INTERNATIONAL JOURNAL OF RESEARCH CULTURE SOCIETY

ISSN: 2456-6683

Monthly Peer-Reviewed, Refereed, Indexed Research Journal

UGC approved Journal with Global Indexing

Impact Factor: 3.449

Publishes original research papers/articles, reviews, mini-reviews, case studies, synopsis, research project and short research communications of all subjects/topics

Special Issue : 8

Second National Conference on

"RECENT ADVANCES IN APPLIED NANO MATERIALS"

(RAANM-2018)

17th February, 2018

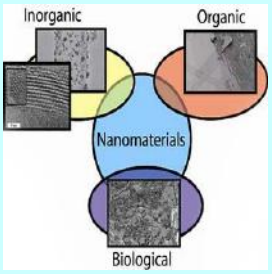

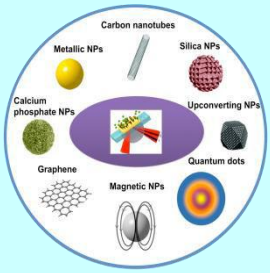

Benefits to publish the Paper in IJRCS

- **IJRCS is an Open-Access, peer reviewed, Indexed, Refereed International Journal.**
- **Author Research Guidelines & Support.**
- **Platform to researchers and scholars of different field.**
- **Reliable and Rapidly growing Publication with nominal publication fees.**
- **Prestigious Editorials from different Institutes of the world.**
- **Communication of authors to get the manuscript status time to time.**
- **Quick and Speedy Review Process.**
- **Full text of all articles in the form of PDF format.**
- **Individual copy of "Certificate of Publication" to all Authors of Paper.**
- **Indexing of paper in all major online journal databases like Google Scholar, Academia, Scribd, Mendeley, and Internet Archive.**
- **Open Access Journal Database for High visibility and promotion of your article with keyword and abstract.**
- **Provides ISSN to Conference / Seminar Proceeding papers.**

RESEARCH CULTURE SOCIETY & PUBLICATION

Email: editorijrcs@gmail.com

Web Email: editor@ijrcs.com

Cont. No: +91 9033767725

WWW.IJRCS.ORG

SECOND NATIONAL CONFERENCE

PROCEEDINGS

RECENT ADVANCES IN APPLIED NANO MATERIALS

16th & 17th February, 2018

The Managing Editor:

Dr. Chirag M. Patel

(Research Culture Society & Publication – IJRCS)

Co- editors:

Dr.V.Nathanial

Asst. Professor,
Dept. of Physice
University College of Science, Sifabad
Osmania University, Hyderabad

Organized by :

Department of Physics,
University College of Science, Saifabad,
Osmania University, Hyderabad - 500 004.
TELANGANA STATE

ABOUT THE CONFERENCE:

The department of Physics, University College of Science, Saifabad, Osmania University, Hyderabad is organizing a Second National Conference on Recent Advances in Applied Nano Materials during 16-17 February -2018. Nanoscience is an emerging interdisciplinary science which integrates Physics, Chemistry, Biology, Materials Engineering, Earth Science and Computer Science. The National conference covers a wide range of topics in Nano and Bio-sciences. The scope of this program is to gain fundamental understanding on Recent Advances in Applied Nano Materials. The need for nano materials in bio sciences for drug delivery systems, magnetic cell separation, cancer treatment, etc.is ever increasing. There is a flourishing interest in nanoscience and its applications in Hi-tech areas such as super capacitors, spintronics and magnetic imaging.

ABOUT THE COLLEGE:

The University College of Science, Saifabad was established in 1951, as a constituent college of Osmania University, which is accredited with A grade. The college campus is centrally located in the city of Hyderabad and provides an excellent academic environment. Highly qualified faculty and advanced equipment available with the college made it one of the best centers for research, training and learning. The college has various Under Graduate and Post Graduate courses in six subjects including Physics. Choice Based Credit System in Post Graduate programmes has been adopted from the current academic year. This college is proud of academic achievements by its teaching faculty.

ABOUT THE DEPARTMENT:

The department of Physics was established as one of the core departments of the college in 1951, offering under Graduate courses. In 1991 its activities were upgraded to include teaching at the Post-Graduate level with introduction of M.Sc. course in Physics with Condensed Matter Physics as specialization. This department is funded by the DST under FIST Programme.

DISCLAIMER

CONFERENCE COMMITTEE:

Chief Patron
Prof. S. Ramachandram, Vice-Chancellor, Osmania University, Hyderabad

Patrons
Prof. CH. Gopal Reddy, Registrar, Osmania University, Hyderabad
Prof. T. Krishna Rao, OSD to Vice Chancellor, OU, Hyderabad
Prof. T. Parthasarathy, Dean, Development & UGC Affairs, Osmania University, Hyderabad
Prof. Ch. Venkata Ramana Devi, Dean, Faculty of Science Osmania University, Hyderabad
Prof. J. Siva Kumar, Head, Department of Physics, Osmania University, Hyderabad

Chairman
Prof. S.K. Mahmood, Principal,University College of Science, Saifabad, Osmania University, Hyderabad

Co-Chairman
Dr J. Laxman Naik, Head, Dept.of Physics, UCS, Saifabad, Osmania University, Hyderabad

Convener & Organizing Secretary
Dr. V. Nathanial, Assistant Professor, Department of Physics,, University College of Science, Saifabad
Osmania University, Hyderabad - 500 004

Co-Convener
Dr. T. Somaiah, Department of Physics, University College of Science, Saifabad
Osmania University, Hyderabad - 500 004

NATIONAL ADVISORY COMMITTEE

Prof. R. Sayanna, VC-KU,Warangal
Prof. K.V. Ramanujachary, USA
Prof. Khaja Althaf Hussain, VC - MGU, Nalgonda
Prof. Subhash Kondawar, RTM university, Nagpur,
Prof.S.Natarajan, IISc, Bangalore
Prof. Ashok K Ganguli, IIT Delhi
Prof. I. Pandu Ranga Reddy, Registrar, Palamur Univ.
Prof. M.S.Ramachandra Rao, IIT Chennai
Dr. A.K.Tyagi, IGCAR, Kalpakkam
Prof. V.R.K. Murthy, IIT, Chennai
Prof. Satish Ogale, Pune
Prof. R. Jayavel,
Prof. H.H. Joshi, SU, Rajkot
Prof. D.G. Kubekar, SU, Rajkot
Dr. K.B. Modi, SU, Rajkot
Prof. K.M. Jadhav, Dr. B A M University
Prof. Parimal H. Trivedi, Gujarat University
Dr. V. Rajendran, KSRCT, Tamilnadu
Dr. Y. Purushotham, CMET,Hyd.
Dr. K. Vijaya Kumar, JNTUH
Dr. R.K.Kotnala, NPL, Delhi
Dr. Sangeeta Kale, Pune
Dr. U.S. Jhoshi, Gujarat University
Dr. G. Aravind, Methodist Engg. College, Hyd

SCIENTIFIC ADVISORY COMMITTEE

Prof. H. Venkateshwarlu, Special Officer, Centenary Celebrations, OU
Prof. C.Vishnuvardhan Reddy, BOS, Physics, OU
Prof. G. Prasad, BOS, Electronics
Prof. Ch. Abraham Linkan,OU
Dr.M.Raghavender Sharma. VP-UCSS, Saifabad
Prof. S. Chandra Lingam, JNTUH
Prof. B. Krishnamarajulu Naidu, OU
Prof. D. Karunasagar, OU
Dr. G. Prabhakar, Dept. of Geology, OU, UCSS
Dr. P. Jalapathy, Dept. of Chemistry, UCSS

UNIVERSITY ADVISORY COMMITTEE

Prof. D. Ravinder
Prof.K.Madhukar
Prof.M.V.Ramana Reddy
Prof.A.Sadananda Chary
Prof. Syed Rahman
Dr.S.Narender Reddy
Dr.K.Uma Sundari
Dr.C.P.Vardhani
Dr.Aparna Dode
Dr.P.Hima Bindhu
Dr.Kaleem Ahmed Jaleeli
Dr.Y.Kalyana Laxmi
Mrs.K.Kirana
Dr. D.Madhuri
Dr.S.Narendra Babu
Dr.N.Narsimulu
Dr.M.Prasad
Dr.N.V.Prasad
Dr.R.Sandhya
Dr. Md. Shareefuddin
Dr.M.Sreenath Reddy
Dr.D.Sreenivasu
Dr.Ch.Srinivas
Dr.M.Srinivas
Dr.G.Upender
Dr.M.Venkata Narayana

LOCAL ORGANISING COMMITTEE

Dr.B.Ravinder Reddy
Dr.K.Sadhana
Dr. B.Ramaiah
Dr.Ch.Venkateshwarlu
Mr.G.Sreeramulu
Mr.P.Naresh
Mrs.P.Neeraja
Dr. M. Purnima
Ms. K. Vara Laxmi
Mr. A.Ranjith
Mrs. Ch. Sumalatha
Mr. T. Rambabu
Ms. Tahreema Nousheen
Mr. B. Naresh
Mr. Y. Sandeep

A brief Report of National Confernce

The two-day National Conference on "Recent Advances in Applied Nano Materials" (NCRAANM 2018) on the occasion of National Science Day celebrations, being organized by Department of Physics, University College of Science, Saifabad was attended by more than 300 participants. The conference was well attended by eminent academicians, faculty members and students from reputed technical and educational institutions from different parts of the country and representatives of governmental bodies and industries.

The conference was inaugurated by **Prof.R.Sayanna, Vive-Chancellor, Kakatiya University, Warangal, Prof. Althaf Hussain, Vice Chancellor, Mahathma Gandhi University, Nalgonda**, Prof. Ramanuja Chary, Rowan University, USA, Prof. J.Shiva Kumar, Head, Dept Of Physics, University College of Science, OU, Hyderabad , Prof.S.K.Mahmood, Principal, University College of Science, Saifabad, and Dr.V.Nathanial, Organising Secretary of this conference were participated. On 16thmorning in the inaugural session, all the dignitaries on the dias were released the Conference Souvenir and share their views on the conference by addressing the gathering. The Chief Guest and Guest of Honors were gave their valuable speeches. Further they spoke about recent developments in Nano Science and Technology. The inauguration was soon followed by the key note address of Prof K.V.Ramanuja Chary, Rowan University, USA. Then after high Tea Break, the first technical session started, chaired by **Dr. J. Laxman Naik** and co-chaired by **Prof Subhash Kondavar** and two invited talks were presented during the session one of them by Dr.T.Theivasanthi, Kalasha Lingam University, Madhurai, Tamilnadu on Applications of Nano aterials.

After the lunch break, the second session started with Prof K.V. Ramanuja Chary, Rowan University, USA delivered a talk on Fossil fuel rapid depletion of non-renewable resources is poising an imminent threat to the energy and supply of fine chemicals that are vital to the global economy. After this talk, few of the oral presentations given by the participants were completed. After this, Prof G. Prasad, Osmania University was giving the invited talk on Properties and Applications of Nano ferro electric materials, followed by cultural sessions.

The second day program was started with oral presentations by the participants followed by the invited talk by the Prof.Subhash kondawar, RTM University, Nagpur delivered an inspirational talk on Enhanced Sensor Functionality of Polyaniline Hybrid Nano fibers for chemical vapors. After lunch break, Prof.D.Ravinder, Department of Physics, Osmania University delivered a lecture on Applications of Nano ferrites followed by Poster session.

During the **valedictory program** conducted in the evening, the chief guest Prof R. Limbadri, Vice Chairman, Telangana State Council of Higher Education, Guest of honour Prof.D.Ravinder, Program presiding by Dr.G.Prabhakar Former Vice Principal, University College of Science, Saifabad, Prof.Theivasanthi, Prof.S.Kondawar were participated. A few participants who gave their feedback on the conference praised the institution for hosting its first ever conference in such an impeccable manner and said that they were overwhelmed by the hospitality offered by the organizers. Best Oral and best Poster Presentations were given in the program.

Conference Photos – RAANM-FEB-2018

The Chief Guest, Prof R. Sayanna Vice Chancellor, Kakatiya University is giving inaugural speech in the Inaugural session of the two-day National Conference on Recent Advances in Applied Nano Materials (NCRAANM-2018).

Releasing of the Conference by the Dignitaries on the dias of Two-day National Conference on Recent Advances in Applied Nano Materials (NCRAANM-2018).

Audience in the Conference while delivering the Lecture.

A Participant from Mangalure University sharing his experience of Two-day National Conference on Recent Advances in Applied Nano Materials (NCRAANM-2018).

Best Oral Presentation received by Mrs Purnima Setty Department of physics O.U. in Two-day National Conference on Recent Advances in Applied Nano Materials (NCRAANM-2018).

Appreciation Memento to Dr B. Ramaiah, Department of Physics, UCS Saifabad a member in organizing committee of Two-day National Conference on Recent Advances in Applied Nano Materials (NCRAANM-2018).

INDEX

Second National Conference on
RECENT ADVANCES IN APPLIED NANO MATERIALS
February 16-17, 2018 at Department of Physics, University College of Science, Saifabad, Osmania University, Hyderabad, Telangana State, India.

Ultrasonic Effect on Rheological Parameters of Human Blood

Mohd Abdul Saleem and Kaleem Ahmed Jaleeli
Biophysics Research Laboratory, Department of Physics Nizam College (Autonomous),
Osmania University, Hyderabad-500001, India.
Email - saleemsaqibi25@gmail.com, kaleemjaleeli@gmail.com

Abstract: *The present paper reports the data on Rheological parameters of normal and ultrasonic irradiated human blood. The blood samples were collected from the healthy donors and were stored in heparin as anticoagulant. The samples were irradiated with ultrasonic interferometer at a frequency of 3MHz.*

In the present investigation, the Rheological parameters (viscosity, volume flow Rate and surface tension) of normal and ultrasonic irradiated human blood are determined employing capillary viscometer technique. Blood samples are irradiated with ultrasonic standing waves at an interval of 30 min upto 2 hours using ultrasonic interferometer. The data reveals variation in the rheological parameters of normal and ultrasonic irradiated blood samples.

Key Words: *Human blood, Ultrasonic interferometer, Ultrasonic Standing waves, Viscometer, Viscosity, Volume flow rate, Surface Tension*

1. INTRODUCTION:

Ultrasound refers to sound with a frequency above that which can be detected by the human ear. It is a cyclic sound pressure with a frequency greater than the upper limit of human hearing. Its interaction with living system leads to a special branch of physics called Ultrasonic Biophysics. Ultrasonic biophysics is the study of mechanisms responsible for how ultrasound and biological materials interact. Ultrasound induced bioeffects focus on issues related to the effect of ultrasound on biological materials.

Rheology is the study of the flow and deformation behavior of materials. It is a specialized part of fluid mechanics and is concerned primarily with Non-Newtonian substances like Blood. Blood is a vital fluid found in human being and other animals. It contains many chemical compounds to perform various functions.

Watchier [1] reported the absorption of ultrasound in water, blood, milk and other biological fluids at 1-10 GHz using damped oscillation.

G Gopala Krishna et al [2] determined the absorption of ultrasound in human blood. The study suggests that the absorption of ultrasound in human blood is due to viscous interaction between the fluid and the suspended cells.

S Chien et al [3] carried out the work on effects of hematocrit and plasma proteins on human blood Rheology at low shear rates. The Viscosity of whole blood, defibrinated blood and Ringer suspension of cells was determined at low shear rates and was observed that the Viscosity of each system rises as the hematocrit is increased.

Somayeh Arain Rad et al [4] studied the mobile phone effects on viscosity of human blood. The study reveals that viscosity increases linearly with the exposure time.

Naresh Kaul [5] using simple approach of viscometer technique studied the rheological behavior of blood and observed that Viscosity is affected by various factors and concluded that it depends on the amount of plasma proteins, the number and volume of corpuscles.

Barbee JH [6] studied the effect of temperature on relative viscosity of human blood. Blood viscosity is a measure of the resistance of blood to flow, which is being deformed by either shear stress or extensional stress.

Lowe GD et al [7] examined the relationship of Blood viscosity and risk of cardiovascular events. The finding suggests that the increased blood viscosity may be one plausible biological mechanism through which increase in haematocrit and fibrinogen may promote ischaemic heart disease and stroke.

Sahar E et al [8] analyzed the effect of electric field on hematological parameters and biophysical blood properties for diagnosing anemia in rats and concluded that Electric field exposures may alter the blood mechanical and rheological properties. EF exposure originated different metabolic and hematological effects, which appeared to be related to the duration of exposure.

G.B. Thurston [9] studied the Viscoelasticity of Human Blood. The study reveals that viscoelastic properties are strongly dependent upon both the hematocrit and the velocity gradient, at low hematocrits the viscosity of blood is not dependent upon shear rate and hence is Newtonian while at higher hematocrits it is Non Newtonian.

2. MATERIALS AND METHODS:

Blood samples of volume 4 ml were collected from the healthy donors and were stored in Heparin as anticoagulant. Each sample was divided into two parts. One was a control sample and the other was test sample. The test sample was irradiated using Ultrasonic interferometer. Rheological parameters such as coefficient of Viscosity, Volume flow rate and Surface tension of normal and ultrasonic irradiated blood samples exposed upto 2 hours at an interval of 30 min were determined using capillary viscometer technique, developed in Biophysics Research Laboratory, Nizam College, Hyderabad.

The viscometer is a simple capillary tube of length of about 30cm and with a radius of 0.05cm. The capillary tube was marked with two preset points A and B the distance between them is 10 cm. A sample of blood of length 2 to 6 cm was sucked by one end of the capillary tube. The flow of blood column in the capillary tube was controlled by closing and opening upper end of the tube. The time required for the sample to travel a fixed distance of 10 cm was recorded and velocity was calculated from the ratio of preset distance (10 cm) and time.

A plot is drawn between 1/L on X- axis and V on Y-axis and it is a straight line with intercept on Y- axis. The intercept of the straight line is measured which gives the maximum velocity (V_o). Viscosity, Volume flow rate and Surface tension were calculated from the intercept of the straight line using the following formulas

1. Coefficient of Viscosity has been calculated using the equation

$$\eta = R^2\rho g / 8V_o$$

η-Coefficient of viscosity (poise);
g – acceleration due to gravity (cm/s^2);
R-Radius of capillary tube (cm);
ρ- Density of blood (gm/cc);
V_o - Y- intercepts.

2. Volume flow rate (Q) has been obtained using the equation
3.

$$Q = V_0 (\pi R^2)$$

V_0 – Maximum Velocity;
R –Radius of Capillary tube (0.05cm)

4. Surface Tension has been calculated using the relation

$$T = (4\eta Tan\alpha) / RCos\theta$$

η – Coefficient of viscosity (poise);
R – Radius of capillary tube (cm);
θ- Angle of contact of sample with capillary wall- 30^0
α- slope of the straight line between L^{-1} on X- axis and velocity on Y- axis

A simple viscometer Technique

3. RESULTS AND DISCUSSIONS:

Table 1 presents the data on coefficient of Viscosity, Volume flow rate and Surface tension of normal and ultrasound irradiated blood using ultrasonic interferometer upto 2hours with an interval of 30 min.

Table1: Data on Coefficient of Viscosity, Volume flow rate and Surface tension with respect to Time (min)

Time(min)	0	30	60	90	120	%change for 2hours
Coefficient of Viscosity(poise)	0.046	0.047	0.050	0.059	0.062	34.7
Volume Flow Rate($cm^3.sec^{-1}$)	0.054	0.053	0.050	0.042	0.040	-25.92
Surface Tension($dyne.cm^{-1}$)	47.21	48.24	51.32	49.54	52.06	10.27

Fig 1: Plot between Coefficient of Viscosity (η) and time

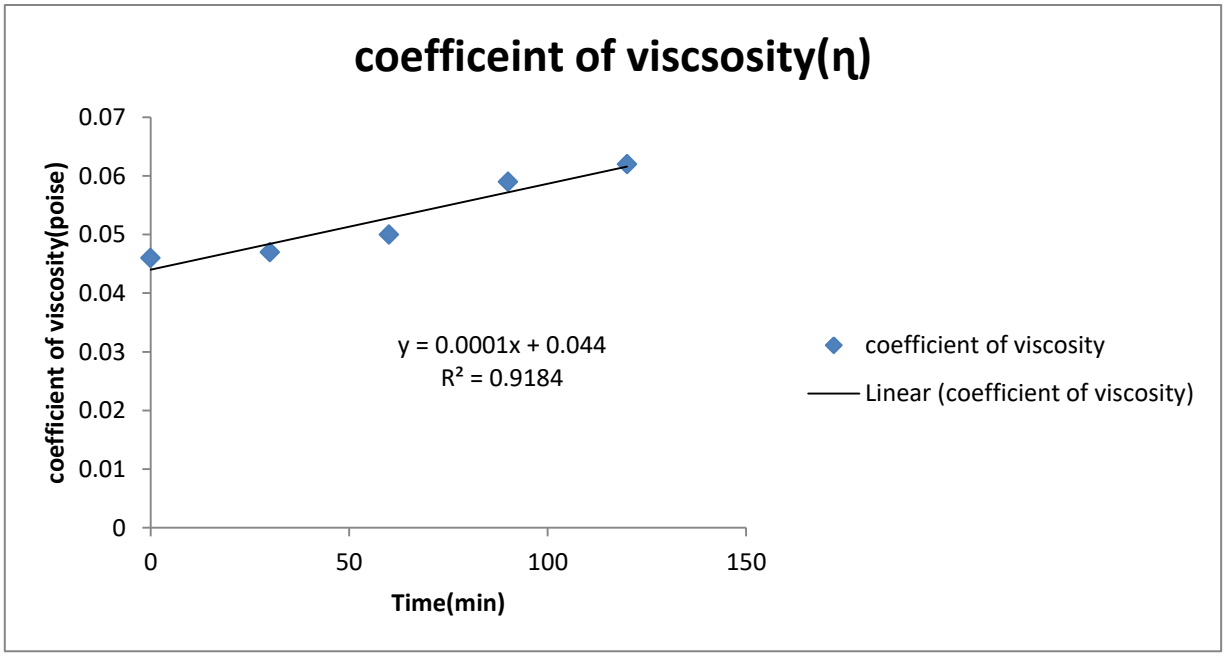

Fig 2 : Plot between Volume Flow Rate (Q) and time

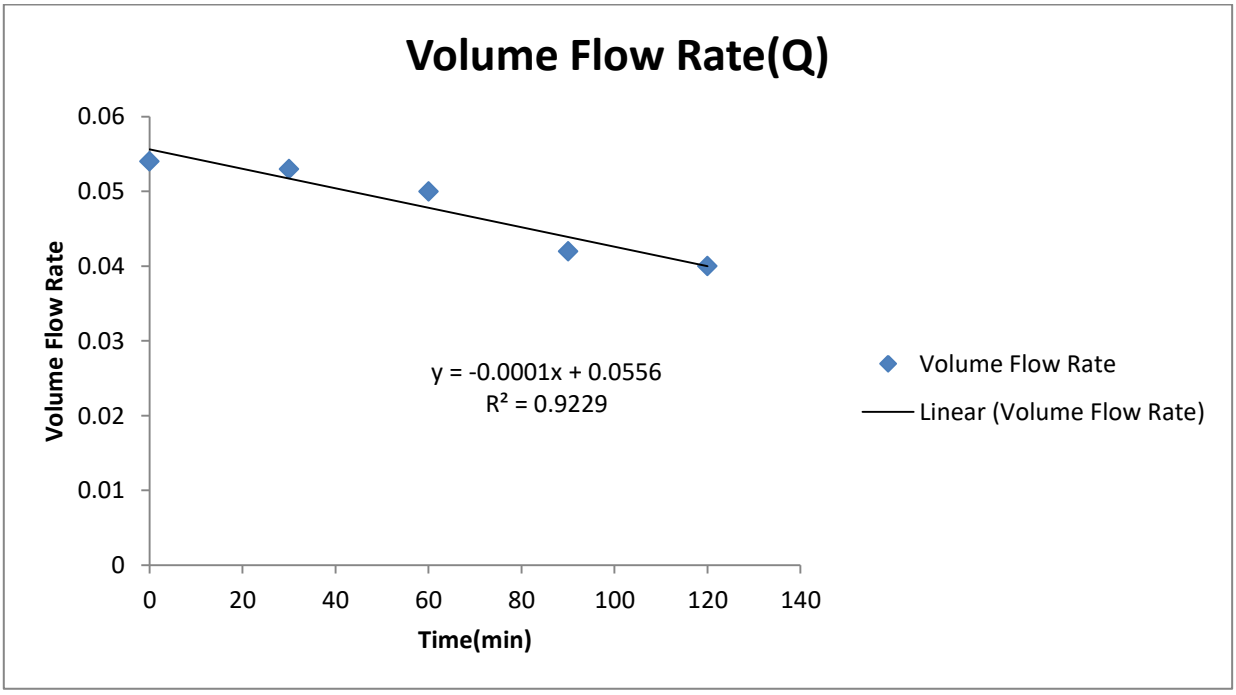

Fig 3 : Plot between Surface Tension(T) and time

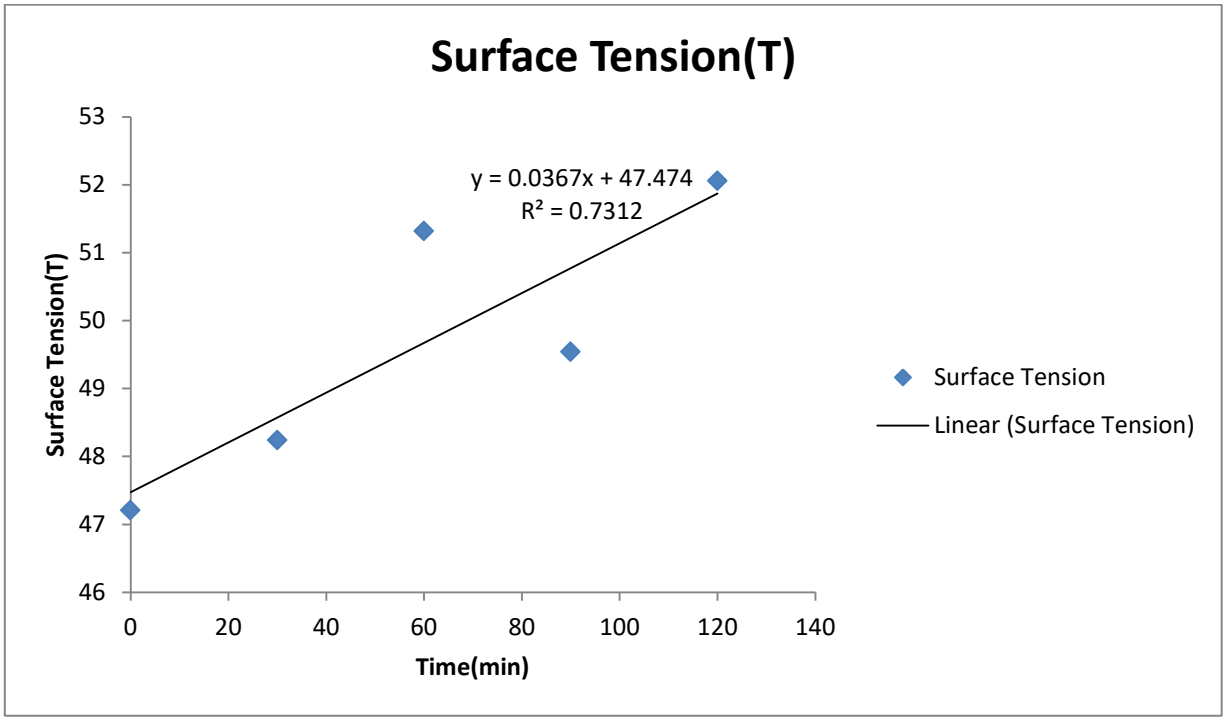

It is evident from Fig 1, 2 & 3 that the Coefficient of Viscosity and Surface tension increases linearly with exposure time whereas the Volume Flow Rate decreases.

The present study demonstrates that the erythrocyte membrane physiology is influenced due to the exposure of ultrasonic standing wave. The increase in Viscosity and decrease in Volume flow rate of ultrasonic irradiated sample may be due to aggregation of erythrocytes. The increase in Surface Tension of ultrasonic irradiated sample may be due to the changes in physical properties of Plasma.

REFERENCES:

1. Watchier , Fundamentals of Radiology Ed. G .Reimer ,Berlin (1939)
2. G. Gopal Krishna, A. Anwar Ali and Adeel Ahmad; Absorption of Ultrasound in Human Blood. Journal de Physique Colloques, (1990), 51 (C2), pp.C2-311-C2-314.
3. Chien S, Usami S, Taylor HM, Lundberg JL and Gregersen MI. Effects of hematocrit and plasma proteins on human blood rheology at low shear rates. J Appl Physiol. (1996) Jan; 21(1):81-87.
4. Somayeh Arian Rad, Kaleem Ahmed Jaleeli and Adeel Ahmad, Influence of EM radiation produced by mobile phone on viscosity of human blood. International journal of science, Environment and Technology, Vol.4, No.6 , (2015) 1469-1475.
5. Naresh Kaul ; A study on Rheological behaviour of blood: An alternate approach. Scholedge International Journal of Multidisciplinary and Allied studies. Vol.2, issue 6(June 2015) ISSN-2394-336X.
6. Barbee JH, The effect of temperature on relative viscosity of human blood, Biorheology, Vol.10 (1993), PP.1-5
7. Lowe GD, Lee AJ, Rumeley A Blood viscosity and risk of cardiovascular events: the endinburgh Artey study . Br J Haematol (1997); 96:168-173.
8. Sahar E, Hassein A & Hassan M MarzogaF .Occupational study of electric field on haematological parameters and biophysical blood properties for diagnosing anemia in rats. Int.J.Adv.Sci.Tech. Res., Vol.2 (2015), PP.143-155.
9. G.B. Thurston. Viscoelasticity of Human Blood. Biophysical Journal,(1972) 12(9):1205-1217.

Second National Conference on
RECENT ADVANCES IN APPLIED NANO MATERIALS
February 16-17, 2018 at Department of Physics, University College of Science, Saifabad, Osmania University, Hyderabad, Telangana State, India.

Review Article

Applications of Nano particles for MRI Cancer Diagnosis and Therapy

Kotte shylaja [1*], ch.Vinuthna [2], Dongamanti Ashok [1]
[1, 2] Green and Medicinal Chemistry Laboratory, Department of Chemistry, Osmania University, Hyderabad-500007, Telangana, India.
[*]Corresponding author: Tel: +91-9398306434, Email address: k.shylajasatyam@yahoo.in

Abstract: *Recent technological advances in nanotechnology, molecular biology, and imaging technology allow the application of nano materials for early and specific cancer detection and therapy. As early detection is a prerequisite for successful treatment, this area of research has been rapidly growing. This paper provides an overview of recent advances in production, functionalization, toxicity reduction, and application of nano particles to cancer diagnosis, treatment, and treatment monitoring. This review focuses on super paramagnetic nano particles used as targeted contrast agents in MRI, but it also describes nano particles applied as contrasts in CT and PET. A very recent development of core/shell nano particles that promises to provide positive contrast in MRI of cancer is provided. The authors concluded that despite unenviable obstacles, the progress in the area will lead to rapidly approaching applications of nanotechnology to medicine enabling patient-specific diagnosis and treatment.*

Key Words: *Review Article, Nano, MRI, Diagnosis and therapy*

1. INTRODUCTION:

Despite many efforts, cancer is among the top three causes of death in modern society [1], demanding improved treatment, that currently includes surgery, chemotherapy, and various types of radiation therapy. Although there is a substantial progress in effective cancer treatment and many forms of cancer are treatable, the therapies are not always effective and often have undesired side-effects [1]. As early diagnosis is essential for successful therapy, both new diagnosis and treatment methods need to be developed. Nanotechnology, combined with other disciplines such as molecular biology and imaging technology, provides unique capabilities and enables innovative diagnosis and therapy. Furthermore, it also allows individualized treatment and treatment monitoring, taking into account patients' variability and thus their response to treatment, ensuring optimal efficacy of the applied therapy. While this technology is currently mostly applied to various types of cancer, it could soon find applications to other diseases.

2. NANO MATERIALS:

In Cancer Diagnosis As early diagnosis is associated with positive outcome, using any type of therapy, there are many incentives for developing technologies that can detect cancer at its earliest stages. In most cases, detection of stage 1 cancers is associated with a higher than 90% 5-year survival rate [2, 3] due to availability of curative treatment. Currently, cancer is detected using various medical tests such as blood, urine, or imaging techniques followed by biopsy. Conventional anatomical imaging techniques typically detect cancers when they are few millimeters (e.g., MRI) or centimetres (e.g., PET) in diameter, at which time they already consist of more than a million cells. Recently proposed molecular imaging aims at rectifying this disadvantage. The development of this new imaging modality became possible due to the recent progress in nanotechnology, molecular and cell biology, and imaging technologies. While molecular imaging applies to various imaging techniques such as Positron Emission Tomography (PET), computed tomography(CT), or ultrasound, of particular interest is magnetic resonance imaging (MRI) that provides the best spatial resolution when compared to other techniques and is noninvasive or at least minimally invasive. Unfortunately, MRI has not been applied to its full potential for the diagnosis of cancer mostly because of its low specificity (false-positive rate of 10% for breast cancer) [4–8]. The lack of MRI specificity can be, however, rectified using cell markers and unique properties of paramagnetic and super paramagnetic nano particles (NP), which can be utilized to be detected with MRI in small quantities. Super(paramagnetic) nano particles when

placed in the magnetic field disturb the field causing faster water proton relaxation, thus enabling detection with MRI. Nano particles, typically smaller than 100 nm, have been applied to medicine [9, 10] due to their unique magnetic properties and sizes, comparable to the largest biological molecules, such as enzymes, receptors, or antibodies, that enable diagnostic, therapy as well as combined therapy and diagnostic (known as theranostics) [11, 12]. Nano particles with potential MRI-related medical applications comprise various materials, such as metals (gold, silver, and cobalt) or metal oxides (Fe3O4, TiO2, and SiO2). A passive or active method can be used to deliver nano particles to the specific site. An example of passive application of iron-based nano particles is liver cancer that lacks an efficient method of early diagnosis. Current techniques, including ultrasound, CT, and MRI, detect liver tumors only when they have grown to about 5 centimeters in diameter. By that time, the cancer is especially aggressive, resisting chemotherapy, and difficult to remove surgically.

3. CORE-SHELL NANO PARTICLES:

The very recent development in nanotechnology enabled the production of complex particles consisting of the core and shell, each made of different atoms, such as FePt@Au [13].In principle, there are two types of core/shell nano particles used in imaging applications: inorganic/organic and inorganic/ [14]. The most common organic shell is silica(SiO2),while inorganic material comprises various metals. Many inorganic core-shell nano particles have been constructed ,including Au@Ag [123], Au@Co [15], Au@Pt [16],Au@TiO2 [17],Au@Fe2O3 [18],Ni@Ag [19], Fe@Ag [20],Ni@Pt [21], Co@Au [22], Fe@Pt [23], LaF3@Eu [24] or β-NaYF4 : Yb3+, and Er3+/β-NaYF4 [25].This development allowed new applications of nano particles, for example, as targeted contrast agents generating positive contrast in MRI. Standard contrast agents shortening$T2$ have been developed, yet efficient targeted contrast agents shortening both $T1$ and $T2$ are still an area of research as the core/shell nano particles could provide improved tumor delineation and hyperintense tumor MRI due to shortening both $T1$ and $T2$, unlike standard iron-based nano particles that shorten mostly T2 [26, 27–31].

4. PRODUCTION OF NANO PARTICLES:

A commonly used method of magnetite synthesis is the coprecipitation of iron salts in aqueous media at room temperature under basic, inert conditions [7, 8]. This relatively straightforward method results in the formation of large amounts of magnetic core clusters of about 36nmcomposedof single particles around 10 nm; however, the generated clusters are very polydisperse. Difficult control of aggregation and particle size distribution are the disadvantages of the coprecipitation method. An alternative to coprecipitation is the thermal decomposition method[32,33,34,35,36,37].In this method, an iron oleate precursor is prepared which isthen decomposed into an iron oxide at high temperature in an organic solvent. The resulting nanoparticles have narrow size distributions but unfortunately are coated with a hydrophobiclayer of oleic acid. In order to obtain stable aqueous dispersions of these particles in water, OA on the surface of the particles is exchanged for another ligand [38] which not only stabilizes the particle in suspension but can also serve to covalently attach other molecules to the surface of the particle [8].The most common synthesis methods of core/shell nanoparticles are chemical vapor deposition, laser-induced assembly ,self-assembly, and colloidal aggregation [39, 40].In the microemulsion method [40], surfactants allow the homogenization of all types of reactants, and the particles formed are capped by the surfactant molecules [41]. Thus, the size of the nanoparticles can be controlled varying a concentration of surfactant .Mandal et al. used glucose .to control shell growth of gold or silver onto Fe3O4 particles upon heating of the mixture of Fe3O4 particles. To coverFe3O4 nano particles with gold or silver, a modified micro emulsion method has been used . This method allows shell thickness of the core-shell particles to be tunable and allowed production of structures of size from18 to30nmwithvarying proportion of Fe3O4 to the noble metal precursor salts [41].Very recently a very promising method of production of3D colloidal spheres containing various nanoparticles was proposed [42]. These multifunctional nanoparticles may be used for different applications such as multimodal imaging, remotely controlled release, targeted drug delivery, or simultaneous diagnosis and therapy [43]. This so-called template assisted fabrication process uses porous calcium (CaCO3) microspheres as a sacrificial template. This method allows easy control of the size of the spheres, flexible tuning of their biochemical and physical properties, and encapsulation of various nanoparticles. The process comprises adsorption of nanoparticles into the porous CaCO3 sphere, encapsulation of polyelectrolytes, and removal of the template by crosslinking. The end product is a colloidal sphere. Using this method, Au nanoparticles and cross-linked poly-L-lysine(PLL) (P-AuNPs) [43], citrate-stabilized gold nanoparticles(C-AuNPs) [44], cetyl trimethylammonium bromide(CTAB) capped gold nanorods (GNRs) [45], and magnetic nanoparticles (γ-Fe2O3) were used to create 3D hybridcolloidal spheres [46]

5. NANOPARTICLES FOR MULTIMODAL IMAGING:

While various imaging techniques, such as MRI, CT, Positron Emission Tomography (PET), and infrared (IR) imaging ,have been used for diagnosis and treatment monitoring, eachone delivers different information on disease and its location. There is no perfect imaging method, as each technique hasits advantages and disadvantages. MRI

provides the best soft tissue contrast but its sensitivity is low; PET is more sensitive than MRI but its spatial resolution is low; CT is fast but soft tissue contrast is low; and finally infrared imaging is fast and very sensitive but the depth of penetration is very low. Nanotechnology allowing production of multimodal contrastagents ("all in one") takes advantages of all these modalities.Of particular interest is the recent development of rare earth up conversion nanophosphors (RE-UCNPs) [47–51]as potential contrast agents because of their optical and biochemical properties, such as sharp emission lines, long life times, and nonphoto blinking. In particular, Yb3+ and Tm3+codoped RE-UCNPs emitting at 800nm have been used for a whole-body small-animal near-infrared imaging .This technique allowed detection of only 50 cells in a whole body mouse imaging . Unfortunately, photo luminescent imaging has a low light penetration depth, but this limitation could be rectified by simultaneous application of MRI or/and CT with a contrast agent suitable for all these techniques. Therefore, Gd3+ was synthesized with RE-UCNPs creating magnetic-luminescent RE-UCNPs contrast agent for bimodal imaging, allowing *T*1-enhanced MRI and up conversion luminescence imaging (UCL) . Furthermore, to enable CT, MRI, and luminescence imaging using the same contrast, super paramagnetic nano particles have been synthesized with RE-UCNPs using a cross linker anchoring method. An example isNaYF4 : Yb,Er@Fe3O4@Au,which could be used for MRI, optical, and CT imaging . NaYF4 : Yb,Tm @Fe*x*O*y* core-shell nanostructure was used for *T*2-weighted MRI and UCL bimodal lymphatic imaging . Of particular interest for multimodal contrasts may be NaLuF4because RE-UCNPs based on the NaLuF4 have high UCL uantum yield and high X-ray absorption co efficient. Another example of multimodal application of nano particles is their simultaneous utilization in high-resolution MRI and high-sensitivity PET for more accurate disease detection. The PET marker (e.g., Cu64) can be added to an MRI marker creating a MRI/PET contrast agent. Furthermore, radionuclide attachment can be achieved via chelating agents.[41-47].

9. CONCLUSIONS:

Recent developments in nano materials, molecular and cellular biology, and imaging technology enabled to enhance our diagnostic and therapeutic capabilities, improving detection limits tissue down to the cell and even to the molecular level. We can now combine atom and bio molecular Journal of Nano materials 7manipulation applying quantum physics, molecular chemistry, biology, and genetics to fabricate minute synthetic structures and to apply them along with high-resolution noninvasive imaging technologies for diagnosis, therapy, and treatment monitoring. Current investigation of nano materials in animal models has offered less invasive diagnosis and induced fewer side-effects due to improved targeting, yet up to date their clinical applications have been limited. The major obstacle seems to be the long time needed for clinical trials and associated costs. Despite that nano materials will likely have a significant impact on patient care in the future.

REFERENCES:

1. Y. Liu, H.Miyoshi, andM. Nakamura, "Nanomedicine for drugdelivery and imaging: a promising avenue for cancer therapy and diagnosis using targeted functional nanoparticles," *International Journal of Cancer*, vol. 120, no. 12, pp. 2527–2537, 2007.
2. R. Weissleder, "Molecular imaging in cancer," *Science*, vol. 312,no. 5777, pp. 1168–1171, 2006.
3. R. Etzioni, N. Urban, S. Ramsey et al., "The case for early detection,"*Nature Reviews Cancer*, vol. 3, no. 4, pp. 243–252, 2003.
4. L.M. Parkes,R.Hodgson, L.T. Lu et al., "Cobalt nanoparticles asa novel magnetic resonance contrast agent—relaxivities at 1.5 and 3 Tesla," *Contrast Media and Molecular Imaging*, vol. 3, no.4, pp. 150–156, 2008.
5. J. D. G. Dur'an, J. L. Arias, V. Gallardo, and A. V. Delgado,"Magnetic colloids as drug vehicles," *Journal of PharmaceuticalSciences*, vol. 97, no. 8, pp. 2948–2983, 2008.
6. K. Gupta and M. Gupta, "Synthesis and surface engineeringof iron oxide nanoparticles for biomedical applications," *Biomaterials*,vol. 26, no. 18, pp. 3995–4021, 2005.
7. S. Lefebure, E. Dubois, V. Cabuil, S. Neveu, and R. Massart,"Monodisperse magnetic nanoparticles: preparation and dispersion in water and oils," *Journal of Materials Research*, vol. 13,no. 10, pp. 2975–2981, 1998.
8. A.-H. Lu, E. L. Salabas, and F. Sch · uth, "Magnetic nanoparticles:synthesis, protection, functionalization, and application," *Angewandte Chemie*, vol. 46, no. 8, pp. 1222–1244, 2007.
9. M. Latorre and C. Rinaldi, "Applications of magnetic nanoparticlesin medicine: magnetic fluid hyperthermia," *Puerto Rico Health Sciences Journal*, vol. 28, no. 3, pp. 227–238, 2009.
10. M. C. Roco, "Nanoscale science and engineering: unifying andtransforming tools," *AIChE Journal*, vol. 50, no. 5, pp. 890–897, 2004.
11. J. D.Meyers, T. Doane, C. Burda, and J. P. Basilion, "Nanoparticles for imaging and treating brain cancer," *Nanomedicine*, vol.8, no. 1, pp. 123–143, 2013.
12. S. S. Kelkar and T.M. Reineke, "Theranostics: combining imagingand therapy," *Bioconjugate Chemistry*, vol. 22, no. 10, pp.1879–1903, 2011.

13. H. B. Na, I. C. Song, and T. Hyeon, "Inorganic nanoparticles forMRI contrast agents," *Advanced Materials*, vol. 21, no. 21, pp.2133–2148, 2009.
14. R. Ghosh Chaudhuri and S. Paria, "Core/shell nanoparticles:classes, properties, synthesis mechanisms, characterization, and applications," *Chemical Reviews*, vol. 112, no. 4, pp. 2373–2433,2012.
15. R. G· ·uzel, Z. ·· Ust· ·unda^g, H. Eks ¸ i et al., "Effect of Au and Au@Agcore-shell nanoparticles on the SERS of bridging organic molecules," *Journal of Colloid and Interface Science*, vol. 351, no.
16. F. Bao, J. F. Li, B. Ren, J. Yao, R.Gu, and Z. Tian, "Synthesis andcharacterization ofAu@Co andAu@Ni core-shell nanoparticles and their applications in surface-enhanced Raman spectroscopy,"*Journal of Physical Chemistry C*, vol. 112, pp. 345–350, 2008.
17. S. Kumar and S. Zou, "Electrooxidation of carbon monoxideand methanol on platinum-overlayer- coated gold nanoparticles: effects of film thickness," *Langmuir*, vol. 23, no. 13, pp.7365–7371, 2007.
18. Y. Chen, B. Zhu, M. Yao, S.Wang, and S. Zhang, "The preparationand characterization of Au@TiO2 nanoparticles and their catalytic activity for CO oxidation," *Catalysis Communications*,vol. 11, no. 12, pp. 1003–1007, 2010.
19. H. Yin, Z.Ma,M. Chi, and S. Dai, "The preparation and characterizationof Au@TiO2 nanoparticles and their catalytic activity for CO oxidation," *Catalysis Today*, vol. 160, pp. 87–95, 2011.
20. L. Xia, X. Hu, X.Kang, H. Zhao,M. Sun, and X. Cihen, "A onestepfacile synthesis of Ag-Ni core-shell nanoparticles in waterin-oil microemulsions," *Colloids and SurfacesA*, vol. 367, no. 1–3,pp. 96–101, 2010.Journal of Nanomaterials 11
21. L. Lu, W. Zhang, D. Wang, X. Xu, J. Miao, and Y. Jiang,"Fe@Ag core-shell nanoparticles with both sensitive plasmonic properties and tunable magnetism," *Materials Letters*, vol. 64,pp. 1732–1734, 2010.
22. G. Wang, H. Wu, D. Wexler, H. Liu, and O. Savadogo, "Ni@Ptcore-shell nanoparticles with enhanced catalytic activity foroxygen reduction reaction," *Journal of Alloys and Compounds*, vol. 503, no. 1, pp. L1–L14, 2010.
23. W. R. Lee, M. Kim, and J. Choi, "Redox-transmetalation processas a generalized synthetic strategy for core-shell magnetic nanoparticles," *Journal of Analytical and Applied Chemistry*, vol.127, pp. 16090–16097, 2005.
24. X.-B. Zhang, J.-M. Yan, S. Han, H. Shioyama, and Q. Xu, "Magnetic ally recyclable Fe@Pt core-shell nanoparticles and their use as electrocatalysts for ammonia borane oxidation: the role of crystallinity of thecore," *Journal of the American Chemical Society*, vol. 131, no. 8, pp. 2778–2779, 2009.
25. J. W. Stouwdam and F. C. J. M. van Veggel, "Improvement inthe luminescence properties and processability of LaF3/Ln and LaPO4/Ln nanoparticles by surface modification," *Langmuir*,vol. 20, no. 26, pp. 11763–11771, 2004.
26. Y.Wang, L. Tu, J.Zhao, Y. Sun,X.Kong, andH.Zhang, "Upconversion luminescence of β-NaYF4: Yb3+, Er3+β-NaYF4 core/
27. shell nanoparticles: excitation power density and surface dependence,"*Journal of Physical ChemistryC*, vol. 113, no. 17, pp. 7164–7169, 2009.
28. N. J. J. Johnson,W.Oakden, G. J. Stanisz, R. ScottProsser, and F.C. J. M. van Veggel, "Size-tunable, ultrasmall NaGdF4 nanoparticles: insights into their T1 MRI contrast enhancement," *Chemistryof Materials*, vol. 23, no. 16, pp. 3714–3722, 2011.
29. G. K. Das, N. J. J. Johnson, J. Cramen et al., "NaDyF4 nanoparticlesas T2 contrast agents for ultrahigh fieldmagnetic resonanceimaging," *Journal of Physical Chemistry Letters*, vol. 3, no. 4, pp.524–529, 2012.
30. C. Dong, A. Korinek, B. Blasiak, B. Tomanek, and F. C. J.M. van Veggel, "Cation exchange: a facile method to make NaYF4:Yb,Tm-NaGdF4 core-shell nanoparticles with a thin,tunable, and uniform shell," *Chemistry of Materials*, vol. 27, no. 4, pp. 1297–1305, 2012.
31. Y. Y. Wang, K. F. Cai, and X. Yao, "Facile synthesis of PbTenanoparticles and thin films in alkaline aqueous solution at roomtemperature," *Journal of SolidStateChemistry*, vol. 182, no.12, pp. 3383–3386, 2009.
32. S.-H. Yoo, L. Liu, and S. Park, "Nanoparticle films as a conductinglayer for anodic aluminum oxide template-assisted nanorod synthesis," *Journal of Colloid and Interface Science*, vol. 339, no.1, pp. 183–186, 2009.
33. M. A. L'opez-Quintela and J. Rivas, "Chemical reactions inmicroemulsions: a powerful method to obtain ultrafine particles," *Journal of Colloid and Interface Science*, vol. 158, no. 2, pp.446–451, 1993.
34. M. Mandal, S. Kundu, S. K. Ghosh et al., "Magnetite nanoparticles with tunable gold or silver shell," *Journal of Colloid and Interface Science*, vol. 286, no. 1, pp. 187–194, 2005.
35. M. Mandal, S. Kundu, T. K. Sau, S. M. Yusuf, and T. Pal, "Synthesisand characterization of super paramagnetic Ni-Pt nanoalloy," *Chemistry of Materials*, vol. 15, no. 19, pp. 3710–3715, 2003.
36. X. Yan, J. Li, and H. Mohwald, "Templating assembly ofmultifunctionalhybrid colloidal spheres," *Advanced Materials*, vol. 24, pp. 2663–2667, 2012.
37. X. Yan, P. Zhu, J. Fei, and J. Li, "Self-assembly of peptideinorganichybrid spheres for adaptive encapsulation of guests," *Advanced Materials*, vol. 22, no. 11, pp. 1283–1287, 2010.

38. S. Link and M. A. El-Sayed, "Size and temperature dependence of the plasmon absorption of colloidal gold nanoparticles," *Journal of Physical Chemistry B*, vol. 103, no. 21, pp. 4212–4217,1999.[146] B. Nikoobakht and M. A. El-Sayed, "Preparation and growth mechanism of gold nanorods (NRs) using seed-mediated growth method," *Chemistry of Materials*, vol. 15,no. 10,pp. 1957–1962, 2003.
39. J. Johnson and F. C. J. M. van Veggel, "Sodium lanthanide fluoridecore-shell nanocrystals: a general perspective on epitaxial shell growth," *Nano Research*, 2013.[148] J. Zhou, Z. Liu, and F. Li, "Upconversion nanophosphors forsmall-animal imaging," *Chemical Society Reviews*, vol. 41, no. 3,pp. 1323–1349, 2012.
40. J. Shen, L.-D. Sun, and C.-H. Yan, "Luminescent rare earthnanomaterials for bioprobe applications," *Dalton Transactions*, no. 42, pp. 5687–5697, 2008.
41. X. Zhu, J. Zhou, M. Chen, M. Shi,W. Feng, and F. Li, "Core-shellFe3O4@NaLuF4: Yb,Er/Tm nanostructure for MRI, CT and upconversion luminescence tri-modality imaging," *Biomaterials*,vol. 33, no. 18, pp. 4618–4627, 2012.
42. F. Wang, Y. Han, C. S. Lim et al., "Simultaneous phase and size control of up conversion nanocrystals through lanthanide doping," *Nature*, vol. 463, no. 7284, pp. 1061–1065, 2010.
43. S.Wu, G. Han, D. J. Milliron et al., "Non-blinking and photo stable up converted luminescence from single lanthanide-doped nanocrystals," *Proceedings of the National Academy of Sciencesof the United States of America*, vol. 106, no. 27, pp. 10917–10921,2009.
44. M. Nyk, R. Kumar, T. Y. Ohulchanskyy, E. J. Bergey, and P. N.Prasad, "High contrast in vitro and in vivo photoluminescence bioimaging using near infrared to near infrared up-conversionin Tm3+ andYb3+ doped fluoride nanophosphors," *Nano Letters*,vol. 8, no. 11, pp. 3834–3838, 2008.
45. Q. Liu, Y. Sun, T. Yang, W. Feng, C. Li, and F. Li, "Sub-10 nmhexagonal lanthanide-doped NaLuF4 upconversion nanocrystals for sensitive bioimaging in vivo," *Journal of the American Chemical Society*, vol. 133, no. 43, pp. 17122–17125, 2011.
46. J.Zhou, Y. Sun,X.Du, L. Xiong, H. Hu, and F. Li, "Dual-modalityin vivo imaging using rare-earth nanocrystals with nearinfrared to near-infrared (NIR-to-NIR) upconversion luminescence and magnetic resonance properties," *Biomaterials*, vol. 31, no. 12, pp. 3287–3295, 2010.
47. J. Shen, L.-D. Sun, Y.-W. Zhang, and C.-H. Yan, "Super paramagnetic and upconversion emitting Fe3O4/NaYF4:Yb,Er heteronanoparticlesvia a crosslinker anchoring strategy," *ChemicalCommunications*, vol. 46, no. 31, pp. 5731–5733, 2010.
48. L. Cheng, K. Yang, Y. Li et al., "Facile preparation of multifunctional up conversion nano probes for multimodal imaging and dual-targeted photothermal therapy," *Angewandte Chemie*, vol., no. 32, pp. 7385–7390, 2011.

Second National Conference on
RECENT ADVANCES IN APPLIED NANO MATERIALS
February 16-17, 2018 at Department of Physics, University College of Science, Saifabad, Osmania University, Hyderabad, Telangana State, India.

Excess Permittivity, Dielectric Relaxation and Membrane Capacitance of Erythrocytes of Human Blood

[1]Mohd Abdul Malik, [2]Dr. Mohd Khalid Mubashir Uz Zafar

[1]Ph.D Research Scholar, Department of Physics, Dravidian University,Kuppam, India
[2]Associate Professor, Maulana Azad National Urdu University, Hyderabad, India
Email –[1]malik.dawoodi@gmail.com, [2]mkmzafar@gmail.com

Abstract:*The paper reports data on excess permittivity, dielectric relaxation time and membrane capacitance of human blood of groups A, B, AB and O using the technique of dielectrophoresis. In this technique, dielectrophoretic collection rate (DCR) of erythrocytes is measured, when they are suspended in glycine - glucose medium and subjected to non- uniform electric field (NUEF), produced by pin - pin electrode configuration or spherical field geometry at the frequency ranging 1 MHz to 10 MHz and applied voltage of 30 Vpp. Knowing DCR and other parameters concerned with electrode chamber and electric field strength, excess permittivity; relaxation time; and membrane capacitance of erythrocytes are calculated.*

Key Words: *Excess Permittivity, Relaxation Time, Membrane Capacitance Dielectrophoresis, Pin - Pin Electrode Configuration, Human Erythrocytes, Glycine-Glucose medium.*

1. INTRODUCTION

Pohl (1951) observed the translational motion of neutral matter caused by polarization effect in a non-uniform electric field and named it as dielectrophoresis. Till then the study of non-uniform field effects (NUFE) on neutral matter was not recognized as a separate phenomenon. It was used as early as 600 B.C. by Thales of miletus to sort out fluff from other matter [1]. The same phenomenon was observed by Gilbert (1600) and he reported the change in shape of water drops when they were brought closer to electrified amber [2].

Winckler (1748) and Priestly (1769) noticed non-uniform field effect on organic matter [3] [4]. However, NUFE for the separation of materials was realized in 19th century when Lowden (1891) reported a technique for the removal of metal particles from used lubricating oils [5]. Dow (1926) used NUFE for the removal of emulsions of water from petroleum [6]. Pohl (1951) used the NUFE for analysing plastic pigments at the Naval Research Laboratory. The phenomenon was rather fully defined and explored by Pohl and his co-workers treating non-biological matter with non-uniform electric fields. These studies paved the way for biological dielectrophoresis [7].

The first application of non-uniform electric field effects on biological matter or in other words biological dielectrophoresis was described by Pohl and Pylmale (1960a) [8] [9]. The separation of living cells from dead was made by Pohl and Hawk (1966) [10]. Mason and Twonsley (1971) made use of DEP technique to separate living cells and organelles of the same species that differ only in diet [11]. Chen and Pohl (1974) described a technique known as single cell dielectrophoresis to find excess permittivity of a single cell [12]. Pohl (1973) characterized single cell organism and organelles by their characteristic yield spectra [13]. Eisenstadt and Schienberg (1972) determined the diffusion coefficient of proteins in solution [14]. Pohl and his collaborators made dielectrophoretic analysis on biological matter at cellular, particulate and molecular levels.

Gopala Krishna et al (1981 & 1983 a) reported the dielectrophoretic collection rate (DCR) of yeast cells *saccharomyces cervisiae* considering cylindrical field geometry [15] [16]. The excess permittivity of individual yeast cells was determined by subjecting them to both dynamic and static single cell dielectrophoresis (Gopala Krishna et al 1983b) [17].

Gopala Krishna et al (1992) reported the influence of thrombosis on dielectrophoretic collection of human erythrocytes. The dielectrophoretic collection rate (DCR) of normal and diseased human erythrocytes was studied by varying the frequency of applied field from 1 MHz to 10 MHz, keeping all other parameters constant. Characteristic frequencies were measured from dielectrophoretic spectra [18].

Dielectrophoreticcharacterization of normal and diseased blood was reported by Gopala Krishna et al (1994) [19]. The dielectrophoreticbehavior of human red blood cells (HRBC) from patients suffering from diabetes mellitus and jaundice was observed. The dielectrophoretic collection rate (DCR) of HRBC was studied in the β -dispersion region keeping all other parameters constant by applying spherical field geometry. Unique frequency dependent spectra, characteristic of HRBC physiology have been obtained for normal and diseased cells examined under identical conditions.

Gopala Krishna et al (1995) studied human red blood cells (HRBC) of normal and leukemic blood by using the principle of dielectrophoresis. The threshold voltage for the dielectrophoretic collection of the normal and diseased HRBC collected from healthy persons and patients suffering from leukemia were reported, in the β- dispersion region under the action of non-uniform electric field set by spherical field geometry. Significant variation was observed in the threshold voltage for collection of normal and cancer samples at the same frequencies under identical conditions of the experimentation [20].

Malik Dawoodi and Zafar studied excess permittivity of human erythrocytes of groups (A, B, AB and O by measuring their velocity when subjected to NUEF [21].

2. MATERIALS AND METHODS

2.1 Dielectrophoretic Set up

The experimental arrangement for biological cell dielectrophoretic study is shown in Fig.1. A signal generator of frequency ranging from 1 MHz to 10 MHz and voltage of range 30 volt is connected to electrode chamber so as to produce non-uniform AC field between the rounded tips of the electrodes of the chamber. The frequency of the AC signal is measured directly from signal generator. An Oscilloscope to monitor the AC signal and to measure the voltage of the signal accurately is connected to the electrodes of the electrophoretic chamber. A CCTV system consists of video camera and video monitor is attached to a trinocular microscope (Labo Triumph 90066) to observe the collection of erythrocytes or formation of pearl chains at the electrodes. The motion of erythrocytes has to be observed under the microscope continuously for a long duration of time. The CCTV system provides the facility of microscopic observation and measurements with ease.

2. 2. Construction of Electrode Chamber

In the present investigation, erythrocytes were subjected to non-uniform electric field produced by spherical field geometry. A pair of platinum wires of diameter 500 µm were placed 1 mm above the surface of a glass slide in such a way that these axes lie along the same straight line with the rounded tips facing each other and were separated by distance of 750 µm. The wires were placed through a non-conducting ring of 1.0 cm internal diameter. When this ring is cemented on a glass slide it forms pin-pin electrode chamber which canproduce non-uniform electric field when A.C. voltage is applied between the electrodes. The chamber can hold about 0.3 ml of cell suspension (Fig. 2.).

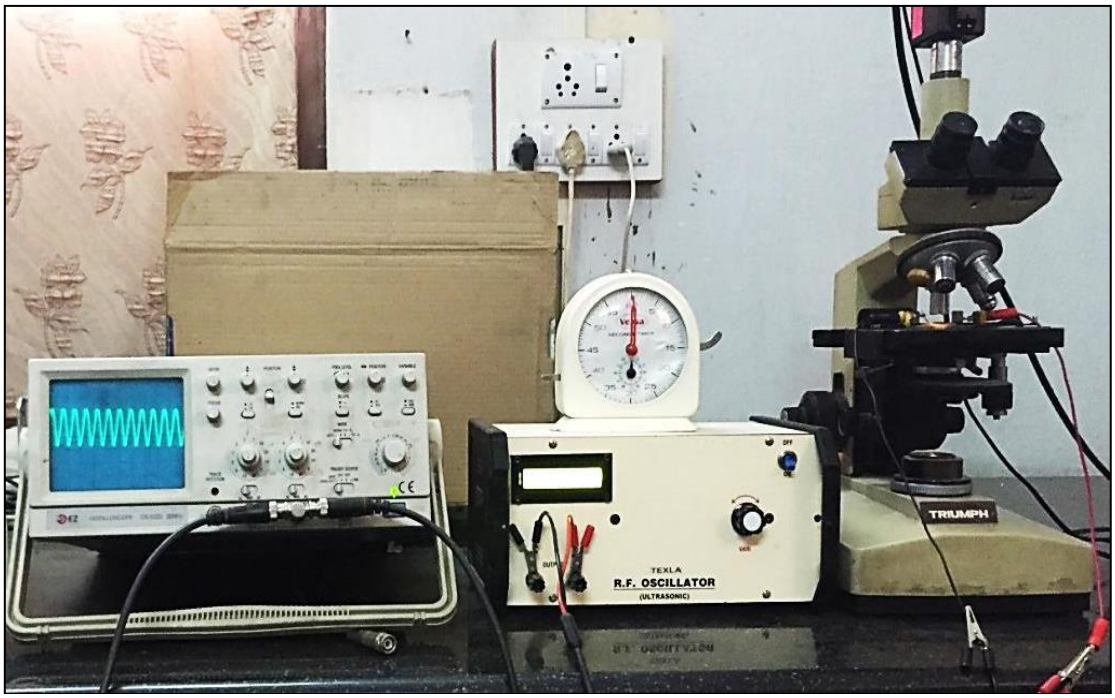

Fig. 1. Experimental setup of Dielecrophoresis

Fig. 2.Electrode chamber of dielectrophoresis

2. 2. Experimental Procedure

The erythrocyte suspension of 0.3 ml filled in the electrode chamber was subjected to NUEF produced by pin-pin electrode configuration.Dielectrophoresis has been carried out in the frequency range 1-10 MHz to realize the formation of the pearl chains.The average length of the pearl chain formed of cells in one minute termed as dielectrophoretic collection rate (DCR).The DCR, studied as a function of frequency gives dielectrophoretic spectrum.

The electrode chamber was mounted on a conventional microscope and the observations were made with an eyepiece micrometer marked into 100 div/cm, each division corresponds to 10 µm at 10x of the objective. The AC signals were drawn from R.F. oscillator. The cell suspension of fixed volume (0.2 ml) was dropped into the chamber and the electrical signals were applied between the platinum electrode or 1 minute for a fixed rms voltage of 30V. The cells were collected at round tips of the electrodes along the field lines in the form of pearl chains due to mutual dielectrophoresis (Fig.3.).

(a). Without electric field

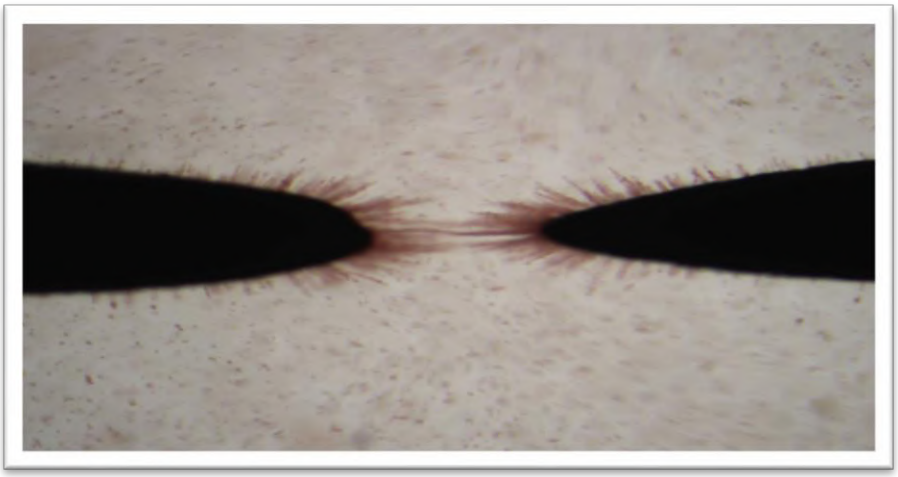

(b). With electric field

Fig. 3.Dielectrophoretic Collection of Erythrocytes

The average chain length was measured for 1 min which gives yield or dielectrophoretic collection rate (DCR). Keeping electric conductivity of cell suspension cell concentration, applied voltage and elapsed time to be constant, DCR of erythrocytes was measured as a function of frequency in the range 1 – 10 MHz both for normal and exposed human erythrocytes. The parameter *Excess Permittivity (K_e)*, which involves permittivity of erythrocytes as well as suspending medium, was calculated using the relation,

$$K_e = \frac{9r_1^2(r_2-r_1)^2 d\omega B Y^2}{64\pi^2 a^6 C^2 \emptyset^2 r_2^2 t}$$

Where,

r_1: radius of the electrode = 250 µm

r_2: Distance between the electrodes = 750 µm

d: Density of blood = 1045 kg.m3

ω: Angular frequency (MHz)

B: Micropolar parameter

a: Radius of the erythrocytes = 3.5 µm

ϕ: Applied voltage = 30 volt

t: Elapsed time = 60 sec

Y: Yield or DCR (µm. Sec-1)

C: Concentration of the cellular suspension = 8.48 x 109 cells / m3

The micropolar parameter (B) is frequency dependent. It is measured by drawing the plot between Relaxtion time (τ) is the reciprocal of characteristic angular frequency (ω) of DCR spectrum, ie.,

$$\tau = \frac{1}{2\pi\upsilon}$$

whereυ is the frequency of applied voltage.

Membrane capacitance (Cm) is calculated using the relation,

$$C_m = \frac{\tau}{\rho_i R}$$

Where,

τ = Relaxation time; ρ_i = internal resistivity of the cell = 100 ohm.cm; R = radius of erythrocyte = 3.5 µm

3. RESULTS AND DISCUSSION

Fig. 1. shows both DCR and Ke spectra i.e., the plot between Ke or DCR of erythrocytes on Y-axis and frequency of applied a.c. field on X-axis for human blood of groups A, B, AB and O. Two peaks are observed in Ke spectrum. It is interesting to note from the figure the peaks at the frequencies 5 and 8MHz for A, B and AB groups; and 4 and 8 MHz for O group. The peaks in the DCR and Ke spectra may perhaps reveal Maxwell-Wagner or interfacial polarisation of erythrocyte membrane.

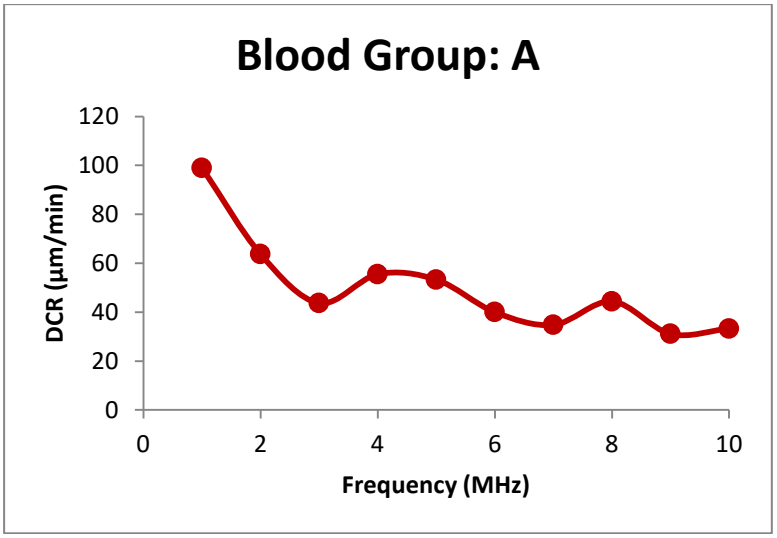

Fig. 1.1(a). DCR spectrum of erythrocytes of A group blood

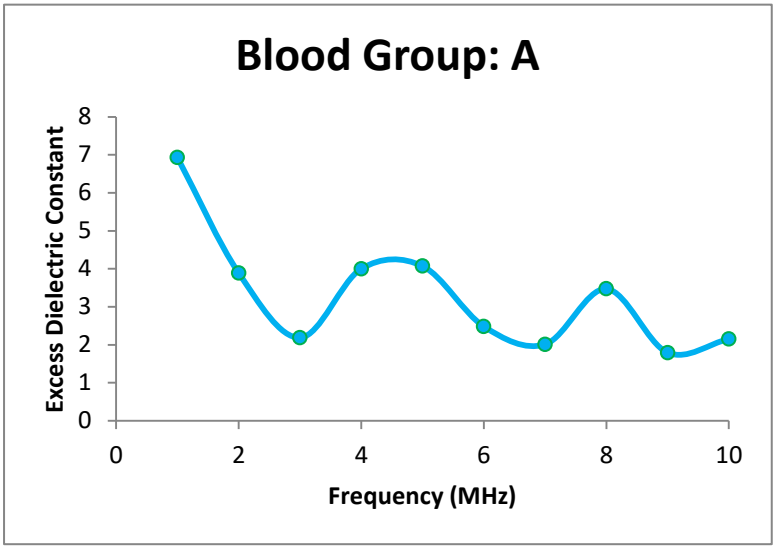

Fig. 1.1(b).Ke spectrum of erythrocytes of A group blood

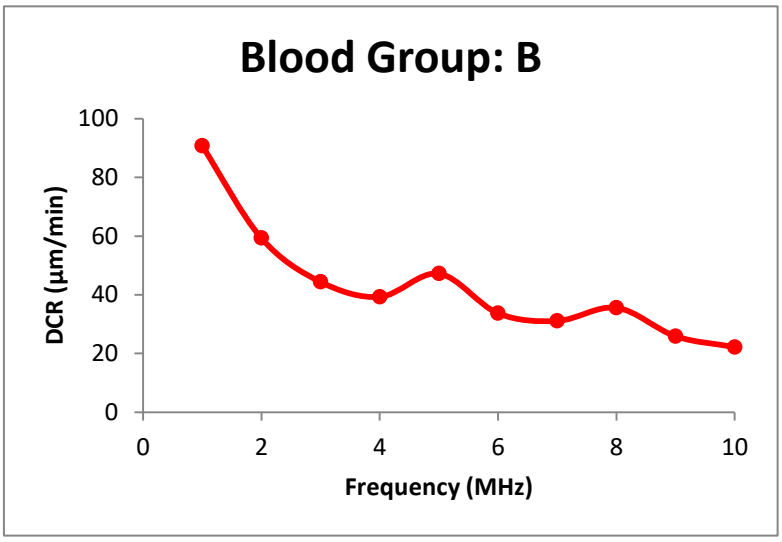

Fig. 1.2(a). DCR spectrum of erythrocytes of B group blood

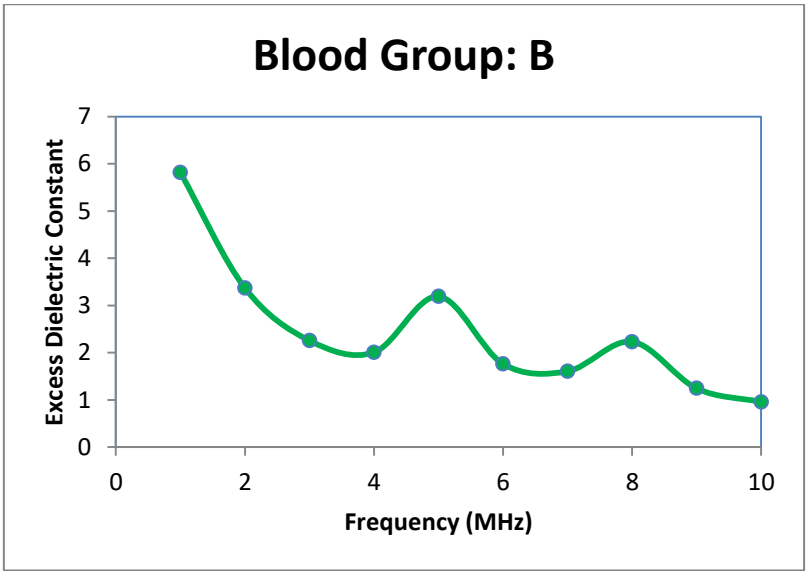

Fig. 1.2(b).Ke spectrum of erythrocytes of B group blood

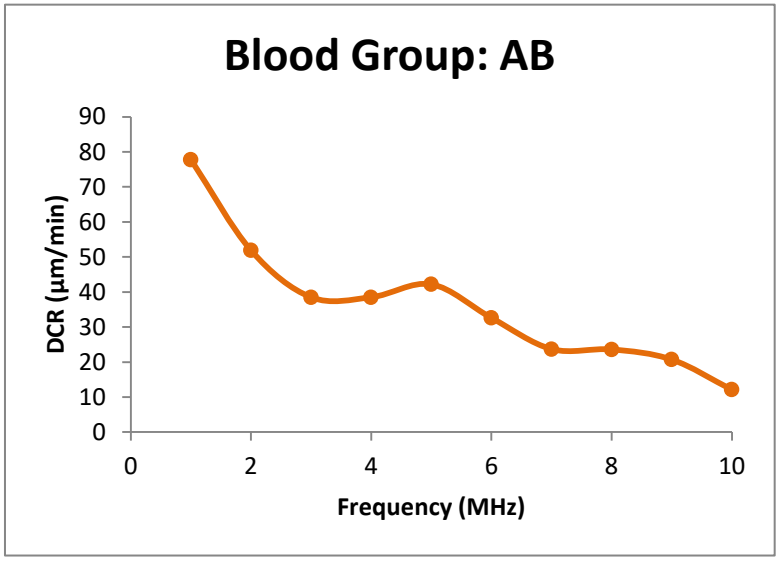

Fig. 1.3(a). DCR spectrum of erythrocytes of AB group blood

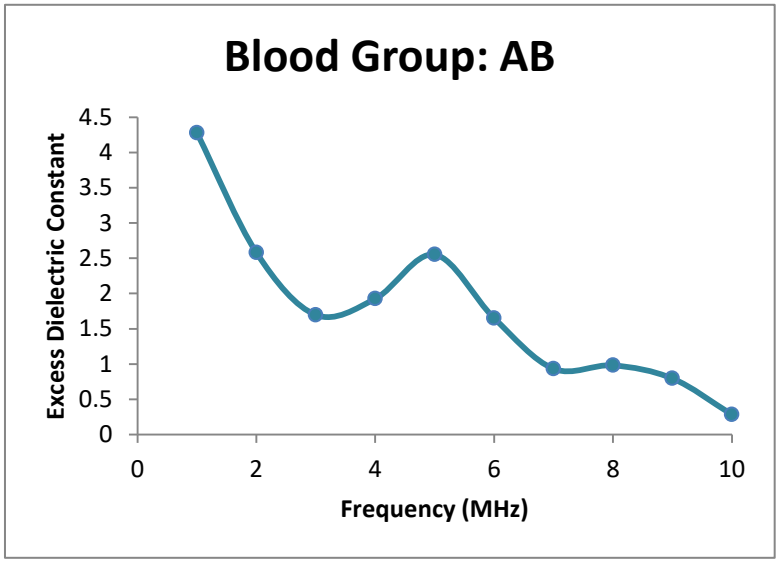

Fig. 1.3(b).Ke spectrum of erythrocytes of AB group blood

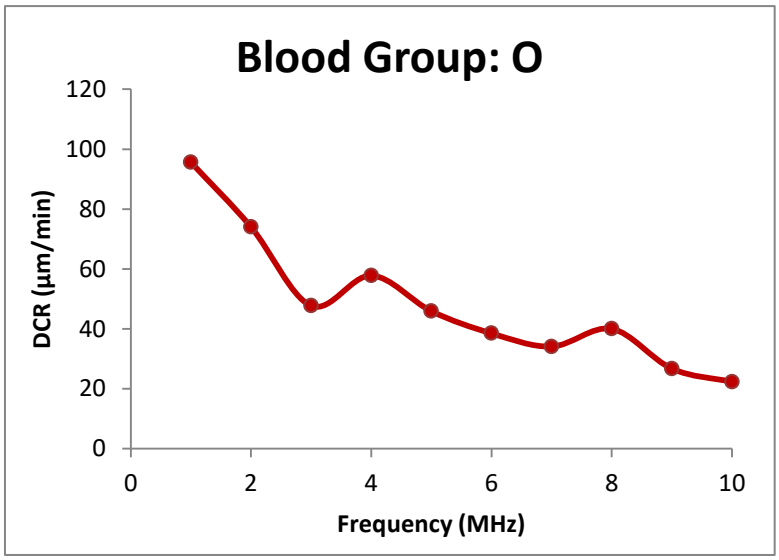

Fig. 1.4(a). DCR spectrum of erythrocytes of O group blood

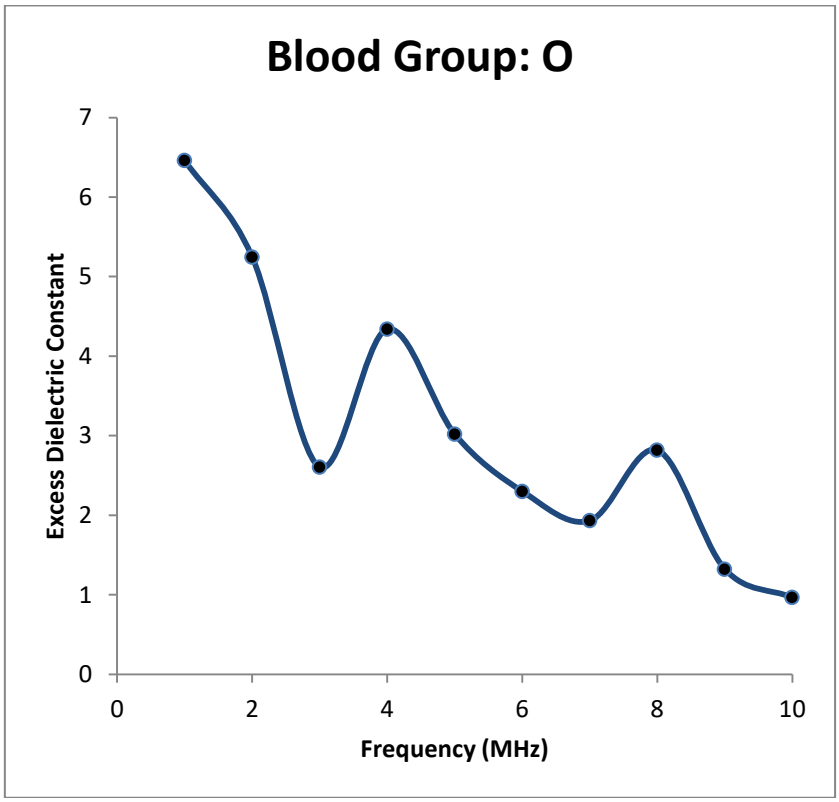

Fig. 1.4(b).Ke spectrum of erythrocytes of O group blood

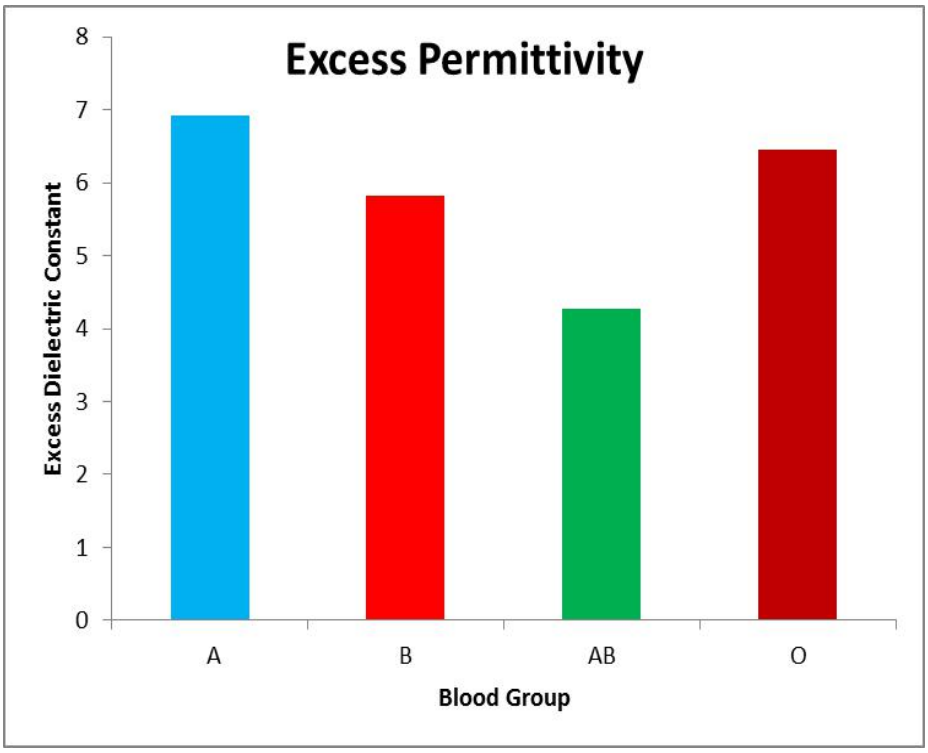

Fig.2. A comparison Ke of erythrocytes of blood groups A, B, AB and O

Fig.2. presents a comparison $K_e$of erythrocytes of blood groups A, B, AB and O. It is observed that

$$K_e(A) > K_e(O) > K_e(AB) > K_e(B)$$

Fig. 3.Gives a comparison of dielectric relaxation time of erythrocytes of blood groups A, B, AB and O. Two dielectrophoretic relaxation time can be seen.

$$\tau1\ (O) > \tau1\ (A) = \tau1\ (B) = \tau1(AB)$$
$$\tau2\ (A) = \tau2\ (B) = \tau2\ (AB) = \tau2(O)$$

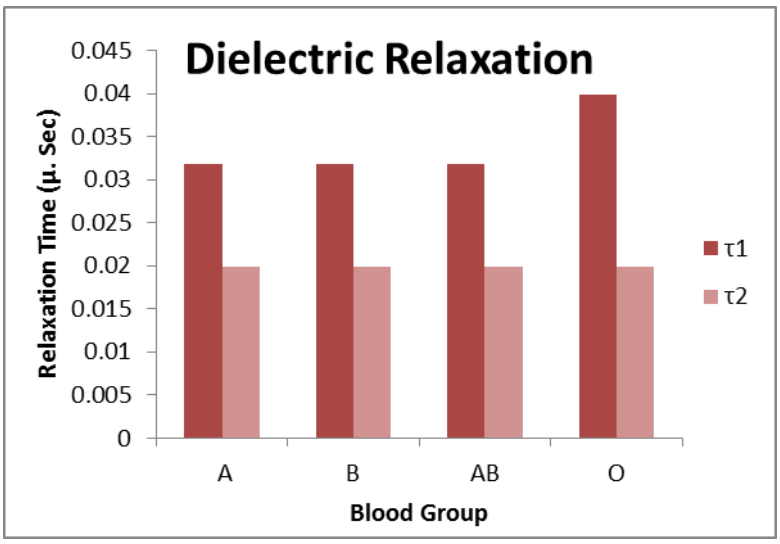

Fig. 3.A comparison of dielectric relaxation time of erythrocytes of blood groups A, B, AB and O.

Fig. 4.Presents a comparison on membrane capacitance of erythrocytes of blood groups A, B, AB and O.

Cm1 (O) > Cm1 (A) = Cm1 (B) = Cm1 (AB)

Cm2 (A) = Cm2 (B) = Cm2 (AB) = Cm2 (O)

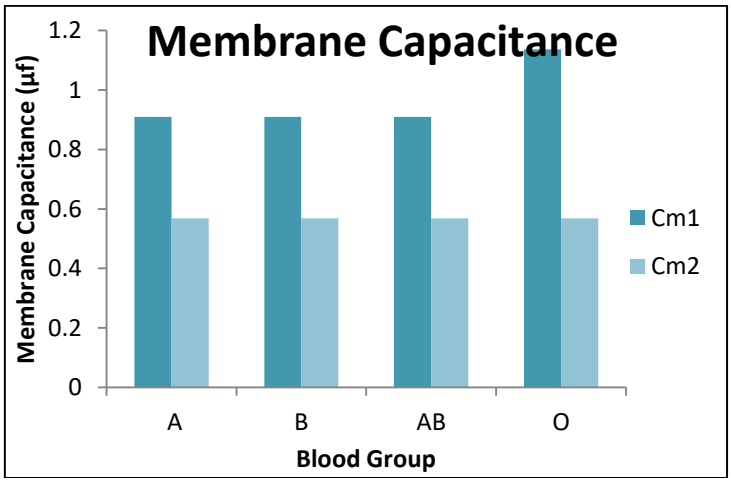

Fig. 4. A comparison of membrane capacitance of erythrocytes of blood groups A, B, AB and O.

Blood type A is formed through the addition of the A antigen, which has *N-acetylgalactosamine* (GalNAc) glycosidically bonded to the O antigen.

Similarly for blood type B, the B antigen has an additional *galactose* forming a glycosidic bond to the O antigen. In both the A and B blood types, the new antigen forms an α-1,3 linkage to the outermost galactose component of the O antigen through the help of glycosyltransferases. GalNActransferase adds the extra N-acetylgalactosamine for the A antigen while Galtransferase adds the extra galactose for the B antigen.

Excess permittivity of blood of group A is more, less in groups B and AB than that of O group blood. It shows that in case of A group blood, GalNAc attached to O antigen icreasesK_e, while Galactose attached to O antigen (ie antigen B) decreases K_e. Regarding relaxation time (and membrane capacitance, one can say that both Antigen A and B decrease τ and C_m. Finally, the study conclude that the blood antigen influence the dielectric properties of erythrocytes of human blood.

REFERENCES

1. Pohl H.A.(1951) J. Appl. Phys. 22. 869

2. Gilbert 1600 D C Magnite, Book-II, Chapter II pater short, London on Readex Micro Print, Lnadmarks of Science, New Yourk and London (1967)
3. Winckler F.H. (1748)Essaisurla nature on Readex microprint landmarks of science, New York and London.
4. Priestly (1769) The history present state of electricity with experiments, 2nd Ed., -London, on Readex microprint, landmarks of Science, N.Y and London. (1974)
5. Lowden. J.J (1891) (To Henry G. Thomas) U.S. Pate. 465822
6. Dow D.B (1926) U.S.Beaureau of Mines Bulletin No. 250.
7. Pohl H.A. (1958) J. App. Phys. 22, 869
8. Pohl H.A. and Plymale G.E. (1960a) J. Electrochem. Soc., 197, 368
9. Pohl H.A and Plymale C.E (1960b) J. Electrochem. Soc, 107, 390
10. Pohl H.A., Hawk I. (1966) Science, 152, 647
11. Mason B.D and Townsley P.M (1971) Can. J. Microbiol., 17, 879
12. Chen C.S and Pohl.H, (1974) Ann. N.Y. Acad. Sci, 238, 176
13. Eisenstadt H.M and Schienberg J.H. (1972) Science, 176, 1325
14. GopalaKrishana G, Anwar Ali A.K.W and Adeel Ahmad (1981) National Seminar on Acoustics and Ultrasonics, Dept. of Physics, University of Cochin, 37
15. Gopala Krishna. G. Anwar Ali A.K.W and Adeel Ahmad (1983a) Ind. J. Exp. Bio, 21, 283.
16. Gopala Krishna G, Adeel Ahmad and Anwer Ali AKW (1983b) Curr. Sci, 52(23), 1085.
17. Gopala Krishna G. RajiniKumari K and Adeel Ahmad (1992) Current science, 62(16), 684
18. Gopala Krishna G., Jaleeli K.A, Adeel Ahmad and Rama Krishna P (1994) Indian J. Comp Animal Physiol, 12,23
19. Gopala Krishna G., Jaleeli K.A and Adeel Ahmad (1995) National Symposium on Cellular and Molecular Biophysics, Hyderabad.
20. Mohd. Abdul. Malik, M. K. M. Zafar, Int. J.Innov.Res. Sci.Engg. Tech., Vol. 6, Issue 5, May 2017, pp. 9318-9323

Second National Conference on
RECENT ADVANCES IN APPLIED NANO MATERIALS
February 16-17, 2018 at Department of Physics, University College of Science, Saifabad, Osmania University, Hyderabad, Telangana State, India.

SEM Analysis of Human Hair

[1] Mohammed Abdul Mujeeb and [2] Mohd Khalid Mubashir Uz Zafar
[1]Department of Physics, Dravidian University, Kuppam A.P-517425, India
[2]Associate Professor, Maulana Azad National Urdu University, Hyderabad-500032, India
E- mail- abdulmujeeb250977@gmail.com, [2]mkmzafar@gmail.com

Abstract: *The paper presents scanning electron micrographs of human hair. The hair samples were selected from males and females of different age ranging from new born to 75 years in order to examine the influence of age and sex on morphological structure of hair. The diameter and scale index are measured and noted a significant variations with respect to age and sex. Diameter tends to peak at about age 50 for male and 45 for female. It is interesting to note that no of scales per unit length more or less remains the same whatever may be age or sex. Further it can be noted that there appears no deposition of inorganic material in the organic matrix of human hair fiber. That is the reason human hair is highly elastic in nature.*

Key words: *Hair, SEM, keratin, cortex, cuticle, medulla, Morphological Parameters*

1. INTRODUCTION

Human hair morphology has been extensively discussed in recent decades due to the interests of those engaged in the cosmetic industry, dermatological and forensic sciences [1]. With advances in microscopic techniques, it is possible to obtain additional physical and chemical information about morphological hair structures, using atomic mass spectroscopy or image mass spectroscopy [2]. Despite more difficult sample preparation methods, the classical electron microscopy techniques (TEM and SEM) are still very much used to study human hair morphology [3]. SEM has been substituted by AFM for analyzing hair. Human hair is composed mainly of keratin which is α- helical protein with high cystine content [4]. Morphological human hair is divided into 4 layers cortex, cuticle, intercellular material and medulla. The cuticle has an amorphous character. Each cuticle is formed by 4 subunits that have distinct chemical composition and reactivity. Their reticulated structure depends on the cystine content. The cellular membrane complex (CMC), which is found between cuticles, is a hydrophilic material rich in polar amino acids and lysine [5]. CMC and endocuticle are believed to be the main diffusion pathways in to human hair [6]. The cortex is formed by elongated cortical cells surrounded by the CMC. The cortical cell has an inner fibrillar structure embedded in sulphur rich matrix [7].The medulla is localized in the centre of the fiber and could be absent, fragmented or continuous [8]. It has high lipid content compared to the rest of the fiber [8] and it is poor in cystine but rich in citrulline [10]. Thus disulphide bonds are replaced by peptide bonds that maintain cohesion in the structure which is the reason for the insolubility of medulla proteins. Morphologically it has been reported that medulla has a porous structure formed by spongy keratin [11]. Since human hair is a biological material that has a crystalline portion and amorphous structures with different degree of reticulation due to its sulphur content. Scoble and Litman (1978) found a method of washing of human hair and nail samples to examine by neutron activation and gamma - ray analysis [12]. The amounts of Na, K, Br, Au, Zn and La that are removed by successive washings determine the optimum number of washing for removing these trace elements as surface contaminants. Acidic and basic hair-nail hard keratins their colocalization in upper cortical and cuticle cells of the human hair follicle and their relationship to soft keratins was studied by Lynch et al (1986). Marshall (1983) studied the Low-sulfur and high-sulfur proteins from human hair and nail were characterized by 2-dimensional polyacryl amide gel electrophoresis [13]. Mercury in hair and nails was determined by Suzuki et al (1989) with speciation of chemical forms of mercury [14]. Total mercury (THg) and inorganic mercury (I Hg) were determined. No sex-related differences were found in mercury levels in hair and nails. Tazawa - Toshio et al (1997) investigated the fetal development of the nail epithelium, the expression of hard keratin and epidermal keratin in human fetal skin at various stages of gestation by immunofluorescence microscopy using anti-hair keratin and anti-epidermal keratin 10 monoclonal antibodies [15]. Marchisio et al (2001) studied the morphological expression of human hair and nail invasion in vitro by 31 isolates

of nine Scopulariopsis species was studied by light microscopy on whole material and on semi-thin sections, as well as by transmission electron microscopy.

2. MATERIALS AND METHODS

The human hairs of different age of male and female totaling 13 samples were collected from donors. The hair samples were washed three times, and dried at room temperature till further analysis. SEM images of hair samples were recorded directly using scanning electron microscope of make (CarnZeiss merlin compact) and model 30Kv-OXFORD EDAX. The SEM images for hair samples of 6 males and 7 females of age ranging from new born to 75 years, at the magnification 10K X are presented in Fig 3-15.

3. RESULTS AND DISCUSSION

Table 1 presents average values of diameter of 6 hair samples of males, measured at their two positions. Also, age of male subjects ranging from 0.5 – 60 years is shown in the table. Similar data is presented in Table 2 for hair samples of 7 females whose age ranges between 0.25 and 75 years.

Table 1: Data on Diameter of male human hair of different age

Age (Year)	Diameter (µm)		
	Position 1	Position 2	Mean
0.5	13.39	13.80	13.50
5	53.60	54.25	53.90
25	83.19	83.32	83.25
30	93.54	90.68	92.11
50	97.93	97.62	97.77
60	66.46	68.02	67.24

Table 2: Data on Diameter of female human hair of different age

Age (Year)	Diameter (µm)		
	Position 1	Position 2	Mean
0.25	34.55	34.18	34.37
10	67.32	66.31	66.82
20	80.41	75.91	78.16
37	89.18	88.15	88.67
45	98.45	95.25	96.85
55	86.98	94.34	90.16
75	56.06	55.32	55.69

Figs 1 and 2 depict plots between age in years on X - axis and diameter of hair in micro meter on Y-axis. The graphs are curves. Their equations along with R^2 are also presented in the Figs. 1 and 2. It is evident from the figures that diameter of hair tends to peak at about age 50 for males and age 45 for females. It is interesting to note that the diameter human hair more or less the same irrespective of sex.

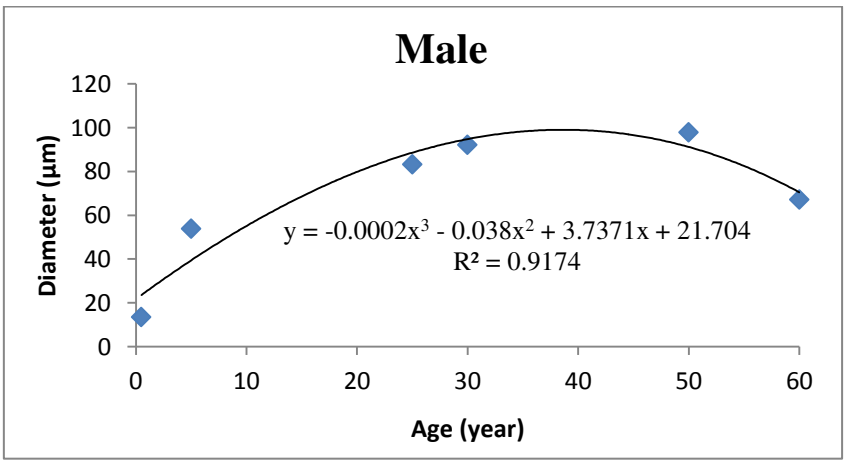

Fig.1. A plot between diameter of hair and age of males

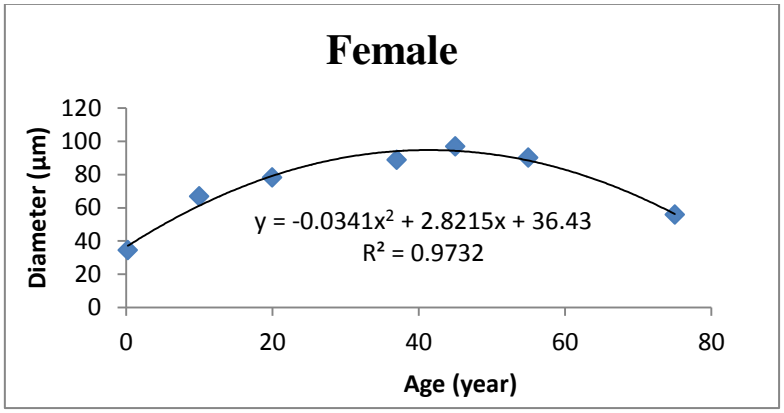

Fig. 2. A plot between diameter of hair and age of females

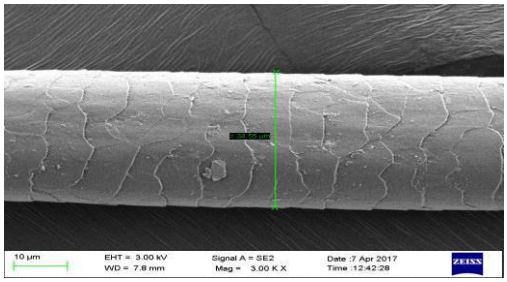

Fig.3. SEM Micrograph of Female human hair of age 3 months of Magnification 10K X

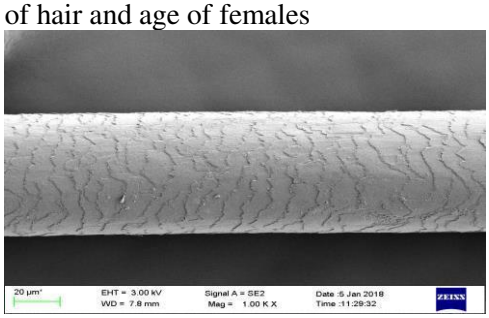

Fig.4. SEM Micrograph of Female human hair of age 10 years at Magnification 10KX

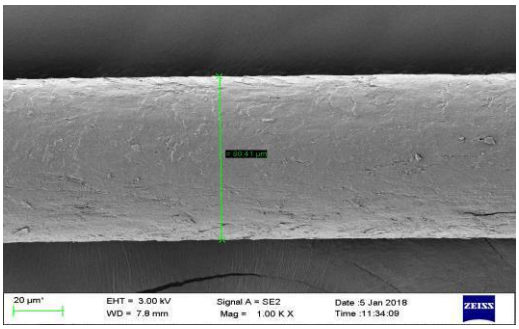

Fig.5. SEM Micrograph of female human hair of age 20 years at Magnification10KX

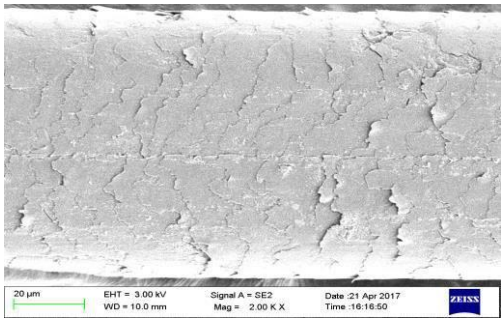

Fig.6.SEM Micrograph of female human hair of age 37 years at Magnification 10 KX

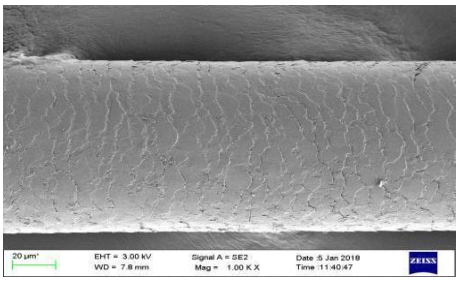

Fig.7. SEM Micrograph of female human hair of 45 years of Magnification 10KX

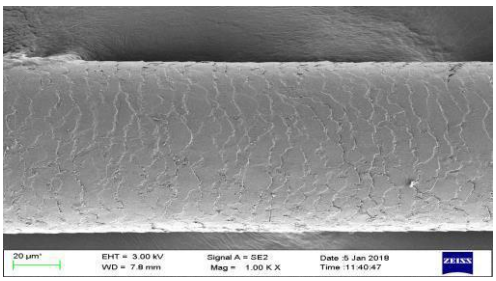

Fig.8. SEM Micrographs of female human hair of age 55 years of Magnification 10KX

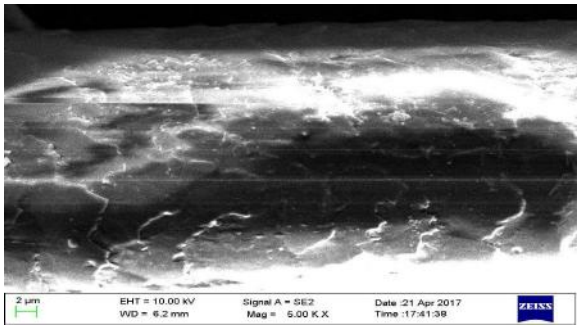

Fig.9. SEM Micrograph of female human Hair of age 75 years of Magnification 10KX

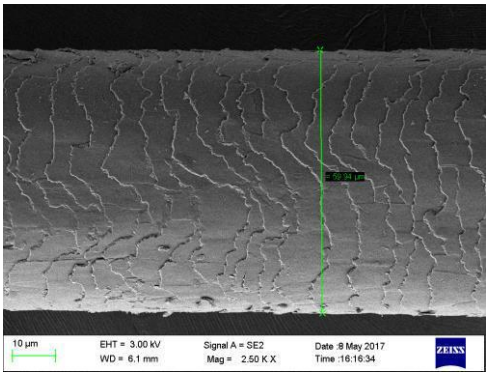

Fig.10. SEM Micrograph of male human hair of age 5 years of Magnification 10KX

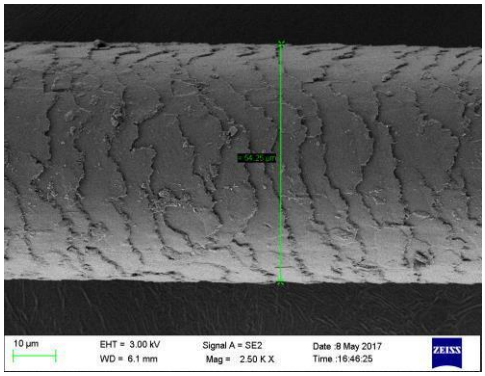

Fig.11. SEM Micrograph of male human hair of age 25 years of Magnification 10KX

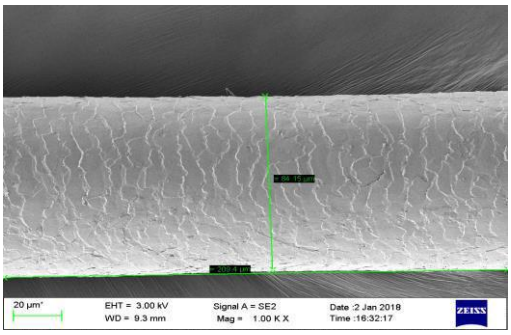

Fig.12. SEM Micrograph of male human hair of age 30 years of Magnification 10KX

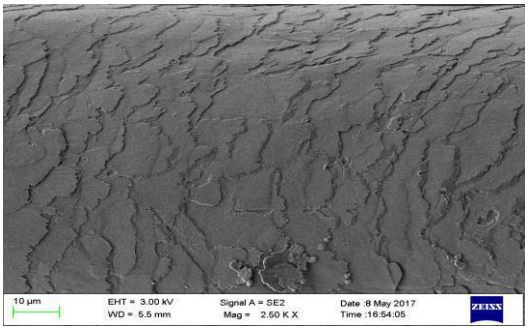

Fig.13. SEM Micrograph of male human hair of age 50 years of Magnification 10KX

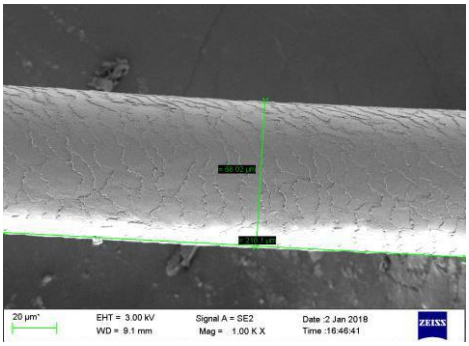

Fig.14. SEM Micrograph of male human hair of age 60 years of Magnification 10KX

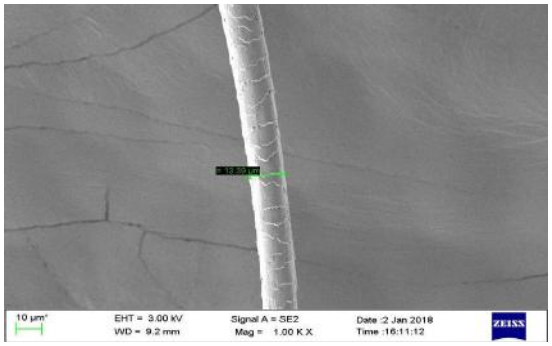

Fig.15. SEM Micrograph of male human hair of age 6 months of Magnification 10KX

The results are based on the morphology and cuticular scale pattern of the hair obtained using most advanced investigation method. Diameter tends to peak at about age 45 years irrespective of sex. It can be noted that there appears no deposition of inorganic material in the organic matrix of human hair fiber. That is the reason human hair is highly elastic in nature. The significant changes in diameter of human hair, irrespective of sex , can be attributed to the variations in molecular composition mainly lipids and proteins, however carbohydrate content does not vary considerably as reviled by IR study on hair [16].

REFERENCES

1. Clement, J.L., pareux, p. f., A. & Ceccaldi, P.F. (1981) *contributional etude lamedulla despoils. Annal. Dermatol, Venereol.,* 108,849-857.
2. Deedrick, D.W. (2004) *Microscopy of hair part 1: a practical guide and manual for hairs. Forensic Sci. common*. 1.1-7
3. Jones, L.N. & Rivetti, D.E. (1997) *The role of 18- methyleicosanoic acid in the structure and formation of mammalian hair fibres, Micron*28, 469-485.
4. Kelch, A., Wessel. S., Will. T., Hintze. R., Wepf & Wiesendanger, R. (2000) *penetration pathways of fluorescent dyes in human hair fibres investigated by scanning near field optical microscopy.j. Microsc*.200,179-186

5. Kreplak, L., Briki, F., Duvault, Y., Doucet. J., Merigoux. C., Leroy, F., Leveque, L., Miller, L. et.al (2001) *profiling lipids across Caucasian and Afro-American hair transverse cuts, using synchrotron infrared microspectrometry. Int. j. cosmet*. Sci.23, 369-374.
6. Mahrle, G. & Orfanos, C.E. (1971) *The spongious keratin and the medulla of human scalp hair. Arch. Derm. Res,* 241, 305-316.
7. Roper, K., Fohles, J., Peters, D. & Zahn, H. (1984) *Morphological composition of the cuticle from chemically treated Wool,1*. Calculating endocuticle content in isolated cuticle from results of amino acid analysis. Text, Res. J. 54, 139-143.
8. Smith, J.R. (1998) *A quantitative methods for analyzing AFM images of the outer surfaces of human hair.*j. Microsc. 191, 223-228.
9. Swift. J. A. & Smith, J.R. (2000) *Atomic force microscopy of human hair Scanning*22. 310-318.
10. Wagner, R.D.C & Joekes. I. (2005) *Hair protein removal by sodium dodecyl sulfate. Colloid surf*, B. Biointerfaces 41, 7-14.
11. Zanh,H., Jolles, P. & Hocker. H. (1997) *Formation and structure of human Hair*. Pp. 59, 148. Birkhauser Veriag, Basel, Switzerland.
12. Litman IM (2012). *Simple modified freezing technique for identification fo human scalp and public hairs* Egypt. J. Forensic Sci.2 (2): 69-72.
13. Marshal (1983) *scanning electron microscopy study of different hair types . part II: Talanta* 123: 54-62.
14. Tazawa- Toshio et al (1997) content and relationship of elements in human hair for a non industrialized *population in Poland Sci. Total. Environ*. 209(1): 59-68.
15. Marchisio et al (2001) studied the morphological expression of human hair and nail in vitro by. J. Cosmet. Sci.53.89-100.
16. Mohammed Abdul Mujeeb and Khalid. M. Zafer (2017), FTIR Spectroscopic studies on human hair, Int. J. Innov. Res. Sci. Engg. Tech., 6(5): 9327 – 9332.

Second National Conference on
RECENT ADVANCES IN APPLIED NANO MATERIALS
February 16-17, 2018 at Department of Physics, University College of Science, Saifabad, Osmania University, Hyderabad, Telangana State, India.

A comparative study on auto catalytic ion efflux of carbohydrate rich *sorghumcontroversum* (white jawar) & lipid rich *helianthus oannuus* (sunflower) seeds

[1]M. A. Hakeem and [2]Dr. MohdKhalid Mubashir Uz Zafar

[1]Ph.D Research Scholar, Department of Physics, Dravidian University,Kuppam, India
[2]Associate Professor, MaulanaAzad National Urdu University, Hyderabad, India
Email –[1]ahqamer83@yahoo.com, [2]mkmzafar@gmail.com

Abstract: *The paper presents a comparative study on auto catalytic ion efflux of carbohydrate rich Sorgumcontroversum(White Jawar) and lipid rich Helianthus annuus(Sunflower) seeds, placed in the imbibition medium water and also 0.9% NaCl solution in order to assess the effect of salinity on ion efflux of seeds. The autocatalytic ion efflux constant is calculated measuring electrical conductivity of imbibition medium, when the seeds are under the process of imbibition. It is noticed that the value of ion efflux constant is more for fat rich seeds than that of carbohydrate rich seeds. It is interesting to note that ion efflux constant of seeds increases, when seeds are subjected to 0.9% NaCl solution instead of water for imbibition irrespective of type of seed.*

Key Words: *Autocatalytic Ion Efflux Constant; Electrical Conductivity; White Jawar; sunflower seeds.*

1. INTRODUCTION:

Seeds normally take up only water and oxygen during germination. However during the initial stages of germination many substances are lost from the seed accompanied by a net loss of dry weight which is due to the oxidation of substances on one hand and a leakage out of the seed on the other hand. The aqueous medium namely water, in which seeds are placed during germination is generally referred to variously as the bathing medium, Studies on seed germination are usually confined to the changes in mass or volume of the seed as a function of time during the process of imbibition to evaluate the time of germination. In view of this the study of seeds germination is considered a useful biophysical phenomenon to understand. The seed kinetics may be assessed from knowledge of electrical behavior of imbibition medium, Hence, the present study is an attempt to assess a comparative study on auto catalytic ion efflux constant of carbohydrate rich Sorgumcontroversum(White Jawar) and lipid rich Helianthus annuus(Sunflower) seeds when they placed in distilled water and 0.9% NaCl solution as imbibition medium irrespective type of seed.

2. LITERATURE REVIEW:

Obendorf and Hobbs [1] studied the temperature sensitivity during imbibition of soyabean.
Keller and Bleak [2] studied the factors influencing imbibition by seeds of the crested Wheat –grass complex. Shaykewich and Williams [3] have studied the resistance to water absorption in germination rape seed. The concept of hydraulic conductivity for a seed was introduced by them and the dynamic of the imbibition phase has been examined. Fensom [4] has studied the bioelectric potential of plants and has detected change in the electrical properties of the surface of the tissue. ShanmugaSundaram et al [5] reported that the ion efflux from whole seedling increases the specific conductance of the bathing medium. The increase in electrical conductivity in leachates of imbibing seeds is due to the increased leakage of these electrolytes.

Kotowski and Brauner [6] has studied influx of water and the seed coat permeability by method of electrical conductivity. Gopala Krishna et al [7] showed that water uptake by seeds resulted in an efflux of ion into the imbibition medium, causing an increase in the specific conductance of water from its initial value.

Mujeeb et al [8] calculated auto catalytic ion efflux constant of Barley, Mung bean and Jawar, as a function of time. Hakeem et al [9] calculate the autocatalytic ion efflux constant of Mung bean seeds placed in imbibition medium water and NaCl solution of different concentration.

3. MATERIALS AND METHODS

Sorgumcontroversum(White Jawar) and *Helianthus annuus*(Sunflower) seeds were cleaned with wet cloth and dried at room temperature then allowed to imbibe in water. Then specific conductance of imbibition medium (water) was measured for a period of time 3 hours with an interval of 0.25 hour. From the data on specific conductance of imbibition medium as a function of time, autocatalytic ion efflux constant can be calculated using that differential equation,

$$\frac{d\sigma}{dt} = k_i\sigma_t\,(\sigma_\infty\text{-}\sigma_t\,)$$

Where, σ_t is the specific conductance at any time t, and $\sigma_\infty$is the specific conductance at infinite time. 10 gmof *Sorgumcontroversum*(White Jawar) and *Helianthus annuus*(Sunflower) seeds were taken. They were cleaned with wet muslin cloth and dried at room temperature and were allowed to imbibe in 40 ml of distilled water and 0.9% NaCl solution. The specific conductance of imbibition medium was determined with the help of electrical conductivity meter (ELICO – CM 180), at an interval of 0.25 hour of imbibition. The increase in the specific conductance at every 15 min was determined as a percentage of the conductance of taken 0.9% NaCl solution at time at t = 0.

3. RESULTS AND DISCUSSION

Table-1, Auto Catalytic ion efflux constant of two seeds in water and 0.9% NaCl

S.No	Scientific Name	Common Name	K_i in Distilled Water	K_i in 0.9 NaCl
1	*Sorgumcontroversum*	White Jawar	0.879	1.775
2	*Helianthus annuus*	Sunflower	1.145	1.886

The rate of water uptake $\left(\frac{dw}{dt}\right)$ was assumed to be controlled by osmosis and at the rate of ion efflux (from the seed system to the imbibition medium could be a differential equation. A plot of log ($\frac{\sigma_t}{\sigma_\infty - \sigma_t}$) against time‘t’ should be a straight line from the slope of which the value of K_i the auto catalytic ion efflux constant is calculated.

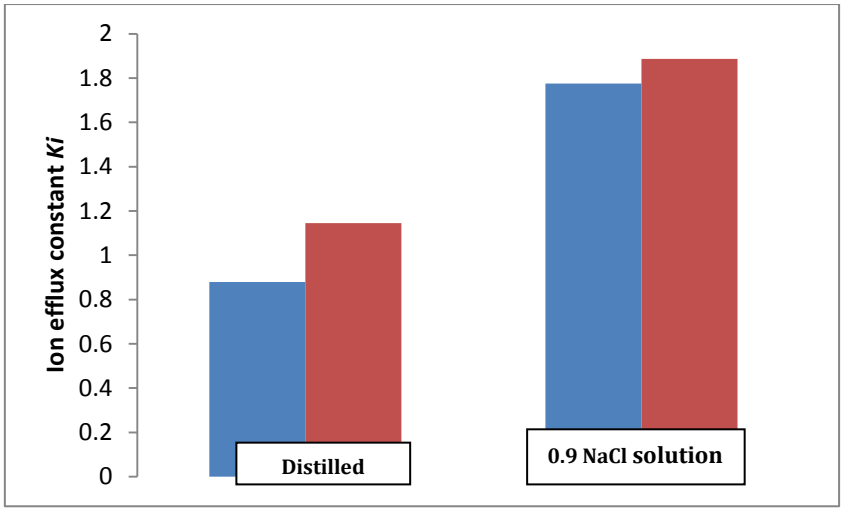

Fig.1, A Comparison on auto catalytic ion efflux constant of seed in Distilled water and 0.9% NaCl Solution

Autocatalytic Ion efflux Constant of selected seeds, determined by ion efflux method, considerably high in 0.9% NaCl solution compared to distilled water as shown in Fig.1, It is noticed that the value of ion efflux constant is more for fat rich seeds than that of carbohydrate rich seeds. It is interesting to note that ion efflux constant of seeds increases, when seeds are subjected to 0.9% NaCl solution instead of water for imbibition irrespective of type of seed.

REFERENCES:

1. ObendorfR.L., & Hobbs P.R, (1970): Crop science, 10, 563
2. Keller W. and Bleak A.T, (1970): Crop science, 10, 424.
3. Shaykewich C.F., and Williams J, (1971): Exp. Bot, 22, 19.
4. Fensom D.S., Cand. J, (1959): Bot, 37, 1003.
5. ShanmugaSundaramE. R. B., SivasithamparamN., JanardanaRao G., and Govindaraju C,(1982): Effect of culture filtrates of Aspergillusterric acid on cell permeability of green gram (Vigna radiate (Linn) Wilczek) seedlings, Current Science 51, 370-1.
6. Kotowski and Brauner F. (1926): Proc. Am. Soc. Hort. Sci., 23, 176.
7. Gopala Krishna G., and Latha L, (1986): Assesment of time of germination in pulses and Cereals by ion efflux and water uptake method, Idian J. Ari. Sci, 56(2): 107-14.
8. Mohammed Abdul Mujeeb, S.VenkateswaraRao, M.K.M. Zafar,andAdeel Ahmad, (2016): Auto-catalytic Ion Efflux Constant of Seeds, 05, 07.
9. Hakeem M., A, and Khalid M. Zafar, (2017): Effect of Salinity on Auto catalytic Ion Efflux Constant of VignaRadiata (Mung bean) seed, 6, 3.

Second National Conference on
RECENT ADVANCES IN APPLIED NANO MATERIALS
February 16-17, 2018 at Department of Physics, University College of Science, Saifabad, Osmania University, Hyderabad, Telangana State, India.

A Comparative Study on FTIR spectroscopy of some Carbohydrate Rich Seeds

[1]Shaik Jainul Pasha and [2]Dr. Mohd Khalid Mubashir Uz Zafar

[1]Ph.D Research Scholar, Dravidian University, Kuppam, India
[2]Associate Professor, MaulanaAzad National Urdu University, Hyderabad, India
Email – [1]zain3110@gmail.com, [2]mkmzafar@gmail.com

Abstract:*The paper presents a comparative study on FTIR spectroscopy of carbohydrate rich seeds. The seeds selected for the study are: Hordeumvulgare (Barley), Sorghum controversum (white jawar), Triticumaestivum (Common wheat), Vigna radiate (Mung bean). The seeds are cleaned and powdered to fine grade. The FTIR spectra are recorded at the wavelength in the range of 400 cm-1 to 4000 cm-1. It is interesting to note that the principal bands at about 1020 cm-1, 1649 cm-1and 2926 cm-1, common in all seeds with different intensities, are related to Carbohydrates, proteins and fats respectively. The seeds of the present study show relatively high absorbance for the band at 1020 cm-1, compared to other two bands pertaining to protein and fat, revealing the fact that the seeds are carbohydrate rich.*

The presents study concludes that absorbance of bands observed can be used with ease for identification and estimation of macro molecular composition.

Key Words:*Seeds; Carbohydrates; Proteins; Lipids; FTIR spectroscopy*

1. INTRODUCTION:

Seeds are the important part of human life, without which one can simply not exist. The food supply to mankind totally depends on seeds and seed stock, many other natural resources that we use as human beings, such as cotton, paper, timber, and edible oils, all begin their live as seeds. Seeds are part of the ever evolving constant of nature that is maintained by complex series of inter-relationships between her different component parts, of which seeds play a central role.

Seeds are basically very small embryonic plants that are enclosed and sealed by a covering that is referred to as the seed coat. A typical seed includes three basic components, an embryo, a supply of nutrients from the embryo and the seed coat Seeds come in all sizes and shapes and need particular conditions for their development into plants, in terms of the size of seeds, they vary from the size of a pinhead to a coconut, plants can contain a few seeds or thousands of seeds.

As is known, infrared spectroscopy is a potential tool to provide valuable information in the study of biomaterials with respect to structure of macromolecular components and their conformations within the tissue. It can also supplement other physical and chemical methods of analysis for the qualitative and quantitative determinations of different components present in the biomaterials.

In specific cases infrared spectroscopy is helpful for the identification of inorganic and organic constituents of biomaterials. In general, spectral analysis of tissues of biological system depends upon the material present and the analyte being sought. The tissue itself is dominated by the spectrum of the macromolecular components, which are present in the large quantity. If living tissue is being examined, it is dominated by the water spectrum.

For the spectroscopic analysis, the biological material may be classified into four types:

- Organic tissues like muscle (skeletal, cardiac and visceral), brain liver, kidney, spleen, tongue, etc.
- Mineralised tissues such as teeth, bone, integuments, nail, hair, calculi, gallstones, etc.
- Body fluids, such as cerebral fluid, spinal fluid, pleural fluid, saliva, blood, urine, bile juice, etc.
- Biological macro molecules, such as nucleic acids, carbohydrates, amino acids, proteins, lipids, fatty acids, waxes, oils, etc.

It is well known that the visible region of electromagnetic radiation extends from 390 to 700 nm. The infrared radiation extends from the end of the visible region at 700 nm to the microwave region with wave length of 1mm. In general IR spectrum is divided in to three regions.

The region between visible and mid infrared (700 nm – 1400 nm) is called Near Infra red. This region of IR is being used for many applications, especially quantitative analysis. The region used by the material scientists is the mid infra red region extending from 1400 nm to 3000 nm. The region beyond 3000nm to 1 mm is called the Far Infra red region. This region is concerned with low frequency vibrations and molecular rotations.

2. LITERATURE REVIEW:

Heinz Fabian and Werner Mantele(2002) described IR instrumental techniques for steady state absorbance and reaction – induced difference spectra and reported sampling procedures available to obtain IR spectra of proteins, peptides, amino acids and more complex enzymes [1].

Andreas Barth (2007) reviewed and discussed the application of infrared spectroscopy to the study of proteins. He focused on the mid-infrared spectral region in the study of protein reactions by reaction-induced infrared difference spectroscopy [2].

Andreas Barth (2007) studied on the protein reactions by focusing on the mid-infrared spectral region [3].

VijayaUshasree and Adeel Ahmad (2017) has made an IR analysis on 90% packed erythrocytes by using IR spectroscopic data on human blood groups A, AB, AB and O [4].

VijayaUshasree and Adeel Ahmad (2017) reported IR spectroscopic data on blood of patients suffering from Diabetes mellitus. IR analysis was made on whole blood, plasma and serum. The characteristic spectral bands pertaining to glucose in the medium of blood were identified. [5].

Search of literature reveals that FTIR studies have not been done on seeds. Hence, an attempt has been made to study carbohydrate rich seeds using the technique of IR spectroscopy

3. MATERIALS AND METHODS

The seeds selected for the study are: Hordeumvulgare (Barley), Sorghum controversum (white jawar), Triticumaestivum (Common wheat), Vigna radiate (Mung bean). The seeds are cleaned and powdered to fine grade.FTIR spectra were recorded in FTIR spectrophotometer (Shimadzu FTIR - 8400S) in the range of 4000 cm^{-1} to 400 cm^{-1}.

For the study, a small quantity of seed powder was mixed with potassium bromide (KBr) in the ratio of 1:4 and pressed in a stainless steel die to produce thin KBr wafer, containing a relatively high concentration of seed sample in IR transparent KBr matrix.

4. RESULTS AND DISCUSSION

Fig. 3. Presents FTIR spectra of the seeds Hordeumvulgare(Barley), Sorghum controversum (White Jawar), Triticumaestivum (wheat) and Vigna radiate (Mung bean). Spectra reveal a series of bands along with % transmittance related to the functional groups of lipids, proteins, carbohydrates and also inorganic material presents in the seed powder.

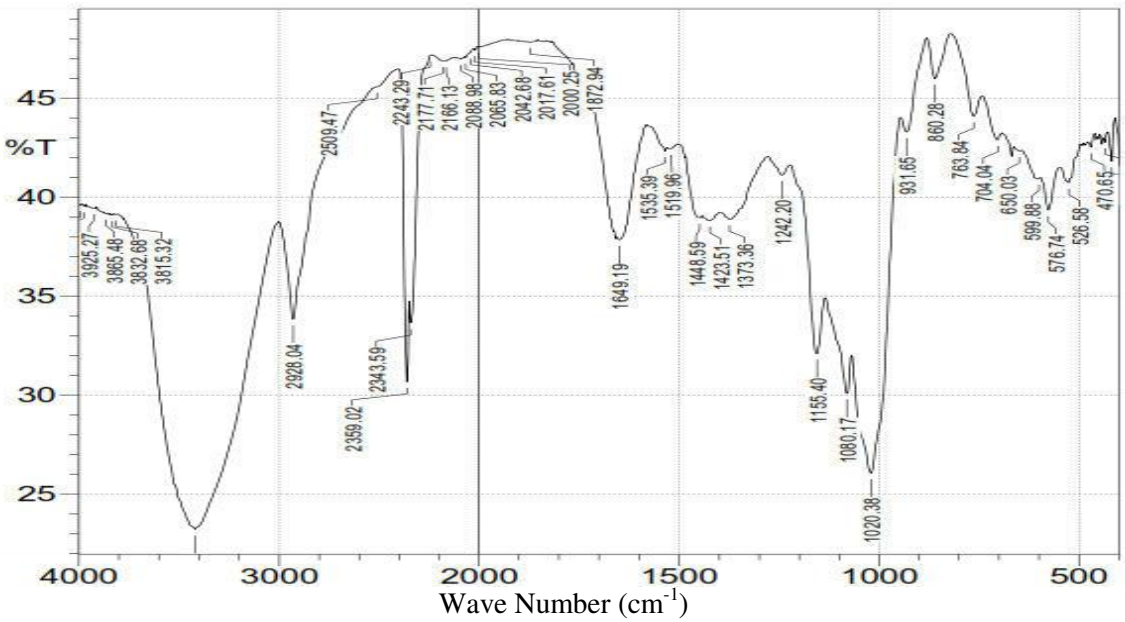

Fig. 1.1. FTIR spectrum of Hordeumvulgare (Barley) seeds

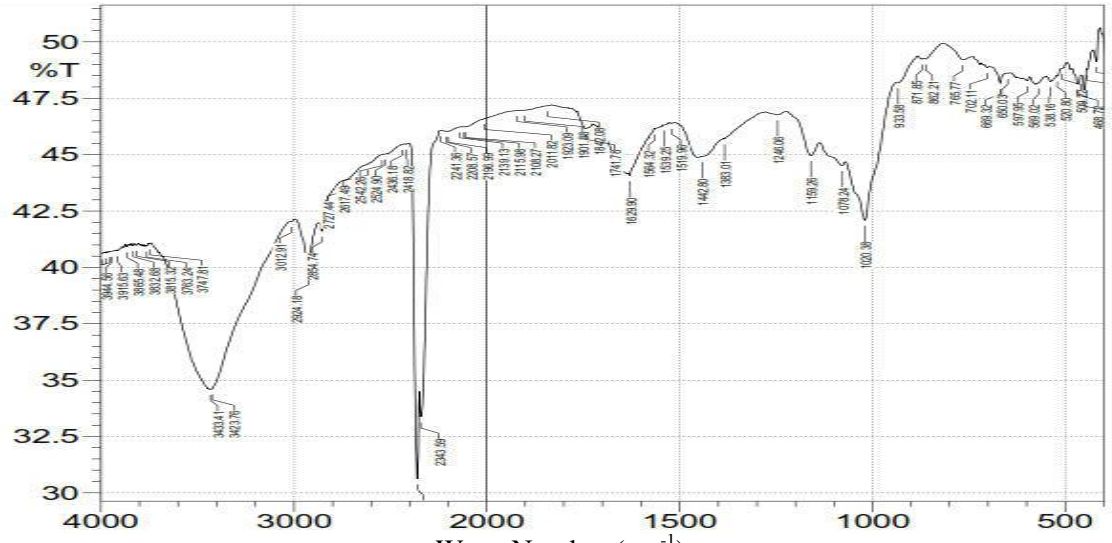

Fig. 1.2. FTIR spectrum of Sorghum controversum (white jawar)

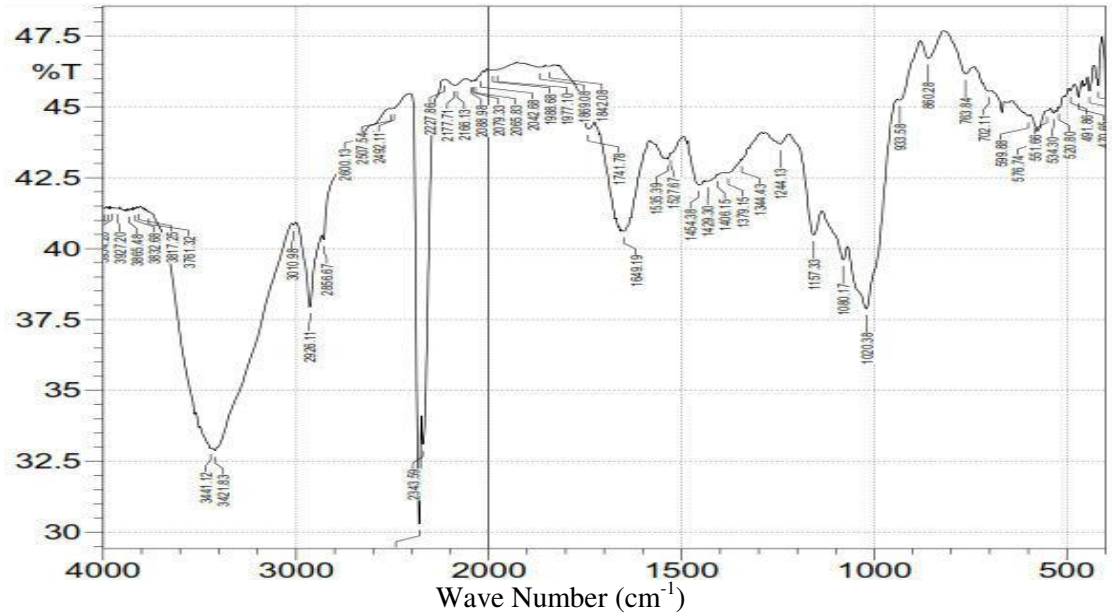

Fig. 1.3. FTIR spectrum of Triticumaestivum (wheat)

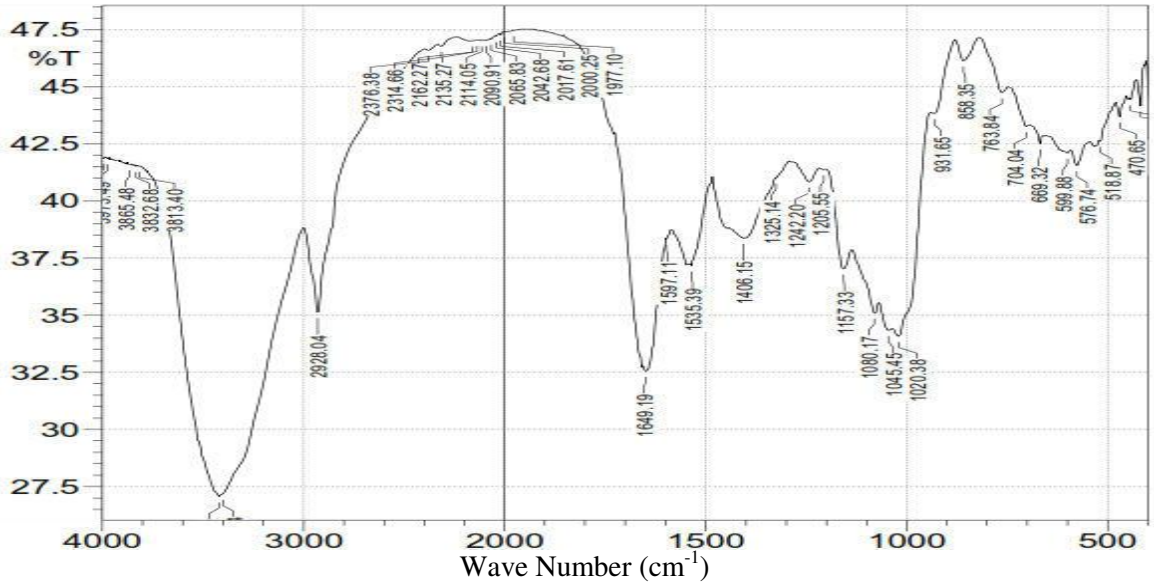

Fig. 1.4. FTIR spectrum of Vigna radiate (Mung bean)

Table 1 gives FTIR data obtained from IR spectra of the seed powder under investigation. Transmittance (%) for specific bands at 1020 cm^{-1}, 1649 $cm^{-1}$and 2926 cm^{-1} is presented in the table.

Scientific Name	Common Name	Transmittance (%) of bands at		
		1020 (cm^{-1})	1649 (cm^{-1})	2938 (cm^{-1})
Hordeumvulgare	Barley	26.05	37.83	33.82
Sorghum controversum	White Jawar	42.08	44.07	39.71
Triticumaestivum	Common wheat	37.88	40.61	37.94
Vigna radiate	Mung bean	34.08	32.55	35.13

It is interesting to note that the principal bands at about 1020 cm^{-1}, 1649 $cm^{-1}$and 2926 cm^{-1}, common in all seeds with different intensities, are related to Carbohydrates, proteins and fats respectively. The seeds of the present study show relatively high absorbance for the band at 1020 cm^{-1}, compared to other two bands pertaining to protein and fat, revealing the fact that the seeds are carbohydrate rich.

REFERENCES:

1. Heinz Fabian and Werner Mantele, Infrared spectroscopy of proteins, John Wiley & Sons, 2002.
2. A. Barth, Infrared Spectroscopy of Proteins, Biochim. Biophys.Acta, Vol. 1767(2007),pp. 1073–1101.
3. Andreas Barth, Infrared Spectroscopy of Proteins, Biochim. Biophys.Acta, Vol. 1767(2007),1073–1101.
4. U VijayaUshasree and Adeel Ahmad, “FTIR spectroscopic analysis on human blood groups”, International Journal of Science, Environment and Technology, Vol.6, No 3, 2017
5. U VijayaUshasree and Adeel Ahmad, “A study on Infrared Spectroscopy of human blood of patients suffering from Diabetes mellitus”, Int. J. Innov. Sci. Res., 2017.

Effect of ZnO on Physical and Optical Properties of Tellurite Lithium Borate Glasses

P.Naresh[1, 2a], B.Kavitha[1], S. Ashwini Priya[1],D.Sreenivasu[1],N.Narsimlu[1], Ch.Srinivas[1]
J. Laxman Naik[2], K. Siva Kumar[1]
[1]*Department of Physics, Osmania University, Hyderabad, Telangana, India 500007.*
[2]*Department of Physics, University College of Science, Saifabad, Osmania University.*
[a)] Corresponding author; nareshosmania13@gmail.com

Abstract: *To study physical, and optical properties of glass samples of the Quaternary system (60-x) B_2O_3−10TeO_2-(30-x) Li_2O-x ZnO with x=0,5,10,15, and 20 mole percentage were prepared by conventional melt quenching technique. XRD confirmed the amorphous nature of all samples. Physical parameters like density, molar volume, Oxygen packing density and etc. calculated. Density of glass samples non-linearly increased with the increase of ZnO concentration due to the replacement of lighter Li_2O with heavy metal oxide ZnO. Optical properties has studied with the help of UV-Visible absorption spectra .Cut off wavelength is increases non linearly whereas E_{opt} and Urbache energies is also changes with addition of ZnO into glass network.*

Keywords*: Density, Optical band gap energy, Refractive index, Cutoff Wave length.*

1. INTRODUCTION:

TeO_2 based glasses possess excellent optical properties, as they exhibit good light transmission in the visible and infrared regions along with low phonon energies. For this reason tellurite glasses are important and widely using for many photonic device applications [1-3]. Optically transparent TeO_2 based glasses showing second harmonic generation have been discovered [4, 5].Synthesis, physical, optical and structural properties of heavy metal oxide glasses like ZnO are very interesting due to their high density, high refractive index and high IR transparency [6, 7].B_2O_3 is a familiar glass former. Boro Tellurite glasses holds good physical and optical properties with the addition of glass modifiers like Li_2O and ZnO produces low rates of crystallization and increase glass forming ability [8].Main objective of the present glass system is to study the effect of conditional glass former ZnO on physical and optical properties of Boro Tellurite lithium glasses with various amounts of Zinc Oxide.

2. EXPERIMENTAL:

2.1.0020Preparation of glasses

Glass system of 60B_2O_3-10TeO_2-(30-x)Li_2O-xZnO with x =0, 5,10,15, and20was prepared using conventional melt-quenching technique. Each component oxide of AR grade used in the experiment was weighed using electronic balance with an uncertainty of ±0.0001g and was mixed using mortar and pestle. The mixtures were transferred to furnace at 950^{o}C for 30minutes.It was stirred to get homogeneity. The melted molten was poured onto a preheated metal plate. Transparent glasses were formed and it was annealed at 150^{o}C to remove thermal strains.

Table.1.Detailed composition

Sample code	Composition in mole percentage			
	B_2O_3 %	TeO_2%	Li_2O %	ZnO %
BTL1	60	10	30	0
BTLZ 2	60	10	25	5
BTLZ 3	60	10	20	10
BTLZ 4	60	10	15	15
BTLZ 5	60	10	10	20

2.2. Characterization techniques

2.2.1. Density related physical parameters

The density (ρ) of the glasses was measured using electronic densimeter based on Archimedes' principle at room temperature xylene as immersion liquid. Therefore, we calculate density (ρ) , molar volume(V_m) , Oxygen packing density(OPD)values were calculated from the relation for all glasses as follows:

$$\text{Density } (\rho) = \left[\frac{a}{a-b}\right] * 0.86 \quad (1)$$

a- weight in air, b - weight in xylene

$$\text{Molar volume } \quad Vm = \frac{\Sigma XiMi}{\rho} \quad (2)$$

Mi –Molecular weight

$$\text{Oxygen packing density } (OPD) = 1000 * \frac{Cp}{Mi} \quad (3)$$

Where C- number of oxygen ions present in the formula.

2.2.2. X-ray diffraction

To determine the nature of the prepared glass samples X-ray diffraction technique have been carried out using X-ray diffractometer with k_α radiation ($1.54A^0$) at room temperature .The patterns (Philips PW 1140) were recorded Bragg angle in the range of 10^0-80^0 with counting rate 0.2/sec.

2.2.3. UV-Absorption Spectra

The Optical absorption spectra of the glass samples were recorded at room temperature in the wavelength region 200-1000 nm by using Shimadzu 8400S UV-Visible spectrophotometer in order to study optical properties i,e cutoff wavelength, optical band gap energy, Urbach energies(E) and evaluated refractive index,molar refraction and electronic polarizabilities.

3. RESULTS AND DISCUSSION:

3.1. XRD

The XRD patterns of all the glass samples are found that there is no sharp peak in the patterns therefore it is confirmed the glasses are amorphous in nature as shown in figure.1. Approximately at 24 degrees it is found a Bragg's hump.

3.2. Density and Molar volume

Density of the prepared glass samples was found nonlinear increase from 3.06-3.44 gr/cc with addition of ZnO into glass system. ZnO is a heavy metal oxide when it is entering to glass system the host and major dominating B_2O_3 and TeO_2 bonds will be broken therefore density is non-linearly increasing whereas molar volume is also behaves the same as shown in figure.2

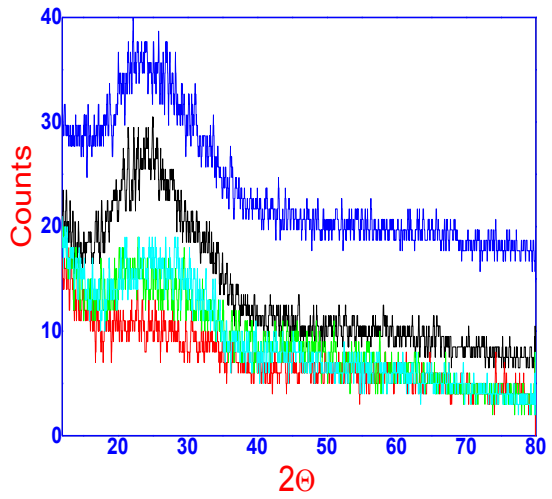

Fig.1.XRD patterns

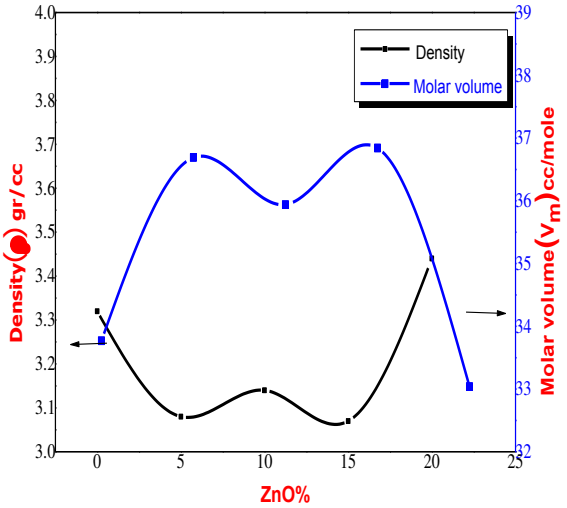

Fig.2. Density and V_m with ZnO.

Density dependent physical properties was calculated and shown in Table.2.

Table.2. Physical properties of glass system

Sample	Density (gr/cc)	Molecular weight(M) gr/mole	Molar volume(V_m) cc/mole	OPD (g atm/1)	Molar refraction (R_m)	Polarizability $\alpha_{e\,(10^{-24})}$
BTL 1	3.32	112.32	33.77	69.15	18.86	7.40
BTLZ 2	3.08	113.32	36.96	74.48	22.14	8.70
BTLZ 3	3.14	113.07	35.94	73.24	20.47	8.10
BTLZ 4	3.07	113.44	36.84	74.69	20.95	8.30
BTLZ 5	3.44	113.82	33.04	66.78	18.77	7.44

3.3. Optical properties

The optical absorption spectra of the glass system with different mole fractions of ZnO do not show any sharp absorption edges, which is the characteristic nature of the glassy state. It is also observed that the fundamental absorption edge shifts to higher wavelengths then shifted to lower wavelengths as the concentration of ZnO increases Optical band gap energy is decreased then suddenly increased as shown in figure.3 and the values shown in Table.3.

The optical band gap of the amorphous materials closely relative to the energy gap between valence band and conduction band [9]. The glass forming anions influences the conduction band whereas cations play an indirect but significant role [10]. The optical band gap energies (Eg) of the glasses were obtained from UV-absorption edge by plotting $(\alpha h\nu)^{1/2}$ as a function of photon energy $h\nu$ using Davis and Mott relation. The direct and indirect band gap energies calculated by extrapolating the linear region of the graph towards X-axis to meet at $(\alpha h\nu)^{1/2}= 0$. It was observed that the value of optical band gap energies non linearly decreases with increase of ZnO concentration and results in the increase of bonding defects and non-bridging oxygen [11]. BTL sample exhibits lowest cut off wavelength and highest band gap energies as shown in figure.4,5.

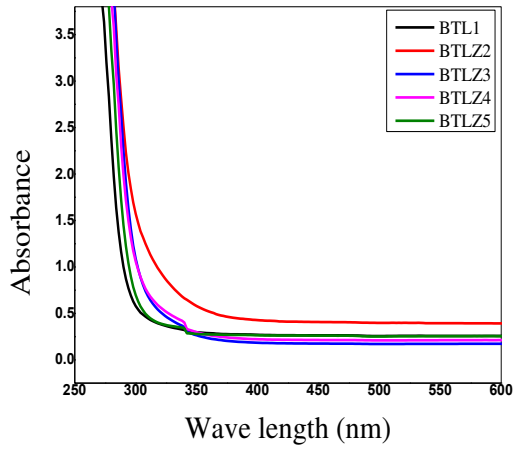

Fig.3.Optical Absorption spectra of glasses

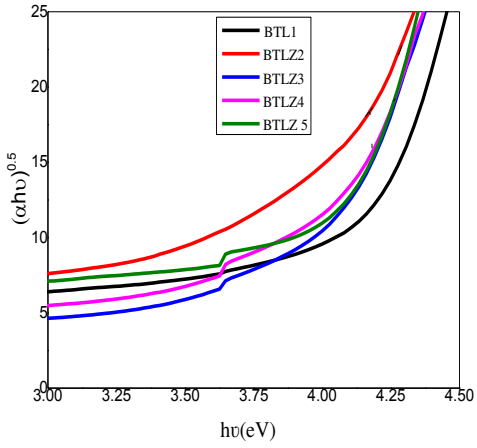

Fig.4. Tauc plots for indirect bandgap

Table.3.Optical properties of glass system

Sample	Cut off wavelength(nm)	Indirect band gap in eV	Direct band gap in eV	Urbache energy(E)	Refractive index(n)
BTL 1	303.4	3.80	3.99	0.45	2.19
BTLZ 2	334.5	3.09	3.65	0.56	2.36
BTLZ 3	322.6	3.68	3.90	0.49	2.23
BTLZ 4	316.6	3.70	3.92	0.53	2.22
BTLZ 5	308.9	3.72	3.94	0.59	2.22

Along the absorption coefficient curve and near the optical band edge there is an exponential part called Urbache tail. This exponential tail appears in the low crystalline, poor crystalline, the disordered and amorphous materials because these materials have localized states which extended in the band gap. Urbache plots drawn between hν and log(α) as shown in Figure.5.Urbach energy of the prepared glass samples is found to change non linearly with addition of ZnO as shown in figure.5

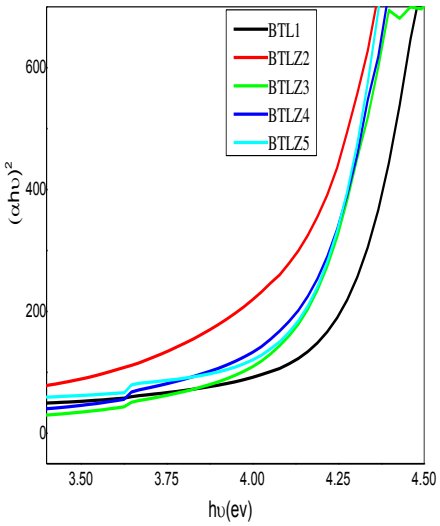

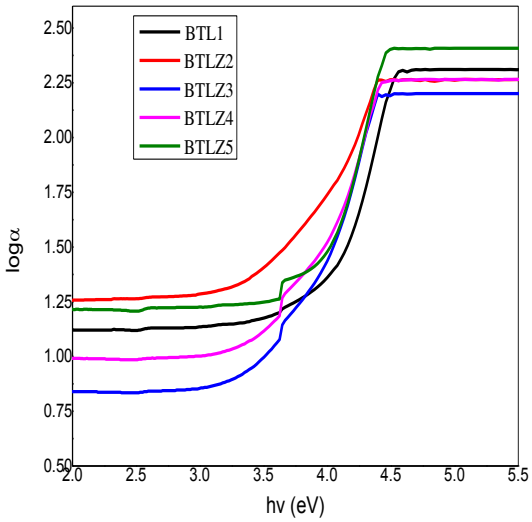

Fig.5. Direct band gap energy **Fig.6. Urbache plots**

4. CONCLUSIONS:

All the glass samples were prepared by melt quenching technique. Density of glasses non linearly increased with addition of ZnO. Direct and indirect band gap energies were found to decrease non linearly whereas Urbache energy is increased non linearly. Refractive index of the samples was increased non linearly.

5. ACKNOWLEDGEMENTS:

The authors are thankful to Head, Department of Physics, Osmania University for providing experimental facilities.

REFERENCES:

1. Stanworth, J. E. *J. Soc. Glass Technol*., 1952, 36, 218.
2. Yakhkind, K. *J. Am. Ceram. Soc*., 1966, 49, 670.
3. Shioya, K., Komatsu, T., Kim, H.G., Sato, R. & Matusita,K. *J. NonCryst. Solids*,1995,189,16.
4. M. Imoka, T. Yamazaki, J. Ceram. Soc. Jpn. 76 (1968) 160.
5. S.K. Lee, M. Tatsumisago, T. Minami, Phys. Chem. Glasses 35 (1994).
6. C.E. Stone, A.C. Wright, R.N. Sinclair, S.A. Feller, M. Affatigato, D.L. Hogan, N.D. Nelson, Y.B. Dimitrov, E.M. Gattet, D. Ehrt, Phys. Chem. Glasses 41 (2000) 409.
7. A. Pan, A. Ghosh, J. Non-Cryst. Solids 271 (2000) 157.
8. P. GayathriPavani et al. / Physica B 406 (2011) 1242–1247.
9. Materials Science-Poland, Vol. 28, No. 1, 2010
10. B. Sumalatha et al. / Journal of Non-Crystalline Solids 357 (2011) 3143–3152.
11. M. Altaf, M.A. Chaudhry, S.A. Siddiqi, Glass Phys. Chem. 31 (5) (2005) 597.

Second National Conference on
RECENT ADVANCES IN APPLIED NANO MATERIALS
February 16-17, 2018 at Department of Physics, University College of Science, Saifabad, Osmania University, Hyderabad, Telangana State, India.

Structural and Impedance Studies of $NiFe_2O_4$ Nanofibers Synthesized by electrospinning technique

[1,*] Kamatam Hari Prasad, [2] Dr. J. Laxman Naik, [3] K. Sai Baba, [4]Dr. B. Ramaiah
[1]Assistant Professor, [2]Associate Professor, [3]Assistant Professor & [4]Asst. Professor
[1, 3] Institute of Aeronautical Engineering, Hyderabad, India
[2, 4]University College of Science, Saifabad, Osmania University, Hyderabad.
Email:- [1,*] hariprasad.kamatam@gmail.com, [2] laxmannaikj@gmail.com, [3] saibaba021@gmail.com

Abstract: *Nanocrystalline ferrites (MFe_2O_4) are current focus of researchers because of their usage in numerous applications like recording media, ferro fluids, magneto optics, spintronics, microwave devices, etc. Apart from the electronic and magnetic applications, ferrites are also used as a gas, humidity sensor material and as an anode material for lithium-ion battery. $NiFe_2O_4$ nanofibers were prepared by using electrospinning technique. X-ray diffraction, and Fourier transform infrared spectrum (FT-IR) spectroscopy results confirm the formation of cubic spinel structured $NiFe_2O_4$ nanofibers. Atomic force microscopy (AFM) results confirm the formation of $NiFe_2O_4$ nanofibers and the roughness parameters. The impedance measurements were carried out at different temperatures and frequencies, were analyzed to obtain the electrical conductivity of spinel $NiFe_2O_4$ nanofibers at 300 K is found to be 6.39 x 10^{-6} S cm^{-1}.*

Key Words: *$NiFe_2O_4$ nanofibers; Electrospinning; XRD; FT-IR, AFM; Impedance studies;*

1. INTRODUCTION:

Nanocrystalline ferrites (MFe_2O_4) are current focus of researchers because of their usage in numerous applications like recording media, ferrofluids, magneto optics, spintronic, and microwave devices, etc. [1-3]. Apart from the electronic and magnetic applications, ferrites are also used as a gas, humidity sensor material and as an anode material for lithium ion battery [4, 5]. Superior magnetic, dielectric and mechanical properties of nanocrystalline materials, compared to their respective conventional bulk, are due to the occupancy of majority of atoms at the grain boundaries. Different chemical routes are currently used for the synthesis of nanoparticles including co-precipitation, combustion, polyol, sol–gel, spray pyrolysis, micro emulsion and hydrothermal routes [6-10]. Among the various available methods, for the synthesis of $NiFe_2O_4$, electrospinning method is found to be simple, cost-effective, and also large-scale production is possible for producing one-dimensional nanostructures of organic, inorganic, and composite nanofibers. In our present study, nanocrystalline $NiFe_2O_4$ nanofibers are prepared using electrospinning process. The structure, crystalline phase, morphology, roughness and electrical conductivity of the prepared one-dimensional $NiFe_2O_4$ nanofibers, were respectively by using the X-ray diffraction (XRD), Fourier transform infrared spectroscopy (FTIR), atomic force microscopy (AFM), and impedance spectroscopy techniques.

2. METHOD:

$NiFe_2O_4$ nanofibers was prepared using Poly (vinyl alcohol), citric acid, urea assisted sol-gel route followed by electrospinning method. Analar grade precursor chemicals of Poly (vinyl alcohol) (PVA, Mw = 80,000), nickel nitrate hexahydrate, ferric nitrate monohydrate, citric acid and urea were used for the synthesis of nanocrystalline $NiFe_2O_4$ nanofiber. Firstly, the PVA solution was prepared by dissolving 3 g of PVA in 40 mL of deionized water at 50 ^oC under constant stirring. Simultaneously, in another beaker the required quantity of metal nitrate solutions was taken and sonicated for 10 minutes. The mixture of solution was continuously stirred at 353 K for an hour. The required amount of citric acid and urea solutions were added to the above solution on continuous stirring. The solution was evaporated at 353 K for 8 hours under constant stirring, which results the polymeric resin. The resins were further dried in an oven at 333 K for 24 hours to remove the excess water and the drying process caused the formation of

dried foamy polymeric intermediate. Nanocrystalline $NiFe_2O_4$ powders were obtained by calcining the polymeric intermediates at 448 K and above. The complete process was investigated through XRD, FTIR, AFM and Impedance spectroscopy techniques.

2.1 CHARACTERIZATION TECHNIQUES:

The powder X-ray diffraction patterns were recorded on a PANalytical XPert-Pro X-ray diffractometer with Cu K_α radiation of wavelength λ=1.5418 A^o and scanned from 80-10^o. FTIR spectra were recorded on pellet samples using Shimadzu FTIR/8300/8700 spectrophotometer in the range of 4000 – 400 cm^{-1} with 2 cm^{-1} resolution for 20 scans. Thin transparent pellet samples were prepared using the dried gel sample, heated from room temperature to higher temperatures (623 K), and grounded well with spectra pure KBr powder taken in 1:20 ratio. Three-dimensional (3D) AFM micrographs of the $NiFe_2O_4$ nanofibers, the sample of 5µm x 5µm scan size, were recorded by using the NanoScope-V Multimode^{TM} SPM, Veeco Instruments, USA. The AFM was operated in tapping mode (non-contact) to prevent damage to the surface of nanofibers, and also, to provide optimal image and quality data. From the 3-D AFM images of the $NiFe_2O_4$ nanofibers, diameter size and surface roughness parameters like root mean square (RMS) roughness (R_q), arithmetic average surface roughness (R_a), and maximum height (R_{max}) asymmetric values were determined by using NanoScope analysis software. The prepared $NiFe_2O_4$ nanofibers sample was pressed into a pellet of 10 mm diameter and 1.24 mm thickness using a KBr hydraulic press. Silver paste was applied on both sides of the $NiFe_2O_4$ nanofibers pellet as electrodes and heated at 200 ^{o}C for half an hour to ensure maximum contact and good adherence. The prepared pellet was placed between two platinum meshes and measured the impedance data at room temperature (25 ^{o}C) and frequencies (10 MHz to 100 Hz) using an Alpha A high- performance frequency analyzer, Novo-control, Germany. The measured impedance data were analyzed using 'Win-fit' software to obtain the resistance for calculating the conductivity and activation energy of the prepared $NiFe_2O_4$ nanofibers sample.

3. RESULTS AND DISCUSSION

3.1. XRD analysis

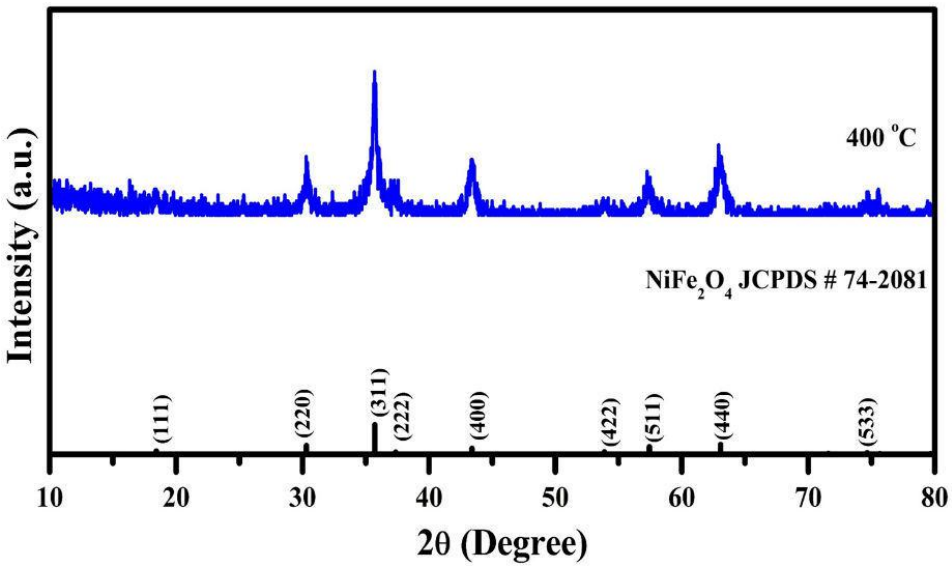

FIGURE 1. X-ray diffraction patterns of the $NiFe_2O_4$ nanofibers

Figure. 1, shows the X-ray powder diffraction patterns of $NiFe_2O_4$ nanofibers sample prepared by electrospinning method. The formation of $NiFe_2O_4$ crystalline phase was confirmed by comparing the diffraction patterns with the JCPDC # 74-2081 data. The crystallite size of the $NiFe_2O_4$ nanofibers sample was calculated by using Scherer's formula and it is found to be 20 nm.

3.2. FTIR analysis

Figure. 2 shows the Fourier transform infrared spectra of $NiFe_2O_4$ nanofibers. The observed vibrational bands at 600 and 430 cm^{-1}, which corresponds to the formation of tetrahedral and octahedral structured spinel $NiFe_2O_4$ nanofibers and also confirms the removal of organic residuals [9-10]. $NiFe_2O_4$ nanofibers sample with high purity was observed. The organic impurity free $NiFe_2O_4$ nanofibers sample is taken for further studies.

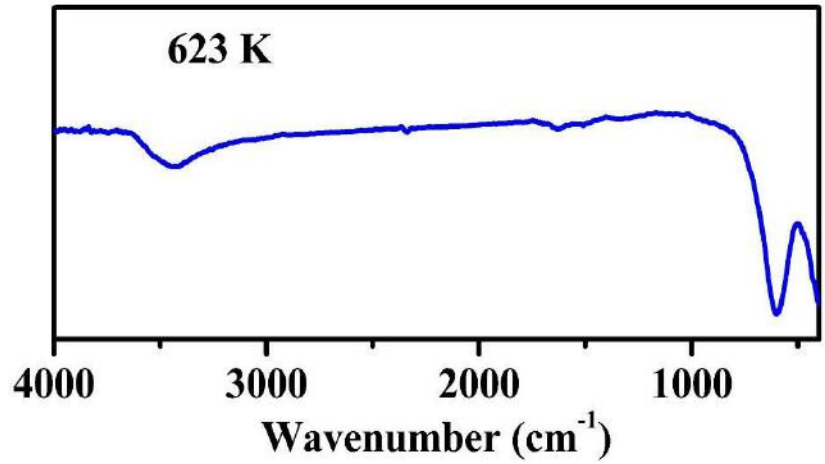

Figure. 2 shows the Fourier transform infrared spectra of $NiFe_2O_4$ nanofibers

3.3 AFM

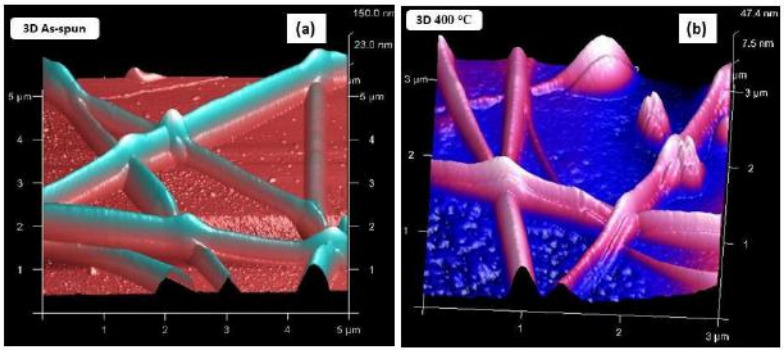

Figure. 3 (a) & (b), shows the 3D AFM micrographs of PVA/$Ni(NO_3)_2.6H_2O$/$Fe(NO_3)_2.H_2O$ composite fibers and $NiFe_2O_4$ nanofibers (calcined at 400 ^oC).

From figure. 3 (a) and (b), it is observed that the fiber diameters are found to be 250-650 nm and 150-350 nm, respectively, for the as-spun and calcined at 400 ^oC PVA/$Ni(NO_3)_2.6H_2O$/$Fe(NO_3)_2$ .H_2O composite fibers. The root means square (RMS) roughness (R_q), arithmetic average surface roughness (R_a) and maximum height (R_{max}) values were evaluated using NanoScope analysis software. It is also found that the calcined fibers show the smallest surface roughness (i.e. R_a=10 nm, R_q=15 nm, and R_{max}=73.2 nm) compared to PVA/$Ni(NO_3)_2.6H_2O$/$Fe(NO_3)_2.H_2O$ composite fibers (i.e. R_a = 25.6 nm, R_q = 32.3 nm, and R_{max} = 150 nm).

3.4. IMPEDANCE analysis

Figure. 4 (a) shows the Nyquist [imaginary (-Z′′) vs. real (Z′)] plots obtained at room temperature for the $NiFe_2O_4$ nanofibers pellet sample. From fig. 4 (a), it is observed that the Nyquist plots of $NiFe_2O_4$ nanofibers show the two semicircles for room temperature in the measured frequency range. The measured impedance data of $NiFe_2O_4$ nanofibers was analyzed by using the winfit software and obtained resistance (R) and electrical behavior, in terms of equivalent circuit, shown in the inset of fig. 4 (a). The formation of two semicircles corresponds to the parallel combination of two constant phase element (CPE) and two resistances of the $NiFe_2O_4$ nanofibers. The obtained total resistance from the impedance plot is used to calculate the electrical conductivity (σ) of the $NiFe_2O_4$ nanofibers sample, by using the following equation [11-20].

$$\sigma = \frac{1}{R}\frac{t}{A} \qquad (1)$$

Where t is the thickness of the $NiFe_2O_4$ nanofibers sample and A is the area of the sample. The observed electrical conductivity of the $NiFe_2O_4$ nanofibers samples is found to be 6.39 x 10^{-6} S cm^{-1} at 25 ^oC.

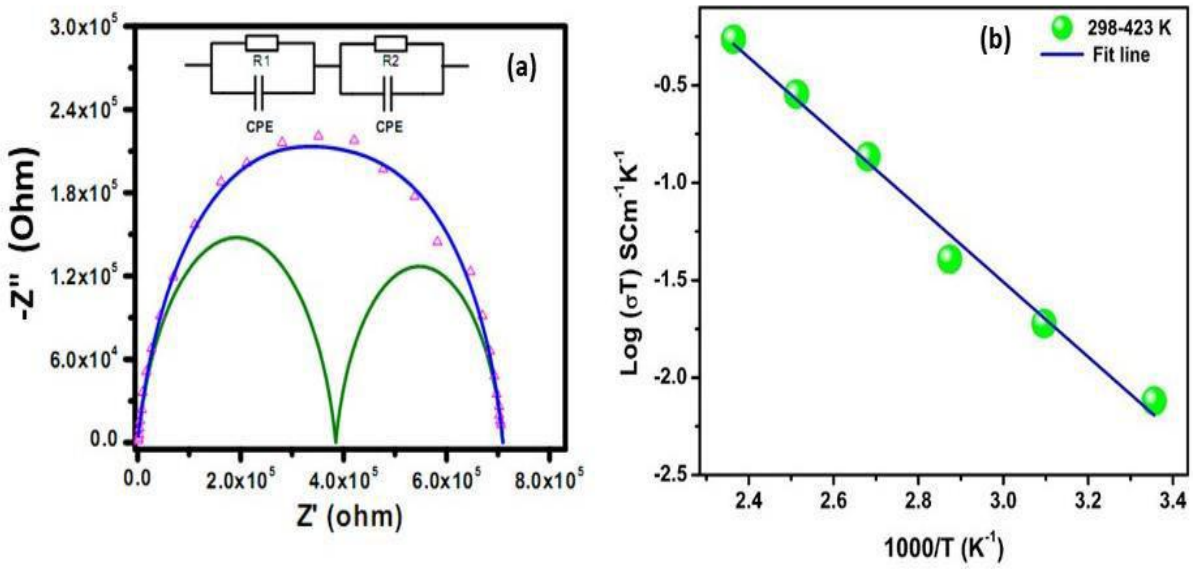

Figure 4 (a) shows the Nyquist [imaginary (-Z′′) vs. real (Z′)] plots obtained at room temperature for the $NiFe_2O_4$ nanofibers pellet sample; (b) shows the log (σT) vs. 1000/T plot of the prepared $NiFe_2O_4$ nanofibers sample.

3.4.1. Temperature dependence conductivity

The obtained electrical conductivity of the $NiFe_2O_4$ nanofibers sample at different temperatures is fitted to the following Arrhenius equation using the least square fit [11-20].

$$\sigma T = \sigma_o \exp\left(\frac{-E_a}{KT}\right) \qquad (2)$$

Where σ is the conductivity, T is the absolute temperature, σ_0 is the temperature independent conductivity, K is the Boltzmann constant and E_a is the activation energy. Fig. 4 (b), shows the log (σT) vs. 1000/T plot of the prepared $NiFe_2O_4$ nanofibers sample. In fig. 4 (b) all the symbols are measured data and the straight line is the fitted data. The activation energy (E_a) is calculated from the slope of the log (σT) vs. 1000/T plot in the temperature range 25 ^oC to 150 ^oC. The calculated activation energy (E_a) for the migration of the charge carriers in the $NiFe_2O_4$ nanofibers sample is found to be 0.33 eV.

4. CONCLUSION:

One-dimensional $NiFe_2O_4$ nanofibers, with diameter ranges from 150 to 350 nm, were synthesized by simple electrospinning technique. The phase and structure respectively confirm the formation of $NiFe_2O_4$ nanofibers. XRD, FTIR results confirm the formation of the pure crystalline phase of spinel structure nanosize one-dimensional $NiFe_2O_4$ nanofibers. The morphology, roughness features of the newly developed one-dimensional $NiFe_2O_4$ nanofibers were confirmed from the AFM results. The observed total electrical conductivity of $NiFe_2O_4$ nanofibers sample is found to be 6.39 x 10^{-6} S cm^{-1} at 298 K and the calculated activation energy is 0.33 eV. The observed high conductivity and low activation energy of the developed $NiFe_2O_4$ nanofibers may be due to the one-dimensional (1-D) nanostructured properties, which may help to enhance the mobility of the charge carriers in the compound. Hence, the developed high porous structured 1D $NiFe_2O_4$ nanofibers may be useful for various applications. The developed electrospinning process can be used to scale up to produce a large quantity of 1D $NiFe_2O_4$ nanofibers and it can also be used to develop many other types of nanofibers materials for various applications.

ACKNOWLEDGEMENT:

Authors are grateful to CIF, Pondicherry University for using characterization facilities.

REFERENCES:

1. M.P. Pileni, (2001): Adv. Funct. Mater., 11, 323–336.
2. F.Y. Cheng, C.H. Su, Y.S. Yang, C.S. Yeh, C.Y. Tsai, C.L. Wu, (2005): Biomaterials, 26, 729–738.
3. Q. Song, Z.J. Zhang, (2004): J. Am. Chem. Soc., 126, 6164–6168.
4. R.B. Kamble, V.L. Mathe, (2008): Sensors and Actuators B, 131, 205–209

5. Y.N. Nuli, Q.Z. Qin, (2005): J. Power Sources 142, 292.
6. A. Chatterjee, D. Das, S.K. Pradhan, D. Chakravorty, (1993): J. Magn. Magn. Mater., 127, 214–218.
7. S.G. Doh, E.B. Kim, B.H. Lee, J.H. Oh, (2004): J. Magn. Magn. Mater. 272–276, 2238–2240.
8. B. Baruwati, R.K. Rana, S.V. Manorama, (2007): J. Appl. Phys., 101, 014302–221-5.
9. J.L. Gunjakar, A.M. More, K.V. Gurav, C.D. Lokhande, (2008): Applied Surface Science 254, 5844–5848
10. G. Socrates, (2001): Infrared and Raman Characteristic Group Frequencies, John Wiley and Sons, New York.
11. A. Ratnakar, K. Hari Prasad, S Vivekananthan, P C Karthika, Aashutosh Kumar, Material Today: Proceedings, 3(10) (2016) 4052-4057.
12. P Jena, N. Nallamuthu, K. Hari Prasad, M. Venkateswarlu, N. Satyanarayana, (2014): Structural characterization and electrical conductivity studies of $BaMoO_4$ nanofibers prepared by sol–gel and electrospinning techniques. *Journal of Sol-gel Science and Technology*, 72, 480–489.
13. K. Hari Prasad, S. Vinoth, P. Jena, M. Venkateswarlu, and N. Satyanarayana, (2017): Structural characterization and impedance studies of PbO nanofibers synthesized by electrospinning technique, *Mater. Chem. Phys.*, 194, 188–197.
14. Kamatam Hari Prasad, S. Subramanian, T.N. Sai Ram, G. Amarendra, E.S. Srinadh, N. Satyanarayana, (2017): Structural, Electrical and Dielectric properties of Nanocrystalline $LiMgBO_3$ particles synthesized by pechini process, *Journal of Alloys and Compounds*, 718, 459-470.
15. K. Hari Prasad, A. Ratnakar, N. Satyanarayana, (2016): Structural and Electrical Conductivity Studies of $LiMgBO_3$ Nanoparticles prepared by Pechini Process, *Material Today: Proceedings*, 3, 4064-4069.
16. K. Hari Prasad, N. Naresh, and N. Satyanarayana, (2016): Preparation of $LiMn_2O_4$ Nanorods and Nanoparticles for Lithium-Ion Battery Applications, *Materials Today Proceedings*, 3, 4040-4045.
17. K. Hari Prasad, S. Vinoth, A. Ratnakar, M. Venkateswarlu, N. Satyanarayana, (2016): Structural and Electrical Conductivity Studies of Spinel $LiMn_2O_4$ Cathode films grown by RF Sputtering, *Material Today: Proceedings*, 3, 4046-4051.
18. Kamatam Hari Prasad, P. Muralidharan, E.S. Srinadhu, N. Satyanarayana, (2017): Morphological, A.C. conductivity, dielectric properties of $LiCoO_2$ cathode films grown by RF Magnetron sputtering, *Advanced Materials – TechConnect Briefs*, 2, 90-93.
19. Kamatam Hari Prasad, P. Muralidharan, E.S. Srinadhu, N. Satyanarayana, (2017): A.C. conductivity, dielectric and electric modulus properties of $Li_4Ti_4O_{12}$ anode films grown by RF Magnetron sputtering, *Advanced Materials – TechConnect Briefs*, 2, 114-117.
20. Kamatam Hari Prasad, P. Muralidharan, E.S. Srinadhu, N. Satyanarayana, (2017): A.C. conductivity, dielectric and electric modulus studies of $LiMn_2O_4$ cathode films grown by RF Magnetron sputtering, *Advanced Materials – TechConnect Briefs*, Vol.2, pp.106-109.

Second National Conference on
RECENT ADVANCES IN APPLIED NANO MATERIALS
February 16-17, 2018 at Department of Physics, University College of Science, Saifabad, Osmania University, Hyderabad, Telangana State, India.

Structural and Impedance Studies of Nanocrystalline ZrO_2 Nanoparticles by Polyol Method

[1,*] K. Hari Prasad, [2] S. Devaraj, [3] Dr. J. Laxman Naik, [4]Ch. Venkateshwarlu
[1]Assistant Professor, [2]Assistant Professor, [3]Associate Professor & [4]Asst. Professor
[1,2] Institute of Aeronautical Engineering, Hyderabad, India
[3, 4]University College of Science, Saifabad, Osmania University, , Hyderabad.
Email:- [1,*] hariprasad.kamatam@gmail.com, [2]sandiri.devaraj30@gmail.com, [3] laxmannaikj@gmail.com

Abstract: *Nanocrystalline ZrO_2 nanoparticles have been synthesized by polyol method using zirconium oxychloride as the metal ion source. The complete process for the synthesis of nanocrystalline ZrO_2 was monitored by TG/DTA, XRD, TEM, and Impedance. Thermal behavior of the intermediate powder was investigated using TG/DTA analysis. The phase of the intermediate, as well as synthesized ZrO_2 powder, was investigated by XRD. The microstructure of the synthesized nanocrystalline ZrO_2 powder was identified using transmission electron microscopy. The impedance measurements were carried out at different temperatures and frequencies, were analyzed to obtain the electrical conductivity of ZrO_2 powder at 300 K is found to be 3.46 x 10^{-6} S cm^{-1}.*

Key Words: *Nanocrystalline ZrO_2 Powder; Polyol synthesis; TG/DTA, XRD; TEM; Impedance.*

1. INTRODUCTION:

Zirconium oxide has wide range of applications, including high temperature ceramics, catalysis, restorative dentistry, etc., due to its properties [1-3]. Recently, it was observed that nanostructured ZrO_2 powder exhibits enhanced performance in many applications. Wide range of wet chemical routes such as sol-gel, combustion, hydrothermal, co-precipitation, and polyol method, etc., have been investigated for the synthesis of nanocrystalline metal oxides, including ZrO_2 powders [1-5]. Among them, ethylene glycol mediated polyol synthesis have been used for the preparation of nanostructured metal and metal oxides because of its high boiling point (~197 ^oC) as well as strong reducing power. In this process, ethylene glycol acts as a solvent for the precursor chemicals due to its high relative permittivity and lead to hydrolysis reactions under atmospheric pressure. Thus, the polyol route involves hydrolysis and inorganic polymerization carried out on the salts dissolved in a polyol medium. In the present work, polyol route was used for the synthesis of nanocrystalline ZrO_2 powder was investigated by TG/DTA, XRD, TEM, and impedance techniques.

2. METHOD:

The Stoichiometric amount of zirconium oxychloride (AR Grade, S.D-Fine Chemicals Pvt. Ltd., India) was added to ethylene glycol (S.Q Grade, Qualigens, India) under stirring condition by keeping the total metal ions to ethylene glycol ratio of 1:40. The resulting clear solution was heated at 175 ^oC for 100 minutes in an Erlenmeyer flask. During heating, the clear solution turned into a white color, turbid suspension, which may indicate the formation of zirconia polymeric intermediates. After cooling to room temperature, colloidal stable suspensions were obtained. The suspended particles were separated from ethylene glycol by centrifugation at 2500 revolutions per minute for 5 minutes. Repeated washing was performed on the obtained particles using distilled water and dried in an oven at 80 ^oC for 10 h. The dried polymeric intermediate particles were further calcined at 600 ^oC for 5 hours to obtain nanocrystalline ZrO_2 powder.

2.1 CHARACTERIZATION TECHNIQUES:

Thermal behavior of the polymeric intermediates was investigated by simultaneous TG/DTA measurement (Lybsys thermal analyzer, Setaram, France). Approximately, 3 milli grams of polymeric intermediate was heated at a rate of 10 ^oC/min between 30 and 600 ^oC. All thermal studies were performed in flowing oxygen. The powder X-ray diffraction patterns were recorded on a PANalytical XPert-PRO X-ray diffractometer with Cu K_α radiation of

wavelength λ=1.5418 A^o and scanned from 80-10^o. Microstructure of the polymeric intermediate was identified using transmission electron microscope (TEM), Jeol**,** Japan. The prepared ZrO_2 powder sample was pressed into a pellet of 10 mm diameter and 1.45 mm thickness using a KBr hydraulic press. Silver paste was applied on both sides of the ZrO_2 powder pellet sample as electrodes and heated at 200 ^{o}C for half an hour to ensure maximum contact and good adherence. The prepared pellet was placed between two platinum meshes and measured the impedance data at room temperature (25 ^{o}C) and frequencies (10 MHz to 100 Hz) using an Alpha A high- performance frequency analyzer, Novo-control, Germany. The measured impedance data were analyzed using 'Win-fit' software to obtain the resistance for calculating the conductivity and activation energy of the prepared ZrO_2 powder sample.

3. RESULTS AND DISCUSSION

3.1. TG/DTA analysis

TG/DTA thermogram of the intermediate particles obtained from the ethylene glycol mediated polyol process is shown in Figure 1. From figure 1, the observed broad endothermic peak in DTA curve between 50 and 150 ^{o}C with ~3 % weight loss is due to the removal of absorbed water. Further heating of the intermediate particles caused the broad exothermic peak between 200 and 350 ^{o}C, which is attributed to the decomposition of organic derivatives (glycolates) and the respective ~ 2 % weight loss observed in the TGA curve. The exothermic peak at approximately 455 ^{o}C corresponds to crystallization of the ZrO_2 phase. There is no significant weight loss observed beyond 500 ^{o}C, which indicates the complete decomposition of organic derivatives and also the formation of ZrO_2 phase, further it was confirmed by XRD analysis.

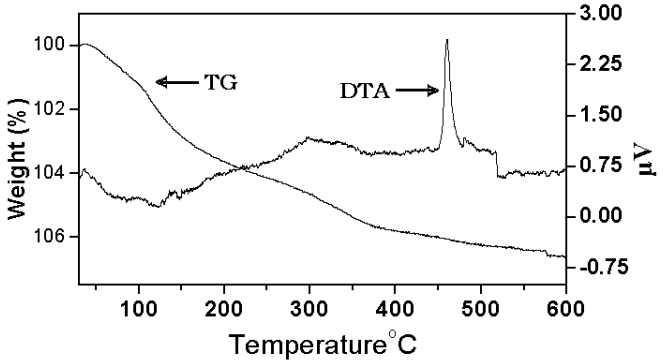

FIGURE 1. TG/ DTA Thermogram of the collected suspension (ZrO_2 intermediate)

3.2. XRD analysis

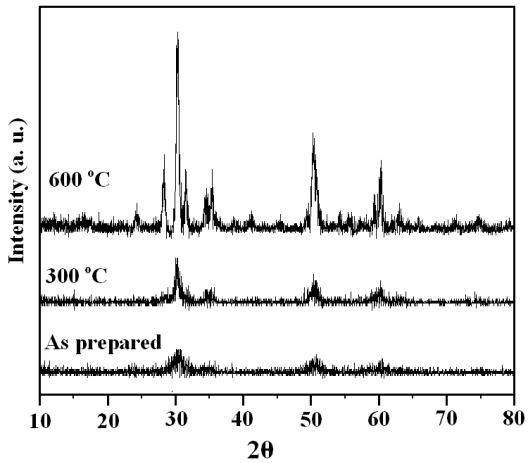

FIGURE 2. X-ray diffraction patterns of the as-prepared as well as calcined suspensions at 300 ^{o}C and 600 ^{o}C for 5 h.

Figure 2. shows the X-ray diffraction patterns of the as-prepared as well as calcined polymeric intermediate at 300 ^{o}C and 600 ^{o}C. The peaks of the as-prepared, as well as calcined polymeric intermediate at 300 ^{o}C indicate the formation of a tetragonal ZrO_2 phase only. However, the calcination of polymeric intermediates at 600 ^{o}C yields a mixture of both metastable tetragonal ZrO_2 and monoclinic ZrO_2 phases. The XRD patterns indicate that both crystalline phases were independently formed during the calcination since the small intense peak at ~32^o related to the monoclinic ZrO_2 phase is observed in the XRD pattern of the polymeric intermediate calcined at 300 ^{o}C. The

diffraction patterns also showed that the increasing calcining temperature leads to the increment of ZrO_2 crystallinity. XRD analysis confirmed the formation of organic-free ZrO_2 powder with t-ZrO_2 and m-ZrO_2 phases at 600 ^oC for 5 hours. The volume fraction and their respective crystallite sizes were calculated by using XRD data. The obtained volume fraction for the tetragonal phase and crystallite size are respectively found to be 44 % and 20 nm. Also, the calculated volume fraction for the monoclinic phase and crystalline size it is found to be 48 % and 22 nm respectively [4-6].

3.3. TEM analysis

Transmission electron micrographs of the ZrO_2 powder synthesized by ethylene glycol mediated polyol method at 600 ^oC for 5 hours with 100 nm magnifications is shown in figure 3. The micrograph shows that the agglomeration of ZrO_2 particles of the size of 24 nm, which is comparable with the crystallite size calculated using X-ray diffraction data [4-5].

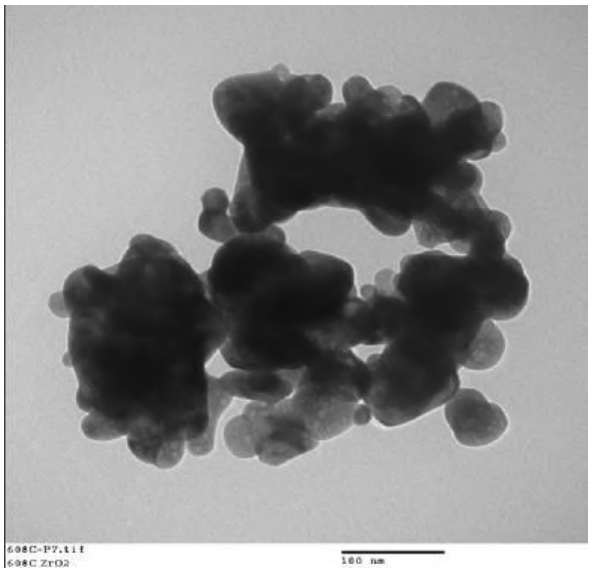

FIGURE 3. TEM micrograph of the nanocrystalline ZrO_2 powder synthesized at 600 ^oC

3.4. IMPEDANCE analysis

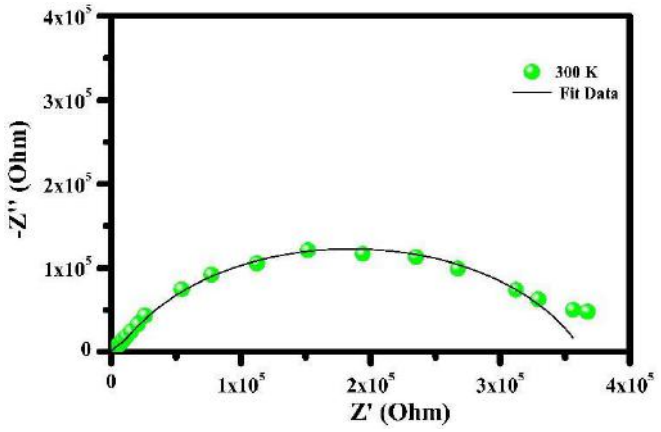

FIGURE 4. Room temperature impedance curve of ZrO_2

Figure 4. shows the complex impedance plots of ZrO_2 sample. The electrical behavior of the sample has been studied in the frequency range of 10 MHz to 1 MHz. Figure .4 shows the Cole –Cole plot of the ZrO_2 sample. The intercept of depressed semicircle with the real axis gives the bulk resistance (R_b). The impedance curve was fitted by using Win fit software and calculated bulk resistance [4-12]. The conductivity of the ZrO_2 sample was calculated by using following equation

$$\sigma = \frac{t}{RA}$$

Where σ is the electrical conductivity of the sample, t is the thickness of the pellet, A is area of the pellet sample and R is the bulk resistance of the sample. The conductivity of the ZrO_2 sample at room temperature was found to be 3.46 x 10^{-6} S/cm.

4. CONCLUSION:

The nanocrystalline ZrO_2 powder was successfully synthesized by employing ethylene glycol mediated polyol process. From TG/DTA and XRD results, it is found that the organic free nanocrystalline ZrO_2 particles are formed at 600 ^oC with two different phases of tetragonal and monoclinic. Their volume fraction was calculated using X-ray diffraction data and it is found to be 44 % for the t-ZrO_2 and 48 % for m-ZrO_2. The average crystallite size of the synthesized ZrO_2 powder was calculated using Scherer's formula and found to be in the range of ~20 nm for t-$ZrO_2$and ~ 22 nm for m-ZrO_2. TEM analysis of the synthesized ZrO_2 particles shows agglomeration of primary ZrO_2 particles size of ~ 24 nm. The electrical conductivity of ZrO_2 powder at 300 K is found to be 3.46 x 10^{-6} S cm^{-1}.

ACKNOWLEDGEMENT:

Authors are grateful to CIF, Pondicherry University for using characterization facilities.

REFERENCES:

1. Srinivasan R, Hubbard CR, Cavin OB, Davis BH, (1993): *Chem Mater,* 27, 5.
2. Angeles-Chavez C, Cortes-Jácome MA, Torres-Garcia E, Toledo-Antonioa JA, (2006): *J Mater Res*, 21, 4: 807.
3. Tan GL, Wu XJ, (1998): *Thin Solid Films*, 330, 59, 1998.
4. P Jena, N. Nallamuthu, K. Hari Prasad, M. Venkateswarlu, N. Satyanarayana, (2014): Structural characterization and electrical conductivity studies of $BaMoO_4$ nanofibers prepared by sol–gel and electrospinning techniques. *Journal of Sol-gel Science and Technology,* 72, 480–489.
5. K. Hari Prasad, S. Vinoth, P. Jena, M. Venkateswarlu, and N. Satyanarayana, (2017): Structural characterization and impedance studies of PbO nanofibers synthesized by electrospinning technique, *Mater. Chem. Phys.*, 194, 188–197.
6. Kamatam Hari Prasad, S. Subramanian, T.N. Sai Ram, G. Amarendra, E.S. Srinadh, N. Satyanarayana, (2017): Structural, Electrical and Dielectric properties of Nanocrystalline $LiMgBO_3$ particles synthesized by pechini process, *Journal of Alloys and Compounds*, 718, 459-470.
7. K. Hari Prasad, A. Ratnakar, N. Satyanarayana, (2016): Structural and Electrical Conductivity Studies of $LiMgBO_3$ Nanoparticles prepared by Pechini Process, *Material Today: Proceedings*, 3, 4064-4069.
8. K. Hari Prasad, N. Naresh, and N. Satyanarayana, (2016): Preparation of $LiMn_2O_4$ Nanorods and Nanoparticles for Lithium-Ion Battery Applications, *Materials Today Proceedings*, 3, 4040-4045.
9. K. Hari Prasad, S. Vinoth, A. Ratnakar, M. Venkateswarlu, N. Satyanarayana, (2016): Structural and Electrical Conductivity Studies of Spinel $LiMn_2O_4$ Cathode films grown by RF Sputtering, *Material Today: Proceedings*, 3, 4046-4051.
10. Kamatam Hari Prasad, P. Muralidharan, E.S. Srinadhu, N. Satyanarayana, (2017): Morphological, A.C. conductivity, dielectric properties of $LiCoO_2$ cathode films grown by RF Magnetron sputtering, *Advanced Materials – TechConnect Briefs*, 2, 90-93.
11. Kamatam Hari Prasad, P. Muralidharan, E.S. Srinadhu, N. Satyanarayana, (2017): A.C. conductivity, dielectric and electric modulus properties of $Li_4Ti_4O_{12}$ anode films grown by RF Magnetron sputtering, *Advanced Materials – TechConnect Briefs*, 2, 114-117.
12. Kamatam Hari Prasad, P. Muralidharan, E.S. Srinadhu, N. Satyanarayana, (2017): A.C. conductivity, dielectric and electric modulus studies of $LiMn_2O_4$ cathode films grown by RF Magnetron sputtering, *Advanced Materials – TechConnect Briefs*, Vol.2, pp.106-109.

Second National Conference on
RECENT ADVANCES IN APPLIED NANO MATERIALS
February 16-17, 2018 at Department of Physics, University College of Science, Saifabad, Osmania University, Hyderabad, Telangana State, India.

Effect of Mg(x) Doped in ZnO Nano materials

[1]Paluri Anjaiah, [2] T V D Prasadh
[1]Research scholar, Department of ChemistryOsmania University Hyderabad-500007, Telangana, India.
[2]Department of Chemistry, Osmania University Hyderabad-500007, Telangana, India.
Email - anjichem420@gmail.com

Abstract: *This paper reports Mg doped ZnO Nano thin films with Mg is varying with various concentrations ratio ranging from0.07to0.57werepreparedby sol-gel spin coating method. To investigate the effects of Mg in the host ZnO the structural and the optical properties of the Mg doped ZnO nano thinfilms,ScanningElectronMicroscopy(SEM)andX-raydiffraction(XRD)arecarriedout.WithincreaseintheMg concentration ratio, the grain size of the Mg doped ZnO thin film was found to be increased. The energy dispersive analysis by X-ray(EDAX) confirmed the element of Mg in the ZnO films. Growth of high quality MgZnO nano structured thin films opens-up numerous possibilities for the development of ultraviolet opto-electronic devices. In the present work, ZnO Nano thin films were grown on microscope glass substrate using solution growth technique from solutions of triethanolamine (TEA), ammonia (NH3) and thioacetamide (TA). The method is relatively simple easy to control, sufficient to produce large area and good adherence to the substrate films. The properties of the films grown at different temperatures with different concentrations were characterized using various techniques.*

Key Words: *Mg doped ZnO,Nano structured thin film,spin coating.*

1. INTRODUCTION:

Semiconductor nanoparticles show unique, size-dependent optical properties due to quantum confinement effect. Zinc Oxide (ZnO) is a wide -band gap II-IV semiconductor material with 3.2 eV optical band gap and having large exciton binding energy of ~60 meV which causes the stimulated emission at room temperature.Hall mobility ZnO single crystal is on the order of 200 cm2 v -1 s -1 at room temperature. An emerging material that holds promise for flexible applications is ZnO. Due to its deep excitonic energy level, thermal stability, and chemically benign nature[1-4], ZnO is Increasingly become an attractive wide band gap semiconductor [5]. Most of the group II–VI binary compound semiconductors crystallize in either cubic zinc blende or hexagonal wurtzite structure where each anion is surrounded by four cations at the corners of a tetrahedron, and vice versa. This tetrahedral coordination is typical of sp3 hybridized covalent bonding. It has a polar hexagonal axis, the c axis, chosen to be parallel to z. This is a hexagonal lattice, with lattice parameters a = b = 0.3296 and c = 0.52065 nm, and is characterized by two interconnecting hexagonal sub lattices of Zn2+ and O2−, such that each Zn ion is surrounded by tetrahedral of O ions and vice versa. This tetrahedral coordination gives rise to polar symmetry along the hexagonal axis.

2. METERIALS AND METHODS:

Zinc oxide (ZnO) and its alloys are semiconductors which offer potential applications such as solar cells, dis-play panel electrodes, light emitters, sensors, modulators and acoustic surface wave devices[6,7]. Mg is incorporated as substitution type material to control the bandgap in ternary oxide semiconductors [8, 9] . Although Mg2+ (0.57 Å) has a similar ionic radius to Zn2+ (0.60 Å), the solid solubility of MgO in the ZnO matrix is limited due to its different crystal structure. MgO has a cubic rock salt structure, [10] while ZnO has a hexagonal wurtzite structure [11]. So, the reports have demonstrated that the MgZnO alloy thin films with a wide range of Mg2+ from 0 to 36% still maintained the hexagonal lattice structure due to the similar ionic radius of Mg2+ and Zn2+, and corresponding energy bandgap could be increased from 3.34 to 3.96 eV[12]. MgZnO films can be prepared by several techniques such as molecular beam epitaxy (MBE) [10], metal-organic chemical deposition (MOCVD) [11], RF mag-netron co-sputtering [12], pulse laser. The sol–gel method has several advantages such as simple and low cost. The most wide spread use of sol-gel is in coating of devices such as in antireflective coatings with Index gradation; optical or infaredabsorbing coatings and electrically conductive coatings. Until now, very little work has been done in MgZnO thin films by using sol-gel

method. In this study, sol-gel spin-coating method was adopted to deposit the MgxZn1-xO thin films with various Mg mole fractions because spin-coating technique has distinct advantages such as easy and cheap operation, excellent compositional control and homogeneity on the molecular level.

3. EXPERIMENTAL DETAILS:

The MgxZn1-xO thin films were grown on Si (100) sub-strates by using sol-gel spin-coating method. The Si substrates were cleaned by immersion in an acetone for 24 hours and then also cleaned with 55 deg0C of 10% NaOH solution and then rinsed with deionized water. The preparation of MgxZn1-xO thin films is illustrated schematically in Figure 1. The precursor sol solution was prepared by dissolving 0.6 M zinc acetate dihydrate [Zn (CH3COO)2·2H2O] in 0.6 M 2- methoxyethanol as a solvent, and monoethanol-amine (MEA) was added to the stable solution. The molar ratio of zinc acetate dihydrate to 2-methoxyethanol was maintained at 1:1. The Mg mole fraction was controlled by the change in the wt % ratio of magnesium acetate tetrahydrate [Mg (CH3COO)2·4H2O] to zinc acetate dihydrate from 0.07 to 0.57. The resultant sol solution was stirred at 60 °C for 2 h to yield a clear and homogenous solution. The sol solution was preserved for 1 day before the growth of the MgxZn1-xO thin films. The sol solution was spin-coated onto Si substrate, rotated at 3000 rpm for 20s. The MgxZn1-xO thin films were heated at 300 °C for 10 min to evaporate the solvent and remove the organic residuals (named as pre-heat treatment). After the pre-heat treatment, the MgxZn1-xO thin films were cooled with a cooling rate of 5oC/min to avoid cracks. The spin-coating and pre-heating processes were repeated three times. In order to crystallize, the MgxZn1-xO thin films were heated in a furnace under an air atmosphere at 500 °C for 1 h (named as post-heat treatment). The effects of Mg mole fraction on the structural and the optical properties of the MgxZn1-xO thin films were investigated by Scanning Electron Microscopy (SEM), X-ray diffraction (XRD), and Fourier transform infrared spectroscopy (FT – IR).

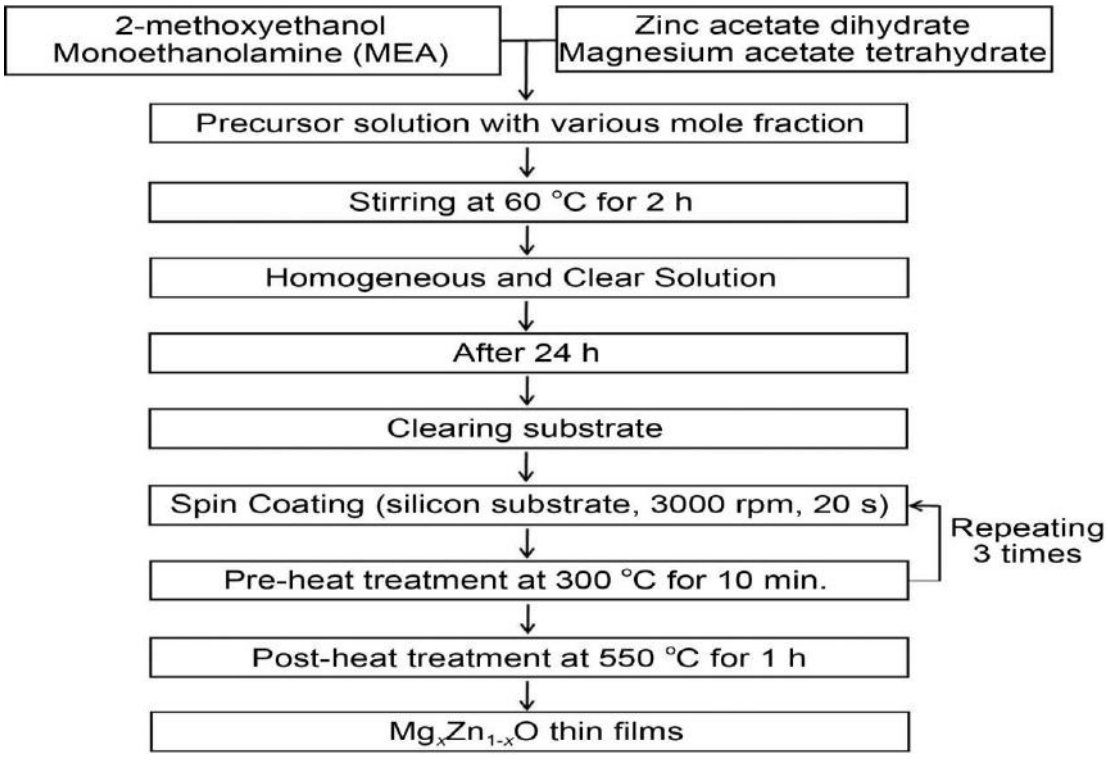

The prepared samples are as follows in the below table

Sample name	Doping base	Mol(%) of Mg
1	99.93	0.07
2	99.83	0.17
3	99.73	0.27
4	99.63	0.37
5	99.53	0.47
6	99.43	0.57

4. RESULTS AND DISCUSSIONS:

SEM:

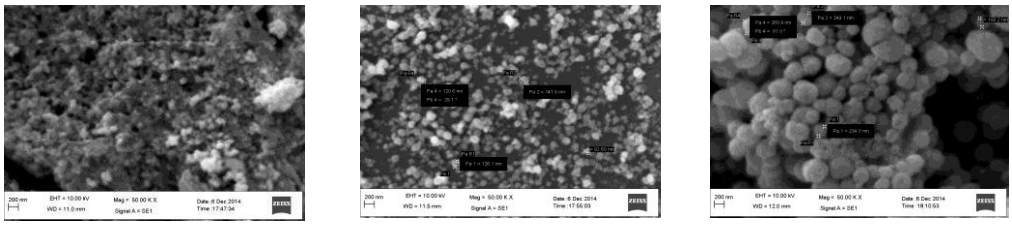

EDX:

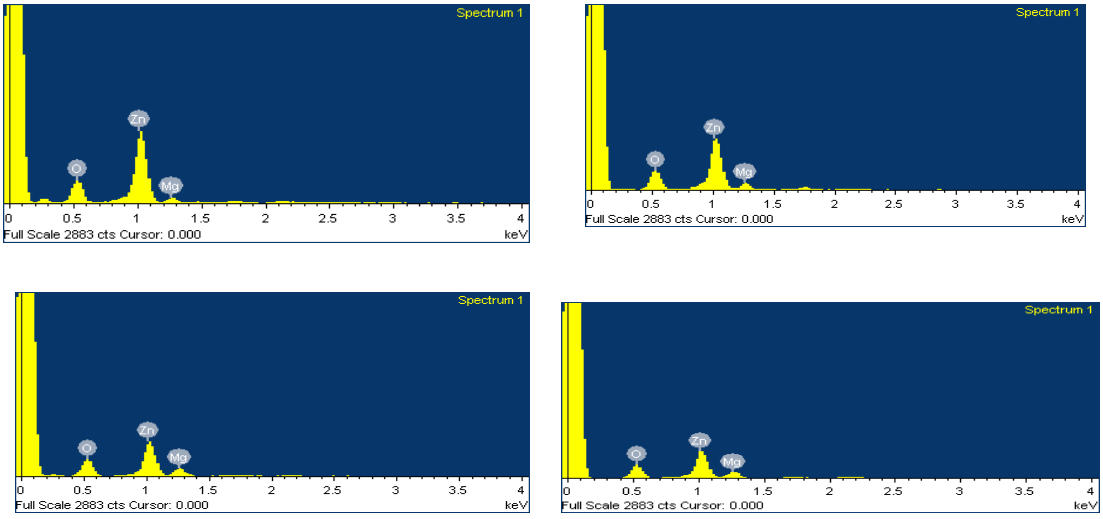

REFERENCES:

1. Ravichandran C, Kumar J, Srinivasan G, Lennon Craig, Sivananthan S. J Mater Sci Mater Electron 2015;26:5489–94.
2. Kılınç N, Arda L, Öztürk S, Öztürk ZZ. Cryst Res Technol 2010;45:529–38. Minami T. New n-type transparent conducting oxides. MRS Bull 2000;25:38–44.
3. Minami T, Nanto H, Sato H, Takata S. Thin Solid Films 1988;164:275–9.
4. Jayadevan KP, Tseng TY. J NanosciNanotechnol 2012;12:4409–57.
5. Chen CY, Retamal JR, Wu IW, Lien DH, Chen MW, Ding Y, et al.ACS Nano 2012;6:936672.
6. Chen CY, Chen MW, KeJJ, Lin CA, Retamal JRD, He JH.PureApplChem 2010;82:2055–73.
7. Narayanan GN, Ganesh RS, Karthigeyan A. Thin Solid Films 2016;598:39–45.
8. Kaushal A, Kaur D. Sol Energy Mater Sol Cells 2009;93:93–198.

Second National Conference on
RECENT ADVANCES IN APPLIED NANO MATERIALS
February 16-17, 2018 at Department of Physics, University College of Science, Saifabad, Osmania University, Hyderabad, Telangana State, India.

Targeted therapy for cancer: An *In silico* approach

Aruna Airva, Upender Bowroju, Vasavi Malkhed & Navaneetha Nambigari*
Department of Chemistry, University College of Science, Saifabad, Osmania University, Hyderabad -500 004 Telangana State, INDIA.
*E mail: nitha379@yahoo.com

Abstract: *Drug discovery has undergone a sea change with technological innovation. The application of computational techniques has been quickly lapped up by the scientists in the field of targeted drug delivery systems. The Wnt proteins are active in cancer by various signaling pathways through Frizzled (Fz) receptor binding, leading to gene expression.*

In the present study comparative modeling method was used to generate the 3D structure of the Wnt - 4 target protein. The structure is refined and validated using bioinformatic tools. The active site residues of the protein are identified. These residues are important for the identification of leads.

Key Words: *Wnt protein, Comparative Modeling, Active site residues.*

1. INTRODUCTION:

Drug Discovery has become truly an interdisciplinary with the advent of genomics and informatics. Starting from late 90s, it has spread its domain quickly from traditional synthesis, pharmaceutical formulations to high throughput screening and combinatorial synthesis [1]. The application of computational techniques has been quickly lapped up by the scientists in the field of drug discovery. Recent approaches on drug discovery has been identifying and targeting novel proteins [2]. Biological phenomena are highly regulated and it is recognized that therapeutic interference with mechanism of signaling cascade offers a tool for clinical applications in various pathologies [3].

The challenge in drug discovery for cancer is to eradicate tumor cells and spare normal cells. Like all other regulated biological phenomena, Wnt pathway activation in breast cancer cells increases the cell motility while its blockade suppresses their aggressive behavior in vitro [4]. Practically every medicine interacts with a targeted protein, either boosting or inhibiting its function. Validating the protein function is a crucial step in the drug discovery process. Once the molecular mechanism of a disease is understood you have a clue to design a therapeutic. Finding drugs that focus on the cancer cells without effecting normal cells in the body, is the need of the hour.

Cancer is a life threatening disease characterized by uncontrolled growth of tumor cells. Cancer is a major global problem and is the second leading cause of death in developed countries. The major setbacks of cancer management – drug resistance, disease relapse, and metastasis [5]. Wnt pathway is disregulated in many types of cancers and hence could provide an excellent therapeutic target [6].The Wingless-type MMTV integration site family, (WNT gene) it encode signaling proteins. These proteins have been implicated in oncogenesis. One potential signal transduction is via the Wnt ligand, a critical signaling molecule in mammary gland development regulated, *Wnt - 4* signaling may represent a novel target [7]. Activation of the Wnt signaling pathway is primary cause in oncogenesis, affecting cell proliferation, morphology and contact inhibition, as well as co-operating with other oncogenes in multistep tumor progression. Knowledge of signaling mechanisms including binding interaction of Wnt ligand - receptor, are important for the designing of antagonist against cancer using *in silico* techniques.

2. METHODOLGY

Homology modeling of the Wnt - 4 protein

Comparative modeling techniques are widely used by computational chemists to predict the three-dimensional (3D) models of proteins [8, 9]. The 3D structure of the protein is essential to know the biochemistry of the protein, comparative modeling method is applied to build the 3D structure of the *Wnt - 4* protein.

The amino acid sequence of the target protein (UniProt ID: P56705) is retrieved in FASTA format from the ExPASy Swiss-Prot (Expert protein analysis system) server (http://www.expasy.org) [10]. The template selection is carried out using template search tools such as Position-Specific Iterative Basic Local Alignment Search Tool (PSI-BLAST) [11, 12] for sequence, Jpred3 for Secondary structure [13], and Protein Homology/analogy Recognition Engine (PHYRE) for fold similarities [14], respectively. Proteins with the lowest E – score value are considered as templates. The pair wise alignment of the target protein, with the sequence of selected template is carried out with ClustalW tool [15]. MODELLER program is used to obtain 3D structure of protein [16]. The 3D model of the protein with the lowest MODELLER objective function is selected for further studies [17]. Loop building is carried out for the amino acids with low stereochemical quality in the 3D model of the target protein using build loop module in Swiss-PDB Viewer (SPDBV), which calculates bad contacts, clashes, and hydrogen bonds. The protein structures are visualized and analyzed with SPDBV, which is an interactive molecular graphics program [18, 19].

Validation of WNT - 4 protein 3D model

The refinement of the initial model of the target protein is followed by energy minimization. Energy minimization is carried out using SPDBV with the default cutoff root mean square deviation (RMSD) value of 0.3 Å. The model is validated by PROCHECK [20, 21] from the Structural Analysis and Verification Server (SAVES). The stereochemical quality of the resulting protein 3D model is interpreted with Ramachandran plot [22] by checking the dihedral angles phi and psi of the amino acid residues. The local model quality is assessed by ProSA server [23].

Active site prediction

The binding domain mediates interaction of *Wnt - 4* and Fz receptor proteins initiating a conserved pathway that regulates crucial aspects of cell fate determination, cell migration, and cell polarity. The active site region of the *Wnt - 4* protein is identified by using Computed Atlas of Surface Topography of Proteins (CASTp) [24] server tool. CASTp server measure systematically the area and volume of each cavity to assess the active site domain.

Further to validate the domains, Protein–protein (P-P) docking is carried out between *Wnt - 4* and its receptor Fz with the help of Patch Dock server [25, 26] and identify the specific binding residues within the binding domain of the target protein.

3. RESULTS AND DISCUSSION

The Wnt signaling pathway is ancient and evolutionarily conserved pathway [27].The Wnts are secreted glycoproteins (19 proteins) in humans hinting to complexity of signaling regulation. To date major signaling pathways downstream of the Fz receptor have been identified

As Planar Cell Polarity [28] and the Wnt/Ca^{2+} pathways. The Wnt4, Wnt5a and Wnt11 ligands express signal via the non-canonical pathway. Over expression of these Wnts (Figure 1) were found to disrupt cell fate both Xenopus and zebrafish, which is regulated by the canonical pathway [29].

The 3D model of the *Wnt - 4* protein (Figure 2) was generated using homology modeling techniques, based on its sequence similarity with proteins of known structure (template). The retrieved amino acid sequence of the *Wnt - 4* protein was subjected to BLAST, Jpred3, and PHYRE search, against the PDB, to identify suitable template structures for comparative modeling. Protein with PDB ID, 4Foa B was selected as suitable template, based on lowest E score values (Table 1). Similar protocols have been followed to build the model [30, 31]

The 3D model the protein is validated using PROCHECK measures the angular distribution of psi/ phi torsion angles of backbone residues of the protein model and is given in the form of Ramachandran plot. The Ramachandran plot (Figure 3) of the model revealed that phi/psi angles of 90% residues are in the favored regions, 10% in the generously allowed region and none of the residues (0%) were in disallowed region. The stereochemical quality of any protein structure of a good quality model is expected to have over 90% in the most favored regions [A, B, L] [32].

ProSA server calculates the energy needed for the architecture of the protein folding energy as a function of the amino acid sequence. The low z-score indicates an overall model quality and also compares the deviation of the total energy of the structure with respect to an energy distribution derived from native conformations [33]. Figure 4 shows the location of the *z*-score for modeled, *Wnt - 4* as a black spot located within the space of proteins determined by NMR .Overall folding energies of the residues of the protein are highly negative, the folding energy for the model protein with a z- score of —6.4, in the range of native conformations.

The region of *Wnt - 4* protein binding to its receptor was taken as reference to determine the putative binding domain (Figure 5)/ active site. The binding pocket volumes were identified using CASTp and were found to have two cavities with area 3807.9 & 2588.3 $Å^3$. Proteins interact with each other to produce a particular cellular effect / signal transduction. P – P docking was carried out between WNT - 4 and Fz receptor to identify the binding residues of importance in the complex formation between the two proteins. In the most stable docked complex from the two hydrogen bonds, Ser 109: HG – Glu 324 :OE1 (2.2934 Å) and Lys 101: O – Arg 228 : N (3.180 Å) was observed as represented in Figure 6. The hydrogen bonding interactions play an important role for the stability of the complex.

4. CONCLUSION :

The homology modeling method provided a reliable structure of *Wnt - 4* for further investigation. The docking studies conclude that Lys 101, Ser 109 of *Wnt - 4* are involved in the hydrogen bonding. These interactions lead to binding of wnt protein to Fzd receptor signals via downstream effectors that result in the inhibition of beta-catenin phosphorylation, thereby preventing degradation of beta-catenin. Stabilized beta-catenin can then accumulate and travel to the nucleus to trigger changes in transcription of target genes. The investigation of docking site of *Wnt - 4* with its receptor domain helps in identifying new molecular entities as *Wnt - 4* antagonist. The results provide valuable information for the design of new leads targeting *Wnt - 4* for the treatment of cancer.

Figure 1. The planar cell polarity (PCP) pathway is triggered by Wnt protein. *Wnt - 4* binds Frizzled receptor leading to the activation gene expression

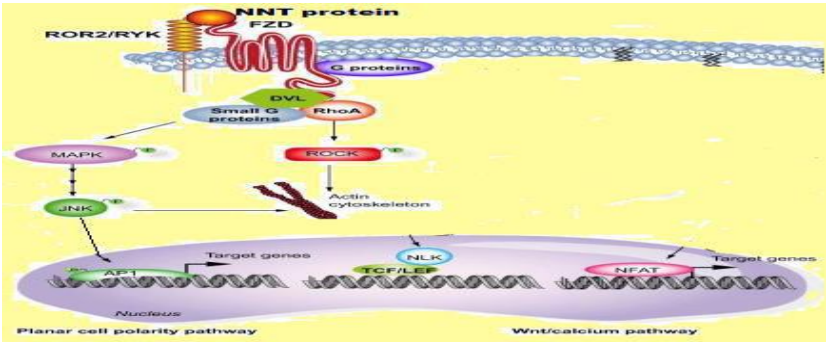

Together these proteins trigger the activation of the small GTPases RHOA and RAC-1 that leads to the activation of the kinases JUN kinase (JNK) and ROCK. These signaling pathways are involved in cell adhesion, migration, and cell cytoskeleton organization. The stress response pathway involves the activation of JNK, which phosphorylates the transcriptional factors AP-1 and JUN leading to their translocation to the nucleus to regulate the gene expression.

Figure 2. 3D model of *Wnt - 4* protein

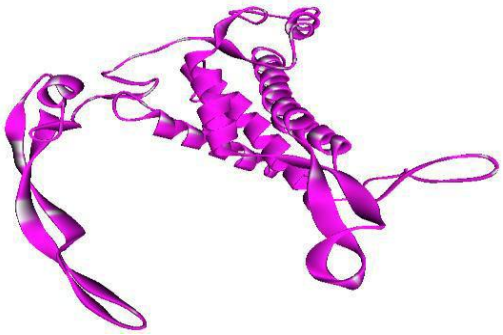

3D model of protein generated using MODELLER showing the Helices and Sheets in violet color.

Figure 3. Ramachandran plot, conformational analysis of protein

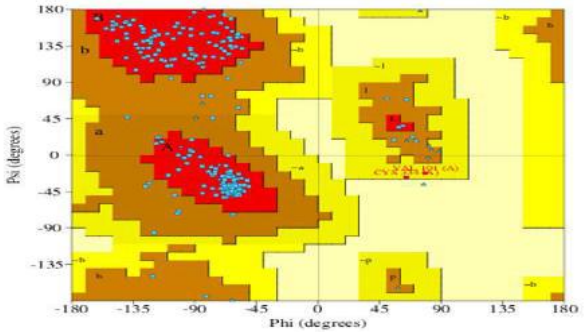

The most favored regions residues (90.0%) are colored red, additionally allowed, generously allowed region residues (10.1%) and disallowed regions (0%) are indicated in yellow, light yellow and white field respectively.

Figure 4. The overall quality of the protein by ProSA

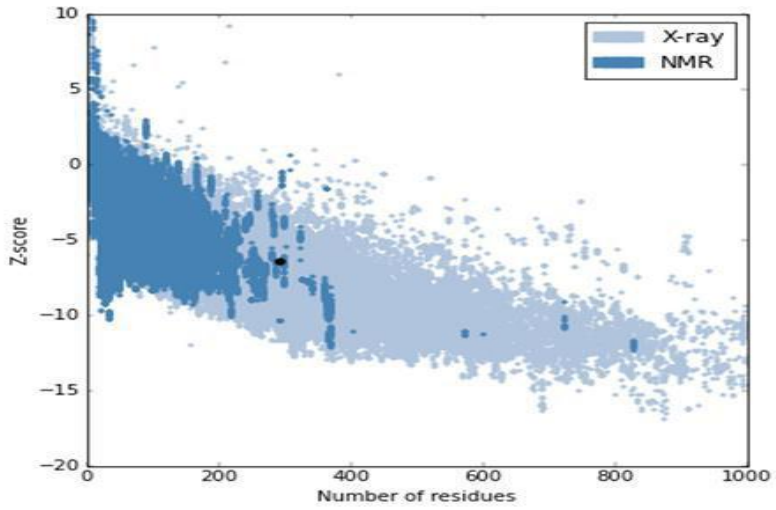

*ProSA - web z-score of all protein in PDB determined by X-ray crystallography (light blue) and by NMR spectroscopy (dark blue). The black spot corresponds to Wnt - 4 protein. Z-Score = -**6.4***

Figure 5. Conserved motifs in *Wnt - 4* protein

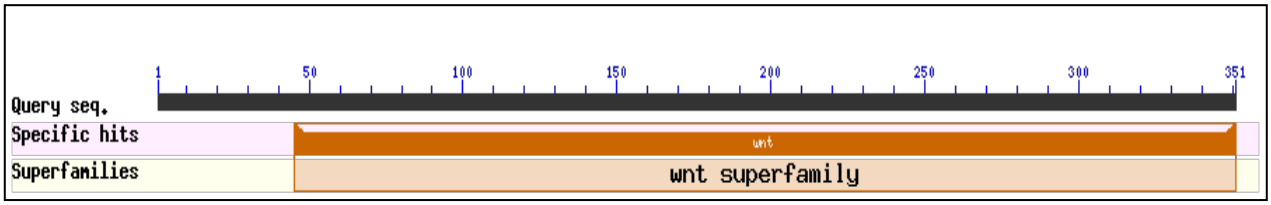

Wnt domain is identified as conserved domain

Figure.6. The binding interactions of *Wnt - 4* – Frizzled (Fz) receptor docked complex.

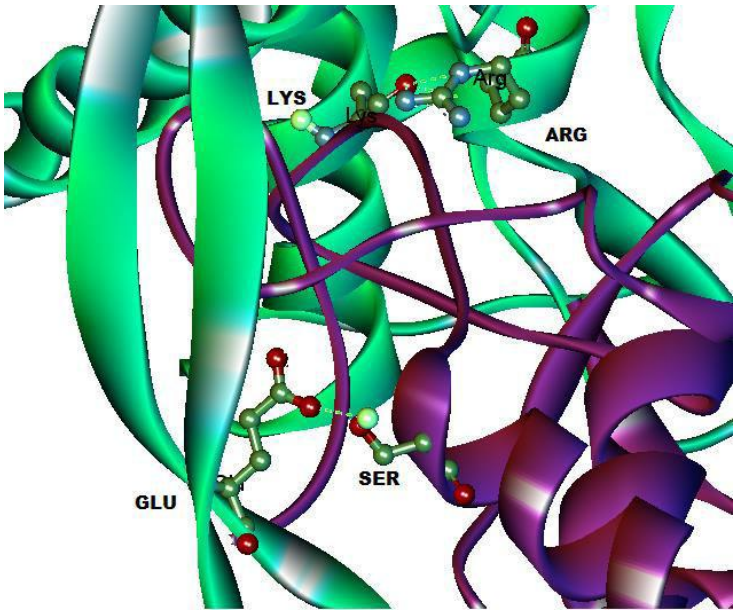

The best docked complex from the protein–protein docking studies using patch dock server. Fz is represented in green solid ribbon and Wnt - 4 in pink. Two hydrogen bonds are shown in green dotted lines.

Table 1. Comparison of the template search results (E-values and PDB codes) obtained from various servers for the Wnt - 4 protein.

S.No	Name of the protein database	Parameter(s) considered	E-value	PDB code
1.	BLAST	Sequence position specificity	2e - 76	4Foa B
2.	JPred3	Secondary structure prediction, solvent accessibility and coiled-coil region prediction	1e - 65	4Foa B
3.	PHYRE	Protein fold recognition (threading)	100%	4Foa B

BLAST: Basic local Alignment Search Tool; JPred3: Secondary Prediction Server;
PHYRE: Protein Fold Recognition Server.

REFERENCES

1. Irwin D. Kuntz, (1992), Structure-Based Strategies for Drug Design and Discovery, Science 257: 1078-1082.
2. Kang Choon Lee and Seulki Lee (2017) Brushing Off antigencity. Nat.Biomed. Eng, 1, 0019. Doi: 10.1038/s41551 – 016 – 0019.
3. M. Korc and R. E. Friesel (2009) The role of fibroblast growth factors in tumor growth, Curr. Cancer Drug Targets 9: 639-651.
4. Mahnaz M. Kazi, Trupti I. Trivedi, Toral P. Kobawala, Nandita R. Ghosh (2016) The Potential of Wnt Signaling Pathway in Cancer: A Focus on Breast Cancer. Cancer Transl Med. 2(2):55–60.
5. Han L, Shi S, Gong T, Zhang Z, Sun X (2013) Cancer stem cells: therapeutic implications and perspectives in cancer therapy. Acta Pharm Sin B. 3 (2): 65–75.
6. Dahmani R, Just PA, Perret C (2011) The Wnt/β-catenin pathway as a therapeutic target in human hepatocellular carcinoma. Clin Res Hepatol Gastroenterol 35 (11): 709–13
7. Matthew J. Sikora et al (2016) Breast Cancer Res.18:92.DOI: 10.1186/s13058-016-0748-7.
8. Anderson AC (2003) The process of structure-based drug design. Chem Biol 10:787–797.
9. Dorn M, E Silva MB, Buriol LS, Lamb LC (2014) Three dimensional protein structure prediction: methods and computational strategies. Comput Biol Chem 53PB:251–276.
10. Gasteiger E, Gattiker A, Hoogland C, Ivanyi I, Appel RD, Bairoch A (2003) ExPASy: the proteomics server for in-depth protein knowledge and analysis. Nucleic Acids Res. 31:3784–3788.
11. Altschul SF, Gish W, Miller W, Myers EW, Lipman DJ (1990) Basic local alignment search tool. J Mol Biol 215:403–410.
12. Altschul SF, Madden TL, Schäffer AA, Zhang J, Zhang Z, Miller W, Lipman DJ (1997) Gapped BLAST and PSIBLAST: a new generation of protein database search programs. Nucleic Acids Res. 25:3389–3402.
13. Cole C, Barber JD, Barton GJ (2008) The Jpred 3 secondary structure prediction server. Nucleic Acids Res. 36:W197–W201.
14. Kelley LA, SternbergMJ (2009) Protein structure prediction on the web: a case study using the Phyre server. Nat Protoc 4:363–371.
15. Thompson JD, Higgins DG, Gibson TJ (1994) CLUSTALW: improving the sensitivity of progressive multiple sequence alignment through sequence weighting, position specific gap penalties and weight matrix choice. Nucleic Acids Res 22:4673–4680.
16. Sali A, Potterton L, Yuan F, van Vlijmen H, Karplus M (1995) Evaluation of comparative protein modeling by MODELLER. Proteins 23:318–326.

17. Martí-Renom MA, Stuart AC, Fiser A, Sánchez R, Melo F, Sali A (2000) Comparative protein structure modeling of genes and genomes. Annu Rev Biophys Biomol Struct 29:291–325.
18. Fiser A, Do RK, Sali A (2000) Modeling of loops in protein structures. Protein Sci 9:1753–1773.
19. Guex N, Peitsch MC (1997) SWISS-MODEL and the Swiss-Pdb viewer: an environment for comparative protein modeling. Electrophoresis 18:2714–2723.
20. Laskowsky RA, MacArthur MW, Moss DS, Thornton JM (1993) PROCHECK: a program to check the stereo chemical quality of protein structures. J Appl Crystallogr 26:283–291.
21. Morris AL, MacArthur MW, Hutchinson EG, Thornton JM (1992) Stereochemical quality of protein structure coordinates. Proteins 12:345–364.
22. Ramachandran GN, Ramakrishnan C, Sasisekharan V (1963) Stereochemistry of polypeptide chain configurations. J Mol Biol 7:95–99.
23. Wiederstein M, Sippl MJ (2007) ProSA-web: interactive web service for the recognition of errors in three-dimensional structures of proteins. Nucleic Acids Res 35:W407–W410.
24. Dundas J, Ouyang Z, Tseng J, Binkowski A, Turpaz Y, Liang J (2006) CASTp: computed atlas of surface topography of proteins with structural and topographical mapping of functionally annotated residues. Nucleic Acids Res 34:W116–W118.
25. Duhovny D, Nussinov R, Wolfson HJ (2002) Efficient Unbound Docking of Rigid Molecules. In Gusfield et al., Ed. Proceedings of the 2'nd Workshop on Algorithms in Bioinformatics(WABI) Rome, Italy, Lecture Notes in Computer Science 2452: 185-200, Springer Verlag.
26. Schneidman-Duhovny D, Inbar Y, Nussinov R, Wolfson HJ (2005) PatchDock and SymmDock: servers for rigid and symmetric docking. Nucl. Acids. Res. 33: W363-367.
27. Yuko Komiya and Raymond Habas (2008) Wnt signal transduction pathwaysOrganogenesis 4(2): 68-75.
28. Seifert JR, Mlodzik M (2007) Frizzled/PCP signalling: a conserved mechanism regulating cell polarity and directed motility. Nat Rev Genet. 8:126-38.
29. Tao Q, Yokota C, Puck H, Kofron M, Birsoy B, Yan D, Asashima M, Wylie CC, Lin X,Heasman J (2005) Maternal wnt11 activates the canonical wnt signaling pathway required for axis formation in Xenopus embryos. Cell.120:857-71.
30. Navaneetha Nambigari, Kiran Kumar Mustyala, Vasavi Malkhed et al., (2012). Angiogenesis: an in silico approach to angiogenic phenotype. Journal of Pharmacy Research. 5 (1): 583 - 588.
31. Rajender Vadija, Kiran Kumar Mustyala, Navaneetha Nambigari et al., (2017) Homology modeling and virtual screening studies of FGF-7 protein—a structure-based approach to design new molecules against tumor angiogenesis. J Chem Biol DOI 10.1007/s12154-016-0152-x.
32. Schneider G (2010) Virtual screening: An endless staircase? Nat Rev Drug.Discov.9: 273-276.
33. Chen IJ, Foloppe N (2010) Drug-like bioactive structures and conformational coverage with the ligprep/confgen suite: Comparison to programs moe and catalyst. J Chem Inf Model.50: 822-839.

Second National Conference on
RECENT ADVANCES IN APPLIED NANO MATERIALS
February 16-17, 2018 at Department of Physics, University College of Science, Saifabad, Osmania University, Hyderabad, Telangana State, India.

Structural Characterization of Nano Crystalline Ni $Er_xFe_{2-x}O_4$ferrites

Gopal boda[1], Nehru boda[2], G. Aravind[2], A. Panasa Reddy[1*], D.Ravinder[2*]
[1]*Department of chemistry,University college of Engineering,Osmaniauniversity, Hyderabad.*
[2]*Department of physics, Osmania University, Hyderabad, 500007, Telangana, India.*
[*]*Correspondence author email: ravindergupta28@rediffmail.com*

Abstract: *Nano crystalline Erbium doped Nickel ferrites, which can be represented compositional formula* $NiEr_xFe_{2-x}o_4$ *where(X=0.00 to 0.10 with a step of 0.01) were synthesized by the citrate-gel auto combustion method. Synthesized powders are sintered at* 500^0C *for four hours in air and characterized by XRD, SEM, EDS, and FTIR studies. X-ray diffraction analysis of the investigated samples showed cubic spinel structure of the ferrites without any impurity peak and the values of lattice parameter (a)and X-ray density(*d_x*) increases with the increase of Ercontent. Scanning electron microscope (SEM) studies revealed morphology of the Nano crystalline samples. An elemental composition of the sample was studied by Energy Dispersive spectroscopy (EDS). FT-IR measurements show the characteristic ferrite bands. The observed results can be explained on the basis of composition.*

Key Words: *Ni-Er Nano ferrites, citrate-gel auto combustion method, XRD, SEM EDS, FT-IR.*

1. INTRODUCTION:

Erbium substituted nickel Ferrites have diverged practical applications as high density magnetic data storage, particularly important because of their excellent Microwave absorbing materials [1]. Most of ferrite materials belonging to semiconductors with good magnetic properties [2]. Magnetic resonance imaging contract agents and targeted release of drugs, preparation conditions influence the cation distribution. Which in term reflectsIn the chemical and physical of ferrites to a great extend [3]. Theinteresting physical and chemical properties of the ferrites arise from their ability to distribute the cations among the tetrahedral (A) and octahedral (B) sites [4].Properties of ferrites are highly sensitive to the substitution of different metal ions in its tetrahedral and octahedral sites. Properties of ferrites are highly sensitive to the substitution of different metal ions in its tetrahedral and octahedral sites [5].
Substitution of large rare earth ions In place of small ions will result in strain which induce structural distribution and there by modify the properties of samples in Nano-region
The properties of ferrites are dependent on several factors, chemical composition, method of preparation, grain size, sintering temperature and atmosphere [6].

2. EXPERIMENTAL DETAILS:

The Nickel-Erbiumnano ferrites having the chemical formula $NiEr_xFe_{2-x}O_4$ were synthesized by citrate gel auto combustion method using the below raw materials

2.1 Raw Materials:

- Nickel nitrate 99%pure(AR Grade)[$Ni(NO_3)_2$]
- Erbium nitrate 99.9% sigma Aldrich [$Er(NO_3)_3$] $6H_2O$
- Ferric nitrate –99.9%pure(AR Grade) ($Fe(NO_3)_3$ $9H_2O$
- Citric acid –99%pure(AR Grad) ($C_6H_8O_7.H_2O$)
- Ammonia Solution -99%pure(AR Grade)(NH_3)

2.2. The flow chart of synthesis of Ni-Er Nano ferrites:

The calculated quantities of metal nitrates were dissolved in minimum amount of distilled water to get clear homogeneous solution an aqueous solution of citric acid was added to the metal nitrate solution. The molar ratio of

citric acid to the total moles of citric acid to the total moles of nitrate ions was adjusted to 1:3 .The mixture was slowly stirred.

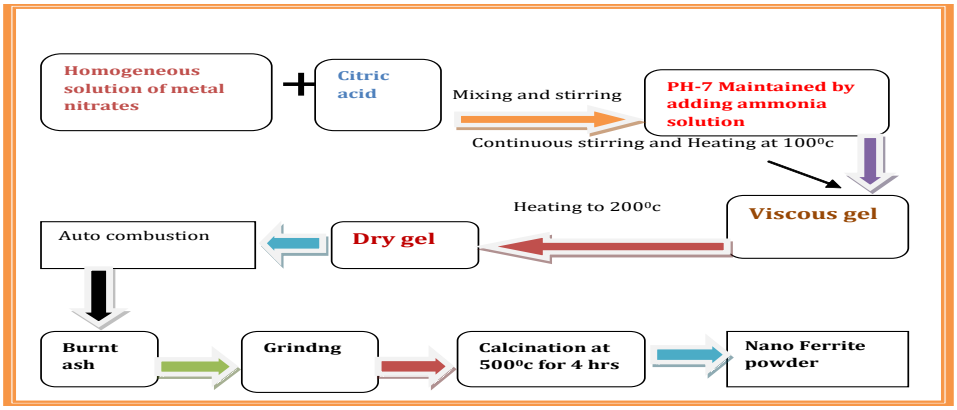

2.3 Structural characterization by XRD:

In order to characterize the phase purity and structural characterization was done by X-Ray Diffract meter were recorded using Regakumaniplex powder X-ray diffractometer (Cu-Kαλ=1.5406A$^{\circ}$)with diffracted mono chromatic beam with radiationof wave length (1.5405A^{0}) to study the diffraction pattern of Ni-Er between brag Angles 10^{o} to 80^{o} in the steps of 0.04°/sec. nano ferrites particles Were shown in Figure.
The crystalline size was calculated for the sample using the high intensity 311 peak and using DebayScherrer formula **[7]** while taking into account the intensity broadening [8].

Crystalline size of the sample $\boldsymbol{D = \frac{0.91\lambda}{\beta \cos\theta}}$

Where $\lambda$the wavelength of X-ray is used [9]. βIs the width of diffraction peak i,e. full width Half Maximum(FWHM) , θ is the peak position.

Lattice parameter (a) of the sample was calculated by the formula. $\boldsymbol{a = d * \sqrt{h^2 + k^2 + l^2}}$[10] Where a=Lattice constant, (hkl) are the Miller indices, d is the inter planner space The X-ray density of the prepared sample was calculated using the relation $\boldsymbol{dx = \frac{8M}{a^3 N}}$(g/cm^3) [11] where **M**= molecular weight of the sample,**a** is the lattice parameter and **N** is the Avogadro number.

3. RESULT AND DISCUSSION:

3.1. XRD Analysis

The X-ray diffraction(XRD)technique was performed to confirm the Erbium substituted Nickel ferrites to form a single-phase cubic spinel structure as shown in Figure-(2).With no extra lines corresponding to any other crystallographic phase. The results obtained from XRD pattern for all the samples of $NiEr_xFe_{2-x}O_4$ with the (hkl) values corresponding to the diffraction peaks of different planes (220), (311), (400), (422), (511), and (440) are spinel cubic phase

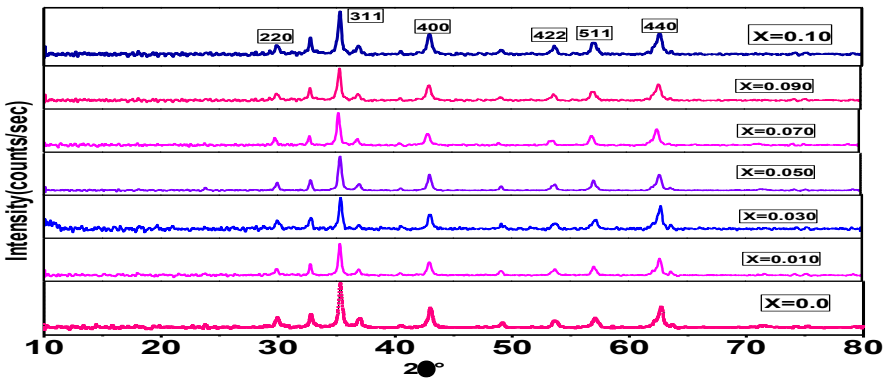

Figure.1. XRD pattern of $NiEr_XFe_{2-X}O_4$ nano crystalline ferrites

The calculated values of crystalline size for the different compositions are given in the table (1).
It can be seen from the table that the values of the crystal size varies from 15.36nm to 39.45nm of the various Er concentrations

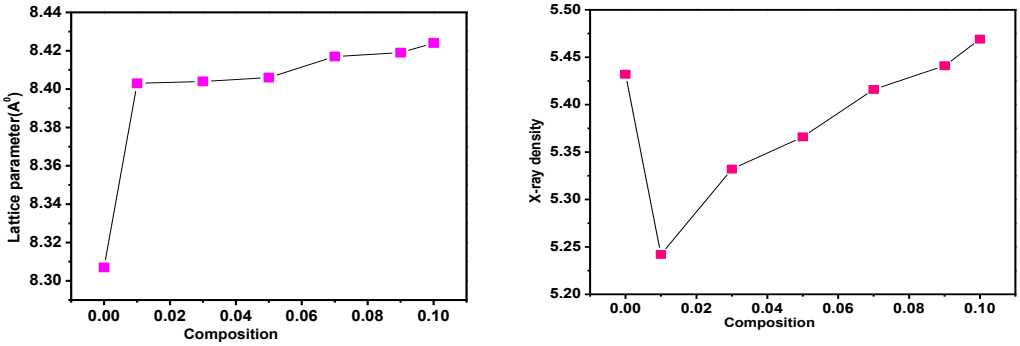

Figure (2) variation of lattice constant with Er^{+3} content and Figure (3) shows the X-ray (d_x) vs Er^{+3} concentrations

The lattice parameter values of all the composition of Erbium doped Iron ferrites have been calculated from the d- spacing and are given in the table. A plot is drawn between the lattice parameter vs Erbium composition is shown in Figure (2) variation of lattice constant with Er^{+3} content in $NiEr_xFe_{2-x}O_4$is (x=0.00 to 0.10 with a step of 0.01)is observed that the Lattice parameter increases with increase in Ercontent. This is attributed to replacement of smaller ionic radii Ni (0.78A°) by larger ionic radii Er^{+3} (A°) ions. This linear variation indicates that the Ni-Er ferrite system obeys vegard's law [12] The Figure(3) shows the X-ray density (d_x) vs concentration, The X-ray density (d_x) is depend on the lattice parameter and molecular weight of the sample. From the table one can observe that molecular weight of the sample is increases with Erbium concentration and lattice parameter is also increases with the increase of Er compositions. This may due to the grater atomic weight of Er-167.259 gm/mol and lesser atomic weight of Fe-55.845gm/mol shown in below figure Erbium was very small .the calculated values of the lattice constant tabulated in table: 1shows that there has been no structural distortion for the various ratios. The fact that Erbiumgoes as substitution into the cubic spinel lattice evident from the absence of any extra peaks in the XRD spectrum**.**

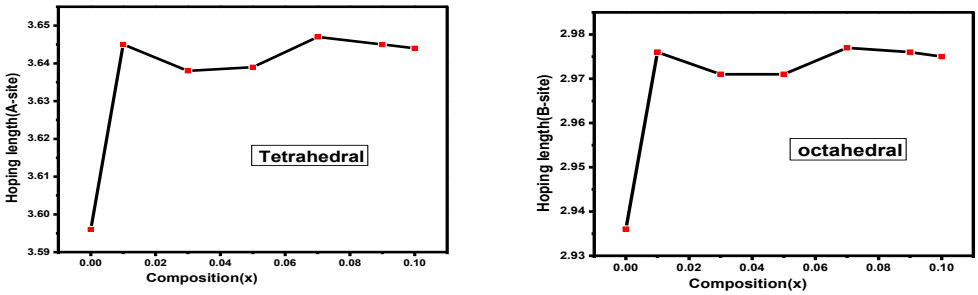

Table1. Crystalline size (D), Lattice parameter (a), X-ray density (d_x), Happing length A, B- site.

Sample	D(nm)	a (A^0)	dx(gm/cc)	A-site	B-site
Pure	39.45	8.307	5.432	3.596	2.936
Er 0.010	21.96	8.403	5.242	3.645	2.976
Er 0.030	21.96	8.404	5.332	3.638	2.971
Er 0.050	21.95	8.406	5.366	3.639	2.971
Er 0.070	21.82	8.417	5.416	3.647	2.977
Er 0.090	17.56	8.419	5.441	3.645	2.976
Er 0.10	15.36	8.424	5.469	3.644	2.975

3.2. Morphology by SEM: Scanning Electron Microscope is the best technique for studying surface morphology of Erbium substituted nickel naono ferrites (prepared samples by Citrate- Gel Auto combustion method was using scanning electron SEM) where the secondary electron images were taken at different magnifications to study the synthesized samples were shown in Figure (4).

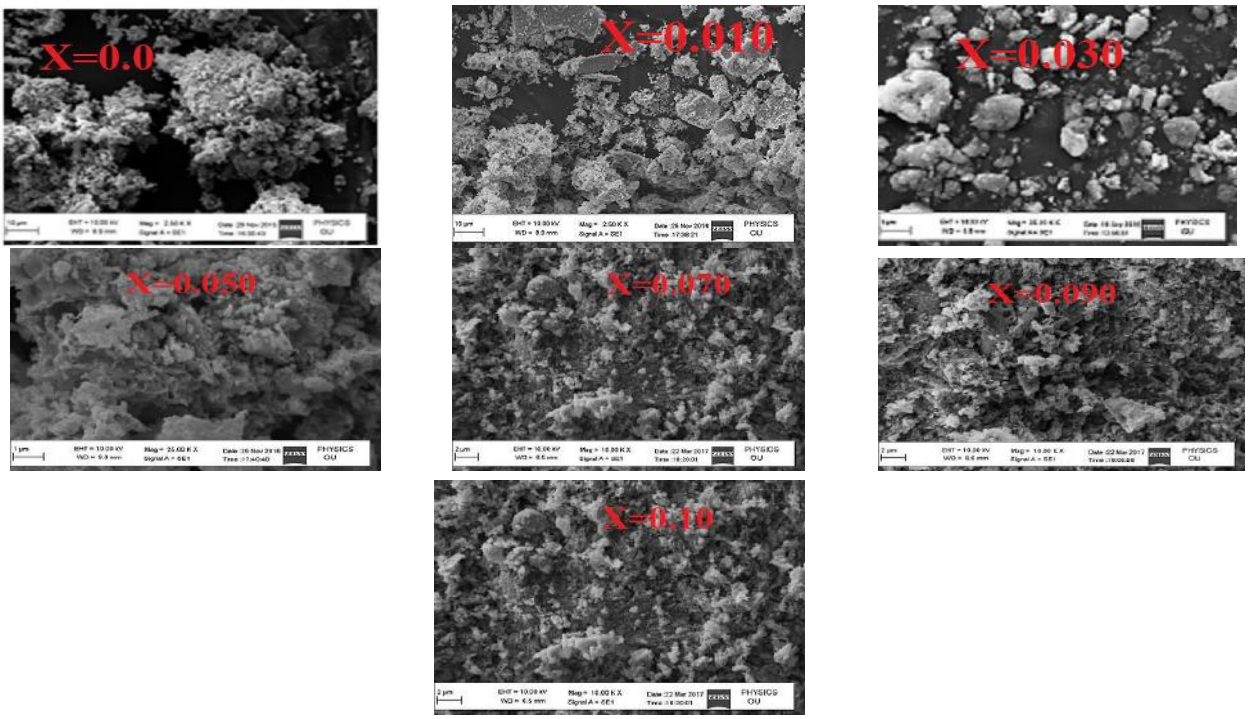

Figure (4)SEM images of$NiEr_xFe_{2-x}O_4$ ferrite samples(X=0.0, 0.010,0.030,0.050,0.070,0.090,0.1).

The SEM imagesof Ni-Er ferrite are shown in the Figur the images show that the particles have an almost homogeneous distribution, andthe morphology is seems to be uniform some of the samples are agglomerated form. it evidenced by SEM images that the agglomeration of particles lies in Nano region.the particles were observed as uniform grain (in different SEM images) sizes

3.3. Elemental Analysis by EDS

The EDS spectra give information about the chemical composition of the elements present from the surface to the interior of the solids, and they are used to confirm the homogeneity of the investigated samples, The spectra indicated the presence of O, Fe, Ni, and Er as the major elements in the synthesized material with no impurities are observed along with elemental mapping. The EDS spectra of the samples are shown in Figure (5)

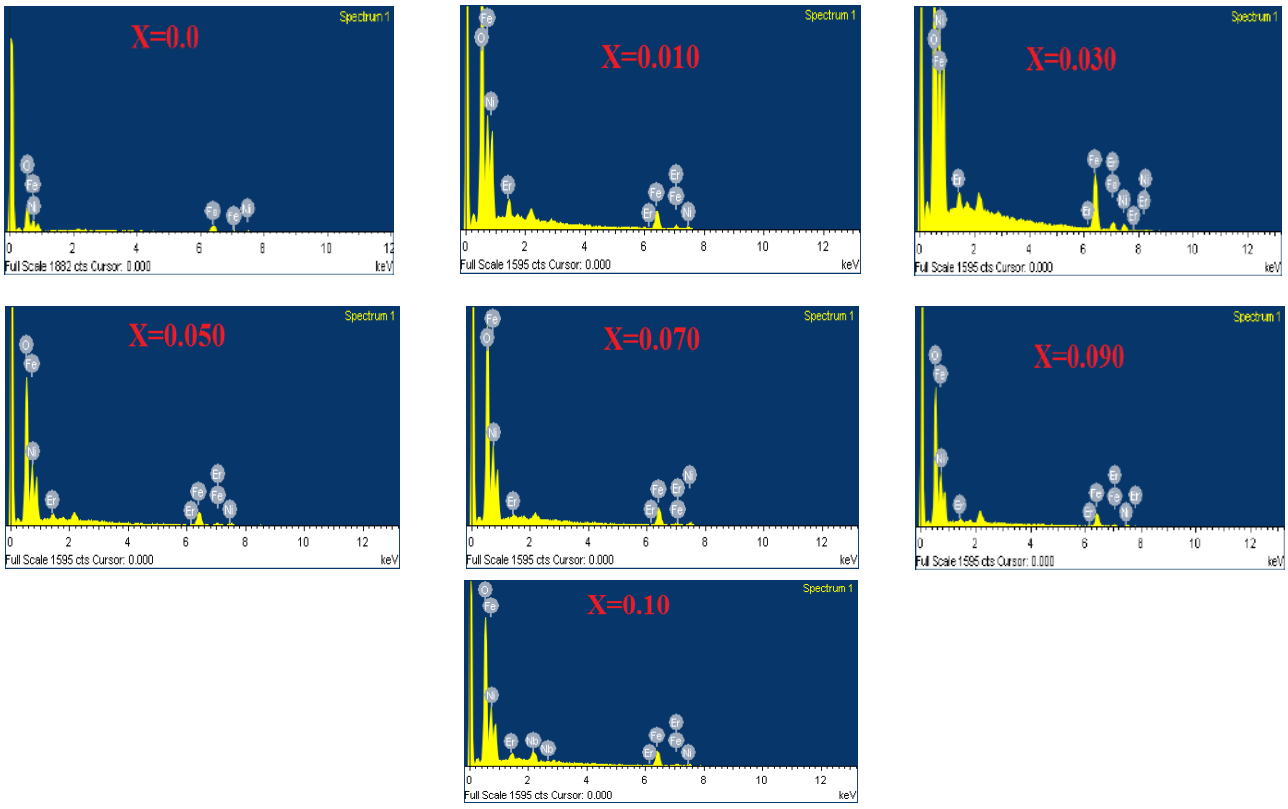

Figure (5) EDS images of$NiEr_xFe_{2-x}O_4$ ferrite samples

3. 4. FTIR Spectral analysis:

FTIR spectra of $NiEr_xFe_{2-x}O_4$nano crystalline ferrites of prepared samplesfrom two absorption bands were recorded in the range of lower frequency band (ϑ_1)387-397cm^{-1} and higher frequency band(ϑ_2)574-580cm^{-1} corresponds to the stretching vibrations of the metal at the tetrahedral site and octahedral site it explain that the normal mode of vibration of tetrahedral cluster is higher than that of octahedral cluster.[13, 14] It should be attributed to the shorter bond length of tetrahedral cluster and longer bond length of octahedral cluster. Shown in below figure (6)

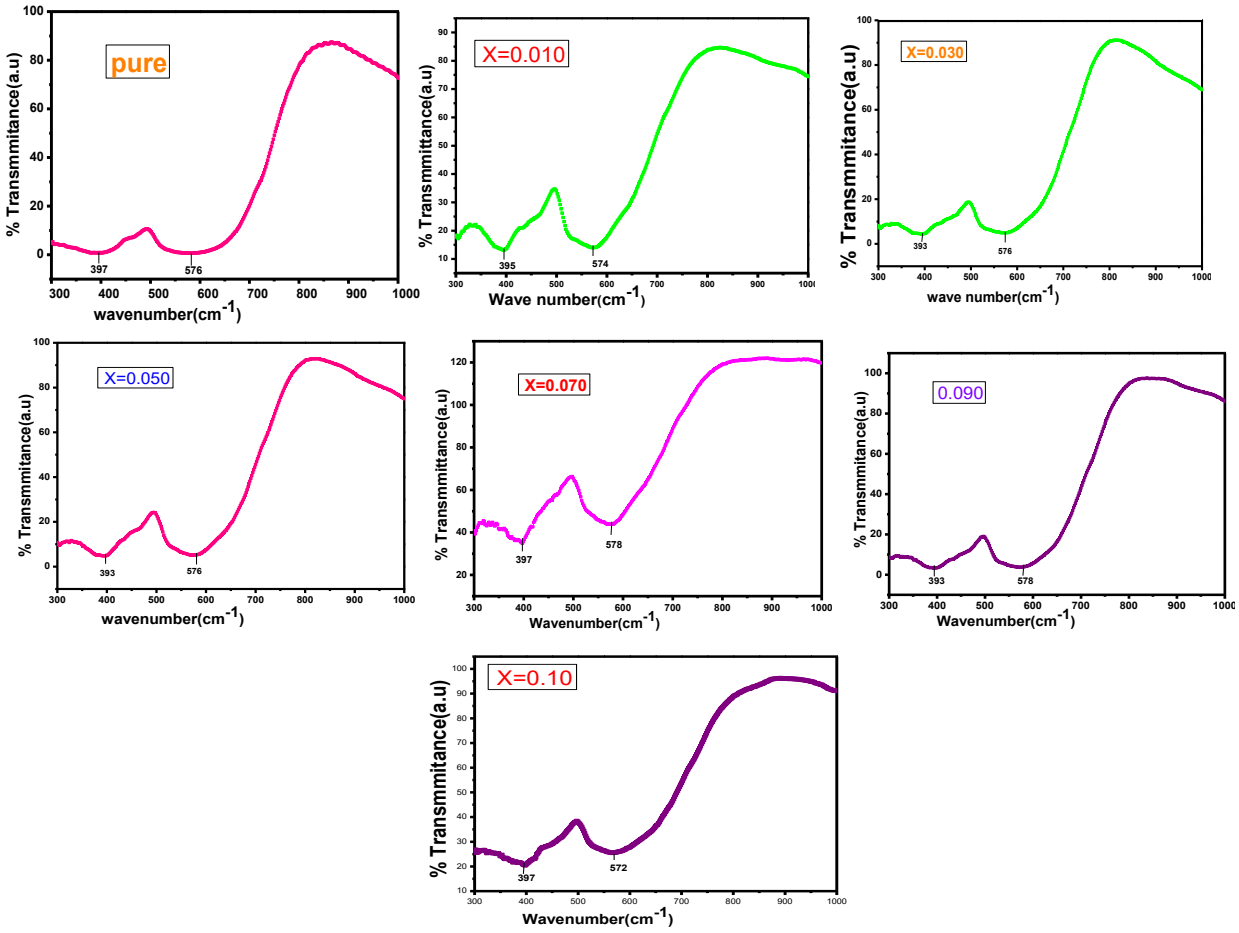

Figure (6) FT-IR images of$NiEr_xFe_{2-x}O_4$ ferrite samples

CONCLUSION:

- Erbium substituted nickel nano ferrites $NiEr_xFe_{2-x}o_4$where(X=0.00 to 0.10 with a step of 0.01) were prepared by Citrate Gel Auto Combustion technique is a convenient way for obtaining a homogeneous nano sized mixed ferrites, it is very simple and economical method where no specific heating or cooling rate is required .
- X-ray diffraction pattern confirms the formation of single phase cubic spinel structure. from standard data JCPDS.
- The crystalline size of the various Ni-Er ferrites was in the range of 15 to 39 nm.
- SEM micrographs of the composition indicate morphology of the particles is similar.They reveal largely agglomerated,well defined nano particles of the sample powder within homogeneous brader grain size distribution.
- EDS data give the elemental % and atomic % in the Ni-Er ferrites and it shows the presence of Ni,Er, Fe and O without precipitating cations
- FT-IR spectra show the two main absorption bands of ferrites it reveals that tetrahedral and octahedral of the spinel ferrits characterization.

ACKNOWLEDGEMENTS

The author **Gopalboda** conveys his sincere thanks to **Prof. A Panasa Reddy**, for his keen encouragement and guidance and RGNF-NFHE, new Delhi for awarding national fellowship to do ph.d. The author also grateful to head, department chemistry, university college of science Osmania University Hyderabad,

REFERENCES:

1. D.Fiorani in: j.l. Dormann.D.Fiorani (Eds),Magnetic properties Of fine Properties, North Holland Delta. Series,1992.
2. B.Visuanathan, V.R.K.Murthy, Ferrite materials Science and Technology, NerosaPublishing,1990
3. S.Gkakade, R.Ckambale, Y.D.kolekar,C.V.Ramana. Dielectric,electrical transport and magnetic properties of Er-Co Nano ferrites.
4. M.Raghasudha D.Ravinder, P.Veerasomaih.Characterization of Cr-Co Nano Ferrites by citrate-Gel auto combustion method.
5. A.Pradeep, G.Chandrasekaran. FTIR study of Ni,Cu and Zn substituted nano-particles of $MgFe_2O_4$Materials Letter 60(2006) 371-374
6. L.Zhao,H.Yang,X.Zhao,L.Yu,Y.Cui,andS.Feng,Mater.Lett.60,1-6(2006)
7. Cullity B D, Elements of X-ray diffraction (addition Wesley, Reading, Mass), 1959. ,p.132.
8. M.S.Ruiz, S.E.Jacobo, Electromagnetic properties of Li-Zn ferrites doped with aluminum, physica B 407(2012) 3271-3277.
9. K.Wykpis,A.Budnoik,E.Lagiewka,Science,Forum.636(2010)1053-1058
10. I.H Gul,W.A.Maqsood,J.Magn.Mater.320 (2008) 270.
11. M.J.Iqbal; m.NAshiqP.Hernadez-Gomezb; J.M. Munoz,J.Magn. Magn. Mater.2008, 320,881.Doi:10.1016/j.jmmm.2007.09.005
12. K.B.Modi,J.D.Gajera, M.P.Pandya,H.GVora,H.H.Joshi,Pramana Journal of Physics, Vol 62, No 5,May,2004,pages 1173-1180
13. N.MDeraj ,J. Anal.Appl. 82(2008) 212.
14. M.Srivastava,A.K. Ojha.S.Chaudary,P.K.Sharma,A.C.Pandey,J.Alloys Comp.494(2010)275.

Second National Conference on
RECENT ADVANCES IN APPLIED NANO MATERIALS
February 16-17, 2018 at Department of Physics, University College of Science, Saifabad, Osmania University, Hyderabad, Telangana State, India.

Synthesis and Characterization of Titanium Dioxide Nanoparticles

Satyanarayana.T[1], N.Usharani[2], J.Siva Kumar[3]
[1]Department Of Physics, Osmania University, Hyderabad, Telangana, India.
[2]Department of Physics, TKR Engineering College, Hyderabad, Telangana, India.
[3] Professor, Department of Physics, Osmania University, Hyderabad, Telangana, India.
Email - [1]satya.thodeti@gmail.com, [2]usha.nannuri@gmail.com

Abstract: *Titanium Dioxide Nanoparticles exhibit good photo catalytic properties. Nano-TiO_2 is chemically stable, relatively nontoxic, environment friendly and is used in antiseptic and antibacterial compositions. TiO_2-nanoparticles were prepared by chemical synthesis method using Titanium tetrachloride ($TiCl_4$) and Sodium carbonate (Na_2CO_3). TiO_2 nanoparticles were annealed at different temperatures and their properties have been evaluated by XRD, PSA, SEM, EDAX, TG/DTA, and UV-V Spectroscopy.*

Key Words: *TiO_2-Nanoparticles, $TiCl_4$, Sodium Carbonate, XRD, SEM, TG/DTA.*

1. INTRODUCTION:

Titanium dioxide (TiO_2) has become part of our everyday lives. It is found in various consumer goods and products of daily use such as cosmetics, paints, dyes and varnishes, textiles, paper and plastics, food and drugs, and even in paving stones. Titanium dioxide (TiO2) exhibits unusual structural, optical, electronic, magnetic and chemical properties. Nano titanium dioxide powder has many good functions and features, such as stable properties, non-toxic, high activity of photo catalysis, low cost and good at resisting chemical attack [1-4]. TiO2 is a well-known wide band gap semiconductor (3.0 to 3.2 eV) with its remarkable advantages of high refractive index, high transparency in the visible and infrared regions, good thermal and mechanical stabilities, high photo-conversion efficiency and good photo-stability which makes it a very important material with wide range of applications. Titanium dioxide exists in both crystalline and amorphous forms and mainly exists in three crystalline polymorphous, namely anatase, rutile and brookite. Anatase and rutile have a tetragonal structure, where as brookite has an orthorhombic structure. [2-3]. Since the physical properties of Nanoparticles depend on the Nanoparticle characteristics such as size and composition, it is essential to have a synthesis process in which these properties are controllable. TiO2 nanomaterials were synthesized using the most convient ways of synthesizing methods namely Sol-gel method [5, 6, 7, 8, 9, 10, 18], hydrothermal method [9, 10, 11, 12] solvothermal method [13, 14,] chemical vapour deposition [15, 16] and physical vapour deposition etc. In the process of synthesis of TiO2, the shape and crystal structure of the product significantly depends on raw materials used. Characterization and manipulation of individual nanostructures of TiO2 require not only extreme sensitivity and accuracy, but also atomic-level resolution. Therefore, this leads to various microscopes that would play a central role in characterization and measurements of nanostructures of TiO2 materials [5]. In this experimental procedure, sol-gel or chemical synthesis method is used for preparation of nanometer TiO2 powder. The products are characterized by XRD, PSA, SEM, EDAX, TG/DTA, and UV-Visible Spectroscopy. The sol-gel method is an attractive method for the synthesis of Titanium dioxide nanoparticles. Since this method is carried out in solution, tailoring of certain desired structural characteristics such as compositional homogeneity, grain size, particle morphology and porosity is possible

2. EXPERIMENTAL PROCEDURE:

Titanium tetrachloride is the inorganic compound and it is an important intermediate in the production of titanium dioxide nano particles. The chemical reaction taking place after adding sodium carbonate (Na_2CO_3) is given below.

$$TiCl_4+2Na_2CO_3 = TiO_2 + 4NaCl + 2CO_2$$

In Synthesis of Nano-TiO_2, initially 8M HCl Solution was prepared in 50 ml distilled water. Then we added 20 ml $TiCl_4$ in the above solution. 2.1M Na_2CO_3 solution was added drop wise until, the whole solution's pH was reached around 9 and precipitates were formed. These precipitates were washed several times. Then after washing

CH_3COOH (0.075M) was added in above solution, under vigorous stirring. Again solution was washed several times. After washing HNO_3 was added drop wise into above solution until solution pH was down to 1.2. Then Solution was centrifuged. Precipitates were dried in furnace at 100°C for 24 hours. After drying, sample was annealed at 650°C for 2 hours. The samples were grinded to form a fine nano powder.

3. RESULTS & DISCUSSIONS:

3.1. X-RAY DIFFRACTION

XRD analysis was carried out for TiO_2 nano material. The synthesized nano material is matched with the PCPDF card no **89-4921**, where the lattice constants for this material is **a = 3.777A° ,b= 3.777A° , c= 9.501A° ; α = 90° β = 90° Y = 90°**, the structure is Tetragonal, molecular weight is **79.90g,** Average crystalline size (D) is **36.61 nm** and d-spacing is calculated to be **0.35 nm**.

Figure.3.1. X-Ray Diffraction Patterns of Nano-TiO_2

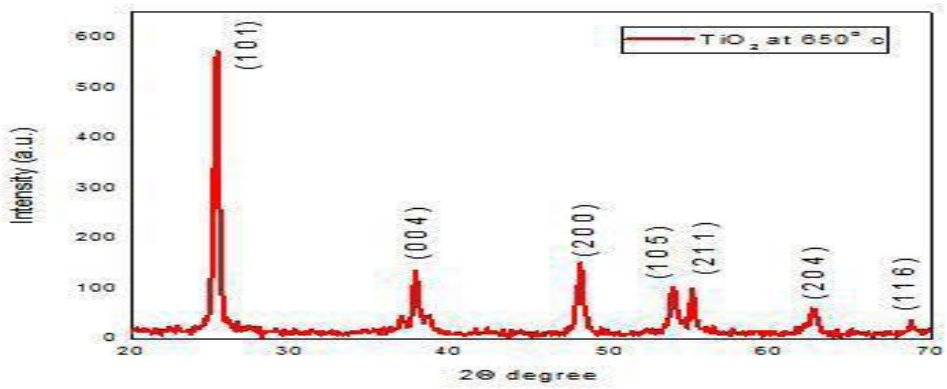

Theta(θ) Degrees	Theta(θ) Radians	FWHM(β in Degrees)	FWHM(β in Radians)	Cos(θ)	Crystallite size (D) = Kλ/βcosθ
14.35965	0.2506	0.17963	0.00313634	0.968758058	42.81100756
15.9632	0.2786	0.13848	0.002417861	0.961438534	55.11292497
17.9100	0.3125	0.16983	0.002965232	0.951540611	44.47663374
22.8644	0.3990	0.31969	0.005581787	0.921427005	22.87972897
24.3450	0.4249	0.24558	0.004287827	0.911079433	29.44979248
27.4282	0.4787	0.28244	0.004931402	0.887588775	24.94621089
				Total	219.6762986
				Average	**36.61271644**

Table.3.1. XRD data of TiO_2

3.2. PARTICLE SIZE ANALYZER (PSA):

TiO_2 nano material synthesized was characterized by PSA for particle size distribution analysis.

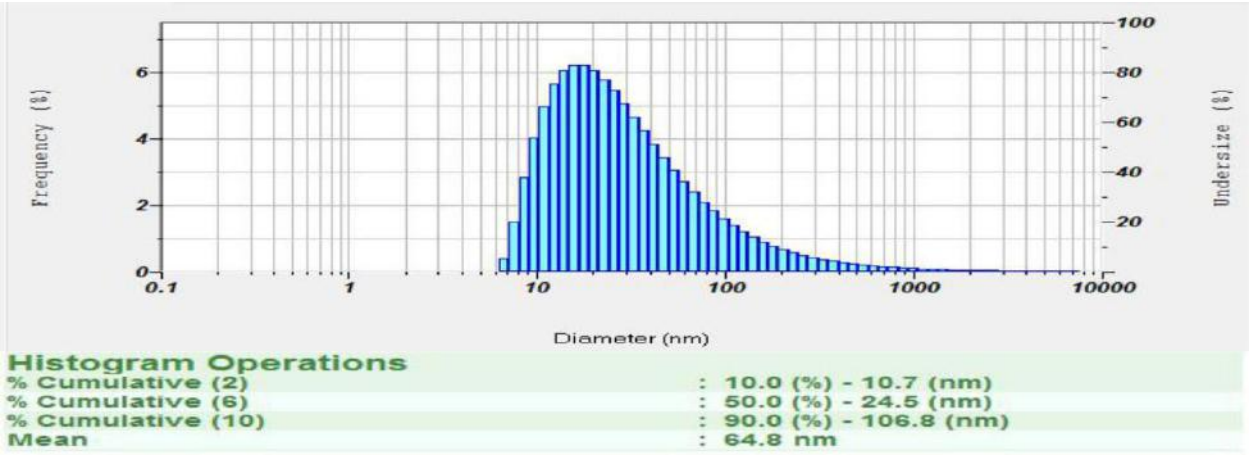

Figure .3.2.Particle distribution in the Particle Size Analyzer of Nano-TiO_2

The measurement of particle size distribution of TiO_2 nano material was characterized by Particle Size Analyzer. In the prepared sample it was observed that, particles have a wide size distribution, but the majority of them were dispersed within a narrow range, as shown in Fig.3.2. The average particle size of TiO_2 nano material from the histogram was found to be 64.8 nm.

3.3 SCANNING ELECTRON MICROSCOPY (SEM):

The surface morphology of TiO_2 nano material was investigated by using SEM and morphology images are shown in below Figure.3.3 which shows morphology of TiO_2 nano material with different scale 10µm, 10µm, 5µm, 4µm. From the below shown SEM images, we can infer that the obtained TiO_2 nano material is crystalline and contains non-porous surface morphology.

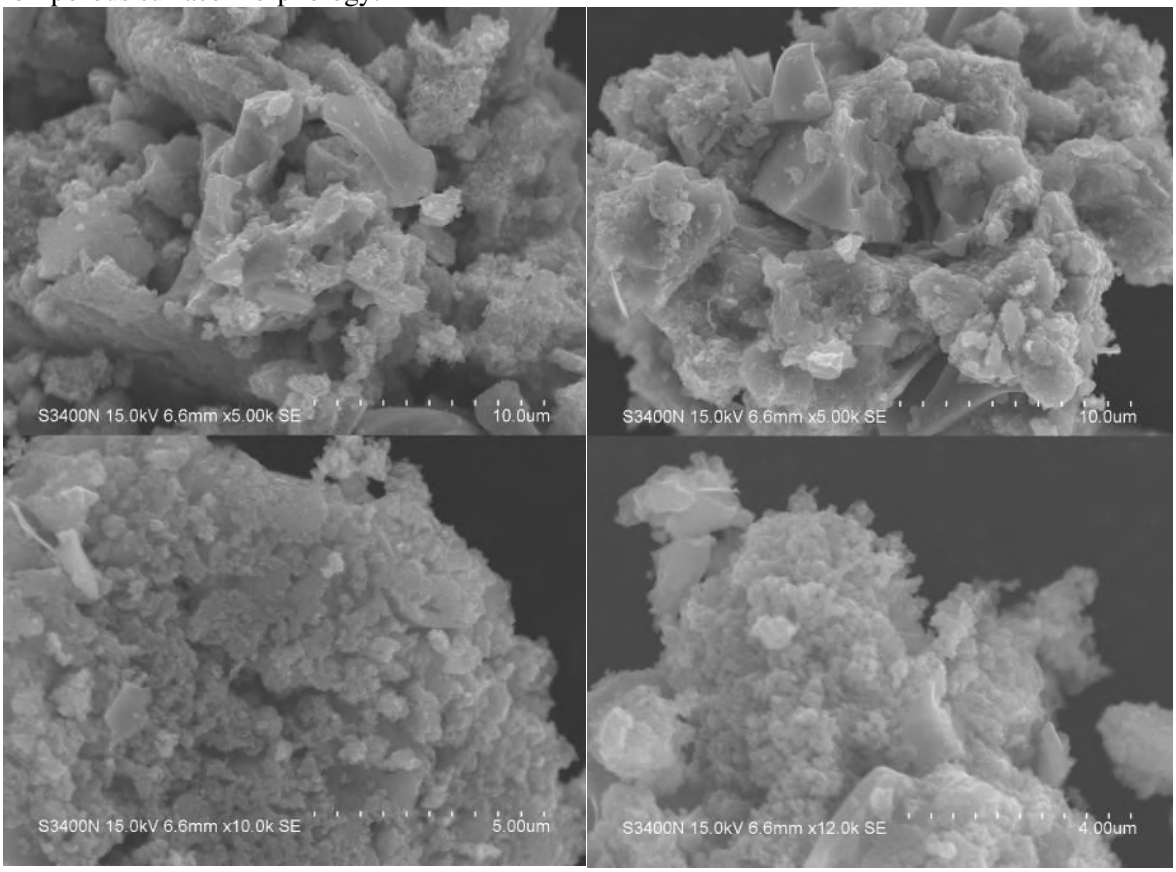

Figure.3.3.SEM images of Nano-TiO_2

3.4. ENERGY DISPERSIVE ANALYSIS OF X-RAY (EDAX):

EDAX studies are generally carried out to test the purity of the sample by giving us the details of all the elements present in the given sample. Below figure 3.4 shows EDAX results of synthesized TiO_2 nano material. Here by from the results we can exactly know whether we obtained the exact material or not. The elements present in the material are clearly known and whether the obtained material has any contamination can be known by EDX results.

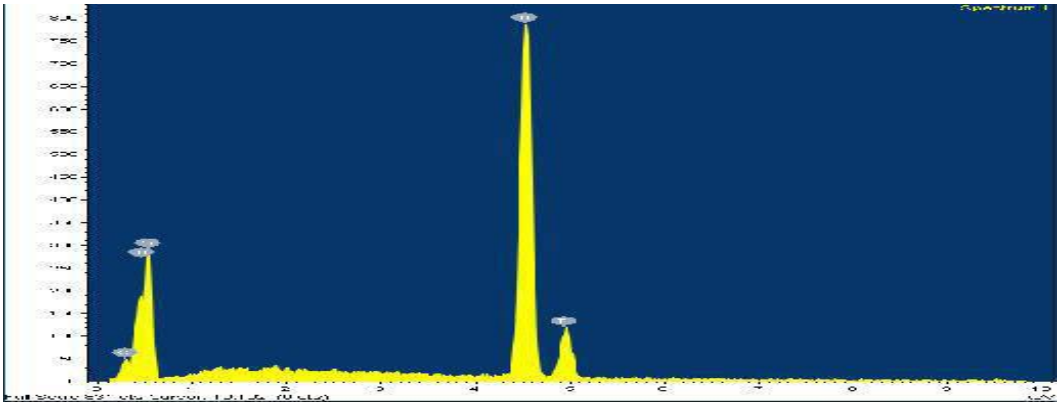

Figure.3.4. EDAX image of Nano-TiO_2

Element	Weight %	Atomic %
Titanium (Ti)	57.01	30.24
Oxygen (O)	40.17	63.80
Carbon (C)	2.82	5.96
Total	100%	100%

Table.3.2. EDAX result of TiO2 nano material

The EDAX analysis shows that the samples of TiO_2 nano material Table 3.2 contain Titanium 57.01%, Oxygen 40.17% and Carbon 2.82% elements in its composition i.e., the energy-dispersive spectroscopy (EDAX) of the nano particles dispersion confirmed the presence of elemental Titanium and oxygen. The presence of these compounds is assumed to be present as components of TiO_2 nano material.

3.5. THERMO GRAVIMETRY/DIFFERENTIAL THERMAL ANALYSIS (TG/DTA):

TG/DTA-analysis gives a lot of information about the compound tested. By making the measurements it is possible to understand the thermal stability and other properties correlated to the thermal stability, such as the ability of the reducing agent to restore the crystal structure of the TiO_2 nano material which may be altered during the oxidation. In Differential Thermal Analysis (DTA) the material under study and the inert reference material are made to undergo identical thermal cycles to record any temperature difference between sample and reference. There are two obvious weight loss stages. The first stage is from temperature 35.87°C to 131.192°C (0.54% wt loss) which can be attributed to the dehydration process of water molecules in the interlayer of TiO_2 nano material. The second is from 196.90°C to 794.79°C (0.801%), it is due to the burning decomposition of oxygen containing groups and due to the burning decomposition of carbon attached to TiO_2 nano material. The total weight loss is 1.44%.

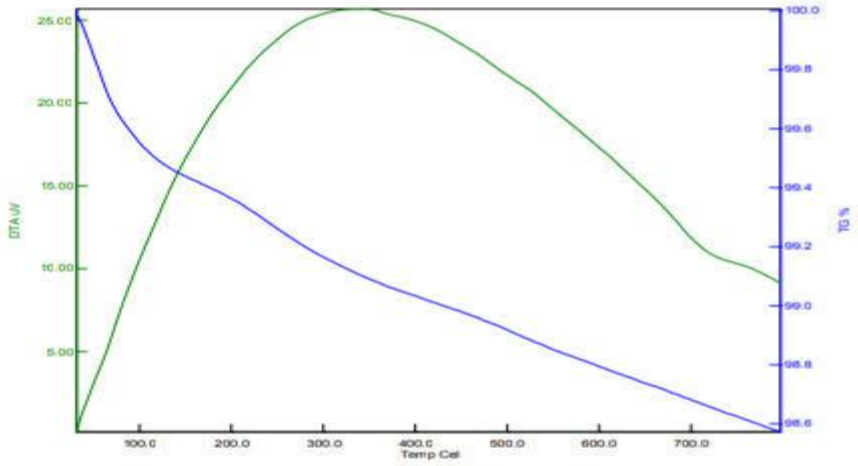

Figure.3.5. TG/DTA curves of Nano-TiO_2

3.6. ULTRAVIOLET-VISIBLE:

An Ultraviolet- Visible spectroscopy measurement was carried out to monitor the absorbance of TiO_2 nano material. The TiO_2 nano material that is formed has an absorbance maximum at 325nm.

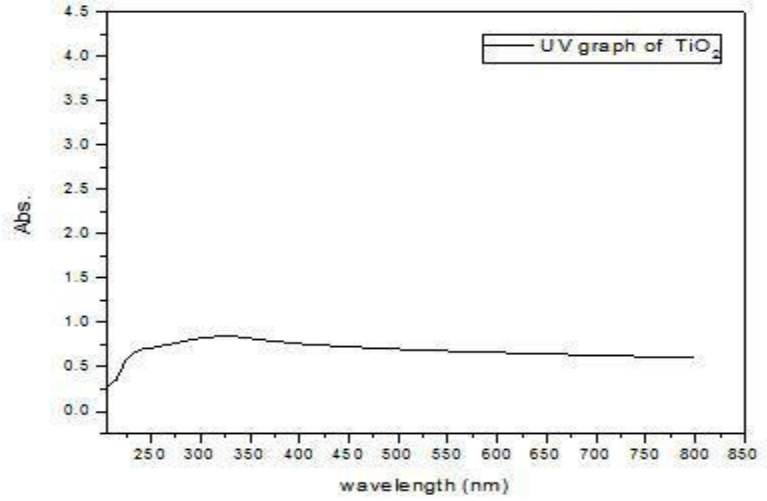

Fig.3.6. UV-VIS Absorption Spectra of the TiO_2 nano material

The TiO_2 sample was dispersed in distilled water by using ultra-sonication. Figure 3.6 show that the UV-Visible spectrum of TiO_2 nano material exhibited a strong absorption peak at 325 nm. Since TiO_2 nano material is an insulator material, absorption coefficient versus photon energy (eV) graph is plotted to determine it's bandgap as shown in the figure 3.7. From the graph, the bandgap is obtained as 6.08 eV.

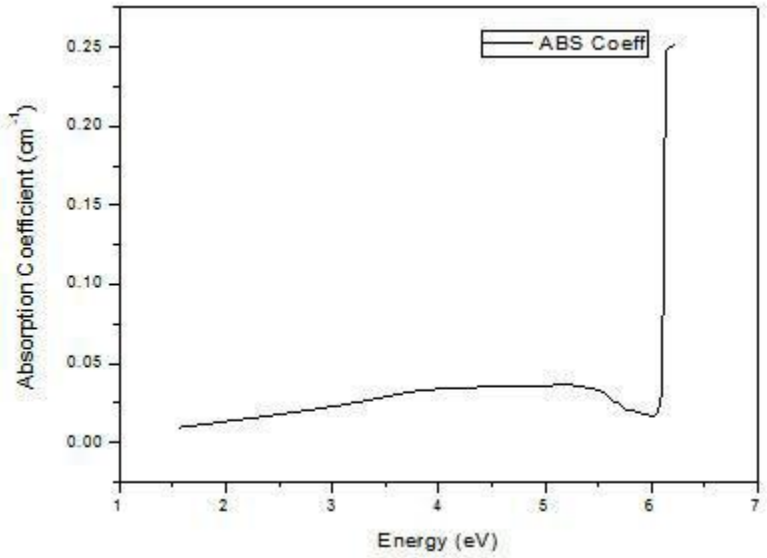

Figure.3.7.Photon energy (Band gap (eV)) vs. Absorption coefficient

4. CONCLUSION:

TiO2 nano material was synthesized by sol-gel method (Chemical synthesis) and characterized by XRD, PSA, SEM, EDAX, TG/DTA, and UV-Visible Spectroscopy. FromXRD, the average crystallite size was calculated as 36.61nm and average d spacing was calculated as 0.35nm. From Particle size analysis, the average particle size was observed as 64.8nm. From SEM images, the TiO2 nano material was crystalline and has non-porous surface morphology. From EDAX results, 57.01% Ti, 40.17% O and 2.82% C was contained in the synthesized TiO2 nano material which confirmed the formation of TiO2. From TG/DTA, the total weight loss was calculated as 1.44%. From UV-Visible spectroscopy, the band gap was observed as 6.08eV.

REFERENCES:

1. Ziquan Liu, Ruming Wang, Fangjun Kan And Fuyi Jiang , Synthesis and Characterization of TiO2 Nanoparticles- -Asian Journal of Chemistry; Vol. 26, No. 3 (2014), 655-659.
2. Venkatraman Madurai Ramakrishnan,Muthukumarasamy Natarajan, Agilan Santhanam,Vijayshankar Asokan, Dhayalan Velauthapillai , Size controlled synthesis of TiO2 nanoparticles by modified solvothermal method towards effective photo catalytic and photovoltaic applications - -Materials Research Bulletin 97 (2018) 351–360.
3. R.SharmilaDevi,Dr.R.Venckatesh, Dr.RajeshwariSivaraj , Synthesis of Titanium Dioxide Nanoparticles by Sol-Gel Technique -ISSN: 2319-8753.
4. On the Sol-gel Synthesis and Characterization of Titanium Oxide Nanoparticles
5. Varun Chaudhary, Amit K. Srivastava and Jitendra Kumar-Materials Research Society-DOI: 10.1557/opl.2011.759.
6. Stotaw Talbachew Hayle, Girma Goro Gonfa , Synthesis and characterization of titanium oxide nanomaterials using sol-gel method- -American Journal of Nanoscience and Nanotechnology
7. 2014; 2(1): 1-7.
8. Ajay Sharma, R.K. Karn, S.K. Pandiyan , Synthesis of TiO2 Nanoparticles by Sol-gel Method and Their Characterization- -ISSN: 2350-0255.
9. S.Perumal, C.Gnana Sambandam, K.Monikanda prabu, S.Ananthakumar , Synthesis And Charecterization Studies Of Nano Tio2 Prepared Via Sol-Gel Method -IJRET-eISSN: 2319-1163.
10. Y. Bessekhouad, D. Robert, and J. V. Weber , Preparation of TiO2 nanoparticles by Sol-Gel route- -Vol. 05 International Journal Of Photoenergy 2003.
11. R. Vijayalakshmi and V. Rajendran , Synthesis and characterization of nano-TiO2 via different methods- -ISSN 0975-508X-CODEN (USA) AASRC9.
12. Mrs.M. Kavitha, Dr.C.Gopinathan and P.Pandi , Synthesis and Characterization of TiO2 Nanopowders in Hydrothermal and Sol-Gel Method- -ISSN 2278-7763.

13. Bruna Andressa Bregadiolli, Silvia Leticia Fernandes, and Carlos Frederico de Oliveira Graeff , Easy and Fast Preparation of TiO2 - based Nanostructures Using Microwave Assisted Hydrothermal Synthesis- -DOI: http://dx.doi.org/10.1590/1980-5373-MR-2016-0684.
14. G. C. Collazzo1, S. L. Jahn, N. L. V. Carreño and E. L. Foletto , Temperature And Reaction Time Effects On The Structural Properties Of Titanium Dioxide Nanopowders Obtained Via The Hydrothermal Method -ISSN 0104-6632.
15. C. S. Kim, B. K. Moon, J. H. Park, S. T. Chung, S. M. Son, J. Cryst. Growth,254 (2003) 405.
16. G. Melcarne, L. D. Marco, E. Carlino, F. Martina, M. Manca, R. Cingolani, G.Gigli, G. Ciccarella, J. Mater. Chem., 20 (2010) 7248.
17. S. Seifried, M. Winterer, H. Hahn, Chem. Vap. Deposition, 6 (2000) 239.
18. J. A. Ayllon, A. Figueras, S. Garelik, L. Spirkova, J. Durand, L. Cot,
19. J. Mater. Sci. Lett., 18 (1999) 1319.
20. Shipra Mital Gupta, Manoj Tripathi , A review on the synthesis of TiO2 nanoparticles by solution route- - DOI: 10.2478/s11532-011-0155-y.
21. S. Mahshid , M. Askari, M. Sasani Ghamsari , Synthesis of TiO2 nanoparticles by hydrolysis and peptization of titanium isopropoxide solution- -Journal of Materials Processing Technology 189 (2007) 296–300- doi:10.1016/j.jmatprotec.2007.01.040.
22. Z R Ismagilov, L T Tsykoza, N V Shikina, V F Zarytova, V V Zinoviev (deceased), S N Zagrebelnyi , Synthesis and stabilization of nano-sized titanium dioxide- - DOI 10.1070/RC2009v078n09ABEH004082.
23. Ruud J.B. Peters, Greet van Bemmel, Zahira Herrera-Rivera, Johannes P.F.G. Helsper, Hans J.P.Marvin, Stefan Weigel, Peter Tromp, Agnes G. Oomen, Anton Rietveld, and Hans Bouwmeester , Characterisation of titanium dioxide nanoparticles in foodproducts: Analytical methods to define nanoparticles- -J. Agric. Food Chem.
24. Matteo Crosera,Andrea Prodi ,Marcella Mauro ,Marco Pelin,Chiara Florio , Titanium Dioxide Nanoparticle Penetration into the Skin and Effects on HaCaT Cells- - Int. J. Environ. Res. Public Health 2015, 12, 9282-9297; doi:10.3390/ijerph120809282.
25. Gigliola Lusvardi , Corrado Barani, Federica Giubertoni and Giulia Paganelli , Synthesis and Characterization of TiO2 Nanoparticles for the Reduction of Water Pollutants- - Materials 2017, 10, 1208; doi:10.3390/ma10101208.
26. Syed Niaz Ali Shah, Zahir Shah, Muzammal Hussain, and Muzaffar Khan , Hazardous Effects of Titanium Dioxide Nanoparticles in Ecosystem- - https://doi.org/10.1155/2017/4101735.

Second National Conference on
RECENT ADVANCES IN APPLIED NANO MATERIALS
February 16-17, 2018 at Department of Physics, University College of Science, Saifabad, Osmania University, Hyderabad, Telangana State, India.

FTIR Spectroscopic Study on Inner Membrane of Egg Shell of Chicken *Gallus gallus domesticus*

Juveria Iram, Kaleem Ahmed Jaleeli & Adeel Ahmad

Biophysics Research Laboratory, Department of Physics, Nizam College (Autonomous), Osmania University, Hyderabad – 500 001, India
Email - dr_adeelahmad@yahoo.com kaleemjaleeli@gmail.com

Abstract: *The paper presents FTIR analysis of inner membrane of eggshell of chicken Gallus gallus domesticus. Fresh samples of egg shells are cleaned; dried and inner membrane of the shell is separated carefully for FTIR analysis. FTIR spectrum reveals a series of bands related to fats and proteins. Calcium carbonate is the major constituent (about 90%) of the shell, but it is absent in the inner shell membrane as characteristic band at 712 cm^{-1} is not seen in the spectrum. However, characteristic bands at 870 cm^{-1} and 1450 cm^{-1} suggest that inner shell membrane possesses carbonate ion.*
The study concludes that the major constituent of inner shell membrane is organic (protein and fat) in contrast to the shell.

Key Words: *Egg shell; chicken; FTIR; Carbonate ion; fats; proteins; inner membrane of shell.*

1. INTRODUCTION:

The egg is composed of a central yolk surrounded by the albumin (egg white), egg shell membranes (inner and outer shell), and calcified egg shell. The meshwork of interlaced fibers is organized into morphologically distinct inner and outer sheets that enclose the egg albumin. The fibers of the outer shell membrane become incorporated into the base of the eggshell.

The structure of the egg shell in relation with its quality, as commercial interest, has been investigated using various microscopy techniques [1, 2]. Simons [3, 4] reported results of a comprehensive study of hen's egg shell and membrane involving the techniques of optical microscopy, TEM and SEM and also reviewed previously published data.

Hui, et al [5] made Fourier transform infra-red spectroscopic study on hen's egg shell alone. Reaction of discarded hen egg shell with tri-calcium phosphate in presence of steam at 900 ^{0}C and subsequent aging for 24 hrs resulted in the formation of synthesized Hydroxyapatite. The FTIR investigation of these samples showed all the characteristic bands for Hydroxyapatite [6, 7].

A search of literature reveals that there exists no information on FTIR analysis of inner membrane of eggshell in its natural state. In view of this, the aim of this paper is to analyse spectroscopically inner membrane of egg shell of the chicken *Gallus gallus domesticus* in its natural condition.

2. MATERIALS AND METHODS:

The egg shell samples of chicken *Gallus gallus domesticus* were collected, cleaned with water thoroughly and dried in room temperature. The inner membrane was removed mechanically and was powdered using pestle and mortar for the use of FTIR analysis.

Infrared spectrum of the inner shell membrane (ISM) powder was recorded in FTIR spectrometer (Shimadzu FTIR – 8400S) in the range of 4000 cm^{-1} to 400 cm^{-1}. For the spectral recording, a small quantity of powder was mixed with potassium bromide (KBr) in the ratio of 1:4 and pressed in a stainless steel dye to produce thin KBr wafer, containing a relatively high concentration of the sample in IR transparent KBr matrix.

3. RESULTS AND DISCUSSION:

Fig.1. shows FTIR spectrum of inner egg shell membrane of chicken, recorded in the range of 4000 cm^{-1} to 400 cm^{-1}. It reveals a series of bands with different intensities.

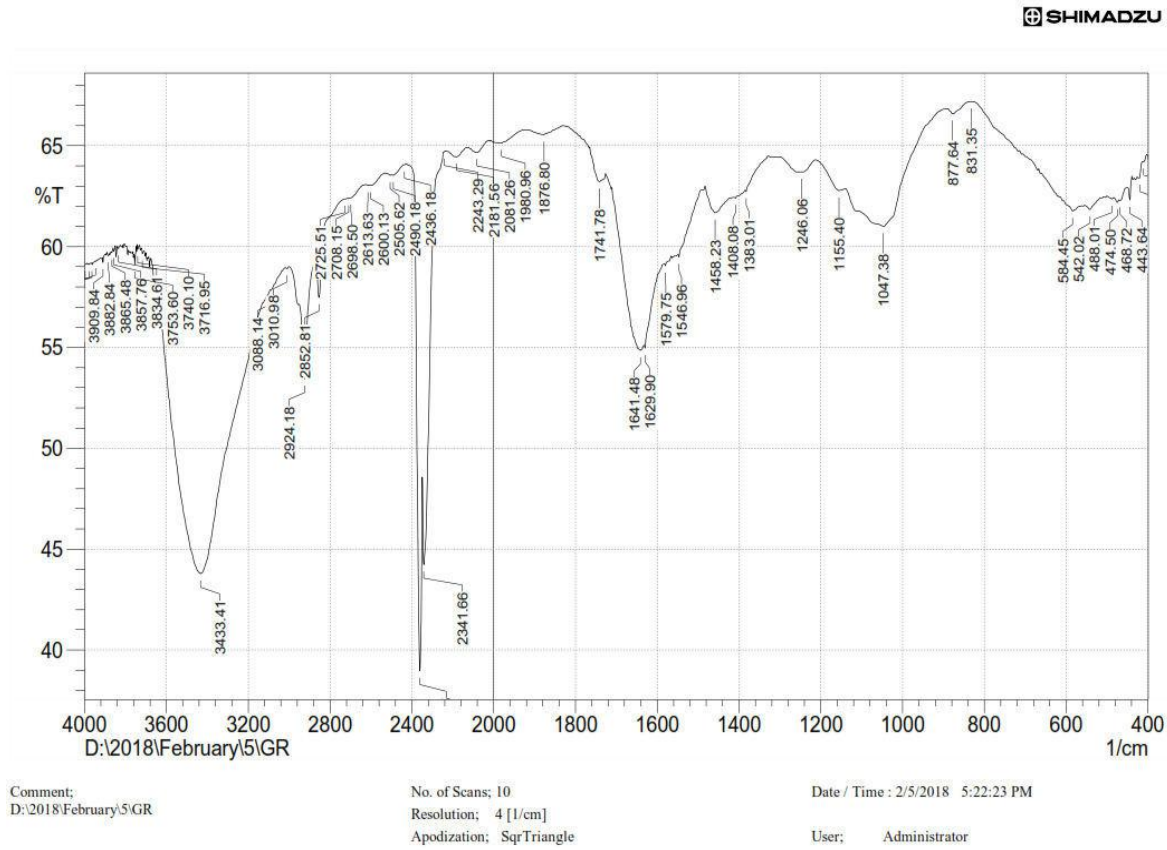

Fig. 1. FTIR spectrum of inner shell membrane of *Gallus gallus domesticus*

Table 1. FTIR data on inner shell membrane of *Gallus gallus domesticus*

Wave Number (cm^{-1})	*Transmittance (%)*	*Characteristic vibrations of functional groups*
3433	43.78	OH stretching mode of water
3088	57.83	Amide B
2924	53.43	CH_2 Asymmetric stretch: mainly lipids
2852	57.48	CH_2 Symmetric stretch: mainly lipids
1641	54.84	C=O stretching vibrations of collagen
1629	54.97	Amide I band of pleated sheath structures of proteins
1546	59.47	Amide II band of protein; N-H stretching
1458	61.67	CH_2 Bending: Mainly lipids
1448	95.03	P-O anti symmetric stretch
1408	62.41	P=O asymmetric stretching of phosphodiesters
1246	63.70	Amide III band components of proteins C-N stretch with N-H bend
1155	62.78	C-O-C, C-O dominated by ring vibrations in Carbohydrates
1047	60.99	
877	66.58	Carbonate ion

The major bands at 1629 cm^{-1} (C - H stretch); 1546 cm^{-1}(N - H stretch and C-O- anti symmetric stretch); and 1246 cm^{-1} (C-H stretch with N-H bend) related to Amide I, Amide II and Amide III respectively in the spectral region 3000 cm^{-1} to 1500 cm^{-1} are attributed to the organic material, which are essentially proteins.

The principal characteristics bands at 2924 cm^{-1} (CH_2 Asymmetric stretch), 2852 cm^{-1} (CH_2 Symmetric stretch) and 1458 cm^{-1}(CH_2 Bend), observed in the spectrum, are concerned mainly with lipids.

But the bands at 1430 cm^{-1}, 875 cm^{-1} and 715 cm^{-1}, concerned with calcium carbonate, are not seen in the spectrum revealing the fact that inner eggshell membrane is free from calcium carbonate. However, characteristic bands at 870 cm^{-1} and 1450 cm^{-1} suggest that inner shell membrane possesses carbonate ion.

The study concludes that the major constituent of inner shell membrane of *Gallus gallus domesticus* is organic (protein and fat) in contrast to the shell.

REFERENCES:

1. Bunk M J, Balloun S L 1978 Ultrastructure of the mammillary region of low puncture avian eggshells. Poultry Science 57: 639–647
2. Carnarius K M, Conrad K M, Mast M G, Macneil J H 1996 Relationship of eggshell ultrastructure and shell strength to the soundness of shell eggs. Poultry Science 75: 656–663.
3. Simons P C M. (197la). Ultrastructure of the hen eggs he 11 and its phys i o 1 ogi ca 1 ; nterpretation. Centre for Agricultural Publishing and Documentation, Wageningen, The Netherlands . pp. 90 .
4. Simons PCM. (l971b). Ultrastructure of the hen eggshell and its physiological interpretation. Figures. Centre for Agricultural Publishing and Documentation, Wageningen, The Netherlands. pp. 46.
5. P. Hui, S.L Meena, Gurbhinder singh, R.D Agarwal, Satyaprakash, Synthesis of hydroxyapatite bio-ceramic powder by hydrothermal method, J. Min. Mater. Char. Engg., Vol. 9, No. 8(2010), pp. 683-692.
6. V. Jokanovic, D. Izvonar, M. D. Dramicanin, B. Jokanovic, V. Zivojinovic, D. Markovic, B. Dacic, Thin films of SiO_2 and hydroxyapatite on titanium deposited by spray pyrolysis, J. Mater. Sci: Mater. Medical, Vol. 17(2006), pp. 539 –546.
7. V. Jokanovic, D. Uskokovic, Calcium hydroxyapatite thin films on titanium substrates prepared by ultrasonic spray pyrolysis, Mater. Transaction, Vol. 46(2005), pp. 228–235.

Second National Conference on
RECENT ADVANCES IN APPLIED NANO MATERIALS
February 16-17, 2018 at Department of Physics, University College of Science, Saifabad, Osmania University, Hyderabad, Telangana State, India.

A Comparative FTIR Spectroscopic Study On Horny Material Of Ox, Sheep And Goat

V.Arun kumar[1], Kaleem Ahmed Jaleeli[2] and Adeel Ahmad[3]

[1, 2, 3] Biophysics Research Laboratory, Department of Physics, Nizam College (Autonomous), Osmania University, Hyderabad – 500 001, India
E- mail: dr_adeelahmad@yahoo.com, mail2arun09@gmail.com

Abstract: *The paper deals with a comparative FTIR spectroscopic study on horny material of Ox, Sheep and Goat. The FTIR spectra of horny material show a series of absorption band with different intensities. These absorption bands identify the various functional groups of the molecule. The IR spectrum reveals the constituents of Horny materials. The constituents Keratin and Calcium phosphate are present in larger quantity but Carbonate and Nitrate ions are relatively lesser whereas water content is very low in the horny material. The study suggests that IR spectroscopy can be used for identification of amino acids and various ions present in the horny materials.*

Key Words: *FTIR, horny material, amino acids, keratin.*

1. INTRODUCTION:

Infrared spectroscopy is a potential tool to provide valuable information in the study of Biological systems. It is very much helpful in the study of structure of various macromolecular components and their conformations within tissue. In most of the cases, infrared spectroscopy gives rapid qualitative and quantitative identification of organic and inorganic constituents and their combinations in mineralized biological tissues.

Li shengqing et al [1] The rhino ceros horn has two absorption peaks of P-H stretching vibration of sphingolipid at 2350cm^{-1}, while other horns only have one or no absorption peak in this region. What's more, compared with other horns, it has weak absorption peaks of C=O stretching vibration of hexosamine at 1733 cm-1, and absorption peaks of S-O stretching vibration of taurine at 881 cm^{-1}. However, other horns have none of these absorption peaks. R. Ashok kumar and M. Ramaswamy [2] (2014) The FTIR spectroscopic studies revealed different characteristic peak values with various functional compounds in the extracts. The FTIR of methanol leaf confirmed the presence of amide, alcohols, phenols, alkenes, carboxylic acids, aldehydes, ketenes, alkenes, primary amines, esters which showed major peaks. Dominique M.R et al [3] The effect of temperature on wheat gluten conditioned at the following water contents, 0%, 13%, and 47% (wet weight basis), was studied by FTIR spectroscopy over the temperature range of 25-85°C. A detailed discussion of the assignment of the amide I band is given. At 0% hydration no changes in the secondary structure with temperature could be detected; spectra were consistent with a tight disordered structure with many protein-protein interactions. At 13% hydration, distinctive changes occurred in the low-frequency region of the amide I band (1630 -1613 cm-1). This was attributed to changes in the, sheet structure. On cooling to 25°C, these changes were mainly reversed. It was noted that most of the changes observed occurred above the glass transition temperature. At 47% hydration, more complex changes took place: as the temperature was raised distinct bands at 1630 and 1613 cm^{-1}merged. Rragavender et al [4] (2011) Detected the functional groups in varius extracts of 'Aerva lanata' using spectroscopic method. Ramanamorthi and Kennan. S [5] (2007) screened the bioactive group of chemicals in the dry leaf powder of Calotropis gigantean by FTIR analysis. Jeanette. M and cardamone [6] Investigations of keratins extracted from wool by reduction hydrolysis and by alkaline hydrolysis showed that their chemical compositions and secondary structures were similar to original wool. The keratin iso-lates were similar in amino acid, Amides I and II, and secondary structure to each other and to original wool. Baddiel [7] reports the use of multiple internal reflectances to study the surface structure of human hair directly rather than by grinding to form a KBr pellet. Using this technique, he shows interesting shifts in protein bands of the cuticle layer as compared to the internal cortical material. Low and Severdia [8] report the use of FTIR-photo thermal beam deflection spectroscopy to characterize the spectrum of a single human hair in a non-destructive manner. Weston [9]

and Alter and Bit-Alkhas[10], all use KBr pellet technique. R.Gangadhar at al [11] reports that Ovine scapular cartilage contains mainly collagen and proteoglycan, carbonate ions and phosphate ions are in very small quantity.

A search of literature reveals that in spite of extensive investigations on infrared spectroscopy of human skin, hair, nail, bone and collagen on different aspects and their constituents such as lipids and proteins, no information is available on qualitative and quantitative identification of organic and inorganic constituents and their combinations. In view of this, in the present investigation, infrared spectroscopic study has been made on horny material, in order to assess its molecular composition. IR studies were made on molecular composition.

2. MATERIALS AND METHODS:

Horn samples are collected from Slater house. The samples are cleaned with water and sun dried 4 or 5 days and cut in to the discs. One sample was powdered for FTIR analysis. FTIR spectra of powdered samples were recorded with Thermo - Nicolet Nexus 670 FTIR spectrometer.

3. RESULTS AND DISCUSSION:

Fig. 1, 2, 3 are FT – IR spectrums of Ox, Sheep, Goat horn, which reveals a series of bands with different intensities. Table-1 presents data on wave numbers and corresponding Transmittance (%) obtained from FTIR spectra along with characteristic vibrations of functional groups.

Fig. 1. FT IR spectra of Ox Horn

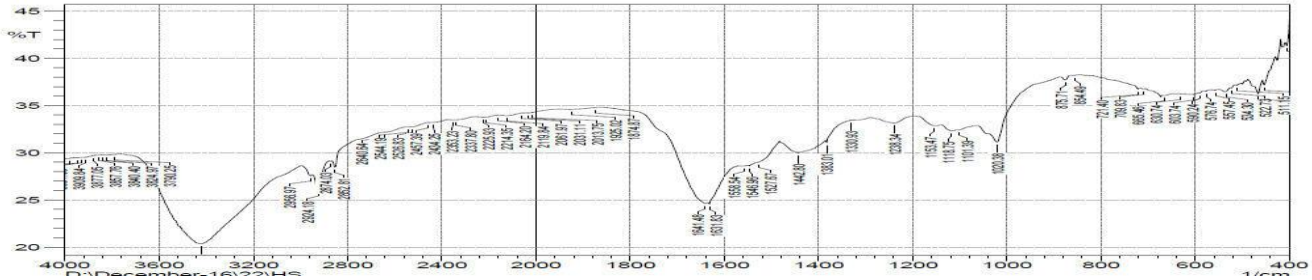

Fig. 2. FT IR spectra of Sheep Horn

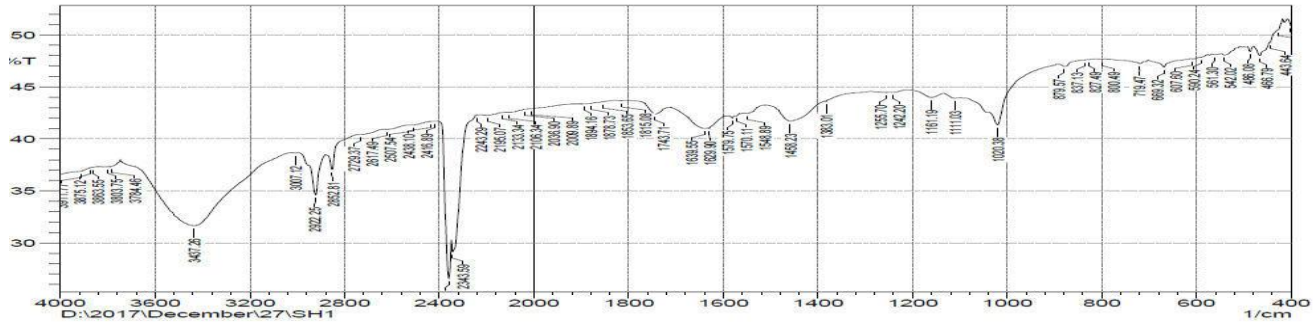

Fig. 3. FT IR spectra of Goat Horn

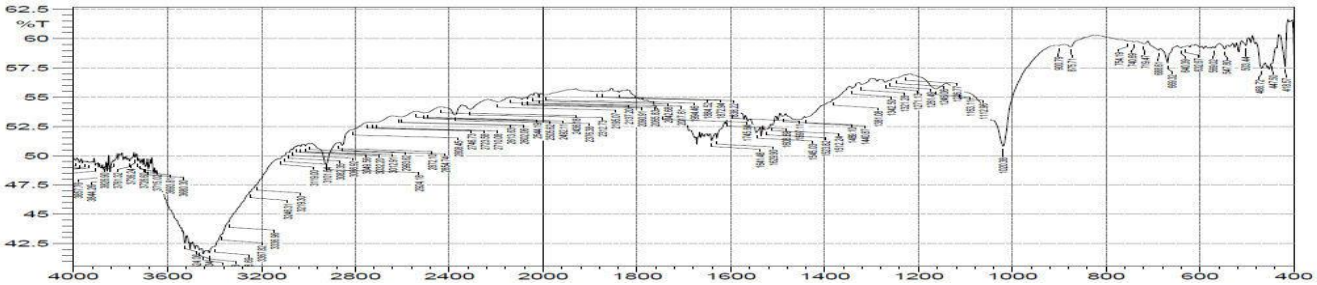

For the systematic analysis, IR spectrum is divided into four regions. Region I is from 4000 cm^{-1} to 3000 cm^{-1} concerned with water and hydroxyl group. This region is of considerable interest, because it reveals the nature of hydrogen bonding. Region II is 3000 cm^{-1} to 1500 cm^{-1}, where in bands for functional groups are observed. In this

region major IR absorption pertaining calcium phosphate occurs. Region III is 1500 cm^{-1} to 600 cm^{-1}, which has significant importance in the context of biological minerals and their combinations. The spectra of horn powder indicate the presence of bands characteristics of calcium phosphate ion, carbon ion and water molecule and also of some functional groups. Region IV is 600cm^{-1} to 400cm^{-1} are related to disulphide and phosphorus. Most intensive bands are centered at 1641$cm^{-1}$and 1545cm^{-1} in FTIR spectrum. They correspond to Amide-I and Amide-II. Both bands are representative of secondary structure of protein. Amide-I peak arises from C=O hydrogen bonded starching vibrations. Amide-II is attributed to C-N stretching. Amide-I and Amide-II absorption bands are associated also with specific secondary sub- structure such as α- helix, β-plated sheet. The bands at1238cm^{-1}, 1242cm^{-1} and 1246cm^{-1} are related to Amide-III band component of proteins. The dominative bands at 1639cm^{-1} provide the β-plated structural conformation of protein. Amide-I and Amide-II regions are conformed that keratin protein present in the sample. The bands 446$cm^{-1}$and 448cm^{-1} pertains to phosphate ion. That bands conforming major inorganic component presents in the sample was calcium phosphate. The band at 590cm^{-1} shows the crystalline nature of the sample. According to beers law we can easily find the absorbance from percentage of transmittance data. The Relation between absorbance and transmittance → $A=2- \log_{10} \%T$

Table: 1 FTIR data on horny material

Wave Number in cm^{-1} (% Transmittance)			Characteristic vibration of functional groups
Ox	Sheep	Goat	
3840(29.7)	3784(37.3)	3844(48.41)	H2O (atmospheric absorption)
3790(29.8)	3437(31.6)	3462(41.9)	H-O-H stretching of hydroxyl group
		3446(41.57)	Week N-H (2^{o} amine)
		3246 (46.8)	Amide-A N-H stretching of protein
	3007 (38.6)	3066 (50.4)	Amide-B N-H stretching of protein
	2729 (40.4)	3032(50.77)	Stretching vibration CH_3, CH_2, CH
2956 (27.5)	2922(34.60)	2993(51.01)	Aliphatic C-H stretching
2874(29)	2852(37.06)	2854(51.08)	CH symmetric stretching of CH_2,in fatty acids
2544(32.7)	2507(41.33)	2505(53.78)	-SH
1925(34.5)		1994(55.21)	Strong C=C asymmetric state
1874(34.7)	1894(43.4)	1884(55.4)	High content unsaturated fatty acids
	1743(42.4)	1745(53.5)	C=O stretching vibrations of ester functional groups in phospholipids, carbonates
1641(24.5)	1639(41)	1641(51.2)	β plated sheet structure of protein, Amid-I band component region. α- helical structure of(C=O) different conformations .
1558(28.5)	1548(42.44)	1523(52.2)	Amide-II peak region of protein (NH,C-N)
1442(29.9)		1440(53.2)	P-O anti symmetric stretch
1238(33.1)	1242(42.48)	1246(56.6)	Amide-III bond components of protein(C-N)
		900 (59.4)	C-O, C-C Stretching
875 (37.7)	879(46.9)	875(59.2)	NO_2^- ,NO_3^-
630 (36.2)		632(59.3)	C-H bending
603(36.14)	542(48)	547(59.1)	S-S disulphide(week)
576(36.5)			P-O anti symmetric stretching
	466(48)	468(57.4)	P-O symmetric stretch

4. CONCLUSION:

The study conclude that the constituents of horny materials are mainly keratin, Calcium phosphate are present in larger quantity but Carbonate and Nitrate ions are relatively lesser whereas water content is very low in the horny material.

REFERENCES:

1. Li shengqing, Zu Endong and , Li u Lijun(2011), Advanced Materials reach. Vol.177, pp; 636- 639.
2. R. Ashok kumar and M. Ramaswamy(2014), Int. J. Curr. Microbiol. App. Sci., Vol.3, pp:395- 406.
3. Dominique. M.R, Georget and Peter S. Belton; Biomacromolecules, Vol.7, No.2, (2006), pp: 469- 475.
4. Ragavendran. P, Sophia.D, Arul Raj.C, and Gopala Krishnan. V. K: Functional group analysis of various extracts of 'Aerva lanata' by FTIR Spectrum. Pharmacologyonline.1, pp: 358- 365.
5. Ramanamurty. N and Kennan(2007). S. Fourior transform infrared spectroscopic analysis of a plant . Romanian Journal of Biophysics. 17(4), pp; 269- 276.
6. Jeanette. M , Cardamone(2010); Journal of molecular structure, 969, pp;97-105.
7. C. B. Baddiel(1998), Structure and reactions of human hair keratin: An analysis by infrared spectroscopy, J. Mol. Biol., 38,pp;181-199.
8. M. J. D. Low and A. G. Severalia(1983), Infrared spectra of a single human hair, Spectrosc. Lett., 16(11) , pp;871-877.
9. G. J. Weston(1955), The infra-red spectrum of peracetic acid-treated wool, Blochim. Biophys. Acta., 47, pp;462-464.
10. H. Alter and M. Bit-Alkhas(1969), Infrared analysis of oxidized keratins, Text. Res. J., 39, pp;479-481.
11. R.Gangadhar, Kaleem Ahmed jaleeli, Adeel Ahmad(2015), FTIR Spectroscopy of ovine scapular cartilage , Int.J.of.sci.Environment and Tech,Vol.4, No.4, (2015),PP.1-5.

Second National Conference on
RECENT ADVANCES IN APPLIED NANO MATERIALS
February 16-17, 2018 at Department of Physics, University College of Science, Saifabad, Osmania University, Hyderabad, Telangana State, India.

FTIR Spectroscopic Study on Skeletal Muscle of Chicken*Gallus gallusdomesticus*

Mallika kamilekar [1], Kaleem ahmed jaleeli[2], Adeel ahmad[3]
[1.]Assistant Prof. in physics,Arjuncollege of science and technology,Hyderabad
[2]Biophysics Research laboratory, Department of Physics, Nizam College (Autonomous), Osmania University, Hyderabad - 500001, India
Email - kaleemjaleeli@gmail.com

Abstract: *The paper presents FTIR spectroscopic data on skeletal muscle of chicken Gallus gallusdomesticus. The studyreveals the presence of glycogen, contractile proteins, fatty acids, phospholipids, triglycerides and cholesterol along with phosphates in the skeletal muscle. Conformations of proteins are also evident from the spectral study. Amide I and Amide II concerned bands present in the spectrum suggest that proteins in chicken muscle exist in both α and β conformations. The bands related to phosphate ion and carbonate ion can be seen in the IR spectrum.*

Key Words: *FTIR; Chicken; Muscle.*

1. INTRODUCTION:

Fourier transform infrared (FTIR) spectroscopy is a potential tool to extract vital information in the study of biological system. Extensive research work is being done on biological apatite and other biological inorganic materials.

EbruDeniz, et. al., [1] studied to detect the meat types at different concentrations in the mixed raw meat samples by using FT-IR spectroscopy. Mixtures of chicken meat and beef were prepared by adding chicken meat at 0, 20, 40 and 100% (wt/wt) concentrations to beef as the main meat type. They reported that IR spectra were promising and indicating especially five bands (wavenumbers between 2917-2920 cm^{-1}, 2849-2850 cm^{-1}, 1740-1742 scm^{-1}, 1196-1197 cm^{-1}, 1176-1177 cm^{-1}) and concluded that FTIR could be used in identifying species in the beef and chicken meat mixtures.

Gangadhar, et. al.,[2] reported, based on FTIR spectroscopy, that the constituents of ovine scapular cartilage are mainlycollagen and proteoglycans; Carbonate ions and Phosphate ions are in a very small quantity.

NazimaSiddiqui and Adeel Ahmad [3] presented IR spectroscopic data of edible and medicinal oils of plant origin. For IR analysis,Tenedible oils and Fifteen medicinal oils were selected. FTIR spectra were recorded. The FT – IR spectra of edible and medicinal oils showed a series of bands with different intensities and revealed the composition offatty acids and degree of saturation of the selected oils. The study suggested that IR spectroscopy could be considered as a vital technique for identification, analysis, determination of degree of saturation of fatty acids and detection of adulteration of oils of plant origin.

Syed Ismail Ahmed, et. al., [4] studied physical properties such asspecific gravity, viscosity, surface tension, refractive index and electrical conductivity of human urine of healthy donors and of patients suffering from chronic kidney kisease (CKD) for possible early detection of proteinuria. The decrease in surface tension of CKD urines was observed due to high albumin excretion and increased blood urea nitrogen. Fourier transform infrared (FTIR) spectra in the mid IR region were recorded for normal and albumin treated urine. It was observed that peaks at 1641 cm^{-1} and 1450 cm^{-1} in IR spectra were the most specific peaks for urea and albumin, respectively. They concluded that FTIR method of detecting proteinuria is quick and cheaper.

Syed Ismail Ahmed, et. al., [5] quantitated the amount of urea in urine by using FTIR Spectroscopy. FT-IR spectra of urine of healthy persons were recorded at the region 1500 -700$cm^{-1}$by adding urea of concentrations of1.25, 2.5, 5 and 10µ g/mL. The spectra revealed primary peak at 3400cm^{-1}anda secondary peak at 1641cm^{-1}related to urea. A graph between concentration of urea and intensity of IR absorption showed a linear relationship. They reported anincrease in the intensity of absorption at wave number 1641cm^{-1}, which confirmed the specific peak for Urea.

VijayaUshasree, et. al., [6] madeFTIR analysis of whole blood, plasma and serum and reported characteristic spectral bands pertaining to fibrinogen, hemoglobin, erythrocyte membrane, lipids and other plasma proteins.

The present study is an attempt to analyse molecular composition of Chicken skeletal muscle through FTIR spectroscopy.

2. MATERIAL AND METHODS:

The muscle samplesattached to femur boneof chickenwere collected from chicken centre. The samples were cleaned and sun dried. The dry samples were powdered using an agate mortar. Infrared spectrum of the powder was recorded in FTIR spectrometer (Shimadzu FTIR – 8400S) (Fig. 1) in the range of 4000 cm^{-1} to 400 cm^{-1}. For the spectral recording, a small quantity of muscle powder was mixed with potassium bromide (KBr) powder in the ratio of 1:4 and pressed in a stainless steel die to produce thin KBr wafer, containing a relatively high concentration of the sample in IR transparent KBr matrix.
degree of crystallinity of apatite crystallites present in the bone.

Fig. 1. FTIR Setup

3. RESULTS AND DISCUSSION:

Fig. 2.shows FTIR spectrum of chicken muscle recorded in the range of 4000 cm^{-1} to 400 cm^{-1}. It reveals a series of bands with different intensities. Table 1 presents data on wavenumbers and corresponding Transmission (%) obtained from FTIR spectrum along with characteristic vibrations of functional groups.

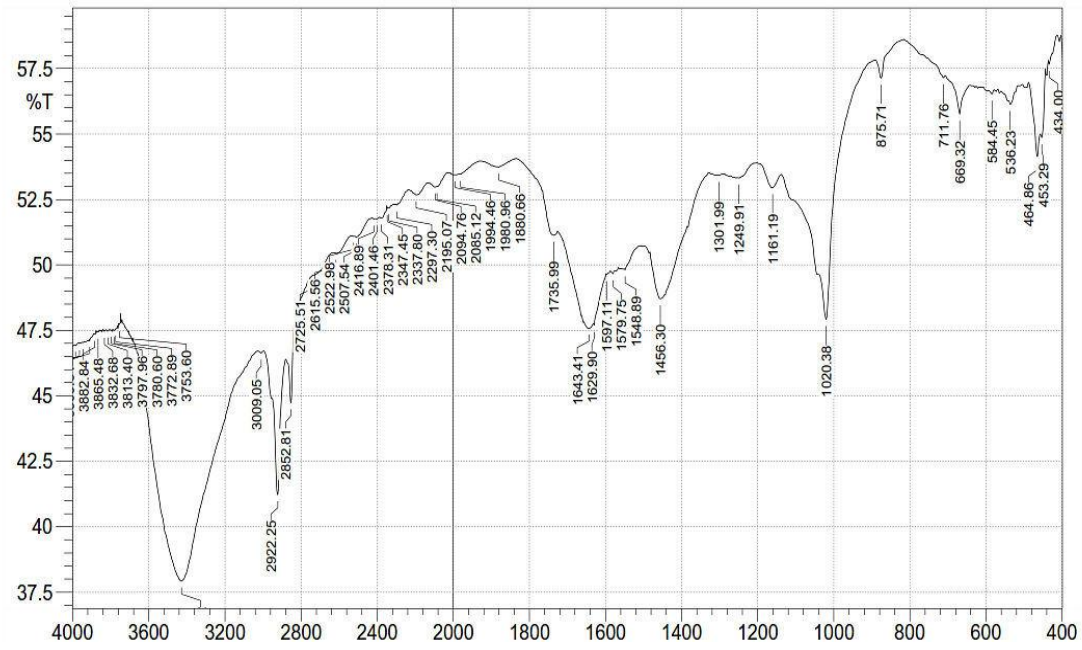

Wave Number (cm^{-1})
Fig. 2. FTIR spectrum of chicken muscle

Wave Number (cm^{-1})	Transmission (%)	Characteristic vibrations of functional groups
3427	37.92	H-O-H stretching
2922	41.23	CH_2 Asymmetric Stretch: mainly lipids, cholesterol
2853	44.74	CH_2Symmetric Stretch: mainly lipids

1736	51.13	C=O stretching vibrations of phospholipids
1643	47.58	C=O stretching vibrations of collagen
1629	47.69	Amide I band of pleated sheath structures of proteins
1548	49.82	Amide II band of proteins, N-H stretching C-O-anti symmetric stretch
1456	48.71	CH_2 Bending: mainly lipids; P-O- anti symmetric stretch
1161	52.92	C-C vibration
1020	47.91	Glycogen
876	57.13	C-O out of plane bending, Carbonate ion
669	55.76	C-S stretch
536	56.53	P-O- Asymmetric bend
464	54.14	P-O- symmetric bend

Table. 1. FTIR data on chicken skeletal muscle

A broad band 3427 cm^{-1} in the region 3500 cm^{-1} to 3000 cm^{-1} is observed. This can be assigned as due to hydroxyl ions involved in hydrogen bonding. The broad band of hydrogen bonded hydroxyl ions in the muscle sample can be attributed to the presence of several hydrogen bonds of different energy.

The major bands observed at 1629cm^{-1} (C-H stretch), 1548cm^{-1}(N-H stretch and C-O- anti symmetric stretch) related to Amide I and Amide II respectively can be attributed to the organic component of the muscle, which isessentially protein, mainly collagen, actin and myosin. Specifically the band at 1643 cm^{-1} (C=O stretch) is of collagen protein.

The band 2922 cm^{-1}(H-C-H asymmetric stretch) of acyl chains, specially cholesterol. The bands at 2853 cm^{-1}(C-H stretch), and 1736 cm^{-1}(C=O stretch are mainly concerned with fatty acids, phospholipids and Triglycerides respectively.

The bands 464 cm^{-1} (P-O- symmetric bend), 1456 cm^{-1} (P-O- anti symmetric stretch) are pertaining to phosphate ion (PO_4^{3-}). The bands 876 cm^{-1} (C-O out of plane bending) and1548 cm^{-1} (C-O-anti symmetric stretch) are characteristic of carbonate ion (CO_3^{2-}).

The IR spectrum of muscle powder indicates the bands concerned with amides of proteins; triglycerides and phospholipids; phosphate and carbonate ions.

REFERENCES:

1. EbruDeniz, BeycanAyhan, EvrimGüneşAltuntaş, DuyguÖzelDemiralp and KezbanCandoğan, 61st International Congress of Meat Science and Technology, 23-28th August 2015, Clermont-Ferrand, France.
2. Gangadhar R, Kaleem Ahmed Jaleeli and Adeel Ahmad, Int. J. Sci. Env. Tech., Vol. 4, No. 4(2015), pp. 1158 – 1162.
3. NazimaSiddiqui and Adeel Ahmad,Int. J. Sci.Env. Tech., Vol. 2, No 6(2013), pp. 1297 – 1306.
4. Syed Ismail Ahmad, Siddiq Ahmed, Iizhar Ahmed Syed, Shakeel Ahmed Ansari and Adeel Ahmad, Oriental Journal of Chemistry, Vol.32, No. 31(2016), pp. 421-1431.
5. Syed Ismail Ahmad, Iizhar Ahmed Syed, P. Ravi Prasad and Adeel Ahmad, Der PharmaChemica, Vol. 6, No. 1(2014), pp.90 – 96.
6. U. VijayaUshasree, Kaleem Ahmed Jaleeli and Adeel Ahmad, Int. J. Sci. Env. Tech., Vol. 5, No 3(2016), pp.1189 – 1192.

Second National Conference on
RECENT ADVANCES IN APPLIED NANO MATERIALS
February 16-17, 2018 at Department of Physics, University College of Science, Saifabad, Osmania University, Hyderabad, Telangana State, India.

Structural Characterization of Samarium substituted Cobalt Nano ferrites by citrate-gel auto combustion method

Nehru Boda[1], GopalBoda[2], G. Aravind[1] , D. Ravinder[1*], A. PanasaReddy[2]
[1.] Department of Physics, Osmania University, Hyderabad, 500007, Telangana, India
[2.]Department of Chemistry, College of Engineering, Osmania University,
Telangana, Hyderabad, 500007
*Corresponding author: ravindergupta28@reddif mail.com

Abstract: *Nano-Crystalline Samarium substituted Cobalt Nano ferrites with chemical formula $CoSm_XFe_{2-X}O_4$ (where X=0.0, 0.010, 0.030, 0.050, 0.070, 0.090 and 0.10) were synthesized by citrate-gel auto combustion method. Synthesized powders were sintered at 500^0C for four hours in air and characterized by XRD, SEM, EDS, FTIR. X-ray diffraction (XRD) analysis showed cubic spinel structure of the ferrites and the values of lattice constant (a) and x-ray density (d_x) increased with the increase of Sm content. The surface morphology of the samples was observed by scanning electron microscopy (SEM). An elemental composition of the sample has studied by Energy Dispersive Spectroscopy (EDS). The FTIR spectra show the two significant absorption bands in the wave numbers around 400 cm^{-1} and 600 cm^{-1} arising due to the inter-atomic vibrations in the tetrahedral and octahedral coordination compounds. The observed results can be explained on the basis of composition.*

Key Words: *Co-Sm Nano ferrites; citrate-gel auto combustion Technique; XRD; SEM; EDS; FTIR.*

1. INTRODUCTION:

Nano spinel ferrites have general formula AB_2O_4 where A is divalent metal ions like Co^{+2} , Cd^{+2}, Zn^{+2}, Ni^{+2} and B is trivalent metal ions like Fe^{+3}, Sm^{+3}, $Al^{+3}$and etc. It constitutes an important class of magnetic materials having several applications like storage devices, microwave devices, magnetic diagnostic, magnetic drug delivery, and etc. [1].

These materials crystallize into a cubic closed packed spinel structure of oxygen ions. The cations occupy two types of interstial sites known as tetrahedral A- site and octahedral B-site, the site occupancy is often depited by the chemical formula $[A^{2+}_{1-\delta}Fe^{3+}_{\delta}][A^{2+}\delta Fe^{3+}_{2-\delta}]O^{2-}_{4,}$where the parentheses and square brackets denote A and B sites respectively, A represents a divalent cation and δ is inversion parameter [2]. Among all spinel ferrites $CoFe_2O_4$ is an interesting magnetic material because due to its high coercively and moderate saturation magnetization as well as remarkable chemical stability, and mechanical hardness and which make it a good candidate for the recording media [3.4].

2. EXPERIMENTAL DETAILS:

The Cobalt Samarium nano ferrites having the chemical formula $CoSm_XFe_{2-X}O_4$ were synthesized by citrate gel auto combustion method using the raw materials are .Samarium Nitrate ($SmNO_3$), Cobalt Nitrate ($CoNO_3$), Ferric Nitrate ($Fe(NO_3)_3$ $9H_2O$), Citric acid ($C_6H_8O_7.H_2O$) and Ammonia solution (NH_3). Thesynthesis of Co- Smnano ferrites: The Chemicals are weighed according to the stoichiometric proportion; the calculated quantities of metal nitrates were dissolved in minimum amount of distilled water to get clear homogeneous solution. An aqueous solution of Citric acid is used as a fuel because; among all other fuels Citric acid has better complexing ability. The metal nitrate to citric acid ratio was maintained as 1:3 for all the samples, and nitrate-citrate solution is obtained to that Ammonia (NH_3) solutions are added drop by drop to maintain PH-7.The solution is mixed and heated by continuous stirring up to100^{o}C for 10-12 hours, then viscous gel is formed, again Water in the mixture is evaporated forming a dry gel generates internal combustion and forms a brown colored product. Which is a desired Sample, collected ferrite powder is subjected to calcinations at 500^0 C for 4hrs these powder are for characterized by XRD, SEM, FTIR and EDS.

The structural characterization was done by X-Ray Diffract meter Bruker D8 advanced system with diffracted monochromatic beam with cu kα radiation of wavelength (1.5405A^0). The diffraction pattern of Co-Sm between the Bragg Angles 10º to 80º in the steps of 0.04º/sec.

The crystalline size was calculated for the sample using the high intensity 311 peak and using DebayScherrer formula [5] while taking into account the intensity broadening

The Crystalline size of the sample $D = \frac{0.91\lambda}{\beta \cos\theta}$ [6]. (1)

Where λ the wavelength of X-ray is used [7]. β Is the width of diffraction peak i, e. full width half Maximum (FWHM), θ is the peak position.

Lattice parameter (a) of the sample was calculated by the formula

$$a = d * \sqrt{h^2 + k^2 + l^2}[8] \quad (2)$$

Where a is Lattice constant, (hkl) are the Miller indices, d is the inter planner space

The X-ray density of the prepared sample was calculated using the relation

$$d_X = \frac{nM}{a^3 N} \text{g/cm}^3 [9] \quad (3)$$

Where n is the number of molecules in a unit cell of spinel lattice (n=8), M= molecular weight of the sample, a is the lattice parameter and N is the Avogadro number.

The experimental density of the prepared samples was calculated by Archimedes' principle with xylene media using following relation.

$$d_E = \frac{\text{Weight of the sample in air}}{\text{Weight of the sample in air} - \text{weight of the sample in xylene}} \times \text{Density of xylene}$$

The Percentage of Porosity P of the ferrite sample was then determined by employing the relation

$$P = \frac{d_X - d_E}{d_X} \times 100 \quad (4)$$

Where d_x is the X-ray density &$d_E$is the experimental density,

The distance between the magnetic ions (hoping length) on A-site (Tetrahedral) and B site (Octahedral) is calculated according to the following relations

$d_A = 0.25a\sqrt{3}$ and $d_B = 0.25a\sqrt{2}$ [10] (5)

The drift mobility (μ_d) of the charge carrier in the synthesized samples is calculated using the fallowing relation

3. RESULT AND DISCUSSION:

3.1. XRD Analysis A phase analysis using X-ray diffraction technique was performed to conform the formation of single-phase cubic spinel structure as shown in figure (1) With no extra lines corresponding to any other crystallographic phase. The results obtained from XRD pattern for all the samples of $CoSm_XFe_{2-X}O_4$ with the (hkl) values corresponding to the diffraction peaks of different planes (220), (311), (400), (422), (511), and (440) are spinel cubic phase

The calculated values of crystalline size for the different compositions are given in the table (1).

It can be seen from the table that the values of the crystal size varies from 11nm to 17nm of the various Sm concentrations

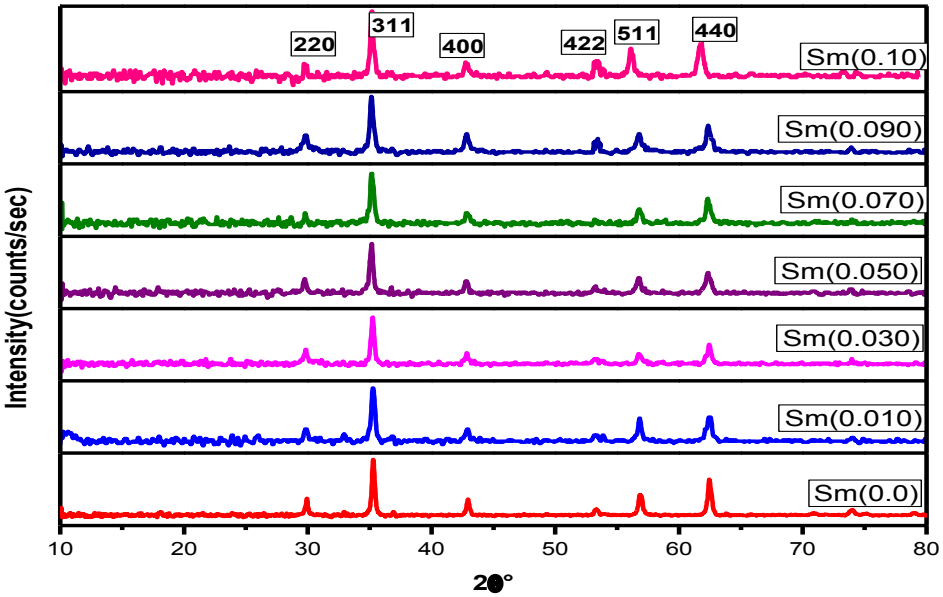

Fig.1. XRD pattern of $CoSm_XFe_{2-X}O_4$ nano crystalline ferrites

Table1. Crystalline size (D), Lattice parameter (a), X-ray density (d_x), Expert density (d_E), Porosity (p)

Ferrite composition	D[nm]	a [A^0]	d_X [gm/cc]	d_E[gm/cc]	p (%)	A-site(d_A)	B-site(d_B)	ϑ_1(cm^{-1})	ϑ_2(cm^{-1})
$CoFe_2O_4$	23.78	8.419	5.222	5.151	1.35	3.6454	2.9761	570	364
$CoSm_{0.010}Fe_{1.99}O_4$	21.95	8.428	5.227	5.165	1.18	3.6493	2.9793	574	368
$CoSm_{0.030}Fe_{1.97}O_4$	14.63	8.431	5.263	5.198	1.23	3.6506	2.9803	570	368
$CoSm_{0.050}Fe_{1.95}O_4$	26.75	8.441	5.286	5.191	1.79	3.6549	2.9838	567	362
$CoSm_{0.070}Fe_{1.93}O_4$	21.94	8.449	5.313	5.255	1.09	3.6584	2.9867	567	364
$CoSm_{0.090}Fe_{1.91}O_4$	21.95	8.453	5.347	5.271	1.42	3.6601	2.9881	570	364
$CoSm_{0.10}Fe_{1.9}O_4$	17.55	8.458	5.358	5.298	1.11	3.6623	2.9899	572	352

The lattice parameter values of all the composition of Samarium doped Cobalt nano ferrites have been calculated from the d- spacing and are given in the table (1). A plot is drown between the lattice parameter vs Samarium composition is shown in Fig. (2).

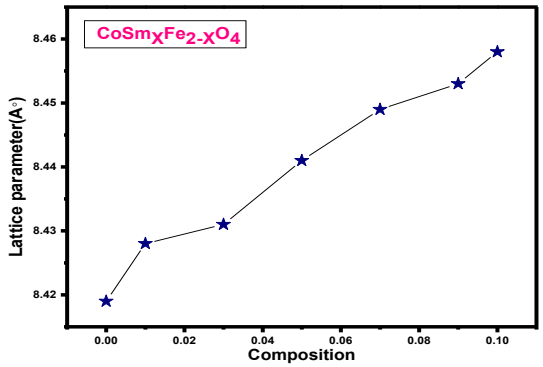

Fig 2. Lattice parameter vsSm composition

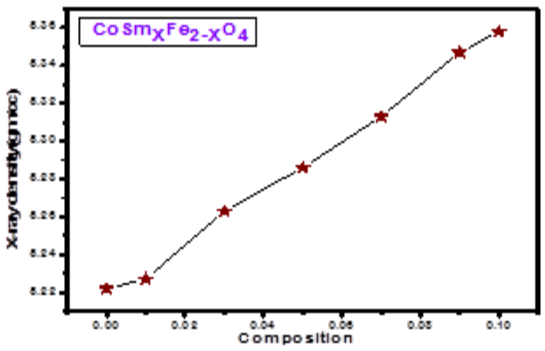

Fig 3. X-ray density vsSm composition

The variation of lattice constant with Sm^{3+} content in $CoSm_xFe_{2-x}O_4$ (where x=0.0, 0.010, 0.030, 0.050, 0.070 0.090 and 0.10) is observed that the Lattice parameter increases with increase in Smcontent. This is attributed to replacement of smaller ionic radii Fe (0.69A°) by larger ionic radii Sm^{3+} (1.098A°) ions. This linear variation indicates that the Co-Sm ferrite system obeys Vegard's law [11].

From fig (3) shows the X-ray density (dx) vsSm concentration, the X-ray density (dx) is depend on the lattice parameter and molecular weight of the sample. From the table (1) we can observe that molecular weight of the sample is increases with Samarium concentration and lattice parameter is also increases with the increase of Sm compositions. This may due to the grater atomic weight of Sm (150.36gm/mol) and lesser atomic weight of Fe(55.845gm/mo)[12] the sample.

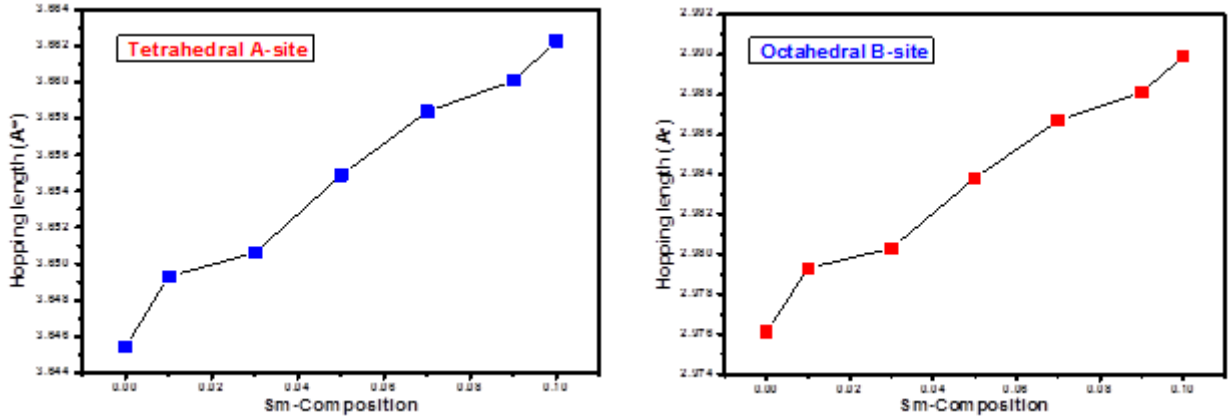

Fig. 4. Tetrahedral A-Site and Octahedral B-Site of $CoSm_XFe_{2-X}O_4$

3.2. Morphology by SEM

Morphology of Co-Sm prepared samples was done by using scanning electron microscope (SEM) as the instrument Ziess special edition-18 where the secondary electron images were taken at different magnifications to study the synthesized samples were shown in fig (5)

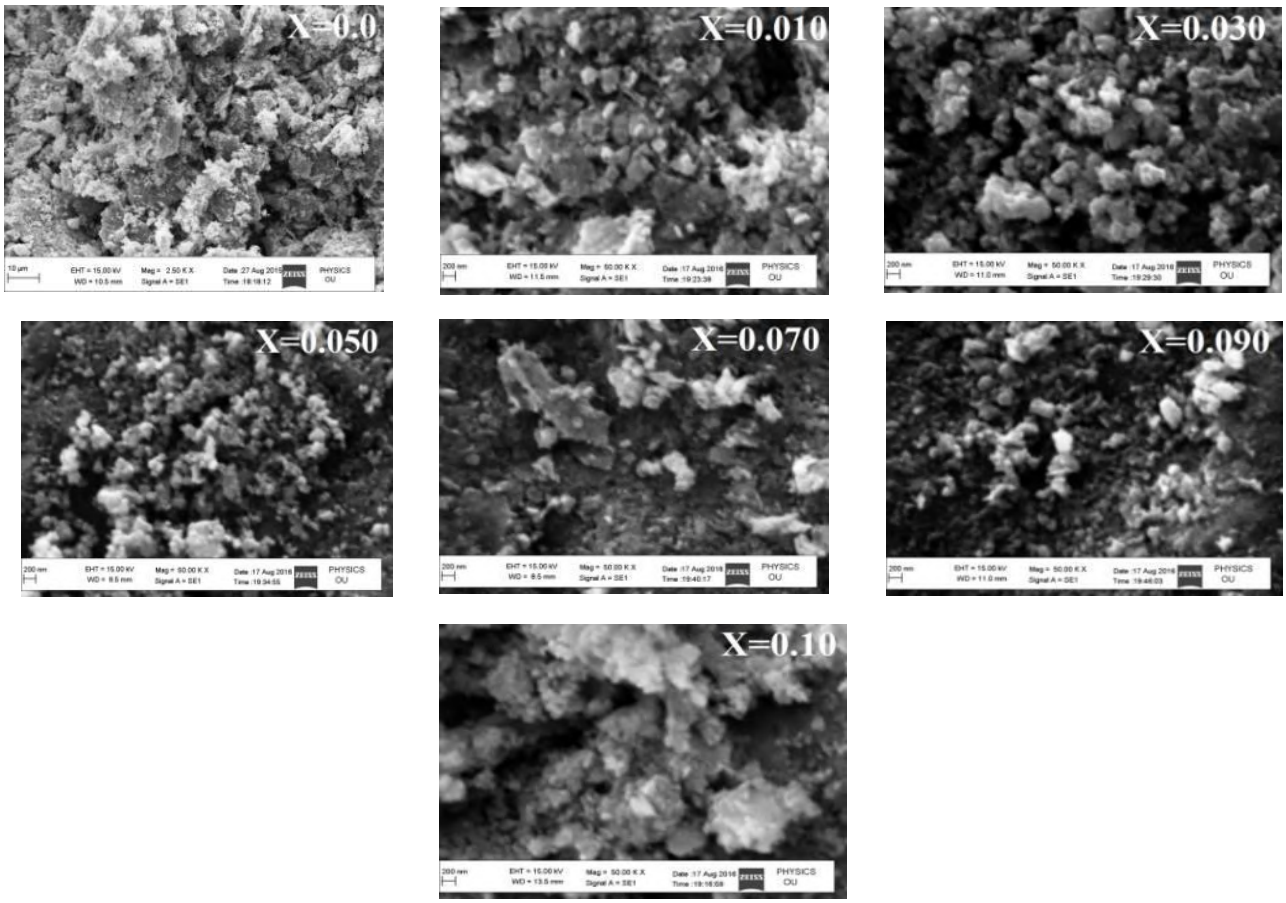

Fig 5. SEM micrographs of $CoSm_XFe_{2-X}O_4$ferrites samples at (x=0.0, 0.010, 0.030, 0.050, 0.070, 0.090 and 0.10)

The Sem images show that the particles have an almost homogeneous distribution, and some of the samples are agglomerated form. It is evidenced by SEM All the samples exhibit a very low porosity and large grain size (52nm-150nm) that the agglomeration of particles lies in nano region. The particles were observed as uniform grain (in different SEM images) sizes, the increasing Sm content particle size will be decreases from 0.010 to 0.050, and again increase Sm content particle size will increases upto 0.10.

3.3. Elemental Analysis by EDS

By using The EDS spectra we observe the chemical composition of prepared samples of the elements present from the surface to the internal of the solids, and they are used to confirm the homogeneity of the investigated samples. The spectra indicated the presence of elements (O, Fe, Co, and Sm) without impurities and which indicates the Completeness of solid state reaction. The EDSmicro graphs of the samples are shown in Fig (6)

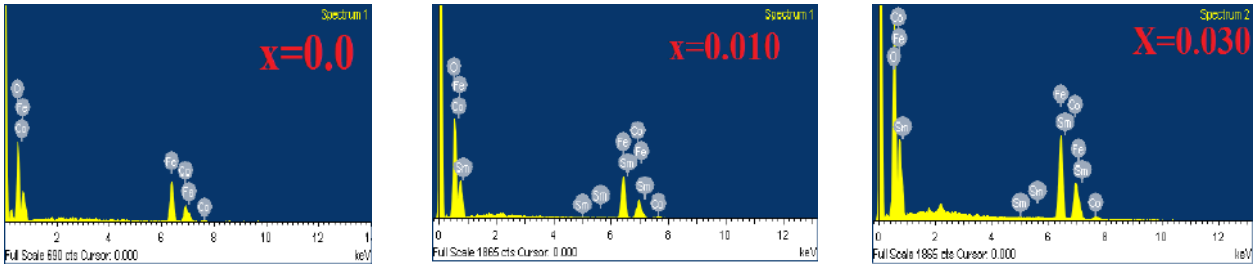

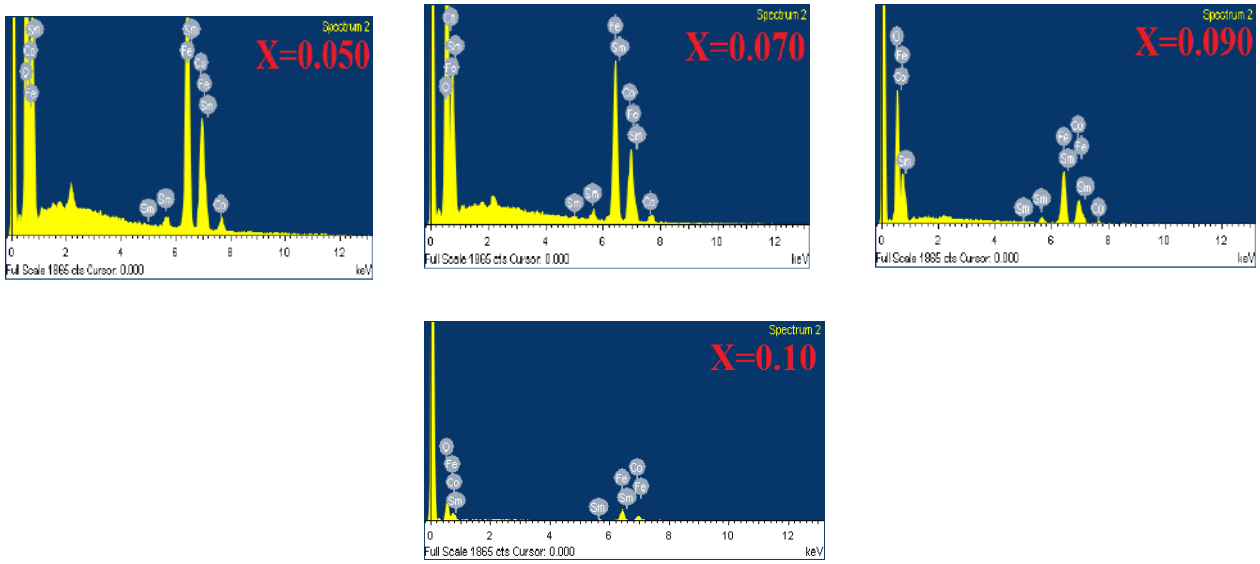

Fig .6.EDS micro graphs of $CoSm_XFe_{2-X}O_4$nano ferrites

Elements	O		Fe		Co		Sm	
Ferrite Composition	Weight %	**Atomic %**	**Weight %**	**Atomic %**	**Weight %**	**Atomic %**	**Weight %**	**Atomic %**
$CoFe_2O_4$	27.24	57.08	48.55	29.15	24.22	13.78	- -	- -
$CoSm_{0.010}Fe_{1.99}O_4$	28.13	58.47	45.82	27.29	24.71	13.94	1.34	0.30
$CoSm_{0.030}Fe_{1.97}O_4$	28.60	59.14	45.49	26.94	24.06	13.51	1.85	0.41
$CoSm_{0.050}Fe_{1.95}O_4$	28.28	59.02	44.87	26.83	23.73	13.45	3.12	0.69
$CoSm_{0.070}Fe_{1.93}O_4$	29.72	61.01	42.84	25.20	23.01	12.82	4.44	0.97
$CoSm_{0.090}Fe_{1.91}O_4$	29.03	60.76	41.64	24.96	22.41	12.74	6.92	1.54
$CoSm_{0.10}Fe_{1.9}O_4$	26.88	57.83	43.14	26.59	24.53	14.33	5.45	1.25

4. FOURIER TRANSFORMATION INFRARED SPECTROSCOPY:

The infrared spectroscopy gives information about the chemical and molecular structure change in ferrites due to the changes in Fe-O bond during heat treatment or when some foreign atom is introduced in the parent ferrite compound, Fourier transformation infra-red spectra of Samarium substituted cobalt nano ferrite which were sintered at 500°C were recorded in the range of 250-4000cm^{-1} at room temperature. In ferrites the bands appearing at the higher wave number (ν_1 567-670cm^{-1}) is assigned to the tetrahedral site, while the band appearing at lower wave number (ν_2 352-368cm^{-1}) is assigned to the octahedral site. The higher wave number ν_1 represents the vibration of Fe^{3+}-O^{2-}in the sub lattice site-A, while the lower wave number band ν_2 represents the trivalent metal oxygen vibration at the octahedral B-sites.[13].

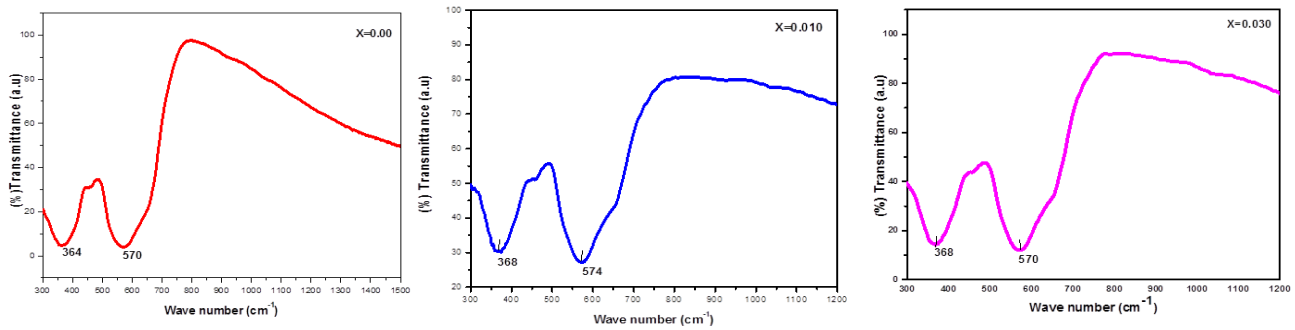

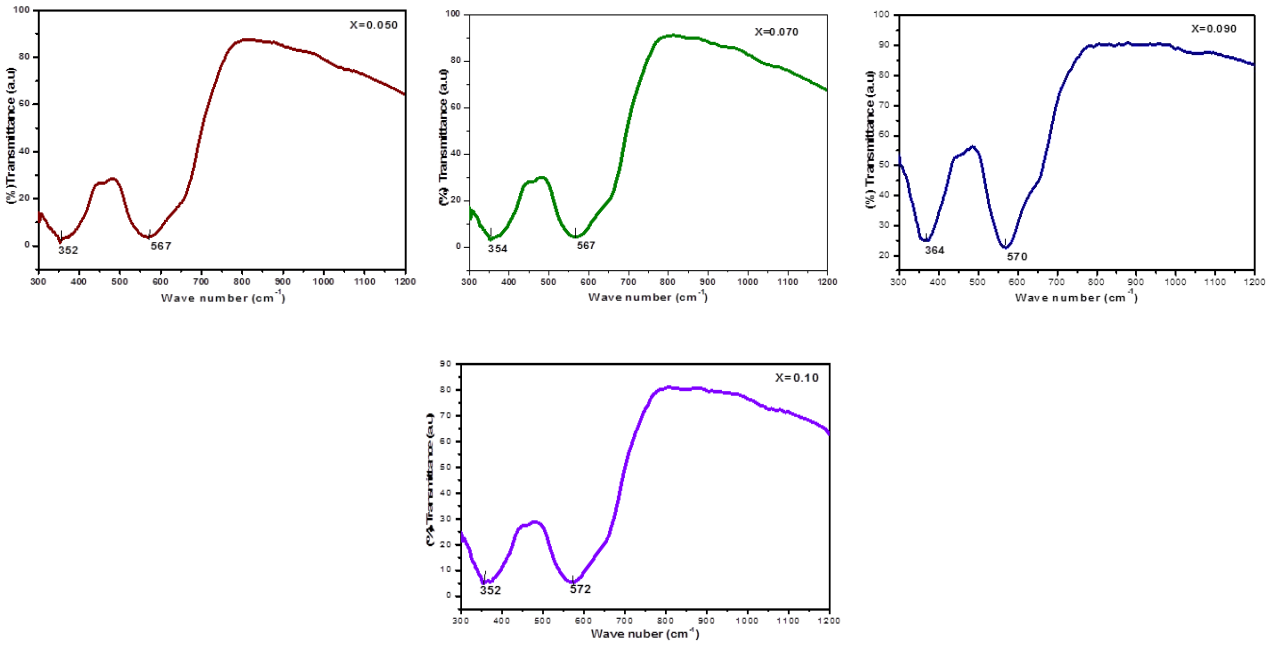

Fig.7. Shows FTIR spectra of the $CoSm_XFe_{2-X}O_4$ ferrite samples (X= 0.0, 0.010, 0.030, 0.050, 0.070, 0.090 and 0.10)

CONCLUSION:

Citrate Gel Auto Combustion technique is a convenient way for obtaining a homogeneous nano sized mixed ferrites, it is very simple and economical method where no specific heating or cooling rate is required. X-ray diffraction pattern confirms the formation of cubic spinel structure in single phase with standard data from JCPDS. The crystalline size of the various Co-Sm ferrites was in the range of 14 to26 nm. The Lattice parameter has increased with the increase of Sm concentration in Co-Sm, ferrites which indicate that the mixed Co-Sm ferrite system obay the vegard's law. SEM micrographs of various compositions indicate the morphology of particles is similar. They reveal largely agglomerated. EDS data give the elemental % and atomic % in the mixed Co-Sm ferrites and it shows the presence of(Co, Sm, Fe and O) without impurities and which indicates the completeness of solid state reaction The FTIR spectra of the ferrite samples in the range of wave numbers from 352 to 670 cm^{-1}. The two absorption bands Observed at (ν_1 567-670cm^{-1}) and (ν_2 352-368cm^{-1}) corresponds to vibrations of tetrahedral and octahedral complexes respectively.

ACKNOWLEDGEMENTS*:*

The authors are very grateful Prof. J. ShivaKumar,, Head, Department of physics, and Prof. C. Vishnuvardhan Reddy, Chairmen Board of studies in physics, University college of science Osmania University Hyderabad, One of the author **Nehru Boda** is very thankful to **UGC, BSR-section** New Delhi, for their financial assistance.

REFERENCES:

1. S. Gubbala, H. Nathani, K. Koziol, and R. D. K. Misra, "Magnetic properties of nanocrystalline Ni–Zn, Zn–
2. Mn, and Ni–Mn ferrites synthesized by reverse micelle technique," *PhysicaB: Condensed Matter*, vol. 348, no. 1–4, pp. 317–328, 2004.
3. B. Viswanathan and V. R. K. Murthy, *Ferrite Materials: Scienceand Technology*, Narosa, New Delhi, India,1990.
4. J.-G. Lee, J. Y. Park, and C. S. Kim, "Growth of ultra-fiecobalt ferrite particles by a sol–gel method and their magneticproperties,"*JournalofMaterialsScience*, vol. 33, no. 15, pp. 3965–3968, 1998.
5. S. N. Okuno, S. Hanshimoto, and K. Inomata, "Preferredcrystal orientation of cobalt ferrite thin fims induced byionbombardment during deposition ," *Journal of Applied Physics*,vol. 71, no. 12, pp. 5926–5929, 1992.
6. Cullity B D, Elements of X-ray diffraction (addition Wesley, Reading, Mass), 1959. P132.
7. Mahmud ST, AktherHossain AKM, Abdul Hakim AKM, Seki M, Kawai T. Tabata H (2006) j MagnMater 305; 269doi; 1016/j.jmmm.2006.01.012.
8. B.D. Cullity, Elements of X-ray diffraction, Wesely Pub,Co,.Massachusetts,1987,101-356
9. B.P.Ladgaonkar, P.P.Bakare,S.R. Sainkar and A.S.Vaingankar, "Influence of Nd+3 substitution on permeability spectrum of Zn-Mg ferrite". Materials Chemistry and Physics, Volume 69,Issues 1- 3,March 1, 2001, pages 19-24.

10. R.C.Kumbale. P.A.Shaikh, S.S. Kamble,Y.D.KolekarJ.Alloys Comp., 478(2009), p.599
11. doi:10.1016/j.jmmm.2005.03.007
12. R.C.Kumbale. P.A.Shaikh, S.S. Kamble,Y.D.Kolekar J.Alloys Comp., 478(2009), p.599 doi:10.1016/j.jmmm.2005.03.007
13. L. Vegard, "The Constitution of Mixed Crystals and the Space Occupied by Atoms," Zeitsch rift fiir Physics, Vol. 5, No. 17, 1921, pp.17-23
14. K.B.Modi, J.D.Gajera, M.P.Pandya,H.G.Vora, H.H.Joshi, Pramana Journal of Physics, Vol 62, No 5,May, 2004, pages 1173-1180

Second National Conference on
RECENT ADVANCES IN APPLIED NANO MATERIALS
February 16-17, 2018 at Department of Physics, University College of Science, Saifabad, Osmania University, Hyderabad, Telangana State, India.

Ultrasonic and Thermo Physical Properties Of Bio-Synthesized Nano (Indium Oxide) Fluids

KanchanaLatha Chitturi[1], Ramchander Merugu[2]
[1]Department of Physics, GDC Khairatabad, Hyderabad-500004, Telangana, India
[2]Department of Bio Chemistry, Mahatma Gandhi University, Nalgonda-508254, Telangana, India

Abstract: *Green Synthesis and Two-step method have been applied for preparing Indium oxide nanoparticles and nanofluids respectively with base fluid as Ethylene Glycol. The Indium oxide nanoparticles were obtained from Indium (III) Acetylacetonate and katira gum as precursors. The effect of surfactant PVP (2-5% volume) and Albumen protein (1% by volume) on Indium oxide nanofluids (1% by volume) is observed. The Indium oxide nanofluids were characterized by SEM and EDAX Spectroscopy. The chemical composition and morphology were done by EDAX and SEM respectively. The effect of PVP and Albumen protein on thermophysical properties (Thermal Conductivity, Viscosity, Density and Ultrasonic Velocity, Adiabatic Compressibility and Surface Tension) of Indium oxide nanofluids were observed in the temperature range 30°C to 60°C confirming the Newtonian behavior of nanofluid.*

Key Words: *Green synthesis, Indium oxide nanofluid, thermophysical properties, two-step method, , SEM and EDAX, katira gum mediated, PVP, Albumen.*

1. INTRODUCTION

Nanofluid is a term proposed by Choi in 1995 of the Argonne National laboratory U.S.A. In recent years, nanofluids have attracted more and more attention [1,2]. Research in nanofluids has many potential applications [3-5]. Most of the reviews were concerned with the experimental and theoretical studies of the Thermophysical properties of nanofluids [6]. The Two-step method is extensively used in the synthesis of oxide based nanofluids. Several authors have argued that thermal conductivity enhancement is due to hydrodynamic effect of nanoparticles Brownian motion. In2O3 nanofluids are very stable due to the protective role of PVP, as it retards the growth and agglomeration of nanoparticles by steric effect. PVP is an efficient agent to improve the stability of suspension [7]. Proteins are polypeptides with a defined conformation whose adsorption change to nanoparticle surface changes with changes in pH. Adsorption of proteins to nanosurface is influenced by solvation forces, hydrogen bonds Van der Waals interactions, etc. PVP and Albumen protein act as efficient agents to improve the stability of suspension [8]. Proteins in vivo are very complex biological systems. Inside the cell the nanoprotein complexes may be processed by different cellular pathways. Temperature induced structural changes can result in different responses in vitro. Thermal vibrations cause polymer to lose its structure allowing greater surface area to nanoparticles to take part in heat transfer.Nanoparticle surface may get pre-coated with specific proteins inside a cellular environment.

Fabrication of In2O3 nanoparticles and In2O3 nanofluid with Albumen protein

The stable In2O3 nanofluid is obtained by using In2O3 nanoparticles synthesized from *Indium (III) Acetylacetonate*and *katira gum*, base fluid (EG), surfactant (PVP) and Albumen protein as shown in the flowchart (**Figure 1**) and the different compositions for synthesis are shown in **Table below**

In_2O_3 : PVP : Gelatin weight ratio	Description
1 : 2 : 1 (Sample-1)	0.2 g of In_2O_3 with 0.4 g of PVP and 0.2 g of Gelatin in 200 ml EG
1 : 5 : 1 (Sample-2)	0.2 g of In_2O_3 with 1 g of PVP and 0.2 g of Gelatin in 200 ml EG

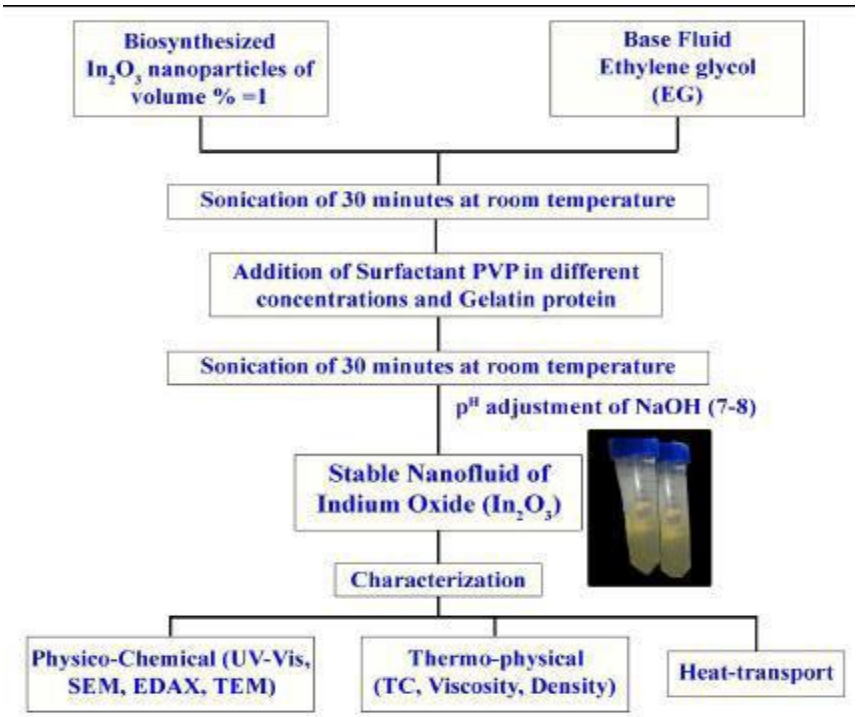

Fig:1 Flowchart for the synthesis of In_2O_3 nanofluids using albumen protein

2. RESULTS AND DISCUSSION:

EDAX and SEM Analysis

In **Figure 2**, the EDAX spectrum of the In_2O_3 nanofluids reveals that the (sample1 and sample2)containing '*In*' and '*O*' as main constituent components indicate no contamination is present due to PVP and Albumen proteins and their atomic and weight ratios confirm the literature values. The SEM images of In_2O_3 nanofluids of (samples 1 and 2) show the random distribution of nanoparticles having *spherical* shape of large surface area with porous nature is observed.

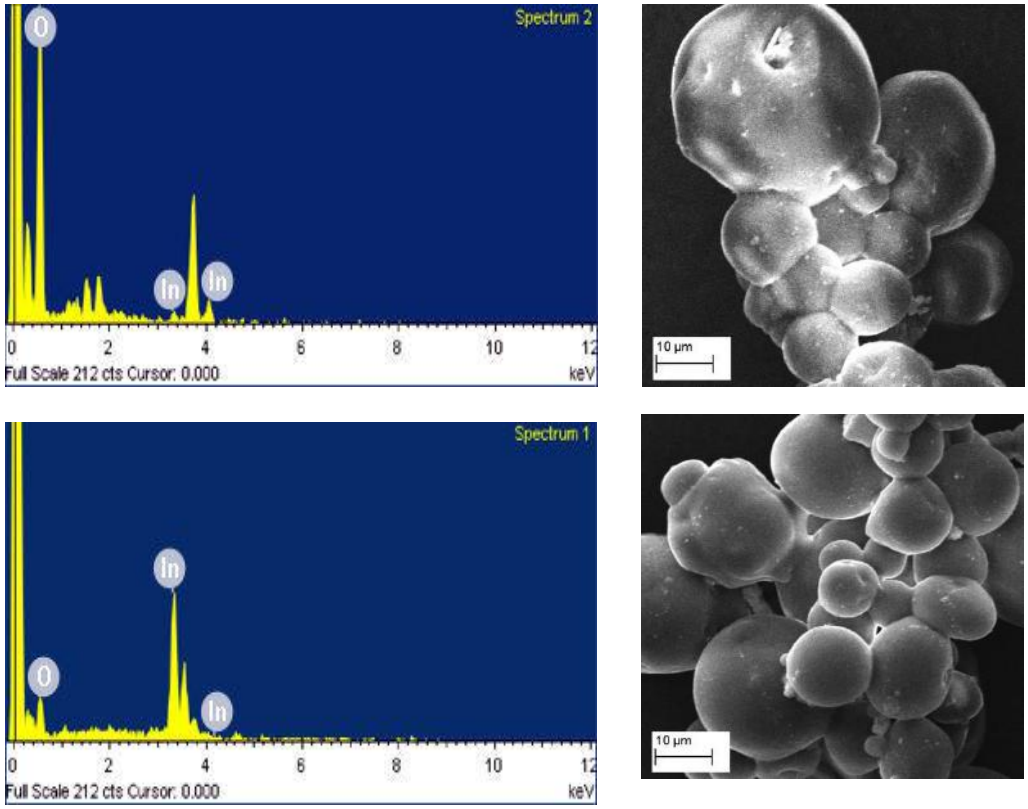

Figure 2. EDAX ***and SEM of sample-1 and sample-2 of Indium oxide nanofluids***

Figure 3. represents the voltage versus thermal conductivity. The ratio of ***Keff/Kb*** is a non-linear behavior in sample 1 and a sharp increase with increase of voltage for sample 2. It can be explained based on Brownian motion nanoparticles freed from PVP binding as the temperature increases **[195]** with increase in temperature nanoparticles diffuse through the polymer matrix. Thermal vibrations cause polymer to lose its structure allowing greater surface area to nanoparticles to take part in heat transfer. The enhancement of thermal conductivity with voltage from 40 V of sample 2 may be due to polymer and Albumen protein ligand binding which are considered as important mechanism for enhancing thermal conductivity of nanofluid**[9-10]**and the percentage of enhancement of sample 2 is found to be 30% compared to that of Ethylene Glycol base fluid.

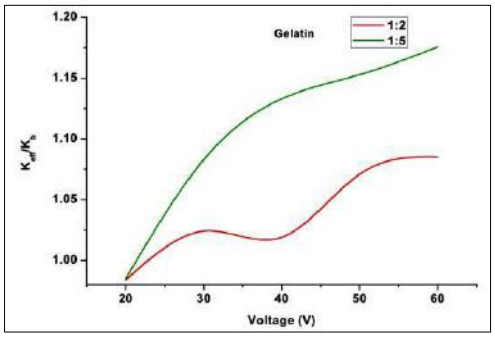

Figure 3: Voltage vs Thermal Conductivity Enhancement Ratio of In2O3 nanofluids using Albumen protein

3. DENSITY AND VISCOSITY ANALYSIS:

Figure 4and Figure 5represents the density vs temperatures ranging from 30oC to 60oC increases with increase of concentration of PVP than that of basefluid. Further, it is observed that at higher temperature (50-60oC) density of sample 2 decreases with that of base fluid Ethylene glycol. **Figure 5**represents the viscosity decreases with increase of temperature and that of base fluid which confirms good heat transfer and reduces pressure drop.

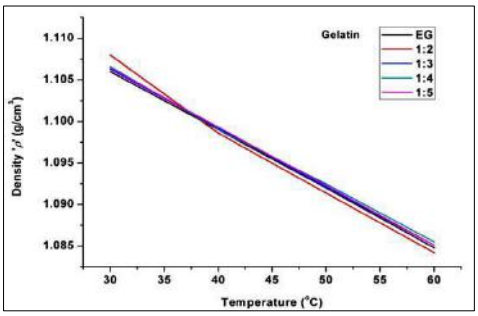

Figure 4: Temperature vs. Density of In2O3 nanofluids using Albumen protein

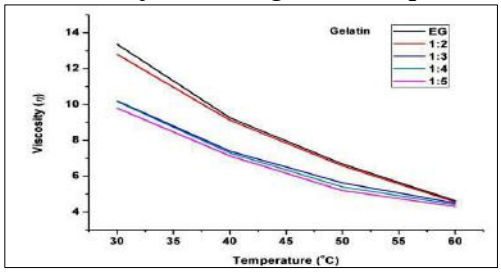

Figure 5 Temperature vs. Viscosity of In2O3 nanofluids using Albumen protein

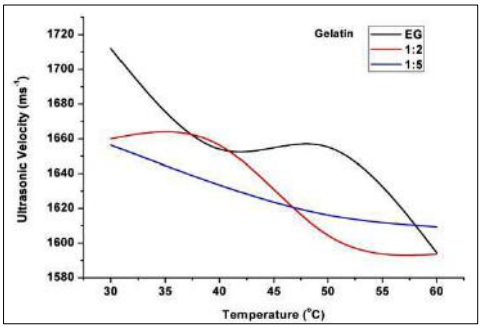

Figure 6 :Temperature vs Ultrasonic Velocity of In2O3 nanofluids using Albumen protein

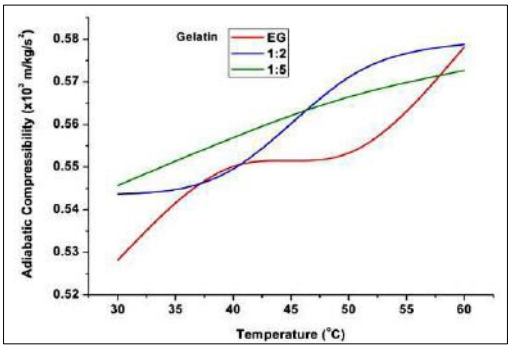

Figure 7 :Temperaturevs Adiabatic Compressibility of In2O3 nanofluids using Albumen protein

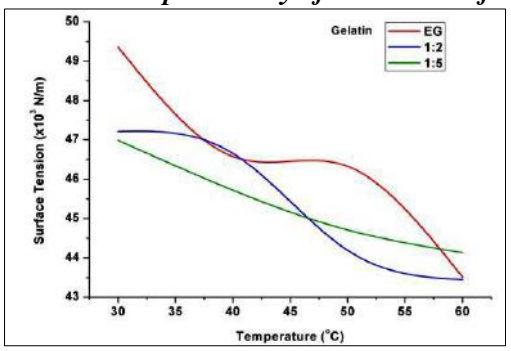

Figure 8 :Temperature vs. Surface Tension of In2O3 nanofluids using Albumen **protein**

In figure (6&7) It is observed that as the concentration of PVP increases ultrasonic velocity decreases and adiabatic compressibility increases with the increase of temperature upto 500c,As proteins contains enzymes and it will destroy at 550c which is attributed to the fact that strong cohesive interaction forces act among the molecules and atoms after the dispersion of In2O3 nanoparticles in PVP and polymer matrix.

In fig (8) the surface tension increases with increase of temperature at about 400C and decreases with increase of concentration of PVP attributed to good heat transfer.

4. CONCLUSIONS:

We have successfully synthesised the Indium Oxide nanoparticles and nanofluid of (sample 1 and sample 2) by green and two step method respectively. The dispersed nanoparticle of In2O3, Albumen protein and different concentration of PVP and their thermo physical properties were observed. It is found that the thermal conductivity enhancement and decrement in viscosity with the increase of concentration of PVP causes heat transfer enhancement in industrial cooling applications.

REFERENCES:

1. Casals E, Pfaller T, Duschl A, Oostingh GJ, Puntes V: Time Evolution of theNanoparticle Protein Corona. ACS Nano 2010, 4:3623–3632)
2. S.Ozerinc, S.Kakac and A.G.Yazlcloglu: “Enhanced thermal conductivity of nanofluids: a state of the art review”, Micro fluidics and Nanofluidics, Vol.8, no.2, pp.145-170, (2010)
3. (Rasa Zūkienė, Valentinas.Zinc oxide nanoparticle and bovine serum albumin interaction and nanoparticles influence on cytotoxicity in vitro.Colloids and Surfaces B: Biointerfaces. Volume 135, 1 November 2015, Pages 316–323).
4. Langmuir. 2013 Dec 3;29 (48):14984-96. doi: 10.1021/la402920f. Epub 2013 Nov 20.
5. Nanoparticle-protein interactions: a thermodynamic and kinetic study of the adsorption of bovine serum albumin to gold nanoparticle surfaces.Boulos SP, Davis TA, Yang JA, Lohse SE, Alkilany AM, Holland LA, Murphy CJ.)
6. Aswathy Ravindran, Anupam Singh, Ashok M. Raichur, N. Chandrasekaran, Amitava Mukherjee¨Studies on interaction of colloidal Ag nanoparticles with Bovine Serum Albumin (BSA). Colloids and Surfaces B: Biointerfaces.Volume 76, Issue 1, 1 March 2010, Pages 32–37)
7. (Monopoli MP, Walczyk D, Campbell A, Elia G, Lynch I, BaldelliBombelli F, Dawson KA: Physical − Chemical Aspects of Protein Corona: Relevance toin Vitro and in Vivo Biological Impacts of Nanoparticles. J Am Chem Soc2011, 133:2525–2534)
8. (Gasser M, Rothen-Rutishauser B, Krug HF, Gehr P, Nelle M, Yan B, Wick P: The adsorption of biomolecules to multi-walled carbon nanotubes isinfluenced by both pulmonary surfactant lipids and surface chemistry.J Nanobiotechnology 2010, 8:1477–3155).
9. Plasma proteins such as human serum albumin (HSA) and transferrinwere shown to adsorb in a monolayer fashion on iron platinum(FePt) NP surface
10. Rezwan K, Meier LP, Rezwan M, Vörös J, Textor M, Gauckler LJ: Bovine Serum Albumin Adsorption onto Colloidal Al2O3 Particles: A New Model Based on Zeta Potential and UV–vis Measurements. Langmuir 2004, 20:10055–10061)

Second National Conference on
RECENT ADVANCES IN APPLIED NANO MATERIALS
February 16-17, 2018 at Department of Physics, University College of Science, Saifabad, Osmania University, Hyderabad, Telangana State, India.

XRD Analysis of Bone of Chicken *Gallus gallusdomesticus*

Sarwath Khalil, Kaleem Ahmed Jaleeli & Adeel Ahmad
Biophysics Research laboratory, Department of Physics, Nizam College (Autonomus), Osmania University, Hyderabad - 500001, India.
Email - skhalil.sk.9@gmail.com, kaleemjaleeli@gmail.com, dr_adeelahmad@yahoo.com

Abstract: *The paper deals with X-ray diffraction analysis of powdered bone of chicken Gallus gallusdomesticus. The study reports that the major inorganic constituents present in the bone is hydroxyl apatite. The crystalline size and lattice strain are evaluated.*

Key Words: *Hydroxyapatite, Bone, X-ray diffraction.*

1. INTRODUCTION

Bone is a dense and constantly changing structure that grows, shrinks and adapts during the entire life time of animals. Bone tissues are classified into two types, compact and cancellous bones. Femur and Tibia are the examples of compact bones and scapula and rib are examples of cancellous bones. The anabolic and catabolic process that takes place in the bone helps in the regulation of mineral metabolism and in the maintenance of the skeleton.

X-ray crystallography is a technique used for determining the atomic and molecular structure of a crystal, in which the crystalline atoms cause a beam of incident X-rays to diffract into many specific directions. By measuring the angles and intensities of these diffracted beams, a crystallographer can produce a three-dimensional picture of the density of electrons within the crystal. From this electron density, the mean positions of the atoms in the crystal can be determined, as well as their chemical bonds, their disorder, and various other information.

Powder diffraction is commonly used to identify unknown substances, by comparing diffraction data against a database maintained by the *International Centre for Diffraction Data* [1]. Therefore it is also helpful in the analysis of unknown biological samples. Many studies have been carried out to learn the x-ray diffraction analysis of eggshell of hen, quil, ostrich, which helped in the synthesis of hydroxyapatite. The Hydroxyapatite (HAp) is one of the most versatile materials used for implantation purpose due to its similarity to natural bone material. Hap has approximate chemical formula Ca10(PO4)6(OH)2 or Ca5(PO4)3(OH), and is the main inorganic constituent of bones in humans. HAp can be successfully synthesized by reaction of discarded eggshell with tri-calcium phosphate in presence of steam at 900 degrees Centigrade and subsequent aging for 24 hrs. Synthetic HAp has been successfully used in hard tissue surgery [2,3]. It is particularly attractive material for the bone and tooth implants since it closely resembles human tooth and bone mineral and has proven to be biologically compatible with these tissues [4-6]. Many studies have indicated that HApcermaics show no toxicity, inflammatory, pyrogenetic responses. It has excellent fibrous tissue formation between implant and bone.[4] It can be revealed stability. The particles are mostly spherical with nano size [7].

Joschek, et. al., [8] studied the properties of porous hydroxyapatite ceramics produced by the sintering of bovine bone. They concluded that ceramics are highly crystalline and porous and have an advantage of high interconnecting pore system and a better drug processing ability.

Gangadhar, et.al., [9] made elemental analysis of ovine scapular cartilage and reported that 13 different elements are present in which percentage of Carbon, Oxygen and Nitrogen is more and molecular composition in is inhomogeneous.

SreenivasaRao, et.al.,[10] made studies on human hair by inductive coupled plasma –atomic emission spectrometry and reported that human hair contains iron, lead, cobalt, nickel, manganese, zinc, copper and calcium.

JayanandManjhi, et.al.,[11] studied the Effect of extremely low frequency magnetic field in the prevention of spinal cord injury-induced osteoporosis. They investigated the effect of extremely low frequency (ELF) magnetic field (MF) by electron microscopic study, which revealed the enhancement of microstructural composition and compactness in cortical and trabecular parts of treated bones.

Jeevan Kumar, et.al., [12] made studies on identification of trace elements in bovine metacarpus bone by Spectro - chemical analysis In their studies Analytical methods are described for the determination of major, minor, and trace elements in bone. Ca, Mo, Pb, Fe, Zn, Cu, Mg, Al, P are identified in the bovine metacarpus bone as major trace elements and 16 more elements are identified as minor trace elements i.e., Os, Sc, Y, K, Mn, La, Cd, Pd, Ru, Na, Sn, Pt, Bi, As, Si and Co.

The present study is an attempt to analyze chicken bone powder by using the technique of x – ray diffraction.

2. MATERIALS AND METHODS

The Bone samples of Chicken *Gallus gallusdomesticus* was separated carefully from the flesh, cleaned thoroughly and dried under the sun for 3 - 4 days, so as remove free water. The bone was powdered using pestle and mortar.

X- ray diffraction of femur bone of Chicken *Gallus gallusdomesticus* was recorded using x-ray diffractometer (Shimatzu – Maxima XRD 7000) in reflection mode with Cu Kα (λ=1.5405 Å) radiation. Sample was made into fine powder for the analysis.

X-rays were produced by a copper target at the voltage 40 kV and current 30 mA. The slits used were divergence slit of 1^0; scatter slit of 1^0; receiving slit of 0.3 mm. In the scanning set up, Driver axis: 2 θ; Scan range: 10 – 80; Mode of scan is continuous scan; Scan speed: 2^0 min^{-1}; Sampling pitch: 0.02^0; Preset time: 0.60 sec.

The size of crystallites, lattice strain and percentage of crystallinity of bone apatite was calculated from XRD data using the formulae[13],

$$\text{Size of crystallites, } L = \frac{K\lambda}{\beta_0 \cos\theta},$$

where λ = 1.54056 Å, K is assumed to be 1

$$\text{Lattice strain, } \varepsilon = \frac{\beta_o}{4\tan\theta}$$

$$\text{Crystallinity (\%)} = \frac{A_t - A_a}{A_t} x\ 100$$

where A_t is total area covered by the peaks and A_a is amorphous area (A_a) covered by the broad peak alone [13].

3. RESULTS AND DISCUSSION

Table 1 gives XRD data obtained from diffractograms. The data includes 2θ, d spacing, relative intensity (I/I_0), FWHM, crystallite size (L) and lattice strain (ε) of diffraction peaks. The data is of machine (diffractometer) generated one. The data of chicken bone reveals principal interplanarspacings (d – spacings) around 2.91 Å, 2.80 Å, 2.21 Å, and 1.81 Å. At these d spacings, crystallite size and lattice strain are calculated. Average values along with SD are also tabulated in the table.

2θ (degree)	d (Å)	I/I_0 (%)	FWHM, β_0 (degree)	Crystallite Size, L (nm)	Lattice strain, ε
30.7410	2.90854	100.00	0.4723	18.23	0.0075
31.9092	2.80467	88.94	0.6298	13.71	0.0096
40.7950	2.21196	11.46	0.7396	11.97	0.0087
50.4920	1.80757	44.17	0.8224	11.16	0.0076
Average:				13.77	0.0084
SD:				±3.160	±0.001

The principal interplanar spacings (d – spacings) observed in the present investigation reveal the fact that mineral present in chicken femur bone ishydroxyl calcium phosphate. Further, calcium phosphate present in bone is of both crystalline and
amorphous in nature. The degree of crystallinity ranges from 50% to 60%.

The broadening of peaks in x – ray diffractograms is because of crystallites of small in size and also inhomogeneous distribution of their size.

REFERENCES

1. Asfiny Nur Laeny, Synthesis of Amorphous Calcium Phosphate by Low Temperature-Precipitation Method from Eggshell: Introduction to X-ray Diffraction Anonim, 2005.

http://www.mrl.ucsb.edu/mrl/index.html. [30 Maret 2007]

2. Dean Mo Liu, Fabrication of hydroxyapatite with controlled porosity, J.Mat.Sci.: Mat. Med., Vol. 8(1997), pp. 227-232.
3. V Jokanovi, B Jokanovi, Kinetics and sintering mechanisms of hydro-thermally obtained hydroxyapatite, Mat. Chem.Phy., Vol. 111(2008), pp. 180-185.
4. L L Hench, Bioceramics: From Concept to Clinic, J. Amer.Cer. Soc., Vol.74(1991), pp. 1487-1510.
5. G. Willmann, Material properties of hydroxyl apatite ceramics, Inter. Ceram, Vol. 42, (1993), pp.206-208.
6. G. Willmann, Medical grade hydroxyapatite: State of the art, British Ceram. Trans.,Vol. 95(1996), pp. 212-216.
7. G. Willmann, J. Min. Mat. Char.Engg., Vol. 9, No.8(2010), pp. 683-692.
8. S Joschek, B Nies, R Krotz andAGopferich, Biomaterials, Vol. 21, No. 16(2000), pp. 1645 - 1658.
9. R Ganghadhar, Kaleem Ahmed Jaleeliand Adeel Ahmad, Int. J. Sci. Engg. Tech., Vol. 4, No. 3(2015), pp.1195 – 1198.
10. K. Sreenivasa Rao, T. Balaji, Talasila Prasada Rao, G.R.K. Naidu, Spectrochimica Acta., Part B. Atomic Spectroscopy,Vol. 57, No. 8(2002), pp. 1333 – 1338.
11. Jayanand Manjhi, Suneel Kumar, Jitendra Behari, Rashmi Mathur, J. Rehabilitation Res. Dev., Vol. 50, No.1(2013), pp. 17 - 30.
12. R. Jeevan Kumar, S. Md. Shoaib, K. Fakruddin, and Adeel Ahmad J. KSU, Sci., Vol.20, No. 2(2008), pp. 17 – 26.
13. Kavesh S, and J M Schultz, Meaning and measurement of crystallinity in polymers: A Review, Polymer Engg. Sci., Vol. 9, No. 5(1969), pp. 331– 338.

Second National Conference on
RECENT ADVANCES IN APPLIED NANO MATERIALS
February 16-17, 2018 at Department of Physics, University College of Science, Saifabad, Osmania University, Hyderabad, Telangana State, India.

Synthesis and Characterization of Ba_2FeMoO_6

G. Rajender[1#], Y. Markandeya[2@] and G. Bhikshamaiah[1*]
[1]Department of Physics, [2]Nizam College, Osmania University, Hyderabad
*E-mail: gbhyd08@gmail.com #E-mail: grphyou@gmail.com @E-mail: markphysics@gmail.com

Abstract: *Double perovskite Ba_2FeMoO_6 samples were prepared by sol-gel method in Ar/H_2 atmosphere. The materials were sintered at different temperatures 1200°C and 1300°C. X-ray diffraction studies showed that the material has cubic crystal structure. The lattice parameter of the samples is found to be 8.0617 and 8.0639 Å for the samples sintered temperature 1200 and 1300°C respectively. The density measurements of the samples were determined experimentally and calculated theoretically using Archimedes principle and X-ray diffraction data respectively. The values of density % are found to be 89.80 and 90.16 for Ba_2FeMoO_6 sintered at1200°C and sintered at 1300 °C respectively. It is known from EDS spectra that the elements Ba, Fe, Mo and O are only present in the sample and no other elements or impurities are present. The FTIR spectra of Ba_2FeMoO_6 sample recorded at RT produced three characteristic absorption bands in the range 850-400 cm^{-1} at around (i) 821 cm^{-1} (ii) 634 cm^{-1} and (iii) 475 cm^{-1} corresponds to the Mo-O symmetric stretching mode of MoO_6-octahedra, anti-symmetric stretching mode of the MoO_6-octahedra and Fe-O vibration absorption of FeO_6- octahedra respectively, confirms the double perovskite phase of Ba_2FeMoO_6 sample.*

Key Words: *sol-gel; double perovskite; X-ray diffraction; scanning microscopy.*

1. INTRODUCTION

The double perovskite of the type $A_2BB'O_6$ (where A is divalent cations such as Sr, Ca and Ba; B is tri/divalent cations such as Fe, Cr, Ga, Mg and Mn; B' is penta/hexa valent cations such as Mo, Re and W;) have been extensively studied due to substantial Low Field Magneto Resistance (LFMR) at room temperature that lead to potential applications of these materials as magnetic field sensors, read heads for magnetic hard disk drives and nonvolatile magnetic computer memory [1–6]. Many researchers prepared Ba_2FeMoO_6 at different sintered temperature and as well as different duration of time period [9-12]. Several investigations such as, XRD, SEM, EDAX, FTIR, Mossbauer spectra, electrical conductivity, Magnetic properties, and Magneto-resistance were done on Ba_2FeMoO_6 [9-12].

In view of this, the authors have taken up to synthesized the Ba_2FeMoO_6 double perovskite at different sintered temperature like as 1200 °C and 1300 °C. These materials were also characterized by various experiments such as X-ray diffraction (XRD), Scanning Electron Microscopy (SEM), Energy dispersive X-ray spectroscopy (EDS) and Fourier transform infrared spectroscopy (FTIR). The authors also observed the effect of sintered temperature on these studies.

2. EXPERIMENTAL

Double perovskite of Ba_2FeMoO_6 at different sintered temperature like as 1200 °C and 1300 °C were synthesized by sol-gel method [7, 8]. Stoichiometric amount of analytical reagent grade $Ba(NO_3)_2$ (Barium nitrite), $Fe(NO_3)_3 \cdot 9H_2O$ (Ferric nitrate), and H_2MoO_4 (Molybdic acid) are separately taken in beakers. Corresponding solutions are formed in the beaker while adding about 100 ml distilled water to Barium nitrite and Ferric nitrate. Ammonium was added to Molybedic acid for converting ammonium heptamolybdate $[(NH_4)_6Mo_7O_{24}]$ latter about 100 ml distilled water is added to get ammonia molybdic solution. The mixture solution was obtained by adding all the three solutions in a single beaker. Citric acid is added to this mixture in the mole ratio of citric acid to metal ions is 2:1. Adjusted the pH of the mixture solution to 7 by adding dilute ammonia solution. After that the beaker contained mixture solution is heated on hot-plate at around 80°C using magnetic stirrer for about a day. Ethylene glycol is added to this solution such that metal ion to ethylene glycol ratio is 1:1.2 and heated until a dark gel is formed. The gel is transformed into precursors in the continuing heating at the same temperature. These precursors are combusted at 250°C using Bunsen burner to get dried loosely powders. The loosely powder are grinned using Agate Motor. Later

the powder are taken into a crucible and heated at 500°C/6 hrs, 700°C/6 hrs, 900°C/6 hrs and 1100°C/6 hrs in a furnace with intermittent grinding. These powders are then pressed into pellets of 1 cm diameter and about 2mm thickness using a die with hydraulic press by applying a pressure of 1 ton. These pellets are sintered at temperatures 1200°C and 1300°C for 6 hrs. Finally double perovskite of Ba_2FeMoO_6 at sintered temperature 1200°C (BFMO1) and Ba_2FeMoO_6 at sintered temperature 1300°C (BFMO2) materials were made when the pellets were annealed at 1000°C in a stream mixture of gas (10% H_2 + 90% Ar) for about 3 hrs for loss of oxygen or reducing the Mo^{6+} to Mo^{5+}. These pellets were subjected to X-ray diffraction studies using Philips PW 1830 diffractometer with Cu-Kα radiation (40 kV × 25 mA) to confirm the crystal structure. Surface morphology of the samples was found using the scanning electron microscope (Model No. Joel JSM-5600) with combined micro analyzer. Fourier transform infrared spectra of the samples were recorded on Bruker Tensor 27 DTGS TEC detector spectrophotometer in the wave number range 400-1000 cm^{-1} by the KBr pellet method.

3. CHARACTERIZATION

Fig. 1. shows X-ray diffraction patterns of BFMO1 and BFMO2 samples obtained at room temperature. Analysis of X-ray diffraction data indicates that these samples comprise a single phase and crystallize in the cubic double perovskite structure with a space group $Fm\bar{3}m$ [13]. All the diffraction peaks of corresponding to BFMO1 and BFMO2 are shown in Fig. 1. The lattice parameter 'a' of BFMO1 and BFMO2 samples has been evaluated using the lattice planes with (h k l) values of (200), (220), (222), (400), (420), (422), (440), (620) and (622) and corresponding Bragg angle (2θ) positions of X-ray diffraction profiles with suitable POWD computer program. The unit cell volume ($V = a^3$) of BFMO1 and BFMO2 was calculated using the calculated lattice parameter 'a'.The values of lattice parameters (*a*) are 8.0617 Å and 8.0639 Å for BFMO1 and BFMO2 respectively. The obtained unit cell volumes are 523.93 $Å^3$ and 524.36 $Å^3$ for BFMO1 and BFMO2 respectively. It is observed that the lattice parameter and unit cell volume of the sample increases with increase of sintered temperature.

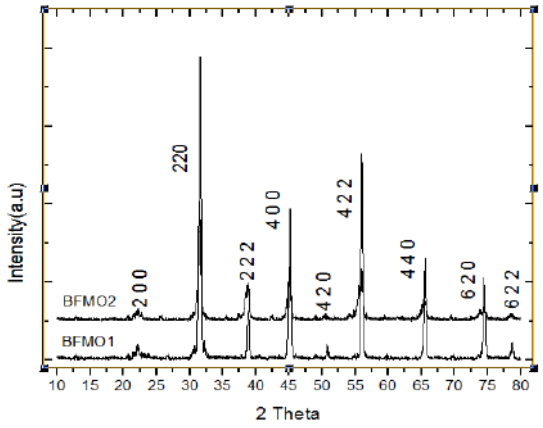

Fig.1. XRD of BFMO1 and BFMO2 samples.

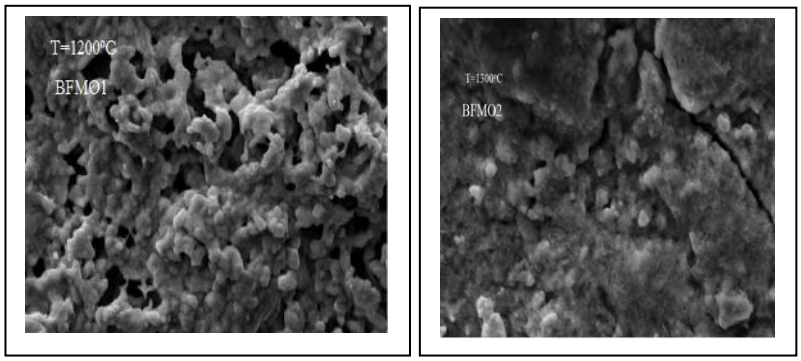

Fig. 2. SEM photographs of BFMO1 and BFMO2 samples.

Fig. 2. show the scanning electron micrographs of Ba_2FeMoO_6 samples sintered at different temperatures as 1200°C and 1300°C. It was observed that porosity is present in the samples as evident in Fig. 2. The pore size of the samples decreases with increase of sintered temperature. The pore size is small and material is closely packed with fewer voids. Some holes defects were observed, but they were probably formed during sample breaking for SEM investigations [14].

The experimental density (d_{exp}) of the BFMO1 and BFMO2 samples was measured by the Archimedes principle using the relation:

$$d_{\exp} = \frac{m_1}{m_1 - m_2} \times d_x$$

where, m_1 is the weight of the sample in air, m_2 is the weight of the sample when immersed in liquid xylene and d_x is density of xylene [d_x = 0.865 gm/cm^3]. The theoretical density (d_{th}) of the BFMO1 and BFMO2 samples from XRD was calculated using the following expression:

$$d_{th} = \frac{zM}{NV}$$

where, z is the number of molecules in unit cell of the crystal (z = 4 for cubic), M is mass per formula unit (gm), N is Avogadro number ($N = 6.023\times10^{23}$ mol^{-1}), V is unit cell volume (cm^3) as determined by XRD. From the values of

density evaluated experimentally and calculated theoretically using X-ray data, one could estimate the percentage of porosity (P %) and percentage of density (d %) of the sample which is calculated by following equations:

$$P(\%) = \frac{d_{th} - d_{\exp}}{d_{th}} \quad \text{and} \quad d(\%) = 100 - P(\%)$$

The values of d_{exp}, d_{th}, P (%) and d (%) of BFMO1 and BFMO2 sample were calculated and are given in Table 1.

Table 1. Values of d_{exp}, d_{th}, P (%) and d (%) of the BFMO1 and BFMO2 samples

Samples	m_1(gm)	m_2(gm)	$d_{(exp)}$(gm/cm^3)	$d_{(th)}$(gm/cm^3)	P (%)	d (%)
BFMO1	0.8318	0.7108	5.9463	6.622	10.20	89.80
BFMO2	0.2910	0.2488	5.9648	6.616	9.84	90.16

Energy dispersive X-ray spectroscopy (EDS) was used to determine the elemental composition of the samples. In the present study, EDS studies of BFMO1 and BFMO2 samples were carried out and the results are shown in **Fig. 3(a, b).** EDS analysis showed that the elements Ba, Fe, Mo and O are present in the samples. It was observed that there were no other elements or impurities in the samples as evident in the EDS spectra.

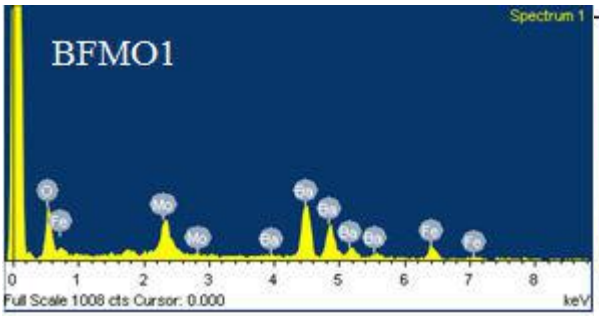

Fig. 3(a). EDS of BFMO1 sample

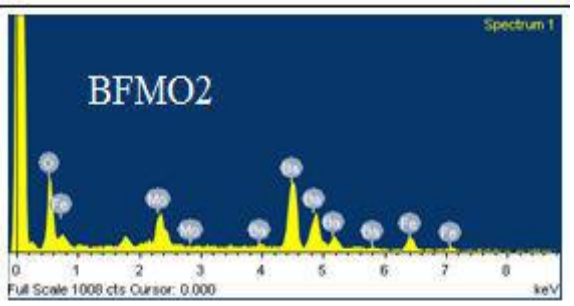

Fig. 3 (b). EDS of BFMO 2 sample

Figure 4 shows FTIR spectra of the BFMO1 and BFMO2 samples in the spectral wave-number range 1000-400 cm^{-1}. The FTIR spectra of the perovskite structure have three characteristic absorption bands between 850- 400 cm^{-1}, respective to composition and these are usually used to identify the perovskite phase formation from the FTIR spectra of the BFMO1 and BFMO2 samples[15]. In the investigation three bands for Fe and Mo are detected. The first strong band in the high-wavenumber

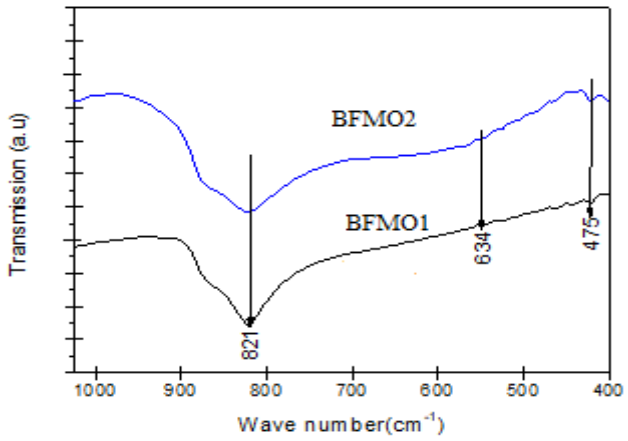

Range ~ 821 cm^{-1} associated to the Mo-O symmetric stretching mode of MoO_6-octahedra. The second band at ~ 634 cm^{-1} assigned to the anti-symmetric stretching mode of the MoO_6-octahedra due to the higher charge of this cation [16]. The Mo-O symmetric stretching mode of MoO_6-octahedra at about 821 cm^{-1} is usually an infrared inactive vibration, but in double perovskite, both Fe and Mo ions exist in Fe and Mo sites, it becomes partially allowed due to lowering site symmetry. The third weak absorption band at about 475 cm^{-1} is ascribed to Fe-O vibration absorption of FeO_6- octahedra. These bands confirm the formation of double perovskite phase of the present samples.

Fig. 4. The FTIR spectra of BFMO1 and BFMO2 samples.

4. CONCLUSIONS

It is noticed that the lattice parameter and unit cell volume of BFMO1 is lower than BFMO2 sample. The density % of BFMO1 is less the BFMO2 samples. The pore size of the samples decreased with increase of sintered temperature from 1200 ^{o}C to 1300^{o}C. It is found from EDS results that no other elements are present in BFMO1 and BFMO2 samples. The three characteristic absorption bands are found in FTIR spectra of Ba_2FeMoO_6 between 850-400 cm^{-1}. These bands confirm the formation of perovskite phase of the present samples.

REFERENCES

1. K. I. Kobayashi, T. Kimura, H. Sawada, K. Terakura, Y. Tokura, Nature(Lond.) 395(1998)677–680.
2. B. Maignan, C. Raveau, M. Martin, J. Hervieu, Solid. State. Chem. 144 (1999) 224.
3. K.I.Kobashi,T.Kimura,Y.Tomioka,H.Sawada,K.Terakuraand, Y. Tokura, Phys. Rev. B. 59, (1999) 11159.
4. W.Prellier,W.Smolyaninova,A.Bisbas,C.Galley,R.L.Green, K. Ramesha, J. Gopalakrishnan, J. Phys. Condens. Matter 12 (2000) 965.
5. H. Han, B.J. Han, J.S. Park, B.W. Lee, S.J. Kim, C.S. Kim, J. Appl. Phys. 89 (2001) 7687.
6. F.K. Patterson, C.W. Moeller, R. Ward, Inorg. Chem. 2 (1963) 196.
7. M. Itoh, I. Ohta, Y. Inaguma, Mater. Sci. Eng. B 41 (1996) 55.
8. M. García-Hernández, J.L. Martynez, M.J.Martynez-Lope, M.T .Casais, J. A.Alons, Phys. Rev. Lett. 86 (2001) 2443.
9. H.Han,C.S.Kim, B.W. Lee ,J.Magnetism Magnetic Materials 254-255(2003)574.
10. A.G.Flores, M.Zazo, J.Iniguez,V.Raposo,C.de Francisco,J.M.Munoz, W.J. Padilla , J.Magnetism and Magnetic Materials 254-255(2003)583-585
11. M.J.Martinez-Lope,J.A.Alonso,M.T. Casais, Z.Naturforsch 58b,571-576 (2003).
12. H.M. Yang, H.Han,B.W.Lee, J.Magnetism and Magnetic Materials 272-276(2004)1831-1833.
13. Anthony Arulraj,K.Ramesha,J.Gopalakrishnan,C.N.R.Rao, J. Solid. State. Chem. 155 (2000) 233-237.
14. G.Aldica,C.Plapcianu,P.Badica,C.Valsangiacom,L.Stoica, J.Magnetism and Magnetic Materials 311(2007) 655-670.
15. Mostafa, M F., Ata-Allah, SS., Youssef, A. A. A., Refai, H.S., J. Magn. Magn. Mater., 320 (2008) 344.
16. Lavat A E, Baran E J, *Vib Spectrosc*, 2003, 32(2),167-174.

Second National Conference on
RECENT ADVANCES IN APPLIED NANO MATERIALS
February 16-17, 2018 at Department of Physics, University College of Science, Saifabad, Osmania University, Hyderabad, Telangana State, India.

Characterization and Conductivity of A_2FeMoO_6 (A = Sr, Ba) double perovskite

Y. Markandeya[1*], G. Rajender[2], Y. Suresh Reddy[2], S. Varaprasad[3], G. Bhikshamaiah[2]
[1]Department of Physics, Nizam College, Osmania University, Hyderabad 500 001, India.
[2]Department of Physics, Osmania University, Hyderabad 500 007, India.
[3]Department of Physics, JNTUA, Ananthapuramu 515 002, India.
[*]Corresponding author E-mail addresses: markphysics@gmail.com

Abstract: *Double perovskite type materials A_2FeMoO_6 (A= Sr and Ba) were synthesized by sol-gel method under H_2/Ar atmosphere at temperature 1000 °C. The materials were analyzed by X-ray diffraction (XRD) and it is found that double perovskite material crystallized in tetragonal structure for Sr_2FeMoO_6 and cubic structure for Ba_2FeMoO_6. Variation of porosity and grain size behavior of samples has been studied by scanning electron microscopy (SEM). The spectra from Energy dispersive X-ray spectroscopy (EDS) showed that all the elements Sr, Ba, Fe, Mo and O are present in the samples and there are no impurities in the materials. It was found from electrical conductivity results in the temperature range from 5-300 K that conductivity of Ba_2FeMoO_6 sample increased compared with Sr_2FeMoO_6. Both samples showed semiconductor to metallic behavior in the temperature range 5-300 K.*

Key Words: *Double perovskite; sol-gel; crystal structure; spectroscopy; conductivity;*

1. INTRODUCTION

Double perovskite materials were extensively studied owing to their important applications such as magneto-electronics, magnetic media, electrical conductors, microelectronics, telecommunications, thermoelectric, magnetic sensors and magnetic read/write heads [1-6]. The general formula of double perovskite is $A_2BB'O_6$, where A is Sr or Ba or Ca atom and, B and B' are transition-metal atoms. The choice of B' and B atoms provides a tunable B'-O-B magnetic interaction, which gives rise to a variety of transport and magnetic properties [4]. The A_2FeMoO_6 compounds crystallize in tetragonal structure with space group I4/mmm for Sr_2FeMoO_6 and in cubic with space group $Fm\bar{3}m$ for Ba_2FeMoO_6 [1, 7]. The structure of A_2FeMoO_6 compound can be viewed as a continuous, regular arrangement of corner sharing MoO_6 and FeO_6 octahedra, alternating along the three directions of the crystal, with the 'A' cations occupying the voids in between the octahedra [1, 6]. Many studies were done to understand the characterization, transport and magnetic structure of A_2FeMoO_6 (A=Sr, Ba,) double perovskite material prepared by solid state method [2-8]. However, there were no conductivity studies reported on A_2FeMoO_6 (A=Sr and Ba) prepared by sol-gel method . In view of this, the authors have taken up to synthesize the A_2FeMoO_6 (A = Sr and Ba) double perovskite and perceived that how the conductivity results reflected by placing Ba and Sr at A-site in A_2FeMoO_6. These materials were also characterized by X-ray diffraction (XRD), Scanning Electron Microscopy (SEM) and Energy dispersive X-ray spectroscopy (EDS).

2. EXPERIMENTAL

Double perovskite of A_2FeMoO_6 (A = Sr and Ba) material were prepared by sol-gel process [9, 10]. The analytical reagent grade $Sr(NO_3)_2$, $Ba(NO_3)_2$, $Fe(NO_3)_3 \cdot 9H_2O$ and H_2MoO_4 are separately taken in beakers. Corresponding solutions are formed in the beaker while adding about 100 ml distilled water to strontium nitrite (or barium nitrite) and ferric nitrate. Required quantity of ammonium was added to H_2MoO_4 for converting ammonium hepta molybdate, latter about 100 ml distilled water is added to get ammonia molybdic solution. The solution mixture was obtained by adding all the three solutions in a single beaker. Citric acid is added to solution mixture in the mole ratio of metal to citric acid ions is 1:2. While ammonia solution is added to the above mixture and pH is adjusted to 7(neutral). After that the beaker containing solution mixture is heated on hot-plate at around 80 °C using magnetic

stirrer for a period of 24 hours. Ethylene glycol is added to solution mixture when solution mixture level reduces to one by fourth of initial level. Ethylene glycol to metal ion ratio is maintained as 1.2:1, continuously heating to solution mixture until a dark gel is formed. The gel is transformed into precursors in the continuing heating at the same temperature. These precursors are combusted by Bunsen burner at 250 ^{o}C to get dry and loose powders. These loose powders are ground using Agate Motor. Later the powder are transferred into a crucible and the powder is burnt at 500 ^{o}C/6 hrs, 700 ^{o}C/6 hrs, 900 ^{o}C/6 hrs and 1100 ^{o}C/6 hrs in a furnace with intermittent grinding. These burnt powders are then pelleted into discs of 1 cm dia and about 2mm thick using a steel die at a pressure of 1 ton. The disc pellets are sintered at temperature 1200 ^{o}C for 6 hrs. Finally double perovskite of A_2FeMoO_6 (A= Sr and Ba) materials were formed and annealed at 1000 ^{o}C in mixture of gas flow (10% H_2 + 90% Ar) for a period of 3hrs to reduce the Mo^{6+} to Mo^{5+}.

These double perovskite materials are exposed to X-rays using Philips PW-1830 diffractometer (40 kV×25mA and Cu-Kα radiation) with a graphite mono-chromator to confirm the crystal structure. A step scan mode was done with a step width of 2θ = 0.02^{o} and 1sec duration of sampling time. The surface morphology and micro structural studies of these materials were analysed using the SEM with (Model No. Joel JSM 5600) combined micro analyser. The elemental analysis of these materials was also determined by EDS (Model: OXFORD). Low temperature electrical conductivity studies were made for these materials in the temperature range 5 to 300 K using the standard four probe method by OXFORD superconducting system.

3. RESULTS AND DISCUSSION

3.1. Characterization

Figure.1 shows the X-ray diffraction (XRD) of A_2FeMoO_6 (A=Sr and Ba) materials. The X-ray diffraction patterns of these materials were analysed. It is found from indexed X-ray results that the Sr_2FeMoO_6 material crystallizes in tetragonal structure with space group *I*4/*mmm* and Ba_2FeMoO_6 material crystallizes in cubic structure with space group $Fm\bar{3}m$[5, 11]. Lattice parameters of A_2FeMoO_6 (A=Sr and Ba) materials were calculated using Bragg angles and (hkl) values in the Cohen's least square method with help of CELEN computer program [10]. The unit cell volume (V) of A_2FeMoO_6 (A=Sr and Ba) were also determined by the formula V= a^2c and V=a^3 for tetragonal and cubic respectively. The values of lattice parameters, unit cell volume are '*a*' =5.574 Å, **'*c*'=** 7.909 Å, **'V'=** 245.73(Å)^3 for Sr_2FeMoO_6 and '*a*' = 8.073 Å 'V'=526.14 (Å)^3 for Ba_2FeMoO_6 respectively. It is understood from XRD analysis that crystal structure changes from tetragonal to cubic when Sr element replaced by Ba element at A-site in the A_2FeMoO_6 double perovskite. Lattice parameters and unit cell volume of Ba_2FeMoO_6 are greater than the Sr_2FeMoO_6. It is due to the ionic radii of Ba^{2+} is larger than Sr^{2+}.

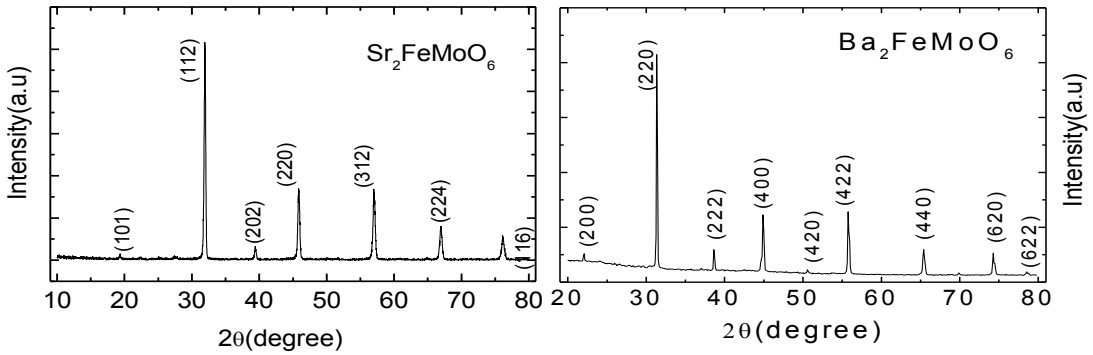

Figure 1. X-ray diffraction patterns along with (hkl) values of Sr_2FeMoO_6 and Ba_2FeMoO_6 materials

Figure. 2 shows the SEM photographs of A_2FeMoO_6 (A= Sr, Ba) materials. It is seen from Figure.2 that slight porosity is present in the materials. The pore size is very small and material is closely packed with fewer voids. The grain size of Sr_2FeMoO_6 sample is slightly smaller than the Ba_2FeMoO_6.

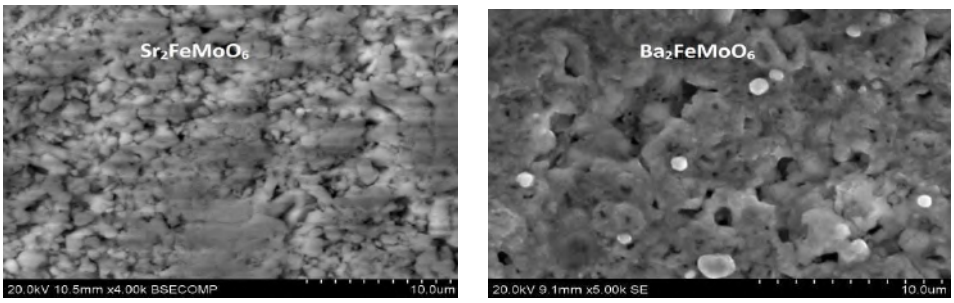

Figure. 2. SEM Photo graphs of Sr_2FeMoO_6 and Ba_2FeMoO_6 materials

EDS of A_2FeMoO_6 (A= Sr, Ba) materials are shown in Figure.3. The results from EDS analysis showed that the elements Sr, Ba, Fe, Mo and O are present and no new impurities exists in the present double perovskite materials.

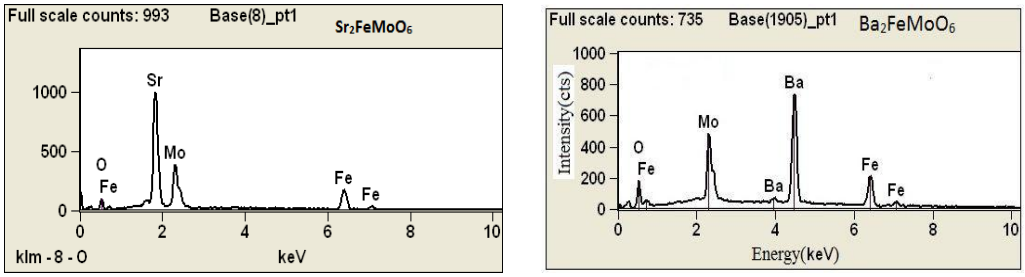

Figure. 3. EDS pattern of Sr_2FeMoO_6 and Ba_2FeMoO_6 materials

3.2. Electrical conductivity

Variation of electrical conductivity (σ) of A_2FeMoO_6 (A= Sr, Ba) as function of temperature in range 5-300 K is shown in Figure.4. It is observed from Figure.4 that the both material exhibits as the transition from semiconductor to metallic nature between temperatures 5 to 300 K [12-15]. The semiconductor-metal transition temperature (T_{SM})are measured from Figure.4. The Sr_2FeMoO_6 material exhibits a semiconducting behavior below transition temperatures 179 K, and a metallic behavior above the same transition temperature. It is expected from the graph of Figure. 4 that the semiconductor-metal transition (T_{SM}) is 50 K for Ba_2FeMoO_6 material. It is noticed that the value of T_{SM} for Ba_2FeMoO_6 decreases compared with Sr_2FeMoO_6. Since the resistivity (1/conductivity) of Ba_2FeMoO_6 is lower than Sr_2FeMoO_6 material in the entire temperature range from 5 to 300 K, hence the T_{SM} of Ba_2FeMoO_6 shifts towards lower temperature region because it has low resistivity.

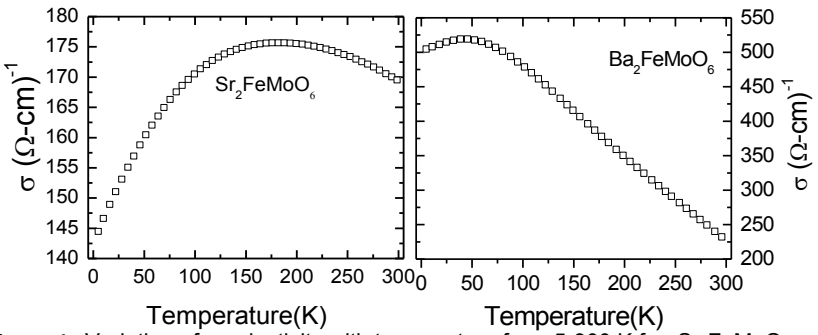

Figure.4. Variation of conductivity with temperature from 5-300 K for Sr_2FeMoO_6 and Ba_2FeMoO_6

It is also seen from Figure. 4 that conductivity (σ) for Sr_2FeMoO_6 is found to be in the range 144-187 $(\Omega\text{-cm})^{-1}$. The value of σ is larger for Ba_2FeMoO_6 compared to Sr_2FeMoO_6, which is of the order ranging from 232-526 $(\Omega\text{-cm})^{-1}$. The difference may be attributed the effect of grain boundary, which appear to influence the conductivity of these present samples [12, 16]. The increase in conductivity regime may be attributed to the decrease in dis-orderness in grain boundaries by substituting Ba element at the place of Sr in A_2FeMoO_6. This corresponds to lowered the scattering of charge carriers, which leads to carrier localization and higher conductivity of the material [6, 17]. It may

be also expected that Ba^{2+} acts as a low barrier to electron transport, growing the number of pathways for electron percolation [18].

The A_2FeMoO_6 (Sr, Ba) materials have semiconductor nature at low temperature and they shows metalic behavior in the high temperature rigime. The elecrons in Fe^{3+} ions move in foward direction (spin up) and the electrons in Mo^{5+} ions moves in reverse direction (spin down) in A_2FeMoO_6 double perovskites with temperature. Since the conductivity of the materials is not linear with temperature and the behavior of material tranform from semiconductor to metalic state.

4. CONCLUSIONS

The value of lattice parameters and unit cell volume of Ba_2FeMO_6 is greater than the Sr_2FeMoO_6. Structural changes occurred from tetragonal to cubic when Sr element replaced by Ba in A_2FeMoO_6. The conductivity of A_2FeMoO_6 material improved by substitution of Ba at A-site in A_2FeMoO_6 in the place of Sr. The grain size of Ba_2FeMoO_6 material is slightly improved compare to Sr_2FeMoO_6.

ACKNOWLEDGMENTS

The authors thank Dr. Rajeev Rawat at UGC-DAE, Consortium for Scientific Research, Indore for providing conductivity and magnetoresitance facilities. The authors acknowledge Department of Science and Technology, New Delhi, India for providing financial assistance to carry out this work under the research project (File No.SB/S2/CMP-004/2013). The authors thank the Head, Department of Physics, University College of Science and Principal and Head, Department of Physics, Nizam College, Osmania University, Hyderabad, India for his encouragement and providing necessary facilities.

REFERENCES

1. Kobayashi K I, Kimura T, Sawada H, Terakura K and Tokura Y 1998 *Nature(London)* 395 677.
2. Zhao H F, Cao L P, Song Y J, Feng S M, Shen X, Ni X D, Yao Y, Wang Y G, Jin C Q and Yu R C, 2015 *Journal of Solid State Communication* 204 1.
3. Gong S, Chen P and Liu B G *2014 Journal of Magnetism and Magnetic Materials* 349 74.
4. Zhang Q, Xu Z F, Pei J and Sun H B 2014 *Journal of Magnetism and Magnetic Materials* 354 231.
5. Lu Min Feng, Wang Jing Ping, Liu Jian Fen, Song Wei, Hao Xian Feng, Zhou De Feng, Liu Xiao Juan, Wu Zhi Jian and Meng Jian 2007 *Journal of Alloys and Compounds* 428 214
6. Gaur Anurag, Varma G D and Singh H K 2008 *Journal of Alloys and Compounds* 460 581
7. Pandey Vibhav, Varma Vivek , Aloysius R P, Bhalla G L, Awana V P S, Kishan H, Kotnala R K 2009 *Journal of Magnetism and Magnetic Materials* 321 2239.
8. Goko Tatsuo, Endo Yoshiyuki, Morimoto Eiji, Arai Juichiro, Matsumoto Takehiko 2003 *Journal of Physica B 329 837.*
9. Markandeya Y, Suresh K and Bhikshamaiah G 2011 *J. Alloys and Compounds* 509 9598.
10. Markandeya Y, Suresh Reddy Y, Shashidhar Bale, Vishnuvardhan Reddy C and Bhikshamaiah G 2015 *Journal of Bulletin of Materials Science* 38 1603.
11. Kim J, Sung J G, Yang H M, Lee B W 2005 *Journal of Magnetism and Magnetic Materials* 290 1009.
12. Liu G Y, Rao G H, Feng X M, Yang H F, Ouyang Z W, Liu W F and Liang J K 2003 J. Physica B 334 229.
13. Feng X M, Rao G H, Liu G Y, Yang H F, Liu W F, Ouyang Z W and Liang J K 2004 *Journal of Physica B* 344 21.
14. Maiti K, Vasanthacharya N Y and Sarma D D 1997 J. Phys. Condens. Matter 9 7507.
15. Inaba F, Arima T, Ishikawa T, Katsufuji T and Tokura Y 1995 J. Phys. Rev. B52 R2221.
16. Chmaissem O, Kruk R, Dabrowski B, Brown D E, Xiong X, Kolesnik S, Jorgensen J D and Kimball C W 2000 J. Phys. Rev. B 62 14197.
17. Hemery E K, Williams G V M and Trodahl H J 2007 *Journal of Physica B* 394 74.
18. Sher Falak, Venimadhav A, Blamire M G, Dabrowski B, Kolesnik S and Attfield Paul 2005 *Journal of Solid State Sciences* 7 912.

Second National Conference on
RECENT ADVANCES IN APPLIED NANO MATERIALS
February 16-17, 2018 at Department of Physics, University College of Science, Saifabad, Osmania University, Hyderabad, Telangana State, India.

Synthesis, Physical Properties and FTIR Structural Studies of TiO_2 doped Mixed Alkali Borosilicate Glass Systems

B. Nagamani[1], Sandhya Cole [2] , Ch. Srinivasu[3]
[1]Dept. of Physics, Dr. LHR Govt. Degree College Mylavaram-521230 ,A.P., India,
[2]Dept. of Physics, ANU, Nagarjunanagar – 522510, Guntur, A.P., India.
[3]Dept. of Physics, Andhra Loyola College, Vijayawada – 520 004, Krishna, A.P., India.
E-mail: nagamani1411@gmail.com

Abstract: *Mixed alkali borosilicate glasses doped with 5% Titanium oxide were synthesized by rapid cooling of bubble free melt in air and their physical parameters were calculated using measured density values. XRD spectra confirm the amorphous nature of samples. FTIR spectra confirm the presence of both BO_4 tetrahedra, BO_3 triangles, B-O-B linkages and Q_4, Q_3 units of Silicon. The absence of peak at 806 cm^{-1} indicates the absence of boroxol ring formation, suggests that the present glass system consists chain type meta borate group.*

Key Words: *Borosilicate glasses, Xylene, TM ions, Diborate*

1. INTRODUCTION

Borosilicate glasses are widely used in many applications, from chemically resistant containers to structural members, and sealing glasses to nuclear waste immobilization. Transition metals effectively change the optical and thermal properties of glasses. Titanium dioxide highly efficient at photo catalysing dirt in sunlight, non-toxic, chemically inert in the absence of light, inexpensive [1].

2. EXPERIMENTAL

2.1 Sample preparation

Transparent Borosilicate glasses of composition xNa_2O-$(30-x)K_2O$-$40SiO_2$-$30B_2O_3$-$5TiO_2$($5 \leq x \leq 25$) ,where x was varied from 5 to 25 in steps of 5 keeping total alkali concentration remain 30 mol% in all samples were prepared by conventional melt-quench method. Analytical grade SiO_2, B_2O_3, K_2CO_3, Na_2CO_3, TiO_2 were used as starting materials. The weighed chemicals were mixed and grinded thoroughly to obtain a homogeneous mixture and was taken in a silica crucible and melted in high temperature furnace at 950°C temperature up to 25-30 minutes until a bubble free liquid was formed. The melt was then quenched to room temperature in air by pouring it on a brass slab and the obtained glasses are annealed about 3 hours at 450°C.

Table 1.The Details of composition (mol %) of present Glass samples

Glass code x (Na_2O Concentration)	Glass system
X_5	$5\ Na_2O$-$25K_2O$-$35SiO_2$-$30B_2O_3$-$5TiO_2$
X_{10}	$10Na_2O$-$20K_2O$-$35SiO_2$-$30B_2O_3$-$5TiO_2$
X_{15}	$15\ Na_2O$-$15K_2O$-$35SiO_2$-$30B_2O_3$-$5TiO_2$
X_{20}	$20Na_2O$-$10K_2O$-$35SiO_2$-$30B_2O_3$-$5TiO_2$
X_{25}	$25Na_2O$-$5K_2O$-$35SiO_2$-$30B_2O_3$-$5TiO_2$

2.2 Physical Parameters

Density of glass samples was measured at room temperature by Archimedes principle by using Xylene as immersion liquid. Using density and the molecular weight values of the samples Physical parameters are evaluated by conventional formulae.

2.3 X-ray diffraction (XRD)

XRD patterns of glass samples were recorded on powder X-ray diffractometer using Cu-K_α radiation for checking amorphous nature of present glass samples.

2.4 Infrared spectra

Glass does not possess long-range order, so no theory of vibrations is available for the interpretation of infrared spectra. But researchers have attempted by simple approaches to correlate certain bands with the presence of certain structural units in glass. The IR absorption spectra of samples were recorded at room temperature between wave number ranges 400-4000cm^{-1}.

3. RESULTS AND DISCUSSION

3.1 Structural effects on Physical parameters

From glass samples x=5 to x=25 as sodium (Na) cation concentration was increased, Na ions replace some of potassium (K) ions. Na cation size is smaller than K cation, it strongly attracts oxygen atoms reducing molar volume. Due to the shrinkage of glass network density of glass sample should increase from x=5 to x=25, was evident by the calculated values of molar volume of present glass samples except for x= 25. For x=25 density slightly decreases may be due to structural changes in glass composition and diffusivity of alkali ions [5].

As due to the reduced molar volume the number of transition metal ion per unit volume (TM ion concentration, N_i) must increase. This leads to decrease the separation between TM ions also (inter ionic distance, ri). Field strength of TM ions also should increase due to reduced molar volume V_m. All these theoretical analysis was exactly proved from the calculated values of physical parameters for the present glass system and are in agreement with the previous studies.

Table 2.Physical parameters of Titanium oxide doped xNa_2O-(30-x) K_2O-35SiO_2-30B_2O_3--TiO_2 glasses

Physical parameter(units)	Glass code				
	X_5	X_{10}	X_{15}	X_{20}	X_{25}
Average molecular weight (g/mol)	72.56	70.94	69.33	67.72	66.11
Density ρ (g/cm^3)	2.17	2.24	2.31	2.41	2.38
molecular volume(cm^3)	33.37	31.66	29.94	28.11	27.77
Concentration N_i (10^{21} ions cm^{-3})	7.21	7.01	8.03	8.55	8.66
Inter ionic distance r_i (A^o)	2.40	2.43	2.32	2.27	2.264
Polaron radius r_p (A^o)	0.968	0.977	0.934	0.914	0.911
Optical basicity (Λ_{th})	0.2479	0.2445	0.2423	0.24	0.238
Field strength F (10^{15} cm^2)	4.07	4.05	4.14	4.18	4.19

3.2 XRD Analysis

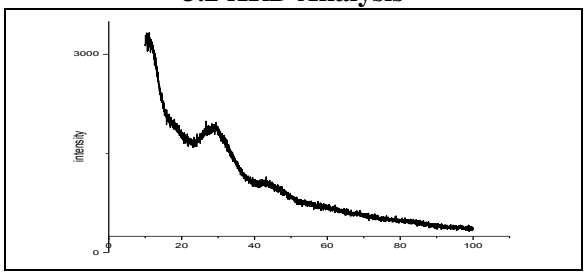

The X-ray diffraction pattern consists of only broad peak, no specific peak of any element confirms the amorphous nature of present investigating system as glass.

Fig1: X-ray diffractiogram of 5Na_2O-(25)K_2O-35SiO_2-30B_2O_3-5TiO_2 glass

3.3 Infrared spectroscopic study of glasses

These vibrational spectra are due to the structural grouping rearrangements with changes in glass composition

Table 3. Wavenumber assignment of infrared transmittance band of present glass system.

S.No	wave number (cm^{-1})	Assigned band
1	**450**	Si-O-S vibrations of SiO_4 tetrahedra
2	467	Si-O-S

3	669	bending mode of B-O-Si
4	719	bending motion of B-O-B center
5	767	6 membered borate group, conversion into BO_4 tetrahedra
6	875	stretching vibrations of tetrahedral BO_4^- units
7	1020	SiO_4 with one NBO
8	1,050	asymmetric vibration of Si-O
9	1259	B-O-B bond constituting the linkage of Boroxol to neighbours
10	1438	antisymmetric stretching vibration of BO_3
11	2924	hydrogen bonding with titanium (metal) oxide
12	3421	fundamental free stretching vibrations of -OH

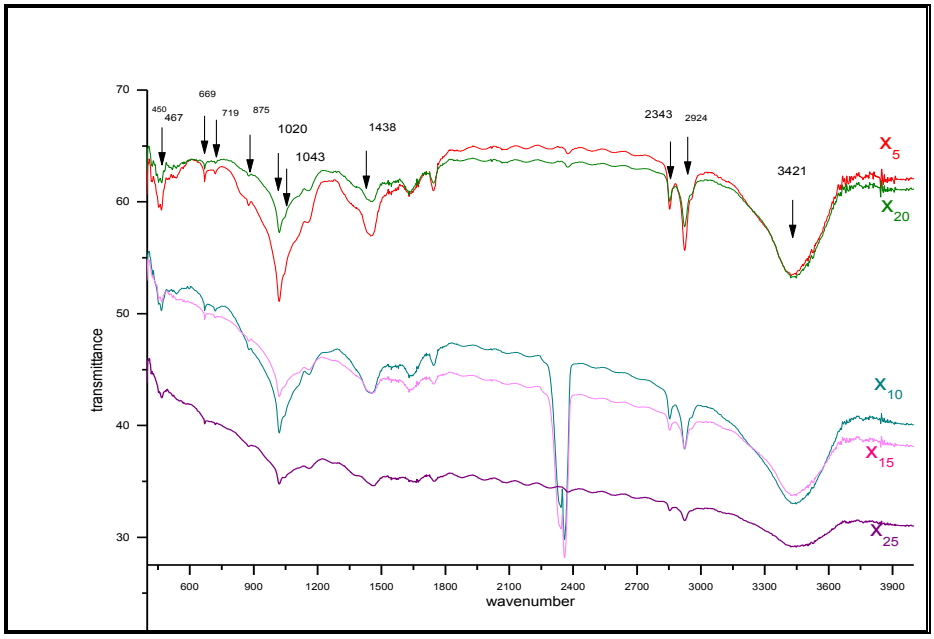

Fig2: FTIR Spectra of xNa_2O-(30-x) K_2O-40SiO_2-30B_2O_3- 5TiO_2

The Si-O-Si band at 450 cm^{-I}, the B-O-B band at 720 cm^{-1} observed in present glasses are in agreement with the earlier reports of FTIR spectra on borosilicate glasses. [6-7]. The band at **720 cm-I** arises from a bond bending motion of the B-O-B centres within the network. Diborate linkage of B-O-B, both boron atoms are tetrahedrally coordinated with triborate structural units. In the present glass system any isotopic shift of intensity was not found, so the concentration of B-O-B bands is same in all glass samples [6, 8]. The weak band at **669 cm^{-1}** is due to Si-O-B vibration [6]. The peak observed at 765 $cm^{-1}$is due to the vibration of the six-membered borate ring [9]. The strongest band at **1050 cm^{-1}** has been assigned to the asymmetric vibration of the Si-O [10, 11].

In this investigating glass samples Alkali/ boron ratio is > 0.5 and SiO_2 mol% is 35% so the glass may consists of diborate, metaborate and SiO_4 (4 bridging oxygens), SiO_4^- (one non bridging oxygen) units which was confirmed by the bands present in FTIR spectra [12]. The absorption band at 1259 cm^{-1} in the spectrum has been assigned to the bond stretching vibration of the boron against the oxygen (B-O-B) [13]. A broad band near 421 cm^{-1} was resulted from the stretching vibrations of Si–OH or Ti–OH groups [14-15].

4. CONCLUSIONS

As the sodium oxide content increases in present glass samples their density, TM ion concentration, field strength are increasing and molar volume, inter ionic distance are decreasing. From FTIR spectra the presence of of Q_4, Q_3 units of Si-O-Si band, B-0-B bands of N_4, N_3 of borate and weak Si-O-B band, molecular water and the absence of ring type Boroxol was confirmed.

REFERENCES

1. Y. Paz and A. Heller, J. Mater. Res., 12, 2759–2766 (1997).
2. F. Auzel, Spectroscopy of Solid State Lasers. [B. Bibartaro, Ed.] Plenum press, New York (1987).
3. G. Guery, J.L. Adam, J. Lum. 42 ,132 (1988) .
4. M. J. Weber, R. Cropp, J. Non- Cryst. Solids 4 (1981) 137.
5. ShenDingkun, Wang Kaitain, Huang Xihuai, Chen Yuxin, BaiJinhua J. Non-Cryst. Solids 52 (1982) 151
6. P. E. Jellyman and J. P. Proctor, J. Soc. Glass Tech. 39, 173T (1955)
7. S. Tenney And J. Wong ,The Journal Of Chemical Physics., 56,11 (1972).
8. Chandkiram Gautam, Avadhesh Kumar Yadav, Vijay Kumar Mishra, Kunwar Vikram Open Journal of Inorganic Non-metallic Materials, 2, 47-54(2012).
9. T.W. Bril, Thesis, Technological University Eindhoven, The Netherlands, 1975.
10. Simon and H. O. McMahon, J. Chern. Phys. 21, 23 (1953).
11. M. Hass, J. Phys. Chern. Solids 31, 415 (1970).
12. Konijnendijk, W. L. (1975). The structure of borosilicate glasses Eindhoven DOI: 10.6100/IR146141
13. J. Krogh-Moe, Phys. Chern. Glasses 6, 46 (1965).
14. Sheng, D.Y. The Application of IR in Polymer Research; Science Press: Beijing, China; 83–88 (1988).
15. M .Haihong, Tiejun Shi and Qiusheng Song; Fibers, 2, 275-284(2014).

Second National Conference on
RECENT ADVANCES IN APPLIED NANO MATERIALS
February 16-17, 2018 at Department of Physics, University College of Science, Saifabad, Osmania University, Hyderabad, Telangana State, India.

Recent Advances and Challenges of Nanotechnology In Drug Delivery Systems

D.SOWJANYA[1], VISHWARAJ SINGH THAKUR[2]
[1] LECTURER IN ELECTRONICS, ST.MARY'S COLLEGE, YOUSUFGUDA
[2] B.Sc (M.E.Cs) II Year, ST.MARY'S COLLEGE, YOUSUFGUDA
Email Id: [1] sowjanya@stmaryscollege.in [2] thakurvishwaraj04@gmail.com

Abstract: *Nano technology is a new novel focus of research which is evolved from convergence and coalescence of many diverse scientific disciplines. It is a general term for the creation, application and manipulation of structures. The use of nano particles plays an effective role in drug delivery. To reduce the problems of gene and drug delivery, nanotechnology is used in medicine known as Nono medicine which reduces the side effects and toxicity of classical drug delivery. One of the main objectives of this nano medicine is to create medically useful nano devices that can be used to treat various diseases inside the body. In this context, the author wants to discus about various developments in drug delivery using nano particles to treat a wide variety of diseases specifically for cancer therapies. Finally, the author also wants to introduce challenges and strategies of nanotechnology in future to overcome limitations in this field.*

Key Words: *Nanotechnology, nanomedicine, drug delivery, cancer therapy.*

1. INTRODUCTION:

Nanotechnology involves a convergence in various areas of science. It not only includes medicine but also includes physics, chemistry, biochemistry, and molecular biology. It is defined as the development of small devices which will be in the range of range of 1 to 100 nm. Such nano-devices can offer to the clinical practice of medicine in general, and to oncology in particular. It is a general term for the creation, application and manipulation of structures. The use of nano particles plays an effective role in drug delivery. To reduce the problems of gene and drug delivery, nanotechnology is used in medicine known as Nano medicine which reduces the side effects and toxicity of classical drug delivery. One of the main objectives of this nano medicine is to create medically useful nano devices that can be used to treat various diseases inside the body.

Nanomedicine is a branch of medicine that applies the knowledge and tools of nanotechnology to the prevention and treatment of disease. Nanomedicine involves the use of nanoscale materials, such as biocompatible nanoparticles and nanorobots, for diagnosis, delivery, sensing or actuation purposes in a living organism. Nanomedicines have been investigated for the drug delivery to treat a large variety of diseases. This industry mainly focusses on oncology-based nanomedicinal therapeutics only, the main aim of these nanomedicines is to improve the therapeutic index of anti-cancer drugs by modifying their pharmacokinetics and tissue distribution .In the enhanced permeability and retention (EPR) effect, and liposomal doxorubicin was the first anti-cancer nanomedicine approved by the FDA in 1995.

Examples of anti-cancer nanomedicines in clinical trials which are in market.

Nanomedicine type	Drug	Product name/company	Indication	Phase
Liposomes	Doxorubicin	Teva	Metastatic breast cancer	Approved
		Janssen	Ovarian cancer	Approved
		Celsion	Refractory chest wall breast cancer	Phase III
		2B3–101/2-BBB Medicines BV	Brain metastases Glioma	Phase II
	Vincristine	Spectrum Pharmaceuticals	leukaemia	Approved

	Cisplatin	Regulon	Non-small cell lung cancer	Phase III
		ALZA Pharmaceuticals	Ovarian cancer	Phase II
		Aronex Pharmaceuticals	Malignant mesothelioma	Phase II
	Paclitaxel	Insys	Breast cancer	Phase II
Polymeric conjugates	Fluorouracil	Cerulean	Renal cancer Small cell lung cancer Ovarian cancer	Phase II
		Baxalta	Acute lymphoblastic leukaemia	Approved
		CTI Biopharma	Ovarian cancer	Phase III maintenance Phase II
		Nektar	Metastatic breast cancer	Phase III
		Cerulean	Ovarian cancer	Phase II
		Mersana	Gastric cancer	Phase II
		ProLindac™	Ovarian cancer	Phase II
		StarPharma	Advanced cancers	Phase I
		Cristal Therapeutics	Solid tumours	Phase I
Polymeric nanoparticles	Mrthotrexate	BIND Therapeutics	Cervical cancer Bladder cancer	Phase II
	Mrthotrexate	AstraZeneca	Advanced solid tumours	Phase I
Polymeric micelles	Pafitaxel	Samyang Biopharmaceuticals	lung cancer Ovarian cancer	Approved
		NanoCarrier	Stomach cancer Breast cancer	Phase III
		NanoCarrier™	Solid tumours	Phase I

Doxorubin		
Time	Drug	
	EA	RA
1	0.01	0.1
2	0.02	0.15
3	0.04	0.2
4	0.05	0.3
5	0.06	0.31
6	0.06	0.33

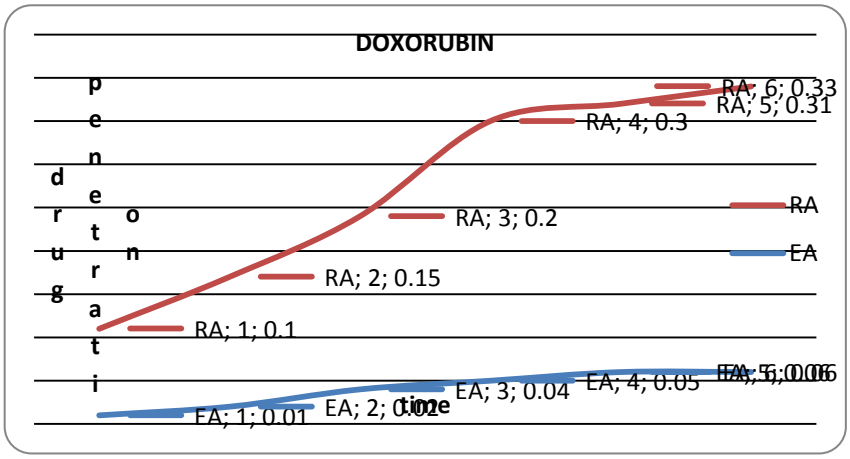

Fluorouracil		
Time	Drug	
	EA	RA
1	0.01	0.05
2	0.04	0.1
3	0.07	0.15
4	0.1	0.2
5	0.11	0.21
6	0.12	0.3

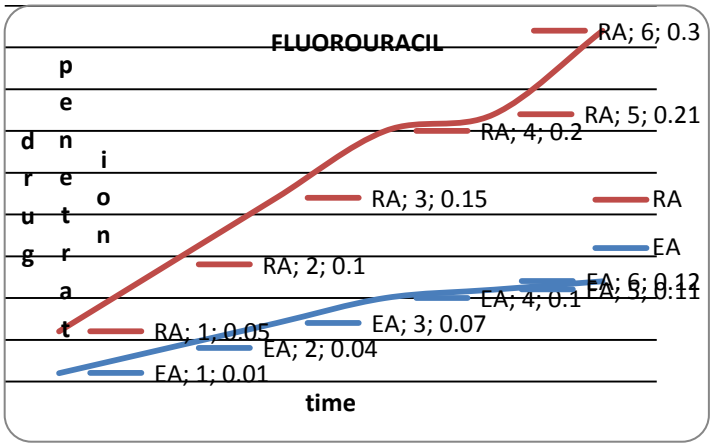

Mrthotrexate		
Time	Drug	
	EA	RA
1	0.01	0.05
2	0.04	0.14
3	0.07	0.18
4	0.09	0.21
5	0.1	0.22
6	0.11	0.29

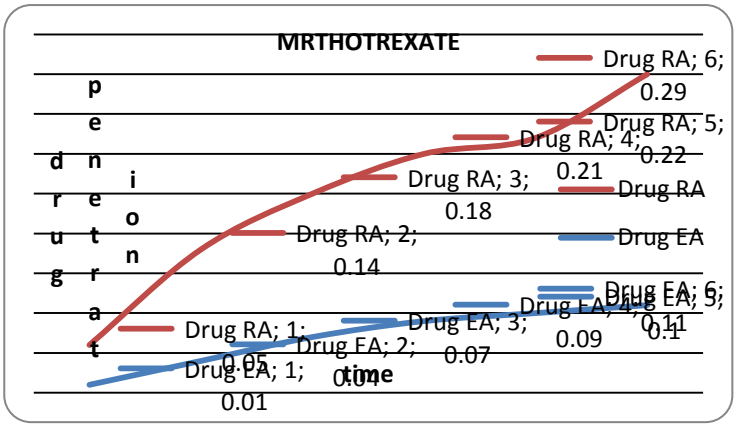

Pafitaxel		
Time	Drug	
	EA	RA
1	0.05	0.06
2	0.08	0.15
3	0.12	0.2
4	0.14	0.21
5	0.15	0.24
6	0.16	0.45

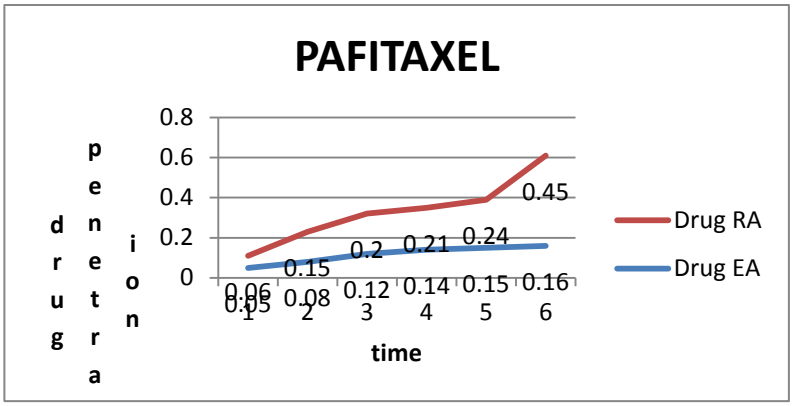

For drug delivery and cancer chemotherapy the ideal nano-carrier should
(i) stabilize without modifying the pharmacological activity of the drug,
(ii) Prevent premature metabolic degradation of the drug
(iii) Release the drug at the intended site/tumor, and
(iv) Exhibit similar or lower toxicity than that of the free drug.

2. NANO-CARRIERS FOR ONCOLOGY:

Cancer is defined as uncontrolled and unregulated tissue growth results in malignant tumors which spreads to other locations from the initiation location and effects other adjacent organs , making the disease life threatening . In spite of many advances in cancer treatment, one of the biggest challenges in cancer treatment is that the normal cells should not get damaged while destroying malignant tumors. In most of the therapy cases drug will be distributed throughout the body, as a result, higher dosages are required. That is the reason why the cancer treatment will be expensive. To overcome the problems which are faced in current methods, scientists are trying to increase

proliferation activity of cancer cells by adopting targeted therapy which uses nano materials. The excellent examples are:

Laser technique :

Lasers are most commonly used to treat superficial cancers like skin cancer, cervical, penil, vulvar, and lung cancer.

There are two types of Laser therapies:

Laser-induced interstitial thermotherapy (LITT) which is used in cancer treatment. It uses heat to shrink tumors and kills cancer cells and Photodynamic therapy (PDT) is the laser therapy which uses a drug called photo sensitizer which is directly injected into patient body and it will be absorbed by all the cells inside the patient body. Then after few days the laser light is used to destroy the cells.

Imaging technology:

Imaging technology has also brought a new dimension to diagnostic procedures like CT scans, MRIs and other techniques which have had a huge impact on the diagnosis. It displays the internal structure of the body including abnormal material, so that the doctor can see the state of the body directly and treat with precision.

Bio Sensors:

A Bio sensor is an analytical device containing an immobilized biological material which can interact with an analyte and produce physical, chemical or electrical signals that can be measured

- The substance which we want to analyse is called analyte
- Biological material may be anything from biological origin such as enzyme, antigen, antibodies, microbials etc
- The analyte will react with the biological substance as a result a sort of signal will be produced that may be Mechanical or electrical, this can be measured which gives the idea regarding the concentration of analyte.

3. THE CHALLENGES AND STRATEGIES IN DRUG DELIVERY USING NANOTECNOLOGY IN FUTURE:

Safety Concern

Few nanotoxicity investigations led to the speculation that nanomaterials may contribute to the formation of free radicals which damage of brain cells and penetrates through the epidermis into areas of the body that are more liable to toxic effects. Several mechanisms have been proposed to affect the toxicity of nanomaterials,

Thus, nanomaterial toxicity should be considered relative to the patient population, as well as the entire manufacturing and disposal processes. Based on safety concerns, the establishments of standards or reference materials and testing protocols that can provide benchmarks for the development of novel classes of materials are needed.

Economic & Financial Barriers

Economic and financial barriers can also stand in the way of implementing nanomedicine. Because of the high development costs of nanodrugs and medical devices, startup companies have little chance of bringing products to the market without support from 'Big Pharma', which is able to provide the financial resources and expertise needed to achieve regulatory and commercial success.

Biological Understanding

In order for bionanotechnologies to progress toward human applications, a better understanding of the mechanisms is needed. Current delivery systems suffer from some major hindrances like rapid clearance by the immune system, low targeting efficiency etc,. To overcome these obstacles, a full understanding of the basic science is needed which will result in achieving the ability to control and manipulate drug delivery.

Manufacturing Issue

Another challenge facing nanodrug delivery is the large-scale production of nanomaterials it is much easier to modify or maintain the size or composition of nanomaterials at the laboratory scale for improved performance than at a large scale. The biomedical community should rethink the level of control needed when working with nanomaterials. Rather than requiring perfect control of the physical dimensions of nanomaterials, a statistical approach may be adopted in order to establish a metric for classifying nanomaterials by material type, average size, aspect ratio and standard deviation.

4. CONCLUSION:

It is noticeable that nano drug delivery systems have great potential to overcome the barriers to target of cells and molecules in cancer treatment. There is a possibility to overcome problems of drug resistance .The challenge, however, remains the precise to ensure that these molecules are expressed only in the targeted organs to prevent effects on other parts of the body. Furthermore, because nanosystems increase efficiency of drug delivery, the doses may need recalibration. Nevertheless, the future remains wide open and exciting.

REFERENCES:

1. Misra R, Acharya S, Sahoo SK (2010) Cancer nanotechnology: application of nanotechnology in cancer therapy. Drug Discov Today 15: 842-850.
2. Robert NJ, Vogel CL, Henderson IC, Sparano JA, Moore MR, et al. (2004) The role of the liposomal anthracyclines and other systemic therapies in the management of advanced breast cancer. Semin Oncol 31: 106-146.
3. Florence AT. Pharmaceutical nanotechnology: more than size. Ten topics for research. Int. J. Pharm. 2007;339:1–2.
4. Damia G, D'Incalci M. Contemporary pre-clinical development of anticancer agents — what are the optimal preclinical models? Eur. J. Cancer. 2009;45:2768–2781.
5. Park K. Nanotechnology: what it can do for drug delivery. J. Control. Release. 2007;120:1–3
6. Ruenraroengsak P, Cook JM, Florence AT. Nanosystem drug targeting: facing up to complex realities. J. Control. Release. 2010;141:265–276.

Second National Conference on
RECENT ADVANCES IN APPLIED NANO MATERIALS
February 16-17, 2018 at Department of Physics, University College of Science, Saifabad, Osmania University, Hyderabad, Telangana State, India.

Effect of Gamma Irradiation on Ag/PVA Nanocomposite Films

Pushpanjali.M.G and Somashekarappa H.M*
*Centre for Application of Radioisotopes and Radiation Technology (CAART) Mangalore University, Mangalagangotri-574199, Karnataka, India
Corresponding Author Email Id: carrtmu@gmail.com

Abstract: *Silver/poly (vinyl alcohol) (Ag/PVA) nanocomposite films with different concentration of AgNO3 (1×10^{-2} M, 5×10^{-2} M and 1×10^{-1} M) were prepared using solvent evaporation method. Synthesized Ag/PVA samples were exposed to gamma radiation of dose 75 kGy. The samples were characterized through UV–Visible spectroscopy, XRD, FTIR, FESEM and EDAX. The absorption spectrum of the film shows the surface plasmon resonance (SPR) peak at 427 nm, confirming the formation of Ag nanoparticles in PVA matrix. The X-ray diffraction analysis reveals the presence of silver metal in face centered cubic (fcc) crystal structure. The change in chemical interaction was analyzed with the help of Fourier Transform Infrared Spectroscope (FT-IR). The morphology of samples was studied using Field Emission Scanning Electron Microscopy (FESEM). The presence of Ag was confirmed by the Energy Dispersive X-ray Spectroscopy (EDX) elemental analysis. The synthesised nanocomposite was subjected to gamma radiation to study the optical and structural changes of Ag/PVA nanocomposites. The discussions on optical and structural changes are presented in this paper.*

Key Words: *Nanocomposites, plasmon, PVA solution*

1. INTRODUCTION

Nanotechnology exactly means any technology performed on a nanoscale that has applications in the actual world. Gamma irradiation offers many advantages for the preparation of metal- nanoparticles. Large number of hydrated electrons produced during γ-irradiation can reduce the metal ions to zero valiant metal particles [3]. An outline made by many authors suggested that irradiation cause a chemical change in polymers, including crosslinking and chain scission Silver nitrate is a fast conducting ion in a number of crystalline and amorphous materials. Ag NPs can be synthesized using various methods some of them are chemical reduction, electrochemical, photochemical, reduction-ray irradiation and UV irradiation. Polymers have been frequently used as particle stabilizer and capping agent [4]. Moreover, it is a water soluble polymer, so it can react with metal salt via formation of chelate with metal cations in an aqueous solution and also act as a capping agent. PVA is a well-known for its wide range of potential applications in optical, pharmaceutical, medical and has been developed for biomedical applications such as artificial pancreas**,** wound dressing and artificial skin. Generally, Polymer/metal nanocomposites can be obtained by two different approaches, namely, ex situ and in situ techniques [2]. The synthesised nanocomposite was subjected to gamma radiation to study the optical and structural changes of Ag/PVA nanocomposites.

2. MATERIALS AND EXPERIMENTAL

2.1. Materials

Nanocomposite films were synthesised by using fully hydrolyzed Poly (vinyl alcohol) PVA (M.wt. 30,000 $gmol^{-1}$) and Silver Nitrate $AgNO_3$ (M.wt. =169.87 g/mol; 99% hydrolyzed) was obtained from Merck. Both the chemicals are analytical grade, and used without further purification. Distilled water was used as a solvent and Gamma Irradiator (GC 5000; BRIT, Mumbai).

2.2. Preparation of Ag/PVA nanocomposites

Poly (vinyl Alcohol) solution was first prepared by dissolving 5 gm in 100 ml distilled water, thoroughly stirred until the polymer became completely soluble. AgNO3 solutions with different molar concentrations (from 0.01 M to 0.1 M), were added to the PVA solution. The solutions were then left to cool at room temperature. Finally, the solution was cast on a petri dish. The films were gamma irradiated at dose 75 kGy using gamma irradiator (GC 5000; BRIT, Mumbai).

2.3. Characterization techniques

Ultraviolet-Visible (UV/Vis) spectroscopy (Shimadzu, UV-1800). Powder X-ray diffraction (XRD) (Rigaku Miniflex). Fourier transforms infrared spectroscope (FT-IR) analysis. Field Emission Scanning Electron Microscopy (FESEM) (ULTRA 55 FESEM, Karl Zeiss). Energy Dispersive X-ray Spectroscopy (EDX) elemental analysis.

3. RESULTS AND DISCUSSION

When $AgNO_3$ is mixed with PVA, the OH^- groups of PVA attracts Ag^+ ions towards it. Fig.1 shows the optical images of pure PVA, Ag/PVA and irradiated Ag/PVA. The PVA films were colourless and Ag/PVA films in yellowish colour, this result confirm the formation of Ag nanoparticles in the PVA matrix [7].

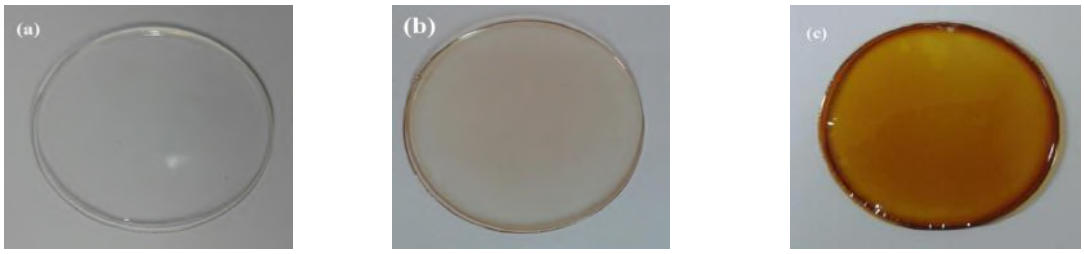

Fig.1. Optical Images of (a) Pure PVA (b) Ag/PVA and (c) Ag/PVA at 75 kGy

Fig.2. There is a band at λ = 276 nm that refer to PVA characteristics compound. As the silver concentration increased ($(1\times10^{-2}$ M - 1×10^{-1} M) the surface plasmon resonance peak is shifted from 422 to 427 nm indicating the presence of red shift and higher content of silver nanoparticles are generates in nanocomposite films [8]**.** Samples were exposed to gamma radiation of dose 75 kGy, the surface plasmon resonance peak is shifted from 427 to 412 nm indicating the presence of blue shift and the formation of smaller metal nanoparticles [9].

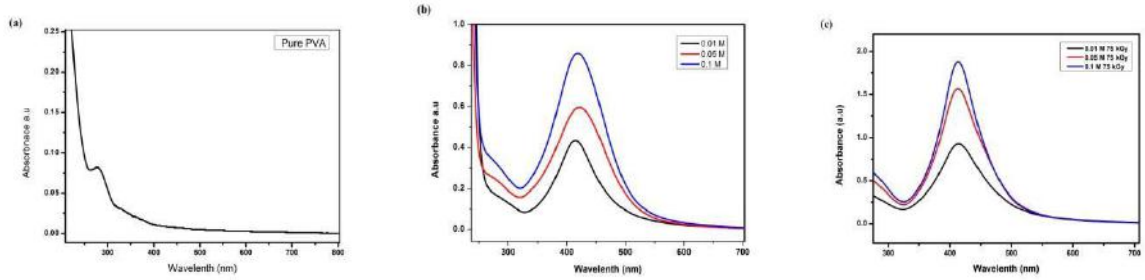

Fig.2. UV-Vis spectroscopy images of (a) Pure PVA (b) Ag/PVA (b) Ag/PVA dose of 75 kGy.

Estimation of particle size of Ag nanoparticles

Assuming that silver nanoparticles have spherical shape, Mie theory [11] was applied for the evaluation of silver nanoparticles size in PVA/Ag nanocomposite films. Particle size experimentally founded by Evanoff and Chumnov [5] was used for the calculation of silver nanoparticles in PVA polymer blends using experimental data:

$$D = 0.715\ \lambda_{max} - 258 \qquad (1)$$

Where D = particle diameter (nm), and λ_{max} is the SPR peak position in UV-Vis absorbance spectrum. The calculated Ag nanoparticles size was listed in Table 1. The obtained data of Ag nanoparticles diameter indicated that the Ag nanoparticles size decreases with irradiation dose

Table 1 Determination of the particle size from UV/Vis spectroscopic analysis

$AgNO_3$ conc.,(M)	Irradiation dose (kGy)	λ_{max} (nm)	Particle Size D (nm)
0.1	0	427	47.30
	75 kGy	412	36.58

Fig.5. The XRD pattern of unirradiated pure PVA exhibits strong and broad diffraction peak located at 2θ = 19.27°. The diffraction peak at 2θ = 19.27° corresponds to the (110) reflection, a plane which contains the extended planar zigzag chain direction of the crystallites [1]. First, the irradiated Ag/PVA nanocomposites show four new diffraction peaks at 2θ = 38.48°, 44.42°, 64.21° and 77.67. These discernible peaks can be indexed to the planes (111), (200), (220) and (311); respectively revealing that the Ag nanoparticles are formed in the PVA matrix and their crystal structure is face centered cubic (fcc) structure according to JCPDS (No.4-0783) [6]. This is a confirmation of spontaneous reduction of Ag^+ ion to Ag^o nanoparticles in the metallic form using PVA chains and irradiation [7].

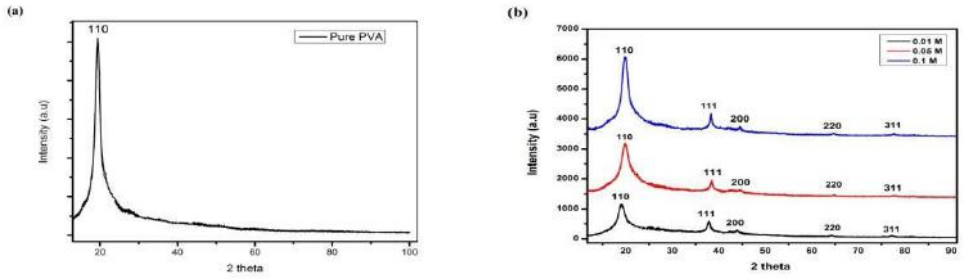

Fig.3. X-Ray Diffraction pattern of Pure PVA (a) and (b) PVA/Ag Nanocomposites at dose of 75 kGy

The particle size 'D' was calculated based on the regular broadening of XRD peaks as a function of decreasing crystallite size [1]. This broadening is a fundamental property of XRD described by well established Scherer theory:

$$D = \frac{K\lambda}{\beta Cos\theta} \qquad \text{(2)}$$

where, D is the particle diameter (nm), K is a constant equals 0.9, λ is the X-ray wavelength; (Cu Kα = 1.540˚ A), β is FWHM of the peak corresponding to plane (111 reflection) and θ is the diffraction angle obtained from 2θ values corresponding to maximum intensity peak in XRD pattern. The calculated values of crystalline particle size (D, nm) are listed in Table 2. The careful analysis for the position of (111) reflection peak illustrates that there is a gradual shift towards lower angle with irradiation dose and it can be seen that with irradiation dose of 75 kGy the particle size decreased.

Table 2: The XRD parameters of Ag/PVA nanocomposite films

AgNO3 conc.,(M)	Dose, (kGy)	size (nm)
0.1	75 kGy	16.88
0.05		14.67
0.01		12.95

Fig.4. shows nanocomposites Films before and after gamma exposure in the range of 4000 cm–1 to 750 cm–1. In pure PVA (curve 'a'), the band observed at around 3271 cm-1 relates to the O-H stretching vibration of hydroxyl group, while the bands observed at 2946 cm–1 & 1719 cm–1 correspond to the C–H and C=O stretching vibration respectively [3]. The occurrence of band at around 1136 cm–1 corresponds to the C-O & C-O-C groups stretching vibrations and the absorption band appeared at 850 cm–1 is due to the out-of-plane vibration of C–H group of PVA, respectively [6]. After embedding Ag nanoparticles in PVA matrix, the decrease in intensity and shifting of the bands observed at 3271 cm-1, 1719 cm–1, 1136 cm–1 and 850 cm–1 towards lower wave numbers suggest the formation of chemical conjugation of Ag nanoparticles with 'O' atoms of PVA chains. After gamma exposure, a further band 1318 cm-1 increase in intensity and shift of the absorption bands at 3271 cm-1 and 1719 cm-1 towards lower wave numbers indicate that after irradiation the structural rearrangement between Ag nanoparticles and PVA chains takes place [7]. The move towards lower wavenumber and broadening of bands observed at1136 cm–1 and 850 cm-1 also indicates that after gamma exposure the structural rearrangements between Ag nanoparticles and PVA molecules take place.

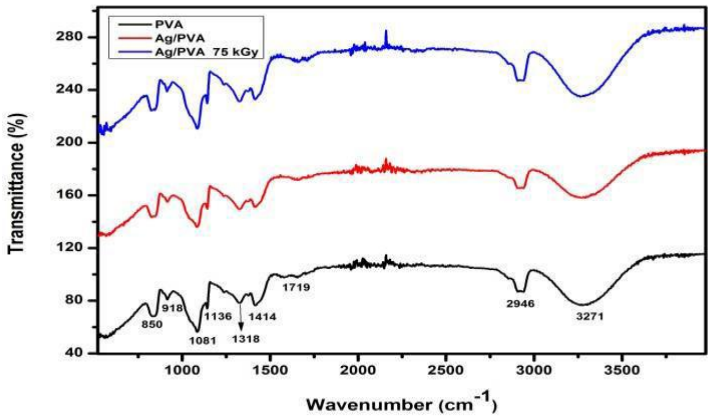

Fig.4. FTIR images of Pure PVA (a) and (b) PVA/Ag Nanocomposites at dose of 75 kGy

The morphological characterization of various composite films was carried out by SEM and elemental analysis by EDAX analysis. Fig. 5 (a-d) shows clearly indicates the formation of silver nanoparticles in the range of 100–200 nm and also realized that the particles were nano in size uniformly dispersed in the PVA matrix [10]. The observation was supported by EDAX analysis.

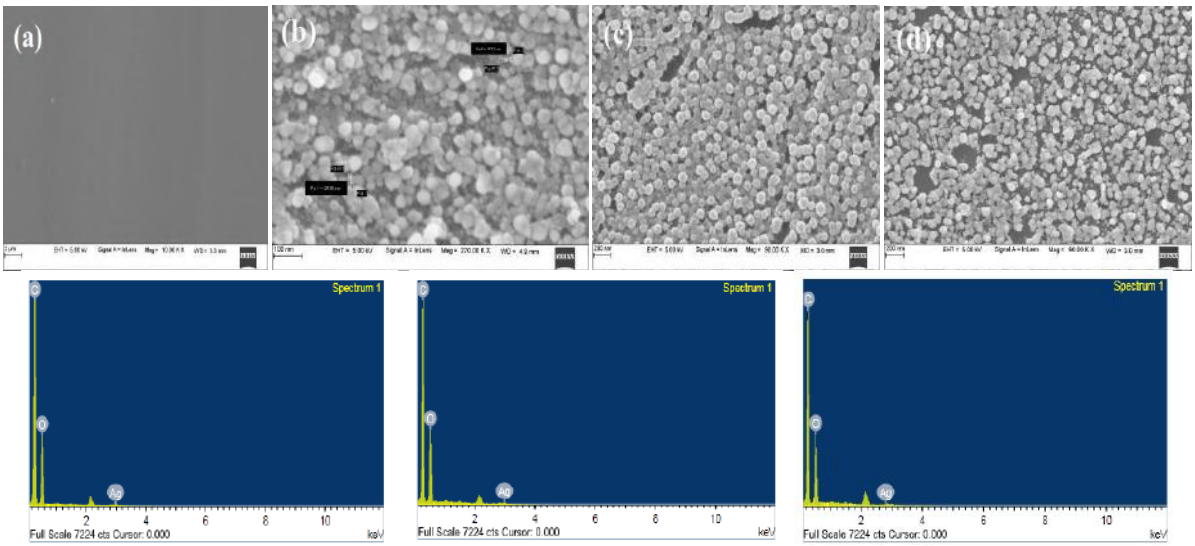

Fig. 5.SEM image of (a) Pure PVA (b) Ag/PVA nanocomposite film at dose of 75 kGy (0.01M) (c) 0.05 M (d) 0.1 M and EDAX of Ag/PVA nanocomposite film (0.01 M, 0.05 M and 0.1 M)

4. CONCLUSION:

In the present study the Ag/ PVA nanocomposites were synthesized through in situ chemical reduction method and films were prepared through solution casting methods. Prepared Ag/PVA samples were exposed to gamma radiation of dose 75 kGy. UV/Vis spectroscopy result shows the surface plasmon resonance at 427 nm confirms the formation of Ag nanoparticles. The absorption peak was increased when films irradiated at the dose of 75 kGy, indicating the formation of more silver nanoparticles in the polymer matrix and more reduction of silver nitrate. The XRD pattern of pure PVA exhibits strong and broad diffraction peak placed at $2\theta=19.27^{o}$ which was due to crystalline part. An irradiated PVA/Ag nanocomposite sample shows four new diffraction peaks at $2\theta = 38.48^{o}$, 44.42^{o}, 64.21^{o} and 77.67 revealed that the Ag nanoparticles were created in the PVA matrix. The FITR analysis reveals that silver nanoparticles attached to polymer chains through some kind of chemical conjugation. The SEM analysis reveals that the particles were nano in size uniformly dispersed in the PVA matrix. The presence of Ag was confirmed by the Energy Dispersive X-ray Spectroscopy (EDX) elemental analysis. Finally, the study concludes that the Ag/PVA nanocomposite films when exposed to gamma radiation it shows the changes in optical and structural behaviour.

5. ACKNOWLEDGMENTS

Coordinator DST-PURSE for permitting the use Field Emission Scanning Electron Microscopy (FESEM) facility, Mangalore University and Manipal Institute of Technology (MIT) for X-Ray Diffraction analysis, Manipal University, Udupi, Karnataka.

REFERENCES:

1. Ali Z.I, Saleh H.H, Afify T.A. 2011. Optical, Structural and Catalytic Evaluation of Gamma-Irradiation Synthesised Ag/PVA Nanocomposite Films. International Journal of Engineering Research & Technology. 3, 1527-1538.
2. Ananth A.N, Umapathy S, Sophia J, Mathavan T, Mangalaraj D.2011. On the optical and thermal properties of in situ/ex situ reduced Ag NP's/PVA composites and its role as a simple SPR-based protein sensor. Appl. Nanosci, 1: 87-96.
3. Chahal R.P, Mahendia S, Tomar A.K, Kumar S. 2016. Optical and structural properties of gamma irradiated PVA/Ag nanocomposite films. Applied Science Letters. 2: 55-58.
4. Eisa W.H, Abdel-Moneam Y.K, Shaaban Y, Abdel-Fattah A.A, Zeid A.M.A. 2011. Gamma-irradiation assisted seeded growth of Ag nanoparticles within PVA matrix. Mater. Chem. Phys.128: 109-113.
5. Evanoff Jr D.D, Chumanov G .2004. Size-controlled synthesis of nanoparticles .1. "Silver-only" aqueous suspensions via hydrogen reduction. **J. Phys. Chem. 108:** 13948-13956.
6. Gautam A, Tripathy P, Ram S. 2006. Microstructure, topology and X-ray diffraction in Ag-metal reinforced polymer of polyvinyl alcohol of thin laminates. J. Mater. Sci. 41: 3007-3016.
7. Ghanipour M, Dorranian D. 2013. Effect of Ag-Nanoparticles Doped in Polyvinyl Alcohol on the Structural and Optical Properties of PVA Films. J. Nanomater. 2013: 1-10.
8. Jabbar W.A, Habubi N.F, Chiad S.S. 2010. Optical Characterisation of Silver Doped Poly (Vinyl Alcohol) Films. J. Ark. Acad. Sci. 64: 101-105.

9. Karthikeyan B. 2005. Spectroscopic studies on Ag–polyvinyl alcohol nanocomposite films. Physica B. 364: 328-332.
10. Omer M.A.A, Saion E, Gar-elnabim E.M, Balla E.A, Dahlan Kh M, Yousif Y.M. 2011. Gamma Radiation Synthesis and Characterisation of Polyvinyl Alcohol/ Silver Nano Composites Film. J. Sc. Tech.12: 104-110.
11. Puišo J, Prosyčevas I, Guobienė A, Tamulevičius S .2008. Plasmonic properties of silver in polymer. Materials Science and Engineering:B. 149: 230-236.

Second National Conference on
RECENT ADVANCES IN APPLIED NANO MATERIALS
February 16-17, 2018at Department of Physics, University College of Science, Saifabad, Osmania University, Hyderabad, Telangana State, India.

Phoshpor Based Iridium Complex for Lighting Industry

A. Sridhar goud*[1], S.Thomas Reddy[2], Ch.Venkateshwarlu[1], V. Nathanial[1], A.Narsaiah[3]
*Research scholar, department of physics,opjs university, churu(raj) india
[1] Department of physics, osmania university, Hyderabad
[2] Department of physics, Kakatiya University, Warangal,
[3] Department of physics, SRR Govt Degree college, Karimnagar.

Abstract: *A phosphoric polymer is employed to host an organometallic iridium complex dopant that is added. In this study, the InGaN which is and iridium complex is used. The quantum dot (QD) phosphor based LEDs consists of the mentioned aspects and is therefore investigated in this paper. The heavy metal iridium complexes dopants added have atoms at the center that exhibits a massive spin-orbit coupling. The use of these phosphorescent materials causes the singlet and triplet interactions to decay with radiation emission. The emitted radiation is the one observed light. The internal quantum efficiency if therefore improved through the process as compared to single inorganic materials for OLEDs, in which the single states are the only ones responsible for light emissions.*

Keywords: *Phoshpor, Iridium, Lighting Industry.*

1. INTRODUCTION:

Solid-state lighting refers to a most recent form of lighting that employs semiconductor light emitting diodes or organic light-emitting diodes to produce light radiation as opposed to the traditional electrical filaments. Phosphor materials are employed in solid state lighting to improve the internal quantum efficiency of OLEDs. The phosphor materials are used as hosts for heavy metallic complexes, forming two states. A single and triplet state, which significantly reduces the band-gap of the phosphor materials and hence increased the internal quantum efficiency of the resulting OLED as far as light radiation emission is concerned (1). The phosphor materials also enable the emission of monochromatic or multicolor LEDs.

2. EXPERIMENTAL DETAILS:

Experimental data is obtained from an insight into the application of OLEDs in lighting purposes. QD phosphor based OLEDs are commonly employed as sources of lighting. As such particular standards are required for the LEDs and particular colors desired for particular solid state lighting functions (2). It, therefore, necessitates the strict limitations on the emission spectrum of an OLED particularly on the red side of the band. This is enabled by the use of the iridium complex. The earlier white fluorescent lighting had a radiance of ˜1×10-6 which was a lot more than the accepted 2.2E-9. The earlier systems of solid state lighting value are as a result of the UV-sensitive phosphors, which have broadband emission and this can only be rectified using filters. The radiance values of the current commercial LEDs is within the range of 1× 10 -7 to 1×10-8. These values fall below the stipulated radiance threshold. Doped nitro does silicates phosphors are used to coat metallic iridium complex InGaN QW LEDs for a mixed color effect on the white output. The Y3Al5O12: Ce3+ and Eu2+ doped with nitro do silicates phosphors have a narrower band gap as compared to UV- sensitive phosphors (3)

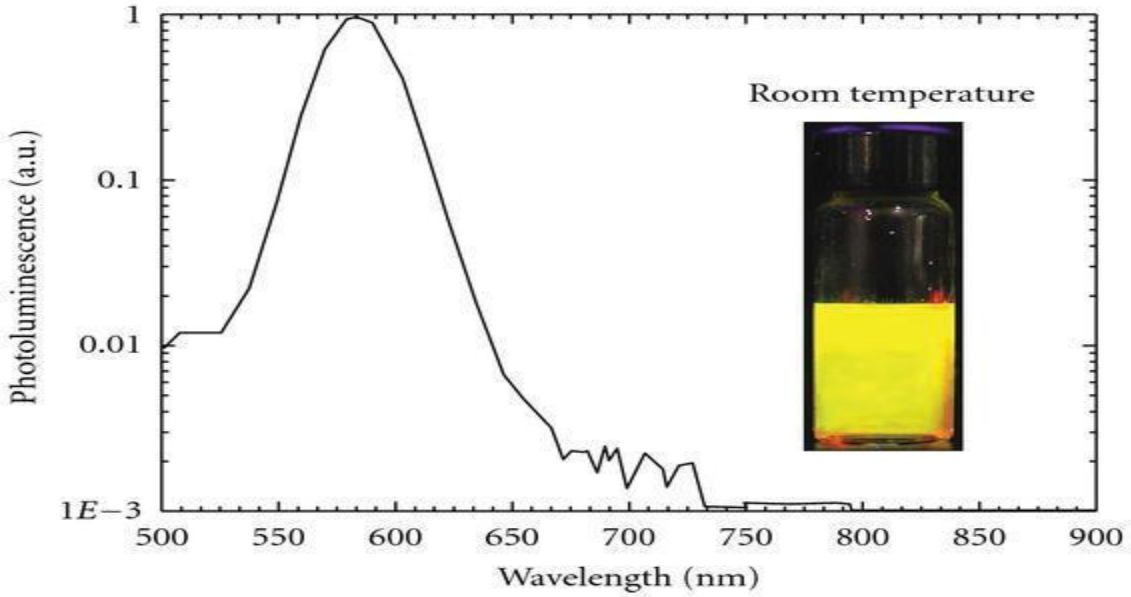

9).

Fig A

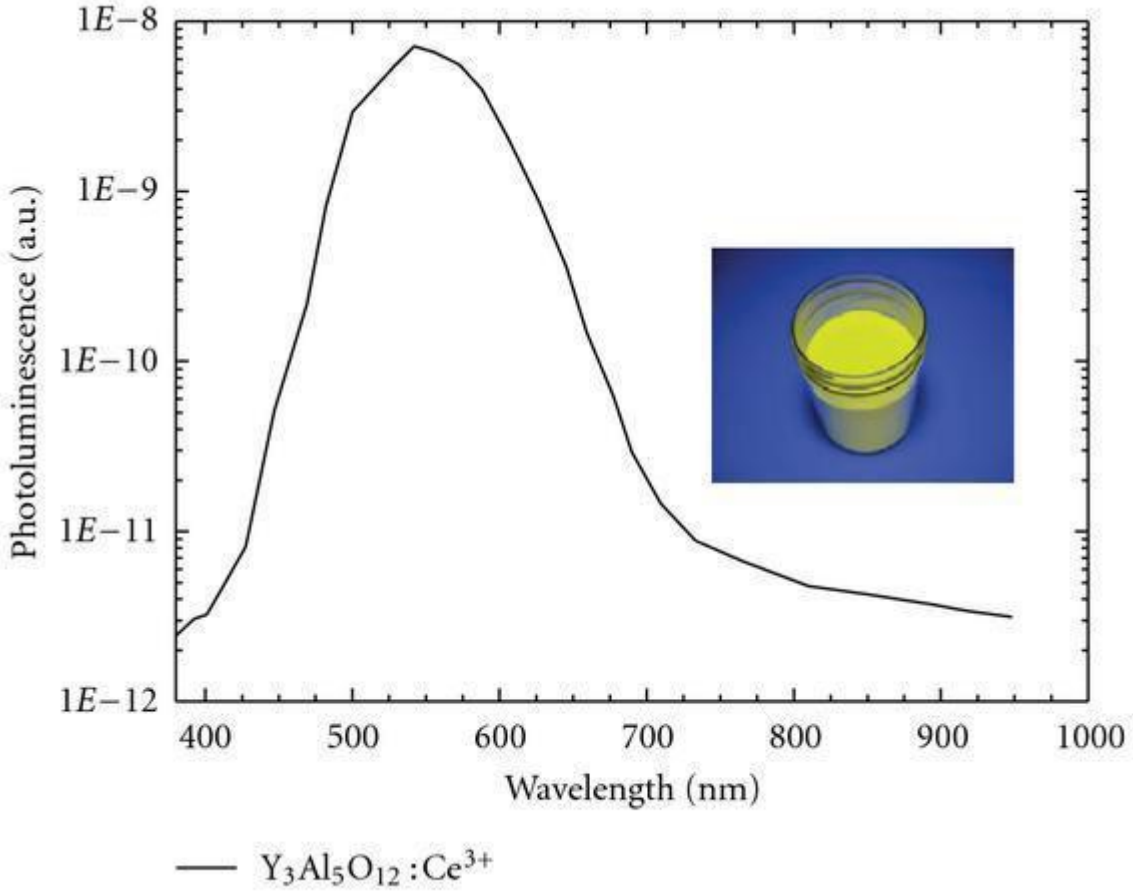

Fig B

Figure A and B above illustrate the distinctions between the spectrum of the metallic complex QD phosphor based LEDs and that of a more traditional Y3Al5O12: Ce3+ phosphor fluorescence spectrum. Calculation from A indicates that the QD iridium metallic complex phosphor based LEDs have a radiance value of 4E-10 at 0.1 brightness. In figure B the Y3Al5O12: Ce3+ phosphor fluorescence spectrum indicates a radiance value of ˜6×10-8 at 0.1 brightness (4).

In a bid to elaborate the concept a QD phosphor-based LED is fabricated through mist-deposition of CdSe/CdS/ZnS shells onto the surface of the iridium complex InGaN, which is responsible for emissions. Electron

microscopy has initiated the process to establish the dimensions and crystalline structure of the phosphors (5). The figure below indicates spherical and almost identical crystals are observed and very well define lattice interference. The lattice interference constitutes the reduced band gap.

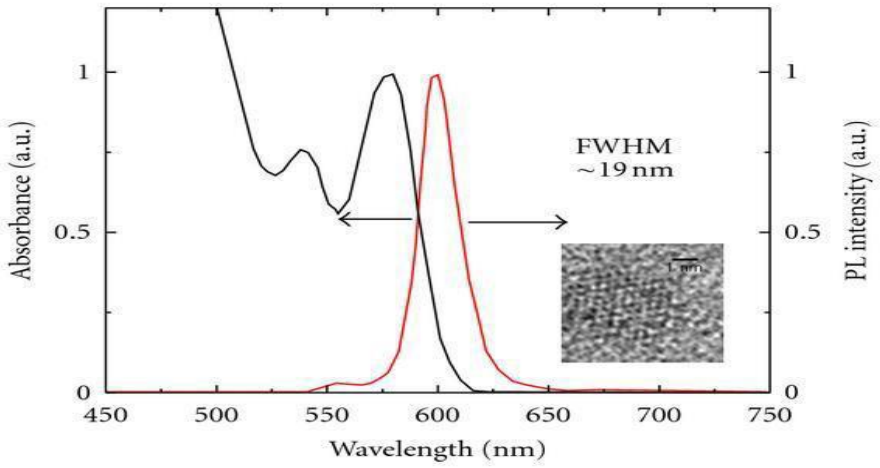

Fig C

The figure above shows lattice distortions and crystal nature as an effect of the introduction nitro do silicate phosphors.

3. RESULTS AND DISCUSSION:

From the above deliberations, it is evident that the available white LEDs used for solid state lighting amount to a radiance value of 10-7. This is way beyond the accepted threshold. That of the iridium metallic complex phosphor based OLEDs is 9.420E-09 for a thickness of 50nm. This is quite effective for solid state lighting. In as much it is still above the stipulated threshold, it is way lower as compared to the former. This value constitutes a reduced bandgap and hence the improved internal quantum radiation (6). The luminescence wavelength also becomes flexible and therefore multiple colors of illumination can be obtained from the iridium-based OLEDs. The spectral response in the phosphor and iridium-based OLEDs is also established as higher than that of the latter.

4. CONCLUSION:

In conclusion, from the observations made it is clear that the phosphor based on the iridium metallic complex are flexible and can, therefore, be applied in a wide range of applications as compared to the traditional white LEDs. The flexibility of the OLEDs is enhanced by the iridium complex and allows for various uses as far as solid state lighting is concerned. From display applications, indicator and light color effects the iridium complex OLEDs can come in really handy. Their increased internal quantum efficiency and color variations enabled by the iridium complex also allows for the usage of less energy but more brightness as compared to the white LEDs.

REFERENCES:

1. Davis, J. V. (2011). *U.S. Patent No. 7,924,371*. Washington, DC: U.S. Patent and Trademark Office.
2. Johnson, R. J. (2005). *U.S. Patent No. 6,842,204*. Washington, DC: U.S. Patent and Trademark Office.
3. Nowatari, H., Ushikubo, T., Ohsawa, N., Seo, S., & Tsutsui, T. (2009, June). 60.2: Intermediate Connector With Suppressed Voltage Loss for White Tandem OLEDS. In *SID Symposium Digest of Technical Papers* (Vol. 40, No. 1, pp. 899-902). Blackwell Publishing Ltd.
4. Simi, C. G., Parish, J., Winter, E. M., Dixon, R., LaSota, C., & Williams, M. M. (2000, August). Night vision imaging spectrometer (NVIS) performance parameters and their impact on various detection algorithms. In *AeroSense 2000* (pp. 218-229). International Society for Optics and Photonics.
5. Thompson, M. E., You, Y., Shoustikov, A., Sibley, S., Burrows, P. E., & Forrest, S. R. (2001). *U.S. Patent No. 6,303,238*. Washington, DC: U.S. Patent and Trademark Office.
6. Yersin, H. (Ed.). (2008). *Highly efficient OLEDs with phosphorescent materials*. John Wiley & Sons.

INTERNATIONAL JOURNAL OF RESEARCH CULTURE SOCIETY ISSN: 2456-6683 Special Issue -8, Feb - 2018
UGC Approved Monthly, Peer-Reviewed, Refereed, Indexed Journal Impact Factor: 3.449 Publication Date: 25/02/2018

Second National Conference on
RECENT ADVANCES IN APPLIED NANO MATERIALS
February 16-17, 2018at Department of Physics, University College of Science, Saifabad, Osmania University, Hyderabad, Telangana State, India.

Luminescence in Ce^{3+} doped phosphate compounds for Energy transfer

S.Thomas Reddy[1], A.Sridhar Goud[2], Ch.Venkateswarlu[2], B.Naresh[2] Y. Sandeep2,.V.Nathaniel[2],
[1.]Dept of Physics,Kakatiya University, Warangal
[2.]Department of Physics, UCS Saifabad, Osmania university, hyderabad

Abstract:*At present days, phosphate compounds are emerging as an important materials because of their special characteristics such as more availability, less cost, environmental friendliness and thermal and charge stabilities. It is known that Ce^{3+} has a strong absorption in many hosts and emission matching with $4f^n$ levels of rare earth impurities, so $Ce3^+$ emission was studied in some phosphate compounds.significance luminescence phenomenon was observed in the compounds and can be made useful as lamp phosphor and for energy transfer study.*

Key Words: *splitting characteristics, RE impurities, Decays time, orthophosphate, pyro phosphate, Energy*

1. INTRODUCTION:

Ce^{3+} ground state is split ($^2F_{5/2}$, $^2F_{7/2}$), these are the only levels possible for 4f configuration. f-f transitions in Ce^{3+} are in IR region. At RT, they occur as unresolved bands with maximum at about 2200- 2300 cm^{-1} and half – width 250-300 cm^{-1}. At low temperature, the band splits into some lines, which are due to f-f transitions and electro-vibronic transitions[1,2,3,4,5]. The excited states above $^2F_{7/2}$ level belong to 5d configuration in the form a of broad bands. Most commonly observed emission is characteristics of 5d $\rightarrow$ 4f transition. Both absorption and emission have usually a broad band character, showing splitting characteristic of ^2F_j states. The Stokes shift is due to interaction with host crystals. As the position of 5d band itself depends on the host, not only the Stokes shift , but also the special positions of both the absorption and the emission bands depends on the host. In (Y, Ce) PO_4, the emission is around 324 nm and 350 nm, while in $(Y, Ce)_3Al_5O_{12}$, the Ce^{3+} emission is in the form of a very broad band stretching from 500 nm to well beyond 700 nm having maximum around 550 nm, and in sulphides such as CaS, Y_2O_2S, it is in green-red region[6,7]. Emission in the UV-blue region is common. Emission at longer wavelengths is obtained[8] when the centre of the 5d level is at relatively low energies. (Strong Nephelauxetic Effect), and the crystal field is very strong. Another feature of Ce^{3+} emission is that both absorption and emission resulting from allowed transitions, the decay time is short, of the order of few ns. Characteristic Ce^{3+}phosphors are thus useful where rapid decay times are required eg. in time of flight camera and scintillators. The luminescence of Ce^{3+} gets concentration quenched at 1-2 % at Ce concentration[9] . $Ce^{3+} \rightarrow Ce^{3+}$ transfer is followed by transport to killer site. Ceusually shows high quenching temperature in silicates, borates and phosphates. Since Ce^{3+} has a strong absorption in many hosts, and emission matching with $4f^n$ levels of other RE impurities, it can be used as a sensitizer for Tm[10], Sm , Dy, Tb[11], Nd[12] ,[13]Gd and Pr.

The study of characteristic luminescence of Ce^{3+} in some phosphate compounds is presented here.

Experimental Details:

Following types of materials were prepared for the study of characteristic emission of Ce^{3+}.

(1) Orthophosphates of the type
i) RPO_4 where R is the rare earth ion
ii) $ABR(PO_4)_2$ where A is the alkali metal ion, B, the alkaline earth metal ion and R is the rare earth ion.
iii) $B_3R(PO_4)_3$ where B is the alkaline earth metal ion and R is the rare earth ion.

(2) Pyrophosphates of the type $M^IM^{III}P_2O_7$, where M^I= monovalent alkali metal ion (K, Na) and M^{II} = trivalent metal ion (Al, La , Gd, Y).

All these compounds were prepared by solid state reaction method (except $KAlP_2O_7$ which is prepared by combustion method[14,15]), where the required ingredients (all of AR grades) were mixed stoichiometrically together and fired at 300^0 C for 12 hrs and then at 750^0C for 2 hrs in reducing atmosphere following with the subsequent grindings.

All these compounds were checked by XRD technique. PL's were taken by using Hitachi F-4000 spectrofluorometer.

2. RESULTS AND DISCUSSION:

Ce^{3+} emissions in various Orthophosphates and pyrophosphates are tabulated in the table below.

Table: Ce^{3+} emission in various Ortho-phosphates

S.N.	Formula	λ_{ex} (nm)	λ_{em} (nm)	Intensity
1	$La_{0.55}Ce_{0.45}PO_4$	254	354	1050
2	$KMgLa_{0.9}Ce_{0.1}(PO_4)_2$	254	340	1800
3	$KMgCe(PO_4)_2$	254	305,340	150
4	$Ba_3La_{0.99}Ce_{0.01}(PO_4)_3$	254 320	340 380	300 240
5	$Ba_3Ce(PO_4)_3$	254	345	Very weak emission
6	$Sr_3Ce(PO_4)_3$	254	340	230
7	$Sr_3La_{0.99}Ce_{0.01}(PO_4)_3$	254	352	120

Table 5:Ce^{3+} emission in various pyro-phosphates

S.N.	Formula	λ_{ex} (nm)	λ_{em} (nm)	Intensity
1	$KLa_{0.99}Ce_{0.01}P_2O_7$	265	318 336	1400
2	$NaGd_{0.99}Ce_{0.01}P_2O_7$	254	315 333	1600
3	$KGd_{0.99}Ce_{0.01}P_2O_7$	250	335	15
4	$KY_{0.99}Ce_{0.01}P_2O_7$	250	344	300
5	$NaY_{0.99}Ce_{0.01}P_2O_7$	254	354 335	300
6	$KAl_{0.99}Ce_{0.01}P_2O_7$	300	380	115

$La_{0.55}Ce_{0.45}PO_4$& $KMgLa_{0.9}Ce_{0.1}(PO)_2$: Fig. 1 shows excitation and emission spectra for the samples $La_{0.55}Ce_{0.45}PO_4$ (curve a) & $KMgLa_{0.9}Ce_{0.1}(PO_4)_2$ (curve b). Strong absorptions are observed for both the samples. Excitation spectra show prominent peaks at 286 nm with a good overlap at 254 nm, which shows the use of the materials as the lamp phosphors. Intense Ce^{3+} emissions were observed around 354 nm and 340 nm for $La_{0.55}Ce_{0.45}PO_4$ and $KMgLa_{0.9}Ce_{0.1}(PO_4)_2$ respectlively. Spectral overlapping of the excitation and emission bands shows a small stoke's shift which indicates that samples can be well studied for energy transfer.

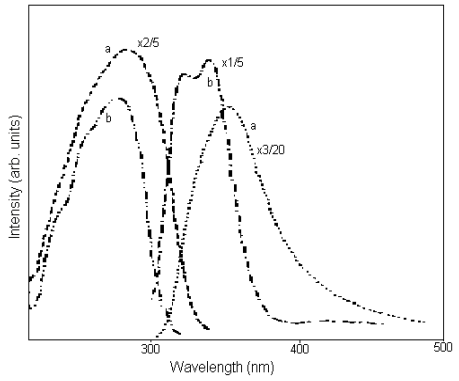

Fig .1:(a)PL excitation(λ_{em}=354nm)and emission(λ_{ex}=254 nm) for $La_{0.55}Ce_{0.45}PO_4$& (b) PL excitation (λ_{em} =340 nm) and emission (λ_{ex} = 254 nm) for $KMgLa_{0.9}Ce_{0.1}(PO_4)_2$

$KMgCe(PO_4)_2$: Fig.2 shows excitation and emission spectra for the sample$KMgCe(PO_4)_2$. The excitation spectrum shows a strong absorption around 270 nm. But the emission intensities are found to be moderate around 325 nm and 340 nm. For this reason, the phosphor is of interest as a lamp phosphor and energy transfer study.

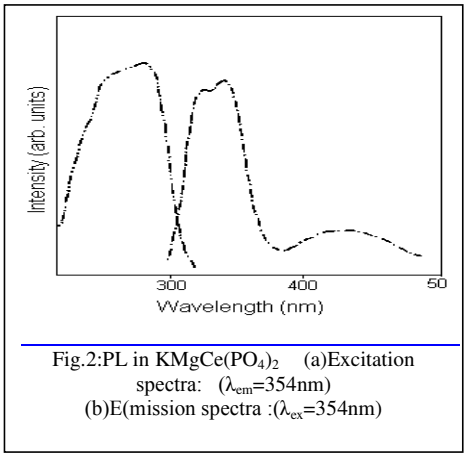

Fig.2:PL in $KMgCe(PO_4)_2$ (a)Excitation spectra: (λ_{em}=354nm)
(b)E(mission spectra :(λ_{ex}=354nm)

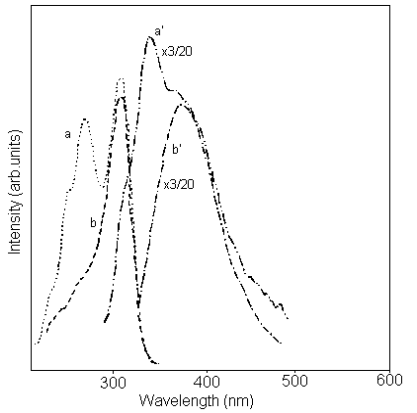

Fig.3.: PL in $Ba_3La_{0.99}Ce_{0.01}(PO_4)_3$.
(a)Excitation spectra:: (λ_{em}=340nm)
(b)Excitation spectra:: (λ_{em}=380 nm)
(a')Emission spectrum(λ_{ex}=254nm)
(b')Emission spectrum (λ_{ex}=3204nm)

$Ba_3La_{0.99}Ce_{0.01}(PO_4)_3$: Fig.3 shows excitation and emission spectra for the sample $Ba_3La_{0.99}Ce_{0.01}(PO_4)_3$.The Excitation spectra are corresponding to the emissions at 340 nm and 380 nm. (curves a & b) having the peak positions at 260 nm and 320 nm respectively with efficient Ce^{3+} absorption. Good overlapping at 254 nm makes sure the use of material as lamp phosphor . Curves a' and b' show two emission spectra peaking at 342 nm and 320 nm for the compound with the excitation at 254 nm and 320 nm respectively. These emissions were found to be weak. Material can be useful for energy transfer study

$Ba_3Ce(PO_4)_3$

Very weak Ce^{3+} emission was observed in the sample with the excitation at 254 nm. PL spectra are not shown for this sample.

$Sr_3Ce(PO_4)_3$& $Sr_3La_{0.99}Ce_{0.01}(PO_4)_3$: Fig 4 shows PL spectra for the two samples $Sr_3Ce(PO_4)_3$& $Sr_3La_{0.99}Ce_{0.01}(PO_4)_3$. Excitation spectrum for both the samples is same which consists of a broad band having two peaks at 260 nm and 270 nm with strong absorption with good overlapping at 254 nm. This ensures the suitability of the phosphor as a lamp phosphor. Broad emission spectrum ranging from 300 nm to 400 nm were observed peaking at 352 nm. Weak emissions of Ce^{3+} were observed around 340 nm for $Sr_3Ce(PO_4)_3$ and around 352 nm for $Sr_3La_{0.99}Ce_{0.01}(PO_4)_3$. These phosphors can be made useful for the lamp application and energy transfer study if the attempts are made to improve the intensity.

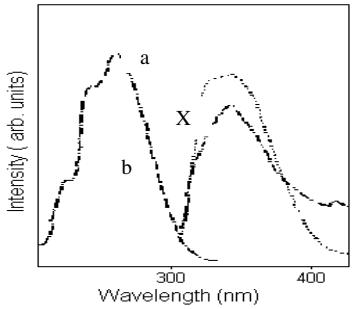

Fig.4: PL excitation (λ_{em}=340 nm) and emission Spectra for (a) $Sr_3Ce(PO_4)_3$&
(b)$Sr_3La_{0.99}Ce_{0.01}(PO_4)_3$($\lambda_{ex}$ = 254 nm)

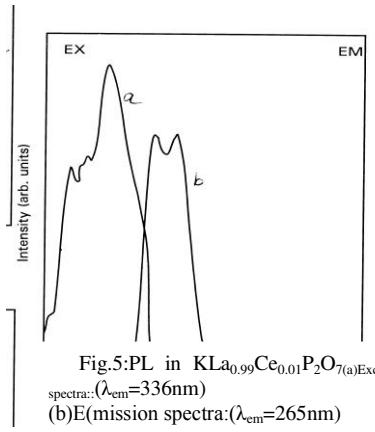

Fig.5:PL in $KLa_{0.99}Ce_{0.01}P_2O_{7(a)Excitation}$ spectra::(λ_{em}=336nm)
(b)E(mission spectra:(λ_{em}=265nm)

$KLa_{0.99}Ce_{0.01}P_2O_7$: Encouraging result is obtained in the sample.(fig.5) shows excitation and emission spectra for the sample$KLa_{0.99}Ce_{0.01}P_2O_7$. Excitation spectrum shows a very strong absorption around 270 nm for the emission at 336 nm, with a good overlap at 254 nm, which shows that material will be useful for lamp purpose. Intense emission peaking at 318 nm and 336 nm was observed with the excitation at 265 nm. Small stoke's shift was observed in the sample which would help in transferring the energy from Ce^{3+} to other ions which plays an important role in the luminescence process[16]. Hence the phosphor will be useful in studying the energy transfer phenomenon.

$NaGd_{0.99}Ce_{0.01}P_2O_7$: The structure of $NaGd_{0.99}Ce_{0.01}P_2O_7$ was found to be in orthorhombicsystem[17]. Fig 6 shows the excitation and emission spectra for the sample. Very strong absorption peaking at 300 nm was observed in the sample with the good overlap at 254 nm, which ensures the use of the material as lamp phosphor. A very strong emission of Ce^{3+} was observed at 315 nm and 333 nm with the excitation at 254 nm. The sample will be useful for the energy transfer study.

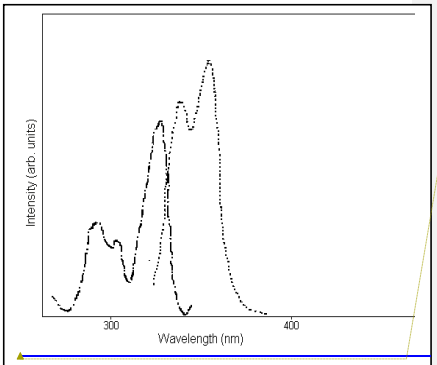

Fig. 6 : PL in $NaGd_{0.99}Ce_{0.01}P_2O_7$
(a):Excitation spectrum : (λ_{em}=333nm)
(b)E(mission spectrum:(λ_{ex}=254nm)

Formatiert: Schriftart: (Standard) +Textkörper (Times New Roman), 11 Pt.

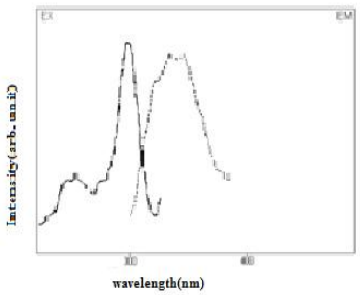

Fig.7:PL in $KGd_{0.99}Ce_{0.01}P_2O_7$
(a):Excitation spectrum : (λ_{em}=333nm)
(b)E(mission spectrum(λ_{ex}=254nm)

$KGd_{0.99}Ce_{0.01}P_2O_7$: Fig.7 shows excitation and emission spectra for the sample$KGd_{0.99}Ce_{0.01}P_2O_7$. Excitation spectra shows the weak absorption around 300 nm, with a poor overlap at 254 nm . Very weak Ce^{3+}emission was observed around 335 nm with the excitation at 250 nm and 285 nm respectively. Poor emission intensity will not allow the phosphor to be used for the study of energy transfer .

$KY_{0.99}Ce_{0.01}P_2O_7$&$NaY_{0.99}Ce_{0.01}P_2O_7$: Fig.8 shows excitation and emission spectra for the two samples (curve a) $NaY_{0.99}Ce_{0.01}P_2O_7$ & $KY_{0.99}Ce_{0.01}P_2O_7$ (curve b). Ce^{3+}emissions of moderate intensities were observed for both the samples. Emission for $KY_{0.99}Ce_{0.01}P_2O_7$ was observed at 344 nm with the excitation at 254 nm while that for .$NaY_{0.99}Ce_{0.01}P_2O_7$ were observed at 335 nm and 354 nm. Excitation peaks were observed with moderate intensities at 250 nm and 307 nm for $KY_{0.99}Ce_{0.01}P_2O_7$and 307 nm for $NaY_{0.99}Ce_{0.01}P_2O_7$at 254 nm. These two samples will be uesful for energy transfer study.

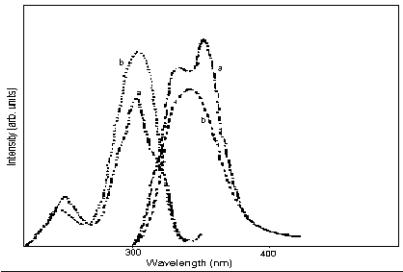

Fig.8: (a):PL Excitation spectrum : (λ_{em}=344 nm)and emissionemission (λ_{em}=254nm)for $KY_{0.99}Ce_{0.01}P_2O_7$
(b).PL Excitation spectrum : (λ_{em}=354 nm) and emission (λ_{ex}=254nm) for $NaY_{0.99}Ce_{0.01}P_2O_7$.

$KAl_{0.99}Ce_{0.01}P_2O_7$: Weak Ce^{3+} emission was observed around 380 nm with the excitation at 300 nm. Fig. 9 shows the PL spectra for the sample. From the excitation spectrum, it is observed that, spectrum has a maximum around 300 nm and does not have a good overlap with the Hg emission. Hence the sample will not be useful for the application of lamps. Weak emission of Ce^{3+} shows that the phosphor will not be useful for energy transfer study also.

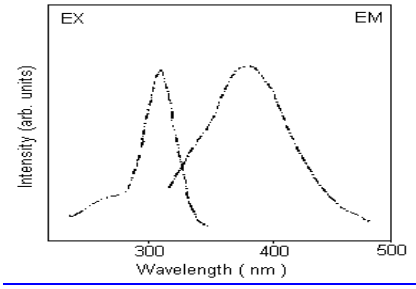

Fig.9: PL in $KAl_{0.99}Ce_{0.01}P_2O_7$
(a) Excitation spectrum : (λ_{em}=380 nm)
(b) Emission spectrum (λ_{ex}= 300 nm)

CONCLUSION :

Ce^{3+} emission was observed to be strong in $NaGd_{0.99}Ce_{0.01}P_2O_7$, $La_{0.55}Ce_{0.45}PO_4$ and $KMgLa_{0.9}Ce_{0.1}(PO_4)_2$, $KLa_{0.99}Ce_{0.01}P_2O_7$, $NaGd_{0.99}Ce_{0.01}P_2O_7$. These phosphors can be made useful as lamp phosphors and for studying energy transfer phenomenon.

REFERENCES:

1. Kaiser W. and Garret C. G. B. 1961 Phys. Rev. Lett. 7, 229
2. Barry T. L. 1968 J. Electrochem. Soc. 115, 1181
3. Blasse G. and Bril A. 1968 Phil. Rws. Rept. 23, 201
4. Blasse G., Wanmaker W. L. terVrugt J. W. and Bril A. 1968a Phil. Res. Rept. 23, 189
5. Blasse G. Bril A. and J. de Vries 1968b J. electrochem. Soc. 115, 977
6. Blasse G. ,Bril A. and J. De Vries 1969 J. Inorg. Nucl. Chem . 31, 568
7. Hoffman M. V. 1968 J. Electruchem. Soc. 115, 560
8. Blasse G. &Bril A. 1969 J. Chem Phys. 51, 3252
9. Palilla F.C., Levin A. K. and Tomkus M. R. 1968 J. Electrochem. Soc. 115, 642
10. Palilla F. C. and O' Reilly B. c. 1968, J. Electrochem. Soc.115, 1076
11. Watchel A. 1969. J. electrochem. Soc. 116,61
12. Wanmaker W. L. and terVrugt J. W. 1967, Phil. Res. Rept 22, 355
13. Wanmaker W.L. and terVrugt J. W. 1968, Phil. Res. Rept. 23, 362
14. A. P. Hardtand P. V. Phung. Combust. Flame 21 (1973) 77.
15. A. P. Hardt and R. W. Holsinger , ibid. 21 (1973)
16. Blasse G. 1986 J. Soild State Chem. 62, 207,211
17. Blasé G. 1966 J. Chem. Phys. 45, 2356

Second National Conference on
RECENT ADVANCES IN APPLIED NANO MATERIALS
February 16-17, 2018 at Department of Physics, University College of Science, Saifabad, Osmania University, Hyderabad, Telangana State, India.

Nanomaterial Risks for Humans and the Environment– Making Innovations Sustainable

K.SOWMYA[1], S.PHANEENDRA[2], S.CHARVANI[3],
[1]Asst.Professor, Institute of Aeronautical Engineering, Dundigal;
[2]Asst.Professor, Balaji Institute of Technoloy and Science, Warangal;
[3]Asso.Professor, Institute of Aeronautical Engineering, Dundigal;

Abstract: *Nanotechnology and manufactured nonmaterials as with any new technology, may bring many advances to society and benefits for the environment, but also pose new challenges in health, environment safety and possible impacts on society. Because of the very broad range of potential applications using nanotechnology and the wide variety of characteristics displayed by manufactured nonmaterial's detailed discussion of both benefits and of health and environmental risks should take place at the level of individual nanotechnology applications.*

Key Words: *Nanomaterial Risks, Humans, Environment, Innovations*

1. INTRODUCTION:

As a result of nanotechnology's rapidly burgeoning growth, it is important that all stake holders' concerned (governments, international, regional and national organizations, industry groups, public interest associations, labour organizations, scientific associations and civil society) engage in discussions to identify and address policy issues. These can include health, safety, moral, ethical, societal, legal and social utility concerns. In view of the predicted great impact of nanotechnologies on the global economy, research and society, and of the expected wide-spread use of nanomaterials, any possible risks should be studied by comprehensive, proactive risk estimation and assessment.

2. EARLY DETECTION AND ASSESSMENT OF RISKS:

A number of research projects have assessed the applicability and relevance of established testing methods and concepts for evaluation of the risks of industrial chemicals to humans and the environment. These focused mainly on nanomaterials already manufactured industrially on a larger scale, such as nanotitanium dioxide, industrial soot (carbon black), nanosilica, nanosilver and other nanoscale pigments. Here the need for further development and specific adjustment of test procedures often became clear.. At the forefront of hazards for occupational safety is the inhalation of respirable and biopersistent dusts. This is especially critical if the dust particles are fibrous. The well-known nanomaterials were therefore assigned into the groups "granular biopersistent particles (GBP)", "biopersistent respirable fibres" and "specific toxicity".

The group assignment addresses different, but already established, testing and protection strategies that can also be applied to nanomaterials in a modified form, if required. The critical fibre dimensions relate to fibre lengths between 5 and 100 microns and fibre diameters of less than 3 microns. This concerns for example characterisations relating to labelling requirements for food and cosmetics, if complex matrices are to be analysed using highly sensitive measuring devices. If nanoparticles were to be absorbed into the body via the intestinal barrier, they could potentially accumulate in different organs. Questions as to the toxicity and degradation of the particles would also have to be taken into account alongside bioavailability and accumulation before any authorisation can be given.

According to state building regulations, buildings are to be constructed such that life, health and the natural foundations of life are not jeopardised. In addition, environmental parameters (pH-value, salt content, content of natural organic substances) influence the mobility, bioavailability and toxic effects of nanomaterials in the environment.

3. CREATING SUSTAINABLE PRODUCT LIFE CYCLES:

Due to their special properties, nanomaterials offer great potential to provide energy-efficient and resource-saving products. The assessment of the opportunities and risks of new product innovations must be conducted on a sound scientific basis. Instruments for the ecobalancing reflection on products containing nanomaterials have already been developed, but so far only a few products have a qualitative and quantitative analysis of their environmental and sustainability potential. Manufacturers and importers are responsible for ensuring that advanced materials and the products manufactured from them meet the legal requirements of European chemical safety. Before being placed on the market, substances and mixtures must be classified according to present findings and be supplied with a hazard label.

A safety data sheet must be produced for commercial customers. Approval and registration obligations apply to certain product groups like food, cosmetics and biocides or additional labelling requirements for consumer information must be observed. To ensure sustainable protection of man and the environment it is essential that regulations keep pace with the rapid and significant progress in material development. This is also to include activities at the end of the life cycle in the event of recycling and disposal

4. INTENSIFYING THE COMMUNICATION OF RISK:

The high dynamics in material development, but also in the generation of risk and scientific data relevant to measures, necessitates special efforts to keep all relevant target groups up to date and ready to act. The development of the competence needed requires long-term vocational and further training opportunities for experts in risk and safety research There are also open questions on the assessment of the risk from nanomaterials for man and the environment when it comes to recycling. 36 Action Plan Nanotechnology 2020 The by now world-wide harmonised hazard labelling using pictograms, hazard and precautionary statements is the most important instrument for risk communication for those involved in the supply chain for substances and mixtures. Commercial customers also receive a comprehensive safety data sheet from suppliers.

The representative population surveys and media analyses as to the perception of nanotechnology in the population are to be continued. One focus is the manner of representation of nanotechnology in the media. Target-group-oriented risk communication strategies are to be derived from the results so that ongoing progress in the description of the risk can be announced in a transparent and comprehensible way to the technical community and other interested groups. Accompanying studies are to evaluate whether the communication of these findings leads to changes in risk perception. The growing importance of social networks is also to be taken into account.

5. CONCLUSION:

The Nation will integrate its nanotechnology activities – including nanosafety – into the “From Material to Innovation” material research programme. Other specialist programmes will also have relationships to nanotechnology. Announcements under the materials research programme will address applications relating to the priority future tasks defined in the Federal Government’s new High-Tech Strategy: Digital Economy 52 Action Plan Nanotechnology 2020 and Society, Sustainable Economy and Energy, Innovative Working Environment, Healthy Living, Intelligent Mobility and Civil Security.

REFERENCE:

1. Publication BekGS 527 on manufactured nanomaterials.
2. www.baua.de/de/Themen-von-A-Z/Gefahrstoffe/ AGS/pdf/A-Staub.pdf
3. Work is carried out on the basis of EU mandate M/461
4. DIN: German Institute for Standardisation, DKE: German Commission for Electrical, Electronic & Information Technologies in DIN and VDE
5. www.oecd.org/chemicalsafety/testing/oecdguidelinesforthetestingofchemicals.htm; ECHA
6. www.oecd.org/science/nanosafety/
7. www.nanoobject.info
8. www.baua.de/de/Themen-von-A-Z/Gefahrstoffe/ Nanotechnologie/Nanotechnologie.html

Second National Conference on
RECENT ADVANCES IN APPLIED NANO MATERIALS
February 16-17, 2018 at Department of Physics, University College of Science, Saifabad, Osmania University, Hyderabad, Telangana State, India.

Biosynthesis, characterization and antidermatophytic activity of AgNPs using seed aqueous extract of *Datura metal* L. (Ummetha)

P Shivakumar Singh[1], GM Vidyasagar[2]
[1]Department of Botany, Palamuru University, Mahabubnagar – 509001, Telangana, India.
[2]Medicinal Plants and Microbiology Research Laboratory, Department of Post-Graduate Studies and Research in Botany, Gulbarga University, Gulbarga – 585 106, Karnataka, India.
Email: - gmvidyasagar@rediffmail.com. Mobile no: 09449258812.

Abstract: *The current work investigated the biosynthesis of silver nanoparticles using Datura metal seed aqueous extract. The biosynthesised silver nanoparticles were confirmed by visual observation and UV-Vis spectroscopy. Appearance of dark brown colour indicated the synthesis of silver in the reaction mixture. The silver nanoparticles were found to be spherical, rod and triangular in shape with variable size ranging from 23.84 to 50.54 nm, as evident by X-ray diffraction studies, TEM. The X-ray diffraction studies, energy dispersive X-ray analysis and TEM analysis indicate that the particles are crystalline in nature. The nanoparticles appeared to be associated with some chemical compounds which possess hydroxyl and carbonyl groups, confirmed by FTIR. This is first and novel report of silver nanoparticles synthesised from Datura metal seeds extract and their antidermatophytic activity.*

Key Words: *Datura metal seed extract, silver nanoparticles, antidermatophytic activity.*

1. INTRODUCTION:

The field of nanotechnology is one of the most active areas of research in modern materials science and technology. It provides the ability to create materials, devices and systems with fundamentally new functions and properties [M. Karkare,2008]. Recently, research in synthesis of Nanoparticles using microbes and plant extracts gaining more importance due to its eco-friendliness, flexible and main point is the evasion of toxic chemicals [S.Mann, 1993]. When compare to microbes, plant mediated synthesis is actively practicing by the researchers for its positive advantages like avoidance of maintaining the microbial culture, time-consuming and cost effective [M.D.A. Farooqui 2010]. Previously, Various plants have been successfully used for the synthesis of biogenic metal nanoparticles (Singh et al. 2011). Nanoparticles are synthesized using plant materials such as *Gliricidia sepium* [W.R. Rajesh, 2009], *Mucuna pruriens* [S.Arulkumar, and M.Sabesan, 2010],*Cassia occidentalis* [V. Arya, 2010], Banana peel [A. Bankar 2010], *Azadirachta indica* [S.S. Shankar,2004], *Aloe vera* (Chandran et al. 2006), *Emblica officinalis* (amla). (Amkamwar et al. 2005), *Capsicum annuum* (Li et al. 2007), *Cinnamomum camphora* (Huang et al. 2007), *Gliricidia sepium* Jacq. (Raut et al. 2009), *Carrica papaya* (Mude et al. 2009), *Opuntia ficus-indica* (Gade et al. 2010), *Murraya koenigii*(Bonde et al. 2010), *Ocimum sanctum* (Mallikarjum et al. 2011), *Saururus chinenis* (Nagajyoti et al. 2011) and the synthesised silver nanoparticles were used effectively against multi-drug resistant bacteria (Ingle et al. 2008), it can be used in many antimicrobial preparations (Gade et al. 2008) and Duran et al. (2007) successfully developed silver nanoparticle impregnated wound dressings and textile fabrics which can be used for burnt patients. Silver nanoparticles are also used for the preparation of surgical masks (Li et al. 2006). *Datura metal* is a semi evergreen plant belonging to the family annonaceae. *D. metal* commonly known as raamphal plant or bullock's heart is widely distributed all over India. The seeds are used as insecticides, anthelmintic, styptic epilepsy, toothache, tumor, fever and dysentery (Mizanur *et al*., 2011) and are also used externally as suppurant. The bark as a powerful astringent is used as antidysentric and vermifuge. Root, bark, seeds and stem possess isoquinoline alkaloids (Nadkarni KM. 2002). Whereas still there is no report on biosynthesis of AgNPs using seeds of raamphal plant.

In the present study, *D. metal* seed aqueous extract was used for the synthesis of silver nanoparticles and their antidermatophytic activity was evaluated against skin diseases causing fungi and bacteria. It is a first and novel report on biosynthesis of silver nanoparticles from *D. metal*.

2. MATERIALS AND METHODS:

Collection of material

Fresh seeds of *Datura metal* were collected from botanical garden of Gulbarga university campus. Silver nitrate ($AgNO_3$) is procured from High Media Laboratories. Solutions were prepared with triply distilled water.

Preparation of the extract

Weighing 25 g of *Datura metal* fresh seeds were thoroughly washed in distilled water, cut into fine pieces and was smashed into 100 ml sterile distilled water and boil plant extract 5 to 6 min& filtered through Whatman No.1 filter paper (pore size 0.45 µm) and was further filtered through 0.22 µm sized filters. The extract was stored at 4^0C for further experiments.

Synthesis of Silver nanoparticles from *Datura metal* fresh seed extract

The aqueous solution of 1mM silver nitrate ($AgNO_3$) was prepared and used for the synthesis of silver nanoparticles. 10 ml of *D. metal* fresh *seed* extract was added into 90 ml of aqueous solution of 1 mM silver nitrate for reduction into Ag+ ions and kept for incubation period of 90min at room temperature. Here the filtrate acts as reducing and stabilizing agent for 1mM of $AgNO_3$.

3. CHARACTERIZATION:

The formation of AgNP is verified by using UV–visible 5704SS ECIL spectrophotometer operated at with 1 nm resolution with optical length of 10 mm. UV–visible analysis of the reaction mixture was observed for a period of 300s. For the study of crystallinity, films of colloidal AgNP formed on Si(III) substrates by drop coating were used for X-ray-diffraction (XRD) study. The data were obtained using Ricago X-Ray Diffractrometer (Japan), operated at 30 kV and 20 mA current with Cu Ka(I = 1.54 A °). The transmission electron microscopy (TEM) images were obtained using Technai-20 Philips instrument operated at 190 keV. Sample for this analysis were prepared by Biosynthesis of Silver Nanoparticles Using *Annon reticulata* seed 109 coating of aqueous AgNPs drops on carbon coated copper grids, kept for 5 min; the extra solution was removed using blotting paper. The film of TEM grid is exposed to IR light for drying. The powder sample of AgNP was prepared by centrifuging the synthesized AgNP solution at 10,000 rpm for 20 min. The solid residue formed is then washed with deionized water to remove any unattached biological moieties to the surface of the nano particles, which are not responsible for biofunctionalization and capping. The resultant residue is then dried completely and the powder obtained is used for FTIR measurements carried out on a Nicolet iS5 FTIR with diamond ATR.

Antidermatophytic activity of AgNPs synthesised from *D. metal* fresh seeds aqueous extract

Test microorganisms: Four fungi *Trichophyton rubrum, Trichophyton tonsurans, Microsporium gypsuam* and *Candida albicans* three bacterial strains *Staphylococcus aureus, Escherichia coli*, *Bacillus subtilis* were used in the present study, all the tested strains were obtained from M.R.M.C medical college, Gulbarga, Karnataka, India. These test cultures were grown in SDB, nutrient broth (Himedia, M002) at 37ºC and maintained on nutrient and potato agar slants at 4ºC.

Agar-well diffusion method: The assay was conducted by agar well diffusion method. About 15 to20 ml of potato dextrose agar medium was poured in the sterilized petri dishes and allowed to solidify. The bacterial strains were suspended in a saline solution (0.85% NaCl) and adjusted to a turbidity of 0.5 Mac Farland standards (108 CFU/ml). 1 ml of fungal strains were spread over the medium using a sterilized glass spreader. Using flamed sterile borer, wells of 4 mm diameter were punctured in the culture medium. Required concentrations (40 mg^{-1}, 20 mg^{-1}, 10 mg^{-1},5 mg^{-1}) were added to the wells. The plates thus prepared were left for diffusion of extracts into media for one hour in the refrigerator and then incubated at 37^oC. After incubation for 48h, the plates were observed for zones of inhibition. The diameter zone of inhibition was measured and expressed in millimetres. 1mM $AgNo_3$ solution and aqueous plant extract was used negative control. Whereas positive control used ketokonazole, streptomycene against fungi and bacteria (1000 μg/ml conc.). The experiments were conducted in triplicates. The same method was followed for testing antibacterial activity using nutrient agar medium incubated at 37^oC for 18h.

4. RESULTS AND DISCUSSION

The biosynthesis of Ag NPs by fresh *D. metal* fresh seed aqueous extract (light yellowish) was carried out and reported in this research work. 2.5ml of *D. metal* seed aqueous extract was added to 250 ml of 1mM $AgNO_3$ solution. The colour of the reaction mixture after 20 minutes at room temperature changes transparent to dark brown colour and this observation is strong sign for the formation of AgNPs is shown in Fig. 2. The formation and stability of the reduced AgNPs in the colloidal solution was examined by using UV–vis spectral analysis. The UV–vis spectrum recorded from reaction mixture plotted and is shown in Fig. 3. The surface plasmon peak observed at 440 nm is further confirmation of presence of AgNPs in the colloidal solution [S. Basavaraja *et.al*.,2008, Ravishankar Bhat *et.al*.,2013].

The XRD pattern of AgNPs which suggest that the particles are of crystalline in nature. The intense diffraction peaks due to AgNPs are clearly observed at (111), (220), and (311), (380). All the peaks match well with the standard JCPDS file 04-0783 of silver shown in figure 4.

TEM procedure was employed to visualize the size and shape of AgNPs formed. A typical TEM image of biologically synthesized AgNPs, which suggests that the particles are uneven in shape. Some are spherical, rod and triangular shaped particles with a varying size of 23.84–50.54 nm shown in figure 6A & 6B.

The FTIR spectroscopy is a useful technique to study the core–shell morphology of AgNPs is as shown in Fig. 7. The two bands at _1650, 53,and 1459,06 are observed and are recognized as

Fig. 1 *Datura metal* seeds used for the synthesis of AgNPs

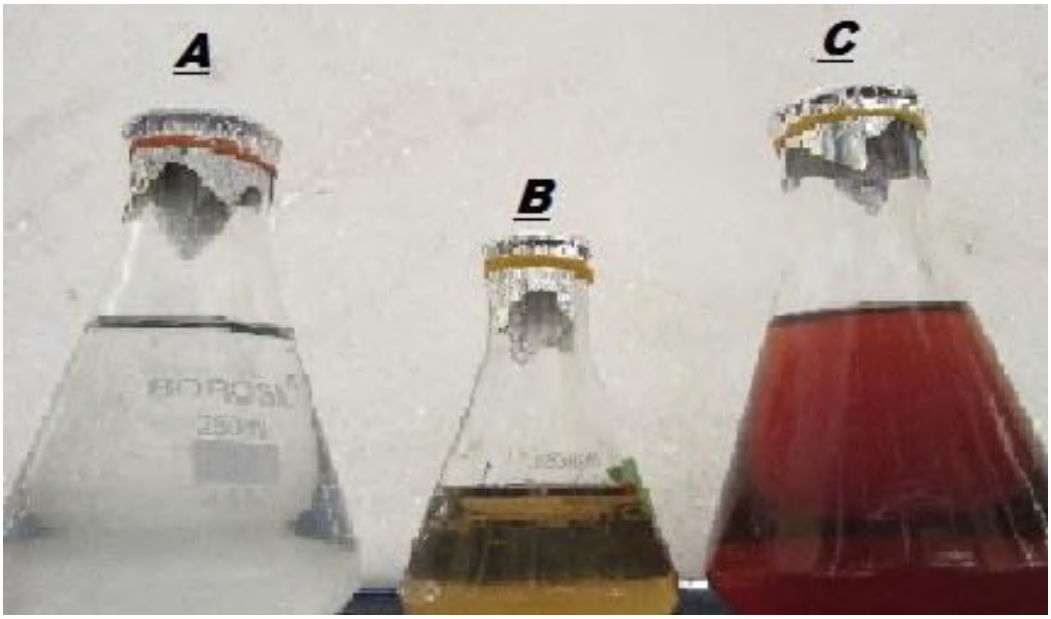

Fig. 2 Synthesis of silver nanoparticles using *Datura metal* aqueous seeds extract treating with AgNO3 solution at room temperature
A) silver nitrate($AgNO_3$) solution, B) *A.reticulata* aqueous seed extract, C)After formation AgNPs change the colour of $AgNO_3$ solution

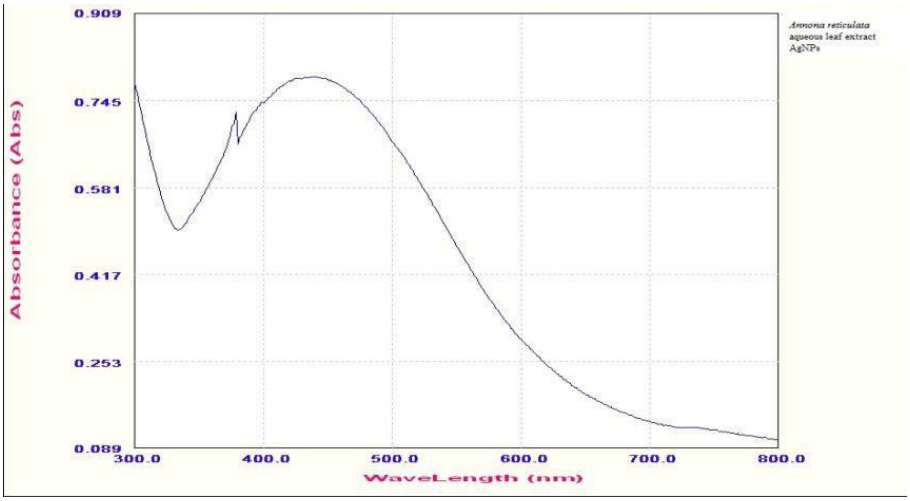

Fig. 3 UV–vis spectrum of bio functionalized AgNPs showing surface plasmon peak at 440 nm

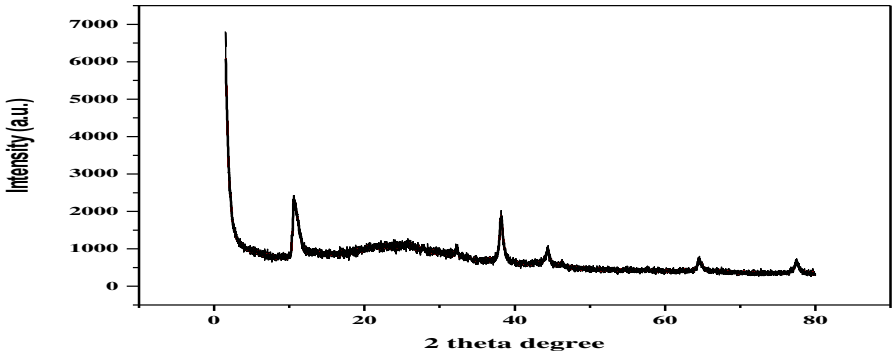

Fig. 4 XRD patterns of bio functionalized AgNPs

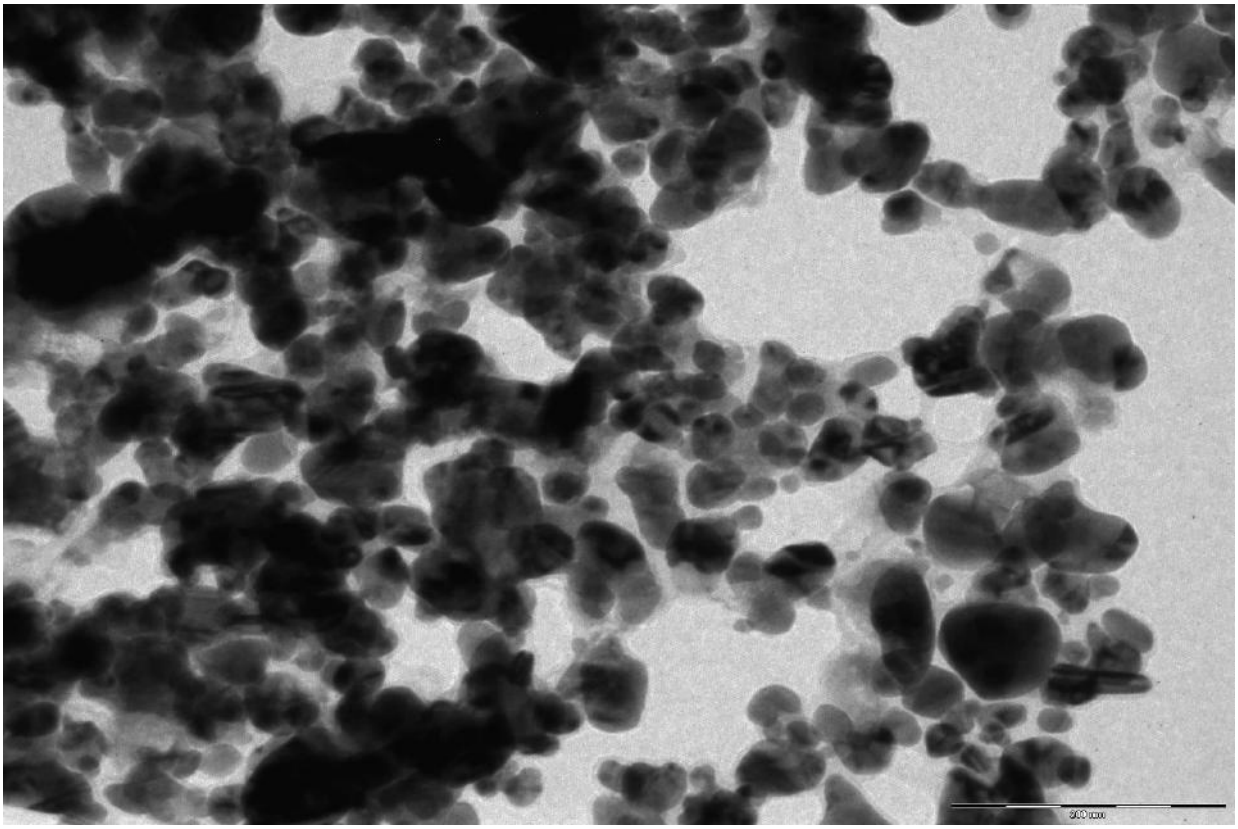

Fig. 5 TEM image of bio-functionalized AgNPs.

Fig. 5 FTIR spectrum of bio functionalized AgNPs

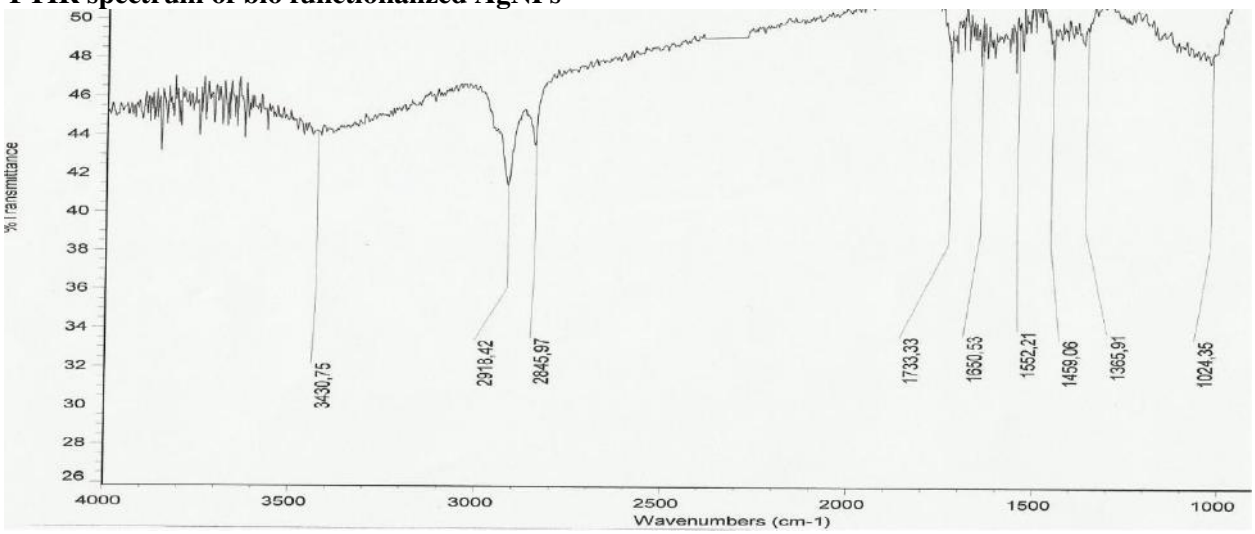

Fig. 6 FTIR spectrum of biofunctionalized AgNPs

Table. 1 Antidermatophytic activity of AgNPs synthesised from aqueous seed extract of *Datura metal*.

Dermatophytic strains	Different conc. of Ag NPs and inhibition zone in mm						
	40 mg^{-1}	20 mg^{-1}	10 mg^{-1},	5 mg^{-1}	Plant aqueous extract	1mM $AgNo_3$ Sol^n	Standard
T. rubrum	14.00	08.00	06.00	-	-	-	22.00
T.tonsurans	12.00	09.00	07.00	-	-	-	23.00
M .gypseum	16.00	12.00	09.00	06.00	-	-	20.00
C .albicans	1800	16.00	11.00	08.00	-	-	26.00
S. aureus	22.00	17.00	12.00	07.00	--	-	32.00
B. subtilis	17.00	14.00	10.00	08.00	--	-	35.00
E. coli	20.0	18.00	14.00	09.00	-	-	30.00

Ag nanoparticles exhibit yellowish brown colour in aqueous solution due to excitation of surface plasmon resonance. On mixing the extract with aqueous solution of the Ag ion complex, a change in the color from colorless to redish brown was observed. It was due to the reduction of Ag+ which indicates the formation of Ag nanoparticles shown in Figure 1&2.

A visible colour change from transparent to yellow within 10 min indicates the formation of silver nanoparticles which was confirmed by UV-visible analysis. Further the colour change to dark-brown is due to increased concentration as well as growth of silver nanoparticles. After 40 minutes there was no significant colour change, which is evidence for the completion of reduction reaction.(fig,2)

ACKNOWLEDGMENTS

Authors are pleased to thank IIT Mumbai for TEM analysis, USIC Gulbarga University for FTIR analysis, Dept of Physics Gulbarga University, Gulbarga for XRD analysis, and Gulbarga University for providing facilities.

REFERENCE:

1. M. Karkare, Nanotechnology fundamentals and applications. IK International publication, (2008) 2- 4.
2. S.Mann, Molecular techonics in biomimetic materials chemistry, *Nature,* 365(1993) 499 - 505.

3. M.D.A. Farooqui, P.S. chauhan, P. krishnamoorthy, and J.shaik, Extraction of silver Nanoparticle from the seed extracts of *clerodendrum inerme,* Digest *journal of nanomaterials and biostructures*,5(2010) 43 - 49.
4. W.R. Rajesh, R.L. Jaya, S.K. Niranjan, D.M. Vijay, and B.K. Sahebrao, phytosynthesis of Silver Nanoparticle Using *Gliricidia sepium*, *Current Nanoscience*, 5(2009)117- 122.
5. S.Arulkumar, and M.Sabesan, Biosynthesis and characterization of gold nanoparticle using antiparkinsonian drug *mucuna pruriens* plant extract. *Int. J. Res. Pharm. Sci,* 4 (2010) 417- 420.
6. V. Arya, S. Yadav, S. Kumar, J.P. Yadav, Antimicrobial Activity of *Cassia occidentalis* L (Seed) against various Human Pathogenic Microbes, *Life Sciences and Medicine Research,* 9 (2010) 1-11.
7. A. Bankar, B. Joshi , A.R. Kumar, S. Zinjarde , Banana peel extract mediated synthesis of gold Nanoparticle, *Colloids and Surfaces B: Biointerfaces*, 80 (2010) 45 - 50.
8. S.S. Shankar, A. Rai, A. Ahmad, M. Sastry, synthesis of Au, Ag, and bimetallic Au core–Ag shell Nanoparticle using Neem(*Azadirachta indica*) seed broth, *J Colloid Interface Sci*, 2(2004) 275- 496.
9. .Singh C, Sharma V, Naik PK, Khandelwal V, Singh H. 2011. A green biogenic approach for synthesis of gold and silver nanoparticles using *Zingiber officinale.* Digest J Nanomat Biostruct 6 (2): 535-542.
10. Bonde SR, Rathod DP, Ingle AP, Ade RB, Gade AK, Rai MK. 2010. *Murraya koenigii* mediated synthesis of silver nanoparticles and its activity against three human pathogenic bacteria. J Exp Nanosci (*in press*).
11. Chandran SP, Chaudhary M, Pasricha R, Ahmad A, Sastry M. 2006. Synthesis of gold nanotriangles and silver nanotriangles using Aloe vera plant extract. Biotech Prog 22: 577-579.
12. Amkamwar B, Damle C, Ahmad A, Sastry M. 2005. Biosynthesis of gold and silver nanoparticles using Emblica officinalis fruit extract, their phase transfer and transmetallation in an organic solution. J Nanosci Nanotechnol 5: 1665-1671.
13. Li S, Qui L, Shen Y, Xie A, Yu X, Zhang L, Zhang Q. 2007. Green synthesis of silver nanoparticles using *Capsicum annum* L. extract. Green Chem 9: 852-858.
14. Huang J, Chen C, He N, Hong J, Lu Y, Qingbiao L, Shao W, Sun D, Wang Y, Wang XH, Yiang X. 2007. Biosynthesis of silver and gold nanoparticles by novel sun dried *Cinnamomum camphora* seed. Nanotechnol 18: 105-106.
15. Raut RW, Lakkakula JR, Kolekar NS, Mendhulkar VD, Kashid SB. 2009. Phytosynthesis of silver nanoparticle using *Gliricidia sepium* (Jacq.). Curr Nanosci 5: 117-122.
16. Mude N, Ingle A, Gade A, Rai M. 2009. Synthesis of silver nanoparticles using callus extract of *Carica papaya*-A first report. J Pl Biochem Biotechnol 18: 83-86.
17. Gade AK, Gaikwad SC, Tiwari V, Yadav A, Ingle AP, Rai MK. 2010. Biofabrication of silver nanoparticles by *Opuntia ficus-indica*: In vitro antibacterial activity and study of the mechanism involved in the synthesis. Curr Nanosci 6: 370-375.
18. Mallikarjun K, Narsimha G, Dillip GR, Praveen B, Shreedhar B, Lakshmi S, Reddy VS, Raju DP. 2011. Green synthesis of silver nanoparticles using *Ocimum* seed extract and their characterization. Digest J Nanomat Biostruct 6 (1): 181-186.
19. Nagajyoti PC, Prasad TN, Shreekanth VM, Lee KD. 2011. Biofabrication of silver nanoparticles using seed of *Saururus chinenis*. Digest J Nanomat Biostruct 6 (1): 121-133.
20. Ingle A, Gade A, Pierrat S, Sonnichsen C, Rai M. 2008. Mycosynthesis of silver nanoparticles using the fungus Fusarium acuminatum and its activity against some human pathogenic bacteria. Curr Nanosci 4: 141-144.
21. Gade AK, Bonde P, Ingle AP, Marcato PD, Duran N, Rai, MK. 2008. Exploitation of *Aspergillus niger* for synthesis of silver nanoparticles. J Biobased Mat Bioengineer 2: 243-247.
22. Li LP, Song QW, Newton E. 2006. Antimicrobial effects of surgical masks coated with 869 nanoparticles. J Hosp Infect 62: 58-63.
23. Duran N, Marcarto PD, De Souza GIH, Alves OL, Esposito E. 2007. Antibacterial effect of silver nanoparticles produced by fungal process on textile fabrics and their effluent treatment. J Biomed Nano 3: 203-208.
24. Nadkarni KM. *Indian Materia Medica*. Mumbai, India: Popular Prakashan; 2002.
25. Mizanur Rahman.S.K, Md. Rashedul Islam, Shahnaz Rahman, Tamim Mosaiab, Rasheda Ahmed,Fatema Khatun, Dilruba Nasrin, Nusratun Nahar, Shamima Ahsan, Mohammed Rahmatullah (2011); *Advances in Natural and Applied Sciences*; 5(2): 218-222, 2011
26. S. Basavaraja, S. D. Balaji, A. Lagashetty, A. H. Rajasab, and A. Venkataraman (2008). Mater. Res. Bull. 43, 1164.
27. Ravishankar Bhat *et.al*., biosynthesis of Silver Nanoparticles Using Areca Nut (Areca catechu) Extract Under Microwave-Assistance. J Clust Sci (2013) 24:107–114

Second National Conference on
RECENT ADVANCES IN APPLIED NANO MATERIALS
February 16-17, 2018 at Department of Physics, University College of Science, Saifabad, Osmania University, Hyderabad, Telangana State, India.

Green synthesis and Characterization of antimicrobial silver Nanoparticles through the leaves of *Bixa orellana*

P Shivakumar Singh[1], DSR Rajender Singh[2] GM Vidyasagar[3]
[1]Department of Botany, Palamuru University, Mahabubnagar – 509001, Telangana, India.
[2]SV Govt UG & PG College Palem, Mahabubnagar Dist. Telangana, India.
[3]Medicinal Plants and Microbiology Research Laboratory, Department of Post-Graduate Studies and Research in Botany, Gulbarga University, Gulbarga – 585 106, Karnataka, India.
Email: shivakumarsinghp@gmail.com Contact: 09989063063.

Abstract: *This is a foremost and new report on extracellular silver nanoparticles synthesis using leaves aqueous extract of Bixa orellana as a sinking agent. The manifestation, size, and shape of the silver nanoparticles are implicit by UV-visible spectroscopy, transmission electron microscopy. The X-ray diffraction studies, energy dispersive X-ray analysis designate that particles are crystalline in temperament. Fourier transform infrared spectroscopy analysis exposed that the nanoparticles are covered with their surface. As can be seen from our studies, the bio functionalized silver nanoparticles thus fashioned have shown commendable antimicrobial effect. The imitation procedure involved is eco-friendly, easy and hence high range production of the same can be considered for using them in many agro-pharmacy applications.*

Key Words: *Bixa orellana, Green synthesis, Silver nanoparticles, TEM, Antimicrobial activity.*

1. INTRODUCTION

A therapeutic plant plays a chief role in the novelty of new remedial agents for drug expansion. *Bixa orellana* is a shrub or small tree with medicinal properties belonging to the family Bixaceae. It is frequently known as sindhurapu in Telugu. *Bixa orellana* is an very important plant as its leaves extract has been used in lesion curing [1], anthelmintic commotion [2] and other pharmaceutical purposes. Nevertheless, the current plant leaves is not being used in the synthesis of silver nanoparticles and their antimicrobial activity has not been mentioned wherever in literature. Hence, captivating into account all these facts the existing search has been intended to optimise the leaves extract deliberation of *Bixa orellana* for the synthesis of AgNPs and their antimicrobial activity.

In the current report, was shown that an extract of *Bixa orellana*, positioned in a strenuous aqueous solution of $AgNO_3$, resulted in the reduction of the silver ions and configuration of silver nanoparticles, and that an extract in aqueous solution of $AgNO_3$ resulted in the lessening of the silver ions and formation of silver nanoparticles. UV-visible (UV-vis) spectroscopy, transmission electron microscopy (TEM), energy dispersive X-ray analysis and Fourier transform infra-red spectroscopy (FTIR) were used to examine size and shape of silver nanoparticles in aqueous extract of *Bixa orellana.*

2. MATERIALS AND METHODS:

Collection of material:

Fresh leaves of *Bixa orellana* were collected from Achampet forests, Mahabubnagar District. Silver nitrate ($AgNO_3$) is procured from High Media Laboratories. Solutions were prepared with triply distilled water.

Preparation of the extract:

Weighing 25 g of *Bixa orellana* leaves were thoroughly washed in distilled water, cut into fine pieces and was smashed into 100 ml sterile distilled water and boil plant extract 5 to 6 min& filtered through Whatman No.1 filter paper (pore size 0.45 µm) and was further filtered through 0.22 µm sized filters. The extract was stored at 4^0C for further experiments.

Figure 1: ***Bixa orellana***

Synthesis of Silver nanoparticles from *Bixa orellana* leaves extract:

The aqueous solution of 1mM silver nitrate ($AgNO_3$) was prepared and used for the synthesis of silver nanoparticles. 10 ml of *Bixa orellana* leaves extract was added into 90 ml of aqueous solution of 1 mM silver nitrate for reduction into Ag+ ions and kept for incubation period of 90min at room temperature. Here the filtrate acts as reducing and stabilizing agent for 1mM of $AgNO_3$.

3. CHARACTERIZATION:

The formation of AgNP is verified by using UV–visible 5704SS ECIL spectrophotometer operated at with 1 nm resolution with optical length of 10 mm. UV–visible analysis of the reaction mixture was observed for a period of 300s. For the study of crystallinity, films of colloidal AgNP formed on Si(III) substrates by drop coating were used for X-ray-diffraction (XRD) study. The data were obtained using Ricago X-Ray Diffractrometer (Japan), operated at 30 kV and 20 mA current with Cu Ka(I = 1.54 A °). The transmission electron microscopy (TEM) images were obtained using Technai-20 Philips instrument operated at 190 keV. Sample for this analysis were prepared by Rapid Biosynthesis of Silver Nanoparticles Using *Cordia dichtoma leaves* 109 coating of aqueous AgNPs drops on carbon coated copper grids, kept for 5 min; the extra solution was removed using blotting paper. The film of TEM grid is exposed to IR light for drying. The powder sample of AgNP was prepared by centrifuging the synthesized AgNP solution at 10,000 rpm for 20 min. The solid residue formed is then washed with deionized water to remove any unattached biological moieties to the surface of the nano particles, which are not responsible for biofunctionalization and capping. The resultant residue is then dried completely and the powder obtained is used for FTIR measurements carried out on a Nicolet iS5 FTIR with diamond ATR.

Antimicrobial activity of AgNPs synthesised from *Bixa orellana* leaves extract:

Test microorganisms: Three fungi *Aspergillus niger, Aspergillus fumigates and Candida albicans, three bacterial strains Staphylococcus aureus, Escherichia coli*, *Bacillus subtilis* were used in the present study, all the tested strains were obtained from Chandighar, sample centres, India. These test cultures were grown in PDA & nutrient broth (Himedia, M002) at 37ºC and maintained on nutrient and potato agar slants at 4ºC.

Agar-well diffusion method: The assay was conducted by agar well diffusion method. About 15 to20 ml of potato dextrose agar medium was poured in the sterilized petri dishes and allowed to solidify. The bacterial strains were suspended in a saline solution (0.85% NaCl) and adjusted to a turbidity of 0.5 Mac Farland standards (108 CFU/ml). 1 ml of fungal strains were spread over the medium using a sterilized glass spreader. Using flamed sterile borer, wells of 4 mm diameter were punctured in the culture medium. Required concentrations (40 mg^{-1}, 20 mg^{-1}, 10 mg^{-1},5 mg^{-1}) were added to the wells. The plates thus prepared were left for diffusion of extracts into media for one hour in the refrigerator and then incubated at 37^{o}C. After incubation for 48h, the plates were observed for zones of inhibition. The diameter zone of inhibition was measured and expressed in millimetres. 1mM $AgNo_3$ solution and aqueous plant extract was used negative control. Whereas positive control used ketokonazole, streptomycene against fungi and bacteria (500 μg/ml conc.). The experiments were conducted in triplicates. The same method was followed for testing antimicrobial activity using nutrient agar medium incubated at 37^{o}C for 18h.

4. RESULTS AND DISCUSSION:

Green synthesis of AgNPs from leaves aqueous extract (slight pink) of *Bixa orellana* was approved out and reported in this research work. 01 ml of *Bixa orellana* leaves aqueous extract was added to 250 ml of 1mM $AgNO_3$ solution. The appearance of the retort concoction subsequent to 18 minutes at room temperature changes transparent to light yellowish colour and this surveillance is strapping signal for the formation of AgNPs is exposed in Fig. 2.

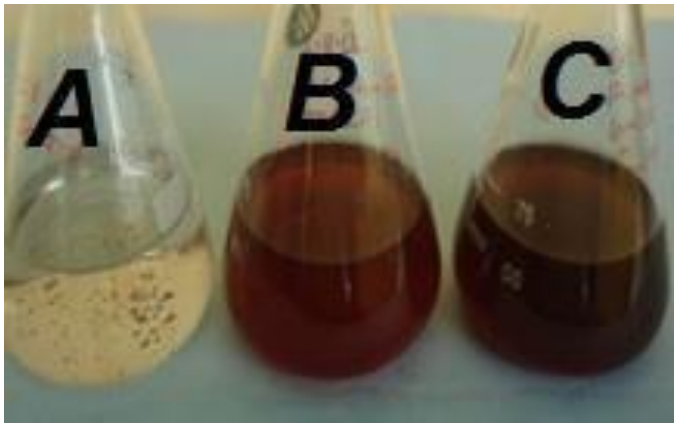

Fig. 2 Synthesis of silver nanoparticles using *Bixa orellana* leaves extract treating with AgNO3 solution at room temperature

A) Formation of AgNPs , B) silver nitrate($AgNO_3$) solution, C) *Bixa orellana* aqueous leaves extract.

The AgNPs formation and constancy of the condensed in the ordeal solution was examined by using UV–vis spectral analysis. The UV–vis range recorded from reaction mixture is shown in Fig. 3.

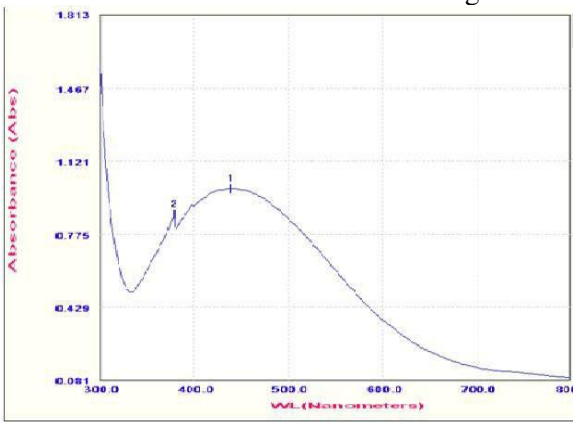

Fig. 3 UV–visa spectrum of bio functionalized AgNPs showing surface plasmon peak at 440 nm

The exterior plasmon height experimental at 440 nm is auxiliary confirmation of occurrence of AgNPs in the ordeal solution [25, 26]. The XRD results of AgNPs which advocate that the particles are of crystalline in nature. The dynamic diffraction peaks like (220), and (311), (380) observed. The recorded peaks competition well with the standard JCPDS file 04-0783 of silver shown in figure 4.

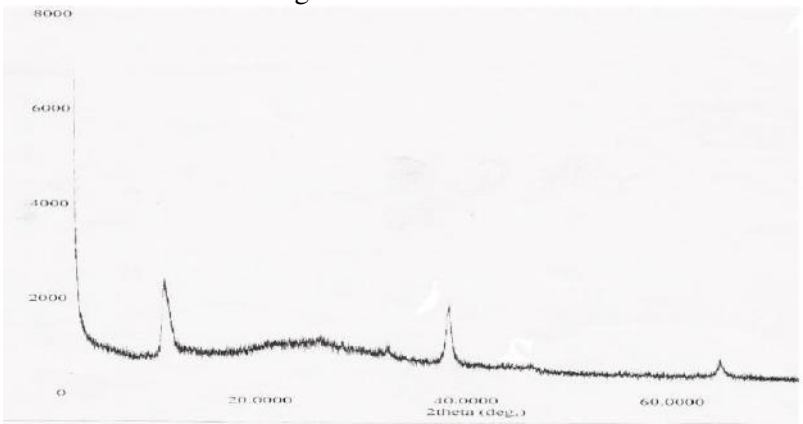

Fig. 4 XRD patterns of bio functionalized AgNPs

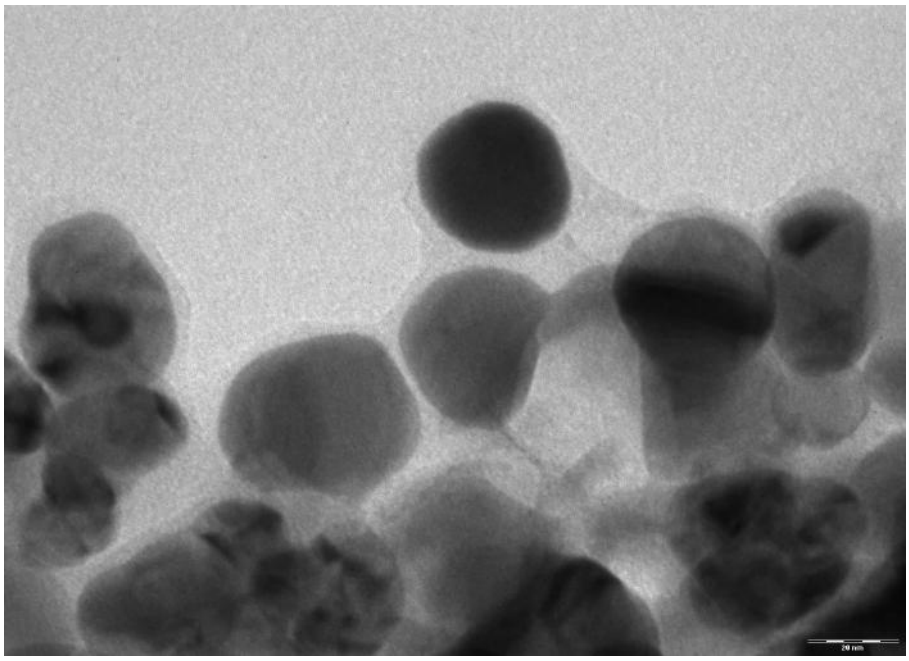

Fig. 5. TEM image of bio functionalized AgNPs, with size pattern

By the TEM results the size and shape of AgNPs was clarified. A classic TEM image of green synthesized AgNPs, which suggests that the particles are uneven in shape. Some are round, spherical and triangular twisted particles with a altering size of 14.88–60.74 nm shown in figure 5.

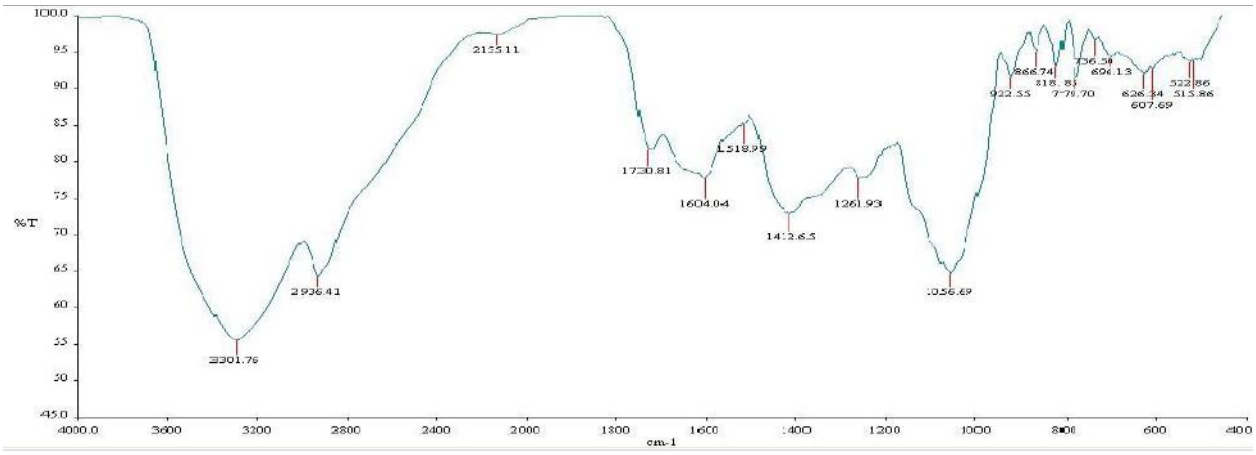

Fig 7. FTIR spectrum of bio functionalized AgNPs

The FTIR spectroscopy is a helpful method to study the middle–shield morphology of AgNPs is as shown in Fig. 6. The strong band at _1650, 53 was observed.

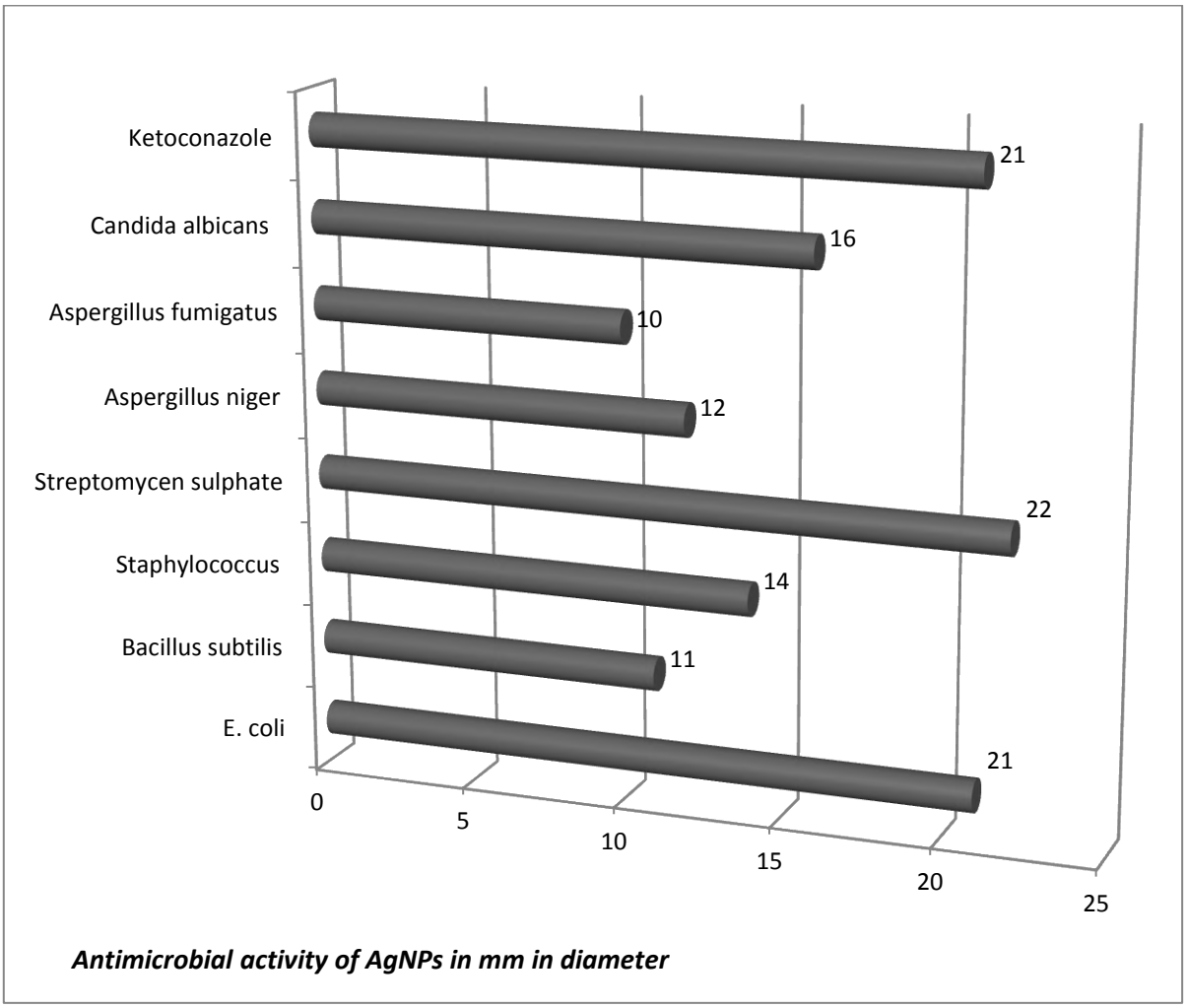

Graph 1: Antimicrobial activity of AgNPs of *Bixa orellana*

Via leaves of *Bixa orellana* based AgNPs antimicrobial activity at 80 µl/well showed maximum antifungal activity against *C. albicans* 16.00 mm followed by *A. niger* 12.00 mm and the least 10.00 mm diameter zone of inhibition showed by *A. fumigatus*. Similarly, against bacteria the maximum activity of 21.00 mm was recorded against *E. Coli* followed by *S. aureus* 14.00mm and *B. Subtilis* 14.00 mm. The antimicrobial activity was straight relative to the meditation of AgNPs. Two negative controls i.e., Plant aqueous extract and $AgNo_3$ solution did not show activity.. Streptomycin sulphate and Ketoconazole used as standards alongside test organisms showed the inhibition zones of 21.00mm & 23.00mm, respectively.(Graph.1).

5. CONCLUSION:

The quick biosynthesis of silver nanoparticles from *Bixa orellana* leaves was shown to be rapid and produce particles of crystallographic irregular shapes. The synthesis technique eco-friendly in nature. The synthesized particles showed antimicrobial activity. The current outcome suggests that they are useful in applications as antimicrobial agent.

6. ACKNOWLEDGMENTS

Authors are pleased to thank IIT Mumbai for TEM analysis, USIC Gulbarga University for FTIR analysis, Dept of Physics Gulbarga University, Gulbarga for XRD analysis, and Gulbarga University for providing facilities.

REFERENCES :

1. M.D.A. Farooqui, P.S. chauhan, P. krishnamoorthy, and J.shaik, “Extraction of silver Nanoparticle from the leaf extracts of *clerodendrum inerme,” Digest journal of nanomaterials and biostructures*, Vol. 5, pp. 43 – 49, 2010.
2. C. Singh, V. Sharma, P.K. Naik, V. Khandelwal and H. Singh, “A green biogenic approach for synthesis of gold and silver nanoparticles using *Zingiber officinale,” Digest Journal of Nanomaterials and Biostructures,*

Vol. 6, No. 2, pp. 535-542, 2011.
3. W.R. Rajesh, R.L. Jaya, S.K. Niranjan, D.M. Vijay, and B.K. Sahebrao, "Phytosynthesis of Silver Nanoparticle Using *Gliricidia sepium*," *Current Nanoscience*, Vol. 5, pp. 117- 122, 2009.
4. S. Arulkumar and M. Sabesan, "Biosynthesis and characterization of gold nanoparticle using antiparkinsonian drug *mucuna pruriens* plant extract," *International Journal of Research in Pharmaceutical Sciences,* Vol. 4, pp. 417- 420, 2010.
5. V. Arya, S. Yadav, S. Kumar and J.P. Yadav, "Antimicrobial Activity of *Cassia occidentalis* L (Leaf) against various Human Pathogenic Microbes," *Life Sciences and Medicine Research,* Vol. 9, pp. 1-11, 2010.
6. A. Bankar, B. Joshi, A.R. Kumar and S. Zinjarde, "Banana peel extract mediated synthesis of gold Nanoparticle," *Colloids and Surfaces B: Biointerfaces*, Vol. 80, pp. 45 – 50, 2010.
7. S.S. Shankar, A. Rai, A. Ahmad and M. Sastry, "Rapid synthesis of Au, Ag, and bimetallic Au core–Ag shell Nanoparticle using Neem(*Azadirachta indica*) leaf broth," *Journal of Colloid and Interface Science*, Vol. 2, pp. 275- 496, 2004.
8. S.P. Chandran, M. Chaudhary, R. Pasricha, A. Ahmad and M. Sastry, "Synthesis of gold nanotriangles and silver nanotriangles using Aloe vera plant extract," *Biotechnolgy Progress,* Vol. 22, pp. 577-579, 2006.
9. B. Amkamwar, C. Damle, A. Ahmad and M. Sastry, "Biosynthesis of gold and silver nanoparticles using *Emblica officinalis* fruit extract, their phase transfer and transmetallation in an organic solution," *Journal of Nanoscience and Nanotechnology,* Vol. 5, pp. 1665-1671, 2005.
10. S. Li, L. Qui, Y. Shen, A. Xie, X. Yu, L. Zhang and Q. Zhang, "Green synthesis of silver nanoparticles using *Capsicum annum* L. Extract," *Green Chemistry,*Vol. 9, pp. 852-858, 2007.
11. J. Huang, C. Chen, N. He, J. Hong, Y. Lu, L. Qingbiao, W. Shao, D. Sun, Y. Wang, X.H. Wang and X. Yiang, "Biosynthesis of silver and gold nanoparticles by novel sun dried *Cinnamomum camphora* leaf," *Nanotechnology,* Vol. 18, pp. 105-106, 2007.
12. R.W. Raut, J.R. Lakkakula, N.S. Kolekar, V.D. Mendhulkar and S.B. Kashid, "Phytosynthesis of silver nanoparticle using *Gliricidia sepium* (Jacq.)," *Current Nanoscience,* Vol. 5, pp. 117-122, 2009.
13. N. Mude, A. Ingle, A. Gade and M. Rai, "Synthesis of silver nanoparticles using callus extract of *Carica papaya*-A first report," *Journal of Pantl Biochemistry and Biotechnology,* Vol. 18, pp. 83-86, 2009.
14. A.K. Gade, S.C. Gaikwad, V. Tiwari, A. Yadav, A.P. Ingle, M.K. Rai, "Biofabrication of silver nanoparticles by *Opuntia ficus-indica*: In vitro antimicrobial activity and study of the mechanism involved in the synthesis," *Current Nanoscience,* Vol. 6, pp. 370-375, 2010.
15. S.R. Bonde, D.P. Rathod, A.P. Ingle, R.B. Ade, A.K. Gade, M.K. Rai, "First report of Murraya koenigii mediated synthesis of silver nanoparticles and its activity against three human pathogenic bacteria," *Nanoscience Methods,* Vol. 1, pp. 25-36, 2012.
16. K. Mallikarjun, G. Narsimha, G.R. Dillip, B. Praveen, B. Shreedhar, S. Lakshmi, V.S. Reddy and D.P. Raju, Green synthesis of silver nanoparticles using *Ocimum* leaf extract and their characterization. *Digest Journal of Nanomaterials and Biostructures,* 6 (1): 181-186, 2012.
17. P. C. Nagajyoti, T. N. Prasad, V. M. Shreekanth, K. D. Lee, "Biofabrication of silver nanoparticles using leaf of *Saururus chinenis*," *Digest Journal of Nanomaterials and Biostructures,* Vol. 6, No. 1, pp. 121-133, 2011.
18. A. Ingle, A. Gade, S. Pierrat, C. Sonnichsen and M. Rai, "Mycosynthesis of silver nanoparticles using the fungus Fusarium acuminatum and its activity against some human pathogenic bacteria," *Current Nanoscience,* Vol. 4, pp. 141-144, 2008.
19. A.K. Gade, P. Bonde, A.P. Ingle, P.D. Marcato, N. Duran, M.K. Rai, "Exploitation of *Aspergillus niger* for synthesis of silver nanoparticles," *Journal of Biobased Matetrials Bioengineer*, Vol. 2, pp. 243-247, 2008.
20. N. Duran, P.D. Marcarto, G.I.H. De Souza, O.L. Alves and E. Esposito, "Antimicrobial effect of silver nanoparticles produced by fungal process on textile fabrics and their effluent treatment," *Journal of Biomedical Nanotechnology,* Vol. 3, pp. 203-208, 2007.
21. L.P. Li, Q.W. Song and E Newton, "Antimicrobial effects of surgical masks coated with 869 nanoparticles," *Journal of Hospital Infection,* Vol. 62, pp. 58-63, 2006.
22. K.M. Nadkarni, "*Indian Materia Medica,"* Mumbai, India: Popular Prakashan; 2002.
23. S. Basavaraja, S. D. Balaji, A. Lagashetty, A. H. Rajasab, and A. Venkataraman *Materials Research Bulletin,* Vol. 43, pp. 1164, 2008.
24. Ravishankar Bhat, Sharanabasava Ganachari, Raghunandan Deshpande, G. Ravindra, A. Venkatraman, "Rapid Biosynthesis of Silver Nanoparticles Using Areca Nut (Areca catechu) Extract Under Microwave-Assistance," *Journal of Cluster Science,* Vol. 24, pp. 107–114, 2013.
25. Kuppasta, I.J. and Nayak, P.V.: Natu. Prod. Rad., 15: 99-102 (2006).
26. Kuppasta, I.J. and Nayak, P.V.: Ind. J. Natu. Prod.,19(3): 27-29 (2003)

Second National Conference on
RECENT ADVANCES IN APPLIED NANO MATERIALS
February 16-17, 2018 at Department of Physics, University College of Science, Saifabad, Osmania University, Hyderabad, Telangana State, India.

Study of recent trends in graphene based electrode materials for solar cells as energy storage devices and sensor applications

Dr K.Vagdevi[1], Dr K.VenkateswaraRao[2], Dr V.Radhika devi[3]
[1] Gokaraju Rangaraju Institute of Engineering & Technology
[2] CNST, IST Jawaharlal Nehru Technological University, Hyderabad
[3] Marri Laxman Reddy Institute of Technology, Hyderabad
Email : vagdevi.kakarla@gmail.com

Abstract: *The interest in dye sensitized solar cells has increased due to reduced energy sources and production costs. Solar cells are important promising material for the conversion of sunlight into electrical energy which offers the low cost and large scale production. We proposed Graphene based nanocompositesas a counter electrode material for the DSSC applicationswhich replaces the existing nano crystalline TiO_2 and ZnO materials deposited as a thin film on conductive glass electrodes. The outstanding mechanical properties of graphene are applicable to prepare flexible, stretchable and foldable electronics.*

Key Words: *Graphene, Properties, applications*

1. INTRODUCTION:

Transparent Conducting Oxides (Tco) Combine Two Physical Properties, Namely, High Electrical Conductivity And Optical Transparency. They Are Achieved By Adding Suitable Dopants And By Creating Defects In The Insulator. These Properties Make Tco An Important Material For Industrial Applications, Such As, Liquid Crystal Display, Plasma Light Emitting Displays, Organic Light Emitting Displays, Touch Screen Sensors, Thin Films, PhotovoltaCells, Smart Windows And Solar Control Films. [1]

Background: Three most common TCOs are tin doped indium oxide In_2O_3: Sn (ITO), fluorine doped tin oxide SnO_2: F (FTO) and aluminum doped zinc oxide ZnO: Al. A very peculiar property to be noticed is that although these TCOs are considered as good conductors, they are, very poor conductors compared to metals. This important factor makes TCO a diverse material for its applications.[2]

CHARACTERISTICS OF TCO

TCO should have the following characteristics when used in technology

- They have to be transparent for visible part of light with transmittance of ≥ 80%.
- They should have high concentration of charge carriers of ≥ 10^{19} cm^{-3} and large mobilities of ≥ 1 cm^2 V^{-1} s^{-1}.

2. CONDUCTIVITY IN TCO:

The material physics of TCO can be understood with the help of simple opinions. The basic idea is to create free charge carriers (electrons or holes) in wide band gap insulators using suitable dopants. For example, the chemical doping of Sn^{4+} for In^{3+} in ITO leads to donor-induced states located close to the host (In_2O_3) conduction band. The oxygen vacancies (In_2O_{3-x}) can also introduce impurity states in the band gap which contribute to conductivity. Further doping of Sn^{4+} leads to a degenerate gas of current-carrying electrons which give rise to far-infrared absorption and high electronic conductivity leaving the host band gap unaffected. Thus the electrically conductive material remains optically transparent in visible region. The mechanism of conductivity in TCO can be understood with the help of classical description of charge transport in metals given by Drude Theory. [3]The charge carriers produced through doping are to be treated as free electron gas. Thus the conductivity (σ) is determined by the density of charge carries and their effective mass.

$$\sigma = \frac{n_e e^2 \tau}{m} = n_e e \mu_e$$

Where n_e = Number of charge carriers,

m_e = Effective mass,

τ = Relaxation time and
$\mu_e = \frac{e\tau}{m_e}$ = Mobility of the charge carriers.
The optical window for ITO is thus set by the Plasmon frequency. Mobility and Plasmon frequency are determined by band gap and effective mass of electron. The response of TCO material to incident light is shown in Fig 1.

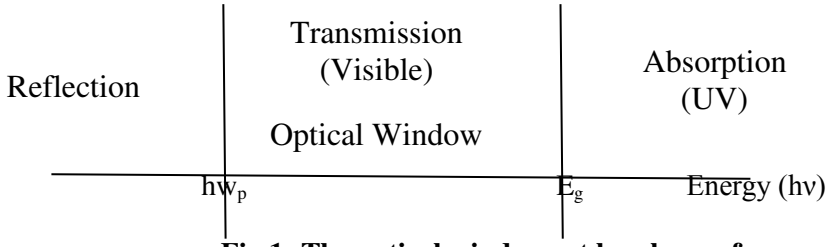

Fig 1: The optical window set by plasma frequency and band gap

From Fig 1, the incident photons with energy lower than the plasmon frequency are reflected and those with energy higher than the band gap are absorbed by TCO. Thus by shifting the Plasmon frequency, the infrared (IR) part of visible spectrum can be transmitted or blocked by TCO material [4]. Also a large secondary band gap which is the difference between two lowest conduction bands is essential. The larger value of secondary band gap lowers the intra band transition of charge carriers and ensures optical transparency.

Brief history of existing TCO materials: Indium Tin Oxide (ITO): At present ITO is the best material for TCO. Lowest resistivity of the order of 1 $\times 10^{-4}$ Ω cm can be obtained in ITO films prepared by different deposition methods. But, one of the greatest disadvantages of ITO is the limited availability of indium on the earth's surface and there is a chance of depletion of element on continuous usage. [5]

Impurity doped ZnO: In 1980, an inexpensive and harmless binary compound of ZnO was developed. Although undoped, ZnO films with resistivity of 4.5 $\times 10^{-4}$ Ω cm were prepared by rf-magnetron sputtering [11], TCO films using ZnO: Al and ZnO: Ga prepared by various deposition methods have attracted much attention for thin film solar cells as resistivity of the order of 1 $\times 10^{-4}$ Ω cm was obtained in these films [6,7]. Among all dopants, Aluminium doped Zinc Oxide is the best and is used in various practical applications.
Limitations of ZnO: As the binding energy between Zn and O is chemically more dynamic, controlling Zn is more difficult in preparing ZnO films. By various deposition methods, resistivity of 1-3 $\times 10^{-4}$ Ω cm, refractive index of approximately equal to 2.0 and average transmittances of above eighty five percentages have been obtained in ZnO doped films. They are unstable at temperatures above 150°c and the optical absorption of ZnO films is lower than that of other TCO films in the visible range. The usage of milky ZnO transparent electrode for solar cells improves the efficiency because of the effect of light confinement [8, 9].

3. DESIGNING NEW TCO MATERIAL:

To overcome limitations of present TCO materials and to meet the required improvements in physical and chemical properties some alternative materials are suggested and the designs are so that they can be used for specialized applications [10].
The following points are considered in designing a new TCO material for commercial applications.

- The resistivity of multicomponent oxide films is similar to the mechanism of metal alloys.
- Optical properties are similar to dielectric materials, and
- The presence of nature and quantity of metal element determine the chemical properties in multicomponent oxide films.

GRAPHENE AS TCO

The non-oxide material graphene is an alternative to the existing TCO materials. The advantage of graphene over the brittle ITO is its mechanical strength and flexibility. It is also economical and obtainable in large quantities. Moreover, large areas of graphene films can be deposited from solutions. Also graphene films are sensitive to surface roughness unlike ITO. However, several technical issues like poor adhesion to peel are to be addressed while applying graphene as a TCL for Light Emitting Diodes. If peeling of graphene occurs, power stops at the position of peeling and does not extend any more in sideways. [11, 12]

Importance of Graphene over ITO and FTO

ITO and FTO have the following disadvantages

- The element indium is scarce.

- They are unstable in the presence of acid and base.
- Structure defects in FTO devices cause current leakage.

PRINCIPLE FOR GRAPHENE APPLICATION

Electrical conductivity of graphene can be changed by adsorbing impurities on the surface of graphene. The carrier concentration of the material is improved as adsorbed molecules acts as donors or acceptors and the conductivity of graphene is altered. In addition, some properties mentioned below increase its sensitivity to single atomic level.

- Graphene is a 2-D material and all its carbon atoms are exposed to the analyte of interest.
- It is highly conductive with low Johnson noise.
- It has very few crystal defects. They ensure a very less intensity of noise caused due to thermal switching.
- Four probe measurements can be done on a single crystal device with electrical contacts of low resistance.
- Moreover it was verified that the mobility of graphene was not affected by heavy doping concentrations of holes and electrons.[13]

Applications of TCO

TCOs are used in many electronic devices. In most of these devices TCO is used as coating on suitable substrates.

- TRANSPARENT CONDUCTING ELECTRODES: Graphene is suggested as an aspirant for TCE applications which replace ITO electrodes. Large continuous area, transparent and highly conductive few layered graphene films produced by CVD are used as anodes for numerous applications.
- SOLAR CELLS: The front surface of solar cells is covered by transparent electrodes. Typical architecture of a thin film solar cell is as shown in Fig 2. TCO layer is used as front contact material for all thin-film solar cells. A reflective contact material is used at the back side. In solar cells, TCO act as contact material for collection of photo-generated carriers and allow the light to reach the active solar absorbing material. [14,15]

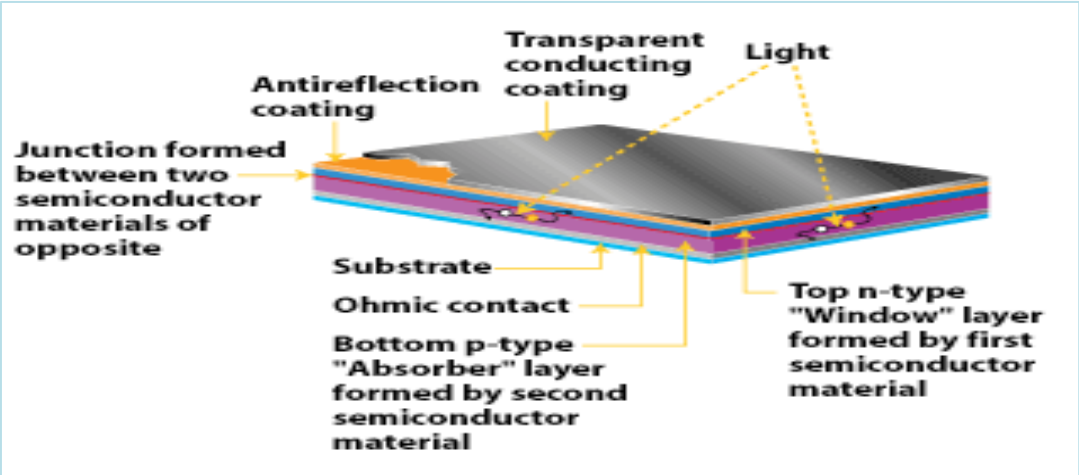

FIG 2: CROSS SECTION OF A SOLAR CELL

4. RESULTS:

Keeping the advantages of graphene in mind, we have studied the electronic and transport properties which consists of DOS, band structure, transmission spectra and I-V characteristics. Variations of all these parameters for pure graphene and graphene adsorbed with Beryllium and Stannic tetra chloride shown in fig 3 and the results are compared and presented in Tab1.

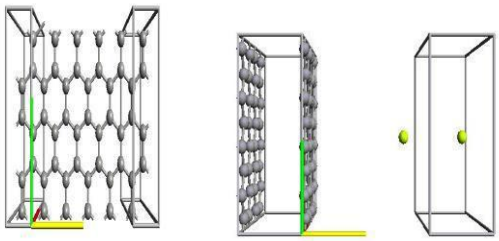

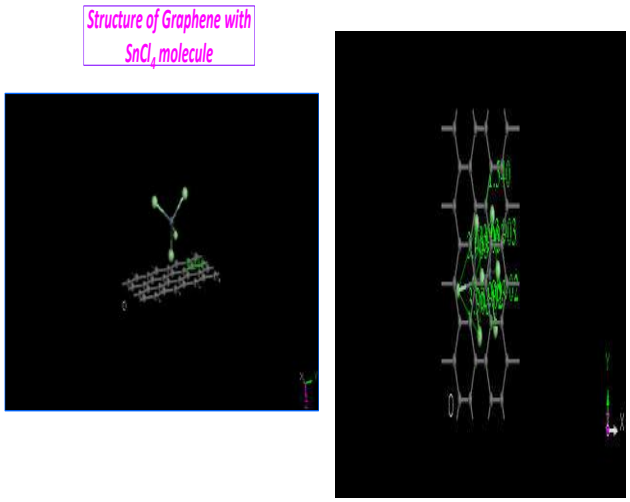

The calculations are done by using DFT and are tabulated in the table below

S.No	Pure Graphene	Graphene with one Beryllium atom	Graphene with two Beryllium atoms	Graphene with one $SnCl_4$ molecules	Graphene with two $SnCl_4$ molecules
Band Gap	0.000 Ha	0.017 Ha	0.021 Ha	0.025 Ha	0.037 Ha
Density of States	80 at -0.2 Ha & 60 at 0.2 Ha	200 at -0.1 Ha & 230 at 0.1 Ha	400 at - 0.1 Ha & 260 at 0.1 Ha	80 at - 0.1 Ha & 65 at 0.1 Ha	850 at - 0.1 Ha & 350 at 0.1 Ha
Negative Differential Resistance	7V to 9V & -9V to -7V	1 to 2V & -5 to - 7V	2 to 5 V	5V to 7V & -5 to -7V	7V to 9V & -7 to -9 V
Negative Differential Conductance	2V to 5V & -2 to -1V	2V to 5V &-2 to -5V	2 to 5 V	5V to 7V & -2 to -1V	7V to 9V & -5 to -7V
Total Energy	-4.64099	-6075.2747	-5075.2747	-6840.6153	-9171.0262
Chemical Potential	-4.21	-5.54	-5.54	-5.54	-5.54

5. CONCLUSIONS:

FromTab1: the band gap of pure graphene is 0 Ha. The band gap increases from 0 to 0.17 Ha, 0.021 Ha when adsorbed with one, two Beryllium atoms and changes to 0.025 Ha and 0.037 Ha when adsorbed with one, two SnCl4 molecules respectively. The density of states has increased from 80 to 850 below Fermi level and 60 to 350 above Fermi level on adsorbing different elements on pure graphene structure. Negative differential conductance is observed in all the cases at different biasing voltages. Total energy has decreased on adsorbing different elements which shows that the system is stable after absorbing the elements.

REFERENCES

1. R.G.Gordan, “Criteria for choosing Transparent Conductors” MRS Bulletin 52 DOI: 10.1557/mrs2000.151, August (2000)
2. T.Minami, “Transparent conducting oxide semiconductors for transparent electrodes” Semiconductor.Sci.Technol.20 S35 (2005)
3. H.KawazoeM.Yasukawa, H.Hyodo, M.Kurita, H.Yanagi and H.Hosono, “Transparent Electronics: From Synthesis to Applications”, Nature (London) 389,939 (1997)

4. H.Yanagi, K.Ueda, H.Kawazoe and Hosono, "Cupric Oxide-based p-type Transparent Conductors", J.Appl.Phys. 88, 4159(2000)
5. K.Ueda, T.Hase, H.Yanagi ,H. Ohta, M.Ortia and M.Hirano, "Epitaxial growth of transparent p-type conducting CuGaO2 thin films on sapphire (001) substrates by pulsed laser deposition" J.Appl.Phys. 89,1790(2001)
6. H.Yanagi, T.Hase, S.Ibuki, K.Ueda and H.Hosono, "A promsing P-type transparent conducting material-layered oxysulfide", Appl.Phys Lett.78,1583(2001)
7. *H Mizoguchi, M Hirano, S Fujitsu, T Takeuchi, K Ueda and H Hosono, "$ZnRh_2O_4$: a P-type semiconducting oxide with a valence band composed of a low spin state of Rh^{3+} in a $4d^6$ configuration", Appl. Phys. Lett. 80 1207,2002*
8. MatthijnDekkers, GuusRijnders and Dave H. A. Blank "ZnIr2O4, a p-type transparent oxide semiconductor in the class of spinel zinc-d6 -transition metal oxide" , Appl.Phys.Lett.90,021903(2007)
9. *P. P. Edwards, A. Porch, M. O. Jones, D. V. Morgan and R. M. Perks*, "Basic materials physics of transparent conducting oxides", *Dalton Trans*., *2004*, *2995-3002*.
10. Chris G. Van de Walle and Jörg Neugebauer, "First-principles calculations for defects and impurities: Applications to III-nitrides", J. Appl. Phys. 95, 3851 (2004)
11. Kiyotaka Wasa[1], Shigeru Hayakawa[1] and Toshio Hada[2], "Electrical and Optical Properties of Sputtered n-p ZnO–Si Heterojunctions", Japanese Journal of Applied Physics, Volume 10, Number 12 p.1732
12. J.Aranovich,A.Oritz and R.H.Bube, J.Vac, "Advances in solar Energy: an annual review of Research and Development", Sci.Technol.16(1979).p994
13. J.Hu and R.G .Gordan, "Deposition of transparent conducting oxides for solar cells chemical laboratories", Sol.cells 30 (1991) P.437
14. T.Minami, "Transparent and conductive multicomponent oxide films prepared by magnetron sputtering", J.Vac.Sci.Technol.A17 (1999)P.1765
15. T.Minami,S.Takata,T.Kakamu and H.Sanohara, "Physics of Very Thin ITO Conducting Films with High Transparency Prepared by DC Magnetron Sputtering", Thin solid Films 270(1-2)(1995)p22.

Second National Conference on
RECENT ADVANCES IN APPLIED NANO MATERIALS
February 16-17, 2018 at Department of Physics, University College of Science, Saifabad, Osmania University, Hyderabad, Telangana State, India.

XRD Analysis of Bone of Chicken *Gallus gallusdomesticus*

Sarwath Khalil, Kaleem Ahmed Jaleeli & Adeel Ahmad
Biophysics Research laboratory, Department of Physics, Nizam College (Autonomus), Osmania University, Hyderabad - 500001, India.
Email - skhalil.sk.9@gmail.com, kaleemjaleeli@gmail.com, dr_adeelahmad@yahoo.com

Abstract: *The paper deals with X-ray diffraction analysis of powdered bone of chicken Gallus gallusdomesticus. The study reports that the major inorganic constituents present in the bone is hydroxyl apatite. The crystalline size and lattice strain are evaluated.*

Key Words: *Hydroxyapatite, Bone, X-ray diffraction*

1. INTRODUCTION:

Bone is a dense and constantly changing structure that grows, shrinks and adapts during the entire life time of animals. Bone tissues are classified into two types, compact and cancellous bones. Femur and Tibia are the examples of compact bones and scapula and rib are examples of cancellous bones. The anabolic and catabolic process that takes place in the bone helps in the regulation of mineral metabolism and in the maintenance of the skeleton.

X-ray crystallography is a technique used for determining the atomic and molecular structure of a crystal, in which the crystalline atoms cause a beam of incident X-rays to diffract into many specific directions. By measuring the angles and intensities of these diffracted beams, a crystallographer can produce a three-dimensional picture of the density of electrons within the crystal. From this electron density, the mean positions of the atoms in the crystal can be determined, as well as their chemical bonds, their disorder, and various other information.

Powder diffraction is commonly used to identify unknown substances, by comparing diffraction data against a database maintained by the *International Centre for Diffraction Data* [1]. Therefore it is also helpful in the analysis of unknown biological samples. Many studies have been carried out to learn the x-ray diffraction analysis of eggshell of hen, quil, ostrich, which helped in the synthesis of hydroxyapatite. The Hydroxyapatite (HAp) is one of the most versatile materials used for implantation purpose due to its similarity to natural bone material. Hap has approximate chemical formula Ca10(PO4)6(OH)2 or Ca5(PO4)3(OH), and is the main inorganic constituent of bones in humans. HAp can be successfully synthesized by reaction of discarded eggshell with tri-calcium phosphate in presence of steam at 900 degrees Centigrade and subsequent aging for 24 hrs. Synthetic HAp has been successfully used in hard tissue surgery [2,3]. It is particularly attractive material for the bone and tooth implants since it closely resembles human tooth and bone mineral and has proven to be biologically compatible with these tissues [4-6]. Many studies have indicated that HApcermaics show no toxicity, inflammatory, pyrogenetic responses. It has excellent fibrous tissue formation between implant and bone.[4] It can be revealed stability. The particles are mostly spherical with nano size [7].

Joschek, et. al., [8] studied the properties of porous hydroxyapatite ceramics produced by the sintering of bovine bone. They concluded that ceramics are highly crystalline and porous and have an advantage of high interconnecting pore system and a better drug processing ability.

Gangadhar, et.al., [9] made elemental analysis of ovine scapular cartilage and reported that 13 different elements are present in which percentage of Carbon, Oxygen and Nitrogen is more and molecular composition in is inhomogeneous.

SreenivasaRao, et.al.,[10] made studies on human hair by inductive coupled plasma –atomic emission spectrometry and reported that human hair contains iron, lead, cobalt, nickel, manganese, zinc, copper and calcium.

JayanandManjhi, et.al.,[11] studied the Effect of extremely low frequency magnetic field in the prevention of spinal cord injury-induced osteoporosis. They investigated the effect of extremely low frequency (ELF) magnetic

field (MF) by electron microscopic study, which revealed the enhancement of microstructural composition and compactness in cortical and trabecular parts of treated bones.

Jeevan Kumar, et.al., [12] made studies on identification of trace elements in bovine metacarpus bone by Spectro - chemical analysis In their studies Analytical methods are described for the determination of major, minor, and trace elements in bone. Ca, Mo, Pb, Fe, Zn, Cu, Mg, Al, P are identified in the bovine metacarpus bone as major trace elements and 16 more elements are identified as minor trace elements i.e., Os, Sc, Y, K, Mn, La, Cd, Pd, Ru, Na, Sn, Pt, Bi, As, Si and Co.

The present study is an attempt to analyze chicken bone powder by using the technique of x – ray diffraction.

2. MATERIALS AND METHODS:

The Bone samples of Chicken *Gallus gallusdomesticus* was separated carefully from the flesh, cleaned thoroughly and dried under the sun for 3 - 4 days, so as remove free water. The bone was powdered using pestle and mortar.

X- ray diffraction of femur bone of Chicken *Gallus gallusdomesticus* was recorded using x-ray diffractometer (Shimatzu – Maxima XRD 7000) in reflection mode with Cu Kα (λ=1.5405 Å) radiation. Sample was made into fine powder for the analysis.

X-rays were produced by a copper target at the voltage 40 kV and current 30 mA. The slits used were divergence slit of 1^0; scatter slit of 1^0; receiving slit of 0.3 mm.In the scanning set up, Driver axis: 2 θ; Scan range: 10 – 80; Mode of scan is continuous scan; Scan speed: 2^0 min^{-1}; Sampling pitch: 0.02^0; Preset time: 0.60 sec.

The size of crystallites, lattice strain and percentage of crystallinity of bone apatite was calculated from XRD data using the formulae[13],

$$\text{Size of crystallites, } L = \frac{K\lambda}{\beta_0 \cos\theta},$$

where λ = 1.54056 Å, K is assumed to be 1

$$\text{Lattice strain, } \varepsilon = \frac{\beta_o}{4\tan\theta}$$

$$\text{Crystallinity (\%)} = \frac{A_t - A_a}{A_t} x\ 100$$

where A_t is total area covered by the peaks and A_a is amorphous area (A_a) covered by the broad peak alone [13].

3. RESULTS AND DISCUSSION:

Table 1 gives XRD data obtained from diffractograms. The data includes 2θ, d spacing, relative intensity (I/I_0), FWHM, crystallite size (L) and lattice strain (ε) of diffraction peaks. The data is of machine (diffractometer) generated one. The data of chicken bone reveals principal interplanarspacings (d – spacings) around 2.91 Å, 2.80 Å, 2.21 Å, and 1.81 Å. At these d spacings, crystallite size and lattice strain are calculated. Average values along with SD are also tabulated in the table.

2θ (degree)	d (Å)	I/I_0 (%)	FWHM, β_0 (degree)	Crystallite Size, L (nm)	Lattice strain, ε
30.7410	2.90854	100.00	0.4723	18.23	0.0075
31.9092	2.80467	88.94	0.6298	13.71	0.0096
40.7950	2.21196	11.46	0.7396	11.97	0.0087
50.4920	1.80757	44.17	0.8224	11.16	0.0076
Average:				13.77	0.0084
SD:				±3.160	±0.001

The principal interplanar spacings (d – spacings) observed in the present investigation reveal the fact that mineral present in chicken femur bone ishydroxyl calcium phosphate. Further, calcium phosphate present in bone is of both crystalline and
amorphous in nature. The degree of crystallinity ranges from 50% to 60%.

The broadening of peaks in x – ray diffractograms is because of crystallites of small in size and also inhomogeneous distribution of their size.

REFERENCES:

1. AsfinyNurLaeny, Synthesis of Amorphous Calcium Phosphate by Low Temperature-Precipitation Method from Eggshell: Introduction to X-ray Diffraction Anonim, 2005.
2. http://www.mrl.ucsb.edu/mrl/index.html. [30 Maret 2007]
3. Dean Mo Liu, Fabrication of hydroxyapatite with controlled porosity, J.Mat.Sci.: Mat. Med., Vol. 8(1997), pp. 227-232.
4. V Jokanovi, B Jokanovi, Kinetics and sintering mechanisms of hydro-thermally obtained hydroxyapatite, Mat. Chem.Phy., Vol. 111(2008), pp. 180-185.
5. L L Hench, Bioceramics: From Concept to Clinic, J. Amer.Cer. Soc., Vol.74(1991), pp. 1487-1510.
6. G. Willmann, Material properties of hydroxyl apatite ceramics, Inter. Ceram, Vol. 42, (1993), pp.206-208.
7. G. Willmann, Medical grade hydroxyapatite: State of the art, British Ceram. Trans.,Vol. 95(1996), pp. 212-216.
8. G. Willmann, J. Min. Mat. Char.Engg., Vol. 9, No.8(2010), pp. 683-692.
9. S Joschek, B Nies, R Krotz andAGopferich, Biomaterials, Vol. 21, No. 16(2000), pp. 1645 - 1658.
10. R Ganghadhar, Kaleem Ahmed Jaleeliand Adeel Ahmad, Int. J. Sci. Engg. Tech., Vol. 4, No. 3(2015), pp.1195 – 1198.
11. K. Sreenivasa Rao, T. Balaji, Talasila Prasada Rao, G.R.K. Naidu, Spectrochimica Acta., Part B. Atomic Spectroscopy,Vol. 57, No. 8(2002), pp. 1333 – 1338.
12. Jayanand Manjhi, Suneel Kumar, Jitendra Behari, Rashmi Mathur, J. Rehabilitation Res. Dev., Vol. 50, No.1(2013), pp. 17 - 30.
13. R. Jeevan Kumar, S. Md. Shoaib, K. Fakruddin, and Adeel Ahmad J. KSU, Sci., Vol.20, No. 2(2008), pp. 17 – 26.
14. Kavesh S, and J M Schultz, Meaning and measurement of crystallinity in polymers: A Review, Polymer Engg. Sci., Vol. 9, No. 5(1969), pp. 331– 338.

Second National Conference on
RECENT ADVANCES IN APPLIED NANO MATERIALS
February 16-17, 2018 at Department of Physics, University College of Science, Saifabad, Osmania University, Hyderabad, Telangana State, India.

FTIR Spectroscopic Study on Quantitation of Urea in Human BloodSerum

U. Vijaya Ushasree[1] & Adeel Ahmad
Biophysics Research Laboratory, Department of Physics, Nizam College (Autonomous),
Osmania University, Hyderabad – 500 001, India.
[1]Department of Physics,Dr.B.R.Ambedkar Open University, Hyderabad - 500033, India.
dr_adeelahmad@yahoo.com

Abstract: *The quantitation of urea has been achieved using FTIR spectroscopy. The FTIR spectra of human blood serum samples are recorded in Mid IR region 4000-400 cm^{-1}.The normal blood serum is treated with urea at different concentrations and FTIR spectra are recorded, which confirm the specific peaks related to urea. A plot between concentration of urea and percentage of absorbancehas shown linear relationship. The study being complementary to chemical analysis is very much useful for the estimation of urea in the blood serum of patients suffering from diabetes and renal diseases.*

Key Words: *FTIR Spectroscopy, Quantitation, Human blood, Serum, Urea.*

1. INTRODUCTION:

IR spectroscopy has been used by Biophysicist and Chemist as a powerful tool to characterize compounds. It has been applied to biology for studying the structure and conformation of molecules like proteins, nucleic acids and lipids. The advances made in instrumentation have paved the way for its utilization in medicine. Besides the application of FTIR for tissue diagnostics, the investigation of body fluids has been gaining importance. The mid –IR region is very use full in the identification of disease patterns using the FT-IR spectrum of human blood serum. Precise quantification of several components such as albumin, total protein, and Urea can be achieved using FT-IR spectroscopy

Zhdanov et al [1] made a comparative study to determine the role of the skeletal base configuration of carbohydrate molecules, using IR and Raman spectroscopy. Theoretical calculations of the vibrational spectra of series of carbohydrates differed in the configuration of CO (CH) bonds in various positions of the pyranosering. The normal vibrations of carbohydrate molecules had, with few exceptions, close or coinciding frequencies; however, they differed greatly in the shape and contribution to the potential energy distribution(PED) of individual groups and bonds. Despite the cooperative character of the vibrations, each compound was characterized by a specific set of frequencies with a prevailing contribution to the PED of particular CO and C - C bondsof the molecule. They concluded that vibrations have a peculiar localization and that steric factors play an important role in the vibrational spectra of carbohydrates.

Minesh Patel et al [2] Studied poly acrylic acid and mucus using infrared, 1H and 13C nuclear magnetic resonance, and X-ray photoelectron spectroscopes and differential scanning calorimetry, which supported the hypothesis that hydrogen bonds, formed between the carboxylic acid functionality of the muco - adhesive material (polyacrylic acid) and the glycoprotein component of mucus, play a significant role in the process of muco-adhesion. They found fewer H-bonded interactions between the components than within the bulk of the pure muco-adhesive agent andpH of the medium influenced the structures of both the poly acrylic acid and the mucus, which, in turn, determine the nature and the extent of muco-adhesive interactions.

Davis and Mauer [3] highlighted the principles of FTIR spectroscopic analysis of bacteria; the advantages and disadvantages of FT- IR applied to bacterial analysis; various sampling techniques; spectral manipulation; statistical analysis of spectra; and applications in pathogen detection.

Jana kopikova et al [4] used FT-IR spectroscopy for the estimation of isolated high molecule fractions and also for the identification of food hydrocolloids in confectionery jellies and food supplements. The simple comparison of spectra of standards and samples proved that this technique is useful for the monitoring of food hydrocolloids in particular food products.

SyedIsmail Ahmadetal[5]estimated concentration of glucosein human urine. They reported specific

bandat1034 $cm^{-1}$for glucose and established a relation between glucose-concentration in urine and Transmission(%)of IR band.

Vijaya Ushasree and Adeel Ahmad[6] reported IR spectroscopic data on human blood and its constituents. IR analysis was made on whole blood, plasma and serum. The characteristic spectral bands pertaining to fibrinogen, hemoglobin, erythrocytemembranelipids and other plasma proteins were identified. They explored the possibility of disease analysis by IR spectroscopy.

Vijaya Ushasree and Adeel Ahmad[7] presented IR spectroscopic data on human blood of groups A,B, AB and O. IR analysis was made on 90% packed erythrocytes. The characteristic spectral bands pertaining to anti genswere discussed. They suggested the possibility of identification of blood antigens spectroscopically.

VijayaUshasree and Adeel Ahmad[8] reported IR spectroscopic data on blood of patients suffering from *Diabetes mellitus*. IR analysis was made on whole blood, plasma and serum. The characteristic spectral bands pertaining toglucose in the medium of blood were identified.

Vijaya Ushasree and Adeel Ahmad [9] made quantification of glucose in human blood seruminmidI Rregion4000-400cm^{-1}using FTIR Spectroscopy. The FT-IR spectraconfirmed the specific peak for glucose. A graph between concentration of glucose and intensity of absorption showeda linear relation. There was an increase in the intensity of absorption.

The present study is an attempt to quantitate glucose in human blood serum by using FTIR spectroscopy.

2. MATERIALS AND METHODS:

The blood samples were collected from healthy donors without adding anticoagulant and serum was separated by removing blood clot. The serum was treated with research grade (SD Fine Chem) glucose at the concentrations of 100,200,300,400 and 500 gm/dL. Infrared spectrum was recorded in FTIR spectrophotometer (ShimadzuFTIR - 8400S) in the range of 4000 cm^{-1} to 400 cm^{-1}. The resolution was kept at 4 cm^{-1} and scanning time was fixed at38 Sec. A total number of 10 scans were carried out on each sample.

3. RESULTS ANDDISCUSSION:

Fig.1. shows FTIR spectra of human blood serum treated with Urea of concentrations 100, 200, 300, 400, 500 mg/dl. Spectra show a series of bands, in the range of 4000 cm^{-1} and 400 cm^{-1}, related to functional groups of proteins, lipids and carbohydrates and other inorganic materials present in the blood serum. Characteristic band for Urea can be seen approximately at 1085 cm^{-1}.

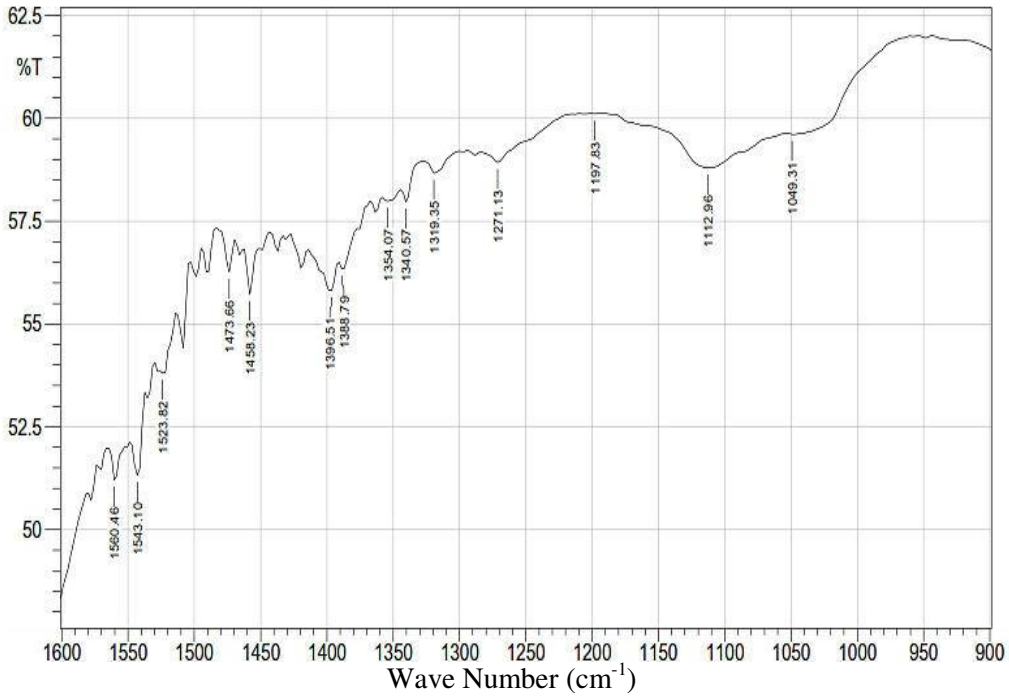

Fig.1.(a). FTIR spectrum of human blood serum treated with Urea of concentration 100 mg/dl

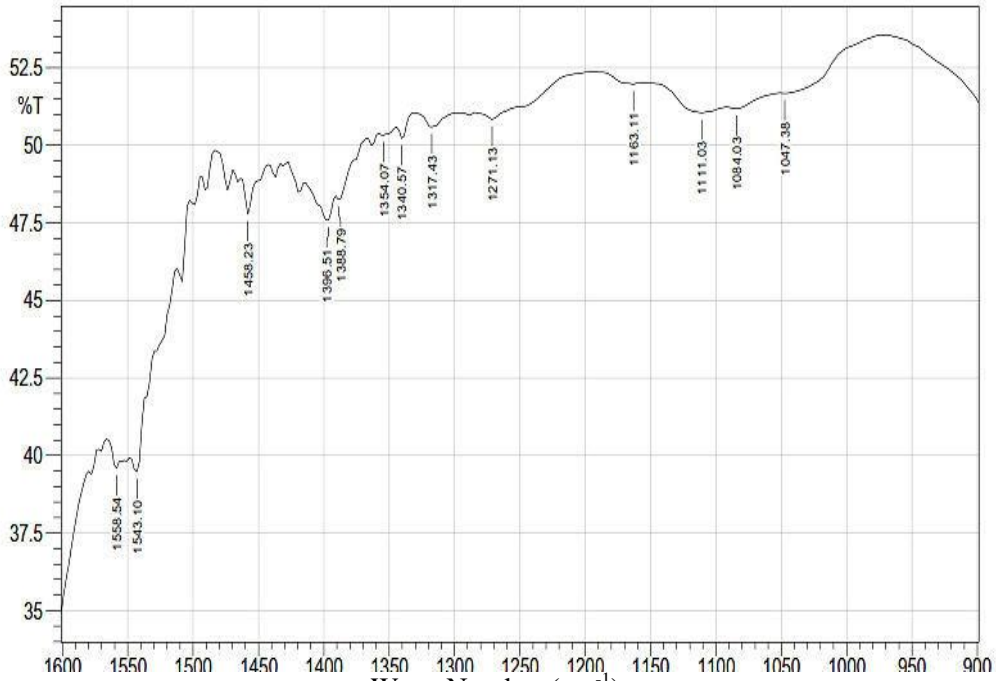

Fig. 1(b). FTIR spectrum of human blood serum treated withUrea of concentration 200 mg/dl

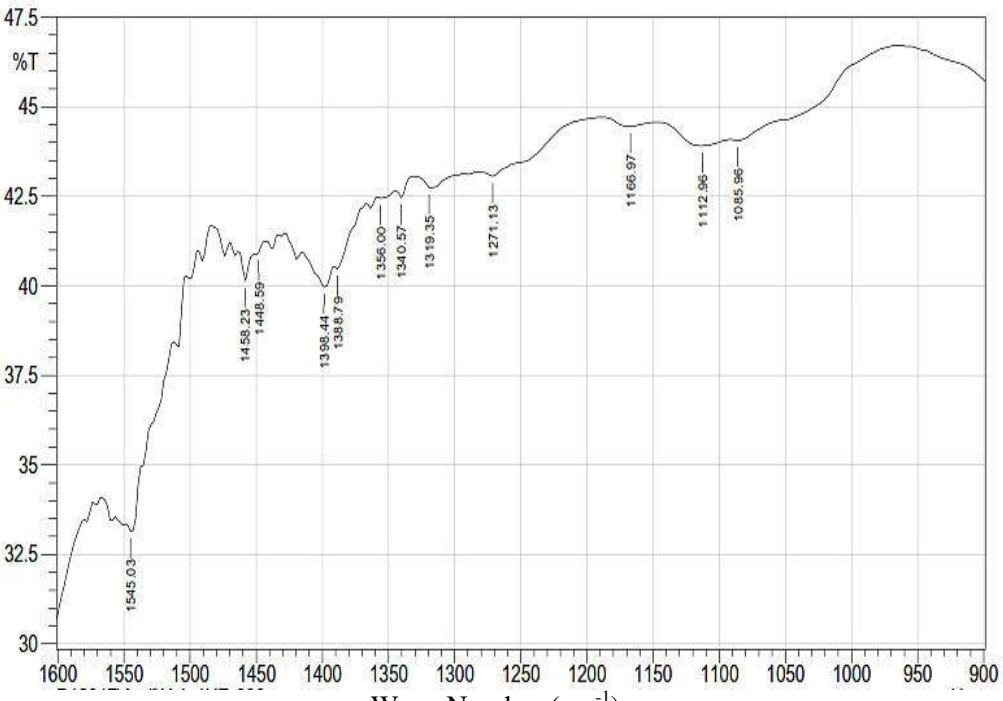

Fig. 1(c). FTIR spectrum of human blood serum treated with Urea of concentration 300 mg/dl

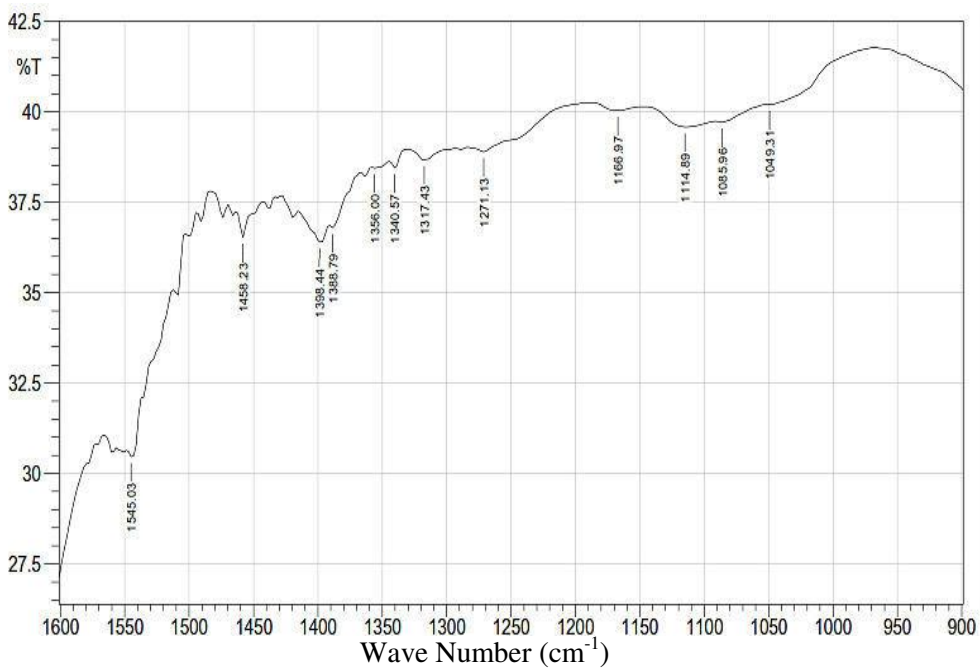

Fig. 1(d). FTIR spectrum of human blood serum treated withUrea of concentration 400 mg/dl

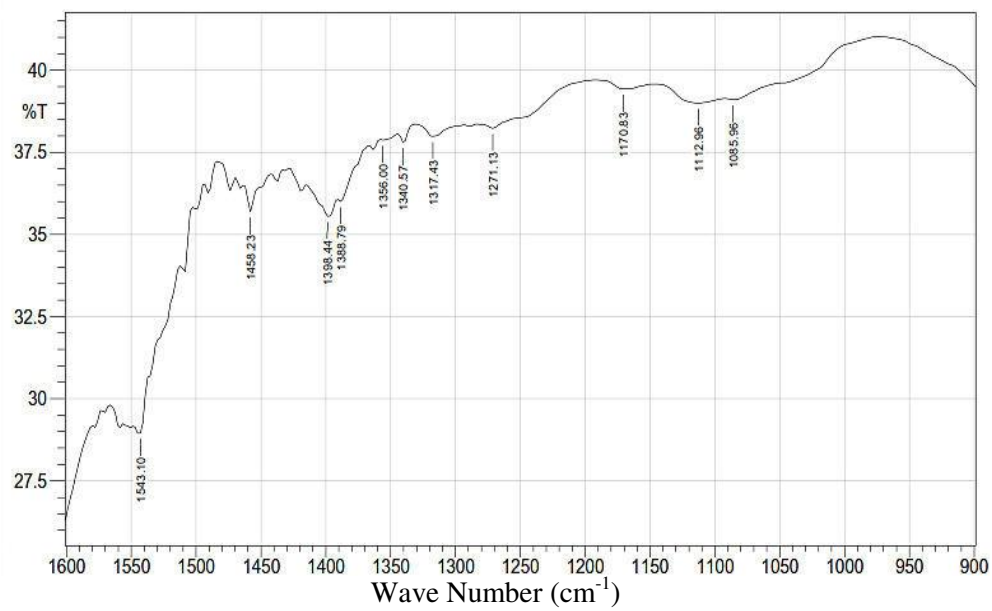

Fig.1(e). FTIR spectrum of human blood serum treated with Urea of concentration 500 mg/dl

Table1 gives FTIR data obtained from Fig1. at1085 cm^{-1}. The table reveals IR absorbance, calculated from transmittance (%), in blood serum treated with Urea of concentration ranging from 100 to 500 mg/dl with an interval of 100 mg/dl. A plot is drawn between Absorbance on Y – axis and glucose concentration (gm/dl) on X – axis (Fig.2.). It is a straight line with +ve slope and also +veY – intercept, the linear regression equation of which is A = 0.0004 X + 0.2134, where A is absorbance and X is glucose concentration, and $R^2 = 0.95$.

Table 1 – Absorbance of IR bands of human blood serum treated withUrea of differentconcentrations(gm/dl)

Concentration of Urea (mg/dl)	Absorbance
100	0.25
200	0.29
300	0.36
400	0.40
500	0.41

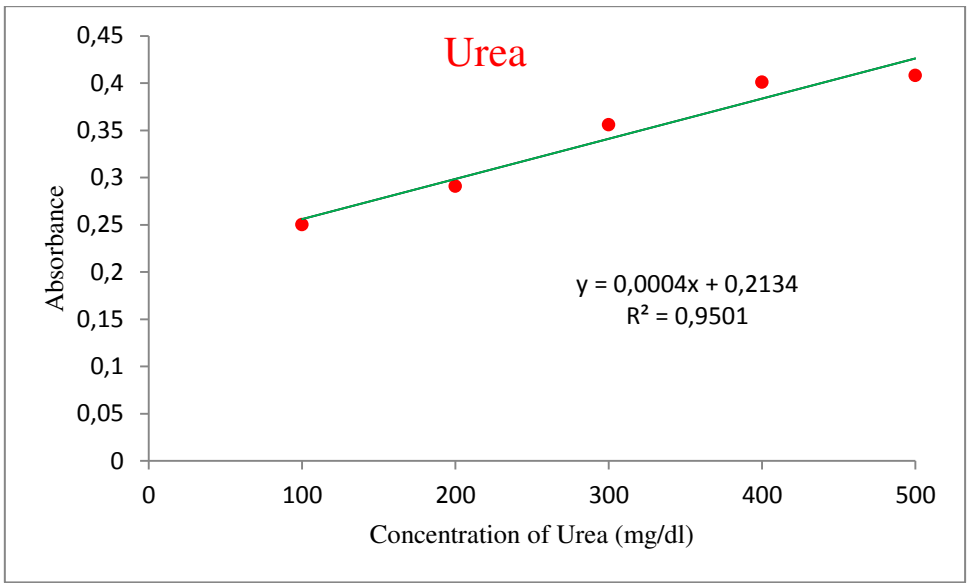

Fig 2.A Plot between Absorbance and concentration of Urea added to blood serum

The study concludes that FT-IR spectrum is a finger print of molecular constituent of the sample. Theabsorbance positions of bandat wave numbers reveal the qualitative characteristics of chemical bonds and structure of the molecule, while the intensities of absorption provide quantitative information of the sample. The present studysuggests that the most specific band for Urea is around at1082cm^{-1} in human blood serum. The quantitation of urea in blood serum IR spectroscopically is very much useful for its estimation in blood of patients suffering from diabetes and kidney diseases.

REFERENCES:

1. R G Zhdanov, V M Andrianov, M K Marchewka, Fourier transform IR and Raman spectroscopy and structure of carbohydrates, J. Mol. Stru.,Vol. 436(1997), pp. 637-654.
2. Minesh M. Patel, John D. Smart, Thomas G. Nevell, Richard J. Wen, Peter J. Eaton, and John Tsibouklis, Mucin/Poly acrylic acid Interactions: A Spectroscopic Investigation of Mucoadhesion, Bio macromolecules, Vol.4(2003), pp. 1184-1190.
3. R Davis and L J Mauer, Fourier transform infrared (FT-IR) spectroscopy: A rapid tool for detection and analysis of foodborne pathogenic bacteria, Curre research, technology and education topics in applied microbiology and Microbial biotechnology, (ed.) A. Mendez Vilas, Formatex, 2010.
4. A Jana copikova, Andriy Synytsya, Marcela Cerna, Jitka Kaasova and Miroslava Novotna, Application of FTIR spectroscopy in detection offood hydro-colloids in confectionery jellies and food supplements, Czech. J. Food. Sci., Vol. 19, No. 2(2001), pp. 51- 56.
5. Syed Ismail Ahmad, PRavi Prasad and Adeel Ahmad, Quantitation of glucoseinurine by Fourier Transform Infrared Spectroscopy, J. Pure &Appl.Phys.,Vol.22,No.4(2010), pp.645–649.
6. U.Vijaya Ushasree, Kaleem Ahmed Jaleeli and Adeel Ahmad, A study on infrared spectroscopy of human blood, Int.J.Sci.,Env.Tech.,Vol.5, No 3(2016),pp. 1189– 1192.
7. U.Vijaya Ushasree and Adeel Ahmad, FTIR spectroscopic analysis on human blood groups, Int.J.Sci.Env.Tech.,Vol.6, No 3(2017),pp. 1685 – 1689.
8. U Vijaya Ushasree and Adeel Ahmad, A study on infrared spectroscopy of human blood of patients suffering from Diabetes mellitus, Int.J. Innov.Sci.Res.,Vol. 6, No. 6(2017), pp. 1025 - 1027.
9. U. VijayaUshasree, and Adeel Ahmad, A FTIR Spectroscopic Study on Quantitation of Glucose in human Blood Serum, Int. J.Innov. Res. Sci. Engg. Tech., Vol. 6, No. 4(2017), pp. 6884 – 6890.

Second National Conference on
RECENT ADVANCES IN APPLIED NANO MATERIALS
February 16-17, 2018 at Department of Physics, University College of Science, Saifabad, Osmania University, Hyderabad, Telangana State, India.

Effect of Solvent on the Anodic oxide films formed on Zr-4 in 0.1MEDTA (Sodium salt): Scanned Electron Micrograph Studies.

V. JeevanaJyothi, B.Suchitha & [1]Ch. Anjaneyulu
Dept. of Chemistry, RBVRR Women's College, Narayanaguda,Hyderabad.
[1]Retd Professor, Department of Chemistry, Osmania University
Email: jeevana.j@rediffmail.com

Abstract: *Anodization of Zr-4 in 0.1M EDTA (Sodium salt)has been carried out. Kinetics of anodic oxidation of Zr-4 has been studied at a constant current density of 8mA.cm^{-2} and at room temperature. The plots of formation voltage vs. time, reciprocal capacitance vs. time and reciprocal capacitance vs. formation voltage were drawn. From these plots, formation rate, current efficiency and differential field were calculated. The Addition of Solvent (Ethylene glycol) showed better kinetic results. For 20%, 40%, 60% and 80% aquo-glycolic media, the dielectric constant values are low leading to the marked improvement in the kinetics. The surface morphology of the anodic films was also studied by Scanning Electron Micrographs (SEM).*

Key Words: *Anodization, formation rate, current efficiency, differential field, Zr-4,EDTA (Sodium salt).*

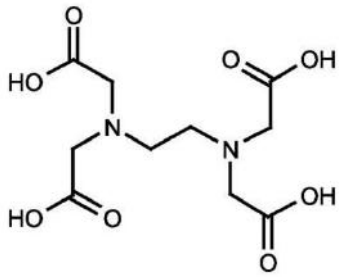

EDTA

1. INTRODUCTION:

Zirconium based alloys are used as structural material in the water cooled thermal reactors [1, 2]. Zr-4, due to their low cross-section for thermal neutrons and because of their relatively good corrosion resistance against water and steam, used in water cooled reactors. Zirconium & its alloys are of primary importance in nuclear technology. Anodization of Zirconium alloys have been studied in some electrolytes [3-6]

In the present work, the kinetics of anodic oxidation of Zr-4 in aqueous solutions of 0.1M EDTA (Sodium salt) and aquo-glycolic media in various proportions (v/v) of water-ethylene glycol mixtures ranging from 0% to 80% ethylene glycol are studied. Scanning Electron Microscopic studies was also carried out to observe the changes in the surface morphology of the anodic films formed.

2. EXPERIMENTAL:

Zr-4 was of 98% nominal purity, supplied in the form of annealed rolled sheet with 0.2mm thickness, supplied by Nuclear Fuel complex, Hyderabad as gift samples.A typical composition of Zr-4 is 0.07wt.% chromium; 0.23 wt.% iron; 1.44 wt.% tin and balance is zirconium.

In the present work, the foil samples used were cut with the aid of a punch into flag-shaped specimens of 1cm^2 working area on both sides and 2cm long tag. The chemical polishing mixture consisted of acids such as HNO_3, H_2O&HF in a definite volume ratio of 3:3:1.

For anodizing, a closed shell of 200ml capacity was used. The cathode used was a platinum foil of 20cm^2 superficial area to make double layer capacitance as large as possible. Electrolytes used were 0.1M EDTA (Sodium salt) in 20%, 40%, 60% and 80% aquo-glycolic mixtures, the solvent being ethylene-glycol.

All the experiments were carried out at a constant current density of 8mA.cm^{-2}. The experimental procedure for the anodization is given elsewhere [7]. The kinetic results calculated are formation rate in Vs^{-1}, current efficiency (ɳ) % and differential fields of formation (F_D) in MV cm^{-1} from the conventional plots V vs. t , 1/C vs. t and 1/C vs. V.

The surface morphology of the anodic film was examined using Scanning Electron Microscope (SEM). The SEM's were taken at IICT-CSIR, Hyderabad.

The surface was thoroughly rinsed with distilled water and dried under infrared lamp and cleaned gently with fine tissue paper. The surface was coated with gold, palladium conducting material using evaporation technique and signal processed secondary electron images were taken from scanning electron microscope model SEM Hitachi- S520 at 10 KV, Hitachi instruments made in Japan (Oxford link ISIS- 300 UK)

3. RESULTS & DISCUSSIONS:

Anodization of Zr-4 was done in 0.1M EDTA (Sodium salt). The formation rate, current efficiency and differential field were calculated. The effect of solvent on Zr-4was studied in 0.1M EDTA (Sodium salt) to check whether there was enhancement in kinetics of film formation[8,9].

4. EFFECT OF SOLVENT:

Anodization of Zr-4 in 0.1M EDTA (Sodium salt) was performed by mixing various proportions of ethylene glycol to the aqueous solution (20%, 40%, 60% and 80%). There was an improvement in the kinetics as given in Table-1. The relevant plots are shown in Figures-1 & 2. Aquo-organic solutions aid in the formation of good oxide films and act as better electrolytic capacitors [10]. These facts support the current results obtained in aquo-organic mixtures of 0.1M EDTA (Sodium salt). It can be explained on the basis of decrease in the dielectric constant of the medium (Table-2)

In solutions of low dielectric constant there is less chance of ion-dipole interactions (solvent-ion interactions) which do not interfere in the oxide film formation. However, the ions in the high dielectric constant solutions interact with oxide ions responsible for oxide film formation due to high solvation with water molecules. In such solutions, the kinetics are poor.

The kinetics are better in low dielectric constant solutions for 20%, 40%, 60% and 80% aquo-glycolic media, the dielectric constant values are low leading to a marked improvement in the kinetics.

5. SCANNING ELECTRON MICROGRAPHS:

Figure -3 and Figure - 4 are the Scanning Electron Micrographs of anodic films formed on Zr-4 in aqueous and aquo-glycolic solutions of 0.1M EDTA (Sodium salt)upto 200V.

Figure 1: Plot of formation voltage as a function of time in aquo-glycolic solution

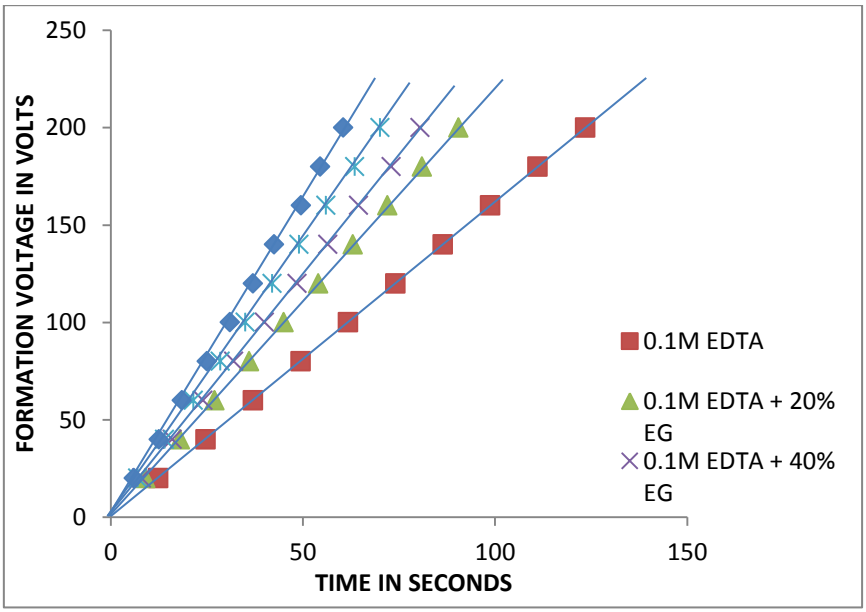

Figure 2: Plot of reciprocal capacitance as a function of time in aquo-glycolic solution.

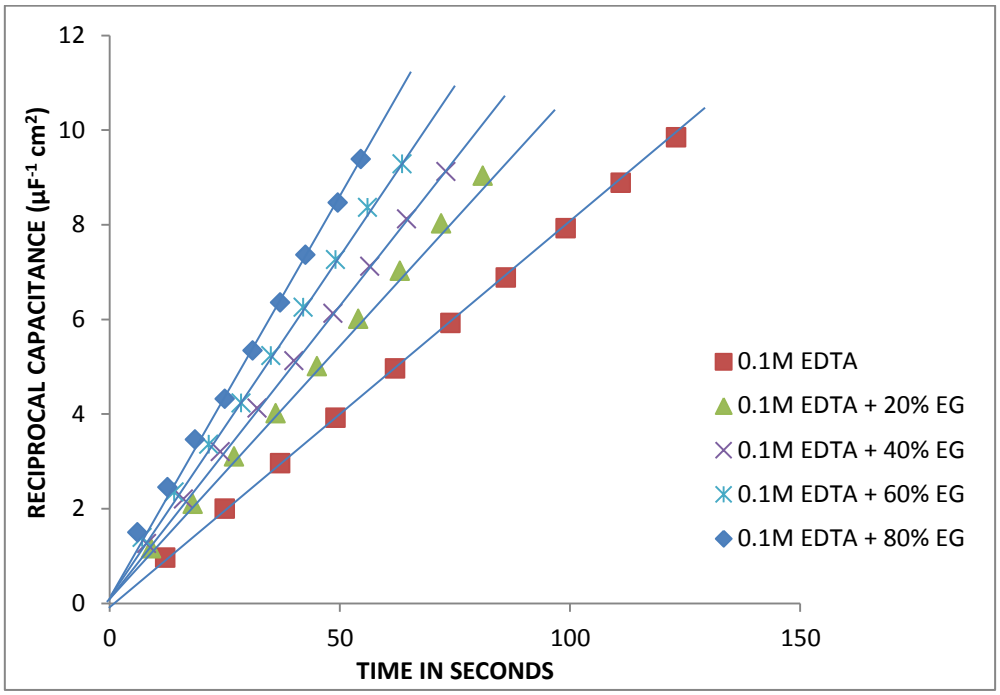

Table- 1
Anodic films formed on Zircaloy-4 in 0.1M Ethylene Diammine Tetra Acetic Acid (sodium salt) both aqueous and aquo-glycolic media.

Electrolyte	Formation Rate, dV/dt ($V.s^{-1}$)	Current efficiency, η (%)	Differential field,F_D ($MV.cm^{-1}$)
0.1M EDTA	1.62	78.1	4.650
0.1M EDTA+ 20% EG	1.70	82.5	4.594
0.1M EDTA+ 40% EG	1.76	85.4	4.549
0.1M EDTA+ 60% EG	1.80	89.0	4.513
0.1M EDTA+ 80% EG	1.88	93.5	4.485

EDTA-Ethylene Diamine Tetra Acetic acid EG-Ethylene glycol

Table 2: Variation of dielectric constant as a function of solution composition

EG , %	0	20	40	60	80	100
Dielectric constant	80.0	72.8	69.2	57.8	43.2	37.7

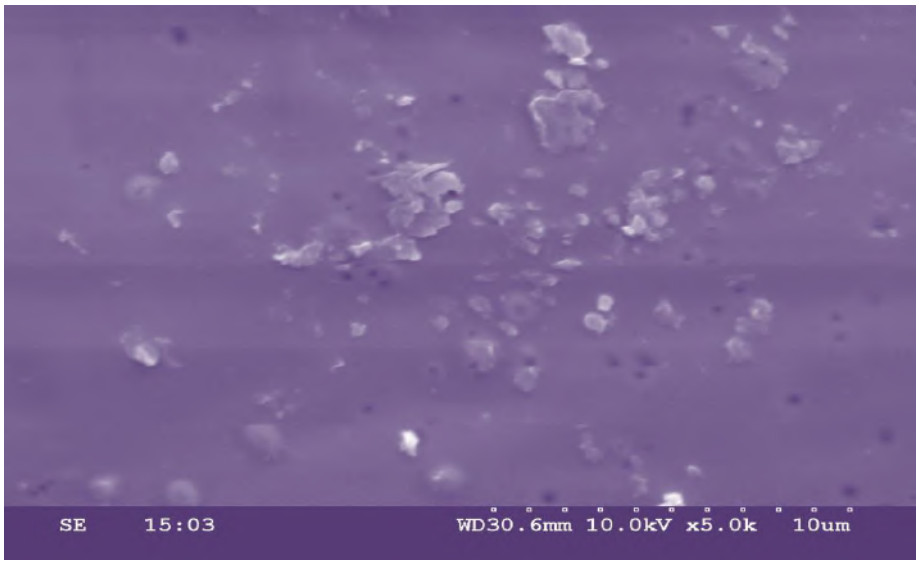

Figure 3: SEM of the film formed upto 220V in 0.1M EDTA (Sodium salt) (aqueous medium) at room temperature (Magnification of the micrograph is X 5000)

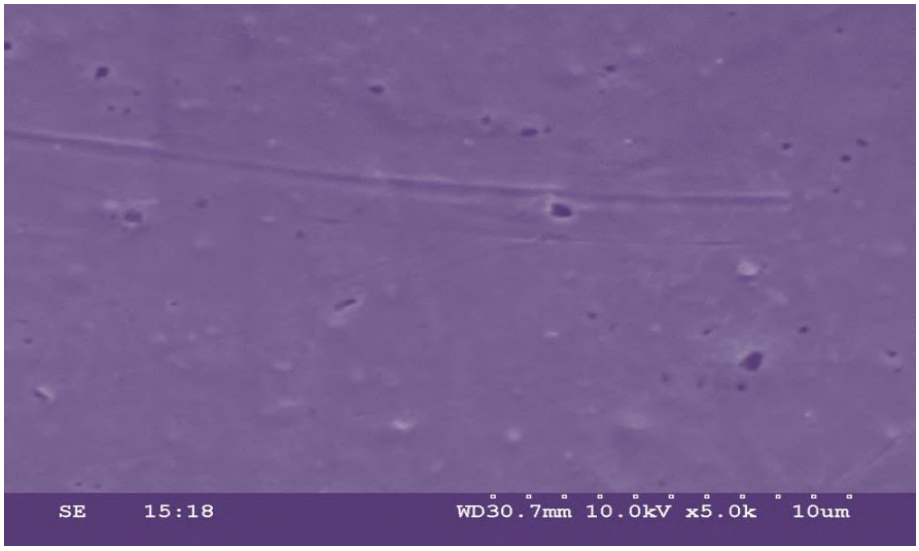

Figure 4: SEM of the film formed upto 220V in 0.1M EDTA (Sodium salt) (glycolic medium) at room temperature (Magnification of the micrograph is X 5000)

When compared, the roughness and non-uniformity of the surface are decreased when electrolytic medium is changed from aqueous to aquo-glycolic medium (fig-4) is observed to be smoother than the film formed in aqueous medium.

Vermilyea studied the formation of anodic films on tantalum in aqueous [11] and non-aqueous [12] solutions. He suggested that the composition of film depends on the solution in which it is formed.

Seregina et al [13] studied the anodization of aluminium alloys in the solution of sulpho-salicylic acid (90g/cc) and found that thick films are possible during anodization at room temperature. Nageshwarrao et al [14] observed a change in the dielectric constant of oxide films by changing the medium from aqueous to glycolic

Aparna [15] also observed the same trend of increasing kinetic results with increase in glycol content in 0.1M Picolinic acid and sodium methoxide for Zr-2 and Ti. Vermilyea[12] reported that the optical thickness was smaller in the non-aqueous solutions, and the increase in weight for a given charge passed could be as much as twice that expected.

Moshashi Koyama [16] carried out anodization of titanium in non-aqueous media and confirmed that the oxide film consists of double layers and suitable for electrolytic capacitors. Wei Wei et al [17] reported the growth of layers by anodization of tantalum in a non-aqueous electrolyte consisting of an optimized glycerol/ethylene glycol mixture with the addition of NH_4F

Schmidt et al [18] observed that the layers of TiO_2 obtained in non-aqueous electrolytes are much adherent and uniform than those realized in aqueous media. ClimentMontoliu et al[19] studied the anodization of titanium in

acid, alkali and neutral baths (aqueous and aquo-glycolic) and suggested from the structure and dielectric properties, that the anodic coatings formed in non-aqueous media acts as better dielectric capacitors.

Panasa Reddy et al[20] and Lavanya et al [21] also studied in trisodium citrate,0.1M KOH(aquo-glycolic) respectively and found that the breakdown voltage was higher when anodized in ethylene glycol medium. This was also supported by other workers [22]. Shukla [23] carried out the study of effect of aquo-glycolic media on Anodization of zircaloy-4 in 0.1M sulphamic acid and found that the addition of solvent improved the kinetic results.

6. CONCLUSIONS:

By changing the solvent medium from aqueous to glycolic, the kinetics of film formation on Zr-4 in 0.1M EDTA (Sodium salt) have been studied and it is observed that the peak voltage, formation rate, current efficiency are increased but differential field of formation decreased with the glycol content of solution. This can be attributed to the decrease in the dielectric constant of the solution with the increase in glycol content of the solution.

Applications of Anodic Oxide Films:

- Capacitors
- Diodes
- Semiconductors
- Resistors
- Photo chemical devices
- As a base for selective electroplating, painting & decorative purposes
- Nuclear technology (nuclear fuel storage & water cooled nuclear reactors)
- Electrolytic condensers
- Insulators
- Good corrosion resistant

7. ACKNOWLEDGEMENTS:

The authors are thankful to Nuclear Fuel Complex, Hyderabad for generous help in providing Zr-4 samples and IICT, Hyderabad for SEM images.

REFERENCES:

1. Williams C D, *Atomic energy of Canada Limited Report*, AECL 1969; 3456.
2. Williams C D, *Reactor technol.,* 1970; **13**,147.
3. Shobha Rani P, AnjaneyuluCh and Sastry K S, *J. Electrochemical Soc India*, 2000; 49,**3**,129
4. Lavanya A and AnjaneyuluCh, *Bull. Electrochem.,* 2004; 20 **4**, 153
5. Lavanya A, Raghunath G and AnjaneyuluCh, *Bull. Electrochem.,* 2004; 20, **7**, 305
6. Ashok Kumar V, Raghunath G and AnjaneyuluCh, *Bull. Electrochem.,* 2005; 21,**1**,17
7. Lavanya A and AnjaneyuluCh, *Bull. Electrochem.,* 2002; **18**, 317
8. Arifuku F, Iwakura C, Yoneyama H and Tamura H, Denki Kagaski, 1978; **46**,19
9. Randal J J, *ElectrochimActa,* 1975; **20**,663
10. Lavanya A, Sarma C S N and AnjaneyuluCh, *J ElectrochemSoc India*, 2001; **50**,164
11. D.A.Vermilyea, *Acta Met.,*1953; **1**,282
12. D.A.Vermilyea, *Acta Met.,* 1954; **2**,482
13. I.E.Seregina, B.Kopara and A.V.Thimoshenko, Deposited Doc. *(Avail SPSTl),* 1982; **10**
14. B.NageshwarRao.V.VenkataRamana&Ch.Anjaneyulu, *J.Electrochem.Soc.India*, 1996; **45**, 27
15. N.N.S.Aparna, Ph.D.Thesis, O.U ,2009.
16. Mashashi Koyama, RikagakuKemyushoHokoku, 1962; **38**, 321,546.
17. Wei Wei, Jan M.Macak, Nabeen, K.Shreshta& Patrick Schmuki, *J.Electrochem.Soc.,* 2009;**156**, K104-K109.
18. HK Schmidt, R.Capellodes&M.I.Vidal, M.T Vida, Lab. Invest. Components, Electron.S.A, *Fr. Rev. Tech. Thomson C.S.F*., 1982; **14**, 657 (FR)
19. F.ClimentMontaliu, R.FartCapellodes&M.I.Vidal, *Plennels An. Quim. Ser.B.,* 1983; **79**, 290
20. A.Panasa Reddy, Ch.Anjaneyulu&K.S.Sastry,*J.Electrochem.Soc.India*., 1990; **39**,183.
21. A.Lavanya, C.S.N.Sarma&Ch.Anjaneyulu, *J.Electrochem.Soc.India*, 2001; **50**,164.
22. A.Panasa Reddy, A.N.Chary, Ch.Anjaneyulu&K.S.Sastry, *J.Electrochem.Soc India.,* 1984; **33,** 229
23. V D Shukla and AnjaneyuluCh, *E-Journal of Chemsistry,* 2011; 8, **1**, 71-76.

Second National Conference on
RECENT ADVANCES IN APPLIED NANO MATERIALS
February 16-17, 2018at Department of Physics, University College of Science, Saifabad, Osmania University, Hyderabad, Telangana State, India.

Physical, Optical absorption & FTIR studies of Na_2O-Al_2O_3-B_2O_3-CuO glasses

B. Ashok , B.Srinivas, Abdul Hammed, M. Narasimha Chary and Md. Shareefuddin.
Department of Physics, Osmania University, Hyderabad-500007, Telangana State.
Corresponding author:ashok.bollam77@gmail.com

Abstract: *This paper reports on different physical, optical and FTIR properties of Cu^{2+} doped bismuth borate glasses.. The glasses containing (30-x)Na_2O-xAl_2O_3-69B_2O_3-1CuO (where x = 0, 5,10 and 15 mol%) have been prepared by melt-quenching method. The physical parameters like density, molar volume, oxygen-packing density, ionic concentration, inter ionic distance, Polaron radius were calculated. Optical absorption spectra of these glasses were recorded in the UV-region using the Shimadzu UV-1800 Spectrometer in the wavelength range350-1100nm. The optical band gap values are determined from Tau'c plots. By using the measured values of the density and optical band gap, the refractive index, dielectric constant, reflection loss, molar refractivity, electronic polarizability and optical basicity were calculated. Results obtained from Fourier transform infrared (FTIR) spectra indicated that sodium plays an important role in converting three coordinated boron atoms [BO3] to four coordinated boron atoms [BO4].*

Key Words: *Physical, Optical, FTIR, Glasses.*

1. INTRODUCTION:

In recent years glasses doped with transition metal ions haveattracted a great deal of attention because of their significant applications in the field of new tunable solid-state lasers, solarenergy converters and fiber-optic communication device [1]. $B_2O_3$is often used as dielectric and insulating material and it exhibit the optical isotropy [2,3]. The oxide glasseswere studied by various authors using EPR, optical, physical and FTIR techniques [5,6]. The addition of alkali oxides such as Li_2O, K_2O, and Na_2O improve theirphysical properties and preparation conditions. Generally Na_2O being a network modifier as it modify the borate network by forming either BO_4 units or non-bridging oxygen ions (NBOs) [7].To improve the physical properties,to increase the glass strength and to decrease the crystallization tendency$Al_2O_3$is added to the glass network [6].Al_2O_3enter into the glass network forming $AlO_4$and AlO_6 structural units, these units are crosslink with the neighboring borate chains.

2. EXPERIMENTAL:

In the present investigation glass samples with general formula (30-x) Na_2O-xAl_2O_3-69B_2O_3-1CuO (with x=0, 5, 10 &15mol%) were prepared by conventional melt-quenching method. For the preparation of glass samples, analar grade chemicals of EMERAK make H_3BO_3, Al_2O_3, Na_2O and CuO were used.The appropriate mole concentrations were weighed in monopan digital balance and finely grounded. These compositions were taken in porcelain crucible and were placed in an electrically heated carbide rod furnace maintained around 1100 ^{0}C. These mixtures took nearly 60minutes to melt congruently. Further these molten mixtures were stirred to achieve homogeneity. These melts were quenched by pouring the melt on pre heated (maintained at 200 ^{0}C) stainless steel plate and pressing with another stainless steel plate. These glasses were annealed at 200 ^{0}C for 24hours to relieve the stresses. The composition of the glass samples prepared are given in Table 1. Optical absorption spectra were recorded using the shimadzu*UV-1800* Spectrophotometer in the wavelength region 350-1100nm. The uncertainty in the measurement was ±1 nm.

3. RESULTS AND DISCUSSIONS

3.1 Physical Parameters:

The density (ρ) of each glass sample was estimated from Archimedes principle using the relation

$$\rho = \frac{Wa}{Wa - Wb} * \rho_b$$

Where ρ_b -density of reference liquid Xylene (=0.865g/cc) while W_a and W_b are the weights of the glass sample in air and Xylene respectively. Using the density values molar volume Vm was calculated using this formula

$$V_m = \frac{M_t}{\rho}$$

From the calculated values of both density (*d*) and molar volume other related physical parameters, such as oxygen packing density (OPD), copper ionconcentration (*N*), interionic distance (r_i), polaron radius (r_P) of the glasses have been computed byusing the relevant expressions available in literature [8].The estimated physical properties of these glasses are given inTable 1.

Table 1:Composition, density (ρ), molar volume (V_M), Oxygen packing density (OPD), copper ion concentration (N_i), Polaron radius(R_p), Inter ionic distance (R_i) of NABC glasses

COMPOSITION	*Density (g/cc)*	V_m (cc/mol)	*OPD* (g.atm/l)	N_i (10^{20}/cc)	*Polaron radius* (10^7 cm)	*Interoinc distance* (10^8cm)
$30Na_2O$-$0Al_2O_3$-$69B_2O_3$-1CuO (NABC-1)	*2.45*	*48.03*	*51.63*	*3.07*	*1.73*	*7.00*
$25Na_2O$-$5Al_2O_3$-$69B_2O_3$-1CuO(NABC-2)	*2.67*	*43.98*	*58.67*	*3.66*	*1.64*	*6.61*
$20Na_2O$-$10Al_2O_3$-$69B_2O_3$-1CuO(NABC-3)	*2.55*	*46.03*	*58.22*	*3.33*	*1.69*	*6.82*
$15Na_2O$-$15Al_2O_3$-$69B_2O_3$-1CuO(NABC-4)	*2.41*	*48.93*	*48.64*	*2.96*	*1.75*	*7.08*

The density (*ρ*) of the present glasses is decreasing from 2.67g/cc to 2.40g/cc with increasing Al_2O_3 mol% from 5 to 15 mol%.The density of Al_2O_3 free glass is found to be 2.45g/cc. The molar volume values are increasing on increasing Al_2O_3mol% from 5 to 15 mol%. The density of Al_2O_3 (3.95g/cc) is greater than the density of Na_2O (2.27). On increasing $Al_2O_3$from 5 mol% to 15 mol% one expects density should increase but on contrary density is decreasing. The decrease density maybe due to the formation of AlO_4 and AlO_6units at the expense of BO_3 and BO_4 units. The bond length of Al-O bond is comparatively larger than B-O bond length. due to this molar volume is increasing and density is decreasing [6]. Hence it is concluded that the density is decreasing while the molar volume is increasing nonlinearly with increasing Al_2O_3 content except the Al_2O_3 absent glasses. The density and molar volume are showing opposite behavior to each other.

3.2. OPTICAL BAND GAP ENERGY (E_{OPT}) AND URBACH ENERGY (ΔE)

The study of the fundamental absorption edge in the UV-region is a useful method for the investigation of optical transitions and electronic band structure in crystalline and amorphous materials. There are two types of optical transitions that can occur at the fundamental absorption edge of crystalline and amorphous. They are direct and indirect transitions. In both the cases, electromagnetic waves interact with the electrons in the valence band, which are raised across the fundamental gap to the conduction band. Davis and Mott gave the following forms of absorption co-efficient α as a function of photon energy for indirect transitions.

$$\alpha(\upsilon) = B(h\upsilon - E_{opt})^2/h\upsilon$$

Where E_{opt} is indirect optical band gap and B is a constant for indirect transitions, Using the above equation, by plotting $(\alpha h\upsilon)^{1/2}$as a function of photon energy $h\upsilon$,one can find the optical energy band gap (E_{opt}) for indirect transitions.

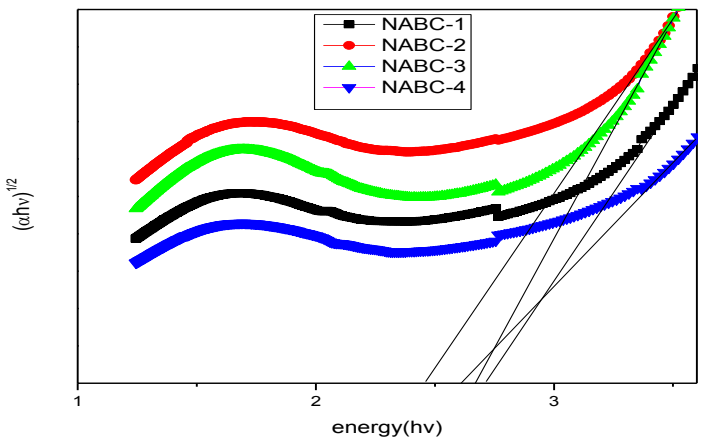

Figure 1. Tauc's plots of NABC glasses

The Urbach energy gives the width of the tails of localized states within the optical band gap. At the absorption edge, random internal electric fields will dominate the broadening of the exciton levels due to the lack of long-range order or presence of defects. The main feature of the absorption edge of an amorphous semiconductors is an exponential increase of the absorption coefficient (α) with photon energy ($h\upsilon$) in accordance with an empirical relation given by

$\alpha=\alpha_0 \exp(h\upsilon/\Delta E)$

here 'α_0' is a constant, 'ΔE' is the Urbach energy which indicates the width of the band tails of the localized states and 'υ' is the frequency of radiation. Urbach energy is a measure of disorder in the amorphous and crystalline solids. The ΔE values are evaluated from the Urbach's plots of ln(α) versus($h\upsilon$) by taking the reciprocal of the slopes of the linear portion of the curves. Optical band gap and Urbach energy values are given in **Table 2**, and it is observed that these values are varying non-linearly with increase of Al_2O_3.

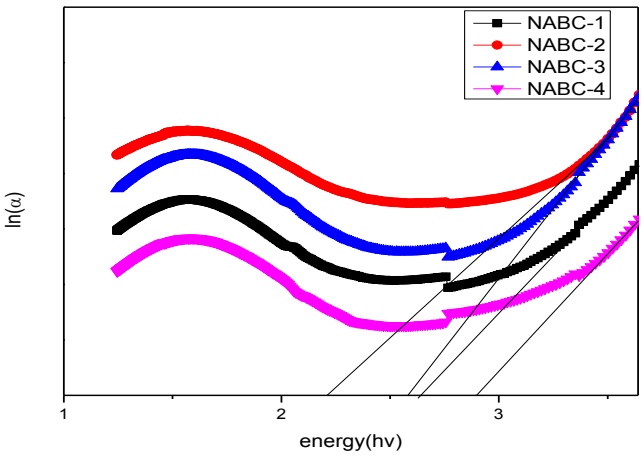

Figure 2.Urbach energy plots of NABC glasses

Table 2:Energy gap (E_{opt}), Urbach Energy(ΔE), Refractive Index (n), dielectric constant (n^2), Reflection loss and molar refractivity (R_m) of NABC glasses

COMPOSITION	E (eV)	ΔE(eV)	n	n^2	R	R_m (cm^{-3})
NABC-1	2.45	0.55	6.03	36.33	0.51	44.27
NABC-2	2.66	0.39	5.89	34.79	0.50	40.39
NABC-3	2.71	0.49	5.87	34.45	0.50	42.24
NABC-4	2.60	0.47	5.93	35.21	0.51	44.98

3.3. FTIR SPECTROSCOPY

The Fourier transform infrared (FTIR) spectroscopy is the most useful technique to identify the functional groups and to know the molecular structure.

Table 3 :FTIR peak positions and their assignments

NABC-1	NABC-2	NABC-3	NABC-4	Bond assignment
463	447	475	464	AlO_4 Vibrations
702	699	701	703	stretching vibrations of Al–O bond in AlO_6 groups combined with B–O–B bending vibrations
820	827	816	-	
928	948	924	936	B-O bond stretching's in BO_4 units and Al-O in AlO_4
1064	1050	1070	1055	Stretching vibration of B-O-B in [BO4] tetrahedron
1188	-	1163	1198	
1352	1353	1359	1377	pyro borate groups containing BO_3^-
1637	1637	1636	1630	Diborate linkage, B-O-B networks

FTIR spectra of (30-x) Na_2O-xAl_2O_3-69 B_2O_3-1CuO recorded in the range 400 to 1600cm^{-1} which exhibited vibrational bands at around 460, 680, 850, 940, 1030, 1150 and 1400cm^{-1} The bands between 463-466cm^{-1} are attributed to AlO_4 vibrations [9, 10], A narrow absorption peak found around 700 cm^{-1} is assigned to the stretching vibrations of Al–O bond in AlO_6 groups combined with B–O–B bending vibrations in BO_3 units.

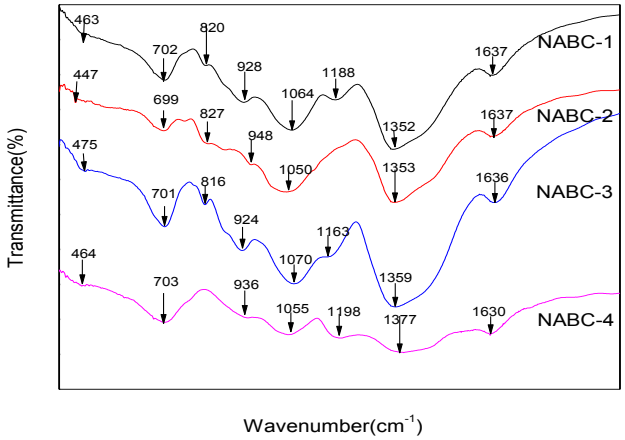

Figure 3. FTIR spectra of NABC glasses

B-O-B bond bending vibrations from penta borate group are assigned to the bands between 669-708cm^{-1}. The bands found between 816-827cm^{-1} are due to diborate linkage, B-O-B networks in the glass system while the bands from 930 to 945cm^{-1} are arised from B-O bond stretching's in BO_4 units and Al-O in AlO_4[11,12]. B-O stretching vibrations of BO_4 units from tri-, tetra-, penta borate groups are arised from the bands 1003-1053cm^{-1}, 1129-1193cm^{-1} are due to diborate groups and 1348-1439cm^{-1} are due to presence of pyro borate groups containing BO_3^-[13-14]. The broad absorption band at around 1630-1637$cm^{-1}$was occurred due to asymmetric stretching relaxation of B-O bonds of trigonal BO_3 units [11].

4. CONCLUSIONS

1. The density is decreasing while the molar volume is increasing nonlinearly with increasing Al_2O_3 content. The density and molar volume are showing opposite behavior to each other.
2. Optical band gap andUrbach energy values are varying non linearly with increase of Al_2O_3.
3. FTIR spectra of the present glasses exhibited vibrational bands at around 460, 680, 850, 940, 1030, 1150 and 1400cm^{-1}.These bands are assigned to AlO_4 vibrations, Al–O bond in AlO_6 groups combined with B–O–B bending vibrations in BO_3 units, B-O-B bond bending vibrations from penta borate group,todiborate linkage, B-O-B networks in the glass system, B-O bond stretching's in BO_4 units and Al-O in $AlO_4$and B-O stretching vibrations of BO_4 units asymmetric stretching relaxation of B-O bonds of trigonal BO_3 units.

REFERENCES

1. G. SivaRamaiah, J. LakshmanaRao, Journal of Alloys and Compounds 551 (2013) 399–404
2. P. Sandhya Rani, R. Singh, J. Mater. Sci. 45 (2010) 2868–2873.
3. S. Simon, D. Eniu, J. Mater. Sci. 42 (2007) 5949–5953
4. Yasser Saleh Mustafa Alajerami, SuhairulHashim, Wan Muhamad Saridan wan Hassan, Ahmad Termizi Ramli, J.Mol. Struct. 1026 (2012) 159–167
5. Abdul Hameed, Gokarakonda Ramadevudu, Siddey Laksmisrinivasa Rao, Mohmmad Shareefuddin1, Mudumba Narasimha Chary,*New Journal of Glass and Ceramics*, 2012, 2, 51-58
6. Mohamed Raheem Ahmed∗, K. Chandra Sekhar, Abdul Hameed, M. Narasimha Chary and MdShareefuddin, International Journal of Modern Physics B Vol. 32 (2018) 1850095
7. R.P. SreekanthChakradhar, B. Yasoda, J. LakshmanaRao, N.O. Gopal, Journal of Non-Crystalline Solids 352 (2006) 3864–3871
8. P. Abdul Azeem a,∗, S. Balaji a, R.R. Reddy, SpectrochimicaActa Part A 69 (2008) 183–188
9. Fatma H. ElBatal and Yousry M. Hamdy, Trans. Ind. Ceram. Soc., 67 (4) 193-202 (2008)
10. F. H. ElBatal, N. Nada, S. M. Desouki and M. M. I. Khalil, Indian J. Pure Appl. Phys., 42, 711-21 (2004)
11. Chandkiram Guatam, Avadhesh Kumar Yadhav, and Arbind Kumar Singh international scholarly Research Network, ISRN Ceramics 2012 Article ID 428497.
12. S. Rani, S. Sanghi, A. Agarwal, N. Kishore, Solid State Phenom. 161 (2010) 51-61.
13. Plyusnina, I.I., Infrakrasnye spektry mineralov (Infrared Spectra of Minerals), Moscow: Moscow State University, 1976.
14. Abdul Hameed, Md. Shareefuddin, S. Laksmi Srinivasa Rao, G. Ramadevudu and M. Narasimha Chary, Int. J. Sci. & Eng. Research, 5(3) (2014) 5-9.

Second National Conference on
RECENT ADVANCES IN APPLIED NANO MATERIALS
February 16-17, 2018 at Department of Physics, University College of Science, Saifabad, Osmania University, Hyderabad, Telangana State, India.

Antibacterial Studies Of Eco-Friendly Phytosynthesized Pva Capped Agnps Using *Passiflora Edulis*

Sandupatla Raju[1], Bolisetty Venkateswarlu[2], Dongamanti Ashok[3*]
[1]Research scholar, [2]Degree lecturer, [3]Assistant professor,
Green and Medicinal Chemistry Laboratory, Department of Chemistry, Osmania University, Hyderabad-500007, Telangana, India.
Email address: [1]rajusandupatla5@gmail.com, [2]venkateswarlu.bolisetty@gmail.com, [3]ashokdou@gmail.com,

Abstract: *The cutting-edge investigation reports about the evaluation of antibacterial studies of AgNPs (AgNPs) using an aqueous leaf extract of Passiflora edulis as reducing agent and polyvinyl alcohol (PVA) as a capping agent. This is simple, one pot, and rapid, eco-friendly, non-toxic and cost-effective method for the synthesis of AgNPs. Synthesis of AgNPs using plant extract has more advanced biological applications as they are the sources of the active compounds which were used in many medical remedies. So this active compound of phytochemicals from the Passiflora edulis plant extracts acts as a reducing agent for the synthesis of AgNPs. The synthesized PVA capped AgNPs were characterized by using diversify instrumental techniques such as UV-Vis spectroscopy reveals the formations of AgNPs as they depicting maximum absorption peak at 436 nm due to surface plasmon resonance. The Fourier transform infrared spectroscopic studies were conducted to know the phytochemicals responsible for the synthesis of AgNPs from the studies of the vibration bands of functional groups. The crystalline nature of the synthesized AgNPs had been studied by X-ray diffraction studies and the average particle size was found to be 24 nm calculated using Debye-Scherrer formula. The morphology of the AgNPs was studied by Scanning electron microscopy and the elemental signal profile carried out automatically with Energy dispersive spectroscopy, which coupled with SEM as it shows spherically shaped particles and the energy dispersive spectroscopy data showing a good atomic and weight content of stable silver. The characterized AgNPs afterward used for the antibacterial studies of the four harmful bacteria Escherichia coli, Bacillus subtilis, Pseudomonas putida, and Staphylococcus aureus, which exhibited high activity. The conducted studies constitute the premise for further investigations of the potential use of AgNPs as a chemotherapeutic.*

Key Words: *PVA capped AgNPs, Passiflora edulis, Scanning electron microscopy, X-ray diffraction, Antibacterial studies*

1. INTRODUCTION:

Currently, the nanoscience and nanotechnology become a broader area because of its increase of usage in the many fields. Nanoparticles possess advanced applications based on their particle size, distribution, capping agents, shape, and other morphological features. They are show difference in properties and applications while compared to their bulk state because they have a large volume to surface ratio as particle size decreases the volume to surface ratio was increasesd due to this fact, nanotechnology becomes the most emerging area in the present era. Nanoparticles can be synthesized various chemical and physical methods. Recently synthesis of nanoparticles using various parts of medicinal plant extracts owning different active compounds of phytochemicals have more advanced improvised properties in medicinal fields as this active compounds were combined with the metal nanomaterials. The metal nonoparticles having distinctive properties in many fields, particularly various applications of silver nanoparticles (AgNPs) includes sensing devices, information storage [1], recording media [2], biosensor design, catalysis [3], optoelectronics4, wound healing [5], pollution control [6], genetic disorders detection [7] and determination of ct-DNA [8].

The selected plant for the phytomediated PVA capped AgNPs was *Passiflora edulis* its common name was passion fruit belongs to the family *Passifloraceae*. It was cultivated commercially for its seedy sweet fruit. The plant has shallow-rooted, woody. The alternate, evergreen leaves with 3 lobes in the mature stage and finely toothed, 3 to 8

in the long, deep-green and glossy look above the leaf and dull beneath, The selected plant leaves were shown in **Figure 1.1.** A single, fragrant flower, 2 to 3 in width, is borne at each node on the new growth. The fruit yellow in color when ripe. The fruit was with a soft to firm, juicy interior filled with numerous seeds. The fruit is both eaten and juiced. The review reveals the presence of wide ranges of phytochemical constituents from the plant like flavonoids, tannins, phenol, glycosides, fatty acids, alkaloids. The leaves and fruit having high medicinal values like seed containing high amounts of piceatannol inhibits melanogenesis and promotes collagen synthesis [9] and possess anticancer properties [10]. The flavonoids from the leaf extract possess the antioxidative capacity [11]. The peptides from seed used against antifungal activity [12]. The plant has anti-inflammatory, anticonvulsant, antimicrobial, antihypertensive, anti-sedative properties, also it can be used in remedial measures for treating conditions like osteoarthritis, asthma and act as a colon cleanser. The different parts of the plants have also been used for the treatment of ulcers, hemorrhoids, as sedatives, a remedy for insomnia, digestive stimulant and a remedy for gastric carcinoma.

The current study reports about the phytomediated PVA capped AgNPs using *Passiflora edulis* aqueous leaf extract as reducing agent, silver nitrate as a precursor and polyvinyl alcohol (PVA) used as a capping agent. Then the phytomediated PVA capped AgNPs were characterized via using various instrumental techniques such as UV-visible spectroscopy (UV-Vis), Fourier transform infrared spectroscopy (FTIR), X-ray diffraction studies (XRD), scanning electron microscopy-energy dispersive spectroscopy (SEM-EDS). The main objectives of the study was to evaluate the antibacterial activity of the *Passiflora edulis* phytomediated PVA capped AgNPs against four human harmful bacteria.

2. MATERIALS AND METHODS:

2.1 Materials

Passiflora edulis plant leaves had been collected from locally from Hyderabad, India. Silver Nitrate ($AgNO_3$) was purchased from SD fine chemicals. The bacterial test strains were procured from IMTECH, Chandigarh. The media for the growth of bacterial strains was purchased from Himedia laboratories, Mumbai, India. Glassware used in the investigation was acid washed then rinsed with distilled water thoroughly. Deionized water used throughout the experiment.

2.2 Preparation of plant extract

The collected plant leaves were cleaned using running tap water followed by rinsing with the distilled water, then dried under shade for 10 days. After drying the plant leaves were ground to fine powder with mortar and pestle. The 5 gm of dried plant powder weighed and mixed with 1000 ml of distilled water and kept for stirring with the heating temp at 60°C for 1 hour. After stirring the plant extract solution filtered and collected in 1000 ml screw cap bottle stored at 4°C for further use in the synthesis of AgNPs.

2.3 Synthesis of phytomediated PVA capped AgNPs

500 ml of the 2M $AgNO_3$ aqueous solution was prepared and mixed with the 500 ml of previously prepared plant extract and kept for stirring at 500 rpm, temp at 60 °C. After 5 minutes of reaction, 30 ml of 1% v/v PVA was added dropwise. After proper mixing of reagents, the solution pH was increased to 8 by adding NaOH dropwise. After 15 min of reaction, the reaction mixture turns deep brown color from pale yellow color shown in **Figure 1.2.** The reaction mixture allowed for 1 more hour to complete the reaction. After completion of the reaction, the colloidal solution subjected to centrifugation with 10000 rpm to collect the concentrated colloidal nanoparticles solution, then kept in a hot air oven at 60 °C for overnight to obtain a moisture free sample then the sample was scraped and ground to fine AgNPs powder.

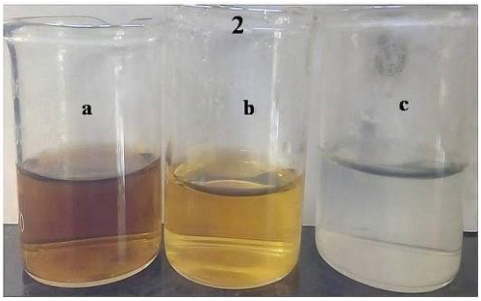

Figure 1. 1. The selected plant leaves, Figure 1. 2. a) Fabricated AgNPs after reaction b) prepared aqueous plant extract c) $AgNO_3$ solution

2.4 Characterization Techniques

The UV spectra of the biosynthesized nanoparticles were recorded by using a UV 2600 UV-VIS Spectrophotometer, Shimadzu by continuous scanning from 200-800 nm and the distilled water was used as the reference for the baseline corrections. FTIR Analysis carried out to identify the phytochemical biomolecules in *Passiflora edulis* which were responsible for the reduction of silver ions to stable AgNPs. Small amount of formed AgNPs used to make KBr pellets then subjected to FTIR analysis using IR Affinity-1 Shimadzu model instrument, with 4500-500 cm^{-1} wavelength range. The crystalline structure of synthesized AgNPs was confirmed by X-ray diffraction studies. X-ray Diffraction analysis of AgNPs was measured by using Philips Xpert PRO, Instrument with Cu Kα X-Ray source with voltage 40kV, with the scanning rate $20min^{-1}$ in θ=2θ configurations. The biosynthesized AgNPs were subjected to ZEISS Special Edition 18 Scanning electron microscope to determine their morphology. A Thin film of the sample was prepared by dropping a small amount of the sample on the carbon coated copper grid, then the film on the SEM grid was allowed to dry by keeping aside for 5 min and the images were taken. The EDS microanalysis system which automatically identifies the elements which were corresponds to the peaks in the energy distribution.

2.5 Antibacterial studies

The antibacterial activity of AgNPs from *Passiflora edulis* was tested by using the well-diffusion method. The fresh cultures of four selected bacteria *Escherichia coli*, *Pseudomonas putida, Staphylococcus aureus, Bacillus subtillis* were prepared. Nutrient agar media was prepared by dissolving 2.8 gm nutrient agar in 100 ml distilled water then autoclaved. Petriplates were made by pouring 20 ml of sterilized media in each plate and spread with 50 µL for different specific bacteria. Then wells were punched and various concentrations of respective samples were added where ampicillin drug used as a control sample, then plates were incubated at 37 °C for 12 hours to observe the zone of inhibition which measured in mm.

3. RESULTS AND DISCUSSIONS:

Formation of AgNPs was confirmed by converting the pale yellow color of the solution to dark brown color, due to surface plasmon resonance (SPR). SPR is the optical property exhibited by some metals nanoparticles [13]. The maximal absorption SPR peak in the UV-Vis spectra of *Passiflora edulis* phytomediated PVA capped AgNPs was noticed at 436 nm was shown in **Figure 2. 1.** which confirmed the formation colloidal nanoparticles as the generally the AgNPs exhibit the characteristic peak between 400-450 nm [14]. The reduction of Ag+ into Ag^0 by using plant extract was confirmed by using FTIR analysis by understanding the vibrational peaks corresponding to the phytochemicals of selected plant leaf extract. The main peaks of FTIR data observed in **Figure 2. 2** at 3331, 1638, 725 which may be due to O-H Stretching or N-H Stretching (alcohols, phenols); -C=C- stretch or N-H Bend (alkenes.1 0 amines), N-H wag or C-H oop (1 0, 2 0amines or aromatics) respectively, same results were observed in articles [15, 16]. The two important bands at 2912 cm^{-1} and 2845 cm^{-1} of C-H stretching corresponded to aldehydes of PVA sample reveals the PVA was acting as capping agent which surrounded the AgNPs. The crystalline nature of the AgNPs was affirmed by using XRD data as the °2 Theta positions at 38.18, 46.17, 67.33, 76.76 were shown in **Figure 2. 3** it is revealing the peaks correspond to the lattice plane of (111) (200) (220) (311) of AgNPs, the data coincide with the JCPDS file no. 04-0783. The average diameter of nanosilver particles found to be 24 nm, calculated using below mentioned Debye-Scherer formula. The particle diameter was distributed between from 13-54 nm. The SEM images of phytomediated PVA capped AgNPs shown in **Figure 3. 1** depicting the nano crystalline particles, with the spherical shape and homogeneous monodispersive in nature. The **Figure 3. 2** of EDS spectral data analysis showing the signals of various corresponding elements with weight % and atomic % of and Ag as 68.68% and 28.09% and to the other elements present.

$$D = K\lambda/\beta \cos\theta$$

Where *K* is the Scherrer constant with a value from 0.9 to 1 (shape factor), λ is the X-ray Wavelength (1.5418 Å), θ is the Bragg angle, β is the FWHM is full width at half maximum in radians.

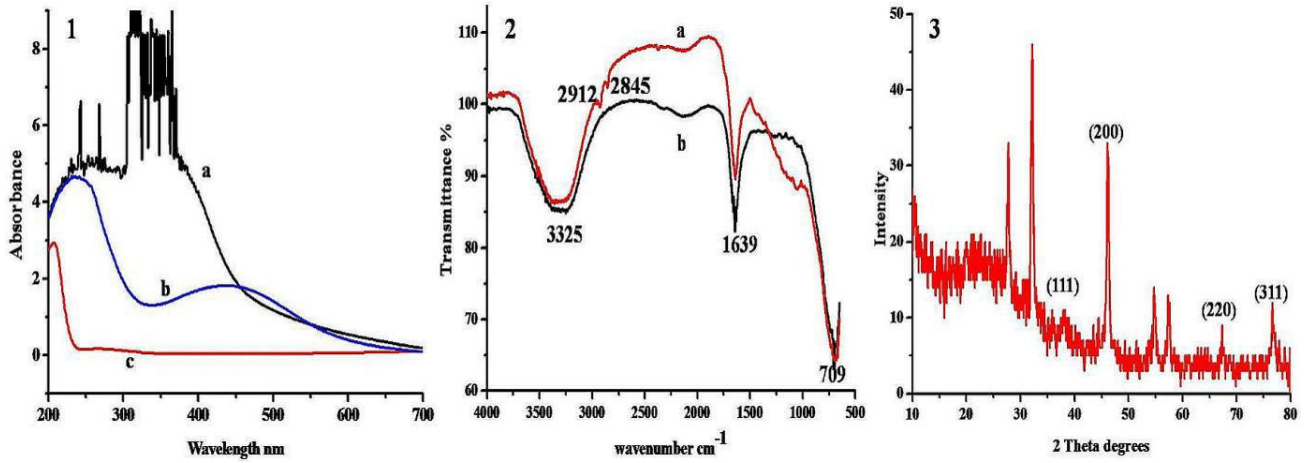

Figure 2. 1. UV-Vis spectral graphs of a) aqueous leaf extract b) fabricated AgNPs c) AgNO3 solution, Figure 2. 2. FTIR spectra of a) fabricated AgNPs b) aqueous leaf extract, Figure 2. 3. XRD data of fabricated AgNPs

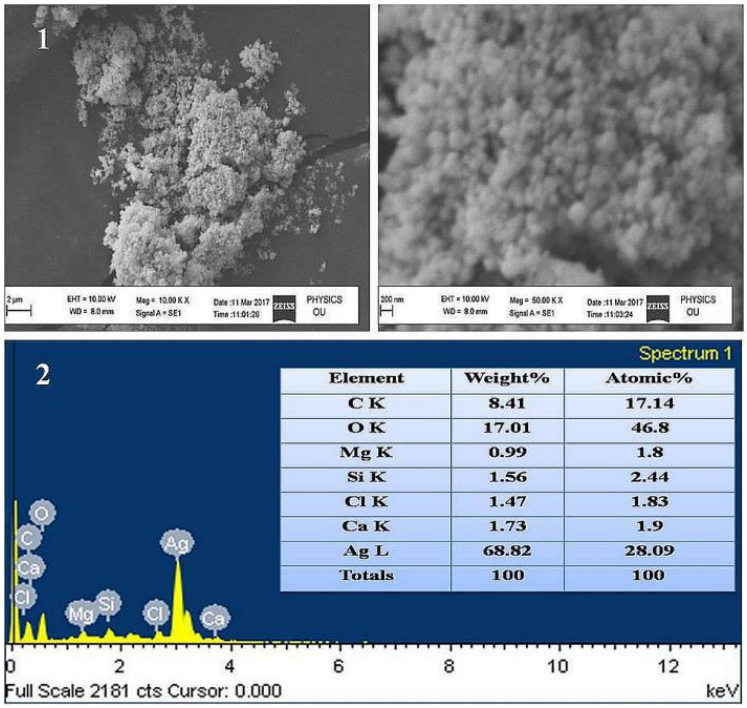

Figure 3. 1. SEM images of fabricated AgNPs at various magnifications, Figure 3. 2. EDS spectral data of elemental signals along with weight % and atomic % of element presence.

3.1 Antibacterial activity

AgNPs was used in medicinal properties for several years [17]. The antibacterial activity of phytomediated PVA capped AgNPs was investigated against harmful bacteria *Escherichia coli, Bacillus subtilis, Pseudomonas putida, and Staphylococcus aureus* using the well diffusion method. The various concentrations of AgNPs were added as 40 µL, 80 µL, 120 µL, 160 µL. The clear zone of Inhibition [18] was observed in **Figure 4** against three tested bacteria where no activity was observed in the case of *Bacillus subtilis.* The highest activity was observed for *Pseudomonas putida.* The linear increase of activity was detected with increasing the concentration of the AgNPs. The zone of inhibition in mm of various concentrations of AgNPs was tabulated in Table 1.

Table1: Zone of inhibition in mm for various concentrations of AgNPs

Bacteria	40 µL	80µL	120µL	160µL	ampicillin
Escherichia coli	16	17	19	19	28
Pseudomonas putida	18	18	20	23	29
Staphylococcus aureus	10	11	12	13	14
Bacillus subtilis	-	-	-	-	-

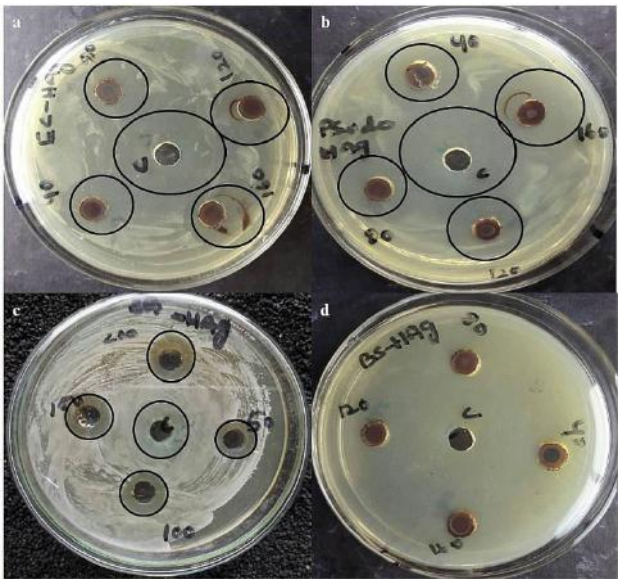

Figure 4: Zone of inhibition of antibacterial activity against *a) Escheritia coli b) Pseudomonas putida c) Staphylococcus areus d) Basillus subtillis*

4. CONCLUSIONS:

The reported study concludes that the phytomediated PVA capped AgNPs was a one-pot, simple, fast, environmentally friendly, nontoxic method, and useful for the bulk preparation of nanoparticles. The fabrication of AgNPs was confirmed by UV-Vis spectroscopy. The FTIR study suggests that the phytochemicals from *Passiflora edulis* leaf extract responsible for the reduction of ionic silver as stable metallic AgNPs and PVA was capped around the particles. The crystalline structure and the average diameter of nanosilver particles found to be 24 nm by using XRD data. The SEM images depicting the nanocrystalline particles, with the spherical shape and homogeneous monodispersive in nature. Based on the study, the prepared AgNPs using leaf extract of *Passiflora edulis* offer effective bioactive factor for growth inhibition of bacteria as it suggests that the phytomediated PVA capped AgNPs can be used as an antibacterial drug in most of the medical fields.

5. ACKNOWLEDGEMENTS:

The authors gratefully acknowledge Department of Chemistry and Department of Biochemistry, University College of Technology, Osmania University to use the facilities therein for characterizing the sample. One of the authors (Raju Sandupatla) thanks and acknowledges UGC for financial assistance and Department of forensic science to provide the facilities to carry out the research work.

REFERENCES:

1. Zhang H.W., Liu Y., and Sun S. H, (2010): Synthesis and assembly of magnetic nanoparticles for information and energy storage applications. *Front. Phys. China, 5*, 347-356.
2. Sun S., Murray C. B., Weller D., Folks L., and Moser A, (2000): Monodisperse fept nanoparticles and ferromagnetic fept nanocrystal superlattices. *Scienc, 287* ,1989-92.
3. Shiraishi Y., And Toshima N, (2000): Oxidation of ethylene catalyzed by colloidal dispersions of poly (sodium acrylate)-protected silver nanoclusters. *Colloids Surf A Physicochem Eng Asp, 169*, 59–66.
4. Mukherjee P., Ahmad A., Mandal D., Senapati S., Sainkar S. R., Khan M.I., Ramani R., Parishcha R., Ajaykumar P. V., Alam M., Kumar R., and Sastry M, (2001): Bioreduction of aucl(4)(-) Ions by the Fungus, Verticillium sp. And Surface Trapping of the Gold Nanoparticles Formed, *Angew Chem Int Ed Engl. 40*(19), 3585-3588.
5. Landsdown A.B., and Williams A, (2007): Bacterial resistance to silver in wound care and medical devices, *Wound Care, 16,* 15-19.
6. Ganaie S.U., Abbasi T., Anuradha J., and Abbasi S.A, (2014): Bio mimetic synthesis of silver nanoparticles using the amphibious weed ipomoea and their application in pollution control, *Journal of King Saud University, Science, 26,* 222–229.
7. Taton T.A., Mirkin C.A., and Letsinger R.L, (2000): Scanometric DNA array detection with nanoparticle probes, *Science, 289*(5485), 1757-60.
8. Liu C., Yang X., Yuan H., Zhou Z., Xiao D, (2007): Preparation of Silver Nanoparticle and Its Application to the Determination of ct-DNA, *Sensors, 7*, 708-718.

9. Yuko Matsui., Kenkichi Sugiyama., Masanori Kamei., Toshio Takahashi.,Tamio Suzuki., Yohtaro Katagata., And Tatsuhiko, (2010): itoextract of Passion Fruit (Passiflora edulis) Seed Containing High Amounts of Piceatannol Inhibits Melanogenesis and Promotes Collagen Synthesis. *J. Agric. Food Chem, 58*, 11112–11118.
10. Lai Thi Ngoc Ha., Bui Van Ngoc., Hoang Hai Ha., and Hoang Thi Yen, (2016): Ultrasound-Assisted Extraction And Anticancer Activity Of Piceatannol From Passiflora Edulis Seed, *Vietnam J. Agri. Sci*, *14*(7), 1016-1025.
11. Federico Ferreres., Carla Sousa., Patrícia Valentão., Paula B Andrade., Rosa M Seabra., And Ángel Gil-Izquierdo, (2007): New *C*-Deoxyhexosyl Flavones and Antioxidant Properties of *Passiflora edulis* Leaf Extract. *J. Agric. Food Chem, 55,* 10187–10193.
12. pelegrini P.B., noronha F.F., muniz M.A.R., vasconcelos I.M., chiarello M.D., oliveira J.T.A., and Franco O.L, (2006): An antifungal peptide from passion fruit (*Passiflora edulis*) seeds with similarities to 2S albumin proteins. *Biochimica et Biophysica Acta (BBA) - Proteins and Proteomics* , *1764 (6*), 1141-1146.
13. Vigneshwaran N., Ashtaputre N.M., Varadarajan P.V., Nachane R.P., Paralikar K.M., Balasubramanya R.H, (2007): Biological synthesis of silver nanoparticles using the fungus Aspergillus flavus, *Mater. Lett, 61*, 1413–1418.
14. Nestor A.R.V., Mendieta V.S., Lopez M.A.C., Espinosa R.M.G., Lopez M.A.C., and Alatorre J.A.A, (2008): Solventless synthesis and optical properties of Au and Ag nanoparticles using Camellia sinensis. *Mater. Lett*, *62* (17), 3103–3105.
15. Perni S., Hakala V., and Prokopovich P, (2014): Biogenic synthesis of antimicrobial silver nanoparticles capped with L-cysteine. *Colloids Surf A*, *460*, 219–224.
16. Prakash P., Gnanaprakasama P., Emmanuel R., Arokiyaraj S., and Saravanan M, (2013): Green synthesis of silver nanoparticles from leaf extract of Mimusops elengi, Linn. For enhanced antibacterial activity against multi drug resistant clinical isolates. *Colloids Surf Biointerfaces,108*, 255–259.
17. Geethalakshmi R., and Sarada D V L, (2012): Gold and silver nanoparticles from Trianthema decandra synthesis characterization and antimicrobial properties. *Int J Nanomed, 7*, 5375–5384.
18. Manisha D.R., Karunakar Rao K., Jahnavi A., Anila M., Sreedhar B., Pratap Rudra M.P, (2013): Synthesis of silver nanoparticles using extracts of Securinega Leucopyrus and evaluation of its antibacterial activity, *Int J. Curr. Sci. 7*, 1-8.

Second National Conference on
RECENT ADVANCES IN APPLIED NANO MATERIALS
February 16-17, 2018 at Department of Physics, University College of Science, Saifabad, Osmania University, Hyderabad, Telangana State, India.

Enhanced sensor functionality of Polyaniline/SnO_2-ZnO hybrid nanofibers for chemical vapors

Akshaya S. Kothare, Hemlata J. Sharma, Subhash B. Kondawar*
Department of Physics, Rashtrasant Tukadoji Maharaj Nagpur University, Nagpur – 440033
*Corresponding Author Email: sbkondawar@yahoo.co.in

Abstract: *Tin dioxide (SnO_2), Zinc oxide (ZnO) and SnO_2-ZnO nanofibers have been fabricated by electrospinning and subsequent calcination process. Polyaniline (PANI) was in-situ grown on SnO_2, ZnO and SnO_2-ZnO nanofibers by chemical oxidative polymerization via chemical bath deposition. The as-prepared PANI/SnO_2, PANI/ZnO and PANI/SnO_2-ZnO nanofibers were characterized by scanning electron microscopy (SEM), energy dispersive x-ray spectroscopy (EDX) and ultraviolet visible (UV-VIS) spectroscopy. SEM micrographs revealed the formation of inorganic electrospun nanofibers with coating of PANI. EDX spectra revealed the presence of elements Zn, Sn, O, N, S and C in PANI/SnO_2-ZnO nanofibers. Sensor functionality of the hybrids was studied toward different chemical vapors at room temperature. In-situ synthesis technique enhanced the conductivity and response of PANI/SnO_2-ZnO nanofibers towards different chemical vapors in comparison to that of pure nanofibers. PANI/SnO_2-ZnO nanofibers have been developed for sensing different vapors at room temperature with high specificity. This is attributed to the formation of greater number of p–n heterojunctions through large surface interaction of the analyte species.*

Key Words: *Nanofibers; Polyaniline/SnO_2-ZnO; Nanocomposites; Electrospinning; Vapor Sensing.*

1. INTRODUCTION:

Vapour sensors have been widely used in a wide range of areas, such as chemical, biomedical, and food industries, wine-quality monitoring, environmental safety and breath analysis. In these applications, it is desired that the vapour sensors exhibit features, such as high sensitivity, high selectivity, high stability, low working temperature, short response and recovery times, etc. The toxic gases HCl (Hydrogen Chloride) and NH_3 (ammonia) are present in the human body as well as evolved during the various processes at the production level in industries, during spraying of pesticides in agricultural farms, while making use of the household cleaning products, etc. Hence there is always a small and finite possibility that these gases get inhaled during respiration. Larger amount of these gases inhaled over longer duration may prove harmful to the living beings. Moreover since both these gases are soluble in water, they not only increase the risk factor of human life but pose a risk to the aquatic life too. Therefore, a great deal of research effort has been devoted to the development of functional materials that may be exploited for the construction of high-performance vapour sensors. Among these, polymer composites reinforced with 1 Dimensional metal-oxide nanostructures have attracted particular attention, primarily because of their unique physical and chemical properties that arise from the large band gap energy, interesting surface chemistry, as well as high surface to volume ratio, high aspect ratio and high porosity [1-2]. SnO_2 and ZnO demonstrate to be excellent candidates for high sensitive gas sensors. In particular, the coupled oxide nanocomposites such as SnO_2/ZnO have received great attention and investigations to improve the gas-sensitive properties of the sensors [3-5]. The sensing mechanism of metal oxide materials mainly relies on the change of electrical conductivity contributed by interactions between metal oxides and surrounding environment. Despite the great success of metal oxide based gas sensors in both scientific research and practical applications, they generally have to work at high temperatures, which bring about the problems such as high power consumption and reduced working life. Moreover, greater efforts have been devoted to the nanocomposites of metal oxides with conducting polymers, including polyaniline (PANI), since the nanocomposites are easy to prepare and could show much improved gas sensing characteristics than the constituent components at room temperature [6-7]. The combination of PANI with metal oxides, create p-n heterojunction seems to be a suitable strategy for the improvement of chemical vapor sensor efficiency at room temperature [8].

2. EXPERIMENTAL:

Preparation of ZnO nanofibers and SnO_2-ZnO/PANI nanocomposites on the substrate

In a typical procedure, 2 g of $Zn(O_2CCH_3)_2$ (H_2O) and 0.5 g of $SnCl_2 \cdot 2H_2O$ was dissolved in 5ml DMF and 5 ml of ethanol under vigorous stirring for 1 h at 60˚C. Subsequently, 1.0 g PVP was added into the above solution under vigorous stirring for 4h. The mixture was loaded into a glass syringe with a needle of 0.5 mm in diameter at the tip and was electrified using a high-voltage DC supply for electrospinning. Electrospinning apparatus consists of a syringe pump, DC high voltage source and rotating or stationary collector. The spinning solution was kept in a vertical syringe with a stainless steel needle having an orifice of 0.5mm. The needle was electrically connected to a positive high voltage. 17 kV was provided between the tip of the spinning nozzle and the collector at a distance of 20 cm and the solution flow rate was kept at 0.4ml/h was maintained using computer control programmer. Thus, the fibers were prepared successfully. Calcination (300˚C in air for 4 h) was performed to remove the organic constituents of PVP and crystallize the SnO_2-ZnO nanofibers. The pristine ZnO nanofibers were also obtained with free addition of $SnCl_2 \cdot 2H_2O$ by the same procedure. The nanofibers of ZnO/PANI and SnO_2-ZnO/PANI composite were prepared by chemical oxidative polymerization of aniline on the substrate bearing pure ZnO and SnO_2-ZnO nanofibers. The concentration of the dopant, CSA was 0.5 M and the oxidizing agent (APS) and the injected aniline was 0.2 M.

RESULTS AND DISCUSSION:

The SEM images show smooth fibers with several millimetres length and an average diameter in the range of about 200 nm of pure ZnO nanofibers and diameter increased to 800 nm when PANI is encapsulated (**Fig.1**).

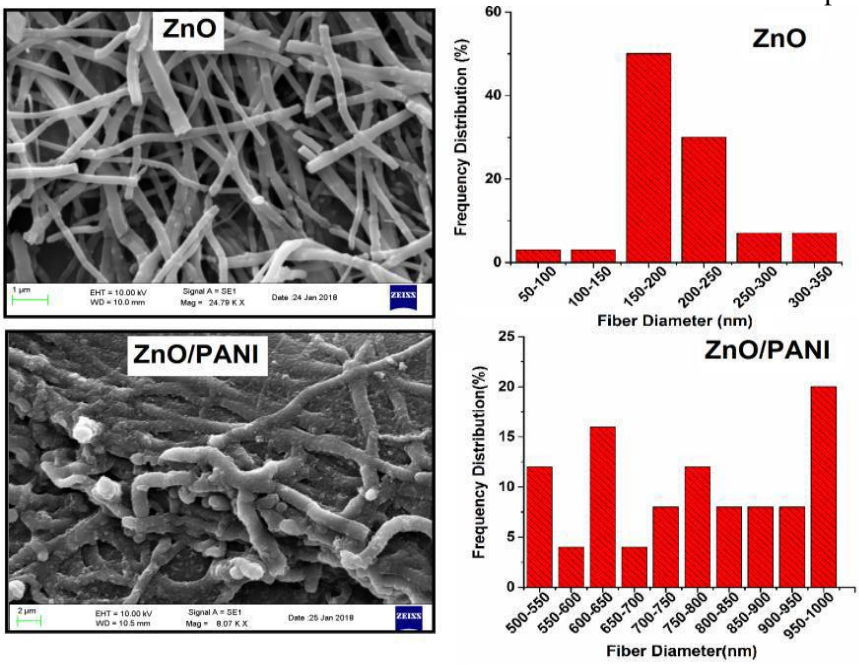

Fig.1: SEM image of pure ZnO and ZnO/PANI nanofibers

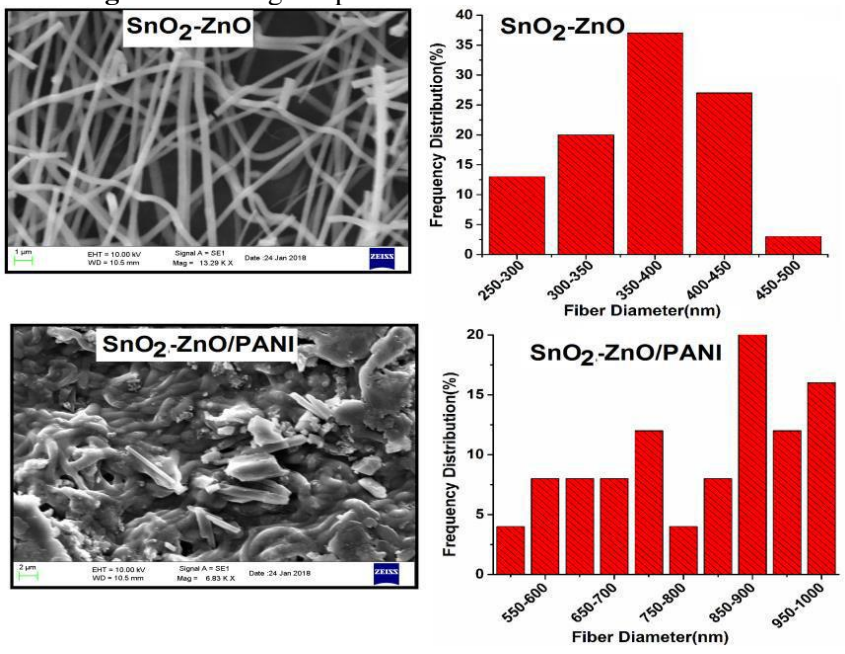

Fig.2: SEM image of SnO_2-ZnO and SnO_2-ZnO/PANI nanofibers

The composite fibers were intertwined forming porous networks that are randomly distributed on the substrate. It indicates that the fabricated film is good for gas sensing. SEM micrographs of SnO_2-ZnO composite nanofibers shows smooth edges and larger diameter around 370 nm compared with pure ZnO nanofibers and diameter of SnO_2-ZnO/PANI composite is increased again as shown in **Fig. 2**. The EDX spectrum of the calcined nanofibers, shown in **Fig. 3**, indicates that the as-prepared SnO_2-ZnO/PANI nanocomposite is composed of O, Sn, C, Zn, S and N elements. SEM image confirmed their polycrystalline nature. The Energy Dispersive X-Ray Spectroscopy (EDX) analysis also confirmed that the composite sample consists of a band attributed to sulfur (sKa 2.21 keV) which indicates the incorporation of $–SO^3$ – as counter ion in the structure of PANI nanofibers. The H signal in composite is not present due to its lower energy and Sn and Zn peaks are related to SnO_2-ZnO composite nanofibers [9-10].

Fig.4 shows UV-VIS spectra of ZnO/PANI and SnO_2-ZnO/PANI nanofibers. ZnO/PANI shows three characteristic peaks of absorption at wavelength 288 nm, 367 nm and 600 nm respectively [5]. The peak at 288 nm in UV region is due to the π-π* transition of benzenoid ring; the peak at wavelength 367 nm, is due to the polaron–π* transition and the peak at wavelength 600 nm, is attributed to the π–polaron transition. In addition, the peaks at wavelength 367 and 600 nm in the visible region arise owing to the doping level and the formation of polarons. Optical absorbance bands for SnO_2-ZnO/PANI composite nanofibers showed red shift and the results are consistent with the SEM Results.

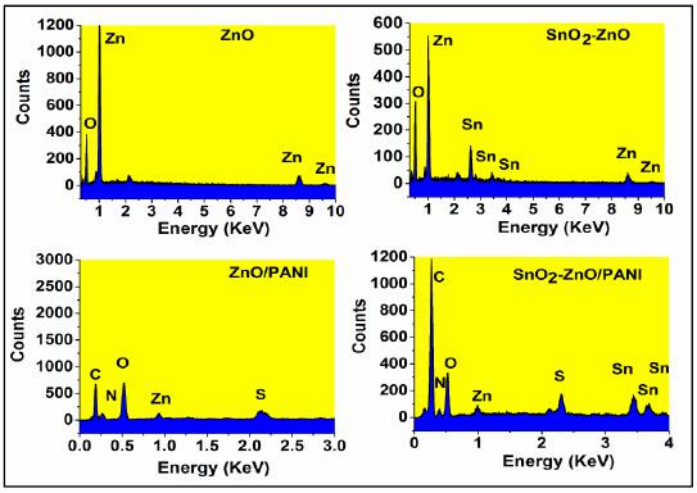

Fig.3: EDX Spectra of pure ZnO, SnO_2-ZnO, ZnO/PANI and SnO_2-ZnO/PANI nanofibers

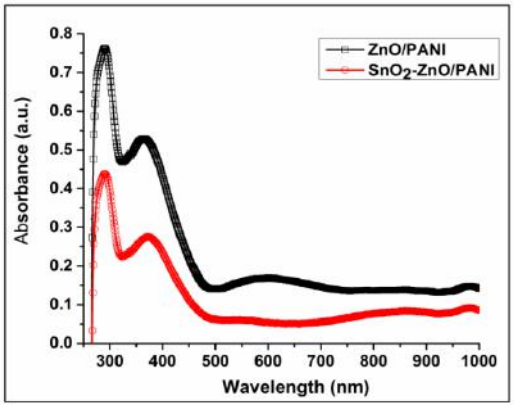

Fig.4: UV-VIS Spectra of ZnO/PANI and SnO_2-ZnO/PANI composite nanofibers

3. CHEMICAL VAPOR SENSING:

On exposure to HCl and NH_3, the composite film (ZnO/PANI and SnO_2-ZnO/PANI) nanofibers resistance changes from its original value, indicating that the electrical resistance is a sensitive parameter in the presence of gas analyte (**Fig.5**). On exposure to ammonia gas (100 ppm in air) at room temperature, it was found that the nanocomposites film resistance increased from the respective unexposed value and decreased for HCl. These changes on removal of ammonia and HCl gas are reversible in nature, and the composite SnO_2-ZnO/PANI showed good sensitivity with relatively faster response/recovery time for both gases while, the pure ZnO, SnO_2 and SnO_2-ZnO composite nanofibers sensor remains insensitive towards different chemical vapors at room temperature [8]. The response ($R=R_g/R_a$) of composite film was calculated. The resistivity of the composites increases in presence of NH_3 because of the undoping of PANI or the reduction of charge carriers by adsorption of ammonia on the surface of material (sensor). Ammonia gas molecules withdraw protons from N^+–H sites to form energetically more favourable NH_4^+ due to which PANI changes from the emeraldine salt state to the emeraldine base state, leading to the reduced hole density in the PANI and thus an increased resistivity. When the sensor is purged with dry air, the process is reversed; NH_4^+ decomposes to form NH_3 and resistance recovered [1]. But for HCl, the process is completely

reversible. The HCl molecule donates H+ ions to the PANI Chain, thus increasing the number of positive charge carriers in the material. This results in decrease in the electrical resistivity of the sensor. Among the composites SnO_2-ZnO/PANI shows enhanced sensing properties such as high response, less response and recovery time and high conductivity as compared with the ZnO/PANI nanofibers at room temperature.

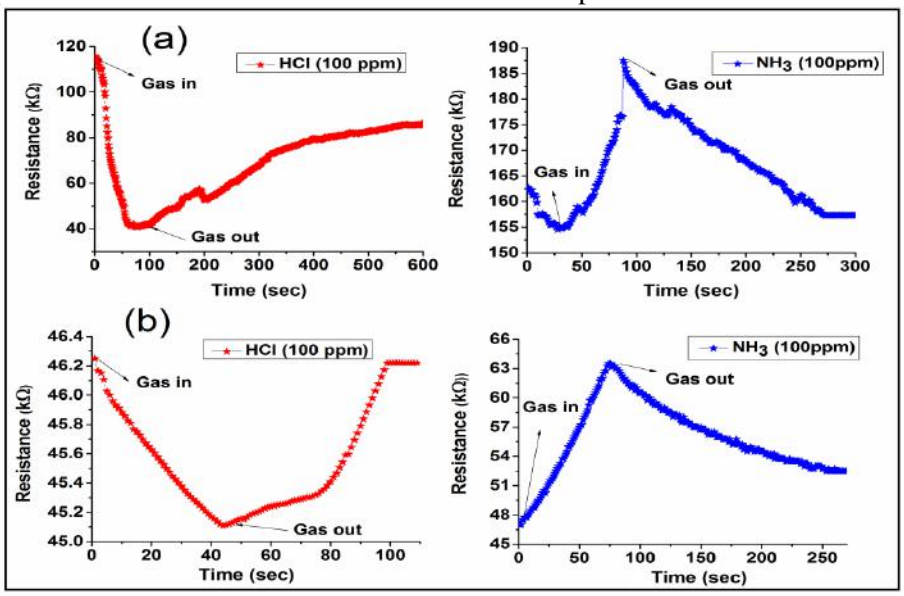

Fig.5: Resistance-Time graph of (a) ZnO/PANI and SnO_2-ZnO/PANI nanofibers at room temperature

Table 1 shows sensing parameters for composite nanofibers at Room Temperature

Parameters	ZnO/PANI		SnO_2-ZnO/PANI	
	HCl	NH_3	HCl	NH_3
Response (R)	0.21	0.8	1	0.84
Response Time (sec)	59	70	42	70
Recovery Time (sec)	505	212	29	182

4. CONCLUSION:

The pure ZnO, SnO_2-ZnO, ZnO/PANI and SnO_2-ZnO/PANI nanofibers were successfully fabricated via electrospinning and oxidative polymerization in chemical bath deposition technique. The as-fabricated SnO_2-ZnO/PANI sensor has shown high response, high conductivity, short response and recovery time at room temperature than ZnO/PANI. Also SnO_2-ZnO/PANI shows good results for HCl vapors than NH_3.

REFERENCES:

1. S. B. Kondawar, S. P. Agrawal, S. H. Nimkar, H. J. Sharma, P. T. Patil. Conductive polyaniline-tin oxide nanocomposites for ammonia sensor, Adv. Mat. Lett. 3(5) (2012) 393-398.
2. I. Fratoddi, I. Venditti, C. Cametti, M.V. Russo. Chemiresistive polyaniline-based gas sensors: A mini review, Sens. Actuators B: Chem., 220(1) (2015) 534-548.
3. Z. Li, F. Blum, M. Bertino, C. Kim. Understanding the response of nanostructured polyaniline gas sensors, Sens. Actuators B: Chem., 183(1) (2013) 419-427.
4. S. Chang, T. Hsueh, I. Chen, S. Hsieh, S. Chang, C. Hsu, Y. Lin, B. Huang. "Highly sensitive ZnO nanowire acetone vapor sensor with Au adsorption, IEEE Transactions on Nanotechnology, 7 (6) (2008) 754-759, 2008.
5. H. Sharma, N. Sonwane, S. Kondawar. Electrospun SnO_2/Polyaniline composite nanofibers based low temperature hydrogen gas sensor, Fibers Polym., 16(7) (2015) 1527-1532.
6. S. Kondawar, S. Acharya, S. Dhakate. Microwave assisted hydrothermally synthesized nanostructure zinc oxide reinforced polyaniline nanocomposites, Adv. Mater. Lett, 2 (5) (2011) 362-367.
7. A. MacDiarmid, A. Epstein. The Concept of secondary doping as applied to polyaniline, Synth. Met., 65 (2-3) (1994) 103-116.
8. H. Khorami, M. Rad, M. Vaezi. Synthesis of SnO_2/ZnO composite nanofibers by electrospinning method and study of its ethanol sensing properties, Applied Surface Science, 257 (2011) 7988–7992.
9. M. Zhang, T. An, X. Hu, C. Wang, G. Sheng, J. Fu. Preparation and photocatalytic properties of a nanometer ZnO–SnO_2 coupled oxide, Applied Catalysis A: General 260 (2004) 215–222.
10. M.S Wagh, L.A. Patil, T. Seth, D.P. Amalnerkar, Surface cupricated SnO_2–ZnO thick films as a H_2S gas sensor, Materials Chemistry and Physics 84 (2004) 228–233.

Second National Conference on
RECENT ADVANCES IN APPLIED NANO MATERIALS
February 16-17, 2018 at Department of Physics, University College of Science, Saifabad, Osmania University, Hyderabad, Telangana State, India.

Development of Polyaniline/ZnO/carbon nanofibers for supercapacitor electrodes

Bhawana A. Manekar, Rounak R. Atram, Shubham N. Gadge, Subhash B. Kondawar*
Department of Physics, Rashtrasant Tukadoji Maharaj Nagpur University, Nagpur – 440033
*Corresponding Author Email: sbkondawar@yahoo.co.in

Abstract: *In this paper, we report the fabrication of ZnO/carbon nanofibers (CNF) through one step electrospinning using zinc acetate and polyacrylonitrile (PAN) followed by stabilization and carbonization process. Polyaniline (PANI) encapsulated ZnO/CNF was prepared by in-situ polymerization for high performance supercapacitor electrodes. Morphology, elemental mapping and electronic states of as-prepared PANI/ZnO/CNF composite electrode were analysed by scanning electron microscopy (SEM), energy dispersive x-ray spectroscopy (EDX) and UV-VIS spectroscopy respectively. The electrochemical performance of the PANI/ZnO/CNF composite electrodes was compared to that of pure CNF, PANI/CNF electrodes in aqueous H_2SO_4 as the electrolyte in three electrodes electrochemical cell. Electrochemical measurements of PANI/ZnO/CNF, PANI/CNF and pure CNF electrodes revealed the maximum specific capacitance, high energy density and excellent cycle life for PANI/ZnO/CNF electrode as compared to that of PANI/CNF and pure CNF electrodes. The combination of electric double layer charge (EDLC) capacitance from high surface area of CNF and pseudo-capacitance from PANI and ZnO facilitates the synergistic effect to enhance the electrochemical performance of PANI/ZnO/CNF composite electrode. This improvement in electrochemical performance suggests that PANI/ZnO/CNF electrodes are promising for the next generation high performance supercapacitors.*

Key Words: *Polyaniline; Carbon nanofibers; Zinc oxide; Electrospinning; Nanocomposites; Electrochemical properties.*

1. INTRODUCTION:

The great energy demand and ever escalating environmental problems can be fulfilled by supercapacitor or ultracapacitor which has features such as more efficient energy supply, high power density, long cycle life (>100,000 cycles), rapid charging/discharging rate, and long-term operation stability and has been extensively studied and considered to be one of the most promising alternative energy storage systems for future [1]. On the basis of energy storage mechanism, supercapacitors are classified into electrical double-layer capacitors (EDLC) and pseudocapacitors. EDLC represents a charge-storage mechanism as a nonfaradaic process, whereas pseudocapacitor is a redox mechanism as a faradaic process. The unique materials related to EDLC are carbonaceous materials, such as carbon nanotubes (CNT), graphene and carbon nanofibers [2]. Among them, carbon nanofibers are displaying outstanding electrical conductivity, high surface area, high pore volume, and adjustable pore sizes. They have been considered as the most promising electrode materials in supercapacitors. To further improve the capacitive performance of carbon nanofibers based supercapacitors, metal oxides and/or conducting polymers have been introduced into carbon electrodes due to their high pseudocapacitance based on fast and reversible surface redox reaction [3, 4]. Among the various metal oxides, zinc oxide is found to be a suitable candidate for supercapacitor applications because of its good electrochemical activity, low cost as a raw material, and environmental friendliness. Recently, ZnO/carbon hybrid materials were used for enhancing the capacity of EDLC and PC. Kim et al have reported the fabrication of ZnO/carbon nanofibers by electrospinning and showed the specific capacitance 275 F/gm [5]. Further, the specific capacitance can be enhanced by using conducting polymer with carbon nanofibers. Conducting polymers such as polyaniline (PANI), polypyrrole (PPy) and polythiophene (PTh), with advantages of good electrical conductivity and multiple intrinsic redox states leading to large theoretical specific capacitance, are better candidates and have attracted growing interests. Among the various conducting polymers, polyaniline (PANI) has been considered as a promising candidate due to its high pseudocapacitance, low cost, facile synthesis and environmental stability. However, because redox reactions are involved in their charge–discharge processes, the conducting polymer-based pseudocapacitors suffer from poor cycling stability and rate capability [6].

Herein, we present the fabrication of the novel hybrid ternary carbon nanofibers/ZnO/polyaniline (CZP) by a facile electrospinning and in-situ polymerization methods. Coating of PANI on ZnO/CNF may help increasing the specific capacitance of supercapacitor due to pseudo capacitance of PANI.The ternary hybrid CZP may utilize the advantages of three kinds of components and avoid the drawbacks of each one, leading to a high specific capacitance.

2. EXPERIMENTAL:

ZnO/PAN-based fibers were prepared by electrospinning. Zinc acetate (10 wt%) as the Zn precursor and a 10 wt% PAN polymer solution dissolved in 20 ml DMF was magnetically stirred for 1 hr at 50°C gives a clear solution for electrospinning. PAN/zinc acetate blend solution was electrospun into nanofibers by using an electrospinning machine (ESPIN-NANO). The nanofibers were stabilized in air at 250°C to induce thermal stability and then held at this temperature for 1 h in air atmosphere. The stabilized fibers were activated at 600° C under nitrogen for 1 hr for carbonization. The carbonized CNF/ZnO fibers were then dipped in 7M HNO_3 solution for 6 hrs to increase its hydrophilicity [5, 7]. CNF/ZnO/PANI composite was prepared by in-situ chemical oxidative polymerization. In a typical process, aniline (0.25M) was added into 1 M HCl (25 mL) and stirred to form uniform mixture. Then acid treated CNF/ZnO (40 mg) was immersed into aniline solution for 30 min and then sonicated to ensure sufficient adsorption of aniline. 1 M HCL solution (25 mL) containing ammonium peroxydisulfate (APS) 0.25M was added drop wise into sonicated solution. The polymerization reaction was carried out at 5°C in ice bath for 6 hrs. The prepared composite was centrifuged and washed with ethanol and distilled water, repetitively [8]. For comparison, CNF/PANI was also synthesized via the similar procedure except the addition of zinc acetate.

3. RESULTS AND DISCUSSION:

Scanning electron microscopy images of as-fabricated CNF, CNF/PANI (CP), CNF/ZnO, and CNF/ZnO/PANI (CZP) are shown in Fig. 1(a-d). SEM image of CNF and CNF-ZnO demonstrates uniform diameter distribution at low range which indicates stable electrospinning process with size of fibers in nanoscale. SEM images of CP and CZP composites indicate the agglomeration of PANI particles over the carbonized fibers of carbon in powder form. EDX is an analytical technique used for the elemental analysis or chemical characterization of a sample. EDX spectrum of CZP composite is shown in Fig. 2. The presence of cabon, zinc, oxygen in CNF/ZnO/PANI indicates the formation of composite material.

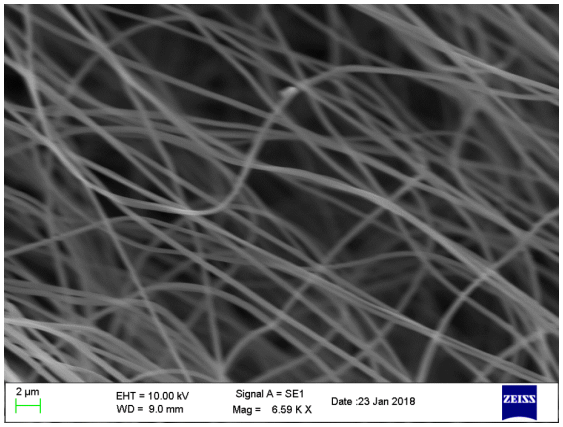

Fig. 1(a): SEM image of CNF

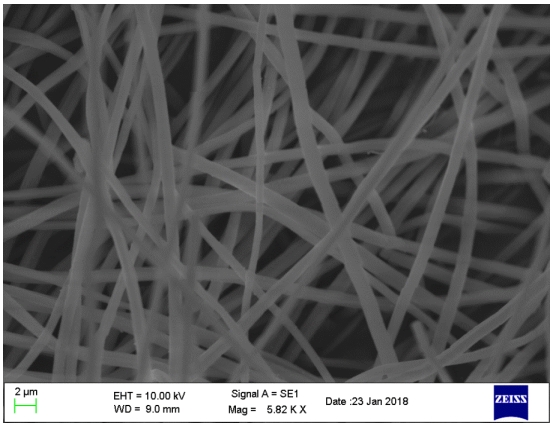

Fig. 1(c): SEM image of CNF/ZnO

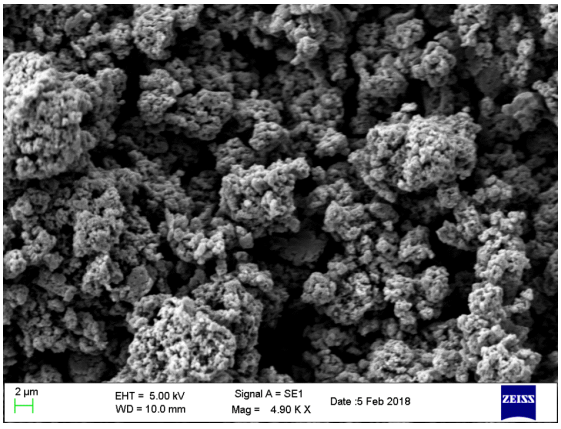

Fig. 1(b): SEM image of CNF/PANI (CP)

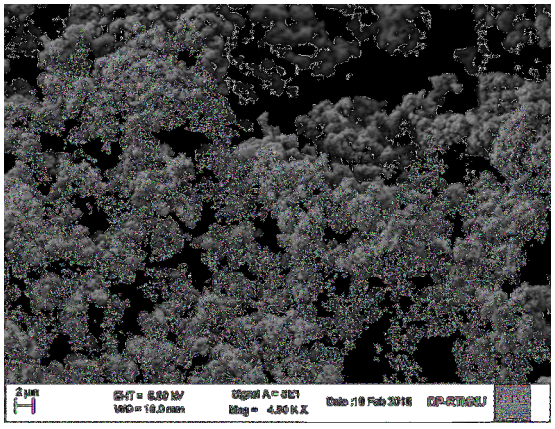

Fig. 1(d): SEM image of CNF/ZnO/PANI (CZP)

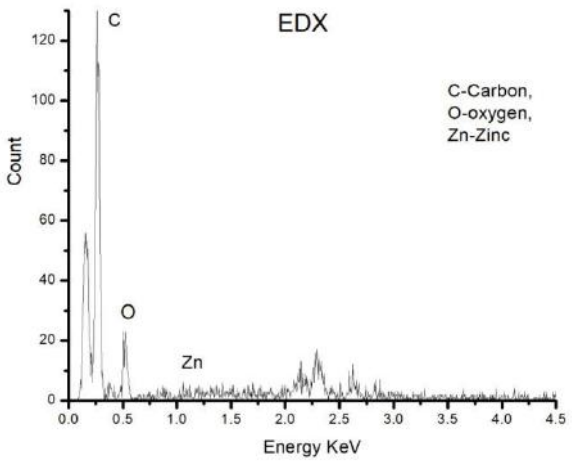

Fig. 2: EDX spectrum of CZP

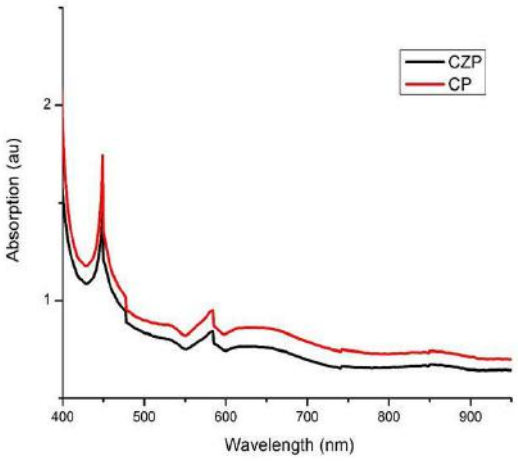

Fig. 3: UV-VIS spectra of CP and CZP

The absorption band at 449 nm corresponds to represents polaronic peak representing the protonation of the polyaniline and the band at 579 nm confirm the presence of conducting emaraldine salt phase of the polymer.

Cyclic voltammetry (CV) is suitable tool to characterize the capacitive behavior of electrode materials. The CV of CP and CZP are performed by cycling the potential of a working electrode, and measuring current with the scan rate of 10 mV/s in 1M H_2SO_4 electrolyte [9]. The quasi-rectangular shape with redox cathodic and anodic peaks in CV indicates the effect of EDLC and pseudocapacitance in the composites. While comparing CV of CP and CZP, more area covered by CZP indicates higher specific capacitance. Ternary composites are found to be potential candidates for supercapacitor electrodes [10-12].

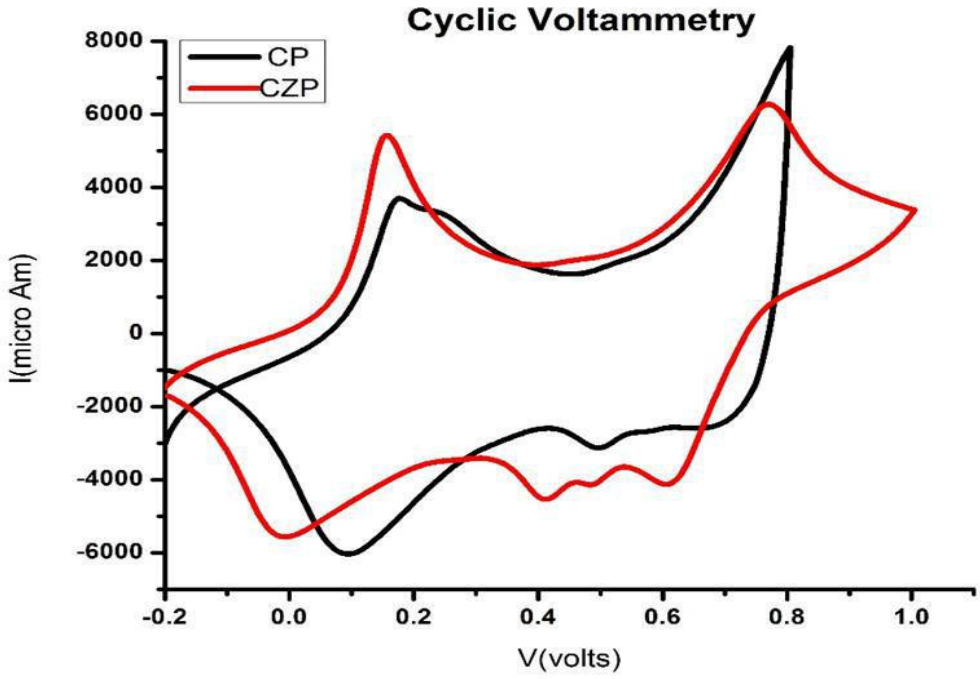

Fig. 4: Cyclic voltammetry of CP and CZP

4. CONCLUSION:

The specific capacitance of CZP is found to be 615 F/gm which is higher than that of CP. Incorporation of ZnO in CNF/PANI increases the specific capacitance. The increase in specific capacitance of CZP is due to synergistic effect of individual components of the composite. Carbon nanofibers based ternary composites are potential candidates as supercapacitor electrodes.

REFERENCES:

1. P. Xiong, J. Zhu, X.Wang, Recent advances on multi-component hybrid nanostructures for electrochemical capacitors. Journal of Power Sources 294 (2015) 31-50.
2. Y. W. Ju, G. R. Choi, H. R. Jung, W. J. Lee, Electrochemical properties of electrospun PAN/MWCNT carbon nanofibers electrodes coated with polypyrrole, Electrochimica Acta 53 (2008) 5796–5803.
3. D. Zhou, H. Lin, F. Zhang, H. Niu, L. Cui, Q.Wang, F. Qu, Freestanding MnO2 nanoflakes/porous carbon nanofibers for high-performance flexible supercapacitor electrodes Electrochimica Acta 161 (2015) 427–435.
4. Z. Tai, X. Yan, J Lang, Q. Xue , Enhancement of capacitance performance of flexible carbon nanofiber paper by adding graphene nanosheets, Journal of Power Sources 199 (2012) 373-378.
5. C. Kim, B. Kim, Zinc oxide/activated carbon nanofiber composites for supercapacitor electrodes. Journal of Power Sources 274 (2015)512-520
6. H. Liu, B. Xu, M. Jia, M. Zhang, B. Cao, X. Zhao, Y. Wang, Polyaniline nanofiber/large mesoporous carbon composites aselectrode materials for supercapacitors, Applied Surface Science 332 (2015) 40–46.
7. X. Song, J. Guo, M. Guo, D. Jia, Z. Sun, L. Wang, Freestanding needle-like polyaniline–coal based carbon nanofibers composites for flexible supercapacitor, Electrochemica Acta 206 (2016) 337-345.
8. F. Miao, C. Shao, X. Li, Na Lu, K. Wang, X. Zhang, Y. Liu, Flexible solid-state supercapacitors based on freestanding electrodes of electrospun polyacrylonitrile@polyaniline core-shell nanofibers, Electrochemica Acta 176 (2015) 293-300.
9. Y. He, L. Wang, D. Jia, Coal/PAN interconnected carbon nanofibers with excellent energy storage performance and electrical conductivity , Electrochemica Acta194 (2016) 239-245.
10. H. Liu, B. Xu, M. Jia, M. Zhang, B. Cao, X. Zhao, Y. Wang, Polyaniline nanofiber/large mesoporous carbon composites as electrode materials for supercapacitors, Applied surface science 332(2015) 40-46.
11. M. Zhi, A. Manivannan, F. Meng, N. Wu, Highly conductive electrospun carbon nanofiber/MnO_2 coaxial nano-cables for high energy and power density supercapacitors, Journal of power Sources 208 (2012) 345-353.
12. G. Xue, J. Zhong, Y. Cheng, B. Wang, Facile fabrication of cross-linked carbon nanofiber via directly carbonizing electrospun polyacrylonitrile nanofiber high performance scaffold for supercapacitors, Electrochemica Acta 215(2016) 29-35.

Second National Conference on
RECENT ADVANCES IN APPLIED NANO MATERIALS
February 16-17, 2018 at Department of Physics, University College of Science, Saifabad, Osmania University, Hyderabad, Telangana State, India.

Effect of Dy^{3+} and Sm^{3+} doping on photoluminescence properties of ZnO nanofibers

Nilam S. Tadas, Chaitali N. Pangul, Subhash B. Kondawar*
Department of Physics, Rashtrasant Tukadoji Maharaj Nagpur University, Nagpur – 440033
*Corresponding Author Email: sbkondawar@yahoo.co.in

Abstract: *Luminescence from nanofibres is capable of providing smart, flexible, light weight, high definition textiles for the variety of application of such brilliant materials. In this paper, we report the fabrication of Dy^{3+} and Sm^{3+} doped ZnO nanofibers by electrospinning and subsequent calcination for photoluminescent fabric designing. Dy^{3+} and Sm^{3+} doped ZnO nanofibers were characterized by scanning electron microscopy (SEM), energy dispersive x-ray spectroscopy (EDX) and photoluminescence (PL) spectroscopy. Morphologically fibers with average diameter 350 nm and 425 nm for Sm^{3+} doped ZnO and Dy^{3+} doped ZnO respectively were observed from SEM. The elemental analysis by EDX revealed the presence of Zn, Dy, Sm and O confirms the formation of doped ZnO. Photoluminescence displays defect free visible emission. Dy^{3+} doped ZnO nanofibers shows emission in white region while Sm^{3+} doped ZnO nanofibers shows emission in orange-red region. Photometric characterisations summarizes the colour- coordinates, correlated colour temperatures (CCT) and luminescence efficacy of radiation (LER) with the help of CIE diagram.*

Key Words: *Dysprosium; Samarium; Zinc Oxide; Nanofibers; Electrospinning; Photoluminescence.*

1. INTRODUCTION:

The very potential 1D nanomaterials had found an extensive interest owing to its very magnificent properties. Nanotubes, Nanowires, Nanofibers etc. had been in constant urge for more development in order to explore more different properties [1]. Nanofibers are one such most potential type of material. Variety of methods are there to fabricate nanofiber but Electro spinning, a top down nano manufacturing method, offers a rapid, facile process for creating high surface are polymer fibers compared to those produced by most bottom up methods [2]. When the diameters of polymer fiber materials are shrunk from micrometers to sub microns or nanometers, there appear several amazing characteristics such as very large surface area to volume ratio (this ratio for a nanofibers can be as large as 10^3 times that of a microfibers), flexibility in surface functionalities, and superior mechanical performance (e.g. stiffness and tensile strength) compared with any other known form of the material. These outstanding properties make the polymer nanofibers to be optimal candidates for many important applications [3].

Electro spinning technique is simple to adopt attractive for its convenience, inexpensive. This technique uses electrostatic forces to produce polymeric, ceramic and composites continuous ultrafine fibers with diameters ranging from microns to few nanometers. Electro spun nanofibers have good orientation, large aspect ratio i.e. length/diameter ratio and dimensional stability. This technique produces flexible, fully light emitting fibers suitable for photonic devices. The nature of the electro spun nanofibers depends on the parameters, molecular weight of the polymer, solution properties, electric potential, flow rate, concentration, distance between the capillary and collection screen, ambient parameters, motion of target screen, needle gauge [4].

In recent years, semiconductor luminescent materials have attracted much attention and a variety of strategies have been explored to optimize the luminescence properties. Among these semiconductors, zinc oxide (ZnO) has become a suitable host material to dope different kinds of dopants [5]. Selective elements doping in semiconductors can offer an effective way to adjust their electrical, optical and magnetic properties, and rare earth is one of the promising materials due to the abundant energy levels and temperature-independent luminescence in the infrared/visible range. The high electron mobility, high thermal conductivity, good transparency, wide and direct band gap (3.37 eV), large exciton binding energy (60eV) and easiness of growing it in the nanostructure form by many different methods make **ZnO** suitable for wide range of applications in optoelectronics, transparent electronics, lasing and sensing applications [6]. In last decade, the number of publications on ZnO has increased annually and in 2007, ZnO has become the second most popular semiconductor after Si and its popularity is still increasing with time [7-8].

Trivalent lanthanide ions doped ZnO has been a topic of great research under this area. Ln^{3+} ions due their unique *f-f* transition nature possess excellent luminescent properties [9]. Lanthanides are set of seventeen chemical elements placed at sixth row of the periodic table stretching from lanthanum to ytterbium. Doping of these ions into ZnO could possibly reveal somany outstanding optical properties for ZnO [10].

This work presents the fabrication of different RE doped ZnO nanofiber using the process of electrospinning. Novel fibres of Dy^{3+} and Sm^{3+} ions doped ZnO nanofiber were successfully fabricated utilising electrospinning-calcination technique which showed intense visible emission overcoming the UV and defect green emission of ZnO. These visible emissions are the characteristic of Dysprosium and Samarium ion resulting from the Magnetic and Electric transition. This is for the first time that the efficient energy transfer had occurred from host ZnO to RE^{3+} ions in nanofiber which originates the intense visible emission. Moreover, it would be interesting to study more effect of various types of doping and co- doping on the luminescence properties of ZnO nanofiber.

2. EXPERIMENTAL:

Starting materials were selected as Zinc Acetate dihydrate ($Zn(CH_3COO)_2\_2H_2O$); LobaChemie with 99.5% purity, RE(III) nitrate hydrate ($RE(NO_3)_3$); Sigma Aldrich with 99.9% purity, Poly Vinyl Alcohol (PVA); Sigma Aldrich Mol.Wt 89,000. All the materials were used without further purification. Initially to prepare pure ZnO nanofiber, 0.5gms of Zinc Acetate dihydrate and RE nitate were dissolved in 1ml of deionised water by magnetic stirring. Another solution was made by dissolving 0.35gms of PVA in 1ml of deionised water at 60°C under continuous magnetic stirring for 2hrs. The two solutions were mixed and allowed to form a homogenous solution by continuous magnetic stirring for another 2hrs with the addition of 0.059ml of glacial acetic acid. The resultant solution was filled in the syringe and electrospinning experiment was carried out. A constant high voltage potential of 20kV was applied to the tip of the syringe and the ground was connected to the surface collector. The distance between the tip of the syringe and ground collector was maintained at 15cms. The fibres so formed were then dried at 120°C in oven for 12hrs. Calcinations were then carried out at 300°C for 2hrs.

3. CHARACTERIZATION:

The prepared samples were studies by using various characterization techniques like SEM and EDX on Carl Ziess EVO 18 SEM revealed that ultralong, smooth and continuous nanofiber were formed. The Distribution graphs confirms diameter size of prepared fibres. PL studies were carried on spectroflurometer Shimadzu RF-5301PC at room temperature on d Dy^{3+} and Sm^{3+} ions doped ZnO nanofiber. Emission and Excitation graphs were studied to confirm the spectra.

4. RESULTS AND DISCUSSION:

Fig.1 and Fig. 2 shows the SEM image of Dy^{3+} ions doped ZnO nanofiber and Sm^{3+} doped ZnO nanofibers both calcined at 300°C respectively. Fig.1 clearly shows that the calcined nanofibers are ultralong and smooth. The distribution graph gives the average diameter of the prepared fibre i.e. 425nm. It can also be seen from the Fig. 2 that the size of nanofiber had reduced considerably but the fibre still retain the form of long and continuous inorganic structures. Distribution curve confirms the reduction in diameter size up to 350nm. Fig. 3 shows the EDX graphs of the prepared samples calcined at 300°C. It confirms the presence of elemental Zn, O, Dy and Sm. Presence of C is due to carbonaceous materials.

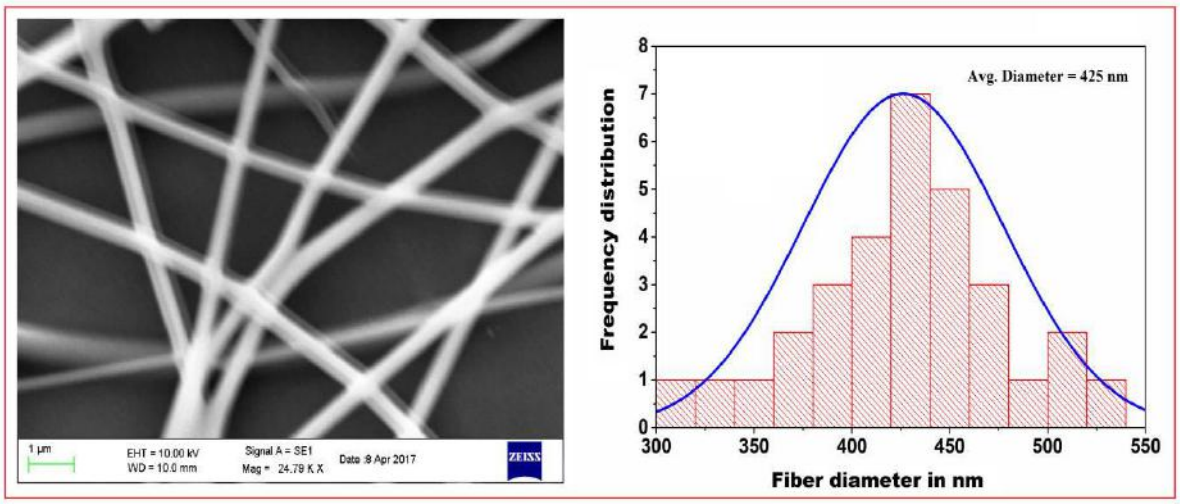

Fig.1 SEM image and histogram of calcined Dy^{3+} doped ZnO nanofibers

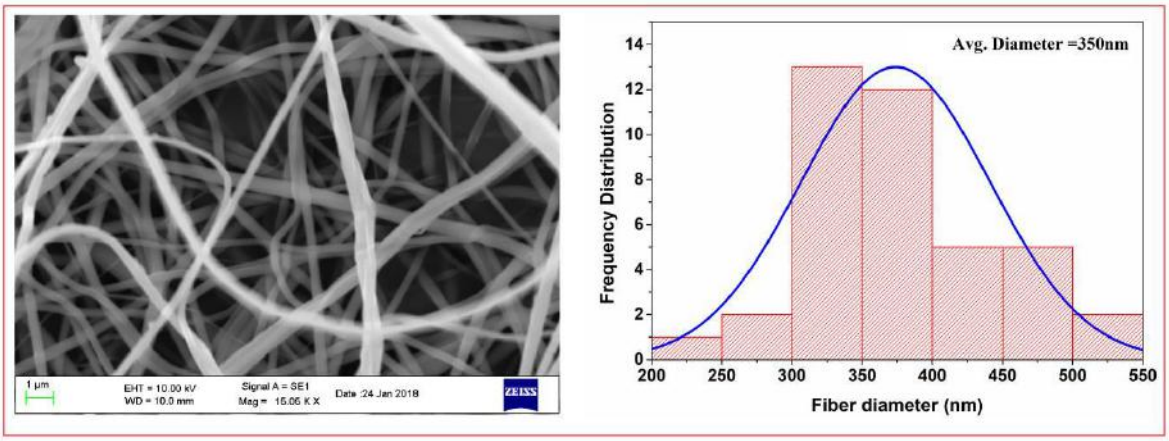

Fig.2 SEM image and histogram of calcined Sm^{3+} doped ZnO nanofibers

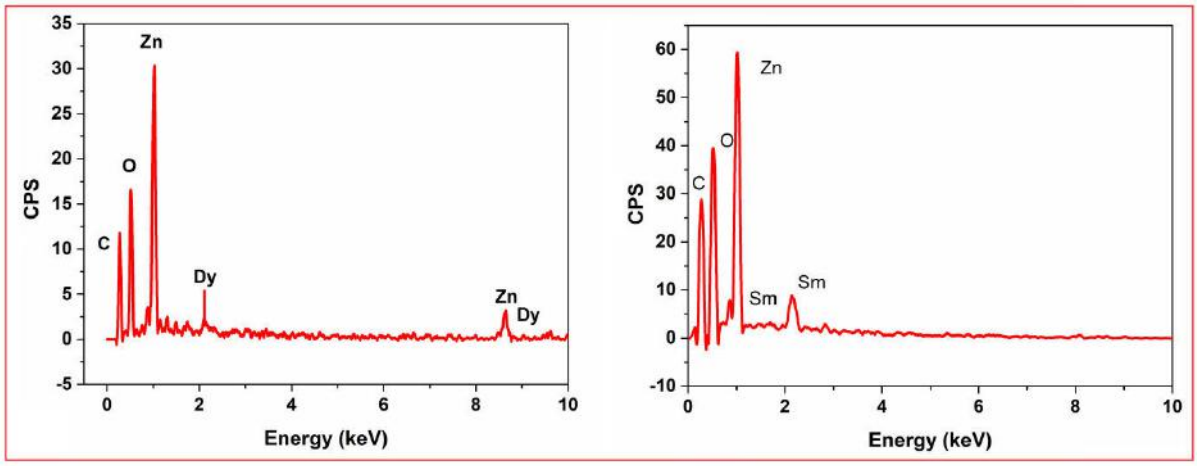

Fig. 3 EDX image of calcined Dy^{3+} doped ZnO nanofibers and Sm^{3+} doped ZnO nanofibers

For better understanding the optical properties of prepared samples photoluminescence excitation and emission spectra RE ions doped ZnO nanofibers were recored. Fig. 4 shows the PL spectra Of Dy^{3+} ion doped ZnO nanofibers. When excited at an excitation wavelength 353nm two spectral peak at 480nm and575 nm are observed in Dy^{3+} ions doped ZnO nanofibres which represents the distinctive emission peak of Dy^{3+} ions, $4F_{9/2} \rightarrow 6H_{15/2}$ and $4F_{9/2} \rightarrow 6H_{13/2}$ respectively. With respect to dysprosium, the $4F_{9/2} \rightarrow 6H_{15/2}$ transition is magnetically allowed transition while $4F_{9/2} \rightarrow 6H_{13/2}$ is forced electrical transition (11). Excitation spectra was record at dominant emission 575nm which gives a broad peak around 350nm.

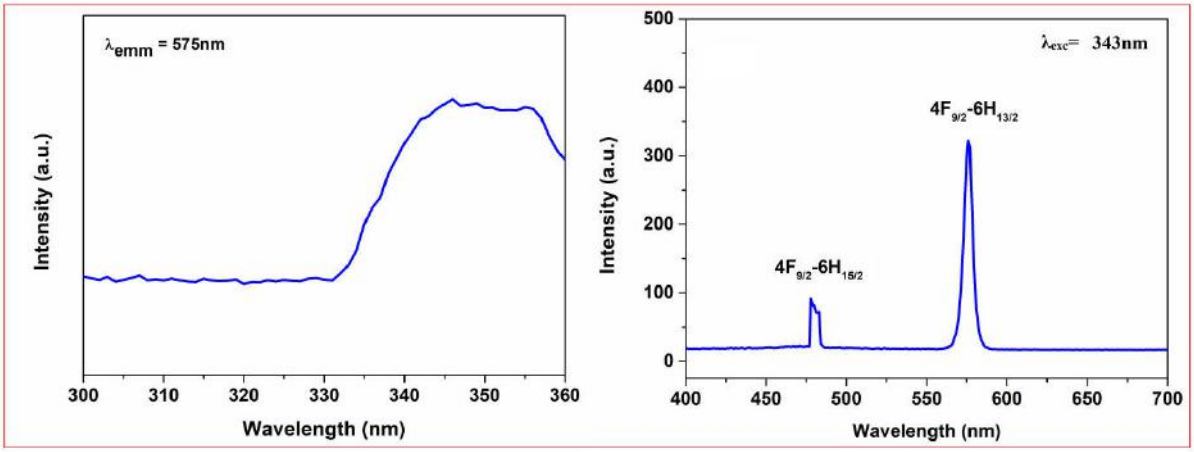

Fig. 4 Photoluminescence spectra of Dy^{3+}doped ZnO nanofibers.

Fig.5 shows the PL spectra Of Sm^{3+} ion doped ZnO nanofibers. When excited at an excitation wavelength 394nm two spectral peak at 606nm and 644 nm are observed in Sm^{3+} ions doped ZnO nanofibres which represents the distinctive emission peak of Sm^{3+} ions. With respect to Samarium, $^4G_{5/2} \rightarrow {}^6H_{7/2}$ transition is magnetically allowed while $^4G_{5/2} \rightarrow {}^6H_{9/2}$ is electrically forced (12). Excitation spectra was recoded at 606nm which gives a broad peak around 390nm.

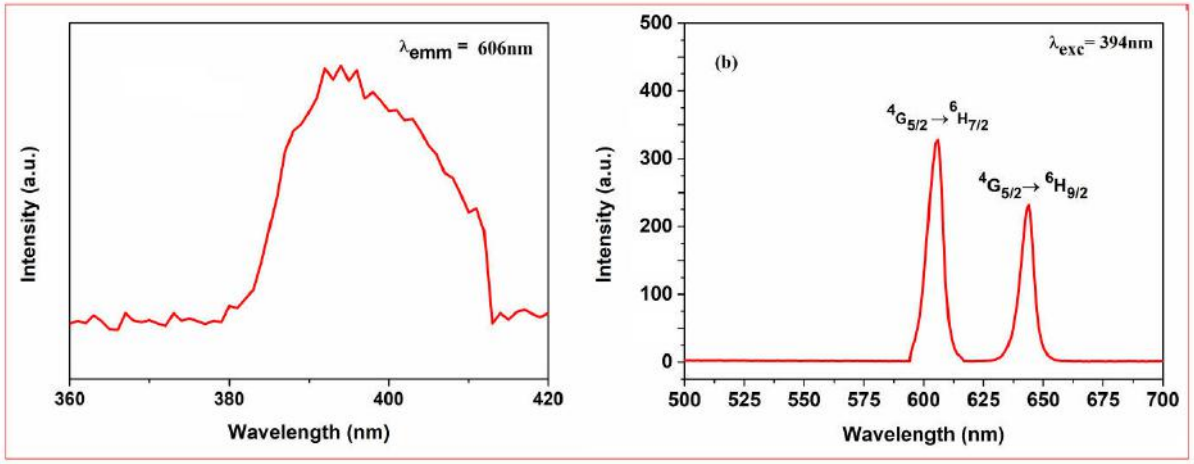

Fig. 5 Photoluminescence spectra of Sm^{3+}doped ZnO nanofibers.

The Commission Internationale de l'Eclairage (CIE) parameters such as colour coordinates, colour co-related temperature(CCT), luminescence efficacy of radiation (LER) were calculated to know the photometric characteristics of the prepared nanofibres. Fig.6 illustrates the CIE chromaticity diagram of emission spectra of prepared samples. The parameters were calculated by the spectrophotometric method using the spectral energy distribution of chromaticity diagram and are summarized in Table 1.

The colour coordinates (x;y) were calculated using the standard procedure. Colour coordinates are one of the important parameter for evaluating luminescent materials performance. From Fig. 6(a), it is seen that the coordinates lie in white region for Dy^{3+} doped ZnO nanofibers while from Fig. 6(b) it is seen the coordinates for Sm^{3+} doped ZnO nanofibers lie in red region. Thus, colour tunability can be achieved by changing the variety of dopants. It is evident from obtained values of CCT and LER as in Table.1, RE ions doped ZnO nanofiber sample calcined at 300°C seem to be a good candidates for warm light LED devices (13).

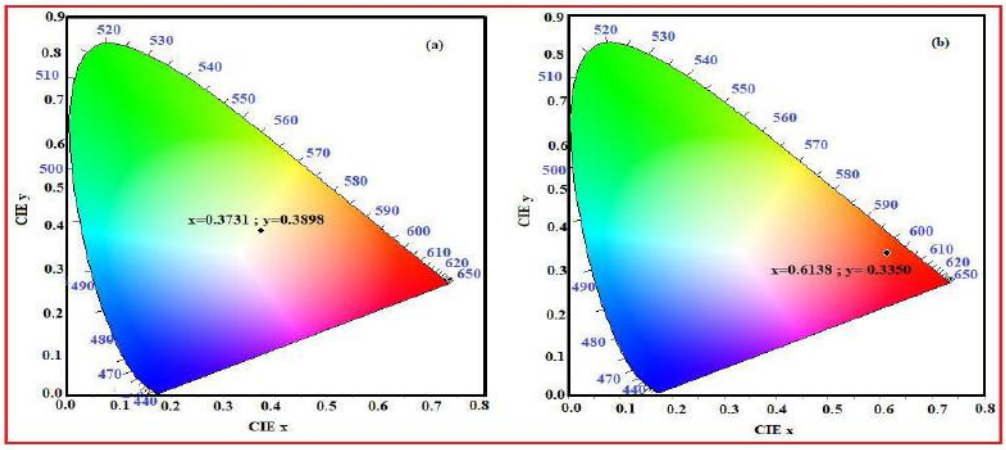

Fig. 6 CIE diagrams of (a) Dy^{3+}doped ZnO nanofibers and (b) Sm^{3+}doped ZnO nanofibers

Table 1 Photometric characteristics of prepared nanofibers.

Sample	**CIE x coordinate**	**CIE y coordinate**	**CCT**	**LER (lm/W)**
Dy^{3+} doped ZnO nanofibers	0.3779	0.3925	4175	315
Sm^{3+} doped ZnO nanofibers	0.6138	0.3350	1106	265

5. CONCLUSIONS:

Dy^{3+} and Sm^{3+} doped ZnO nanofibers with average diameter 350 nm and 425 nm respectively were successfully fabricated by electrospinning and subsequent calcination. The elemental analysis by EDX revealed the presence of Zn, Dy, Sm and O confirms the formation of doped ZnO. From photoluminescence spectra and CIE diagrams, it has been concluded that Dy^{3+} doped ZnO nanofibers shows emission in white region while Sm^{3+} doped

ZnO nanofibers shows emission in orange-red region. Thus, light emitting fibers at nanoscale are the advanced materials for photoluminescent fabric designing.

REFERENCES:

1. Z. M. Huang, Y.Z. Zhang, M. Kotaki, S. Ramakrishna: A review on polymer nanofibers by electrospinning and their applications in nanocomposites, Composites Science and Technology, 63 (2003) 2223–2253.
2. D. Li and Y. Xia : Electrospinning of Nanofibers reinventing the Wheel, Adv. Mater., 14 (2004) 1151-1170.
3. H. Wu, R. Zhang, X. Liu, D. Lin, and W. Pan: Electrospinning of Fe, Co, and Ni Nanofibers: Synthesis, Assembly and Magnetic Properties, Chem. Mater., 19 (2003) 3506-3511.
4. T. Subbiah, G. S. Bhat, R. W. Tock, S. Parameswaran, S. S. Ramkumar: Electrospinning of Nanofibers, Journal of Applied Polymer Science, 96 (2005) 557–569.
5. A. Janotti and C.G. Van de Walle : Fundamentals of zinc oxide as a Semiconductor, Rep. Prog. Phys. 72 (2009) 126501 (29pp).
6. Y.S. Park, C.W. Litton, T.C. Collins, D.C. Reynolds: Exciton Spectrum of ZnO, PhysRev.,143(1966) 512.
7. R. Panda, A. Singh, R. Samal, S. Bhattacharya, P. K. Sahoo, P. K. Datta, S. K. Das: Femtosecond laser excited second harmonic and multiphoton absorption induced UV luminescence generation behaviour of ZnO nanofibers, Optik, 154 (2018) 320–324.
8. H. Yua, H. Fan, X. Wang, J. Wang : Synthesis and optical properties of Co-doped ZnO nanofibers prepared by electrospinning, Optik, 125 (2014) 2361–2364.
9. S. Lymperopoulou, T. Lazarides, C. Papachristodoulou, C. P. Raptopoulou, V.Psycharis, J. C. Plakatouras : Synthesis, structural characterization, and fluorescence of a series of 1D rare earth coordination polymers with a substituted iminodiacetate ligand, Inorganica Chimica Acta, 472 (2018) 276–282.
10. Q. L. Feng, H. Q. Yu, J. X. Fang, X. Z. Chao, Z. C. Wang : Effects of Eu doping and O vacancy on the magnetic and optical properties of ZnO , Physica B: Physics of Condensed Matter, 530 (2018) 133–141.
11. P. Karthikeyan, S. Arunkumar, K. Annapoorani, K. Marimuthu: Investigations on the spectroscopic properties of Dy3+ ions doped Zinc calcium tellurofluoroborate glasses , Spectrochimica Acta Part A: Molecular and Biomolecular Spectroscopy, 193 (2018) 422–431.
12. M. Seshadri, M. Radha, D. Rajesh, L.C. Barbosa, C.M.B. Cordeiro, Y.C. Ratnakarama. : Effect of ZnO on spectroscopic properties of Sm3+ doped zinc phos-phate glasses, Physica B 459 (2015) 79–87.
13. R.Jagannathan, S.P. Manoharan, R.P. Rao, R.L.Narayanan and N. Rajaram: Colour Coordinates of some Photoluminescent Materials, Electrochem 4(6) (1988) 597-600.

Second National Conference on
RECENT ADVANCES IN APPLIED NANO MATERIALS
February 16-17, 2018 at Department of Physics, University College of Science, Saifabad, Osmania University, Hyderabad, Telangana State, India.

Ultrasonic Effect on Rheological Parameters of Human Blood

Mohd Abdul Saleem and Kaleem Ahmed Jaleeli
Biophysics Research Laboratory, Department of Physics Nizam College (Autonomous),
Osmania University, Hyderabad-500001, India.
Email - saleemsaqibi25@gmail.com, kaleemjaleeli@gmail.com

Abstract: *The present paper reports the data on Rheological parameters of normal and ultrasonic irradiated human blood. The blood samples were collected from the healthy donors and were stored in heparin as anticoagulant. The samples were irradiated with ultrasonic interferometer at a frequency of 3MHz.*

In the present investigation, the Rheological parameters (viscosity, volume flow Rate and surface tension) of normal and ultrasonic irradiated human blood are determined employing capillary viscometer technique. Blood samples are irradiated with ultrasonic standing waves at an interval of 30 min upto 2 hours using ultrasonic interferometer. The data reveals variation in the rheological parameters of normal and ultrasonic irradiated blood samples.

Key Words: *Human blood, Ultrasonic interferometer, Ultrasonic Standing waves, Viscometer, Viscosity, Volume flow rate, Surface Tension*

1. INTRODUCTION:

Ultrasound refers to sound with a frequency above that which can be detected by the human ear. It is a cyclic sound pressure with a frequency greater than the upper limit of human hearing. Its interaction with living system leads to a special branch of physics called Ultrasonic Biophysics. Ultrasonic biophysics is the study of mechanisms responsible for how ultrasound and biological materials interact. Ultrasound induced bioeffects focus on issues related to the effect of ultrasound on biological materials.

Rheology is the study of the flow and deformation behavior of materials. It is a specialized part of fluid mechanics and is concerned primarily with Non-Newtonian substances like Blood. Blood is a vital fluid found in human being and other animals. It contains many chemical compounds to perform various functions.

Watchier [1] reported the absorption of ultrasound in water, blood, milk and other biological fluids at 1-10 GHz using damped oscillation.

G Gopala Krishna et al [2] determined the absorption of ultrasound in human blood. The study suggests that the absorption of ultrasound in human blood is due to viscous interaction between the fluid and the suspended cells.

S Chien et al [3] carried out the work on effects of hematocrit and plasma proteins on human blood Rheology at low shear rates. The Viscosity of whole blood, defibrinated blood and Ringer suspension of cells was determined at low shear rates and was observed that the Viscosity of each system rises as the hematocrit is increased.

Somayeh Arain Rad et al [4] studied the mobile phone effects on viscosity of human blood. The study reveals that viscosity increases linearly with the exposure time.

Naresh Kaul [5] using simple approach of viscometer technique studied the rheological behavior of blood and observed that Viscosity is affected by various factors and concluded that it depends on the amount of plasma proteins, the number and volume of corpuscles.

Barbee JH [6] studied the effect of temperature on relative viscosity of human blood. Blood viscosity is a measure of the resistance of blood to flow, which is being deformed by either shear stress or extensional stress.

Lowe GD et al [7] examined the relationship of Blood viscosity and risk of cardiovascular events. The finding suggests that the increased blood viscosity may be one plausible biological mechanism through which increase in haematocrit and fibrinogen may promote ischaemic heart disease and stroke.

Sahar E et al [8] analyzed the effect of electric field on hematological parameters and biophysical blood properties for diagnosing anemia in rats and concluded that Electric field exposures may alter the blood mechanical and rheological properties. EF exposure originated different metabolic and hematological effects, which appeared to be related to the duration of exposure.

G.B. Thurston [9] studied the Viscoelasticity of Human Blood. The study reveals that viscoelastic properties are strongly dependent upon both the hematocrit and the velocity gradient, at low hematocrits the viscosity of blood is not dependent upon shear rate and hence is Newtonian while at higher hematocrits it is Non Newtonian.

2. MATERIALS AND METHODS:

Blood samples of volume 4 ml were collected from the healthy donors and were stored in Heparin as anticoagulant. Each sample was divided into two parts. One was a control sample and the other was test sample. The test sample was irradiated using Ultrasonic interferometer. Rheological parameters such as coefficient of Viscosity, Volume flow rate and Surface tension of normal and ultrasonic irradiated blood samples exposed upto 2 hours at an interval of 30 min were determined using capillary viscometer technique, developed in Biophysics Research Laboratory, Nizam College, Hyderabad.

The viscometer is a simple capillary tube of length of about 30cm and with a radius of 0.05cm. The capillary tube was marked with two preset points A and B the distance between them is 10 cm. A sample of blood of length 2 to 6 cm was sucked by one end of the capillary tube. The flow of blood column in the capillary tube was controlled by closing and opening upper end of the tube. The time required for the sample to travel a fixed distance of 10 cm was recorded and velocity was calculated from the ratio of preset distance (10 cm) and time.

A plot is drawn between 1/L on X- axis and V on Y-axis and it is a straight line with intercept on Y- axis. The intercept of the straight line is measured which gives the maximum velocity (V_o). Viscosity, Volume flow rate and Surface tension were calculated from the intercept of the straight line using the following formulas

1. Coefficient of Viscosity has been calculated using the equation

$$\eta = R^2\rho g / 8V_o$$

η-Coefficient of viscosity (poise);
g – acceleration due to gravity (cm/s^2);
R-Radius of capillary tube (cm);
ρ- Density of blood (gm/cc);
V_o - Y- intercepts.

2. Volume flow rate (Q) has been obtained using the equation

$$Q = V_0(\pi R^2)$$

V_0 – Maximum Velocity;
R –Radius of Capillary tube (0.05cm)

3. Surface Tension has been calculated using the relation

$$T = (4\eta Tan\alpha) / R Cos\theta$$

η – Coefficient of viscosity (poise);
R – Radius of capillary tube (cm);
θ- Angle of contact of sample with capillary wall- 30^0
α- slope of the straight line between L^{-1} on X- axis and velocity on Y- axis

A simple viscometer Technique

3. RESULTS AND DISCUSSIONS:

Table 1 presents the data on coefficient of Viscosity, Volume flow rate and Surface tension of normal and ultrasound irradiated blood using ultrasonic interferometer upto 2hours with an interval of 30 min.

Table1: Data on Coefficient of Viscosity, Volume flow rate and Surface tension with respect to Time (min)

Time(min)	0	30	60	90	120	%change for 2hours
Coefficient of Viscosity(poise)	0.046	0.047	0.050	0.059	0.062	34.7
Volume Flow Rate($cm^3.sec^{-1}$)	0.054	0.053	0.050	0.042	0.040	-25.92
Surface Tension($dyne.cm^{-1}$)	47.21	48.24	51.32	49.54	52.06	10.27

Fig 1: Plot between Coefficient of Viscosity (η) and time

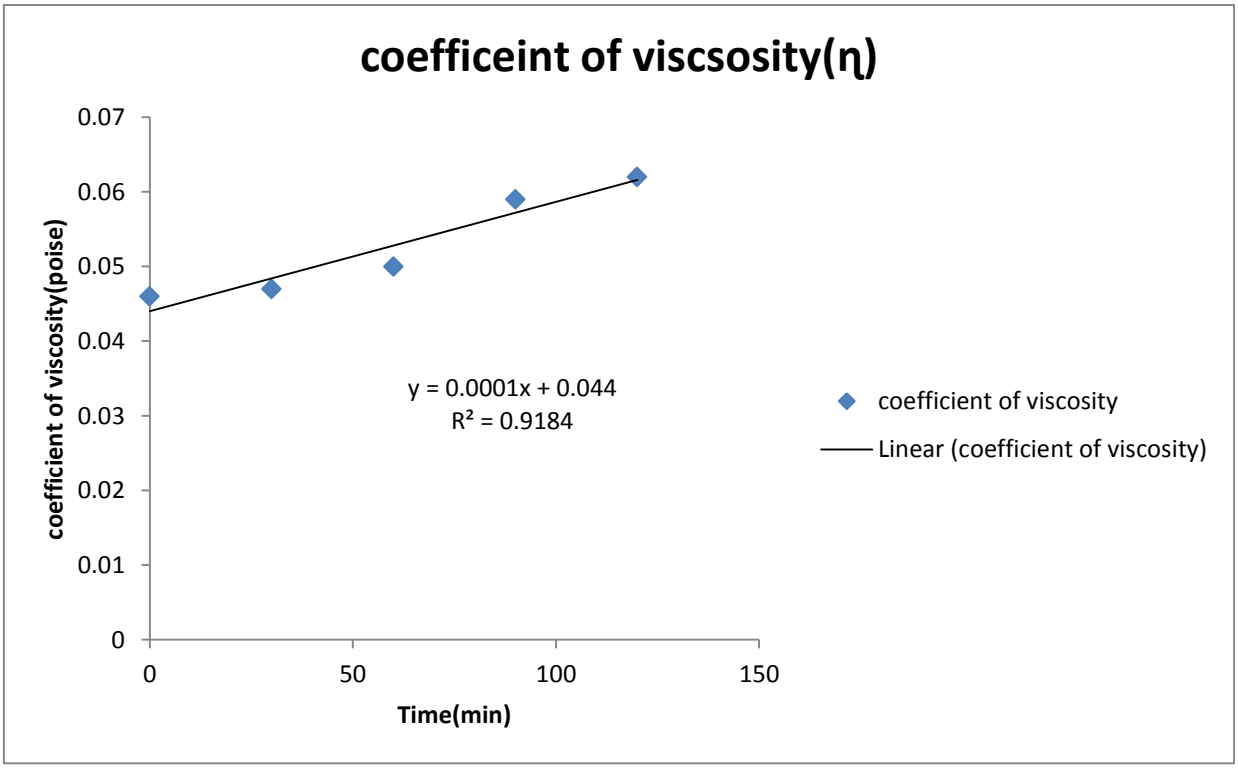

Fig 2 : Plot between Volume Flow Rate (Q) and time

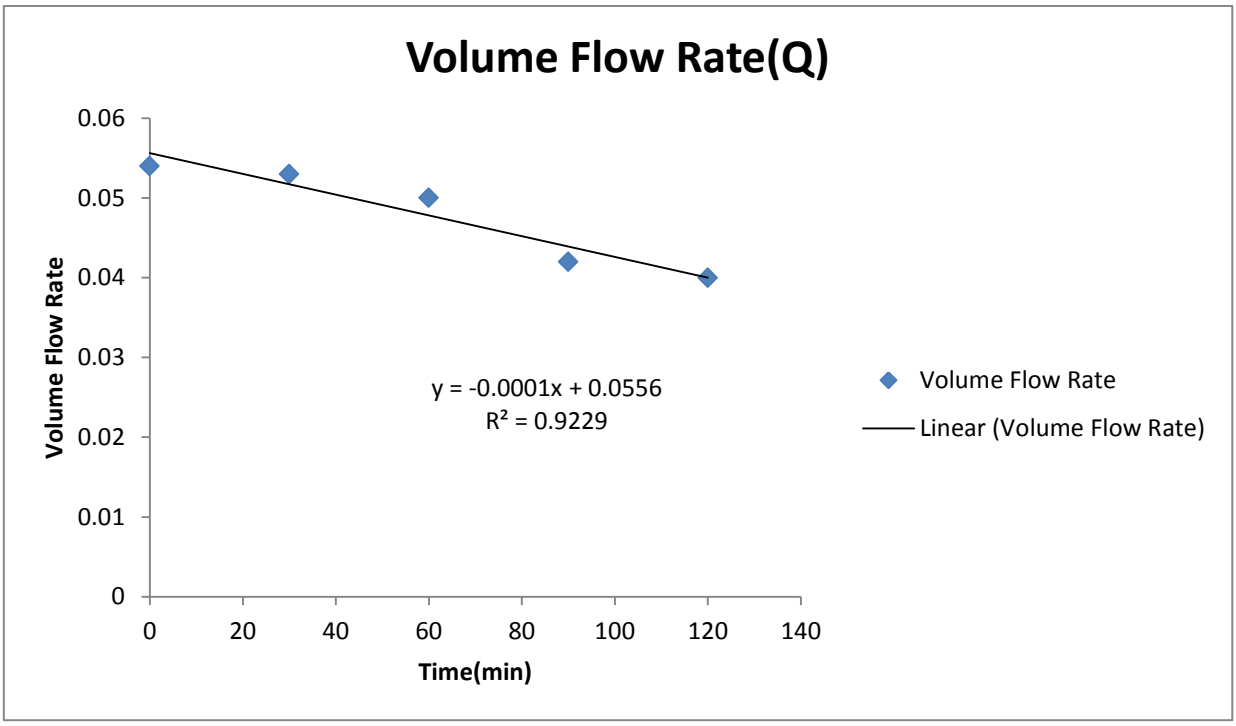

Fig 3 : Plot between Surface Tension(T) and time

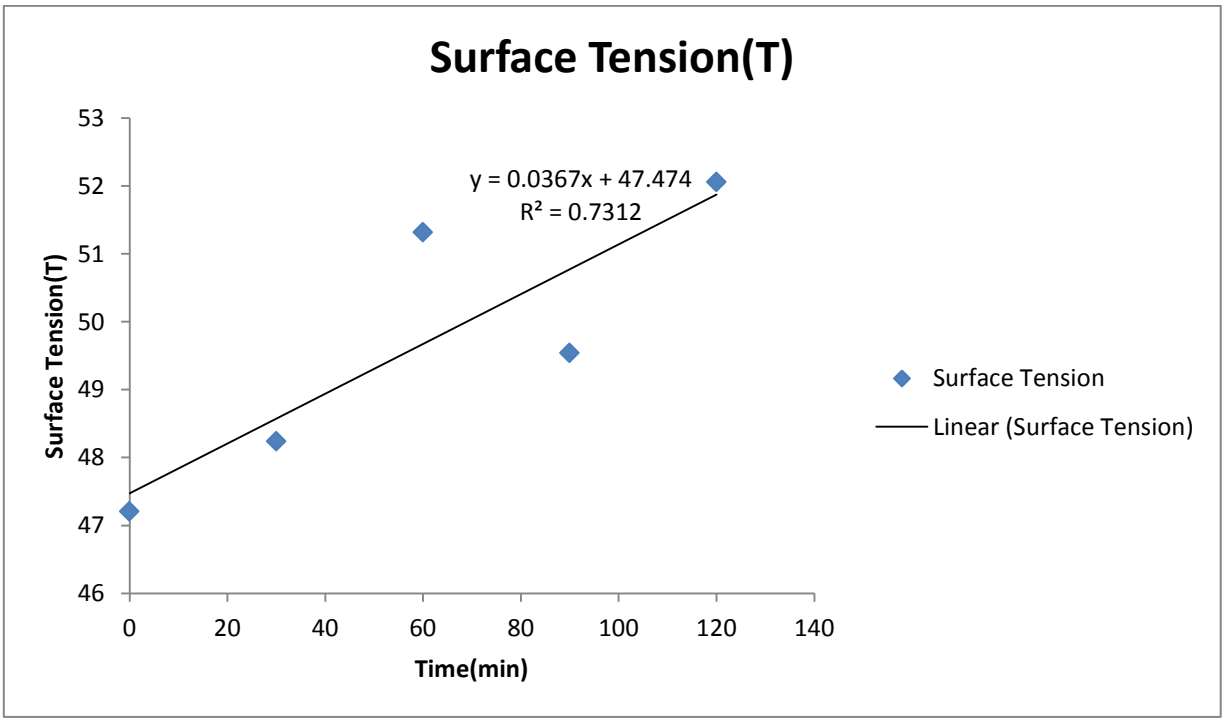

It is evident from Fig 1, 2 & 3 that the Coefficient of Viscosity and Surface tension increases linearly with exposure time whereas the Volume Flow Rate decreases.

The present study demonstrates that the erythrocyte membrane physiology is influenced due to the exposure of ultrasonic standing wave. The increase in Viscosity and decrease in Volume flow rate of ultrasonic irradiated sample may be due to aggregation of erythrocytes. The increase in Surface Tension of ultrasonic irradiated sample may be due to the changes in physical properties of Plasma.

REFERENCES:

1. Watchier , Fundamentals of Radiology Ed. G .Reimer ,Berlin (1939)
2. G. Gopal Krishna, A. Anwar Ali and Adeel Ahmad; Absorption of Ultrasound in Human Blood. Journal de Physique Colloques, (1990), 51 (C2), pp.C2-311-C2-314.
3. Chien S, Usami S, Taylor HM, Lundberg JL and Gregersen MI. Effects of hematocrit and plasma proteins on human blood rheology at low shear rates. J Appl Physiol. (1996) Jan; 21(1):81-87.
4. Somayeh Arian Rad, Kaleem Ahmed Jaleeli and Adeel Ahmad, Influence of EM radiation produced by mobile phone on viscosity of human blood. International journal of science, Environment and Technology, Vol.4, No.6 , (2015) 1469-1475.
5. Naresh Kaul ; A study on Rheological behaviour of blood: An alternate approach. Scholedge International Journal of Multidisciplinary and Allied studies. Vol.2, issue 6(June 2015) ISSN-2394-336X.
6. Barbee JH, The effect of temperature on relative viscosity of human blood, Biorheology, Vol.10 (1993), PP.1-5
7. Lowe GD, Lee AJ, Rumeley A Blood viscosity and risk of cardiovascular events: the endinburgh Artey study . Br J Haematol (1997); 96:168-173.
8. Sahar E, Hassein A & Hassan M MarzogaF .Occupational study of electric field on haematological parameters and biophysical blood properties for diagnosing anemia in rats. Int.J.Adv.Sci.Tech. Res., Vol.2 (2015), PP.143-155.
9. G.B. Thurston. Viscoelasticity of Human Blood. Biophysical Journal,(1972) 12(9):1205-1217.

Second National Conference on
RECENT ADVANCES IN APPLIED NANO MATERIALS
February 16-17, 2018 at Department of Physics, University College of Science, Saifabad, Osmania University, Hyderabad, Telangana State, India.

Development of graphene/CNT/polyaniline and graphene/TiO_2/polyaniline ternary nanocomposites for supercapacitor electrodes

Shubham N. Gadge, Rounak R. Atram, Bhawana A. Manekar, S ubhash B. Kondawar*
Department of Physics, Rashtrasant Tukadoji Maharaj Nagpur University, Nagpur – 440033, India
*Corresponding Author Email: sbkondawar@yahoo.co.in

Abstract: *Among the energy storage devices, supercapacitors exhibit ultrahigh capacitance, high power density, and long cycle due to electrodes made of nanostructure materials. Graphene, as a new emerging carbon material has attracted a lot of attention in energy storage field due to its intrinsic properties. To enhance the specific capacitance of the electrodes for supercapacitors, the combination of carbon nanostructure provides electric double layer charge (EDLC) capacitance and metal oxides or conducting polymers provide pseudo-capacitance have been synergistically used. In this paper, we report the synthesis of ternary graphene/carbon-nanotube/polyaniline (GCP) and graphene/TiO_2/polyaniline (GTP) nanocomposites via in-situ polymerization. As-synthesized nanocomposites have been characterized by scanning electron microscopy (SEM) and energy dispersive x-ray spectroscopy (EDX). Both the ternary nanocomposites have exhibited excellent electrochemical performance suitable for supercapacitors. When compared between the two nanocomposites, GCP exhibited more specific capacitance with high energy density than that of GTP measured in three electrode electrochemical cell with 1 M H_2SO_4. The specific capacitance even of GTP was found to be more than that of binary GP, CP and TP. Though a small amount of CNTs (1 wt.%) is added into graphene, the cycle stability of GCP nanocomposite is greatly improved due to provision of CNTs as conductive wires interconnected among GP particles. The high electrochemical performance of ternary nanocomposites can be attributed to well-designed nanostructure and the synergistic effect of the individual components.*

Key Words: *Nanocomposites; Graphene; Polyaniline; Carbon nanotubes, TiO_2; Electrochemical properties.*

1. INTRODUCTION:

Supercapacitors are new generation of energy storage devices because of fast charge/discharge, high power density and long cycle life compared with batteries and high energy density with large specific capacitance compared with conventional capacitor [1]. Depending on the charge storage mechanism and the active materials used, supercapacitors can be distinguished into Electric Double Layer Capacitors (EDLCs) and Pseudocapacitors. EDLCs store charge electrostatically like conventional capacitors while Psuedocapacitors involve electrochemical redox reaction to store the charge [2, 3]. Carbon has been widely employed as active material for EDLCs due to their very high surface area, high electrical conductivity, abundance, various dimensionalities from zero to three dimensions and more importantly, as environmentally friendly materials. On the other hand, transition metal oxides and electrically conducting polymers are examples of pseudo-capacitive active materials [4, 5]. Among different conducting polymers, polyaniline (PANI) has attracted persistent attention owing to its high pseudocapacitance, light weight, low cost, controllable electrical conductivity, high energy density, environmental friendliness, facile synthesis and fast doping/dedoping rate during charge/discharge process [6, 7]. However, conducting polymers suffer from poor long-term stability that reduces the initial performances due to the repeated swelling and shrinking during charging/discharging cycling [8]. To overcome the poor cycling stability of conducting polymers during charge/discharge processes, much attention has been devoted to the preparation of hybrid electrodes by combining PANI with carbon nanomaterials [9, 10]. Among various carbon materials such as activated carbons, templated carbons, carbide-derived carbons, onion-like carbons, and carbon nanotubes (CNT); graphene has received intensive interest as a new electrode material because of its large surface area, high intrinsic electrical conductivity, and excellent mechanical flexibility [4,11,12]. Each kind of material has its own advantages and disadvantages. Single conducting polymer-based electrodes can provide large specific capacitance, which is substantially larger than that of conventional carbon-based electrodes and comparable to metal oxide-based electrodes. Unfortunately, they suffer from large volumetric swelling and shrinking during charging/discharging processes, which usually leads to structural break down and fast capacitance decay [13]. Metal oxides have excellent property of energy storage which is

responsible for psuedocapacitance, however, they suffers low conductivity [14]. To achieve high performance of SCs by overcoming the cycling instability of single conducting polymer-based electrodes and to improve energy storing capacity it is required to design new hybrid electrode materials to combine EDL capacitance together with fast and highly reversible pseudocapacitance [15, 16]. Considering high surface area of graphene, high energy storage capacity of metal oxide (TiO_2) and conducting nature of polymer polyaniline (PANI), we have prepared graphene/CNT/polyaniline (GCP) and graphene/TiO_2/PANI (GTP) ternary nanocomposites which can be suitable material for the fabrication of supercapacitor electrodes.

2. EXPERIMENTAL:

Functionalization of graphene and CNT

The functionalization of CNTs and graphene is an effective way to prevent their aggregation, which helps to better disperse and stabilize them within a polymer matrix. The carbon nanotubes and graphene were separately functionalized by following typical process. 100 ml solution 6M Sulphuric and Nitric acid each in 3:1 ratio mixed together and stirred for 10 minutes. Graphene and CNTs were added to the mixture and stirring continued for next 10 minutes. This mixture was then sonicated for 4 hours. To remove excess acid, it was centrifuged first and then washed with double distilled water and filtered. The filtrate was then dried for 24 hours at 50 ^oC to get functionalized graphene and CNTs.

Synthesis of graphene/CNT/polyaniline (GCP)

The GCP nanocomposite was synthesized by an in-situ chemical oxidative polymerization. In a typical process, 0.1 g of functionalized graphene (GN) and 10% wt i.e. 0.01 g of CNTs were added to 60 ml deionised water and sonicated for 2 hrs. 0.25 M of aniline monomer solution with 1M HCl was prepared in 60 ml deionised water and stirred for 15 minutes. This solution was added into the graphene/CNT solution with constant stirring and the mixture was again sonicated for 30 min. The 0.25M APS solution was prepared by dissolving required amount of APS into 25 ml distilled water and added drop wise to Aniline/HCl-CNT/graphene mixture solution for 30 min with constant stirring. The stirring was continued for 4 hrs and then kept standing for overnight to obtain polymerized dark-green precipitate. The polymerized solution was then filtered and washed several times with distilled water until the filtrate became acid free, and then washed with acetone, ethanol and methanol. The precipitate was dried in an vacuum oven at 80°C for 12 h to obtain GCP nanocomposite.

Synthesis of TiO_2 nanoparticles

Titanium dioxide nanoparticles were derived from sol–gel process using titanium tetra isopropoxide (TTIP) as precursor. TTIP was dissolved in ethanol and then mixed with water keeping the ratio of TTIP to water as 1:4. The prepared solution was kept under constant stirring on magnetic stirrer at low speed for about 2 hours. Nitric acid (HNO_3) was added drop wise to adjust pH value in acidic range. The rate of hydrolysis is affected by the pH value. A clear yellowish homogeneous transparent stable solution was obtained. The prepared sol was kept 2 hrs for gel preparation at room temperature. The gel was filtered and dried at 110 ^oC for 6 Hrs. The yellow crystals of titanium dioxide were obtained at the end of drying process. These crystals were crushed into fine powder and calcined at 600 ^oC and TiO_2 nanoparticles were formed [17].

Synthesis of graphene/TiO_2/PANI (GTP)

The GTP nanocomposite was prepared by mixing GN and TiO_2 nanoparticles followed by polymerisation. 0.1 g of functionalized GN and 0.1 g of TiO_2 nanoparticles were mixed in 100 ml deionised water and sonicated for 2 hrs. Then the solution was polymerised by the same route as used in the case of GCP nanocomposite.

3. RESULTS AND DISCUSSION:

The SEM images of GCP, TiO_2 and GTP are shown in Figure 1. From the SEM images it is confirmed that the flakes of graphene are clearly seen. Since, CNTs were of only 10 wt% of GN, therefore in GCP, PANI has been mostly covered up GN which might have been interconnected by CNT. In case of GTP, the TiO_2 particles and PANI encapsulated GN is observed. Small TiO_2 particles are distributed on the surface of PANI. From SEM image of TiO_2 particles, it has been observed that the spherical shaped nanoparticles in cluster form are seen. To investigate the chemical composition of the especially in GTP composite to identify the presence of TiO_2, an energy dispersive x-ray spectroscopy was performed by SEM-EDS instrument. From the results of the EDS, energy peaks for carbon, Ti and oxygen are clearly observed indicating the formation of GTP composite.

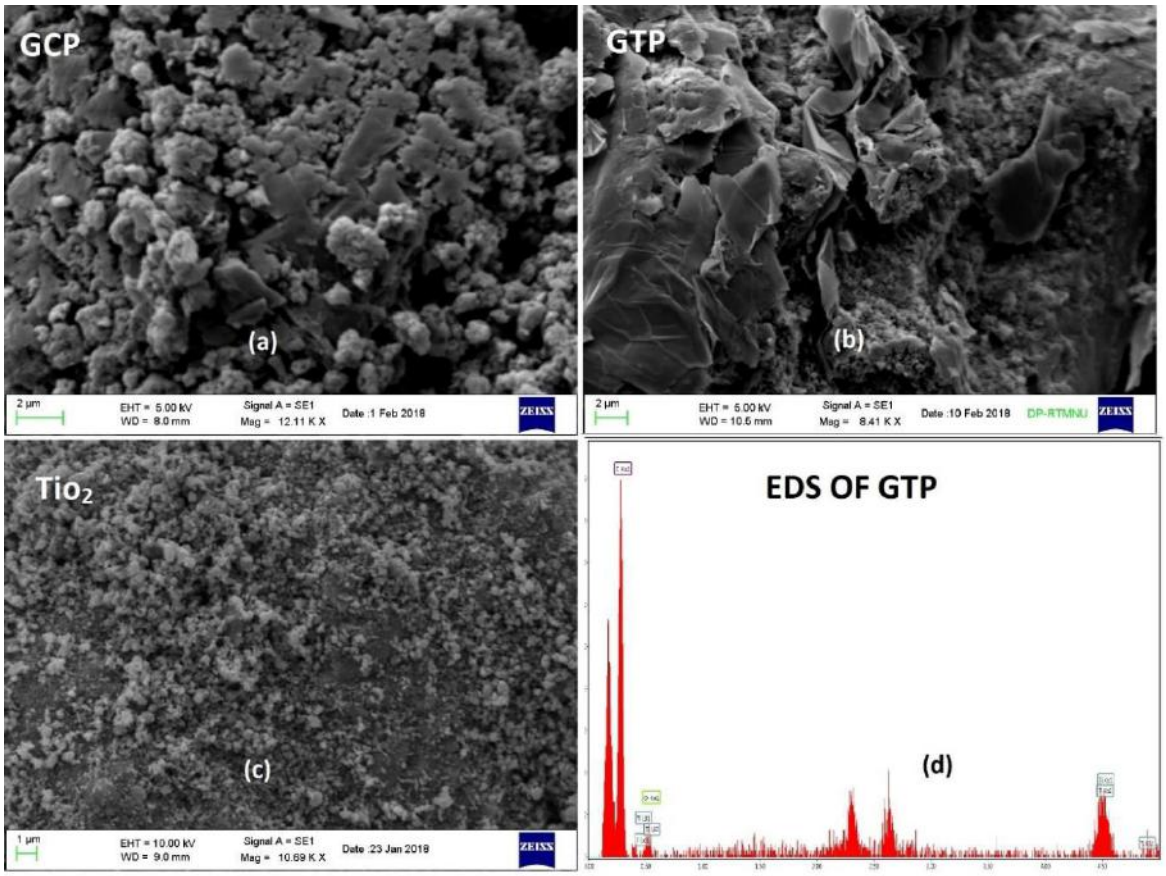

Fig. 1: SEM images of GCP (a), GTP (b), TiO_2 (c) and EDS of GTP (d)

The as-prepared composites were tested for electrochemical performance and the specific capacitance of GCP and GTP was determined from cyclic voltammetry. A three-electrode cell system was used to perform cyclic voltammetry (CV) at room temperature with the electrolyte 1 M H_2SO_4. A platinum electrode and Ag/AgCl electrode were used as the counter and the reference electrodes, respectively. CV of GCP and GTP are shown in Figure 2.

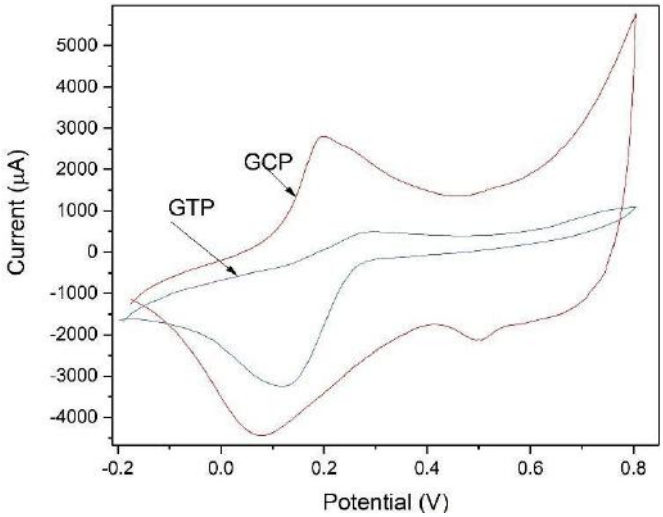

Fig. 2: Cyclic voltammetry of GCP and GTP

Specific capacitance and energy density of GCP were found to be 406 Fg^{-1} and 56.38 Wh Kg^{-1} respectively. On the other hand the specific capacitance and energy density of GTP were found to be 349 Fg^{-1} and 48.47 Wh Kg^{-1} respectively. From the results obtained, it has been confirmed that and the specific capacitance for GTP is found to be 349 Fg^{-1} and its energy density is found to be 48.47 Wh Kg^{-1}. Thus, from the results, GCP exhibited more specific capacitance with high energy density than that of GTP. Though a small amount of CNTs is added into graphene, the cycle stability of GCP nanocomposite is greatly improved due to provision of CNTs as conductive wires interconnected among GP particles. The high electrochemical performance of ternary nanocomposites can be attributed to well-designed nanostructure and the synergistic effect of the individual components.

4. CONCLUSION:

In this paper, we reported a facile strategy for the synthesis of ternary nanocomposites for supercapacitor electrodes. The characterization results show that the integrated composites are composed of graphene, carbon nanotubes, titanium dioxide and polyaniline. Significantly, the intimate and cross binding of the components produced a synergistic effect and afforded facile electron transport among CNTs. GCP showed high specific capacitance compared to that of GTP. These intriguing features make GCP nanocomposite a promising material in supercapacitors or other energy source system.

REFERENCES:

1. M. Hwang, J. Oh, J. Kang, K. Seong, Y. Piao, Enhanced active sites possessing three-dimensional ternary nanocomposites of reduced graphene oxide/polyaniline/Vulcan carbon for high performance supercapacitors, Electrochimica Acta 221 (2016) 23–30.
2. P. Simon, Y. Gogotsi , Materials for electrochemical capacitors, Nature Materials, 7, (2008) 845-854.
3. M. Tran, H. Jeong, Ternary carbon composite films for supercapacitor applications, Chemical Physics Letters 684 (2017) 1–7.
4. Li. Zhanga, X. Zhao, Carbon-based materials as supercapacitor electrodes, Chem. Soc. Rev., 38 (2009) 2520-2531.
5. P. Basnayakaa, M. Ramb, E. Stefanakosb, A. Kumar, Supercapacitors based on graphene -polyaniline derivative nanocomposite electrode materials, Electrochimica Acta 92 (2013) 376– 382.
6. C. Li, H. Bai,G. Shi, Conducting polymer nanomaterials: electrosynthesis and applications, Chem. Soc. Rev., 38, (2009) 2397–2409.
7. C. Meng, C. Liu, L. Chen, C. Hu, S. Fan, Highly Flexible and All-Solid-State Paperlike Polymer Supercapacitors, Nano Lett. 10, (2010) 4025–4031.
8. J. Yan,Q. Wang,T. Wei,Z. Fan, Recent Advances in Design and Fabrication of Electrochemical Supercapacitors with High Energy Densities, Adv. Energy Mater. 4, (2014) 1300816.
9. K. Zhang, L. Zhang, X. Zhao, J. Wu, Graphene/Polyaniline Nanofiber Composites as Supercapacitor Electrodes, Chem. Mater., 22, (2010) 1393.
10. Y. Wang, X. Yang, L. Qiu, D. Li, Revisiting the capacitance of polyaniline by using graphene hydrogel films as a substrate: the importance of nano-architecturing, Energy Environ. Sci., 6, (2013) 477–481.
11. Y. Tana, J. Lee, Graphene for supercapacitor applications, J. Mater. Chem. A, 1, (2013) 14814-14843.
12. N. Mahmood,C. Zhang, H. Yina, Y. Hou, Graphene-based nanocomposites for energy storage and conversion in lithium batteries, supercapacitors and fuel cells, J. Mater. Chem. A, 2, (2014) 15-32.
13. G. Wang, L. Zhang, J. Zhangb, A review of electrode materials for electrochemical supercapacitors, Chem. Soc. Rev., 41, (2012) 797–828.
14. Y. Hou, Y. Cheng, T. Hobson, J. Liu, Design and Synthesis of Hierarchical MnO_2 Nanospheres/Carbon Nanotubes/Conducting Polymer Ternary Composite for High Performance Electrochemical Electrodes, Nano Lett. 10, (2010) 2727–2733.
15. G. Yua, X. Xieb, L. Pand, Z. Baod, Y. Cui, Hybrid nanostructured materials for high-performance electrochemical capacitors, Nano Energy, 2, (2013) 213–234.
16. G. Yu, L. Hu, N. Liu, H. Wang, M. Vosgueritchian, Y. Yang, Y. Cui, Z. Bao, Enhancing the Supercapacitor Performance of Graphene/MnO_2 Nanostructured Electrodes by Conductive Wrapping, Nano Lett. 11, (2011) 4438–4442.
17. V. Kaler, R. K. Duchaniya, and U. Pandel , Synthesis of Nano-titanium dioxide by sol-gel route, AIP Conference Proceedings 1724, (2016) 020127.

Second National Conference on
RECENT ADVANCES IN APPLIED NANO MATERIALS
February 16-17, 2018 at Department of Physics, University College of Science, Saifabad, Osmania University, Hyderabad, Telangana State, India.

Adsorption kinetics for removal of methyl orange dye from aqueous solution by polyaniline based nanocomposites

Sunita C. Manwatkar, Neha V. Nerkar, Subhash B. Kondawar*
Department of Physics, Rashtrasant Tukadoji Maharaj Nagpur University, Nagpur – 440033
*Corresponding Author Email: sbkondawar@yahoo.co.in

Abstract: *Mobility and distribution of dyes in water have been studied extensively due to their effects on environment and other living organisms. Metal oxides and carbon based materials have been continuously used for dyes removal. In this paper, we report the preparation of polyaniline (PANI) based nanocomposites by in-situ chemical oxidation polymerization and the removal of methyl orange (MO) from aqueous solution by using chemical interaction of dye molecule with PANI/TiO_2 and PANI/graphene nanocomposites. Morphology and adsorption kinetics of as-synthesized nanocomposites were studied by scanning electron microscopy and UV-Vis spectroscopy respectively. Percentage of removal of MO dye for PANI/TiO_2 and PANI/graphene was found to be 70% and 65% respectively compared to that of 53% for pure PANI. In order to evaluate adsorption kinetic, the pseudo first order model, pseudo second order model and intra particle diffusion model were tested for their validity by linear equation analysis. The second-order kinetic model was found to be the best linearity for both the nanocomposites compared to other models which indicate that the adsorption of dye is a physical adsorption. The adsorption process was shown to be an efficient for dye removal from water solutions.*

Key Words: *Polyaniline; Nanocomposites; Titanium dioxide; Graphene; UV-Vis spectroscopy, Methyl orange dye.*

1. INTRODUCTION:

In the recent years the distribution of dyes in water have been studied extensively due to their toxic effects to humans, animals, plants and the aquatic organisms. Many of the industries, such as dyestuffs, textile, paper, leather, foodstuffs, cosmetics, rubber and plastics are using much quantity of synthetic dyes in order to give colour for their products and consume substantial volumes of water. As a result, they generate a considerable amount of coloured wastewater [1] . Textile and dyeing industry are among important sources for the continuous pollution of the aquatic environment. Because they produce approximately 5% of total effluents. The textile and dyeing industries effluents are discarded into rivers, ponds and lakes; they affect the biological life various organisms. Dye-containing effluents are undesirable wastewaters because they contain high levels of chemicals, suspended solids, and toxic compounds. Colour causing compounds can react with metal ions to form substances which are very toxic to aquatic habitat and cause many water borne diseases [2]. Dyes are water soluble and non- degradable due to which they are resistant to many materials which limits its removal from water once released into water. Many of the methods are available for the removal of pollutants from water, the most important of which are reverse osmosis, ion exchange, precipitation and adsorption. Of these methods, adsorption technique is a most simple and widely used technique also inexpensive in nature [3]. Metal oxide and activated carbon have been widely used for removal of coloured effluents. TiO_2 and ZnO are metal oxide with nearly same electron affinity so as they are used more for the removal. While CNT's and graphene are carbon based material used for same purpose. The main disadvantage of carbon based materials is that are very expensive. Both Metal oxide and carbon based materials have limitations for removal of dye, this has led many researchers to search for inexpensive and locally available adsorbents so that Photocatalytic activity can be enhanced [3,4]. New organic / inorganic composites have been developed for better removal of dye. One class of such hybrid material is conducting polymer such as Polyaniline (PANI), Polypyrole etc. It is hoped to obtain new composite with synergetic or complementary behaviour between polymer and inorganic substance. The properties of hybrid material become more pronounced if one of the factors goes to nanomaterial scale. PANI has many properties such as low cost, good environmental stability, good electrical conductivity also it provide proper binding site for the adsorption of dye molecules. PANI when composed with inorganic/ organic material improves processability of material [5].

In this paper, we report comparative study of polyaniline/ TiO2 and polyaniline/ graphene can remove anionic (sulfonated) dyes with the application of UV and visible light through a chemical interaction with the sulfonated dyes [6,7] . Thus, the objective of the article is to examine the use of polyaniline/ TiO2 and polyaniline/ graphene composites for the removal of various sulfonated dyes from aqueous solutions and propose a mechanism of chemical interaction between the sulfonated dyes and PANI/ TiO2 and PANI/graphene. Methyl orange is intensely coloured compound used in dyeing and printing textiles. It is also known as C.I. acid orange 52. Chemist used methyl orange as an indicator of weak bases with strong acids. It is water soluble azo dye. It is carcinogenic and mutagenic in nature and hence it has bad impact on nature as well as human habitat.

2. EXPERIMENTAL:

Preparation of PANI-TiO_2 and PANI-GNS nanocomposites

A typical oxidative polymerization method was carried out for polymerization of aniline in the presence of TiO_2 nanoparticles. TiO_2 nanoparticles (0.9313 g) were dispersed by ultrasound in 50ml aqueous solution of aniline monomer (0.2 M) and hydrochloric acid (1M). Aps (0.25M) was dissolved in 50ml de-ionized water and was added drop wise to the mixture of TiO2 and aniline monomer with stirring polymerization proceeded for 6hr. The nanocomposites of PANI with TiO_2 nanoparticle was obtained as precipitate. This precipitate was isolated by filtration, washed with distilled water and ethanol several times and dried at 50 ^{0}C. For PANI-GNS nanocomposites, firstly graphene was functionalized by using mixture of HCl and HNO_3 in 3:1 proportion, and same process of polymerization was followed.

3. RESULTS AND DISCUSSION:

Morphological studied have been done by SEM technique, Fig. 1 shows SEM images for PANI/ TiO_2 and PANI/GNS. PANI/graphene shows smooth layer of PANI coats on layers of functionalized graphene. It increases the dye adsorptivity of PANI/graphene. PANI/ TiO2 image shows incorporation of smooth PANI layer on TiO2 for the formation of core shell type structure. This increases surface area and shows more attraction towards dye molecules [8, 9]. So from morphological view it is clear that in corporation of PANI into metal oxide and graphene increases its adsorptivity by increasing surface area.

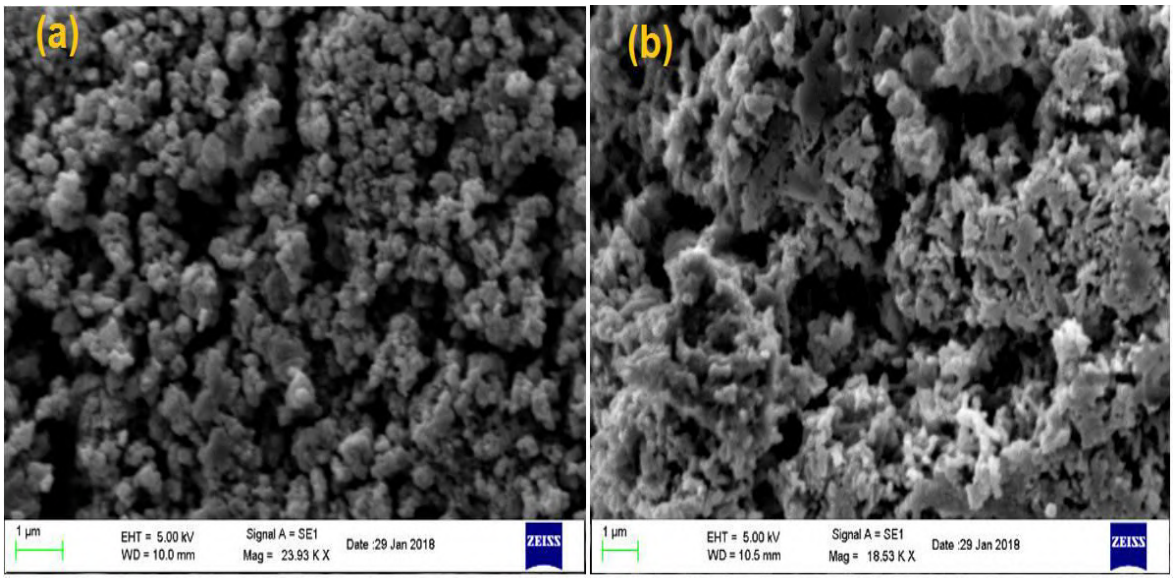

Fig. 1: SEM images of (a) PANI/ TiO_2 and (b) PANI/GNS

UV-Vis spectra were recorded by using LMSP UV-1200 single beam UV- Spectrophotometer and the Photodegradation experiment was carried out. Dye concentration was taken as 100mg/L prepared in de-ionized water and the mixture was stirred and reading were taken after each 15 min and experiment was carried up to equilibrium.

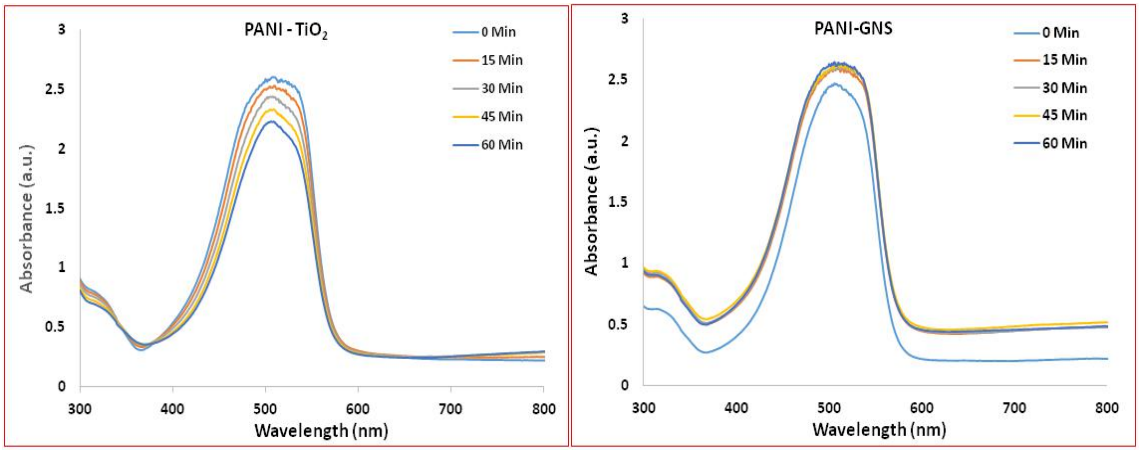

Fig. 2: UV-VIS spectra of (a) PANI/ TiO_2 and (b) PANI/GNS

The characteristic peak of 510 nm in case of PANI/ TiO_2 and 514 nm in case of PANI/GNS assigned to the n-π^* transition from the nonbonding nitrogen lone pair to the conduction band. This peak shows high absorbance with the presence of methyl orange in the solution. With respect to time, the absorbance was found to be decreased. PANI-TiO_2 absorbed more methyl orange compared to that of PANI/GNS. It is well known that the degree of ionization of a dye molecule depends on the pH of the aqueous medium. Methyl orange contains one sulfonated group (-SO_3Na). In acidic aqueous solutions, the functional group of methyl orange (-SO_3Na) gets ionized, and the dye exists in anionic form. When PANI/TiO_2 and PANI/graphene nanocomposites are added to water, the pH of the water becomes acidic (pH= 3.9) and does not change during the course of adsorption. The addition of dyes with sulfonated functional groups to this aqueous solution results in the dissociation of the functional group into its anionic form. The percentage removal of dyes was calculated by equation (1)

$$percentage\ of\ removal = \frac{(C_o - C_e)*100}{C_e} \qquad (1)$$

Where, C_o = Initial concentration and C_e= final concentration

In order to evaluate kinetic mechanism which controls the process pseudo first order model, pseudo second order model and intraparticle diffusion model is tested and the validity of the models were verified by the linear equation analysis $\log(Q_e - Q_t)$ vs time [20, 21]. The pseudo-first-order rate equation is given by equation (2)

$$\log(Q_e - Q_t) = logQ_e - \frac{k}{2.303}t \qquad (2)$$

Where Q_e and Q_t (mg g^{-1}) refer to the amount of dye adsorbed at equilibrium and time t (min), respectively, and k is the rate constant. It is found to be 0.166 min^{-1}. Fig 3 shows the plot of the pseudo-first-order for **PANI/TiO_2 and PANI/GNS** nanocomposites. The pseudo-second-order model can be represented by equation (3);

$$\frac{t}{Q_t} = \frac{1}{k_2}Q_e^2 + \frac{t}{Q_e} \qquad (3)$$

Where k_2 is the rate constant (0.166) of the pseudo-second-order model (g $mg^{-1}min^{-1}$). Fig 4 shows the curve-fitting plot of (t/Qt) vs time PANI/ TiO_2 and PANI/GNS nanocomposites.

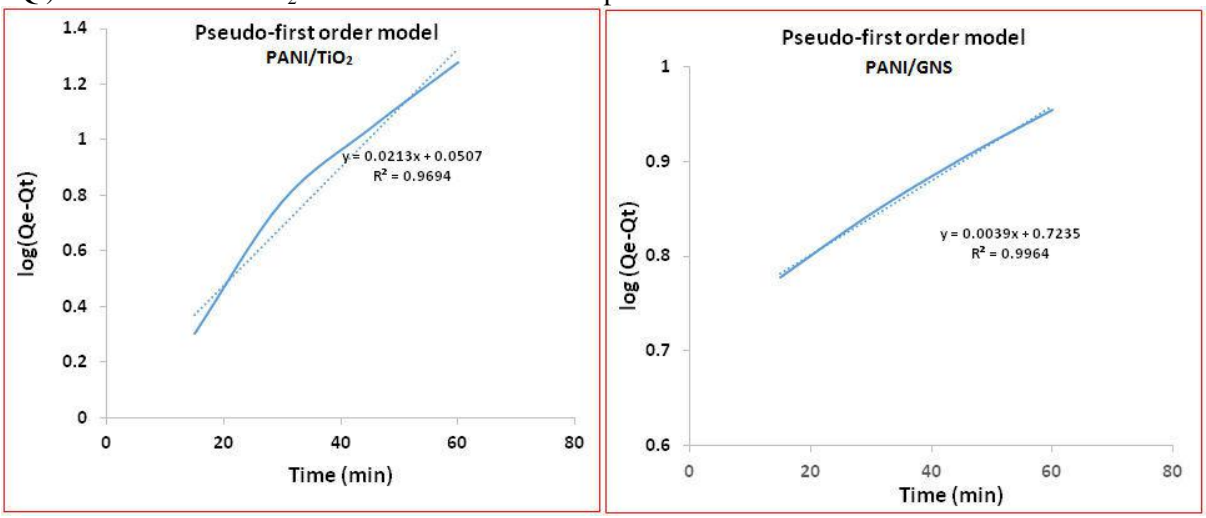

Fig. 3: Pseudo-first-order for plot of (t/Qt) vs time PANI/ TiO_2 and PANI/GNS nanocomposites

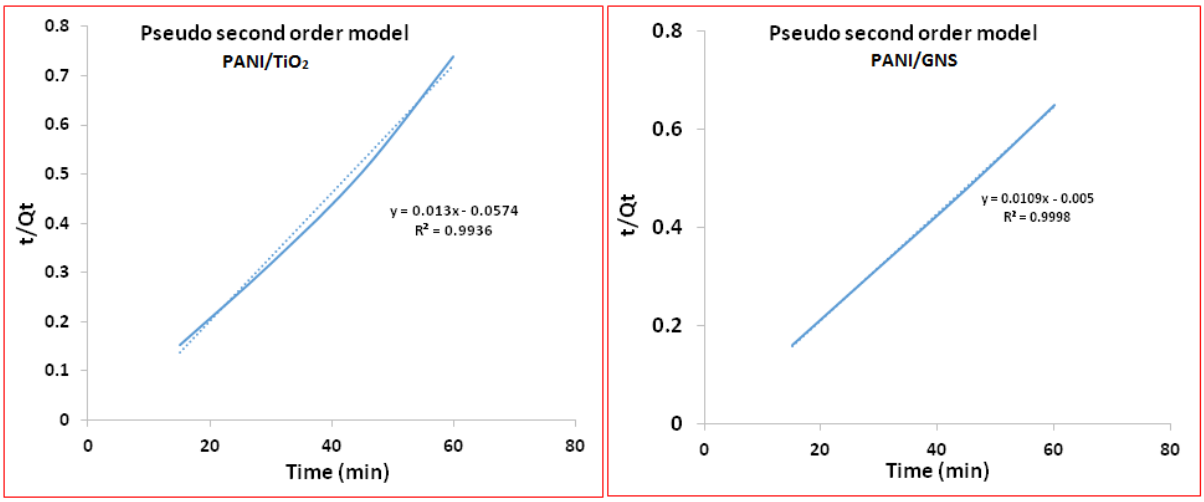

Fig. 4: Curve-fitting plot of (t/Qt) vs time PANI/ TiO_2 and PANI/GNS nanocomposites

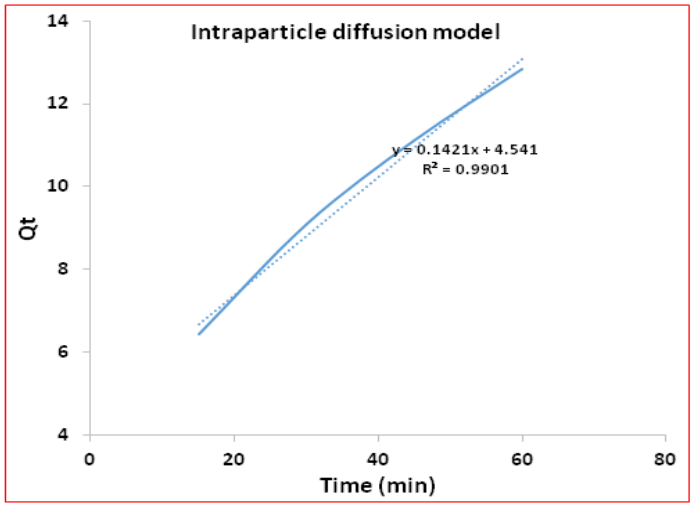

Fig. 5: Intraparticle diffusion model for nanocomposites

4. CONCLUSIONS:

A nanostructured core shell structure of PANI/TiO_2 and layered structure of PANI/ graphene has been successfully synthesized by in situ polymerization. Photocatalytic degradation of MO dye by use of the PANI/TiO2 and PANI/graphene nanocomposite was achieved under visible light irradiation. The nanostructured PANI/ TiO_2 core–shell nanocomposite system prepared in this study has greater photocatalytic activity than PANI/graphene system. For PANI/TiO_2 percentage removal is about 70% while in PANI/graphene shows 65% removal. Further it can be increase by increasing weight percent of PANI/ TiO_2.

REFERENCES:

1. A. S. Ozacan, A.ozacan:" Adsorption of acid dyes from aqueous solutions onto acid-activated bentonite" J. colloid Interf. Sci.276 (2004): p.39-46.
2. E. Forgacs, C. Tibor, and O. Gyula: "Removal of synthetic dyes from wastewaters" Environ. Int. vol.30 (2004) p. 953-971.
3. G. Annadurai, M. Chellapandian, and M. Krishnan" Adsorption of reactive Chitin" Environ. Moni. Vol.59 (1999) p. 111-119.
4. D. Mahanta, M. Giridhar, S. Radhakrishanan and P. satish" Adsorption and desorption kinetics of anionic dyes on doped polyaniline" J. Phys. Chem B113 (2009): p. 2293-2299
5. N.V. Nerkar, S.Kargirwar, S. B. Kondawar, D.V. Burghate And P. D, Burghate" Ultrasonicated organic acid doped polyaniline nanotubes for anionic dye detection in waste water" Int Symp, Ultra. Vol. 22(24) 2015: p. 195-198.
6. G. Hitkari, S. Sing and G. Pandey" Synthesis, Characterization and Visible Light Degradation of Organic dye by Chemically Synthesized ZnO/γ-Fe3O4 Nanocomposites" Int. J. of Advance research in sci.,eng, and tech. : vol 4 (2017) : p, 3960-3965.

7. B. Pant, H.Pant, A.M. Barkat, M. Park, K. Jeon, Y. Choi, H. Kim "Carbon nanofibers decorated (TiO2/ZnO) nanocomposites for the effective removal of organic pollutants and the enhancement of antibacterial activities" ceramic Int. : vol. 39 (2013) : p. 7029-7035
8. R. Saravanan, S. Karthikeyan, V.K. Gupta, G. Sekaran, V. Narayanan and A. Steapha n" Enhanced photocatalytic activity of ZnO/CuO nanocomposite for the degradation of textile dye on visible light illumination" Mate. Sci. and eng.vol.C33 (2013)
9. B. Agarwal, T. Das, S. Baruah. "Improvement of photocatalytic activity of Zinc Oxide nanoparticles using Zinc Sulphide Shell" ADBU J. Of Eng.vol.4 (2016).p.175-180
10. O. Mekasurwandumrong, P. Pawnirat, P. Praserthdam, J. Panpranot "Effects of synthesis conditions and annealing post-treatment on the photocatalytic activities of ZnO nanoparticles in the degradation of methylene blue dye"Chem. Eng. J. : vol.164 (2010) p. 77-84
11. M. Anjum, M. Oves, R, Kumar, MA. Barakat"Fabrication of ZnO-ZnS@ polyaniline nanohybrid for enhanced Photocatalytic degradation of 2- chlorophenol and microbial contamination in waste water"International Journal Biodeterioations and Biodegradation : vol.119 (2017):p.66-77
12. M. Gadyal and K. Venkatesh "Synthesis of Polyaniline-Graphite Nano-Composites"mater. Sci. Rearch : Vol 12 (2015) :p.85-88
13. R. Ahmad, I. Hasan "Efficient remediation of an aquatic environmental contaminated by Cr (VI) and 2,4-Dinitrophenol by XG-g_Polyaniline@ZnO nanocomposites " J. Chem. Eng.data 62 (5)(2017): p. 1594-1602
14. M. Saad , H. Tahir , J. Khan, U. Hameed, A. Saud "Synthesis of polyaniline and their application for removal of crystle violet dye by ultrasonicated adsorption process on surface response methodology" ultrasonic sonochemistry 34 (2017) :p.600-608
15. R. Kobiraj, N, Gupta, A. Kumar Kushwaha, M. Chattopadhyay "Photodegradation of Binary Azo Dyes Using Core-Shell Fe3O4/SiO2/TiO2 Nanospheres" Ind. J. of Chem and tech. 19 (2012) p. 26-31
16. R. Ansari,and Z. Mosaycbzadeh "Removal of Eosin Y, an Anionic Dye, from Aqueous Solutions Using Conducting Electroactive Polymers" Irranian poly. J. 19(2012) p. 26-31
17. H. Qiu, L. Lv, B.Pan, Q. Zhang, W. Zhang, Q. Zhang"Critical review in adsorption kinetic models" Journal of Zhejiang University-Science A. vol.10 (2009).p.716-724
18. YS Ho, Gordon, Mc Kay,"A comparison of chemisorption kinetic models applied to pollutant removal on various sorbents" Process safety and environ. Protection. vol,76.(1998).p.332-340
19. KY Foo, BH Hameed." Insights into the modeling of adsorption isotherm systems" Chemical Engineering Journal vol.156(2010).p. 2-10
20. F.Wu,R. Tseng,R.Juang,"Initial behavior of intraparticle diffusion model used in the description of adsorption kinetics"Chemical Engineering Journal. Vol.153 (2009), p. 1-8
21. J. Lin, L. Wang."Comparison between linear and non-linear forms of pseudo-first-order and pseudo-second-order adsorption kinetic models for the removal of methylene blue by activated carbon" Frontiers of Environ. Sci. & Eng. in China. Vol.3 (2009) .p.320-324

Second National Conference on
RECENT ADVANCES IN APPLIED NANO MATERIALS
February 16-17, 2018 at Department of Physics, University College of Science, Saifabad, Osmania University, Hyderabad, Telangana State, India.

A Comparative FTIR Spectroscopic study on Scapular Cartilage of Camel, Goat and Ox

R. Gangadhar, Kaleem Ahmed Jaleeli and Adeel Ahmad
Biophysics Research Laboratory, Department of Physics, Nizam College (Autonomous),
Osmania University, Hyderabad – 500 001, India
E-mail: dr_adeelahmad@yahoo.com, gangadharphd@gmail.com

Abstract: *The paper reports FTIR data on scapular cartilage of Camel, Goat, and Ox. The study reveals that scapular cartilage consists of mainly collagen and proteoglycans but very less quantity of carbonate and phosphate ions. The FTIR spectroscopy of scapular cartilage powder indicates the presence of bands characteristics of phosphate ion, carbonate ion, water molecule and also some functional groups concerned with protein.*

Key Words: *Scapular Cartilage, Collagen, Camel, FTIR.*

1. INTRODUCTION

Infrared spectroscopy is a potential tool to provide valuable information in the study of biological systems. It is very much helpful in the study of structure of various macromolecular components and their conformations within tissue. In most of the cases, infrared spectroscopy gives rapid qualitative and quantitative identification of organic and inorganic constituents and their combinations in mineralized biological tissues.

Articular cartilage is a connective tissue that covers the end of long bones. The function of articular cartilage is to distribute and absorb contact stresses during joint loading and to provide an almost friction less articulation between bones [1-3]. The possibility to modify the secondary structure of SF has also been acknowledged as a strategy to achieve desirable material properties. The conformation transition of SF with the formation of anti-parallel β-sheets allows improvement of cell adhesion, due to the change in surface roughness, the stiffness of the scaffold and the tailoring of degradability [4–6],[7] reports IR spectroscopic data of edible and medicinal oils of plant origin. For IR analysis, tenedible oils and fifteen medicinal oils were selected. FTIR spectra were recorded. The FT – IR spectra of edible and medicinal oils show a series of bands with different intensities and reveal the composition of fatty acids and degree of saturation of the selected oils.[8] Reported that the characteristic spectral bands pertaining to fibrinogen, hemoglobin, erythrocyte m embrace lipids and other plasma proteins are identified.[9]FTIR spectroscopy techniques are powerful methods to obtain relevant information for understanding protein adsorption to surfaces. Protein quantitation and different interaction studies can be achieved by specific vibration bands associated with chemical groups and proper correlation curves in FTIR spectroscopy. The two dominant bands in any protein's absorbance FTIR-spectrum are the amide I and amide II absorptions.[10,11] Egg shell corresponds to 11% of the total weight of an egg. These eggshells mainly contain calcium carbonate (91% - 94%), calcium phosphate (1%) and other organic matters, which make it preferable for synthesizing CaO.

A search of literature reveals that in spite of extensive investigations on infrared spectroscopy of human skin, hair, nail, bone and collagen on different aspects and their constituents such as lipids and proteins, no information is available on qualitative and quantitative identification of organic and inorganic constituents and their combinations of scapular cartilage. In view of this, in the present investigation, infrared spectroscopic study has been made on scapular cartilage, in order to assess its molecular composition.

2. MATERIALS AND METHODS

The cartilage samples of scapula of the animal Ox,Goat,Camel were collected from beef shop after 4 to 5 hours of slaughtering. The samples were cleaned, flesh attached to them was removed completely and then Sun dried for a day or two. FTIR spectra of powdered samples were recorded with Thermo - Nicolet Nexus 670 FTIR spectrometer and depicted in Fig. 1,2,3. Thedata obtained from FTIR spectra is presented in Table 1.

3. RESULT AND DISCUSSION

Fig.1,2,3is FT – IR spectrum of Ovine scapular cartilage, which reveals a series of bands with different intensities. Table 1 presents data on wave numbers and corresponding Transmittance (%) obtained from FTIR spectra along with characteristic vibrations of functional groups.

Fig.1-Ox Cartilage spectrum

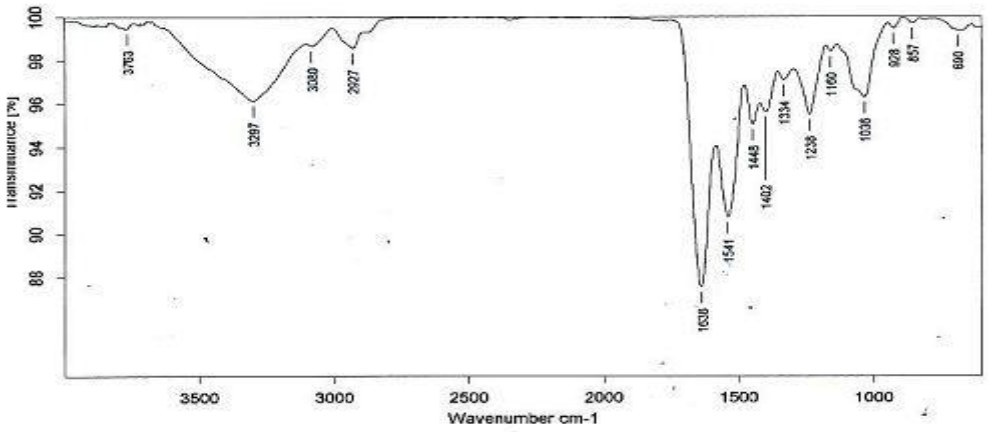

Fig.2-Goat cartilage spectrum

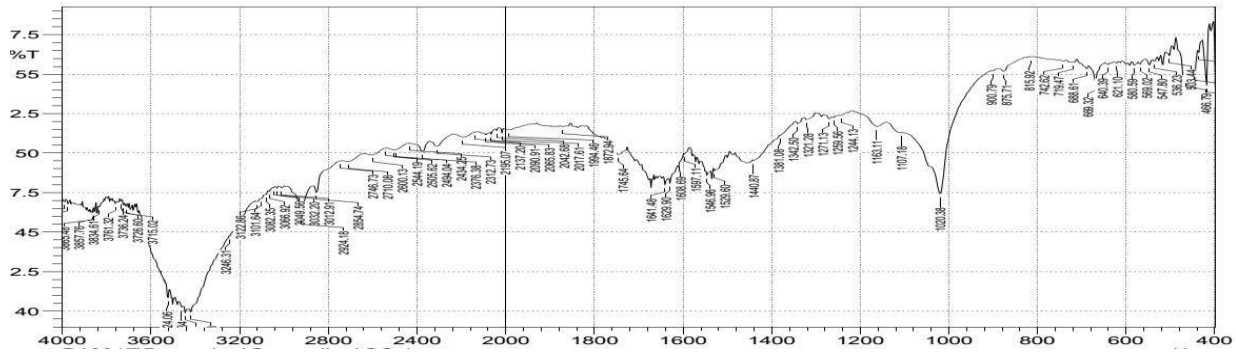

Fig.3 -Camel Cartilage spectrum

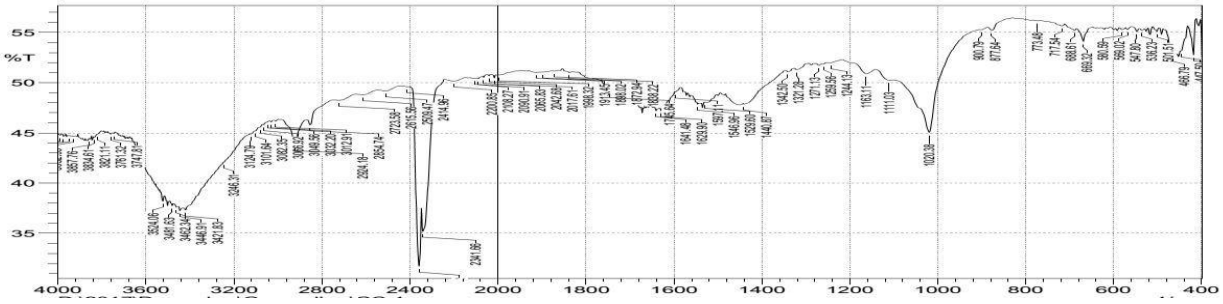

Table-1 FTIR data of Ox, Goat and Camel

Wave Number (Transmittance)			Characteristics Vibrations functional Groups
Ox	Goat	Camel	
3763(99.46)	3761(46.81)	3761(46.88)	Carbonyl C=O Stretching

3297(96.12)	3246(44.71)	3246(42.08)	H-O-H Stretching
3080(98.64)	3082(47.38)	3082(45.56	Amide B
2927(98.56)	2924(45.94)	2924(43.81)	C-H Symmetric Stretching of CH_2
-	1745(49.10)	1745(49.91)	Saturated fatty acids
1638(87.52)	1641(47.99)	1641(47.19)	Amide I of plated sheet structure of Protein
1541(90.74)	1529(48.87)	1529(48.03)	Amide II bond of protein N-H Stretching
1448(95.03)	1440(49.53)	1440(47.86)	P-O Anti Symmetric stretching
1238(95.46)	1259(52.25)	1259(51.84)	Amide III Component of Protein C-N Stretching with N-H band
1160(98.39)	1163(52.25)	1163(51.84)	Ring vibration in carbohydrates C-O, C-C, C-N stretching C-O-H, C-O-C absorption of glycol protein.
	1342(51.87)	1342(51.07)	CH_3 symmetric bending
		717(55.66)	CH_2 rocking
887(99.93)	875(55.17)	877(55.21)	Carbonate ions

For the systematic analysis, IR spectrum is divided into three regions. Region I is from 4000 to 3000 $cm^{-1,}$ concerned with water and hydroxyl group. This region is of considerable interest, because it reveals the nature of hydrogen bonding. Region II is 3000 to 1500 cm^{-1}, wherein bands for functional groups are observed. In this region, major IR absorption pertaining to collagen occurs. Region III is 1500 – 200 $cm^{-1,}$ which has significant importance in the context of biological minerals and their combinations. The spectra of cartilage powder indicate the presence of bands characteristics of phosphate ion, carbon ion, water molecule and also of some functional groups concerned with protein – the collagen. The IR bands at wave number 3080 cm^{-1} is related to Amide B. The dominating bands at 1638 cm^{-1} and 1541 cm^{-1} may be originated due to collagen and proteoglycans and collagen dominates the absorption (Fig. 1,2,3). These bands are related to the stretching vibrations of C=O bonds and N-H bonds respectively. A band around 1238 cm^{-1} is due to the C-N stretch with N-H bending vibrations. These bands are concerned with proteins and the strongest band at 1638 $cm^{-1}$is characteristic of collagen. The bands at 1160 cm^{-1} related to stretching vibrations of C-O and C-OH as well as C-C ring vibrations in carbohydrates. These bands are believed to be more specific to proteoglycans. The bands at 1448 cm^{-1} and 1402 cm^{-1}, originated from P-O anti symmetric stretch arerelated to calcium phosphate ions. The strongest absorption band at 887 cm-1is specific to calcium carbonate ions. The band 712 cm-1 characteristic of calcium carbonate is missing. Hence calcium carbonate is not present in Cartilage.

4. CONCLUSION

The study reveals that scapular cartilage consists of mainly collagen and proteoglycans but very less quantity of carbonate and phosphate ions.

REFERENCES:

1. Mow VC, Guo XE. Mechano-electrochemical properties of articular cartilage: their inhomogeneities and anisotropies. Annu.Rev.Biomed.Eng. 2002;4:175-209.
2. Myers ER, Mow VC. Biomechanics of cartilage and its response to biomechanical stimuli.Cartilage, Volume 1. Structure, Function, and Biochemistry. 1983;1:313-341.
3. Mow VC, Fithian DC, Kelly MA. Fundamentals of articular cartilage and meniscus biomechanics. In: Ewing JW, editor. Articular cartilage and knee joint function: basic science and arthroscopy. New York: Raven Press, Ltd.; 1990:1-18.

4. Leal-Egaña, A.; Scheibel, T. Silk-based materials for biomedical applications. *Biotechnol. Appl. Biochem*. **2010**, *55*, 155–167.
5. Servoli, E.; Maniglio, D.; Motta, A.; Predazzer, R.; Migliaresi, C. Surface properties of silk fibroin films and their interaction with fibroblasts. *Macromol.Biosci*.**2005**, *15*,1175–1183.
6. Min, B.M.; Lee, G.; Kim, S.H.; Nam, Y.S.; Lee, T.S.; Park, W.H. Electrospinning of silk fibroin nanofibers and its effect on the adhesion and spreading of normal human keratinocytes and fibroblasts *in vitro. Biomaterials* **2004**, *25*, 1289–1297.
7. NazimaSiddiqui and Adeel Ahmad; infrared spectroscopic studies on edible and medicinal oils; International Journal of Science, Environment. and Technology, Vol. 2, No 6, 2013, 1297 – 1306
8. U. VijayaUshasree, Kaleem Ahmed Jaleeli and Adeel Ahmad ;a study on infrared spectroscopy of human blood; International Journal of Science, Environment and Technology, Vol. 5, No 3, 2016, 1189 – 1192.
9. R. Copeland, in: *Methods for Protein Analysis*, Chapman Hall, New York, USA, 1994
10. Sasikumar, S.andVijayaraghavan, R. (2006) Low Temperature Synthesis of Nanocrystalline Hydroxyapatite from Egg shells by Combustion Method.Trends in Biomaterials and Artificial Organs, 19,70-73.
11. Rivera, E.M., Araiza, M., Brostow, W., Castaño, V.M.,Díaz-Estrada, J., Hernández, R.,et al. (1999) Synthesis of Hydroxyapatite from Eggshells Materials Letters, 41, 128-134.

Second National Conference on
RECENT ADVANCES IN APPLIED NANO MATERIALS
February 16-17, 2018at Department of Physics, University College of Science, Saifabad, Osmania University, Hyderabad, Telangana State, India.

High Temperature Studies of Nano Crystalline Spinel Ferrites

G. Aravind[a*], Ch.Venkateshwarlu[b], V.Nathanial[b], D. Ravinder[b]
[a]Department of Physics, Methodist College of Engineering & Technology, Abids, Hyderabad
[b.] Department of Physics, Osmania University, Hyderabad, 500007, Telangana, India
***Corresponding author: gunthaaravind@gmail.com**

Abstract:*An attempt has been made to prepare nano-crystalline pure lithium ferrites and metal ion doped lithium ferrites by citrate-gel solution combustion method at low sintering temperatures. This modified method reduces the formation of α- Fe_2O_3 impurity phase in the inverse spinel phase of ferrites. X-ray diffraction analysis of the prepared samples revealed the formation of single phase cubic spinel structure. The dielectric constant (ε') and dielectric loss tangent (tan δ) of the investigated samples has been studied from room temperature to well beyond the Curie temperature using LCR meter at selected frequencies. Seebeck coefficients (S) of the prepared samples were measured from 473-873 K by using differential method. The variation of seebeck coefficient vs temperature shows the semiconducting behavior of the investigated samples. The Curie temperatures for the ferrite specimens under investigation have been determined by using simple Loria technique. The Curie temperature of the samples measured from the both methods is approximately equal.*

Key Words: *High Tem, Nano, Spinel Ferrites.*

1. INTRODUCTION:

Spinel ferrites are the attractive magnetic ceramic material because of their excellent properties like wide and high range of saturation magnetization, low dielectric and magnetic losses, and high Curie temperatures. These are low cost substitutes for expensive garnet ferrites used in microwave electronic devices. The properties and performance of a material are related through the microstructure of the material. The ability to change the properties and performance of a material by suitable processing is what makes most materials useful for mankind. The dielectric properties of these semiconducting spinel nano ferrites play a vital role in determining their suitability for use in particular application [1].

Nano crystalline ferro spinels can be synthesized by various techniques including glass-ceramic method [2], hydrothermal method [3], ultrasonic cavitation method [4], mechanical ball milling method [5], reverse micelle method [6], radio frequency plasma torch method [7], sol-gel εεmethod [8], citrate gel auto combustion method [9] etc. Among these various preparation techniques, citrate gel combustion method has special significances in yielding ultra fine single phase nano powders with better purity along with narrow grain size distribution.

Pure lithium ferrites and metal substituted lithium ferrites are attractive the scientific community due to their technological importance in microwave frequency applications like gyrators, phase shifters, circulators and isolators etc [10]. At high power values, the nonlinearities deteriorate ferrite device applications, to avoid microwave power loss for various applications, the doping of transition metal ions in lithium ferrites are very effective. Metal cations like Co^{+2} and Ni^{+2} are the fast relaxing ions which enhance the microwave properties. Metal ion doped lithium ferrites are also used in cathode material for lithium ion batteries [11]. S.C.Watawe et al [12] studied the microstructure and magnetic properties of Li-Co ferrites prepared by standard double sintering ceramic method. Muthafar et al [13] reported the magnetic and electrical properties of rare earth doped lithium-nickel ferrites synthesized by double sintering ceramic method. In the present communication we report the temperature and frequency dependent dielectric properties and thermo electric properties of pure lithium ferrites and cobalt & nickel doped lithium ferrites synthesized by citrate-gel auto combustion method.

2. EXPERIMENTAL TECHNIQUES:

Nano crystalline spinel ferrites samples having chemical formula $Li_{0.5}Fe_{2.5}O_4$, $Li_{0.3}Co_{0.4}Fe_{2.3}O_4$ and $Li_{0.3}Ni_{0.4}Fe_{2.4}O_4$ were prepared by citrate gel auto combustion method by using their respective nitrates and citric acid as a chelating agent. The overall reaction for the pure lithium ferrites and substituted lithium ferrites are given by

$0.5LiNO_3 + 2.5Fe(NO_3)_3.9H_2O + 3C_6H_8O_7 \rightarrow Li_{0.5}Fe_{2.5}O_4 + 4N_2 + 18CO_2 + 7H_2 + 27.5\ H_2O$

$0.3LiNO_3 + 0.4Ni(NO_3)_2.6H_2O + 2.3\ Fe(NO_3)_3.9H_2O + 3C_6H_8O_7 \rightarrow Li_{0.3}Ni_{0.4}Fe_{2.3}O_4 + 4N_2 +$

$+ 18CO_2 + 7H_2 + 28.1\ H_2O$

The detailed synthesis process of citrate-gel auto combustion method was reported in our earlier publication [14].

The powder x-ray diffraction analysis were recorded at room temperature using Philips X'pert diffractometer in diffraction angle in the range of 20^o-80^o. For measuring the electrical properties, powders were added with a small amount 2% Poly Vinyl Alcohol as a binder to press the prepared powders into circular pellets having 13mm diameter and 2.5mm thickness by applying a pressure of 4 tons. The prepared pellets were sitnered at 500^oC for 4 hours in air in muffle furnace for the densification of the sample. For having a good ohmic contact silver paste was applied on both sides of the pellet. The dielectric properties of the sample were measured by using Agilent E4986 precession LCR meter from room temperature to 450^oC at different frequencies up to 5 M Hz. Thermoelectric power of the prepared samples was measured using differential method between 200-600^oC. The Curie temperatures for ferrite samples under investigation have been determined using Loria technique. Here pure lithium ferrites are represented as LF, cobalt doped lithium ferrites as LCF and nickel doped lithium ferrites LNF.

3. RESULTS AND DISCUSSIONS:

The x-ray diffraction pattern of the prepared samples sintered at 500^oC was shown in figure (1).
From the x-ray diffraction analysis of the investigated ferrites shows the positions of the reflection peaks are almost similar to the corresponding peaks for the bulk material, this implies that the basic structure of the nano crystalline materials is essentially same like the bulk counterparts.
The crystallite size and lattice parameter of the investigated samples were given in the **table1**.

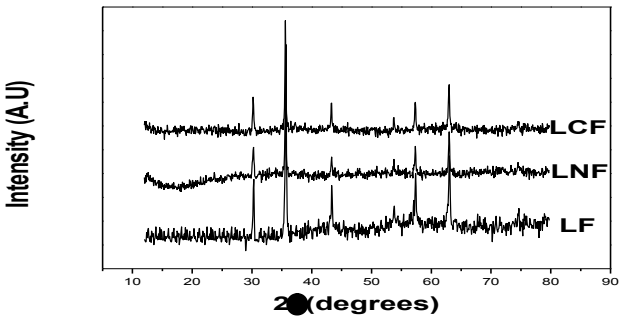

Fig (1) XRD pattern of the synthesized samples

Table1 Structural parameters of the prepared ferrite samples.

Composition	Crystallite Size (nm)	Lattice constant (A^o)	X-ray Density (d_x) (gm/cc)	Seebeck Coeffidient (μV/K)	Curie Temperature (K)
$Li_{0.5}Fe_{2.5}O_4$	41.90	8.356	4.71	5408	873
$Li_{0.3}\ Ni_{0.4}Fe_{2.3}O_4$	45.35	8.358	4.95	4648	840
$Li_{0.3}\ Co_{0.4}Fe_{2.3}O_4$	38.44	8.370	4.93	4413	853

The average crystallite size which are calculated from the Debye-Scherrer's formula were in the range of 38-45 nm which confirms the nano crystalline form.

Shape, size and homogeneity of the investigated samples were confirmed by TEM. The narrow size ranged spherical particles confirm the low temperature controlled synthesis of metal ion substituted nano crystalline ferrites.

The dielectric constant (ε') and dielectric loss tangent (tan δ) of the investigated ferro spinels were found to be depend on the temperature and frequency. The variation of dielectric parameters for pure and metal ion substituted lithium samples with temperature has been studied at different frequencies were shown in **fig(2).** From the figures one can conclude that the dielectric parameters of the samples LF and LNF increases rapidly in the low temperature region, where as in the high temperature region dielectric constant (ε') reaches a stable value (Resonance peak), after that it start to decrease with increasing the temperature. For the low temperature region, the dielectric polarization is improved by the electric field and also by the growing the number of electrons which are increase with temperature, hence the increase in the dielectric constant (ε') at low temperature region is due to both increase in temperature and frequency. For the high temperature region, the saturation in the production of charge carriers is reached. Therefore

the electron exchange between the ions of the same element that are present in more than one valence state (Fe^{+2},Fe^{+3} or Ni^{+2},Ni^{+1}) can not follow the field variation and hence dielectric constant decreases **[16]**. The temperature at which the resonance peak appeared is observed to be shift towards the higher temperature as the frequency is augmented [**17**]. But dielectric parameters of the sample LCF increases slowly in the beginning, it maintains up to a certain temperature and increases rapidly thereafter. Similar behavior can be observed by the various researchers for different compositions **[18]**.

From this figures one can also observed that dielectric constant and dielectric loss tangent of prepared samples were decreased rapidly in the low frequency region and decrease is quite slow in the high frequency region, this can be explained on the basis of Maxwell-Wagner and Koop's theory **[19],** which states that dielectric medium is assumed to be made up of highly conducting grains surrounded by non conducting grain boundaries. The grain boundaries are more effective at low frequencies and grains are more effective at the higher frequencies.

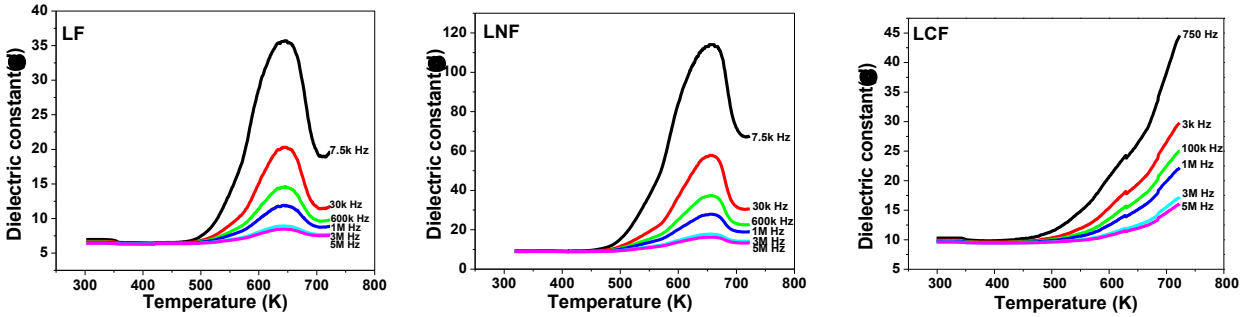

Fig (2) Variation of dielectric parameters of the prepared samples with temperature at different frequencies.

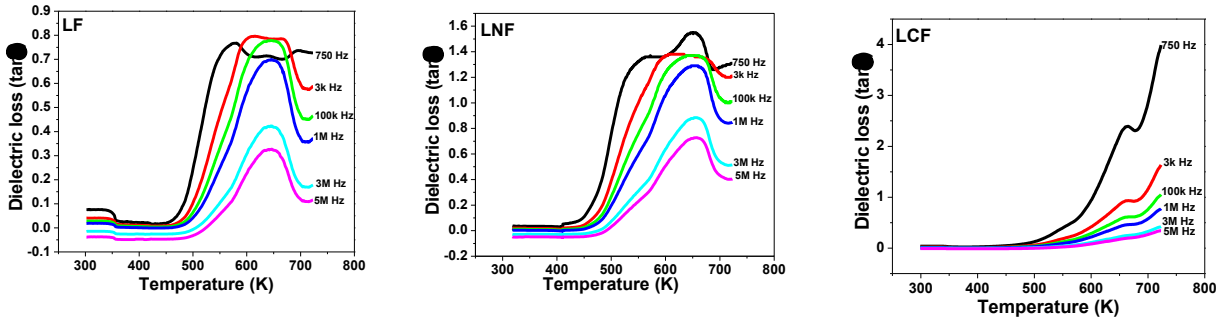

The Variation of Seebeck coefficient with temperature of the prepared LF, LNF and LCF ferrites was shown in **fig(3).** From these figure it was observed that all the investigated samples shows similar thermal variation with See beck coefficient and the value of See beck coefficient increases with increasing the temperature. At low temperature positive value of the S shows the p-type semi conducting nature and increasing the temperature sample changes to n-type semiconductor behavior **[20]**.

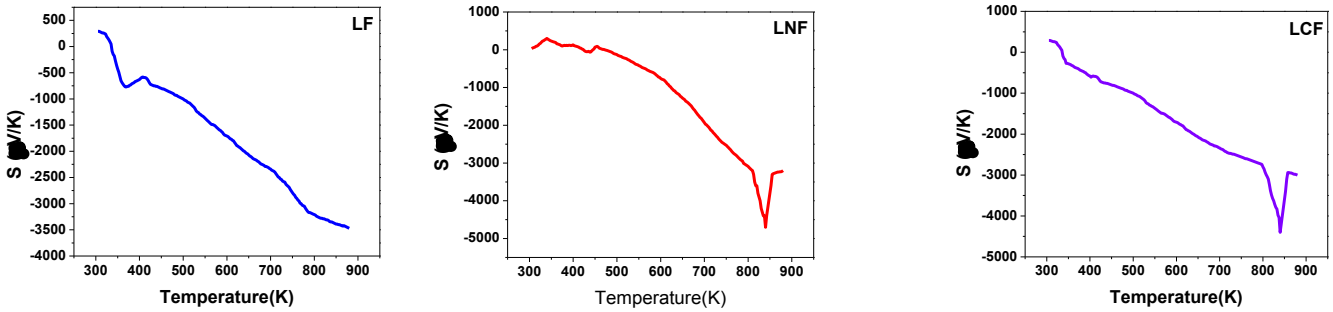

Fig (3) Variation of Seebeck Coefficient with temperature of prepared samples

All prepared nano crystalline ferro spinel samples show an increasing trend in thermo electric coefficient with temperature which indicates the more n-type charge carriers (electrons) are released with an increase in temperature. At a particular temperature an abrupt change was occurring may be due to the presence of Curie point at that temperature. The Curie temperature of the investigated samples measured from the Loria technique have the same values and by doping with the ions in the lithium ferrites Curie temperature of the material decreases [21].

REFERENCES:

1. Mamata Maisnam, Sumitra Phanjoubam, Solid State Communications 152 (2012) 320-323.
2. Ahmed M.El-sayed, Esmat M.A. Hamzavy Monatshefte ftir Chemie 137 (2006) 1119
3. Chaoquan Hu, Zhengong Gao, Xiaorui yang, J of Magn Magn mater 320 (2008)L70
4. Manickam Siva kumar, Atsuya Towata, Kyuichi yasui, Toru Tuzuiti, Yasuo Iida, Curr Appl Phys. 6 (2006) 591
5. Sangeeta Thakur, S.C.Katyal, M.Singh, J of Magn Magn mater, 321 (2009) 1
6. B.P.Rao, O.Caltun, WS.Cho, Chong-Oh Kim, Cheolgi Kim, J of Magn Magn mater 310 (2007) e812
7. S.Son, M.Taheri, E.Carpentur, V.G.Harris, M.E.McHenry, J Appl.Physi 91 (2002) 7589
8. Khalid Mujasam Batoo, Shalendra Kumar, Chan gyu Lee, Alimuddin, Curr Appli Phys 9 (2009) 1072.
9. G.Aravind, M.Raghasudha, D.Ravinder, Advanced Mater Letters 2015, 6(2) 179-185
10. Rajesh Cheraku, G.Govindaraj, Lakshmi Vijayan, Materials Chemistry and Physics (2014) 1-10
11. M.N. Obrovac, O.Mao, J.R.Dahn, Solid State Ionics, 112 (1998) 9-19.
12. S.C.Watawe, B.D.Sarwade, S.S.Bellad, B.D.Sutar, B.K.Chaugale, Materials Chemistry and Physics 65 (2000) 173-177
13. Muthafar F.Al Hilli, Sean Li, Kassim S. Kassim, J of Magnetism and Magn Mater 324 (2012) 873-879.
14. G.Aravind, D.Ravinder, V.Nathanial, Physics Research International, Vol 2014, Article ID 672739, 11 pages http://dx.doi.org./10.1155/2014/672739
15. S.A. Mazen, H.A. Dawoud, Material Chemistry and Physics 82 (**2003**)557-566.
16. Ibetombi, Soibam, Sumitra Phanjobam, H.B. Sharma, H.N.K. Sharma, Effect of Co substituted Li-Zn ferrites, Solid State Communications 148 (**2008**)399-402.
17. Ibetombi Soibam, Sumitra Phanjoubam, H.B. Sharma, H.N.K. Sarma, Solid State Communs 148 **2008** 399-402.**DOI**:10.1016/j.ssc.2008.09.029
18. H.M. Abdelmoneim, Indian J of Pure and Applied Phys, Vol.48, Aug 2010, pp562-570.
19. K. Rama Krishna, Preparation and Electrical Properties of Ni-Zn ferrites by Citrate-gel method, Ph.D thesis submitted to JNTUH Hyderabad-June **2014**
20. A.A. Samokhavalov, A.G.Rustamov,Soviet PhysSolid State,6 (**1964**) 749.

Second National Conference on
RECENT ADVANCES IN APPLIED NANO MATERIALS
February 16-17, 2018 at Department of Physics, University College of Science, Saifabad, Osmania University, Hyderabad, Telangana State, India.

Synthesis Of Citrate Gel Auto Combustion Prepared Li-Cd Nanoferrites Sintered At Reduced Temperature

K. Rama Krishna [1], K. Vijaya Kumar [2] R. Sridhar [3] & D. Ravinder[4]
[1.]Department of Physics, Malla Reddy College of Engineering &Technology, Secunderabad- 500 014
[2.]Department of Physics, JNTUH, College of Engineering Sultanpur, Sanga Reddy-Dist., 502 273,
[3.]Department of Physics, Vignan Institute of Technology & Aeronautical Engineering, Deshmukhi, Nalgonda,
[4.]Department of Physics, Osmania University Hyderabad- 500 004 Telangana, India.
Corresponding Author: ramu521@mail.com

Abstract: *A novel gel auto-combustion method was used to synthesize Li-Cd nanoferrite powder with compositions of* $Li_{0.5-X/2}Cd_XFe_{2.5-X/2}O_4$ *(where x=0.0, 0.2, 0.4, 0.6, 0.8 & 1). X-ray diffraction results showed that synthesized powder from metal nitrites and citric acid is transformed directly into nano-sized ferrites after an auto-combustion process in air. The low-temperature sintered Li-Cd ferrites possess good electromagnetic properties and fine-grained microstructures; hence these samples can be suggestible for multilayer chip inductors with high-performance.*

Key Words: *: Li-Cd ferrite, citrate-gel, lattice parameter, hopping lengths*

1. INTRODUCTION:

Ferrites, which are magnetic oxides, are best examples for very good electrical materials because of their high resistivity and low loss behavior hence these ferrites have vast technological applications over a wide range of frequencies. Lithium-based ferrite is a significant magnetic material for applications because of its better properties at high frequency, high resistivity, high Curie temperature, low dielectric losses and lower densification temperature than other ferrites. Lithium ferrite is one of the most versatile magnetic materials, useful for microwave devices, memory core, power transformers in electronics, antennas, read/write heads for high-speed digital tapes, etc. In particular, mixed lithium ferrites are of much interest because of their application in microwave devices such as isolators, circulators, gyrators and phase shifters. There are several different synthesis methods used to generate ferrites as reported in the literature, including Glyoxylate precursor method [1], sucrose method [2-3], reverse micelle technique [4], hydrothermal method [5]. The objective of this work is to synthesize cadmium doped lithium ferrite produced by Citrate gel method.

.

2. EXPERIMENTAL:

Six different compositions of $Li_{0.5-X/2}Cd_XFe_{2.5-X/2}O_4$ (where x=0, 0.2, 0.4, 0.6, 0.8 & 1) are prepared by citrate gel method. The citrate process [6, 7] is simple, easy and doesn't require any elaborate and expensive experimental setup. The main advantages of this method is

[A] Capacity to yield a homogenous mixture of the constituent ions.
[B] As no ball milling is required in this process, there is a little scope of contamination of materials
[C] In case of conventional methods, there is a possibility of introducing iron impurities during milling this leads in-homogeneity in sample, which affects the magnetic property
[D] This is a simple method which offers a significant saving in time and energy consumption.

The starting materials used in this preparation are Lithium nitrate (Merc, India), Cadmium nitrate (Merc, India), iron (III) citrate (Merc, India) and citric acid (Merc India) having molar ratio of 1:3 were dissolved in de-ionized water. Citric acid acts as chelating agent and helps in the homogenous distribution of metal ions. The P^H of the solution is adjusted to 7 by using ammonia solution. The solution was uniformly heated at 373 K with constant stirring to transform it into a gel and the dried gel was obtained by de hydration process. The dried gel was combusted with evolution of gases and resulted in formation loose powder. This powder is subjected to sintering at 600^0C for 5 hours in air medium to get the final product. The X – ray diffraction patterns of the ferrite powder was taken on powder X-ray diffractometer (X-rd) using Cu-Kα radiation.

3. RESULTS AND DISCUSSIONS:

The X-ray diffraction patters of the samples are shown in Fig.1

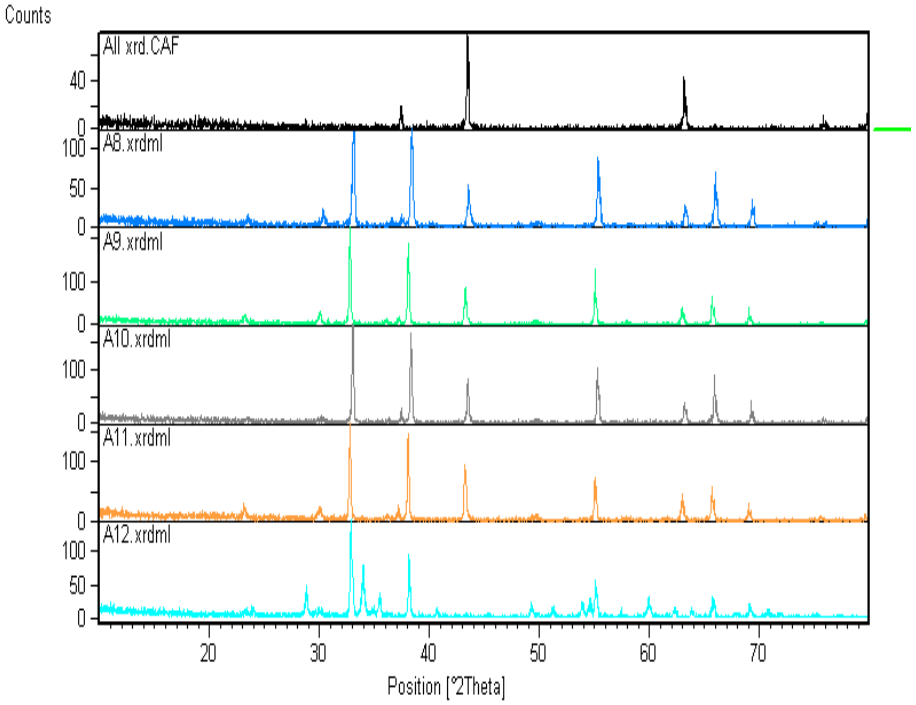

Fig 1.X-rd of Li-Cd ferrites

All the cadmium substituted lithium ferrites of the various compositions show the crystalline cubic spinel structure. The sharp peaks represents that all ferrites are crystalline nature of single phase. The lattice parameter of individual composition was calculated by using the Eq. (1) [8]

$a=d\,(h^2+K^2+l^2)^{1/2}$ (1)

Where, a=lattice constant
d= inter planar distance &
(h, k, l) are the Miller indices

The calculated lattice constant "a" is seen to increase from 8.03 A ^{o} to 8.60 A ^{o} with increase in Zinc content as reported in Table 1, by indicating that the Li-Cd ferrite system obeys Vegard's law [9]. The variation of lattice parameter with cadmium composition is shown in Fig.2. A similar behavior of lattice constant with doping concentration was observed by [10].

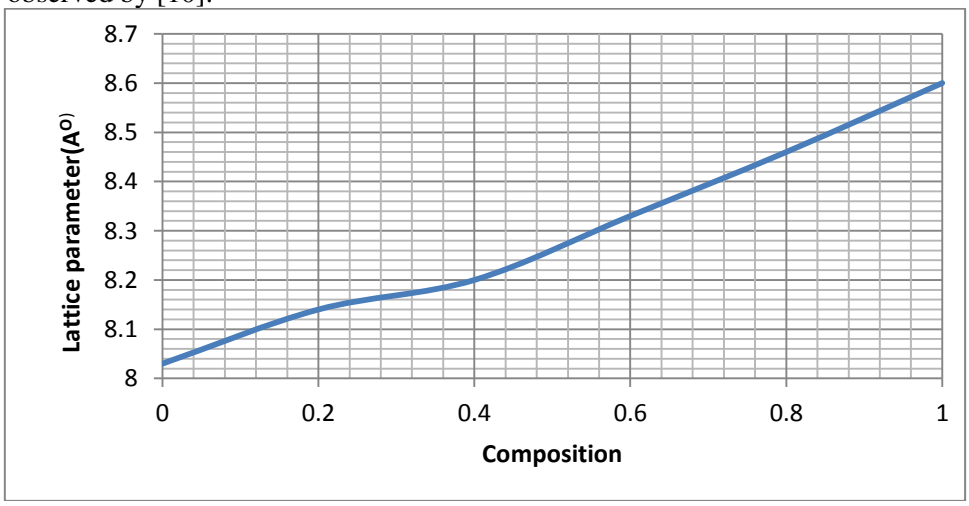

Fig2. Variation of lattice parameter with composition

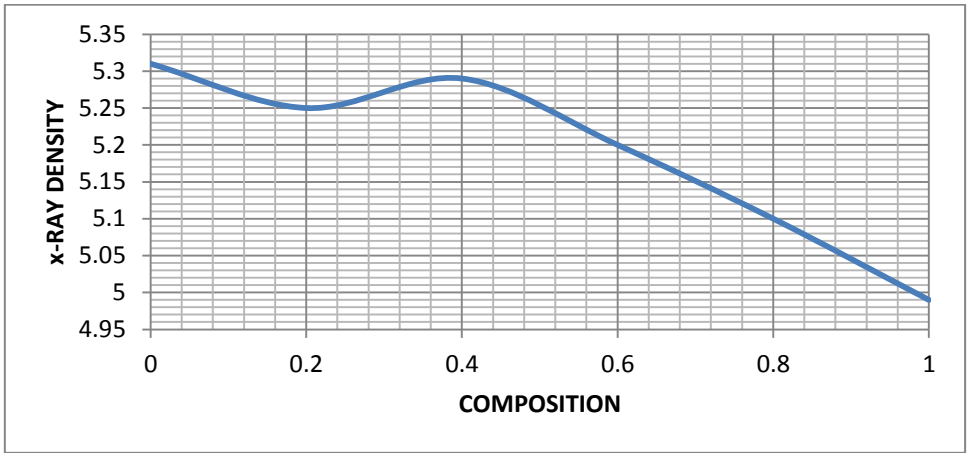

Fig 4. Variation of X-ray with composition

The crystallite sizes of the samples are calculated by using Sherrer's Formula [11] by using equation (2) by taking into account of the instrumental broading **[**12**].**

$$d_{hkl} = \frac{0.91\lambda}{\beta Cos\theta} \quad \text{---} \quad (2)$$

Where

d_{hkl} --- is the crystalline size Perpendicular to (h k l) pane,

λ --- The wave length of X-ray Used,

β --- Width of diffraction peak i.e., Full Width Half Maxima (FWHM)

θ --- The peak position.

X- Ray density (dx) was determined using the following Eq. 3

$$d_x = ZM/Na^3 \quad \text{---} \quad (3)$$

Where 'Z 'is the number of molecules per unit cell (Z=8), 'M' is the molecular weight and 'N' is Avagdro number. The variation of X-ray density with zinc content for mixed Li-Cd ferrite is shown in the Figure 3. It may be seen from the figure that bulk density increases linearly with the increase of cadmium content.

Composition	Lattice Constant (A^0)	X-ray Density (Gm/cm^3)	Crystallite size (nm)	Hopping length Tetrahedral sites (dA)	Hopping length Octahedral sites (dB)
$Li_{0.5}Fe_{2.5}O_4$	8.03	5.31	28	5.31	5.31
$Li_{0.4}Cd_{0.2}Fe_{2.4}O_4$	8.14	5.25	30	5.25	5.25
$Li_{0.3}Cd_{0.4}Fe_{2.3}O_4$	8.20	5.29	38	5.29	5.29
$Li_{0.2}Cd_{0.6}Fe_{2.2}O_4$	8.33	5.20	46	5.20	5.20
$Li_{0.1}Cd_{0.8}Fe_{2.1}O_4$	8.46	5.10	52	5.10	5.10
$CdFe_2O_4$	8.60	4.99	105	4.99	4.99

The hopping lengths of for octahedral (d_A) and tetrahedral (d_B) sites are calculated by using the Equations (3), (4) [13] and tabulated in table 1 along with other data.

$$\left.\begin{aligned} d_A &= 0.25a\sqrt{3} \text{ and} \\ d_B &= 0.25a\sqrt{2} \end{aligned}\right\} \quad 4$$

CONCLUSION:

A series of Li-Cd nano ferrites with composition $Li_{0.5-X/2}Cd_XFe_{2.5-X/2}O_4$ (where x=0, 0.2, 0.4, 0.6, 0.8 & 1) was successfully prepared by using citrate gel method. The lattice parameter, X-ray density, hooping lengths are increasing as cadmium content is increasing from x=0.0 to 1.0

REFERENCES:

1. C.Caizer and M.Stefanescu,J.Phys.D.Appl.Phys.35 (2002) p.3035-3040.
2. P.Pramanik, Bull. Mater. Sci. (1999) p.335.
3. R. N. Das, Mater. Lett. 47 (2001) P.344.
4. S. Gubbala, H. Nathani, K. Koizol, R.D. K. Misra, Physica B 348(2004) p.317-328.
5. Dias, Mater. Resea. Bull. 35 (2000) p. 1439-1446.
6. A.Verma,T.C.Goel,R.G.Mendiratt, M.I.Alam, Mater Sci Eng.B.60 (999) p.156.
7. A.Verma, T.C. Goel, R.G.Mendiratta, J.Magn. Magn. Mater 210 (2000) . p.274-278
8. Iqbal MJ, Siddiquah MRJ Magn Magn Mater 320 (2008) p 487
9. L.Vegard Z.phys vol 5, 1921, p 17.
10. SS Bellad, BK Chougule - Materials research bulletin, 33 1998, p.1165–1173
11. Cullity B D, Elements of X-ray diffraction (Addition Wesley, Reading, Mass), 1959, p132
12. Mahmud ST, Akther Hossain AKM, Abudul Hakim AKM, Seki M, Kawai T, Tabata J Magn Magn Mater (2006) 305 p.269
13. R.C. Kumbale. P. A. Shaikh, S.S. Kamble, Y.D. Kolekar J. Alloys Compd., (2009), 478p. 599.

Second National Conference on
RECENT ADVANCES IN APPLIED NANO MATERIALS
February 16-17, 2018 at Department of Physics, University College of Science, Saifabad, Osmania University, Hyderabad, Telangana State, India.

Preparation and characterization of Barium ferrites Using Microwave-hydrothermal method

P. Phanidhar* and S.R. Murthy#
*Department of Physics, JNTU H, Hyderabad
#Department of Physics, Osmania University, Hyderabad-500007.

Abstract: *Barium ferrite (BaFe12O19) was successfully synthesized by microwave hydrothermal method at a low temperature of 160 C/ 30 min. The synthesized ferrite powders were characterized by X-ray diffraction (XRD) and Scanning Electron Microscopy (SEM). The prepared samples were microwave sintered in the temperature range of 700 to 950 °C for 45 min. The prepared products of barium ferrite were characterized by X-ray diffraction, a scanning electron microscope. The density, lattice parameters were measured and discussed on the variation of sintering temperature*

Key Words: *Barium ferrites, Microwave Hydrothermal Synthesis, Microwave sintering.*

1. INTRODUCTION

Barium hexaferrite (BHF) is one of the interesting material to scientists and researchers to study in\for the application point of view because of its industrial applications like microwave devices ,electromagnetic wave absorbers, computer data storage, high density perpendicular magnetic and magneto-optic recording, disk driver and video recorder as it is having several characteristics like high magnetic moment per formula unit (20 μ_B at 0K), high intrinsic coercivity, large saturation magnetisation, high Curie temperature, fairly large magneto-crystalline anisotropy constant, high permeability with low conduction losses, excellent chemical stability and corrosion resistivity[1-4].Even though it having several applications it is difficult to synthesis BHF due to its complex nature. Ba ferrite nano particles are nowadays generated by a series of different physical and chemical preparation methods. Although such synthetic methods have reached significant advances in terms of homogeneity in the structural/electronic properties of the particles forming the solid, as well as in the size distribution, much work is still needed to obtain full control of the synthesis variables and their influence in the final metal-oxide solid prepared. Problems related to oxide stoichiometry and metal oxidation state (commonly at surface layers) or the presence of impurities and amorphous phases coexisting with the crystalline one are often encountered. A glimpse into these problems would indicate that the structural and electronic properties as well as the primary particle size distribution are strongly dependent on the preparation method, and at the state-of-the-art, a first goal is to perform a detailed and full characterization of the particular solid yielded by the specific preparation method used. To do such a study here we chosen an ecofriendly synthesis and novel method called microwave hydrothermal method. It having several advantages compare to conventional hydrothermal method i.e. (a) high heating rates achieved due to the internal heating manner within the material being processed rather than the heating at the surface; (b) non-contacting heating between the heating source and the reactants and/or solvents; (c) precisely controlling of process parameters; (d) selectively heating compounds with different microwave-absorbing properties; (e) high yields of the products; and (f) both energy and time savings.

In this study, the effect of microwave reaction temperature on the synthesis, phase evolution, and microstructure of barium ferrite has been studied. In particular, we discuss the sintering temperature on the phase composition.

2. EXPERIMENTAL

Barium hexa-ferrite nano particles with different reaction temperature were prepared by M-H method. It provides better control on stoichioetry and structural parameters at nano scale. The chemicals used for the synthesis of samples were Ba $(NO_3)_2.6H_2O$ and Fe $(NO_3)_3 \cdot 9H_2O$. The salts were dissolved in de-ionized water. The solution of both of these precursors with molar ratio (Fe/Ba = 12) was prepared. This solution was heated along with continuous stirring on hot plate. When temperature of solution was reached to 70°C, solution of NaOH was added until required pH value 13 was reached. The aqueous solution was stirred for 1 h to get fine homogeneity. The mixture was then

treated in a Teflon-lined vessel using a microwave digestion system (Model MARS, CEM Corp.). The system is controlled by both pressure and temperature. In the present investigation all the samples were synthesized at different temperatures 170˚C/45min. The final slurry product obtained were filtered, and then washed repeatedly with de-ionized water and ethanol, followed by freeze-drying overnight. The prepared powders were weighted and the percentage yields were calculated from the expected total amount based on the solution concentration and volume and the amount that was actually crystallized. As synthesized powders were granulated and compacted into discs and torroidal specimens by applying uniaxial pressure of 150 MPa and then sintered at different sintering temperature (700, 800, 875, 950˚C/40min) and characterized by using XRD (Philips Model no: PW-1730), structural morphology was studied by FESEM. In this study, the effect of microwave reaction temperature on the synthesis, phase evolution, and microstructure of barium ferrite has been studied. In particular, we discuss the sintering temperature on the phase composition.

3. RESULTS AND DISCUSSION

Fig 1 .Shows the XRD patterns of the as prepared BHF nanopowders with varying the synthesis parameters (i.e. temp). It can be seen from the figure that the powders without microwave treatment gives completely amorphous phase (Fig 1(a)). The powder synthesized at 110°C shows mainly mixture of phase hematite (α-Fe_2O_3),magnetite (γ-Fe_2O_3).The intensity of γ-Fe2O3 decreases markedly with increase of reaction temperature, the $BaFe_{12}O_{19}$ (JCPDS No. 74-1121) and intermediate phase identified as barium iron oxide ($BaFe_2O_4$) were formed at 170°C for 1hr. The efficiency of producing barium hexa ferrite at low temperature increased due to the modified reaction mechanism compare to the other synthesis methods. The mean crystallite sizes were calculated by using Scherrer equation and the crystallite size are in the range of 12 – 18 nm. With increase of reaction temperature the mean crystallite size also increases.

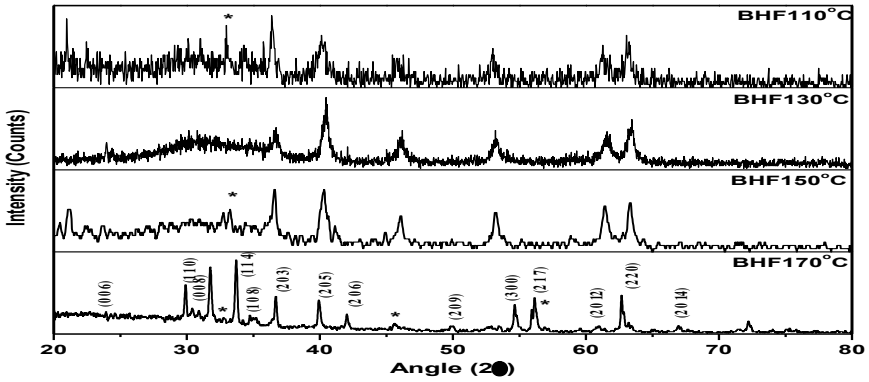

Fig. 1 XRD patterns of as synthesized Barium ferrite nanopowders

Fig 2 shows the FESEM patterns of the as synthesized powders. From the figure it is clearly seen that the particles are regular hexagonal platelets with rather homogeneous particle sizes are in the range from 20nm -25 nm(with a standard deviation of ~2 nm), this is almost in good agreement with XRD peak broadening calculations using scherrer relation.

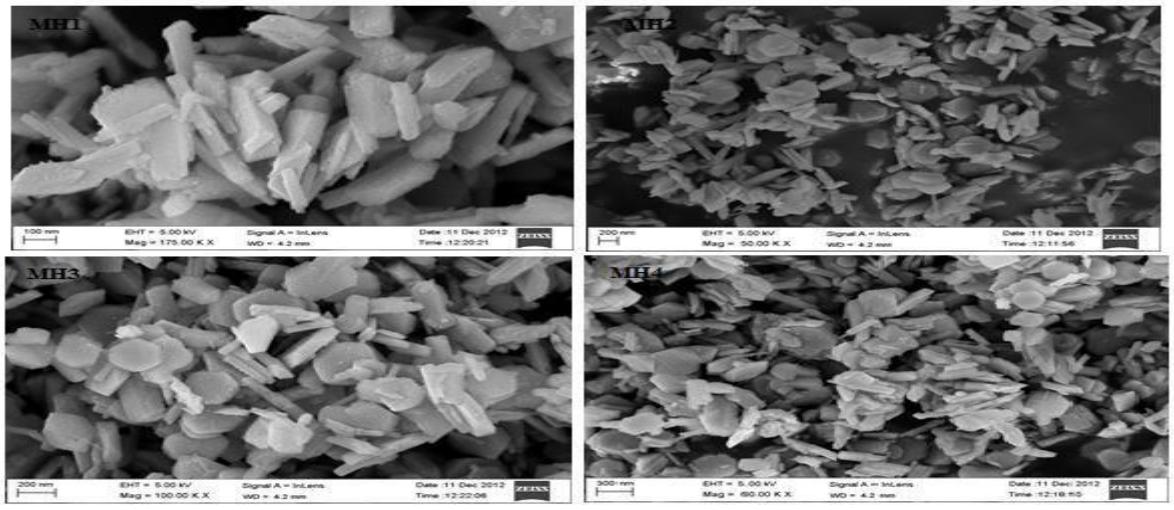

Fig 2 shows the FESEM patterns of the as synthesized powders.

Fig 3 .Shows the XRD patterns of the sintered BHF samples at different sintering temperature (MS1 (700°C), MS2 (800°C), MS3 (850°C) and MS4 (900°C). It can be seen from the figures that the sample sintered at 700°C shows the minute trace of α- Fe_2O_3 and $BaFe_2O_4$ phase with hexaferrite phase. The samples with sintering temperature more than or equal 800°C shows the complete hexaferrite phase without showing any residual phases it is less than the reported temperature by Sadana et.al[5] . This can be achieved mainly due to the applying of higher initial microwave reaction time and sintering time to prepare the powders. With increasing sintering temperature. Therefore it is concluded that a single phase hexaferrite observed when the sintering temperature is more than 800°C. The peaks of BaFe12O19 phase got narrower and sharper, manifesting particle size increase and crystallinity improvement with increasing temperature.The monophasic patterns obtained by these methods match exactlythe reference standard, JCPDS file no: 27–1029.

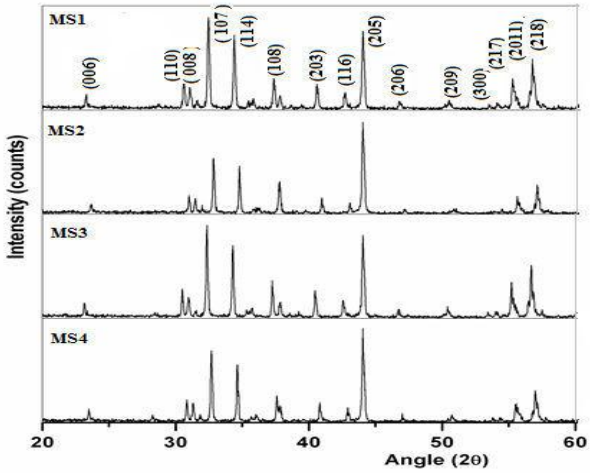

Fig.3. XRD patterns of sintered Barium ferrite

The X-ray diffraction pattern indexed with (hkl) values for each peak of BaFe12O19 nano-hexaferrite is shown in Fig. 1.The observed diffraction lines were found to be corresponding to the standard pattern of the BaFe12O19 ferrite with no extra lines, thereby, indicating that thesample has a single-phase hexagonal structure and no unreacted constituents are present in the sample. Table 1 shows the values of particle size, a,and c for the studied BaFe12O19 nano-hexaferrite. The obtained values are nearly same as reported by other worker [5] which shows the perfectness of crystal structure of the BaFe12O19 nano-hexaferrite. The scanning electron micrograph for studied nanohexaferrite is shown in Fig. 2 which confirms the hexagonal phase of BaFe12O19 nano-hexaferrite.

Table 1: Preparation data of nanocrystalline barium ferrites at room temperature

Sintering temperature (°C)	Crystallite size (nm)	Grain size (nm)	Lattice constant (Å) a	c	Bulk density (g/cc)	X-ray density g/cc
600	40	50	5.865	22.891	4.592	5.372
800	45	58	5.874	23.121	4.664	5.321
700	59	65	5.887	23.165	4.746	5.316
900	66	73	5.892	23.182	4.832	5.302

The average crystallite size was determined from the position of the strongest (1 0 7) diffraction peak via the FWHM using the well-known Scherrer equation, with a constant k of 0.9. The 100% peak (1 0 7) was located at 32.17851 having an FWHM of 0.19981 and therefore an average crystallite size (D) of 4.69 mm. With increasing heat treatment temperatures from 800 to 900°C the relative intensity of the 100% peak increased while the other peaks becoming equally sharper indicating an increase in particle size.

Figs. 4(a)–(d) show the morphology of these particles as synthesized as well as the development of grain structure. The particles following coprecipitation were found to be largely uniform in both shape and size where the majority are of acicular/platelet form and the size ranged from 0.5 to 2 mm. In case for the polished and etched samples sintered at 900 °C, it is clear, from Figs. 2(b) to (d), that the particles are hexagonal platelet crystals and the average grain ranged from 3.5 to 10 mm with the largest grains in the range of 20–25 mm. There is clear evidence that some of these grains have coalesced to form larger grains within the material formed at high temperature as a consequence of thermodynamically driven mass diffusion mechanisms. An example is shown in Fig. 4(b), where the particles are of the order of 25 mm wide by 60 mm long. However, these types are less prevalent throughout the material than those uniformly distributed, the grain size of which lies in the region of approximately 5 mm in

diameter. It is to be noted here that there are some pores present; in the final structure that is unavoidable since 100% theoretical density is never achieved duringany sintering process.

The bulk density of the present investigated samples was accurately measured using the Archimedes's principle by taking an average of eight trials. The bulk density of the sample was calculated from precise measurements of the dry, saturated, and suspended weight. The weight loss of the sample in the water was measured using a digital balance with an accuracy of 0.001mg. The bulk density of a sample was estimated using Eq. 3.6 and the calculated ρ_{bulk} value is presented in Table 3.2.

$$\rho_{bulk} = \frac{M_{air}}{M_{air} - M_{water}} \dots\dots\dots\dots (3)$$

Where M_{air} is mass of the sample in air andM_{water} is mass of the sample in water.

It can be seen from the table that the densification rate has been significantly increased in the microwave sintering process. In the microwave sintering process needs only 20 min to reach 700°C and to obtain a sample with density as high as 90% of TD. The density of Microwave sintered sample has increased to 96% of TD with an increase of sintering temperature from 700°C to 900°C. Thus, higher densification was achieved in a shorter period by using the microwave sintering process.

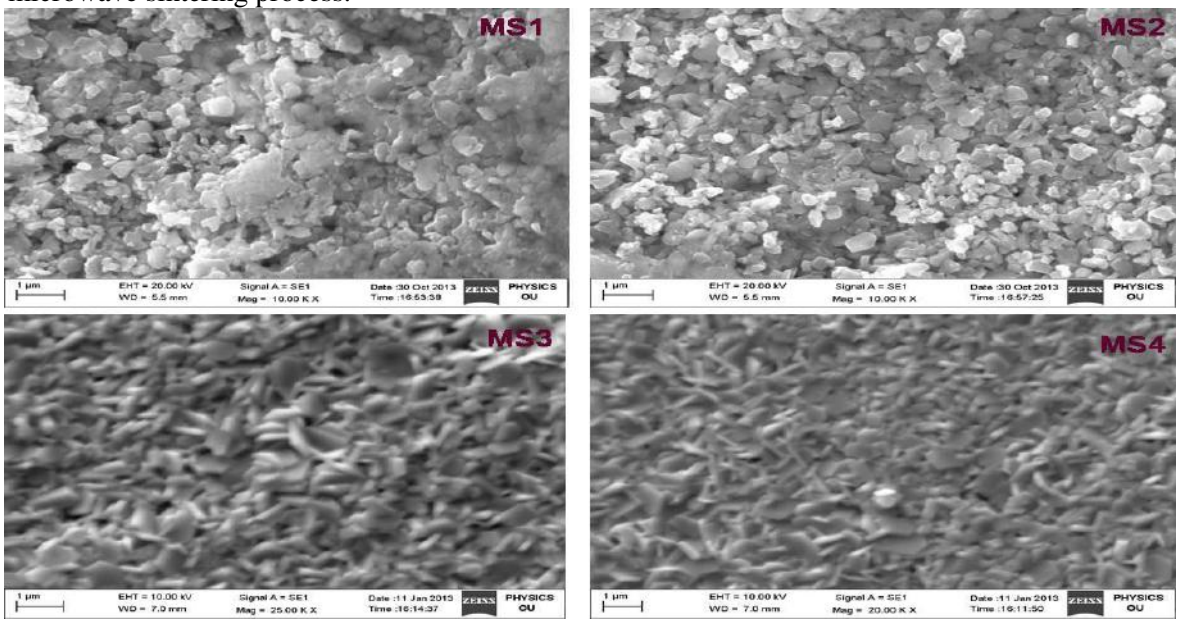

Fig. 4. FESEM pictures on sintered Barium ferrite.

The lattice constant (a) for all the present samples has been calculated with the help of XRD pattern. For a given set of planes (h k l) and from the Bragg's equation [24, 25] the interplanar spacing (d) is given by

$$d_{(hkl)} = {}^{n\lambda}/_{2sin\theta} \dots\dots\dots\dots (1)$$

Where n = order of reflection, λ = wave length of radiation and θ = glancing angle of incident X-ray beam. In general, for Hexagonal structure crystal structure the lattice parameter have been estimated using the following equation:

$$1/d^2_{hkl} = 4/3[\ h^2 + k^2 + hk/\ a^2 + l^2/c^2] \dots\dots\dots 2$$

Lattice parameters (a) for all samples under investigation have been estimated using the above equation, d_{hkl} corresponding to all the diffraction peaks. The average values of lattice constant for nanocrystalline barium ferrite samples are presented in the Table 1.

REFERENCES:

1. J. Qiu, M. Gu, H. Shen,' Microwave absorption properties of Al- and 13 Cr-substituted M-type barium hexaferrite", J. Magn. Magn. Mater. 295(3) (2005) 263-268.
2. A.Ghasemi, A. Saatchi, M. Salehi, A. Hossienpour, A. Morisako, X. Liu, "Influence of matching thickness on the absorption properties of doped barium ferrites at microwave frequencies", Phys. Stat. Sol. (a) 203(2) (2006) 358-365.
3. E. Kiani, A.S.H. Rozatian, M.H. Yousefi, "Structural, magnetic and microwave absorption properties of SrFe12–2x(Mn0.5Cd0.5Zr)xO19 ferrite", J. Magn. Magn. Mater. 361 (2014) 25-29.
4. R.C. Pullar, "Hexagonal ferrites: A review of the synthesis, properties and applications of hexaferrite ceramics", Prog. Mater. Sci. 57 (2012) 1191-1334.
5. K. Sadhana , K. Praveena , S. Matteppanavar ,B. Angadi,, "Structural and magnetic properties of nanocrystalline BaFe12O19 synthesized by microwave-hydrothermal method", Appl Nanosci (2012) 2:247–252.

Second National Conference on
RECENT ADVANCES IN APPLIED NANO MATERIALS
February 16-17, 2018at Department of Physics, University College of Science, Saifabad, Osmania University, Hyderabad, Telangana State, India.

Preparation and characterization of nanocrystalline NiCuZn ferrites

G. Shayam sunder Reddy* and S.R.Murthy#
*Department of Physics, Sri indu college of Engineering and technology, Hyderabad
#Department of physics, Osmania University, Hyderabad-500 007

Abstract: *Ni0.5-xCuxZn0.5Fe2O4 (x=0,0.4, 0.6, 0.8, 0.12mol%) nano powders of ferrite were synthesized using microwave-hydrothermal (M-H) method at 160°C/30 min. The samples were microwave sintered at temperature as low as 900°C/30 min. The sintered samples were characterized using X-ray diffraction (XRD) and Scanning electron microscopy (SEM). The variations of the crystallite size, grain size, sintered density andlattice constant as a function of copper concentration at room temperature have been investigated.*

Key Words: *Ferrites, Microwave Hydrothermal Synthesis, Microwave sintering,*

1. INTRODUCTION

Sintered NiCuZn ferrites was first demonstrated as an electromagnetic wave absorber sheet in HF (3~30MHz) region. Recently, RFID components have become a blossoming communication technique based on high frequency electromagnetic waves and have been used for logistics management. However, poor coupling between tags and readers could be caused by the destructive interference induced by a conductive atmosphere. The electromagnetic absorber sheet can improve the cross talk of RFID tags with their readers in the equipment, and the miniaturization of this component would permit a higher mounting density in equipment, enabling the fabrication of smaller, lighter and more functional electronic products. NiCuZn ferrites are potential materials for HF application due to their high resistivity, high permeability, broad bandwidth, and low price.

Spinel ferrites are commercially important because of their excellent electrical and magnetic properties [1]. The usefulness of ferrites is influenced by physical and chemical properties of the materials and depends on many factors including the methods of preparation. Recently, there has been a grownup interest in low temperature sintered NiCuZn ferrites for the application in producing Multilayer type Chip Inductors(MLCIs) because of their good electromagnetic properties at high frequency and low densification [2-3].

During the manufacture of microwave absorbe, ferrite powder needs to be sintered < 950^0C in order to co-fire with Ag internal electrode [4 -6].Generally, the sintering temperature of these ferrites has been lowered by an addition of sintering aids such as, lead glass, Bi_2O_3, V_2O_5 and WO_3 were added [7-8]. In many ferrites, an addition of aids has been lowered the sintering temperature from 1200^0C to 900^0C and also it was found that the physical and electrical properties were enhanced. However, the values of initial permeability and saturation magnetization were decreased. Now it is well known that the lowering of sintering temperature can also be achieved by choosing pure and fine starting chemical powders.

Out of all methods available for the synthesis of the spinel ferrite nano powders can easily synthesized using a microwave-hydrothermal (M-H) method and which is one of the promising methods for preparing fine ceramic powders. The main advantages of microwave hydrothermal method over the conventional hydrothermal method are: the kinetics of the reaction is enhanced by one to two orders of magnitude, novel phases can be obtained and the rapid heating to treatment temperature saves time and energy. Komarneni et al [9-11] have used the M-H method to prepare nanopowdes of various ferrites with large surface area. Therefore, in the present investigation nanopowders of NiCuZn ferrites were synthesized using M-H method.

Microwave sintering has got many advantages over the conventional sintering method and thus used for the synthesis and sintering of ceramics [12,13]. Hence detailed investigations of the electrical and magnetic properties of NiCuZn ferrites prepared by microwave hydrothermal method and microwave sintered have been undertaken .The obtained results were compared with the conventionally sintered samples and presented in this paper.

2. EXPERIMENTAL

Pure (99.9%) nickel nitrate [$Ni(NO_3)_2.6H_2O$], copper nitrate [$Cu(NO_3)_2.3H_2O$], zinc nitrate [$Zn(NO_3)_2$ $.6H_2O$] and iron nitrate [$Fe(NO_3)_2$ $.9H_2O$] were dissolved in 50 mL of de-ionized water. The molar ratio of powders

was adjusted to obtain composition $Ni_{0.5-x}Cu_xZn_{0.5}Fe_2O_4$ (x=0,4,6,8,12mol%). An aqueous NaOH solution was added to solution until the desired pH (~ 9.45) value was obtained. The products obtained were filtered and washed repeatedly with de-ionized water, followed by drying overnight.

All the synthesized products were characterized using powder XRD. Particle size and morphology were determined using transmission electron microscopy (TEM) (Model JEM-2010, JEOL, Tokyo, Japan).

The obtained ferrite powder was mixed with an appropriate amount of 2wt% polyvinyl alcohol as a binder. Then the powder was uniaxially pressed at a pressure of 1500 kg/cm^2 to form green pellet and toroidal specimens. After binder burnt out at 500^{0}C for 45 min, the compacts were microwave sintered at 850^{0}C (sample MH1, sample MH2, sample MH3, sample MH4 and sample Mh5 respectively) for 30min in air. The microwave sintering process was carried out using a specially designed applicator and which consists of a domestic microwave oven having an output power level tunable up to a maximum of 1100 W and operating frequency of 2.45 GHz.

The structure of the sintered materials was examined using X-ray diffraction. The bulk density of the present samples was measured using the Archimedes method. The dc electrical resistivity for all the samples have been measured using two probe method at room temperature. The dielectric constant and loss were measured at 1 MHz on the NiCuZn ferrites using a LCR meter. All these properties were measured with the variation of copper. The obtained results were compared with the conventionally sintered samples and the results were presented in this paper.

3. RESULTS AND DISCUSSION

The X-ray diffraction pattern of NiCuZn ferrite (MH 1) powder was shown in Fig. 1, suspension with pH ≈ 9.5 were prepared by the M-H synthesis and held at 160°C for 30 minutes. For the optimization of the synthesis temperature initially the suspension with pH ≈ 9.5 was subjected to several temperatures for 30 minutes starting from 120°C. The powders precipitated at room temperature before the M-H treatment was denoted as the precursor. In the reaction conditions synthesized from 120°C to 160ºC for 30 minutes only.

Figs.1 shows the X-ray diffraction pattern for the nano-powders of MH 2 to MH 5 respectively. It is clear from the figures that single-phase spinel structure is seen in all the cases. The broad diffraction peaks observed in XRD pattern indicates the small particle size nature. The intensity, I311 of the 311-reflection peak for the spinel ferrites prepared by the M-H method was compared at different reaction temperatures and holding times. The 311-reflection peak in the present ferrite (NiCuZn ferrite) is the major existing peak at 2θ = 35º. The average particle size of the synthesized powders was estimated from the X-ray peak broadening. Scherer equation was employed on the diffraction lines (2 2 0), (3 1 1), (4 0 0), (5 1 1)/(3 3 3) and (4 4 0) to find out the average crystallite size. The calculated particle sizes for the present powders are in between 50-20 nm.

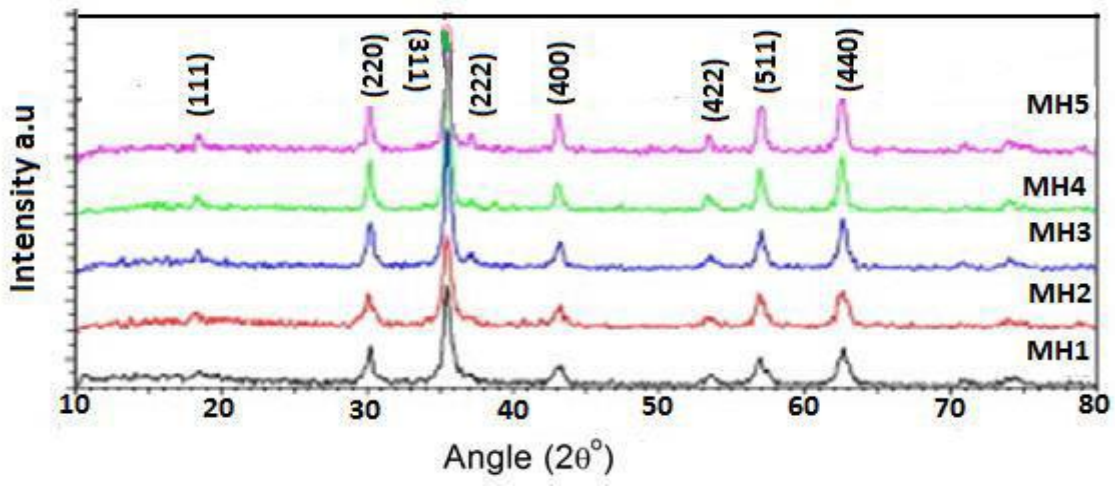

Fig. 1 X-ray diffraction pattern for the nano-powders of NiCuZn ferrites

Conventional technique requires relatively larger time. This places serous limitation on the ceramic method. Microwave sintering method overcomes this limitation of the ceramic method. As sintering temperature plays an important role in the microwave sintering processes of the ferrites, this temperature was selected after conducting a study of effect of sintering temperature on the densification characteristics for NiCuZn ferrites. The samples were sintered at 600,650, 700,750, 800,850 900,950, and 1000ºC for 45 min. Fig.2 gives the results of such an investigation for the $Ni_{0.5-x}Cu_xZn_{0.5}Fe_2O_4$ ferrites (where x= 0, 4,6,8 and 12 mol%). It can be seen from the figure, when the sintering temperature was 800ºC, the ferrite starts to shrink at higher temperature.

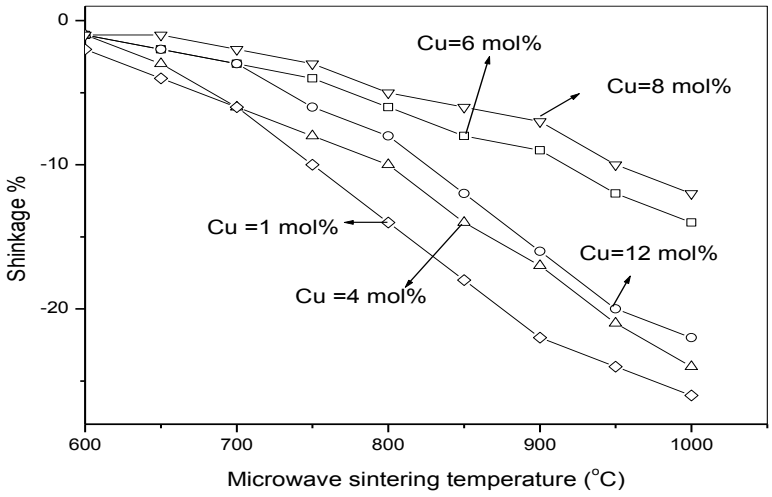

Fig, 2. Shrinkage effect in NiCuZn ferrites

This result is due to hematite component in the ferrite powder and suggests that the firing at a temperature below 700ºC is difficult. The densification curve shifted towards low temperature side with increasing sintering temperature. However, the curve shifted towards the high temperature side for the sintering temperatures more than 900ºC. Thus, for obtaining uniform spinel phase, the sintering temperature should be in between 850ºC- 900ºC is required. Therefore, in the present investigation, the samples were sintered at 900ºC/30 min by using microwave sintering method..

The X–ray diffraction patterns (XRD) of all the ferrites sintered using microwave sintering method have been obtained by using Cu-k_α radiation. Fig. 3 show the X-ray diffraction patterns for all the microwave sintered NiCuZn ferrites. All these ferrites were sintered at a temperature of 900°C/30 min respectively. It can be seen from the figurethat the XRD patterns show that all samples have spinel phase, indicating the absence of any other impurity phase. The line widths observed in the XRD pattern are narrower than that of the line widths of the corresponding nanocrystalline powders. The Scherer's equation is used to estimate the particle size of samples and results are presented in Table 1.

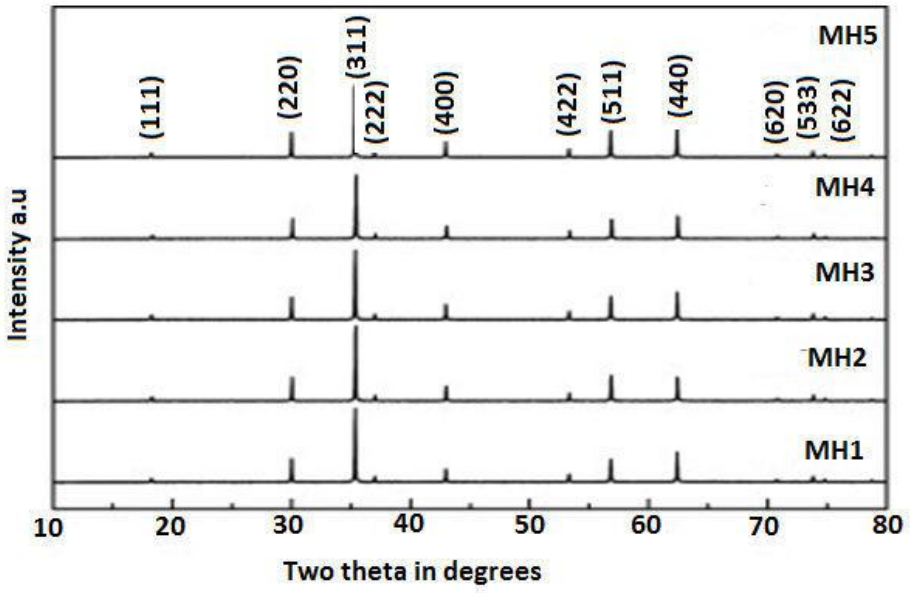

Fig. 3. XRD patterns for microwave sintered NiCuZn ferrrites

The grain size (Dm) of the sintered ferrites has been estimated with the help of XRD patterns using Scherrer's equation:

$$Dm=K\lambda/\beta Cos\theta \quad \ldots.1$$

where K is a constant, β is the full width half maxima and λ is the wavelength of X-rays used and θ is the diffraction angle. The obtained results are presented in the Table1. It can be observed from the table that the grain size of nano-crystalline powders increased with an increase of copper concentration. The grain of these microwave sintered samples were compared with the conventionally sintered samples in Fig.3.It can be observed from the figure that the microwave sintering of the samples resulted a fine grains than that of conventionally sintered samples. Similar behavior was observed with the sintering of other ferrites in our lab [13].

Using the X- ray diffraction patterns, the lattice constant (a) is calculated. For a given set of planes (h k l), the spacing 'd' is given by

dhkl = nl / 2sinq ---------- (2)

Where n = order of reflection, l = wave length of radiation and q = glancing angle of incident X-ray beam. The values of 'd' for the mixed ferrites are calculated using the equation (3.1). Using the values of 'd', the lattice constant (a) for the ferrite is obtained using the following equation

a = d / (h2+k2+ l2)1/2 ---------- (3)

using the equation (3.2) the lattice constants for all the ferrites under investigation has been calculated. From the XRD patterns of the value of lattice parameter for the microwave sintered ferrites are presented in Table 1. It can be seen from the table that lattice parameters for these nanocrstalline ferrites increases with an increase of Cu^{+2} ion concentration. Since Cu^{+2} ions have larger ionic radius (0.87 A^o) than those of Ni^{+2} ions (0.83 A^o), a partial replacement of latter by the former causes the expansion in unit cell dimensions, thereby increasing the lattice parameter.

Table 1: Preparation data for nanocrystalline NiCuZn ferrites

Sample	Crystallize size nm	Grain size (nm)	Lattice constant (Å)	Bulk density P_{bulk} (g/cm^3)	$P_{x\text{-}ray}$ (g/cm^3)	Porosity (%)
MH1	72	76	8.373	4.98	5.37	7
MH2	78	80	8.390	5.07	5.36	6
MH3	85	90	8.393	5.09	5.36	5
MH4	63	70	8.422	5.12	5.28	3
MH5	90	95	8.436	5.00	5.26	5

The bulk density (r) of all the prepared ferrites has been measured accurately by the Archimedes principle. The bulk density of the sample is given by

ρbulk = Mair/ (Mair - Mwater) ---------- (4)

where Mair is mass of the sample in air and Mwater is mass of the sample in water.

This method gives the density values with an accuracy of ± 0.01 gm/cc. The bulk densities for all the presently investigating ferrites are obtained using equation (4) and results are presented in Table 1 for microwave sintered samples.

X-ray densities have been determined using the value of lattice constant (a). The X-ray density (rx-ray) for the ferrite samples is obtained using the relation:

ρx-ray = 8M / Na3 ---------- (5)

Where M = Molecular weight of the ferrite sample
N = Avogadro number
8 = is the number of molecules in the unit cell of spinel lattice
a = Lattice constant

The rx-ray values for the conventionally sintered ferrites were calculated and results were presented in Table 1.

The porosity of the samples is given as:

Percentage porosity (P%) = [1-Bulk density/X-ray density] x 100 ---------- (6)

Using the equation 6 the values of porosity were obtained for all the microwave sintered ferrites under investigation and the values of porosity vary from 3% to 7%.

From table it is also evident for an influence of Cu^{+2} ion concentration on the densification characteristics of the NiZn ferrites. The influence of Cu^{+2} ion concentration on the densification of the NiZn ferrite for different sintering temperatures is presented in Table1. It can be observed from the table that when the Cu^{+2} content increased from 1 mol% to 8mol% the shrinkage or densification curve shifted towards the low temperature side. The densification characteristics are clearly increased with increasing of Cu^{+2} content, the densification temperature of the sample decreases. Thus, the high-density samples were obtained at relatively low sintering temperature (900˚C) by an addition of 8 mol% of Cu^{+2}. For the higher additions of the Cu^{+2}, the density was found to decrease. In general, at higher sintering temperatures a decrease in density was observed. The decreasing has been attributed to increased intragranular porosity resulting from discontinuous grain growth as observed by Burke et al. [14].

The values of lattice parameters are found to increase with increasing Cu^{+2} ion content from 8.373 °A for 1 mol% to 8.437 °A for 12 mol%. This increase is expected in view of the fact that the ionic radius of 0.87 °A for a Cu ion is smaller than that of 0.83 °A for Ni^{+2} ions. It is well known that in NiCuZn ferrites [15] Ni^{+2} ions prefer octahedral sites (B-sites) and Zn^{+2} ions prefer tetrahedral sites (A-sites), also Cu^{+2} ions prefer octahedral sites (B-sites). The increase of the lattice volume usually increases the diffusion path and which in turn increases the rate of cation interdiffussion in the solid solution [16]. But, during the sintering the grain boundary diffusion may play an important role in the grain growth [14]. Thus, the sintering of NiCuZn ferrite may be dominated by the two diffusion mechanisms. Since Cu^{+2} ions have larger ionic radius than those of Ni^{+2} ions, a partial replacement of latter by the former causes the expansion in unit cell dimensions, thereby increasing the lattice parameter.

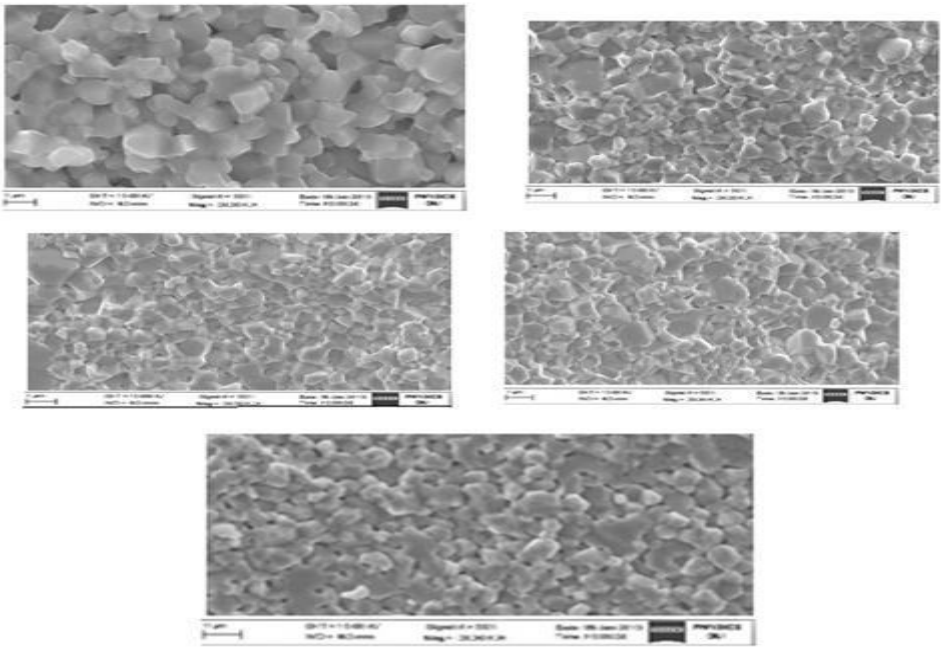

Fig. 4. SEM pictures for microwave sintered NiCuZn ferrites

Fig.4represents the SEM pictures for the microwave sintered samples of the NiCuZn ferrites. It can be seen from the figures that the sintered powders are spherical in shape and the particle size have been estimated from the TEM pictures for all the samples and presented in the Table 1. It can also be observed from the figures that the surface of the sample shows voids and pores formed by the escaping gases during the microwave reaction. This type of porous network is typical of microwave sintered powders. These porous powders are highly friable which facilitate easy grinding to obtain finer particles.

In the Microwave sintering, the local temperature differences at pores and interfaces in the earlier stage of sintering are considered to be the origin of the microwave effect. The microwave radiation effect on grain growth is expected to be smaller than the effect on densification in the case of densified sample as these interfaces disappear in the later stage of sintering. As a consequence, enhanced grain growth is not observed with isothermal microwave sintering. Due to this reason microwave sintered samples possesses small and uniform grain structure.

4. CONCLUSIONS:

A series of NiCuZn ferrites were prepared using microwave hydrothermal method. The powders were sintered at were sintered at 850˚C/30 min. The prepared samples were characterized using X-rays. Grain sizes were calculated with the Scherer formula and a fine grain microstructure was expected. With increasing Cu^{+2} content, the density, electrical resistivity increased upto 8 mol% and then decreases on higher addition. All the properties were compared with the conventionally sintered samples. From the enhancement of all the properties it can be concluded that the microwave sintering is advantageous than the conventional sintering.

REFERENCES:

1. Nakamura, T.J. Magn. Magn.Mater.**1997**,*168*, 285-291.
2. W.C.Kim,S.J.Kim, S.W.Lee and C.S.Kim , J. Magn. Magn.Mater .Vol226- 230, **2001,**pages 1418-1420.
3. Z.Yue, J.Zhou, X.Wang,Z.Gui ,L.Li, J. Mat. Sci. Letters. **2001**,*20*, 1327-1329.
4. K.Y.Kim, W.S.Kim, Y.D.Ju, and H.J.Jung, J.Mat.Sci. vol 27 **1992** 4741-4745.
5. Fujimoto.M., J.Am. Ceram. Soc.**1994**, *77*, 2873-2878.

6. Murthy, S. R. , J. Mat. Sci. Letters. **2002**,*21*,657-660.
7. Z.Y.Hsu, W.S.Ko, H.D.Shen, C.J.Chen , IEEE Trans.on Mag. 30 **1994** 4875-4877.
8. Wang, S.F.; Wang, Y.R.; Yang, T.C.K.; Chen, C.F.; Lu, C.A.; Huang, C.Y. , J. Magn. Magn. Mater. **2000**, *220*, 129-138.
9. Komarneni, S.; Roy, R.; Li, Q.H. ,Mater.Res.Bull. **1992**, *27*,1393-1405.
10. Komarneni ,S.; Li, Q-H.; Stefansson , K.; Roy, R. ,J. Mater. Res.**1993**, *8* ,3176-3183.
11. 11.Komarneni,S.; Roy.R.; Li,Q.H., J. Mater. Res. **1996**,*11*, 1866-1869.
12. K.H.Felgner,T.Muller,H.T.Langhammer and H.P.Abicht, Materials Letters,**2004** 58 1943-1947.
13. A.Bhaskar, B.Rajini Kanth and S.R.Murthy ,J.Mag.Mag.Mater.,**2004** 283 109-116.
14. J. E. Burke, J. Amer. Ceram. Soc. **40** 80 (1957).
15. J. Smit and H. P .J. Wijn, Ferrites Pub. Phillips Tech. Library The Netherlands,150 (1959).
16. R. L. Coble and T. K. Guptha, “Sintering and Related Phenomena” edited by Kuczynski., (1967).

Second National Conference on
RECENT ADVANCES IN APPLIED NANO MATERIALS
February 16-17, 2018 at Department of Physics, University College of Science, Saifabad, Osmania University, Hyderabad, Telangana State, India.

Image acquisition techniques in edge detection – Performance Analysis

M.Parimala,
Associate Professor, Tirumala Engineering college, Bogaram(v), Keesara(m) Medichal
Mailid:pari.parillu@gmail.com,avinpari1224@gmail.com

Abstract: *Image Acquisition is the first stage of any vision systems that refers to the collection of data required to form an image. This Research evaluates three image acquisition methods such as Traditional Monocular vision, RTI (Reflectance Transformation Imaging) and Proposed shadow Stereopsis. These acquired images are then applied into edge detection process for comparison. Analyses are performed in terms of computation time and various performance measures such as Hamming distance, Peak Signal to Noise Ratio (PSNR) and Mean Square Error (MSE). Comparisons with the best available results are given in order to illustrate the best possible technique that can be used as powerful image acquisition method. This research work helps us for improving the perception of details, features and overall shape characteristics from images which are further useful in the study of ancient archaeological stone writings*

Key Words: *Canny edge detection technique, Edge detection, Prewitt edge detection technique*

1. INTRODUCTION

Image acquisition in image processing can be defined as the action of retrieving an image from the source. Performing image acquisition in image processing is always the first step in the workflow sequence. The image that is acquired is completely unprocessed. This unprocessed image is then subjected to edge detection.

Edge detection is the process of identifying and locating sharp discontinuities in an image. It have been used by object recognition, target tracking, object detection etc. Segmentation partition the image into a set of disjoint regions that are uniform and meaningful with respect to some characteristics to enable easy image analysis. Image processing is used in many applications like video surveillance, traffic management and medical imaging. Edge detection is the process of locating an edge of an image. Edges can be classified based upon their intensity profiles like step edge, ramp edge, ridge edge, roof edge. Prewitt, Robert, Sobel and Canny are edge detection algorithms. In edge detection, we used two types of operators namely gradient based edge detection and laplacian based edge detection. The objective of edge detection is to discover the information about the shapes and the reflectance or transmittance in an image and every detector is used to avoid false edges and detected edges should closest to reference edges. Edges can be classified based upon their intensity profiles.

IMAGE ACQUISITION APPROACH

Traditional Monocular Vision: In traditional monocular vision system, localization algorithm is realized by image space transformation, which leads to a trivial calculation process and a complex camera calibration method.
Reflectance Transformation Imaging: The generation of the RTI image requires a set of photos acquired from the same point of view, where in each photo the object is illuminated by a light source from a different direction.
Proposed shadow Stereopsis: Stereopsis is a term that is most often used to refer to the perception of depth and 3-dimensional structure obtained on the basis of visual information deriving from two eyes by individuals with normally developed binocular vision. Calculations based on shadow in the image is performed.

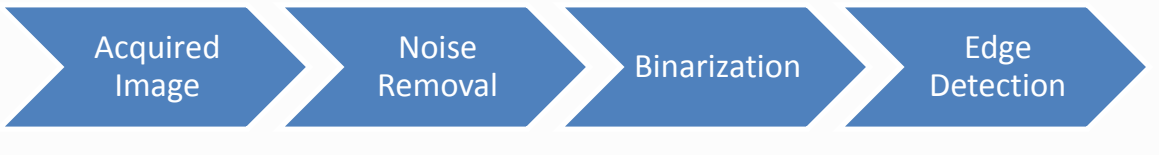

STEPS IN EDGE DETECTION

Edge detection can be done in four steps smoothing, enhancement, detection and localization.

1. Image smoothing: - This step involves filtering the image for noise reduction and improving the performance of edge detector.
2. Enhancement: - This step related with improving the quality of the digital image. We use filter to enhance the quality of the edges in the image.
3. Detection: - Extracting all edge points and determine which edge pixels should be discarded as noise.
4. Localization: - This step used for determine the exact location of an edge (sub- pixel resolution might be required for some applications. It estimate the location of an edge to better than the spacing between pixels).

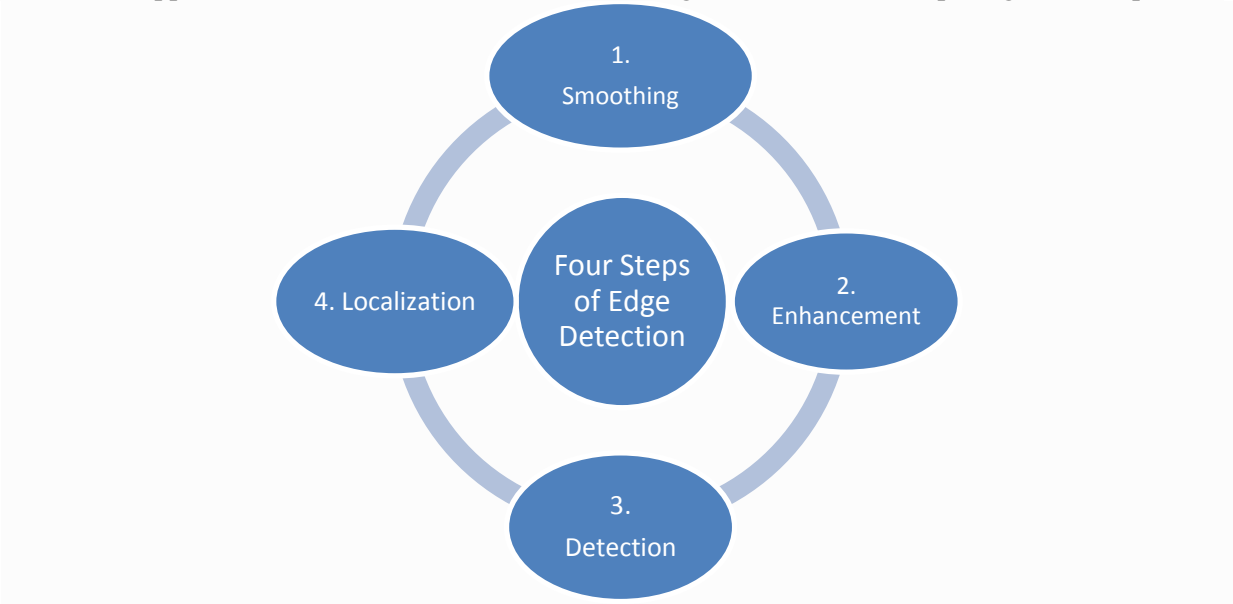

EDGE DETECTION TECHNIQUES

The edge detection algorithms can be generally classified based on the behavioural study of edges with respect to the operators. Different edge-detection approaches can be broadly classified under classical or gradient based edge detectors (first derivative), Zero crossing (second derivative) and optimal edge-detector.

2. EXPERIMENTAL

2.1 EDGE-DETECTION APPROACHES

Edge detection filters out ineffective data, noise and frequencies while preserving the important structural properties in an image.

There are many ways to perform edge detection. However, the majority of different methods may be grouped into two categories namely Gradient and Laplacian.

1. Gradient: The gradient method detects the edges by looking for the maximum and minimum in the first derivative of the image.
2. Laplacian: The laplacian method searches for zero crossings in the second derivative of the image to find edges. An edge has the 1D shape of a ramp and calculating the derivative of the image can highlight its location.

3. RESULTS AND DISCUSSION

3.1 EDGE-DETECTION METHODOLOGIES

Prewitt Edge Detection: The Prewitt edge detector is one of the classical operator used in image processing tools. The prewitt operator have different kernels, where constant c=1. It is the way to estimate the magnitude and orientation of an edge. The prewitt operator is limited to 8 possible orientations.

Canny Edge Detection: It is one of the edge detection method to find edges from the input image without affecting the features of the edges. The canny edge detector first smoothens the image to eliminate noise. Then it finds the image gradient to highlight regions with high spatial derivatives. After that it perform tracking along these regions and suppresses any pixel that is not at the maximum.

4. CONCLUSITON

Edge Detections of images of ancient archaeological stone writings and carvings can be very effective in analysing and studying our cultural heritage. Image Acquisitions needs to be tested along with different edge detection techniques for they performance and accuracy. Detection technique which provides best results in an

intelligent way of detecting edges in which it maintains both precision and image identity at the same time, with and without considering threshold is apt one.

.

REFERENCES:

1. Canny J (1986) A computational approach to edge detection. IEEE Trans Pattern Anal Mach Intell PAMI-8(6):679–698.
2. Bartesaghi, A., Sapiro, G., Malzbender, T., and Gelb, D. 2005. Three-Dimensional Shape Rendering from Multiple Images. Graphical Models, Vol. 67, No. 4 (July).
3. Earl, G.P., Beale, G., Happa, J., Williams, M., Turley, G., Martinez, K., Chalmers, A. A Repainted Amazon. In Proceedings of the 2009 EVA London Conference. Hampton Hill, UK, EVA Conferences International. 2009.
4. Hel-Or, Y., Malzbender, T. and Gelb, D. 2003. Synthesis and Rendering of 3D Textures. In proceedings of Texture 2003 - 3rd International Workshop on Texture Analysis and Synthesis, Nice, France · October 17, 2003.
5. Malzbender, T., Gelb, D., Wolters, H., Zuckerman, B., 2000. Enhancement of Shape Perception by Surface Reflectance Transformation. Tech. Rep. HPL- 2000-38R1, Hewlett-Packard Laboratories, Palo Alto, California, 2000.
6. P. Rakshit, D. Bhaumik and K Bhowmik, "A Comparative Assessment of the Performances of Different Edge Detection Operator using Harris Corner Detection Method", International Journal of Computer Applications (0975 – 8887) Volume 59– No.19, December 2012.
7. J. F. Canny. "A computational approach to edge detection". IEEE Trans. Pattern Anal. Machine Intell., vol. PAMI-8, no. 6, pp. 679-697, 1986.
8. Raman Maini & Dr. Himanshu Aggarwal, "Study and Comparison of Various Image Edge Detection Techniques". International Journal of Image Processing (IJIP), Vol. 3, Issue 1, August 2010.
9. M. Tabb and N. Ahuja, "Multiscale Image Segmentation by Integrated Edge and Region Detection", IEEE Transactions on Image Processing, Vol. 6, No. 5, 642 – 655, May 1997.

Second National Conference on
RECENT ADVANCES IN APPLIED NANO MATERIALS
February 16-17, 2018 at Department of Physics, University College of Science, Saifabad, Osmania University, Hyderabad, Telangana State, India.

Performance Analysis of data Extraction with comparative study of Hive Partitioning and Bucketing

M.Parimala,
Associate Professor, Tirumala Engineering college, Bogaram(v), Keesara(m) Medichal
Email - pari.parillu@gmail.com, avinpari1224@gmail.com

Abstract: *On the basis of the Enterprise/Organization requirement for hadoop/big-data the performance considerations are the pyramids tip. Our research leads on how to overcome the challenges on attaining as much performance optimization we can have for extracting huge data in less time. Here we discuss and compare about the Hive Partitioning and Hive Bucketing we show the comparative study of show data is extracted using Bucketing method where it removes the redundancy of data. Here the main objective is to attain maximum performance while extracting the data.The Aim and Objectives is Optimized Hive Tables, Enables more Efficient Queries, Optimized access to tables to data, Evenly distribute the data.*

Keyword: *Hadoop, Hive, Partitioning, Bucketing*

1. INTRODUCTION:

Map Reduce - Partitioner

A partitioner works like a condition in processing an input dataset. The partition phase takes place after the Map phase and before the Reduce phase.The number of partitioners is equal to the number of reducers. That means a partitioner will divide the data according to the number of reducers. Therefore, the data passed from a single partitioner is processed by a single Reducer.

Partitioner

A partitioner partitions the key-value pairs of intermediate Map-outputs. It partitions the data using a user-defined condition, which works like a hash function. The total number of partitions is same as the number of Reducer tasks for the job. Let us take an example to understand how the partitioner works.

Map Reduce Partitioner Implementation

For the sake of convenience, let us assume we have a small table called Employee with the following data. We will use this sample data as our input dataset to demonstrate how the partitioner works.

Id	Name	Age	Gender	Salary
1201	gopal	45	Male	50,000
1202	manisha	40	Female	50,000
1203	khalil	34	Male	30,000
1204	prasanth	30	Male	30,000
1205	Kiran	20	Male	40,000
1206	laxmi	25	Female	35,000
1207	bhavya	20	Female	15,000
1208	reshma	19	Female	15,000
1209	kranthi	22	Male	22,000
1210	Satish	24	Male	25,000
1211	Krishna	25	Male	25,000
1212	Arshad	28	Male	20,000
1213	lavanya	18	Female	8,000

We have to write an application to process the input dataset to find the highest salaried employee by gender in different age groups (for example, below 20, between 21 to 30, above 30).

Input Data

The above data is saved as input.txt in the "/home/hadoop/hadoopPartitioner" directory and given as input.

1201	**gopal**	**45**	**Male**	**50000**
1202	manisha	40	Female	51000
1203	khaleel	34	Male	30000
1204	prasanth	30	Male	31000
1205	kiran	20	Male	40000
1206	laxmi	25	Female	35000
1207	bhavya	20	Female	15000
1208	reshma	19	Female	14000
1209	kranthi	22	Male	22000
1210	Satish	24	Male	25000
1211	Krishna	25	Male	26000
1212	Arshad	28	Male	20000
1213	lavanya	18	Female	8000

Based on the given input, following is the algorithmic explanation of the program.

Map Tasks

The map task accepts the key-value pairs as input while we have the text data in a text file. The input for this map task is as follows −

Input −The key would be a pattern such as "any special key + filename + line number" (example: key = @input1) and the value would be the data in that line (example: value = 1201 \t gopal \t 45 \t Male \t 50000).

Method − The operation of this map task is as follows −

1. Read the value (record data), which comes as input value from the argument list in a string.
2. Using the split function, separate the gender and store in a string variable.

```
String[] str = value.toString().split("\t", -3);
String gender=str[3];
```

3. Send the gender information and the record data value as output key-value pair from the map task to the partition task.

```
context. write (new Text(gender), new Text(value));
```

4. Repeat all the above steps for all the records in the text file.
5. Output − You will get the gender data and the record data value as key-value pairs.

Partitioner Task

The partitioner task accepts the key-value pairs from the map task as its input. Partition implies dividing the data into segments. According to the given conditional criteria of partitions, the input key-value paired data can be divided into three parts based on the age criteria.

Input − The whole data in a collection of key-value pairs.

key = Gender field value in the record.

value = Whole record data value of that gender.

Method − The process of partition logic runs as follows.

Read the age field value from the input key-value pair.

```
String[] str = value.toString().split("\t");
int age = Integer.parseInt(str[2]);
```

Check the age value with the following conditions.

1. Age less than or equal to 20
2. Age Greater than 20 and Less than or equal to 30.

3. Age Greater than 30.

```
if(age<=20)
{
return0;
}
elseif(age>20&& age<=30)
{
return1%numReduceTasks;
}
else
{
return2%numReduceTasks;
}
```

Output −The whole data of key-value pairs are segmented into three collections of key-value pairs. The Reducer works individually on each collection.

Reduce Tasks

The number of partitioner tasks is equal to the number of reducer tasks. Here we have three partitioner tasks and hence we have three Reducer tasks to be executed.

Input − The Reducer will execute three times with different collection of key-value pairs.

key = gender field value in the record.

value = the whole record data of that gender.

Method −The following logic will be applied on each collection.

1. Read the Salary field value of each record.

```
String [] str = val.toString().split("\t", -3);
```

Note: str[4] have the salary field value.

2. Check the salary with the max variable. If str[4] is the max salary, then assign str[4] to max, otherwise skip the step.

```
if(Integer.parseInt(str[4])>max)
{
max=Integer.parseInt(str[4]);
}
```

3. Repeat Steps 1 and 2 for each key collection (Male & Female are the key collections). After executing these three steps, you will find one max salary from the Male key collection and one max salary from the Female key collection.
4. context.write(new Text(key), new IntWritable(max));

Output −Finally, you will get a set of key-value pair data in three collections of different age groups. It contains the max salary from the Male collection and the max salary from the Female collection in each age group respectively.

After executing the Map, the Partitioner, and the Reduce tasks, the three collections of key-value pair data are stored in three different files as the output.

All the three tasks are treated as MapReduce jobs. The following requirements and specifications of these jobs should be specified in the Configurations –

HIVE is a Data Warehouse infrastructure tool to process the structured data in Hadoop. It is useful in summarizing the data and makes querying &analyzing easy. It provides SQL dialect called HQL(Hive Query Language) for querying the data that is stored in the Hadoop cluster.

Hive Partitioning and Bucketing both are used to performance optimization.

Example of Partitioning and Bucketing:

```
CREATE TABLE newemployee (
employee_idint,
name string,
city string
)
```

PARTITIONED BY (year STRING, month STRING, day STRING)

CLUSTERED BY (employee_id) INTO 64 BUCKETS

Partitioning

Partitioning is nothing but dividing the data into compartments which helps in organizing data in logical fashion. Partitioning data is often used for distributing load horizontally.

With reference to Table creation example above when we insert some data into a partition for 2017-08-16. Hive will then store data in a directory hierarchy, such as:

/user/hive/warehouse/newemployee/y=2017/m=08/d=16

Bucketing

Hive Buckets is a technique of decomposing data or decreasing the data into more manageable parts or equal parts.

So for example as shown above in the newemployee table if we partition by date and bucketing by employee_id. The value of this column will be hashed by a user-defined number into buckets. Records with the same employee_id will always be stored in the same bucket.

2. Hive Partitioning Vs. Bucketing

Partitioning

- Hive Partitioning is dividing the large amount of data into number pieces of folders based on table columns value.
- Partitioning can be done on multiple columns.
- For Partitioning in hive we have to use PARTITIONED BY (COL1,COL2…etc) command while hive table creation.
- Partitioning can be performed on any number of columns in a table by using hive partition concept.
- Partitioning can be performed on Hive Tables like Managed tables or External tables.
- Partitioning works better when the cardinality of the partitioning field is not too high. 'cardinality' means to the number of possible values a field can have. The cardinality of the field relates to the number of directories that could be created on the file system. As an example, if you partition by employee_id and you have millions of employees, you may end up having millions of directories in your file system.
- By using Partitioning we can distribute execution load horizontally.
- Partitioning gives better performance and faster execution of queries in case of partition with low volume of data.
- By partitioning, we can create multiple small partitions based on column values.

Bucketing

- Bucketing AKA Clustering, will result in a fixed number of files, since you specify the number of buckets at the time of table creation. Hive takes the field, calculate a hash and assign a record to that bucket.
- Bucketing can only be applied on one field
- To use bucketing in hive then you should use CLUSTERED BY (Col) command while creating a table in Hive.
- Hive bucketing optimization only on one column only not more than one.
- We can perform Hive bucketing concept on Hive Managed tables or External tables.
- Bucketing works well when the field has high cardinality and data is evenly distributed among buckets. 'cardinality' means to the number of possible values a field can have.
- Hive bucketing divides the data into number of equal parts.
- Bucketing gives better performance and faster execution of queries such as joins with other tables that have exactly the same bucketing
- By using bucketing, we restrict the number of buckets to store the data. This number is defined during table creation scripts.

3. Problem Statement

On the basis of the Enterprise/Organization requirement for hadoop/big-data the performance considerations are the pyramids tip. Our research leads on how to overcome the challenges on attaining as much performance optimization we can have for extracting huge data in less time.

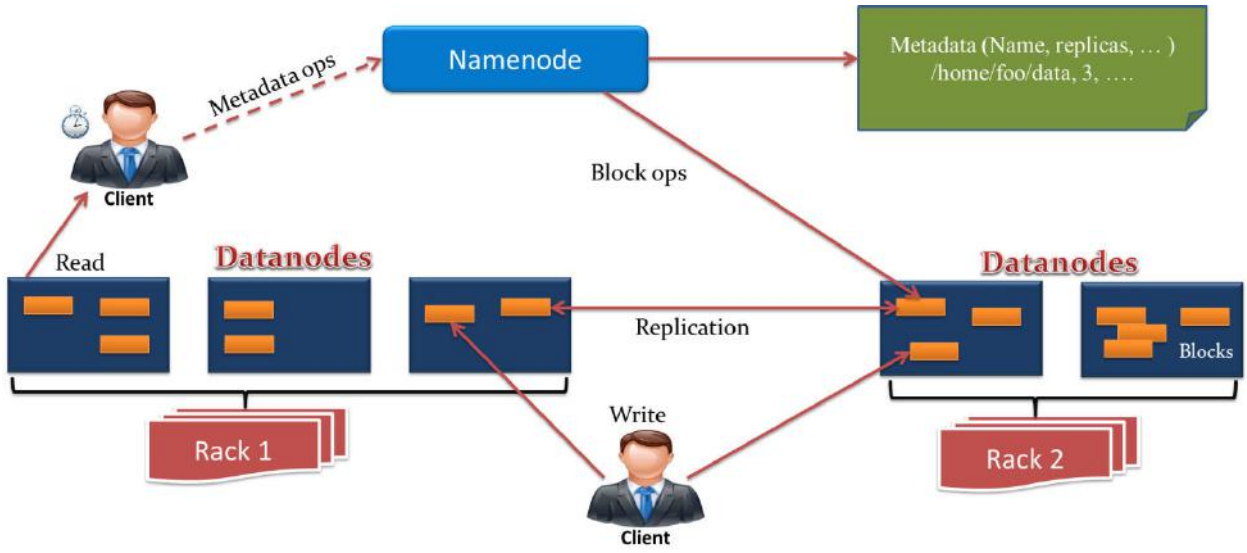

Hadoop Hive bucket is to divide Hive partition into number of equal clusters or buckets. Bucketing is to Organize for table clustering. Hive bucket is reducing the hive partitioned data into more manageable parts.

Let's have the example of Hive bucket.

We have studentsregistration table with registration_date, student_id, course_dtl etc. Hive table will be partitioned on registration_date and student_id as the second-level partition will divide into many small partitions in HDFS.

To overcome this problem, we use Hive bucketing.

Partition by registration_date and bucketing by student_id. The values of this column will be hashed into number of buckets defined by the user. Tuples with the same value of student_id is stored in the same bucket.

```
CREATE TABLE bucketed_table
(
 Col1 integer,
col2 string,
col3 string,
col4 date,
 ...
)
PARTITIONED BY (col4 date)
CLUSTERED BY (col1) INTO user_defined_integer BUCKETS
STORED AS TEXTFILE;
```

One column only should be used to create buckets, no more than one column. Creating Hive buckets on hive tables are hive external tables in on the user requirement and type of SELECT queries on the specific table.

Hadoop Hive Bucketing

Hive bucketing concept is diving Hive partitioned data into further equal number of buckets or clusters. You have to use the CLUSTERED BY (Col) clause with Hive create table command to create buckets.

Difference between Partitioning and Bucketing in hive

1. Hive Partition
2. Advantages with Hive Partition
   2.1 Disadvantages with Hive Partition
3. Hive Bucketing
4. Advantages with Hive Bucketing
   4.1 Disadvantages with Hive Bucketing

Hive Partition

- Hive Partitioning dividing the large amount of data into number pieces of folders based on table columns value.
- Hive Partition is often used for distributing load horizontally, this has performance benefit, and helps in organizing data in a logical fashion.

If you want to use Partition in hive then you should use PARTITIONED BY (COL1,COL2…etc) command while hive table creation.

- We can perform partition on any number of columns in a table by using hive partition concept.
- We can perform Hive Partitioning concept on Hive Tables like Managed tables or External tables
- Partitioning is works better when the cardinality of the partitioning field is not too high .

Supposes if we perform partition on Date column then new partition directories created for every date this very burden to name node metadata.

Partitioning works best when the cardinality of the partitioning field is not too high.Assume that you are storing information of people in entire world spread across 196+ countries spanning around 500 crores of entries. If you want to query people from a particular country (Vatican city), in absence of partitioning, you have to scan all 500 crores of entries even to fetch thousand entries of a country. If you partition the table based on country, you can fine tune querying process by just checking the data for only one country partition. Hive partition creates a separate directory for a column(s) value.

4. Advantages with Hive Partition

- Distribute execution load horizontally
- Faster execution of queries in case of partition with low volume of data. e.g. Get the population from "Vatican city" returns very fast instead of searching entire population of world.
- No need to search entire table columns for a single record.

5. Disadvantages with Hive Partition

1. There is a possibility for creating too many folders in HDFS that is extra burden for Namenode metadata.

Effective for low volume data for a given partition. But some queries like group by on high volume of data still take long time to execute. e.g. Grouping of population of China will take long time compared to grouping of population in Vatican city. Partition is not solving responsiveness problem in case of data skewing towards a particular partition value.

2. So there is no guarantee for query optimization for all the times.

6. Scope of the research

The main scope for the research is to attain the maximum performance for extracting/mining the data from the hadoop/bin-data, on the minimum response time by considering into the usage of data pumping in and out of the hadoop/big-data on the Enterprise/Organization requirements.

As data being stored increases new and latest ideologies & techniques are to be identified which will be a highway for the users who's accessing [read/write] for future or later use.

On the same context huge queues of queries will be flooding, and on the respective query small/medium/large data chunks need to be processed and should be displayed instantly which will be a challenge to the data representatives.

For the above mentioned challenges we propose **Hive Bucketing**

7. Hive Bucketing

- Hive bucketing is responsible for dividing the data into number of equal parts
- If you want to use bucketing in hive then you should use CLUSTERED BY (Col) command while creating a table in Hive
- We can perform Hive bucketing concept on Hive Managed tables or External tables
- We can perform Hive bucketing optimization only on one column only not more than one.
- The value of this column will be hashed by a user-defined number into buckets.
- bucketing works well when the field has high cardinality and data is evenly distributed among buckets

If you want to perform queries on Date or Timestamp or other columns which are having high records fields at that time Hive bucketing concept is perfectible.

- We can assign number of number buckets while creating the table.
- Bucketing also very useful in doing efficient map-side joins etc.

Clustering aka bucketing on the other hand will result with a fixed number of files, since you do specify the number of buckets. What hive will do is to take the field, calculate a hash and assign a record to that bucket.

But what happens if you use let's say 256 buckets and the field you're bucketing on has a low cardinality (for instance, it's a US state, so can be only 50 different values) ? You'll have 50 buckets with data, and 206 buckets with no data.

8. Advantages with Hive Bucketing

1. Due to equal volumes of data in each partition, joins at Map side will be quicker.
2. Faster query response like partitioning
3. Optimized Hive tables and access to the table data

9. Disadvantages with Hive Bucketing

1. You can define number of buckets during table creation but loading of equal volume of data has to be done manually by programmers.

10. CONCLUSION:

This Paper concludes the importance of Hive and Hadoop in Bigdata. Hadoop is Batch oriented system and higher latency due to overhead of Map reduce. Hive is most suited for data ware housing applications, itfast response times are not required and when data is not changing rapidly.

REFERENCES:

1."What is Apache Hadoop," http://hortonworks. com /hadoop/,2011- 2014
2. www.learn4master.com/algorithms/hive-partitioning-vs-bucketing
3.Https://thebytearray.wordpress.com/2016/06/02/hive-performance-optimization/

Second National Conference on
RECENT ADVANCES IN APPLIED NANO MATERIALS
February 16-17, 2018 at Department of Physics, University College of Science, Saifabad, Osmania University, Hyderabad, Telangana State, India.

Thermoelectric behavior of Cr^{3+} ion Substituted Nickel nano ferrites

R.Sridhar[1*], K. Vijaya Kumar [2], K. Rama Krishna[3], D.Ravinder [4]
[1*]Department of BS&H, Vignan Institute of Technology & Science,
Yadadri-Bhuvanagiri-Dist.508284, Telangana State, India.
[2]Department of Physics, JNTUH College of Engineering Sultanpur, Pulkal (M),
Madak-Dist. 502293 Telangana State, India.
[3]Department of Physics, Malla Reddy College of Engineering and Technology, Secunderabad– 500 014,
[4]Department of Physics, Osmania University, Hyderabad-500007, Telangana State, India.
*Corresponding author: +91 9701074722 Email_Id: rapolu31@gmail.com

Abstract: *Nanocrystalline samples of $NiCr_XFe_{2-X}O_4$ (Where X = 0.1, 0.3, 0.5, 0.7, 0.9 and 1.0) were synthesized by Citrate-Gel auto combustion method and sintered at 700^OC for 4 hours. The prepared samples were characterized by X-ray diffraction (XRD) and FT-IR. XRD pattern confirmed cubic spinel structure in single phase and crystallite size was in the range 8 -11nm. The lattice parameter and X-ray density were calculated. FTIR spectra confirm two absorption bands which represent the tetrahedral and octahedral sites. Thermoelectric power was studied from room temperature to well beyond the transition temperature by the differential method. The Seebeck coefficient value illustrates the prepared samples are behave n-type semiconductors at lower temperature and at higher temperature behave as p-type semiconductors. An attempt is made to explain the conduction mechanism in these ferrites.*

Key Words: *Ni-Cr nano ferrites, Citrate-Gel auto combustion method, XRD, FTIR, Thermoelectric power*

1. INTRODUCTION

Nano spinel ferrites illustrate special electric and magnetic properties which are quite different from the bulk ferrite materials. The electrical and magnetic properties of nano ferrites include high electrical resistivity, moderate saturation magnetization and high coercivity, these properties make it suitable for high density recording media, magnetic fluids, sensors and biomedical drug delivery [1].

Ferrites are low mobility semiconductors, the description of the conduction mechanism in semiconductors is demonstrated by thermoelectric power studies and Hall Effect. Analyses of Hall Effect results are make known more straight forwarding specific results. On the other hand, in the case of mobility semiconductors like ferrites, it is sometimes not easy to measure the Hall Effect, in such cases thermoelectric measurements study is the only alternative. The thermo e.m.f measurement gives essential information about the type of conduction in semiconductor, i.e., whether they are n-type or p-type semiconducting nature.

Among the various ferrites, nickel ferrite a typical inverse spinel ferrite has been generally used in electronic devices due to their remarkably high electrical resistivity, mechanical hardness, chemical stability and low cost value [2]. Divalent or trivalent substituted nickel nano ferrite has interested because of its considerable modifies the structural and electrical transport properties, hence they have been used in various fields and many electronic devices such as high density storage devices, batteries [3, 4].

The structural properties and thermoelectric behavior of prepared compositions are effectively influenced by the method of preparation, sintering temperature and with the dopent ions [5]. Among the various chemical preparation techniques citrate gel auto combustion method is a simple process, speeds up the synthesis and offers a significant saving in time, energy consumption over traditional methods.

From the literature study no information is available on thermoelectric behavior of chromium substituted nickel nano ferrites. Hence, to understand the conduction mechanism in mixed Ni-Cr nano ferrites, thermoelectric power as a function of temperature and composition were undertaken. Therefore the author communicating the structural and electrical transport properties of mixed Ni-Cr nano ferrites synthesis by citrate gel auto combustion method.

2. EXPERIMENTAL PROCEDURE

The mixed Ni-Cr nano ferrite system having the compositional formula $NiCr_XFe_{2-X}O_4$ (Where X=0.1, 0.3, 0.5, 0.7, 0.9 and 1.0) were synthesized by citrate-gel auto combustion method. Analytical grade raw materials (Nickel Nitrate ($Ni(No_3)_26H_2O$), Chromium Nitrate ($Cr(NO_3)_23H_2O$), Ferric Nitrate ($Fe(NO_3)_29H_2O$), Citric Acid-Citrate ($C_6H_8O_7H_2O$) and Ammonia (NH_3)) were used to prepare the samples of the Ni-Cr nano ferrite system. The required quantities of metal nitrates are weighed according to the stoichiometry proportion and they were dissolved in minimum amount of distilled water to get clear homogeneous solution. Citric acid is used as a fuel because it has better character ability, the metal nitrate to citric acid ratio was maintained as 1:3 for all the samples and ammonia (NH_3) solution added to obtained nitrate-citrate solution to maintain P^H value at 7. The mixed solution is heated by continuous stirring upto 100°C for 10-12 hours then water is evaporated and viscous gel is formed. By continuous heating a dry gel it generates in internal combustion and forms a powder sample with brown colour. Collect the desired powder sample and it is calcinations at 700^0 C for four hours in muffle furnace. Finally the powder samples are grounded with agate motor to get fine powder ferrite samples.

The structure analysis and phase identification of the sintered samples were performed by X-Ray Diffractometer Bruker D8 advanced system through diffracted monochromatic beam with Cu k_α radiation of wavelength (λ=1.5405Å) in between the Bragg's angles 10° to 80° in the steps of 0.04°/sec. The crystalline size was calculated with using the Debye-Scherrer formula [6].

$$\textbf{The crystallite size } D_{hkl} = \frac{0.91\,\lambda}{\beta\cos\theta} \text{ ------eq 1}$$

Where λ the wavelength of used X-ray beam, β is the full width half Maximum (FWHM)

$$\textbf{lattice parameter } a = d * \sqrt{h^2 + k^2 + l^2} \text{ -------- eq 2}$$

The X-ray density calculated with using the relation [7]

$$X-\textbf{ray density } d_x = \frac{nM}{a^3N}\frac{gr}{cm^3} \text{ -------- eq 3}$$

Where n is the number of molecules in a unit cell of spinel lattice (n=8), M is molecular weight of the sample and N is the Avogadro number (6.022140857×10^{23} mol^{-1})

The absorption spectra of prepared Ni-Cr nano ferrite powders were recorded at room temperature by Fourier Transform Infrared Spectroscopy (Spectrum 100, Perkin Elmer, USA) in the range of 400-4000cm^{-1} with a resolution of 1cm^{-1} using KBr pellet method.

Silver past was applied on either sides of the pellet for having good ohmic contact to measuring the transport properties including thermoelectric power from room temperature to well behind transition temperature.

Differential technique was employed to measure the thermoelectric power (Seebeck coefficient) with the following relation [8].

$$S = \frac{\Delta E}{\Delta T} \text{ -----eq4}$$

Where ΔE is the thermo emf and ΔT is the temperature difference between the two surfaces of the pellet

3. RESULTS AND DISCUSSION

3.1. Structural characterization

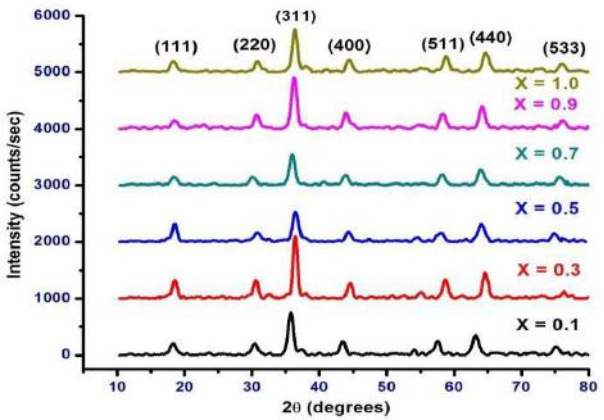

Figure 1: XRD pattern of mixed Ni-Cr nano ferrite system

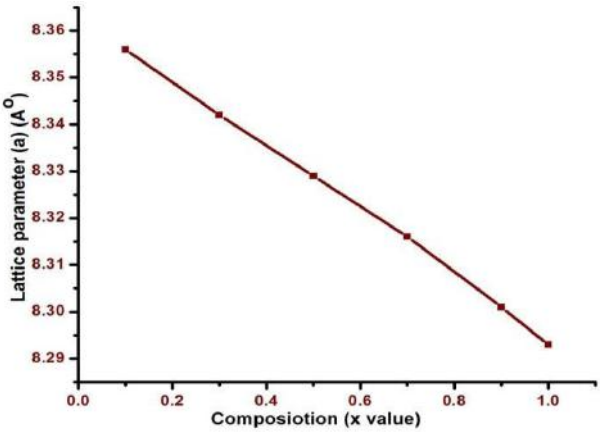

Figure 2 : Variation of lattice parameter with Cr concentration

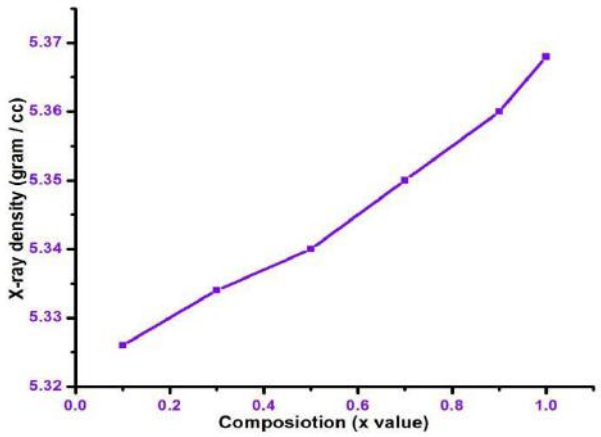

Figure 3: Variation of X-ray density with Cr concentration

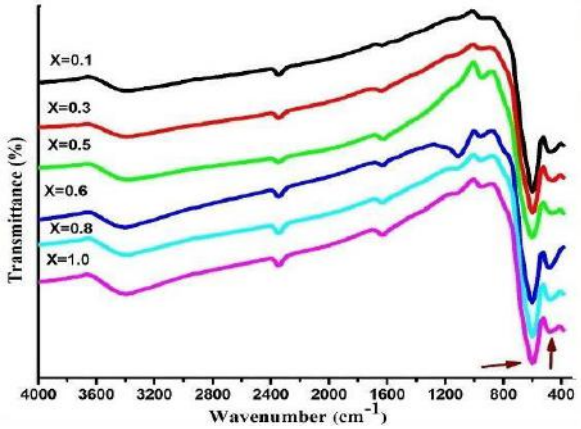

Figure 4: FTIR pattern of Mixed Ni - Cr nano ferrite system

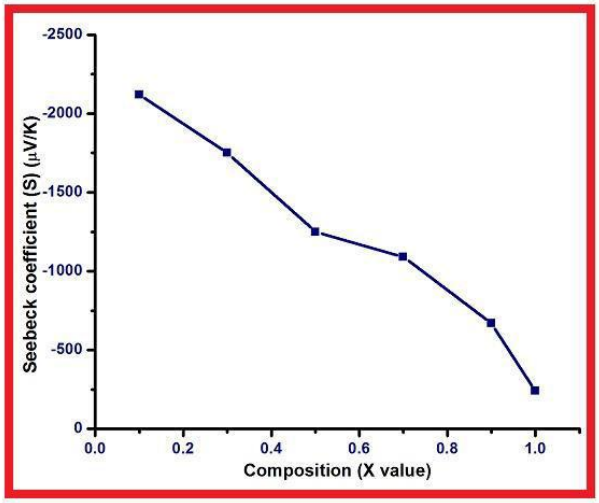

Figuer 5: seebeck coefficient variation with composition

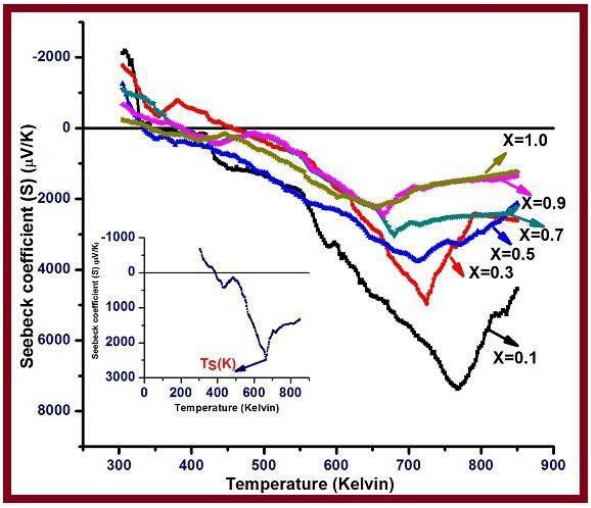

Figure 6: Temperature dependence thermoelectric power

Table – 1: XRD pattern, FTIR pattern analysis and Seebeck coefficient of Ni-Cr nano ferrite system

Sl. No.	Composition	Crystallite size (nm)	lattice parameter (a) (A^o)	X-ray density (gr/cc)	absorption band		Seebeck coefficient (S) (μV/K)
					ν_1 (cm^{-1})	ν_2 (cm^{-2})	
1	$NiCr_{0.1}Fe_{1.9}O_4$	8.96	8.356	5.33	599.96	485.35	-2120
2	$NiCr_{0.3}Fe_{1.7}O_4$	10.36	8.342	5.33	607.03	477.05	-1750
3	$NiCr_{0.5}Fe_{1.5}O_4$	7.95	8.329	5.34	602.45	479.69	-1250
4	$NiCr_{0.7}Fe_{1.3}O_4$	8.55	8.316	5.35	591.43	481.11	-1090
5	$NiCr_{0.9}Fe_{1.1}O_4$	8.84	8.301	5.36	594.86	492.42	-670
6	$NiCrFe_2O_4$	9.26	8.293	5.37	597.13	472.62	-240

Figure 1 shows the X-ray diffraction pattern of mixed Ni-Cr nano ferrite system. It shows the crystalline phases were identified with standard reference data PDF# 862267 for Nickel ferrites ($NiFe_2O_4$) from the international centre for diffraction data (ICDD). It was observed that XRD pattern can be well indexed with peaks corresponding to

cubic spinel structure such as (111), (2 2 0), (3 1 1), (4 0 0), (5 1 1), (4 4 0) and (5 3 3) the strongest reflection comes from (311) plane that indicates spinel phase and all the samples show cubic spinel structure in single phase without showing any other impurity phases [9].

The calculated crystallite size values are reported in **table 1**. From the table the average crystallite size was in the range 8.5-10.5 nm. Best of my knowledge the small size mixed Ni-Cr nano ferrites samples are possible only with the citrate-gel auto combustion method no other method has resulted the such a small size nano ferrites. By this method prepared ferrite samples phase can produce very fast at low temperature but conventional methods need to high temperatures and prolonged heating time [10].

The calculated lattice parameter values are reported in **table 1** as evident in **figure 2.** It shows the lattice parameter decreases with increasing the Cr concentration in Ni nano ferrites, it may be due to the ionic radii difference between Fe^{3+} and Cr^{3+} i.e. the large ionic radii of Fe^{3+} (0.645 Å) is replaced by low ionic radius Cr^{3+} (0.615Å) in octahedral sites [11], that means mixed Ni-Cr nano ferrite system obeys Vegard's law [12]. Decrease in lattice parameter, which may be attributed to shifting on some Fe^{3+} ions form A site to B site for higher composition. A similar behavior of lattice parameter with Cr concentration was observed by several researchers in various ferrite systems [13-14].

Measured X-ray density values are reported in **table 1** as evident in **figure 3**. It shows that the X-ray density increases with increasing the Cr concentration in Ni nano ferrite system, which means it shows the densification of the material. The X-ray density is to dependent on the lattice parameter and molecular weight of the sample, so the Cr^{+3} concentration increase the lattice parameter decreases hence the X-ray density increases. It may be due to greater atomic weight of Fe (55.847 gm/mole) compare with atomic weight of Cr (51.996 gm/mole).

The FTIR spectra of the mixed $NiCr_XFe_{2-X}O_4$ nano ferrite system (Where X=0.1, 0.3, 0.5, 0.7 and 1.0) were recorded in the range of 400 – 4000 cm^{-1} at room temperature shown in the **figure 4**. It shows the two prominent absorption bands ν_1 and ν_2 corresponding to the stretching vibration of the tetrahedral (A-site) and octahedral (B-site) around 600 cm^{-1} and 400 cm^{-1} respectively. These absorption bands represent the spinel ferrites in single phase [15] and the absorption band results are reported in **table 1**. It is clear that the vibrational spectra of ferrites characteristic the high frequency band (ν_1) lies in the range of 591to 607 cm^{-1} corresponds to Fe^{+3}-O^{-2} vibrations in tetrahedral (A site) and low frequency band (ν_2) lies in the range 472 to 492 cm^{-1} corresponds to M^{+2}-O^{-2} vibrations in octahedral sites (B site) [16]. The difference between A site and B site is due to the change in bond length of Fe^{+3}-O^{-2} at the octahedral and tetrahedral sites [17]. The bands around 3400cm^{-1}, 2400 cm^{-1} and 1600cm^{-1} are the contribution of the stretching vibration of free and absorbed water, indicated the removal of the -OH, -CO and -NO groups. Similar trend have been observed by several researchers for the Cr substitution nano ferrite systems [18-19].

3.3. Thermo electric power

Seebeck coefficient of Ni-Cr nano ferrites are measured at room temperature and reported in **table 2**. It observed that the seebeck coefficient decrease from -2120μV/K to -240μV/K as increase of Cr concentration in Ni ferrite as evident in **figure 5.** It explained as motion of charges becomes slow due to resistivity of the material increases. Hence thermo emf developed across the sample was low. So thermo emf is decreases then the seebeck coefficient also decreases. Similar trend was reported by M. Anis-ur- Rehman in the case of Co-Cr [20].

Temperature dependent Seebeck coefficient for all the prepared samples are shown in **figure 6**. It observed that at low temperature the sign of Seebeck coefficient was positive, means hole-type carriers are dominated the thermoelectric transport. Hence they behave like p-type semiconductors. By increasing the temperature, Seebeck coefficient increases and at higher temperature the sign of Seebeck coefficient attained negative, means electron-type carriers are dominated the thermoelectric transport. Hence they behave like n-type semiconductors [21, 22]. The conduction mechanism in the investigated ferrite system is an electron exchange mechanism between Fe^{2+} and Fe^{3+} [23].

$$Fe^{3+} + e^{-} \Leftrightarrow Fe^{2+}$$

4. CONCLUSION

Citrate Gel Auto Combustion technique is a convenient for obtaining a homogeneous nano sized mixed ferrites. X-ray diffraction pattern confirms the formation of cubic spinel structure in single phase with crystalline size in the range of 8 to 11 nm. The Lattice parameter increase with increases Cr concentration, which indicate that the mixed Ni-Cr nano ferrite system obey the Vegard's law. The FTIR spectra illustrates the two absorption bands, which are corresponds the tetrahedral and octahedral sites. The Seebeck coefficient variation wih composition indicating semiconducting nature of the prepared ferrite samples. Temperature dependent Seebeck coefficient is observed that at low temperature they behave like p-type semiconductors and at higher temperature they behave like n-type semiconductors

5. ACKNOWLEDGEMENTS

The authors are grateful to Head, Department of Physics, Osmania University, Hyderabad for provided the facility to synthesis of samples. One of the authors (KVK) is grateful to Dr. K. Eshwara Prasad, Principal JNTUH

College of Engineering, Sultanpur, Pulkal (M), Madak and the author (RS) is grateful to Dr. G. Durga Sukumar Principal, Vignan Institute of Technology & Science, Yadadri-Bhuvanagiri (Nalgonda).

REFERENCES

1. Gopalan V, Joy PA, Al-Omari IA, Kumar DS, Yoshida Y, Anantharaman MR. "Structural, magnetic and Electrical properties of sol-gel derived nanosized cobalt ferrite", J. Alloys compd, 485 (2009) 711-717.
2. K. Ishino and Y. Narumiya, "Development of Magnetic Ferrites: Control and Application of Losses," American Ceramic Society Bulletin, 66 (1987) 1469-1474.
3. O. Silva, P.C. Morais, J. Magn. Magn. Mater. 289 (2005) 136.
4. M. Yokoyama, E. Ohta, T. Sato, T. Sato, "Magnetic properties of ultraÞne particles and bulk material of cadmium ferrite", J. Magn. Magn. Mater. 183 (1998) 173.
5. Goldman A, Modern Ferrite Technology, New York: Van Nostrand Reinhold; 1990.
6. Cullity B D, Elements of X-ray diffraction (addition Wesley, Reading, Mass), (1959) 132.
7. R. C. Kumbale. P. A. Shaikh, S. S. Kamble and Y. D. Kolekar, "Effect of Cobalt Substitution on Structural, Magnetic and Electric Properties of Nickel Ferrite"
8. Raghasudha M, Ravinder D, Veerasomaiah P. "Thermoelectric power studies of Co-Cr nano ferrites" J Alloys Compd 604 (2014) 276.
9. Devan, R.S., Kolekar, Y.D., Chougule, B.K.: J. Phys., Condens. Matter 18, 9809–9821, 2006
10. R. G. Gupta and R. G. Mendiratta, *Journal of Applied Physics*, Vol. 48, No. 2, 1977, pp. 845-848.
11. R.D. Shannon, Acta Crystallogr. Sect. A 32, 1976, 751.
12. L. Vergard, *Zeitschrift für Physik A*: *Hadrons and Nuclei*, Vol. 5, No. 1, 1921, pp. 17-26.
13. Sonal Singhal, Journal of Solid State Chemistry 180, 2007, 296–300
14. R. Arulmurugan, B. Jeyadevan, G. Vaidyanathan and S. Sendhilnathan, *J. Magn. Magn. Mater.* 288, 2005, 470.
15. R.M. Mohamed, M.M. Rashad, F.A. Haraz, W. Sigmund, *J. Magn. Magn. Mater.* 322, 2010, 2058.
16. R. D. Waldron, Phys. Rev. 99, 1955, 1727.
17. A.K. Ghatage, S.C. Choudhari, S.A. Patil, *J. Mater. Sci. Lett.* 15, 1548, 1996.
18. S.M. Patange, S.E. Shirsath, B.G. Toksha, S.S. Jadhav, S.J. Shukla, K.M. Jadhav, *Appl. Phys. A Mater. Sci. Process*. A95, 2009, 429.
19. A.S. Elkady, S.I. Hussein, M.M. Rashad, *J. Magn. Magn. Mater*. 385, 2015, 70.
20. M.Anis-ur-Rehman, A.Abdullah, Mariam Ansari, World Academy of Science, Engineering and Technology, 5, 4, (2011)
21. Y.P. Irkin, E.A.Turor, Sovt. Phys. JEPT 33 (1957) 673
22. Walz, F. "The Verwey transition - a topical review", J. Phys., Condens. Matter., 14 (2002) 285–340 .
23. L. J. Berchmans, R. K. Selvan, P. N. S. Kumar and C. O. Augustin, "Structural and Electrical Properties of $Ni_{1-X}Mg_XFe_2O_4$ Synthesized by Citrate Gel Process", Journal of Magnetism and Magnetic Materials, 279 (2004) 103-110.